NASA TECHNICAL NOTE

NASA TN D-6238

c. 1

NASA TN D-6238

A WIND-TUNNEL INVESTIGATION OF STATIC LONGITUDINAL AND LATERAL CHARACTERISTICS OF A FULL-SCALE MOCKUP OF A LIGHT TWIN-ENGINE AIRPLANE

by Marvin P. Fink, James P. Shivers,
and Charles C. Smith, Jr.

Langley Research Center
Hampton, Va. 23365

NATIONAL AERONAUTICS AND SPACE ADMINISTRATION • WASHINGTON, D. C. • APRIL 1971

1. Report No.
NASA TN D-6238

2. Government Accession No.

3. Recipient's Catalog No.

4. Title and Subtitle
A WIND-TUNNEL INVESTIGATION OF STATIC LONGITUDINAL AND LATERAL CHARACTERISTICS OF A FULL-SCALE MOCKUP OF A LIGHT TWIN-ENGINE AIRPLANE

5. Report Date
April 1971

6. Performing Organization Code

7. Author(s)
Marvin P. Fink, James P. Shivers, and Charles C. Smith, Jr.

8. Performing Organization Report No.
L-7607

10. Work Unit No.
736-01-10-01

9. Performing Organization Name and Address
NASA Langley Research Center
Hampton, Va. 23365

11. Contract or Grant No.

13. Type of Report and Period Covered
Technical Note

12. Sponsoring Agency Name and Address
National Aeronautics and Space Administration
Washington, D.C. 20546

14. Sponsoring Agency Code

15. Supplementary Notes

16. Abstract

The model was a full-scale mockup of a light, twin-engine, low-wing monoplane. Tests were made over an angle-of-attack range of -4° to 24° and over a sideslip range of $\pm 8^{\circ}$ at thrust coefficients of 0, 0.19, and 0.28. Control effectiveness and hinge moments were determined for a full range of deflections on the aileron, elevator, and rudder. Downwash surveys were made in the region of the horizontal tail. Limited tests were made with simulated ice on the wing and horizontal tail. The tests were made at a Reynolds number of 2.94×10^{6}.

17. Key Words (Suggested by Author(s))
Control hinge moments
Light single-engine airplane
Stability and control
Tail downwash

18. Distribution Statement
Unclassified – Unlimited

19. Security Classif. (of this report)
Unclassified

20. Security Classif. (of this page)
Unclassified

21. No. of Pages
268

22. Price*
$3.00

---

*For sale by the National Technical Information Service, Springfield, Virginia 22151

A WIND-TUNNEL INVESTIGATION OF STATIC LONGITUDINAL AND LATERAL CHARACTERISTICS OF A FULL-SCALE MOCKUP OF A LIGHT TWIN-ENGINE AIRPLANE

By Marvin P. Fink, James P. Shivers,
and Charles C. Smith, Jr.
Langley Research Center

SUMMARY

An investigation has been conducted in the Langley full-scale tunnel to determine the static longitudinal and lateral stability and control characteristics of a full-scale mockup of a light twin-engine airplane. Hinge moments were measured on all control surfaces during the investigation, downwash surveys were made at the horizontal tail, and several tests were made to determine the effect of simulated ice on the longitudinal characteristics. The investigation was made over an angle-of-attack range of -4° to 24° at various angles of sideslip between ±8 for various power and flap settings. The thrust coefficients were 0, 0.19, and 0.28, which correspond to either a low-power or a high-speed condition (where the thrust coefficient approaches zero), to a climb condition, and to a take-off or wave-off condition, respectively, for an airplane having an installed power of 260 hp (194 kW) per engine.

The investigation showed that, in general, the model had stick-fixed longitudinal stability through the stall, but a stick-free instability could be encountered at some lift coefficients with an aft center-of-gravity location. The model was directionally stable and had positive effective dihedral for angles of attack up through the stall, although the effective dihedral varied somewhat with angle of attack for different power and flap conditions. Aileron and rudder effectiveness was maintained through the stall and with asymmetric power, the controls were capable of trimming the mockup up to angles of attack through the stall. The model had a fairly symmetrical stall and displayed no tendency for large rolling or yawing moments at the stall.

INTRODUCTION

In recent years the NASA Flight Research Center has been conducting a program to evaluate the flying qualities of a number of general-aviation type aircraft. The results of some of these investigations have been reported in reference 1. As a part of the continuing investigation, one of the airplanes investigated in reference 1, a light twin-engine configuration, was tested in the Langley full-scale tunnel, and the results have been reported in reference 2. In addition, a single-engine version of the airplane of reference 2 was investigated and the results are reported in reference 3. Another single-engine airframe of about the same gross weight as the airplane of reference 3 but with different geometric characteristics and airfoil was tested and reported in reference 4. The present investigation was conducted in the Langley full-scale tunnel to determine the static longitudinal and lateral stability and control characteristics of a mockup of another light twin-engine configuration having geometric characteristics somewhat different from those of the configuration reported in reference 2. Also, a configuration similar to the present model was among those studied by the Flight Research Center and reported in reference 1. The present investigation was made with various power and flap settings over a range of angle of attack from -4° to 24° and over a range of sideslip angles of $\pm 8^{\circ}$. The tests were made at a tunnel speed of about 27 m/sec (90 ft/sec) giving a Reynolds number of about 2.94×10^{6}.

SYMBOLS

Figure 1 shows the stability-axis system used in the presentation of the data and the positive direction of forces, moments, and angles. The data are computed about the moment center shown in figure 2 which is at 25 percent of the mean aerodynamic chord.

Measurements and calculations for this investigation were made in the U.S. Customary Units. They are presented herein in the International System of Units (SI) with the equivalent values given parenthetically in the U.S. Customary Units. Factors relating the two systems of units used in this paper may be found in the appendix.

b	wing span, 11.26 m (36.93 ft)
C_D	drag coefficient, $\frac{\text{Drag}}{qS}$
$C_{h,a}$	aileron hinge-moment coefficient, $\frac{\text{Hinge moment}}{qS_a\bar{c}_a}$
$C_{h,e}$	elevator hinge-moment coefficient, $\frac{\text{Hinge moment}}{qS_e\bar{c}_e}$
$C_{h,r}$	rudder hinge-moment coefficient, $\frac{\text{Hinge moment}}{qS_r\bar{c}_r}$

C_L	lift coefficient, $\frac{\text{Lift}}{qS}$
C_{L_α}	lift-curve slope
C_l	rolling-moment coefficient, $\frac{\text{Rolling moment}}{qSb}$
C_{l_β}	lateral stability parameter; effective-dihedral parameter, $\frac{\partial C_l}{\partial \beta}$, per degree
$C_{l_{\delta a}}$	aileron effectiveness parameter, $\frac{\partial C_l}{\partial \delta_a}$, per degree
C_m	pitching-moment coefficient, $\frac{\text{Pitching moment}}{qS\bar{c}}$
$C_{m_{\delta e}}$	elevator effectiveness parameter, $\frac{\partial C_m}{\partial \delta_e}$, per degree
C_n	yawing-moment coefficient, $\frac{\text{Yawing moment}}{qSb}$
C_{n_β}	directional stability parameter, $\frac{\partial C_n}{\partial \beta}$, per degree
$C_{n_{\delta a}}$	aileron yawing-moment parameter, $\frac{\partial C_n}{\partial \delta_a}$, per degree
$C_{n_{\delta r}}$	rudder effectiveness parameter, $\frac{\partial C_n}{\partial \delta_r}$, per degree
C_Y	side-force coefficient, $\frac{\text{Side force}}{qS}$
$\bar{c}$	mean aerodynamic chord, 1.57 m (5.13 ft)
$\bar{c}_a$	aileron mean chord, 0.43 m (1.42 ft)
$\bar{c}_e$	elevator mean chord, 0.40 m (1.33 ft)

$\bar{c}_r$	rudder mean chord, 0.51 m (1.67 ft)
D	propeller diameter, 2.06 m (6.75 ft)
L/D	lift-drag ratio
n	rotational speed, rps
q	free-stream dynamic pressure, N/m^2 (lbf/ft^2)
q_t/q	ratio of dynamic pressure at tail to free-stream dynamic pressure
S	wing area, 16.65 m^2 (179 ft^2)
S_a	area of one aileron, 0.70 m^2 (7.50 ft^2)
S_e	area of elevator, 1.99 m^2 (21.39 ft^2)
S_r	area of rudder, 1.03 m^2 (11.10 ft^2)
T	effective thrust, $\text{Drag}_{\text{propellers removed}} - \text{Drag}_{\text{propellers operating}}$
T_c'	thrust coefficient, T/qS
V	free-stream velocity, m/sec (ft/sec)
$\frac{V}{nD}$	propeller advance ratio
X	longitudinal axis
α	angle of attack of fuselage reference line, degrees
β	angle of sideslip, positive when nose is to left, degrees
δ_a	total aileron deflection, positive when right aileron is down, $\delta_{aR} - \delta_{aL}$, degrees
δ_e	elevator deflection, positive when trailing edge is down, degrees

δ_f	flap deflection, positive when trailing edge is down, degrees
δ_r	rudder deflection, positive when trailing edge is left, degrees
θ	flow angle in tunnel test section with respect to horizontal plane (downflow is negative), degrees
ϵ	downwash angle at tail relative to free stream, degrees

Subscripts:

L	left
max	maximum
R	right

MODEL

The model tested was a full-scale mockup of a light, twin-engine, low-wing monoplane having a maximum take-off weight of 23 130 N (5200 lb). Figure 2 and table I give the principal dimensions and figure 3 shows the model mounted in the tunnel test section. The model, which was of conventional production-line construction, had a wing span of 11.26 m (36.93 ft), a wing area of 16.65 m^2 (179 ft^2), an aspect ratio of 6.98, and a mean aerodynamic chord of 1.57 m (5.13 ft). The wing had airfoil sections of NACA 23018 at the fuselage center line, NACA 23015 at the nacelle center line, and NACA 23009 at the wing tip. The wing had 5° dihedral, 2.5° incidence at the root, and -0.5° incidence at the tip, resulting in 3° of washout. The thrust axis was parallel to the reference line. The model had a standard three-control system. The horizontal tail was of the stabilizer-elevator type with an elevator travel of $+15^\circ$ to -13.7°. The control deflection range of the ailerons and rudder was $\pm 20^\circ$ and $\pm 25^\circ$, respectively. The controls were remotely operated by electromechanical actuators attached to the bellcrank of each control. The pushrod of each control was strain-gaged to provide the hinge moments. The split-type trailing-edge flap had a maximum deflection of 35°. Power was provided by a 266-hp (198-kW) variable-frequency electric motor in each nacelle.

TESTS

The tests were made to determine the static longitudinal and lateral stability and control characteristics of the model over a wide range of flight conditions. Hinge moments were measured for all control surfaces during the investigation. The model was tested over an angle-of-attack range of -4° to 24°, over a sideslip range of $\pm 8^{\circ}$ for the clean condition $\left(\delta_f = 0^{\circ}\text{; gear up}\right)$, and for flap deflections of 15° and 35° with gear down. A range of elevator deflections of 15° to -13.7° was investigated at zero sideslip, and the aileron and rudder effectiveness was measured over the sideslip range. The tests were made at thrust coefficients of 0, 0.19, and 0.28 which represent a flight condition of low power or high speed (where the thrust coefficient approaches zero), best climb, and full power as in take-off or wave-off, respectively. The thrust coefficients were based on an installed power of 260 hp (194 kW) per engine. The advance ratio for each thrust coefficient was set at a fixed value which was representative of that for flight conditions at which the particular value of thrust coefficient could be achieved. The values of V/nD were 0.95, 0.61, and 0.52 for values of $T_c' = 0$, 0.19, and 0.28, respectively. A propeller blade angle of 20° was used for all tests. Tail downwash surveys were made along the elevator hinge axis with the horizontal tail off at zero sideslip for flap deflections of 0° and 35° for $T_c' = 0$, 0.19, and 0.28. A limited number of tests were made with a cowling nose radius modification shown in figure 4, a short nacelle configuration shown in figure 5, and several patterns of simulated ice on the wing and horizontal stabilizer shown in figure 6. The tests were conducted at a tunnel speed of about 27.5 m/sec (90 ft/sec) which gave a Reynolds number of approximately 2.94×10^{6}.

PRESENTATION OF DATA

The longitudinal data from these tests have been corrected for blockage, airstream misalinement, buoyancy effects, mounting strut tares, and wind-tunnel jet-boundary effects. The lift and drag have been corrected for the integrated average airstream misalinement. The lateral data were not corrected for the lateral variation of the stream angle. It should be pointed out, however, that at least a portion of the positive rolling moment noted at the lower angles of attack for most model conditions can be attributed to lateral variation of the tunnel airstream angle as shown in figure 7. Calculations of section rolling moments using the spanwise variations of stream angle of figure 7 indicated that the total measured out-of-trim rolling moment could be approximately accounted for by the airstream angularity. Similar out-of-trim rolling moments were also noted in references 2, 3, and 4.

The data are presented in the following figures:

Figure
Longitudinal aerodynamic characteristics with propellers removed 8
Longitudinal aerodynamic characteristics with propellers windmilling 9
Longitudinal aerodynamic characteristics with power and flap deflections . . . 10 to 12

Figure

Longitudinal aerodynamic characteristics with asymmetric power 13

Longitudinal aerodynamic characteristics for the short nacelle with power and flap deflections . . . . 14 to 16

Longitudinal aerodynamic chracteristics with engine cowl modification 17

Longitudinal aerodynamic characteristics with horizontal tail removed 18

Longitudinal aerodynamic characteristics with simulated smooth ice on horizontal tail . . . . 19 and 20

Longitudinal aerodynamic characteristics with simulated rime ice on horizontal tail . . . . 21 and 22

Longitudinal aerodynamic characteristics with simulated glaze ice on horizontal tail . . . . 23 and 24

Longitudinal aerodynamic characteristics with simulated glaze ice on wing and horizontal tail . . . . 25 and 26

Variation of pitching-moment coefficient with elevator deflection 27

Variation of pitching-moment coefficient with elevator deflection with simulated ice on horizontal tail only . . . . 28 to 30

Variation of pitching-moment coefficient with elevator deflection with simulated glaze ice on wing and horizontal tail 31

Lateral aerodynamic characteristics with propellers removed 32

Lateral aerodynamic characteristics with power and flap deflections . . . . . 33 to 35

Lateral aerodynamic characteristics with short nacelles, power, and flap deflections . . . . 36 and 37

Lateral aerodynamic characteristics with engine cowl modification 38

Lateral aerodynamic characteristics with asymmetric power . . . . 39 and 40

Lateral aerodynamic characteristics with wing-tip tanks removed 41

Lateral aerodynamic characteristics with ventral fin removed 42

Lateral aerodynamic characteristics with ventral fin and vertical tail removed . . . . 43 and 44

Variation of lateral aerodynamic characteristics with aileron deflection, $\delta_f = 0^\circ$ . . . . 45 to 47

Figure

Variation of lateral aerodynamic characteristics with aileron deflection, $\delta_f = 35^{\circ}$ . . . . 48 to 50

Variation of lateral aerodynamic characteristics with aileron deflection with wing-tip tanks removed 51

Variation of lateral aerodynamic characteristics with rudder deflection, $\delta_f = 0^{\circ}$ . . . . 52 to 54

Variation of lateral aerodynamic characteristics with rudder deflection, $\delta_f = 35^{\circ}$ . . . . 55 to 57

Variation of lateral aerodynamic characteristics with rudder deflection for asymmetric power, $\delta_f = 0^{\circ}$ . . . . 58 and 59

Variation of lateral aerodynamic characteristics with rudder deflection for asymmetric power, $\delta_f = 35^{\circ}$ . . . . 60 and 61

Effective dihedral and directional stability characteristics with propellers removed 62

Effective dihedral and directional stability characteristics with power and flap deflections 63

Effective dihedral and directional stability characteristics with the short nacelle 64

Comparison of effective dihedral and directional stability characteristics with wing-tip tanks on and off 65

Effective dihedral and directional stability characteristics with ventral fin removed 66

Effective dihedral and directional stability characteristics with ventral fin and vertical tail removed 67

Effective dihedral and directional stability characteristics with asymmetric power 68

Aileron effectiveness 69

Yawing effectiveness of aileron 70

Rudder effectiveness 71

Rudder effectiveness with asymmetric power 72

Downwash at tail . . . . 73 and 74

Dynamic pressure of tail . . . . 75 and 76

Figure

Elevator hinge-moment coefficients 77

Elevator hinge-moment coefficients with short nacelle 78

Elevator hinge-moment coefficients with simulated ice on horizontal tail . . . 79 to 81

Elevator hinge-moment coefficients with simulated glaze ice on wing and horizontal tail 82

Aileron hinge-moment coefficients . . . . 83 and 84

Rudder hinge-moment coefficients . . . . 85 and 86

Rudder hinge-moment coefficients with asymmetric power . . . . 87 and 88

Effect of power on longitudinal aerodynamic characteristics 89

Effect of power on lift-curve slope and maximum lift 90

Stick-fixed longitudinal stability characteristics . . . . 91 and 92

Stick-free pitching-moment coefficients 93

Effect of power on stick-free longitudinal stability 94

Elevator control power 95

Comparison of longitudinal characteristics with wing-tip tanks on and off . . . 96

Comparison of longitudinal characteristics with basic and modified cowl . . . 97

Comparison of longitudinal characteristics with basic and short nacelles . . . 98

Effect of ice on longitudinal characteristics 99

Effect of ice on elevator effectiveness . . . . 100 and 101

Flow conditions at horizontal tail 102

Effect of asymmetric power on longitudinal characteristics 103

Effective dihedral characteristics 104

Directional stability characteristics 105

Aileron and rudder effectiveness 106

Effect of wing-tip tanks on aileron characteristics 107

Rolling-moment coefficients for various power conditions 108

Yawing-moment coefficients for various power conditions 109

Yawing-moment coefficients with symmetric and asymmetric power and sideslip 110

Control capability with asymmetric power 111

RESULTS AND DISCUSSION

The basic data obtained during the wind-tunnel investigation are presented in figures 8 to 88 without analysis. Summary plots have been prepared from some of these data to illustrate the general static stability and control characteristics of the model. Only the summary plots are discussed.

Longitudinal Characteristics

The longitudinal aerodynamic characteristics of the model with various power conditions are presented in figure 89 for flap deflections of 0°, 15°, and 35°. As might be expected, increasing thrust coefficient results in an increase in lift-curve slope and maximum lift coefficient because of the increased slipstream velocity over the wing. This effect of power on the lift characteristics is summarized in figure 90 where lift-curve slope and maximum lift coefficient are shown as functions of thrust coefficient.

The pitching-moment curves shown in figure 89 are essentially linear up to angles of attack near the stall and then exhibit a nose-down pitching moment usually associated with straight-wing airplanes at higher angles of attack. The variation of the pitching-moment curves with angle of attack indicates that increasing thrust coefficient reduces the longitudinal stability, particularly with flaps deflected, and causes a fairly large trim change. These effects of power on static longitudinal stability are summarized in figures 91 and 92 where variations of the static stability parameter $\partial C_m/\partial C_L$ are plotted against C_L and T_c', respectively. These data show that, in general, the level of stability remains nearly constant up to the higher lift coefficients where it increases and that increased thrust coefficient caused a decrease in stability. These data also show that the model would have stick-fixed static stability for all test conditions even with the center of gravity at an aft location of 34 percent of the mean aerodynamic chord.

The stick-free static stability characteristics, determined from the pitching- and hinge-moment curves, are shown in figure 93. The data show that the model has stick-free stability in the normal operating range for all flap and power conditions tested. The effect of thrust coefficient on the stick-free longitudinal stability at a lift coefficient of 1.0 is presented in figure 94. These data show that power has a destabilizing effect, as it did for the stick-fixed case, and that the model could have stick-free instability with an aft center-of-gravity loading.

The variation of the elevator effectiveness with angle of attack is presented in figure 95 for flap deflections of 0°, 15°, and 35°. These data show that the effectiveness is reduced at the higher angles of attack, but effectiveness is still maintained through the stall. These data also show that power generally increased the elevator effectiveness.

The effect of the wing-tip tanks on the longitudinal aerodynamic characteristics are shown in figure 96 where the tanks-on and tanks-off data are compared. The tanks appear to have an end-plate effect as evidenced by the increase in lift-curve slope with tanks on. When the tanks-on coefficients are based on an area including the area of the tanks $\left(S = 18.6 \text{ m}^2 \left(200 \text{ ft}^2\right)\right)$, however, the lift coefficients are lower than with the tanks off. This indicates, as might be expected, that the tanks are less effective as a lifting surface than an equivalent area having an airfoil section. The tanks also resulted in a decrease in longitudinal stability at angles of attack near the stall.

Observations of tufts on the upper surface of the engine nacelle indicated that there was some disturbed flow apparently originating from the corners of the cowl which had a rather sharp leading edge. The cowl was modified as shown in figure 4 and the test results are presented in figure 97 compared with the basic configuration. These data show that the modification caused an increase in lift over most of the angle-of-attack range without any effect on the drag. The effect of the modification on the lift-drag ratio is shown in figure 97(b). In the cruise angle-of-attack range ($\alpha \approx 2^\circ$), an increase in L/D of about 1.0 is shown. This modification provided, of course, that it did not effect engine cooling and the benefits that are realized in flight might result in increased performance of the airplane.

Questions have been raised as to what effect the large flat nacelles, currently being used on most twin-engine general-aviation airplanes, have on the airplane aerodynamic characteristics. While the present investigation was not intended to explore the effect of nacelle shape in depth, a few tests were made to determine whether the long aft nacelle had any appreciable effects on the characteristics of the subject model. For these tests, the nacelle was modified as shown in figure 5. The characteristics of the model with the short nacelle are shown in figure 98 compared with those of the model with standard nacelles. The data show an increase in lift and drag with the short nacelle but the changes were relatively small. These differences were likely caused by the increased camber of the nacelle resulting from the change in shape. Observations of tufts on the wing and nacelles during the tests revealed that the flow on the nacelle remained attached over the angle-of-attack range despite the rather abrupt change in shape and the stall pattern on the wing was essentially the same as that observed for the basic configuration. The lift-drag ratio presented in figure 98(b) indicates that only in the cruise angle-of-attack range would the short-nacelle configuration show any increase in airplane performance since at higher angles of attack the drag increase caused an appreciable reduction in maximum lift-drag ratio.

The effect of ice on the variation of lift and pitching-moment coefficients with angle of attack is presented in figure 99 for the model with the glaze-ice formation on both the wing and the horizontal tail. The data show that the ice caused the stall to start at a much lower angle of attack and resulted in a large decrease in maximum lift and a large increase in the nose-down pitching moment near the stall. The effect of ice on the variation of the elevator effectiveness with angle of attack is presented in figure 100. The data show that ice caused some reduction in elevator effectiveness, particularly at angles of attack near the stall, but the reduction was not large enough to result in a loss of control.

Tests were made with the simulated ice formations shown in figure 6 to determine the effect of ice on the elevator effectiveness. Presented in figure 101 is the variation of elevator effectiveness $C_{m_{\delta e}}$ with angle of attack for the several ice formations studied. The data show that with ice only on the tail there was little effect on the elevator effectiveness for any of the test conditions.

One point of interest which may be worthy of comment would be the effect of ice on the landing characteristics of an airplane. For example, an airplane weighing approximately 22 240 N (5000 lbf) and cruising at 175 knots would have a lift coefficient of about 0.29. At this condition the data of figure 99 show that glaze ice does not appreciably affect the lift or pitching moment. In the landing configuration with full-flap deflection, however, the pilot may attempt to rotate the airplane to the ice-free attitude and find that because of the iced condition, the airplane stalls and develops a large diving moment. A nose dive into the ground, or at least a hard landing, might be the result of such a sequence of events with the conclusion that there was a loss of elevator effectiveness. The data show, however, that elevator effectiveness was not appreciably degraded by the ice formations.

Presented in figure 102 is the variation of the average downwash angle and the dynamic-pressure ratio at the tail with angle of attack for the flap and power conditions investigated. These data were obtained from surveys and show an appreciable increase in downwash angle with flap deflection. With the horizontal tail almost completely spanned by the propellers, there is a large increase in the dynamic-pressure ratio at the tail with an increase in thrust coefficient.

The longitudinal characteristics of the model with symmetrical and asymmetrical power are presented in figure 103. These data show that the lift-curve slope and the maximum lift coefficient are reduced with one engine out because of the reduced slipstream velocity over the engine-out wing. As might be expected, the effects on lift are greater with the flaps down than with the flaps up. With flaps down, the slipstream effects of direction of propeller rotation on the pitching moment are more apparent with the right engine out. For this condition, figure 103 shows a reduction in pitching-moment coefficient over most of the angle-of-attack range below the stall, while left-engine-out condition is essentially the same as that for symmetrical power.

Lateral Characteristics

The variation of the effective-dihedral parameter C_{l_β} with angle of attack is shown in figure 104 for the various flap and power conditions tested. These data show that the model has positive effective dihedral $-C_{l_\beta}$ for all conditions to $(C_L)_{max}$. The values of C_{l_β} vary widely depending upon the angle of attack, flap, or power condition, but remained generally high for all conditions. Therefore, the response of the airplane to gusts or to rudder inputs to raise a wing would vary with the airplane configuration. The combination of full-power and full-flap deflection seems to have the most influence on the effective dihedral, causing a reduction in C_{l_β} well below maximum lift. Modifying the nacelle to the short configuration did not appreciably affect the effective dihedral.

The variation of the directional stability parameter C_{n_β} with angle of attack is is shown in figure 105 for the various flap and power conditions tested. These data show that the model is directionally stable in all conditions over the angle-of-attack range. There is a general reduction in directional stability up to the stall. Above the stall C_{n_β} increased for most conditions. With the short nacelle configuration and with the flaps up $(\delta_f = 0^o)$, C_{n_β} was higher than it was for the basic nacelle over the angle-of-attack range for $T'_c = 0.28$, but dropped to a much lower value at angles of attack near the stall for $T'_c = 0$.

The variation of the aileron and rudder effectiveness with angle of attack is presented in figure 106 for the three power test conditions and for flap deflections of 0^o and 35^o. These data show that, in general, the aileron effectiveness remains at a relatively constant high level up to about the stall and the effectiveness is little affected by change in conditions. The rudder effectiveness is also essentially constant through the stall and is relatively unaffected by changes in power but deflecting the flaps resulted in some increase in rudder effectiveness.

The effect of the wing-tip tanks on the aileron characteristics is shown in figure 107. These data show that the tanks increased aileron rolling moment over the entire angle-of-attack range. The tanks, however, did not have any effect on the adverse yawing moment produced by the ailerons.

The basic lateral characteristics of the model, as shown by the variation of the lateral coefficients C_l and C_n with angle of attack for 0^o sideslip, are presented in figures 108 and 109, respectively, for the various power and flap conditions for the basic and short nacelle configurations. The out-of-trim rolling moments noted in figure 108 at the low angles of attack are attributed to the tunnel airstream misalinement as explained earlier. The data show that no large asymmetrical rolling or yawing moments are experienced through the stall ($\alpha \approx 12^\circ$) for all conditions indicating that the flow characteristics were fairly symmetrical. Tuft studies, made along with the force tests, also showed that the flow was symmetrical through the stall. The stall first appeared at the outboard end of the ailerons.

Figure 110 presents the variation of the yawing-moment coefficients with angle of attack for several sideslip angles at $T_c' = 0, 0.19,$ and 0.28 and $\delta_f = 0^\circ$ for symmetrical and asymmetrical power conditions. These data show that for the positive sideslip angles there is a tendency for the yawing moment to decrease with an increase in angle of attack up to angles of attack near the stall. This characteristic was noted in the propeller-removed data of figure 32, but became more pronounced as thrust coefficient was increased as in figure 110. The condition also exists with asymmetric power and does not appear to be associated with the operation of either the right or left engine.

On twin-engine aircraft with right-hand rotating propellers the right engine is sometimes called the critical engine because its failure in flight usually causes greater out-of-trim moments than when the left engine fails. Figure 111 presents the control capability of the model for a right-engine-out condition. The data show that with half aileron and full rudder applied as corrective control, the controls are capable of trimming the asymmetric moments up to angles of attack near maximum lift. The corrective control moments include the adverse yaw of the ailerons and the roll due to rudder deflection.

CONCLUSIONS

A full-scale wind-tunnel investigation has been made to determine the static longitudinal and lateral stability and control characteristics and control hinge moments of a mockup of a light twin-engine airplane. The following conclusions were drawn from the results of the investigation:

1. The model had stick-fixed and stick-free longitudinal stability for angles of attack up through the stall for all the configurations tested with the center of gravity located at 0.25 mean aerodynamic chord.

2. Power has a destabilizing effect, and with an aft center-of-gravity location (0.34 mean aerodynamic chord), the model could have a stick-free longitudinal instability at some lift coefficients.

3. The model is directionally stable and has positive effective dihedral for angles of attack up to the stall but there are large variations of effective dihedral with angle of attack for the different power and flap conditions.

4. Aileron and rudder control effectiveness is maintained through the stall.

5. With asymmetric power the model had sufficient control capability to trim the roll and yawing moments up to angles of attack beyond the stall.

6. The installation of simulated ice lowered the angle of attack for the onset of stall, decreased maximum lift, and increased the nose-down pitching moment near the stall.

Langley Research Center,
National Aeronautics and Space Administration,
Hampton, Va., January 29, 1971.

APPENDIX

CONVERSION FACTORS – U.S. UNITS TO SI UNITS

The following conversion factors from reference 5 are included in this paper for convenience:

Physical quantity	U.S. Customary Unit	Conversion factor (*)	SI Unit
Area	ft^2	0.0929	meters^2 (m^2)
Density	$slugs/ft^3$	5153.8	kilograms/meter^3 (kg/m^3)
Force	lbf	4.448	newtons (N)
Length	in.	0.0254	meters (m)
	ft	0.3048	meters (m)
Moment	lbf-ft	1.356	newton-meters (N-m)
Power	hp	745.67	watts (W)
Pressure . . .	lbf/ft^2	47.88	newtons/meter^2 (N/m^2)
Velocity	ft/sec	0.3048	meters/second (m/sec)

*Multiply value given in U.S. Customary Unit by conversion factor to obtain equivalent value in SI Unit.

REFERENCES

1. Barber, Marvin R.; Jones, Charles K.; Sisk, Thomas R.; and Haise, Fred W.: An Evaluation of the Handling Qualities of Seven General-Aviation Aircraft. NASA TN D-3726, 1966.

2. Fink, Marvin P.; and Freeman, Delma C., Jr.: Full-Scale Wind-Tunnel Investigation of Static Longitudinal and Lateral Characteristics of a Light Twin-Engine Airplane. NASA TN D-4983, 1969.

3. Fink, Marvin P.; Freeman, Delma C., Jr.; and Greer, H. Douglas: Full-Scale Wind-Tunnel Investigation of the Static Longitudinal and Lateral Characteristics of a Light Single-Engine Airplane. NASA TN D-5700, 1970.

4. Shivers, James P.; Fink, Marvin P.; and Ware, George M.: Full-Scale Wind-Tunnel Investigation of the Static Longitudinal and Lateral Characteristics of a Light Single-Engine Low-Wing Airplane. NASA TN D-5857, 1970.

5. Mechtly, E. A.: The International System of Units – Physical Constants and Conversion Factors (Revised). NASA SP-7013, 1969.

TABLE I.- CHARACTERISTICS OF MODEL

Wing:	
Sweepback (0.25 chord), deg	0
Airfoil section:	
Root	NACA 23018
Nacelle	NACA 23015
Tip	NACA 23009
Aspect ratio	6.98
Taper ratio	1.517
Incidence:	
Root	2°30'
Tip	-0°30'
Dihedral, deg	5
Mean aerodynamic chord, m (ft)	1.56 (5.13)
Area:	
Total, m^2 (ft^2)	16.65 (179.08)
Flap, m^2 (ft^2)	2.13 (22.90)
Aileron, m^2 (ft^2)	1.32 (14.17)
Angular travel:	
Flap, deg	35
Aileron, deg	±20
Vertical tail:	
Airfoil section:	
Root	NACA 0009
Tip	NACA 0006
Aspect ratio	1.41
Area:	
Total, m^2 (ft^2)	2.42 (26.02)
Fin and dorsal, m^2 (ft^2)	1.32 (14.20)
Rudder, m^2 (ft^2)	1.09 (11.76)
Angular travel, deg	±25
Horizontal tail:	
Airfoil section:	
Root	NACA 0009
Tip	NACA 0006
Area:	
Total, m^2 (ft^2)	5.05 (54.25)
Stabilizer, m^2 (ft^2)	2.98 (32.15)
Elevator, m^2 (ft^2)	2.05 (22.10)
Incidence, deg	0
Aspect ratio	5.33
Angular travel, deg	+16, -15

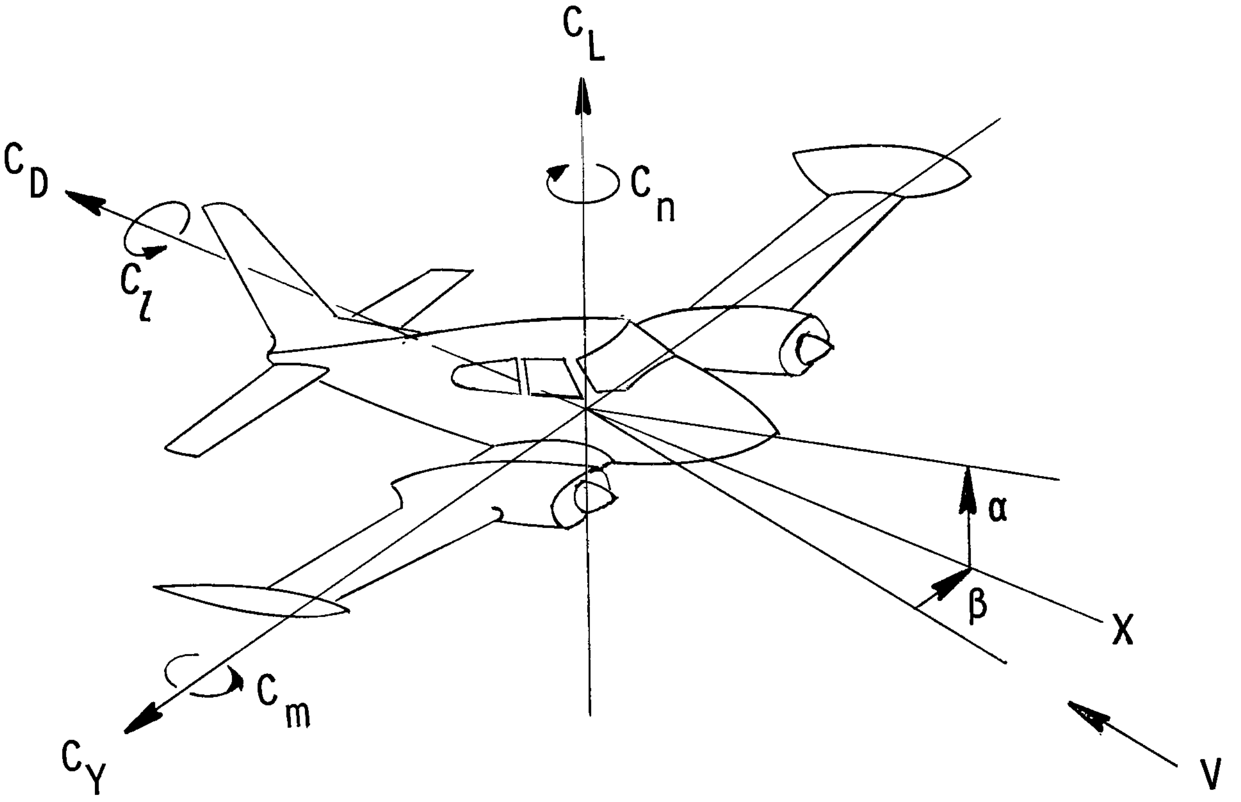

Figure 1.- System of stability axes and positive sense of angles, forces, and moments.

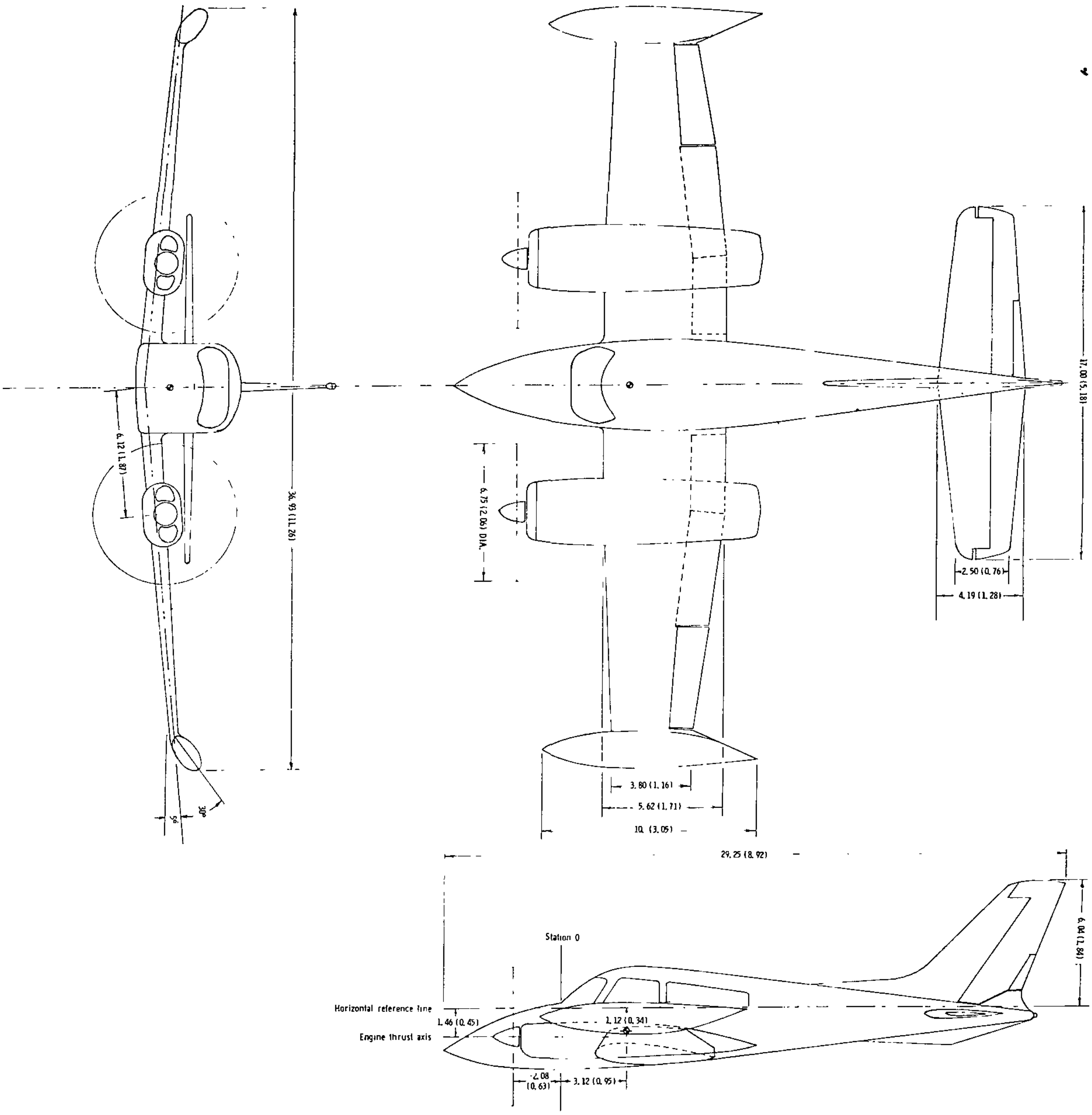

Figure 2.- Three-view drawing of model. All dimensions are in meters (feet).

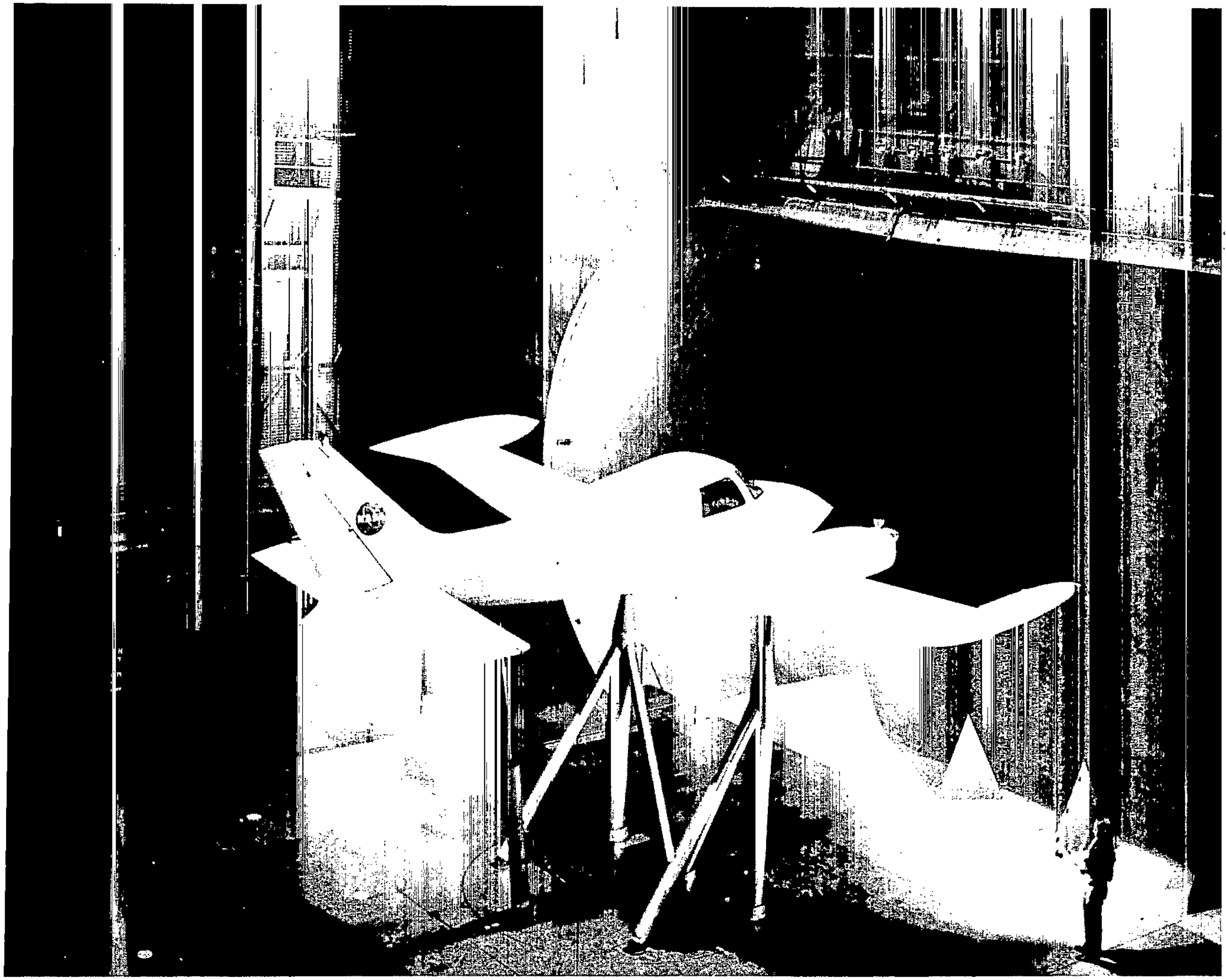

L-70-791

Figure 3.- Photograph of model mounted in Langley full-scale tunnel.

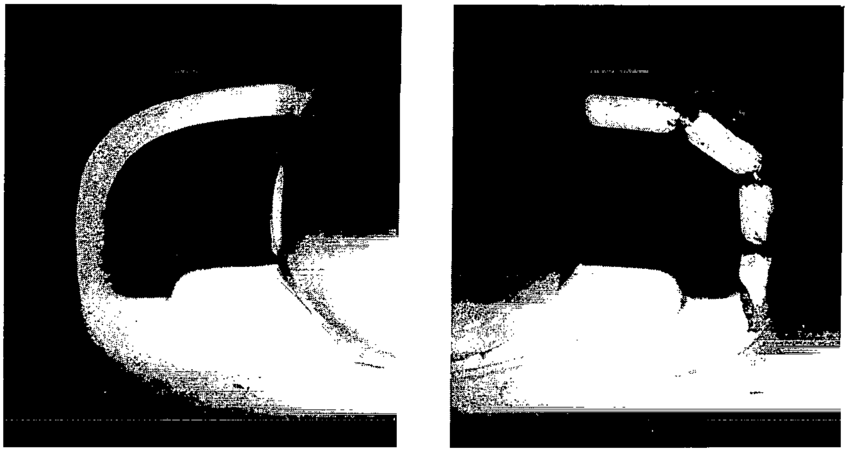

Basic cowl

Modified cowl

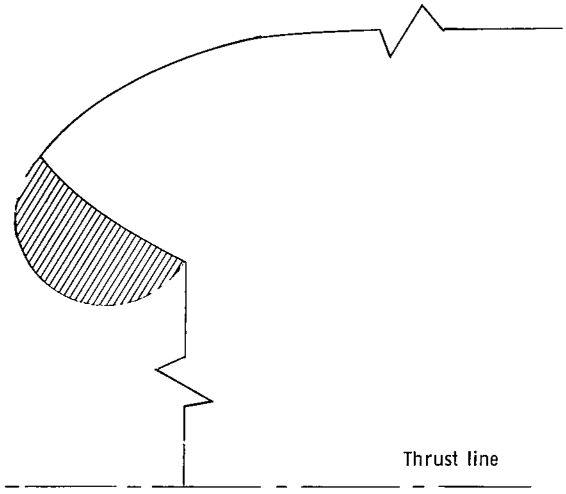

Cross section of cowl leading-edge modification.

L-70-516

Figure 4.- Photograph and cross section of cowl modifications.

L-70-2564

Figure 5.- Photograph of model with short nacelles.

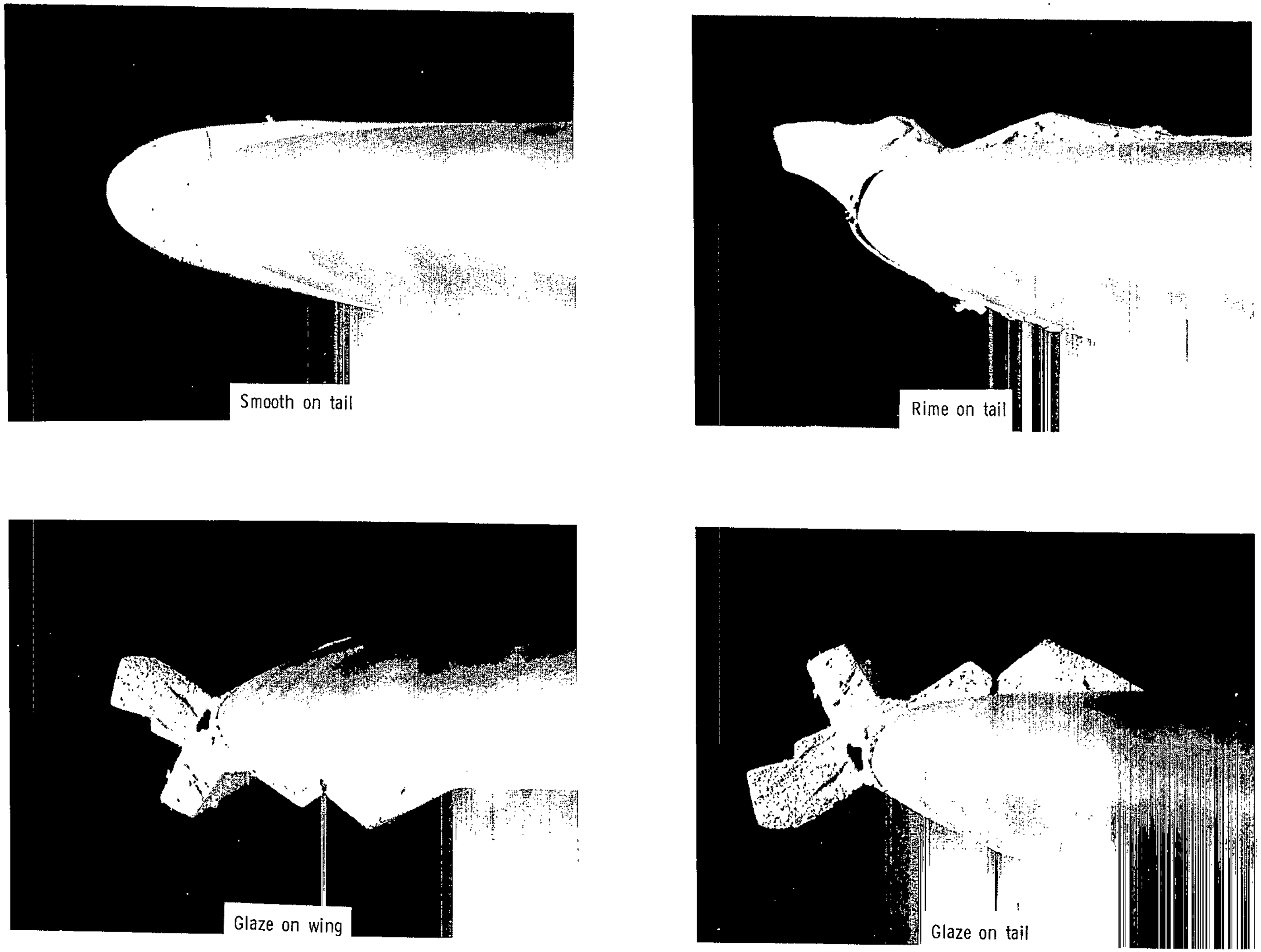

Smooth on tail

Rime on tail

Glaze on wing

Glaze on tail

L-71-517

Figure 6.- Photograph of simulated ice formation on leading edge of wing and horizontal tail.

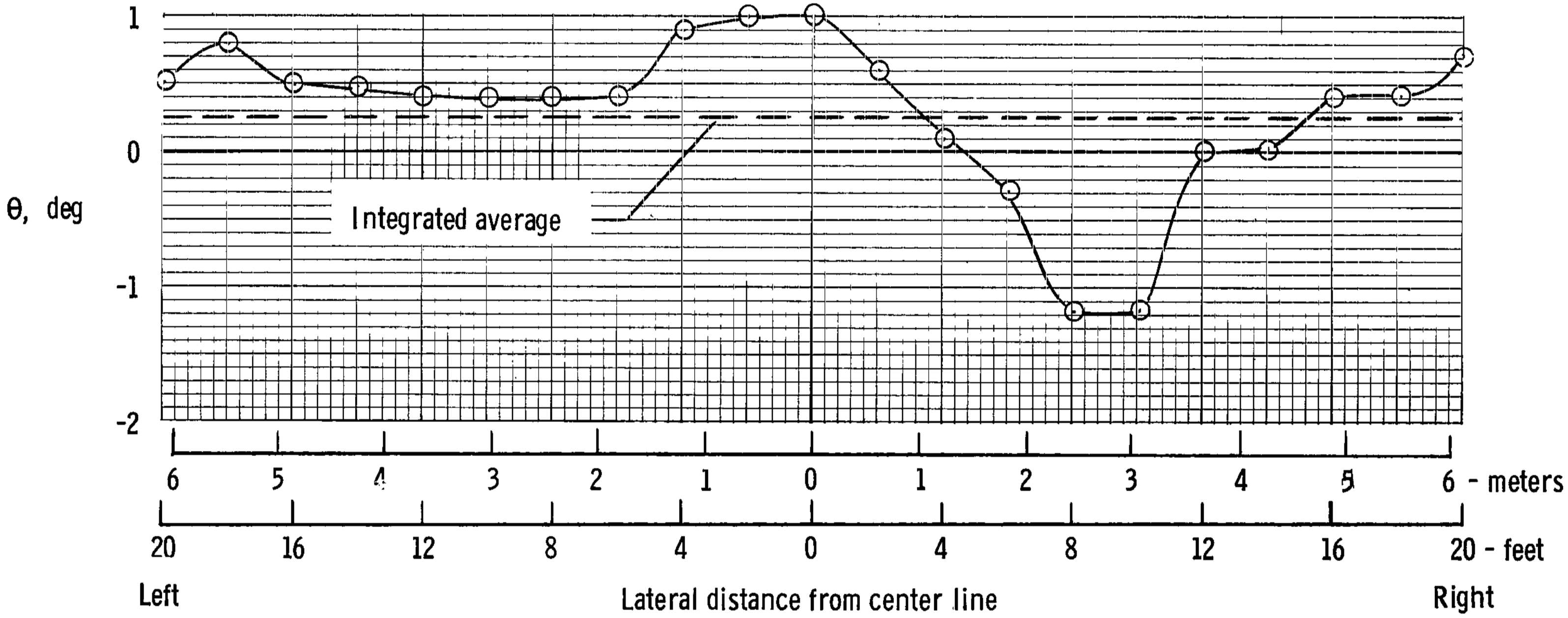

Figure 7.- Lateral variation of airstream angle at the wing location in tunnel.

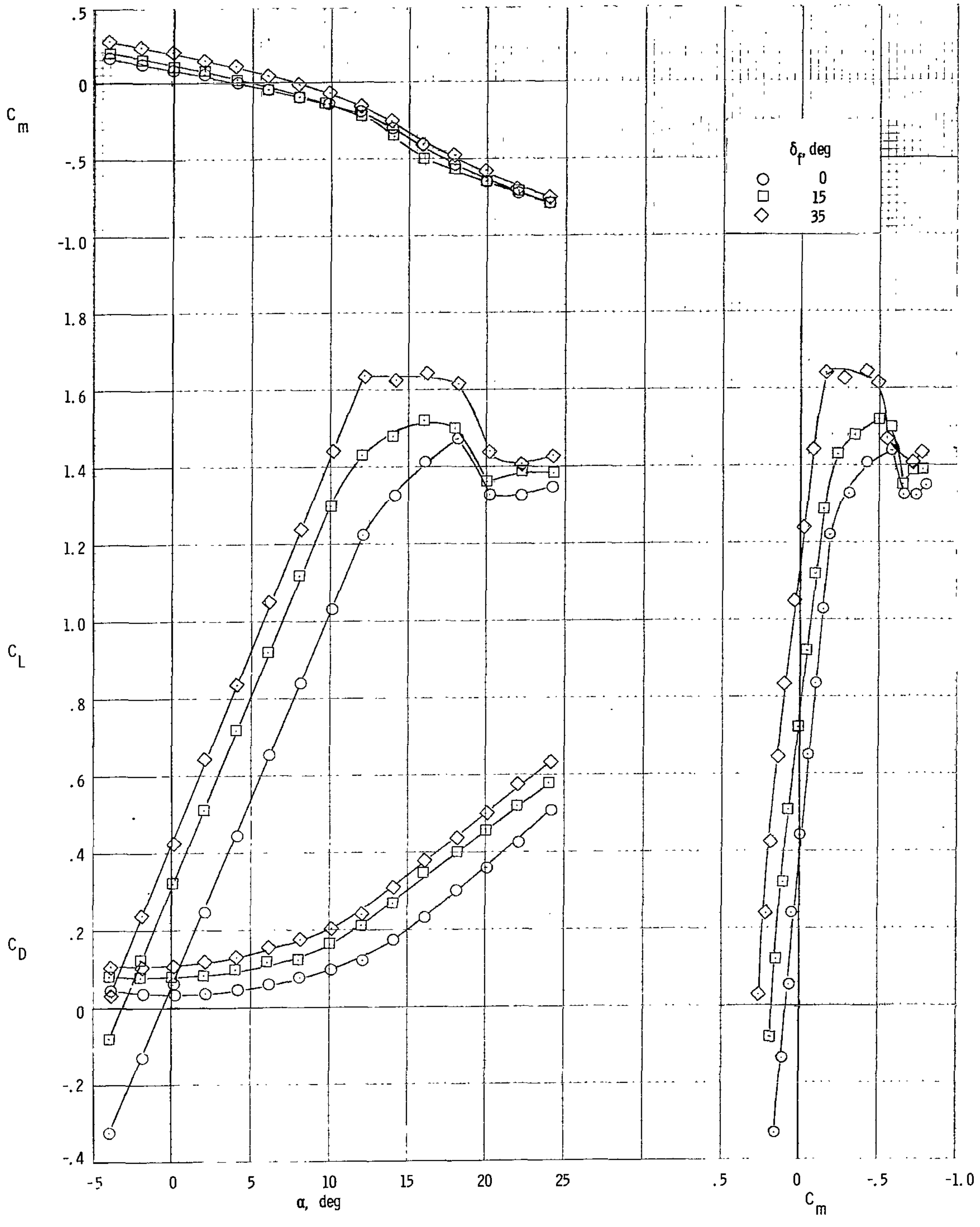

Figure 8.- Longitudinal aerodynamic characteristics of model with propellers removed for several flap deflections.

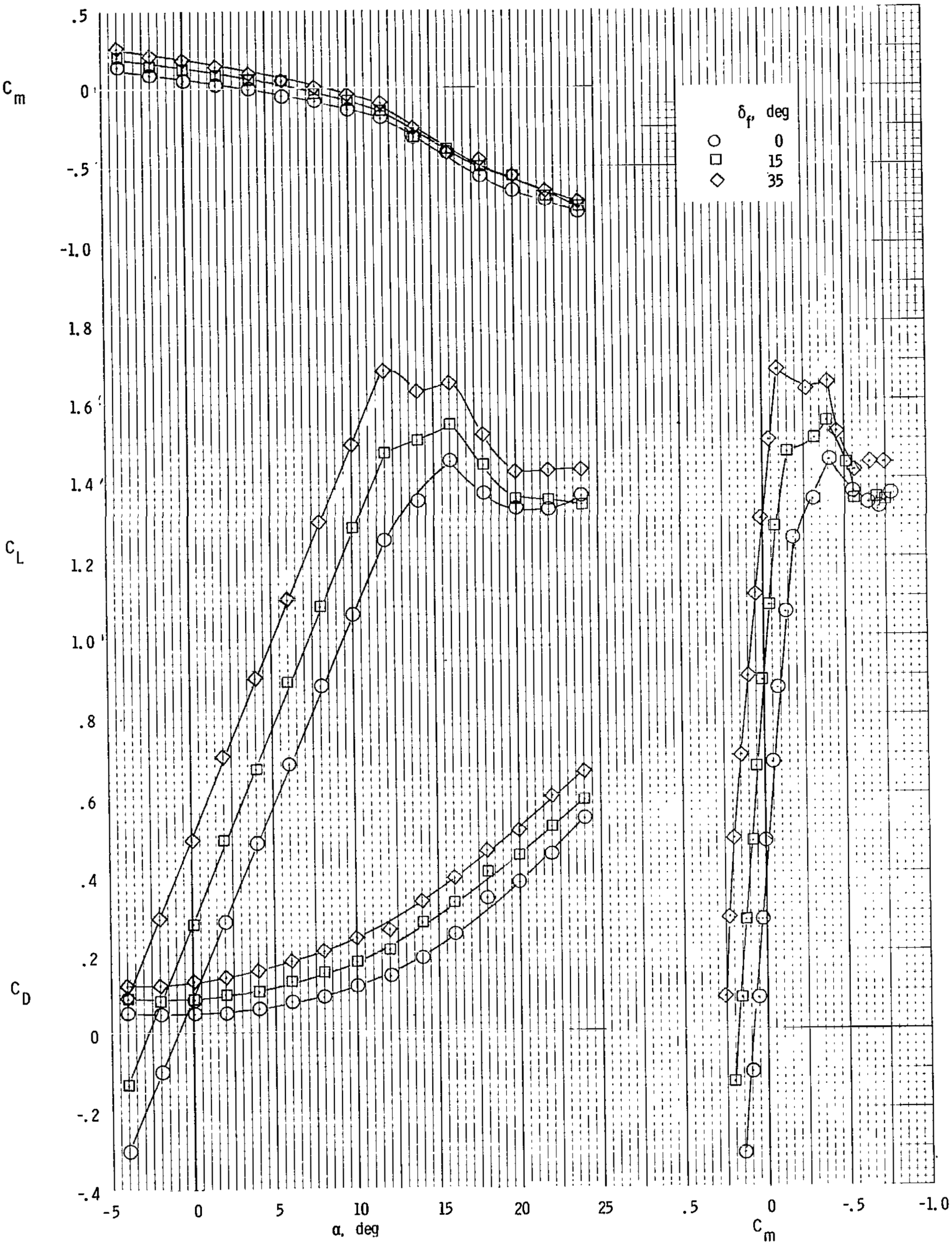

Figure 9.- Longitudinal aerodynamic characteristics of model with both propellers windmilling.

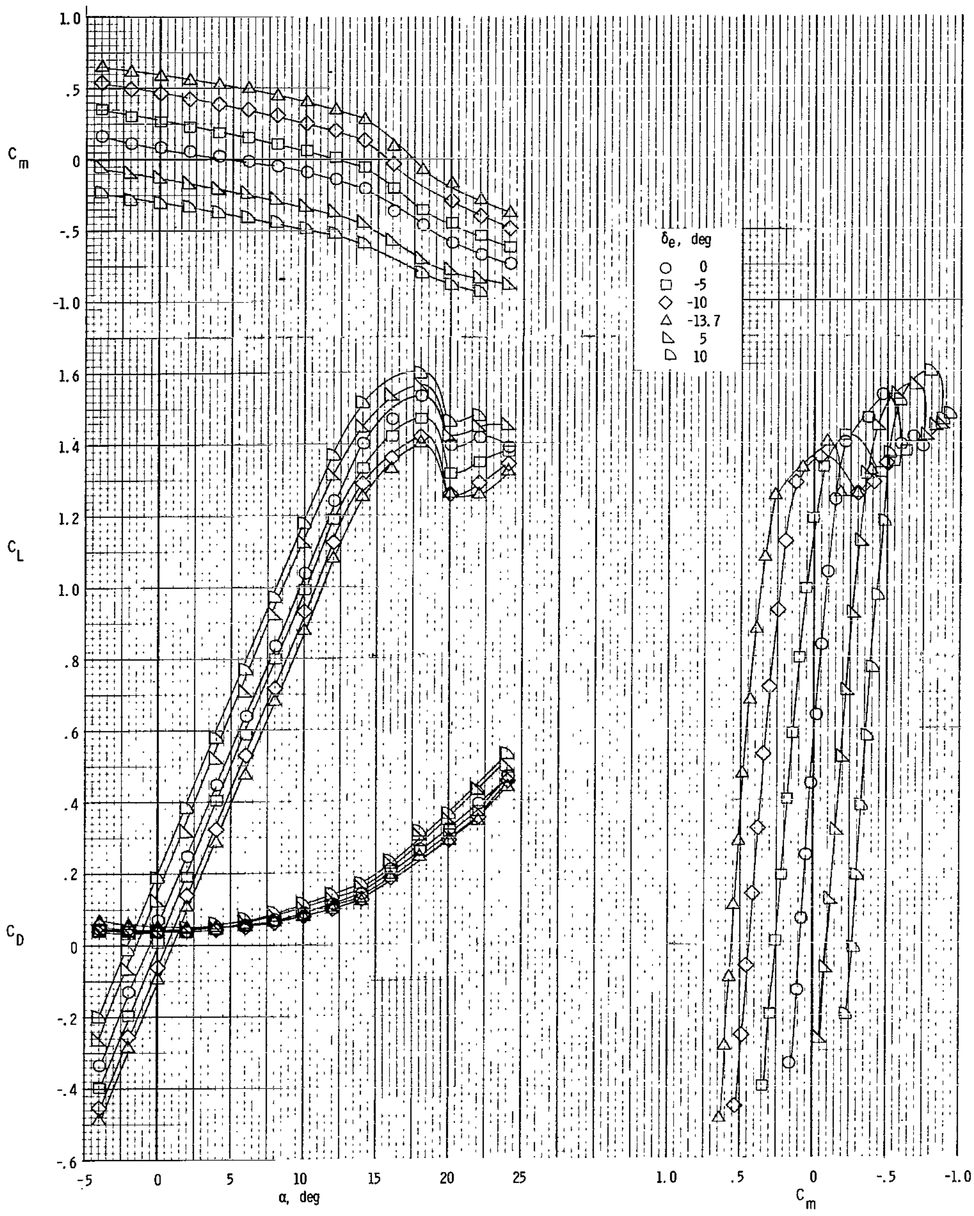

(a) $T_c' = 0$.

Figure 10.- Longitudinal aerodynamic characteristics of model for several thrust coefficients for $\delta_f = 0^0$.

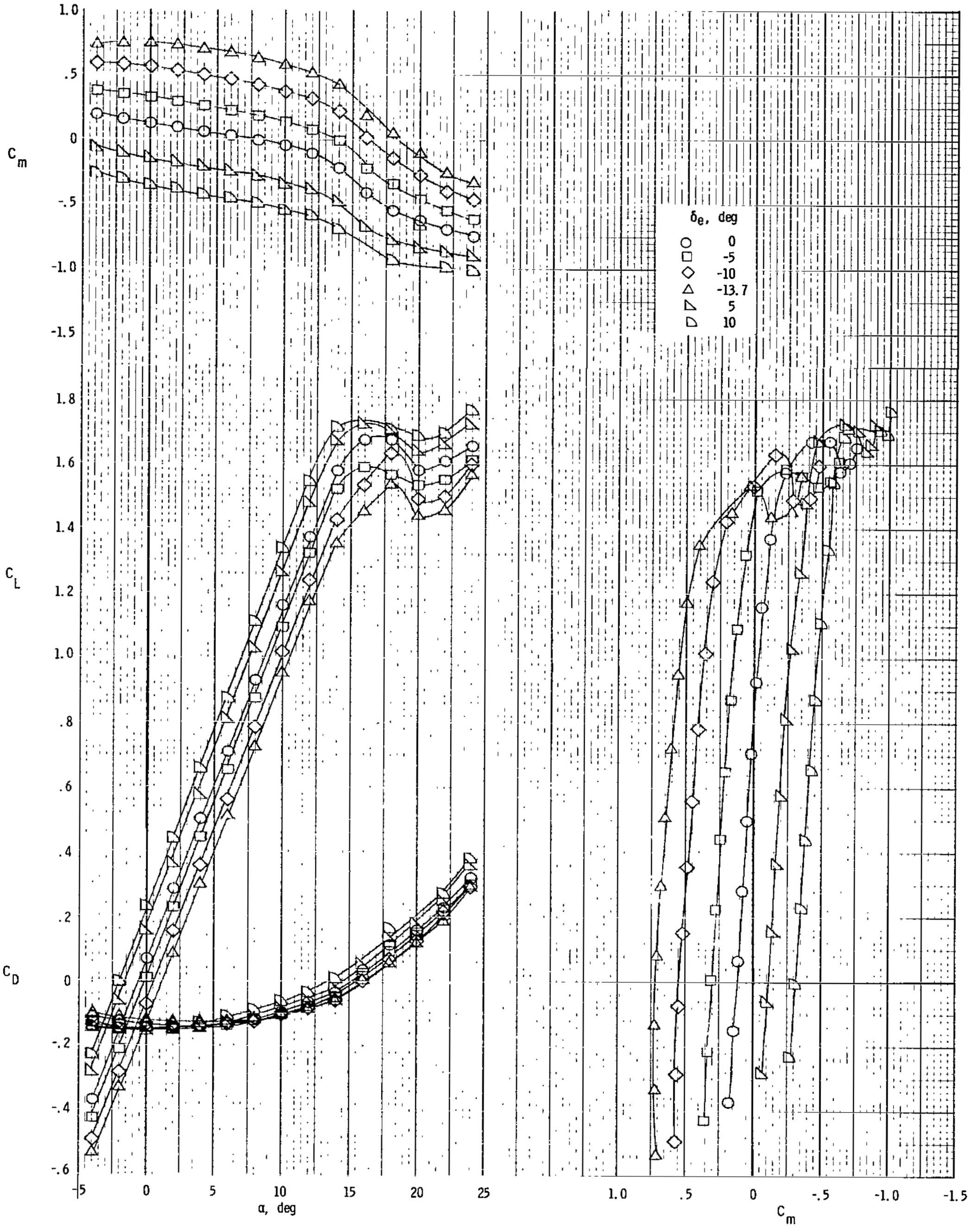

(b) $T_C' = 0.19$.

Figure 10.- Continued.

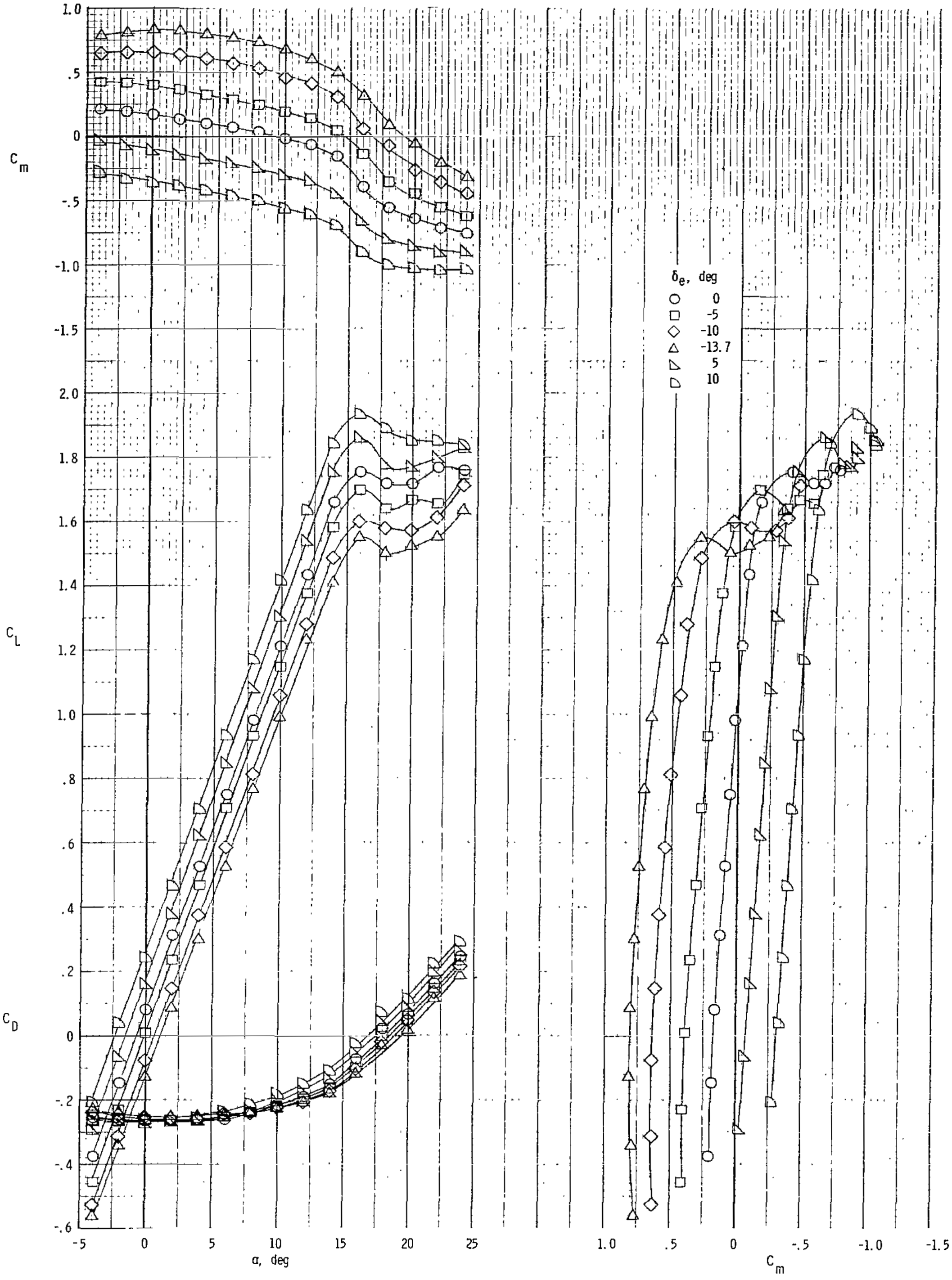

(c) $T_C' = 0.28$.

Figure 10.- Concluded.

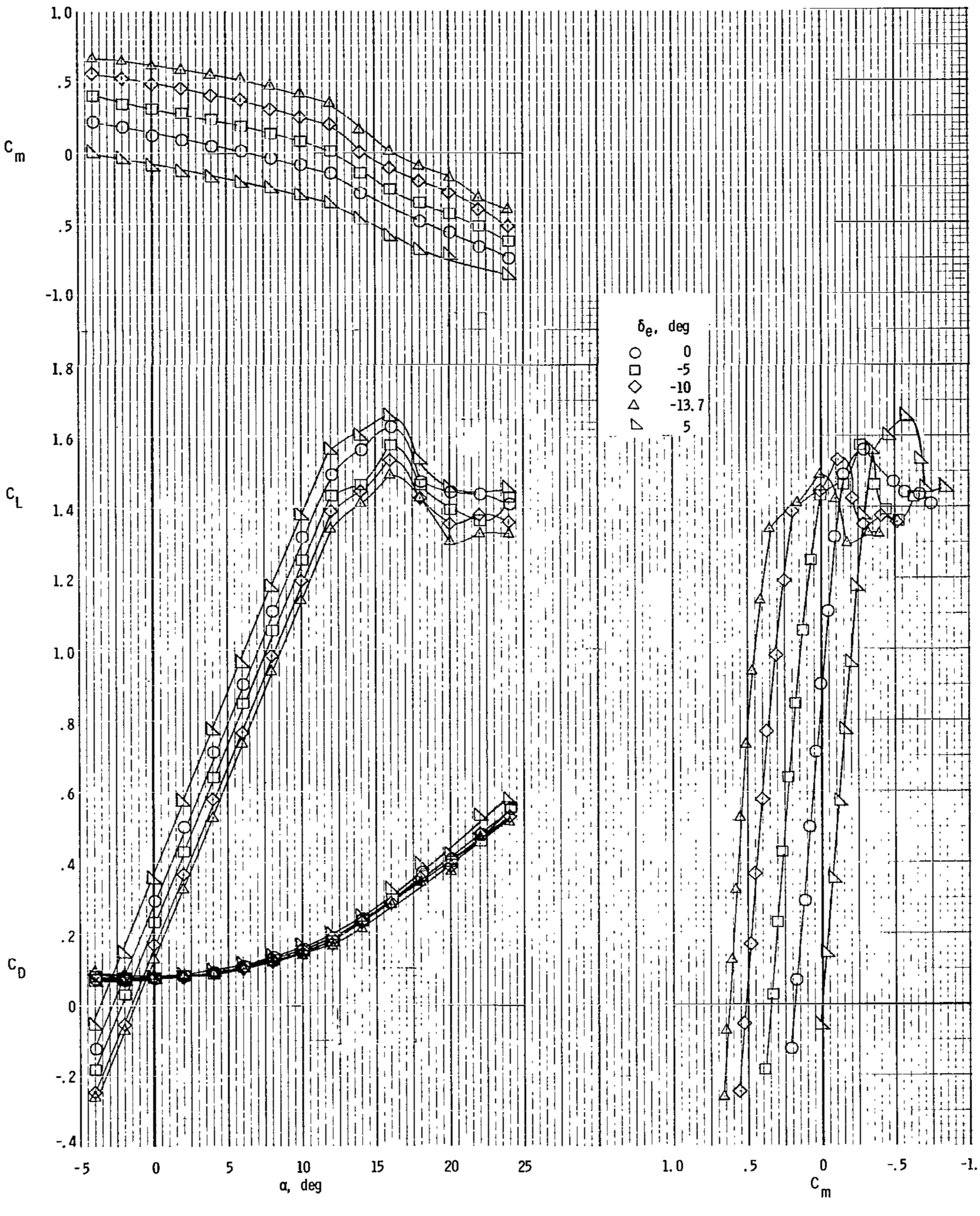

(a) $T_c' = 0$.

Figure 11.- Longitudinal aerodynamic characteristics of model for several thrust coefficients for $\delta_f = 15^0$.

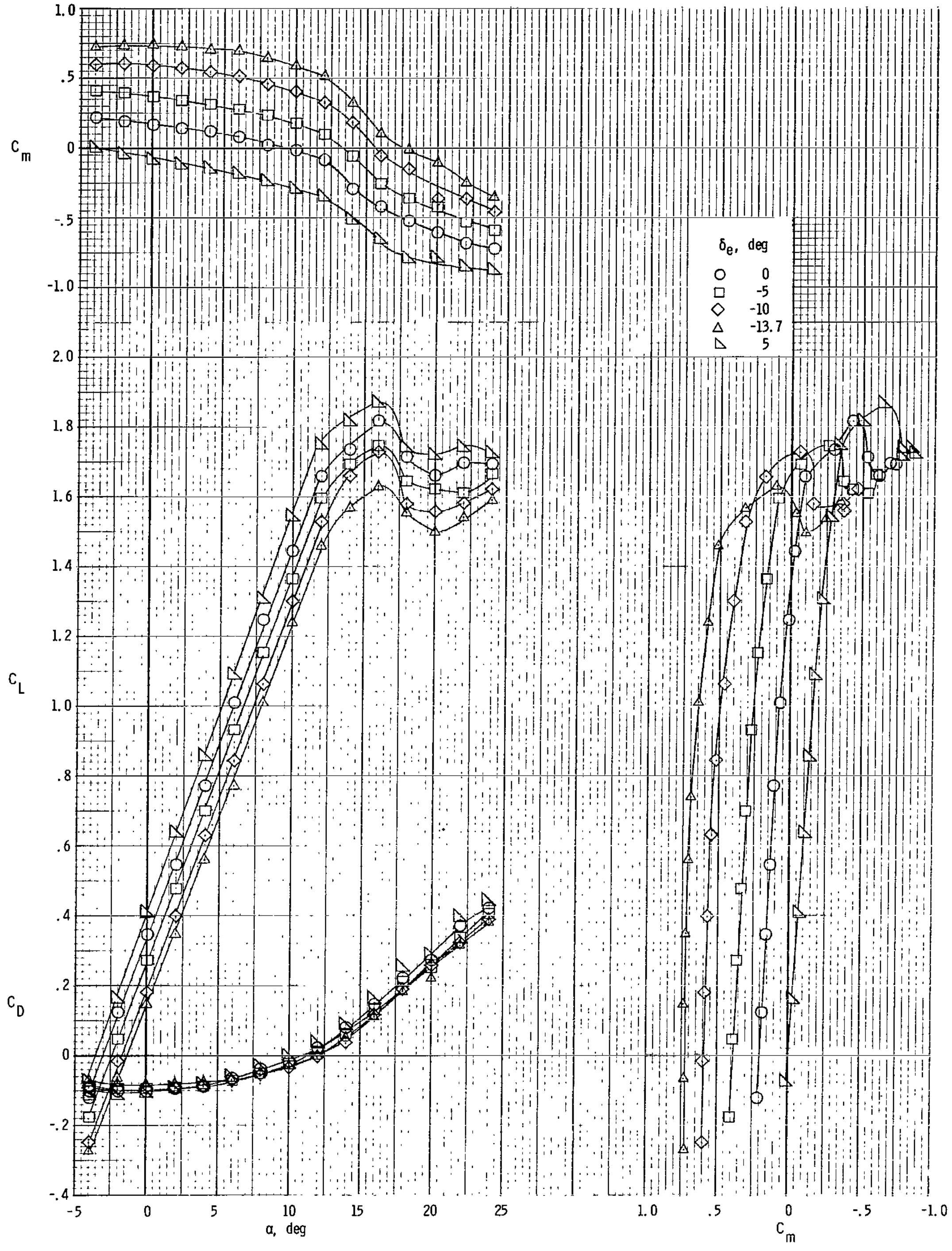

(b) $T_c' = 0.19$.

Figure 11.- Continued.

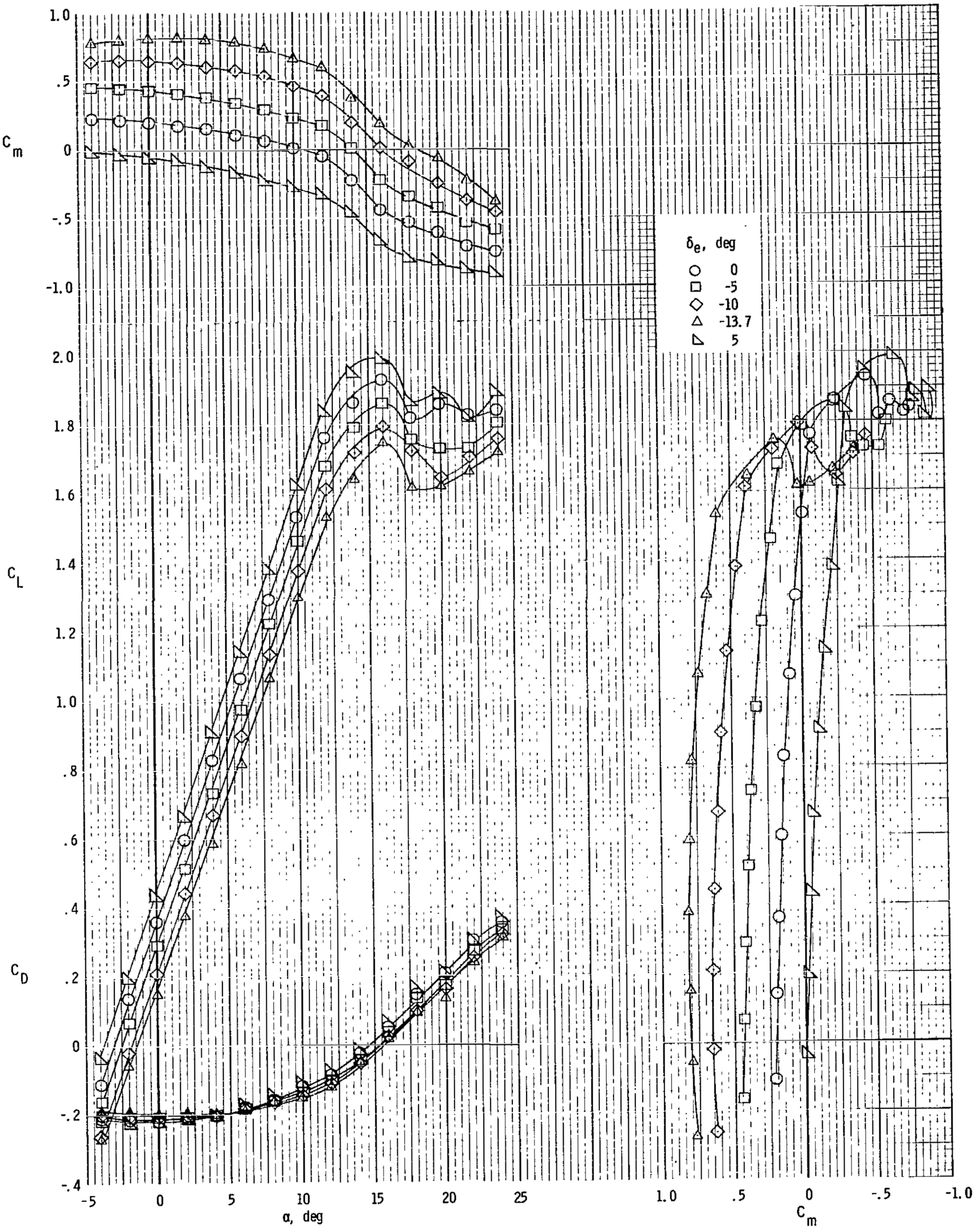

(c) $T_C' = 0.28$.

Figure 11.- Concluded.

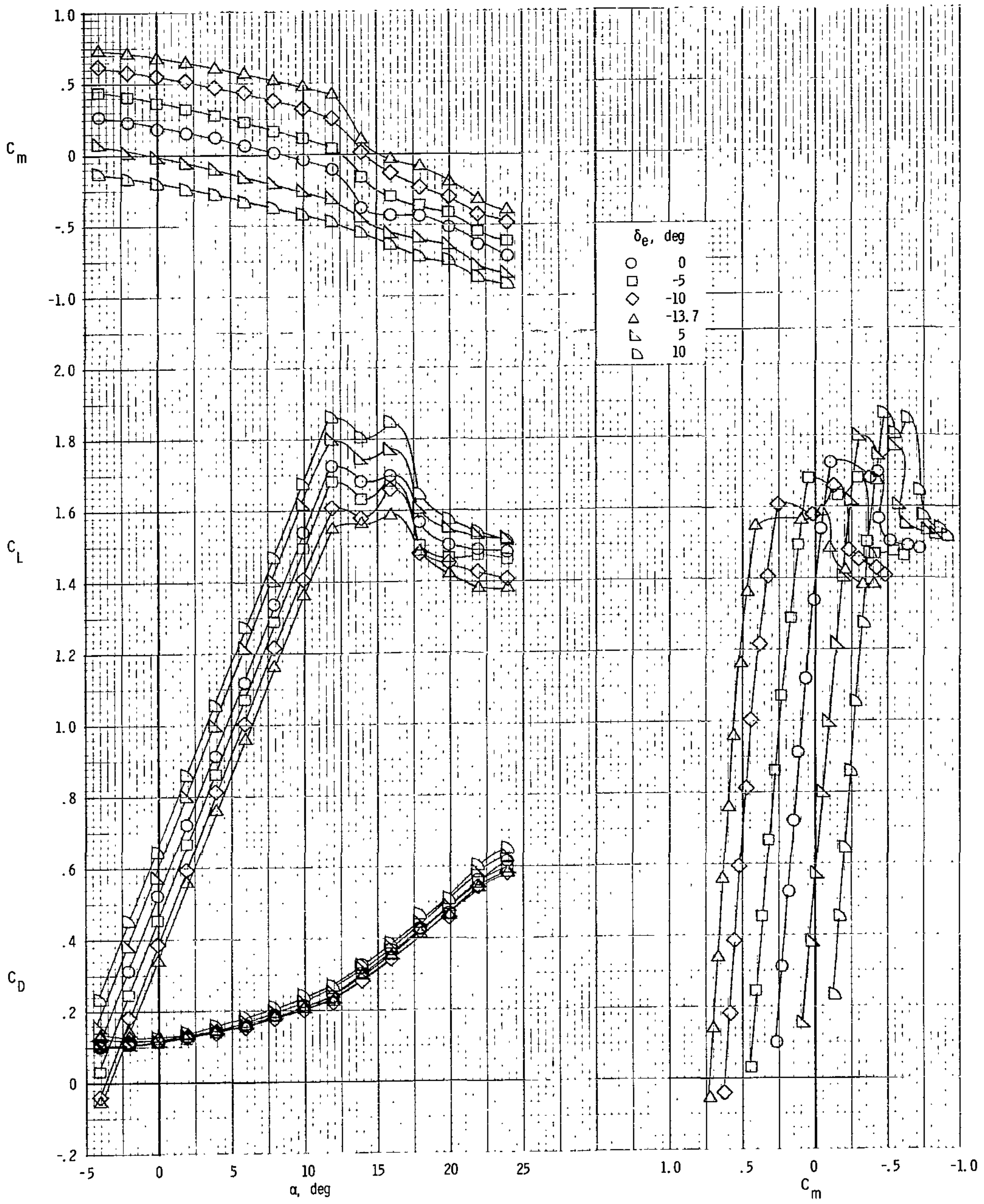

(a) $T_c' = 0$.

Figure 12.- Longitudinal aerodynamic characteristics of model for several thrust coefficients for $\delta_f = 35^\circ$.

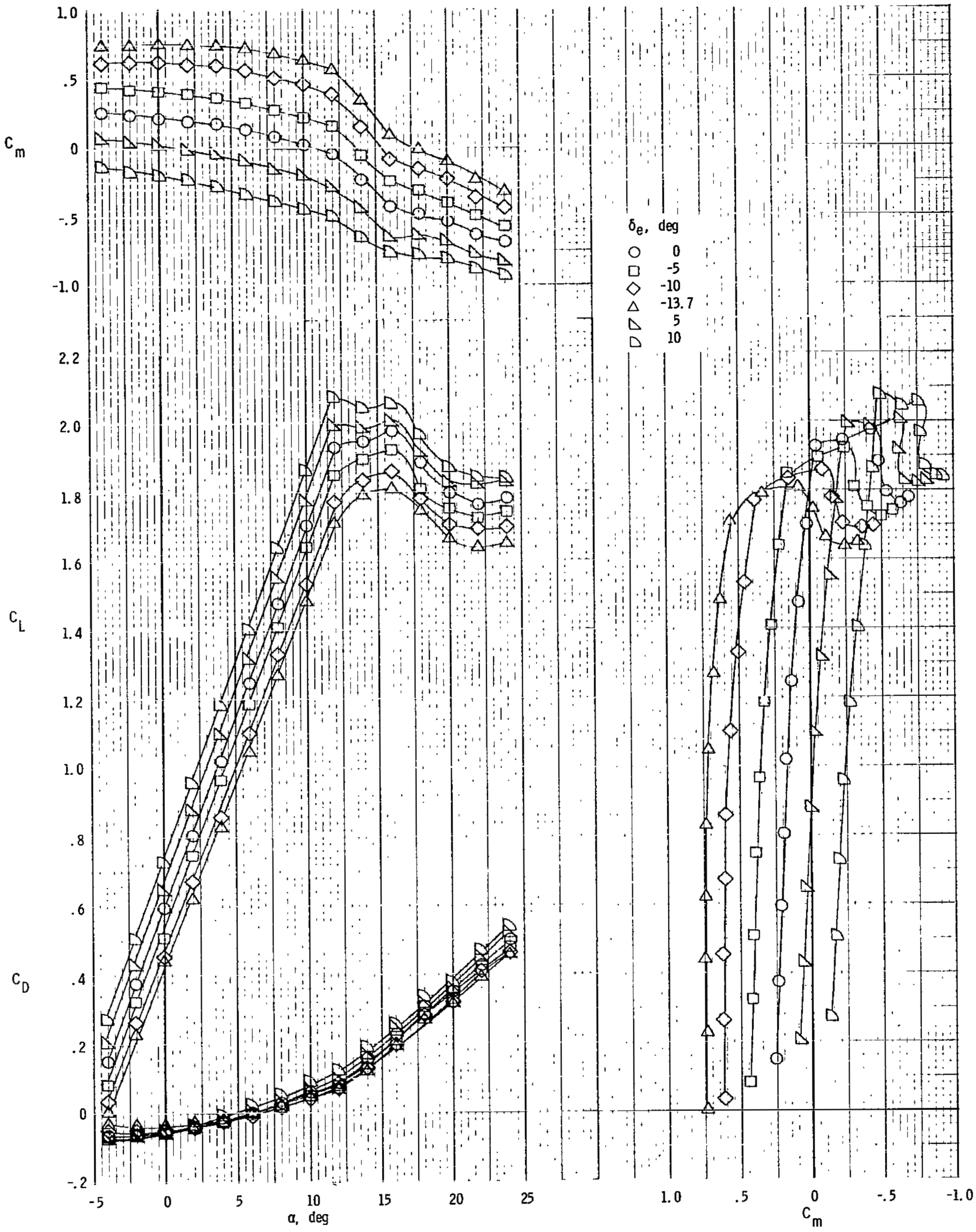

(b) $T_C' = 0.19$.

Figure 12.- Continued.

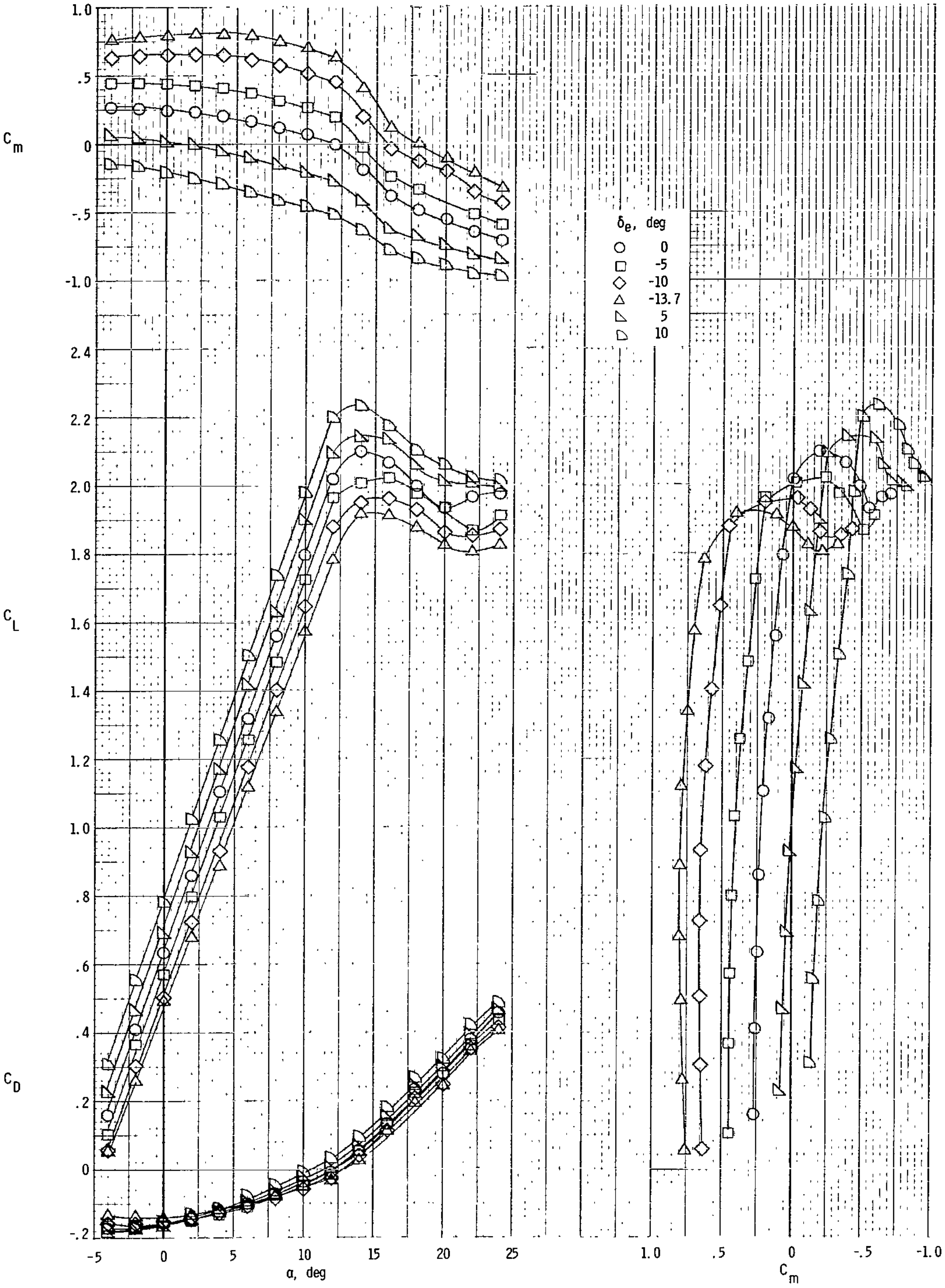

(c) $T_c' = 0.28$.

Figure 12.- Concluded.

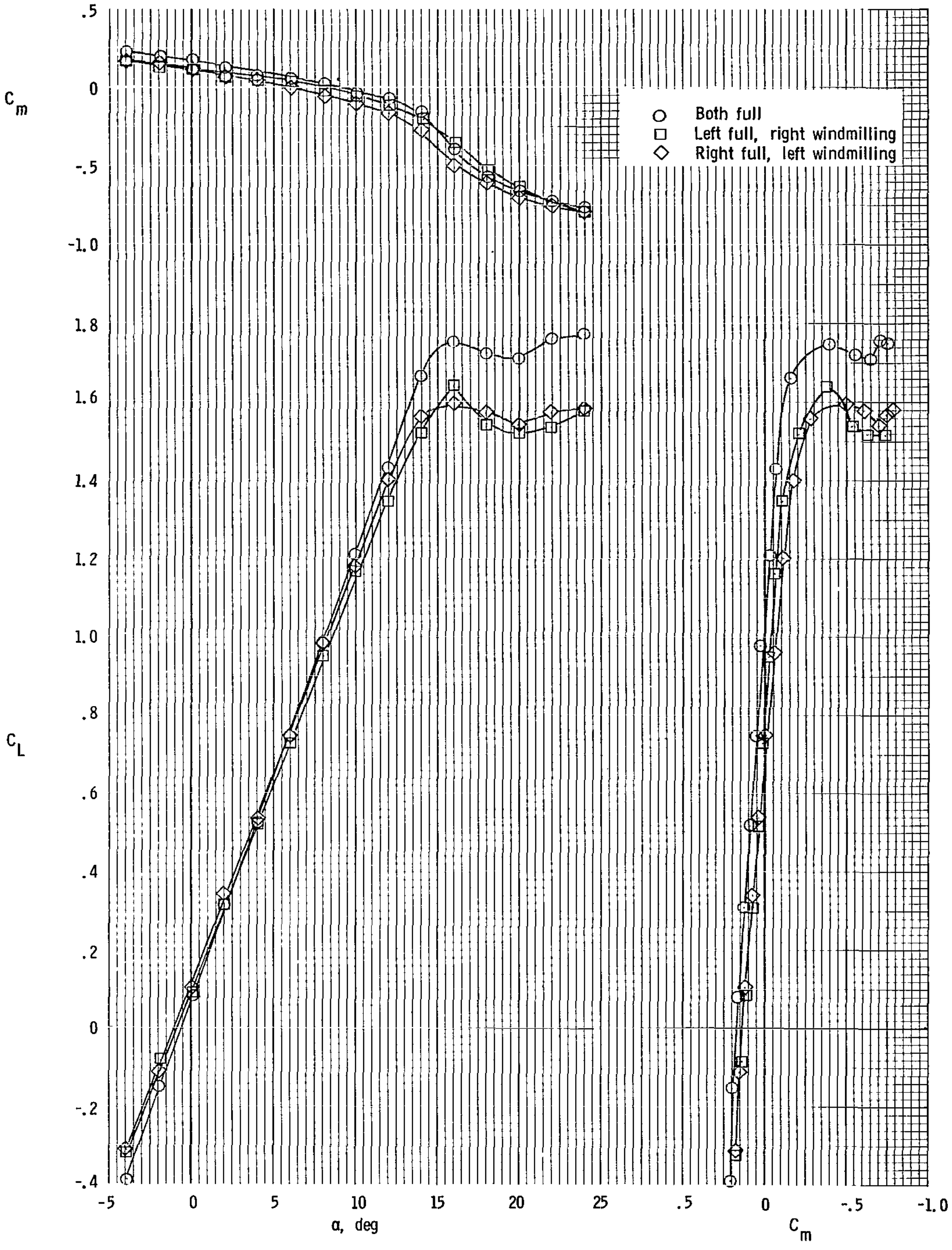

(a) $\delta_f = 0^o$.

Figure 13.- Effect of asymmetric power on longitudinal characteristics for $\beta = 0^o$; $\delta_e = 0^o$.

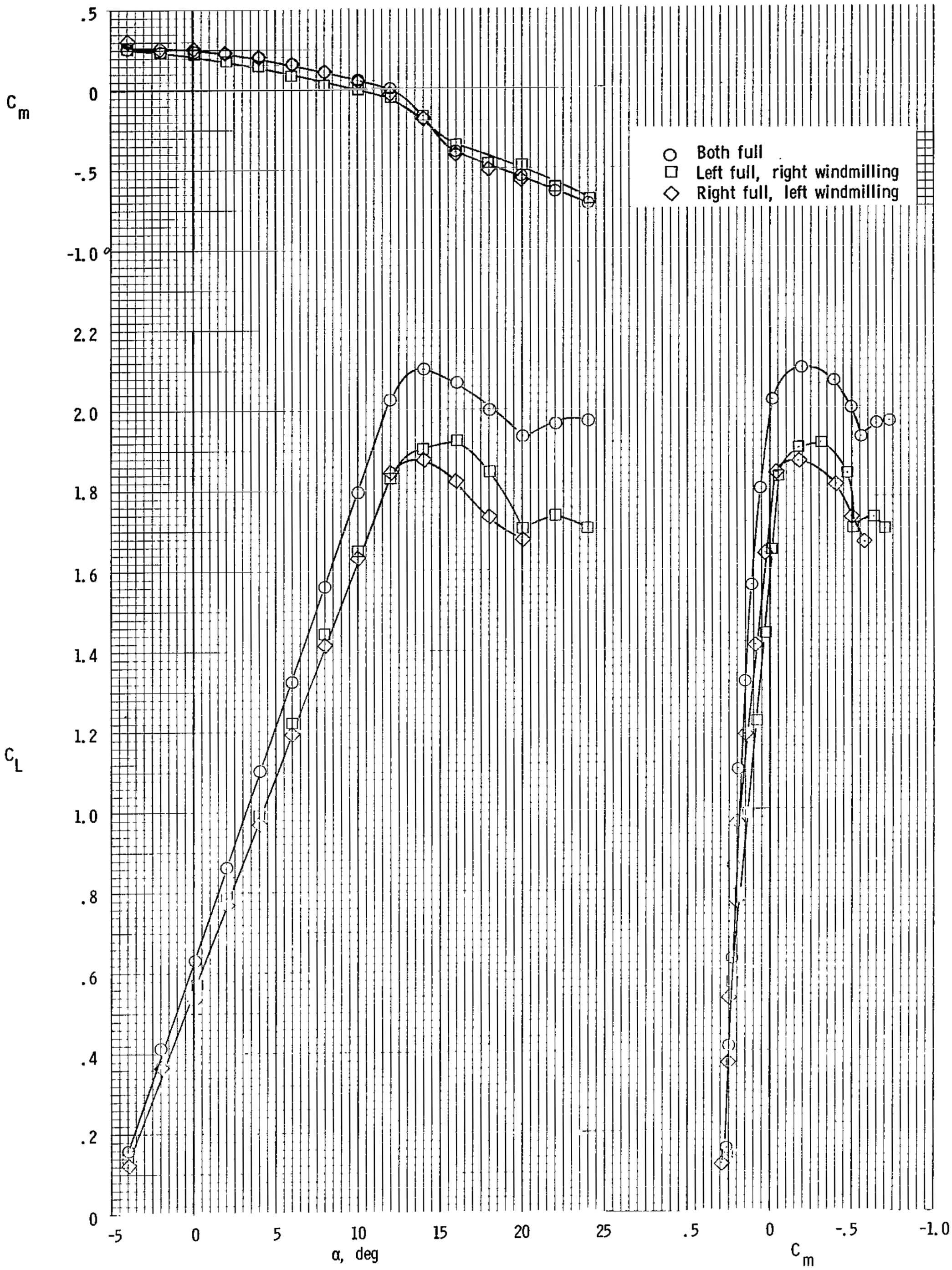

(b) $\delta_f = 35^0$.

Figure 13.- Concluded.

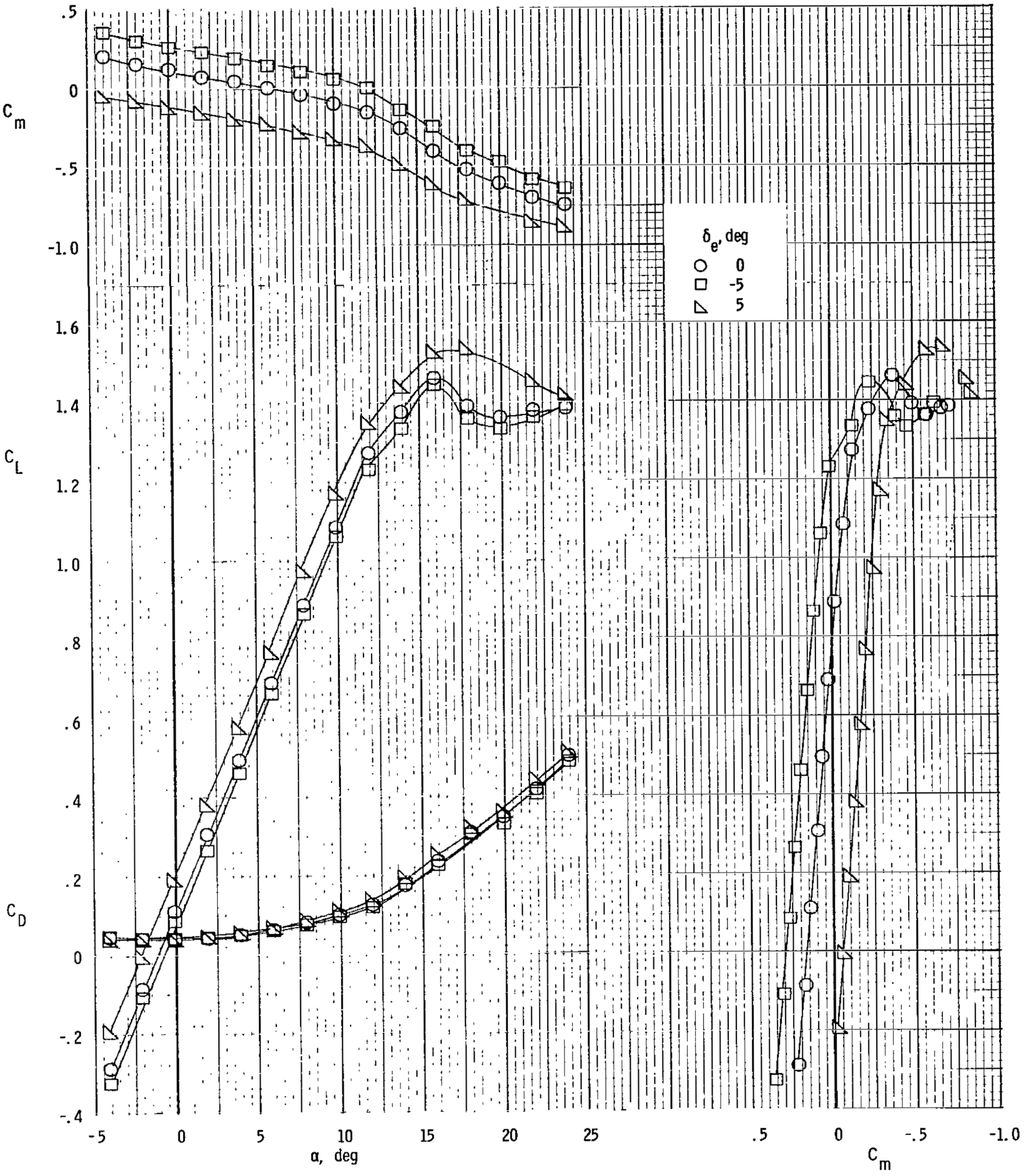

(a) $T'_c = 0$.

Figure 14.- Longitudinal aerodynamic characteristics of model with short nacelle for several thrust coefficients for $\delta_f = 0^0$.

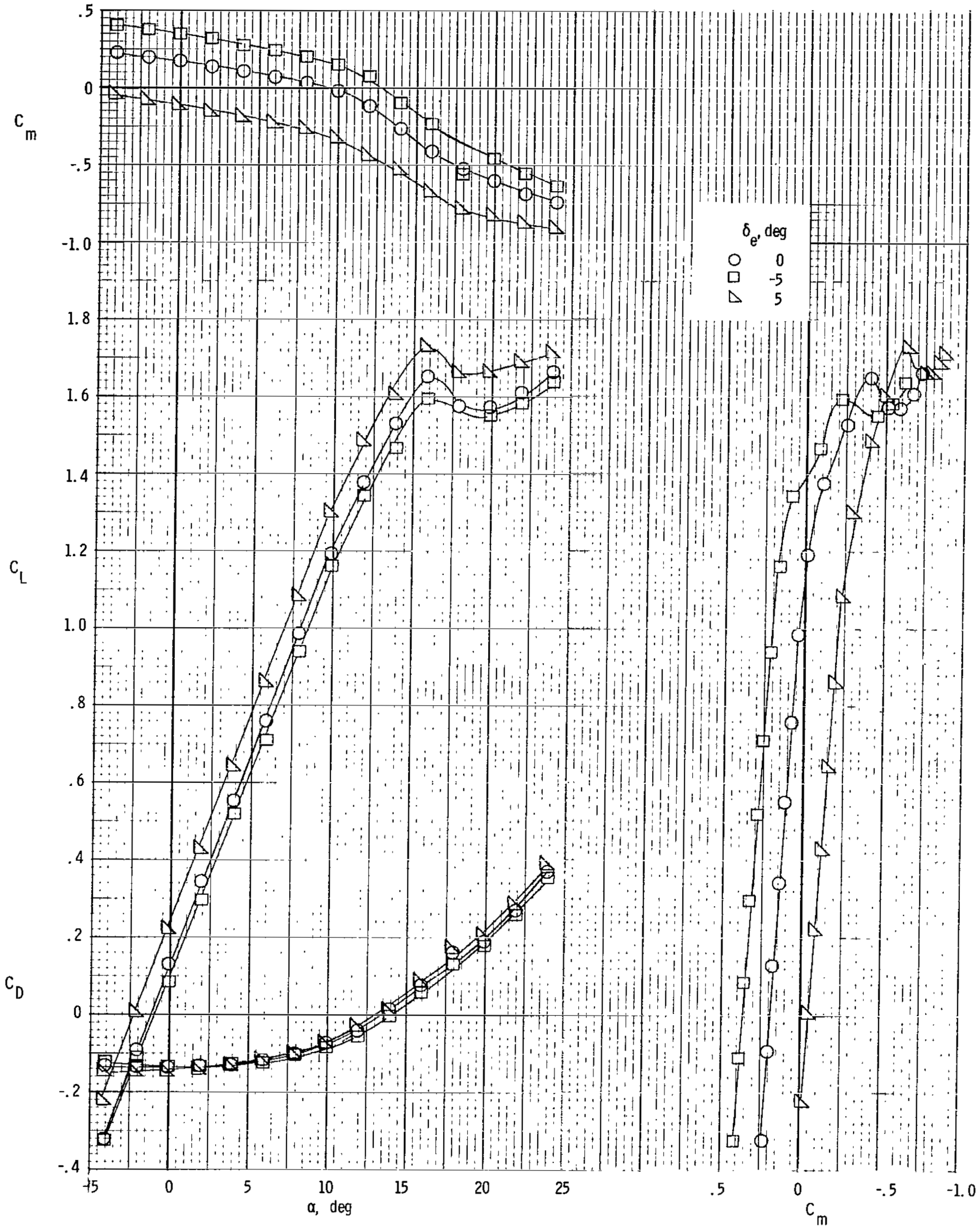

(b) $T_C' = 0.19$.

Figure 14.- Continued.

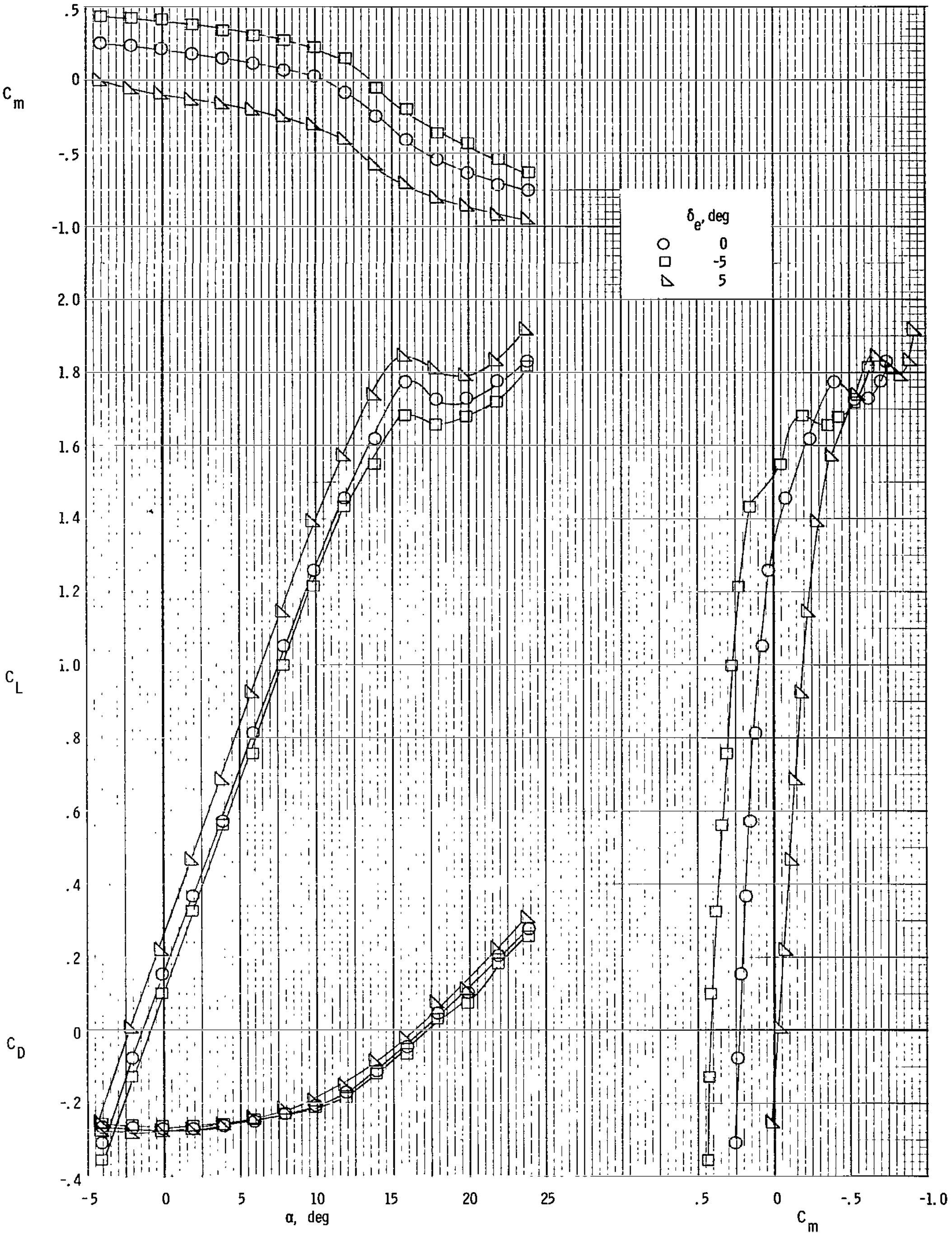

(c) $T'_C = 0.28$.

Figure 14.- Concluded.

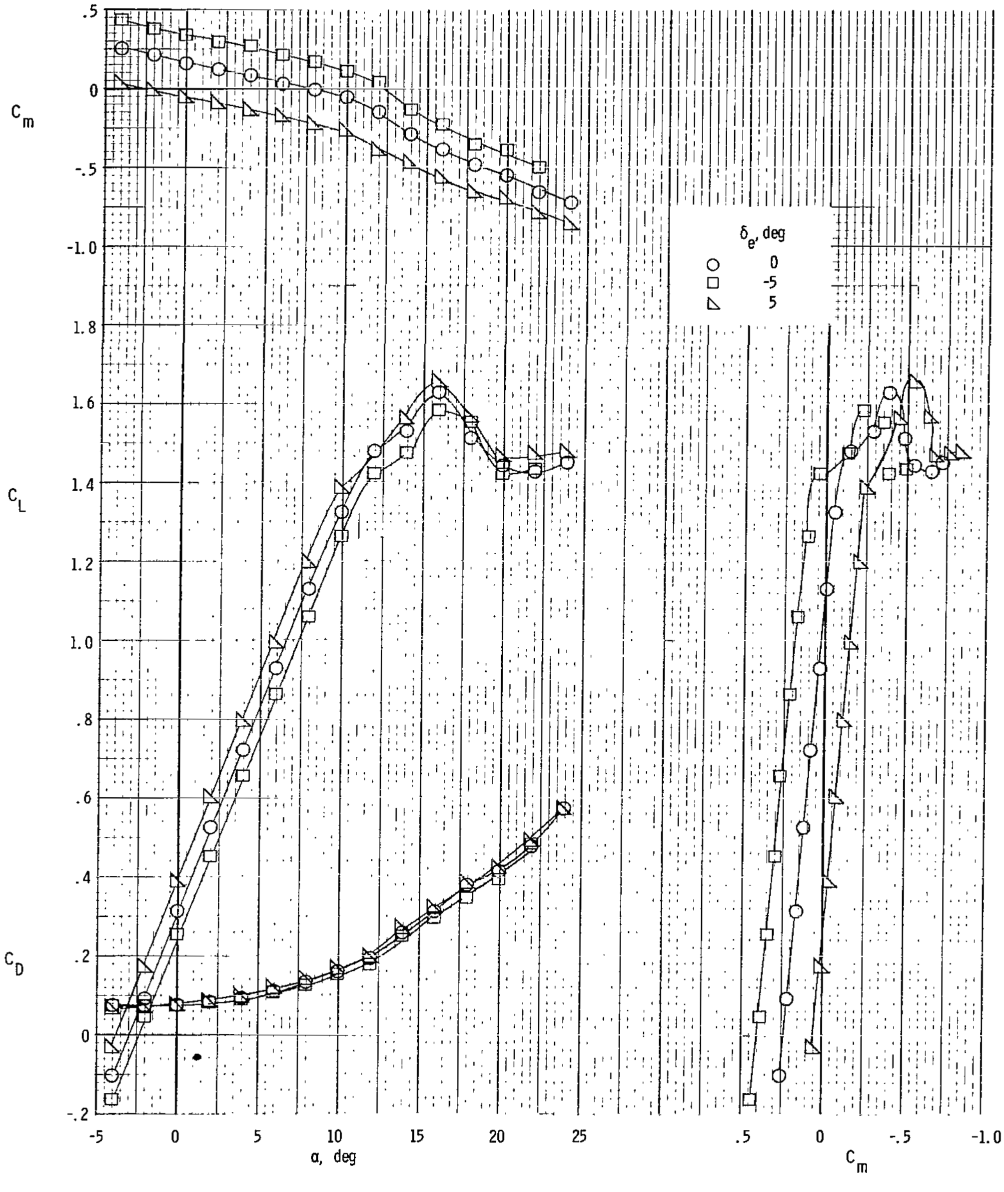

(a) $T'_c = 0$.

Figure 15.- Longitudinal aerodynamic characteristics of model with short nacelle for several thrust coefficients for $\delta_f = 15^\circ$.

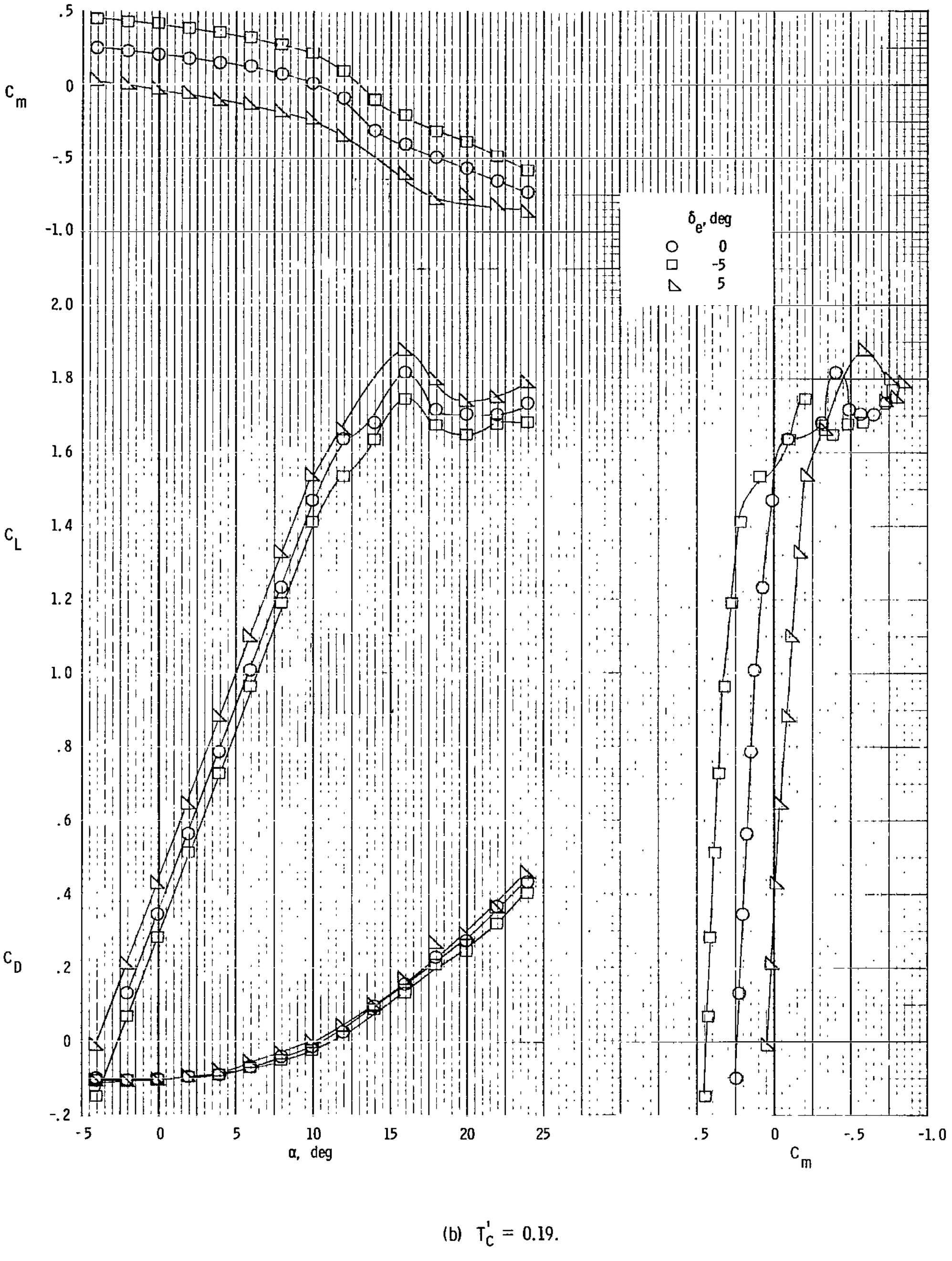

(b) $T_c' = 0.19$.

Figure 15.- Continued.

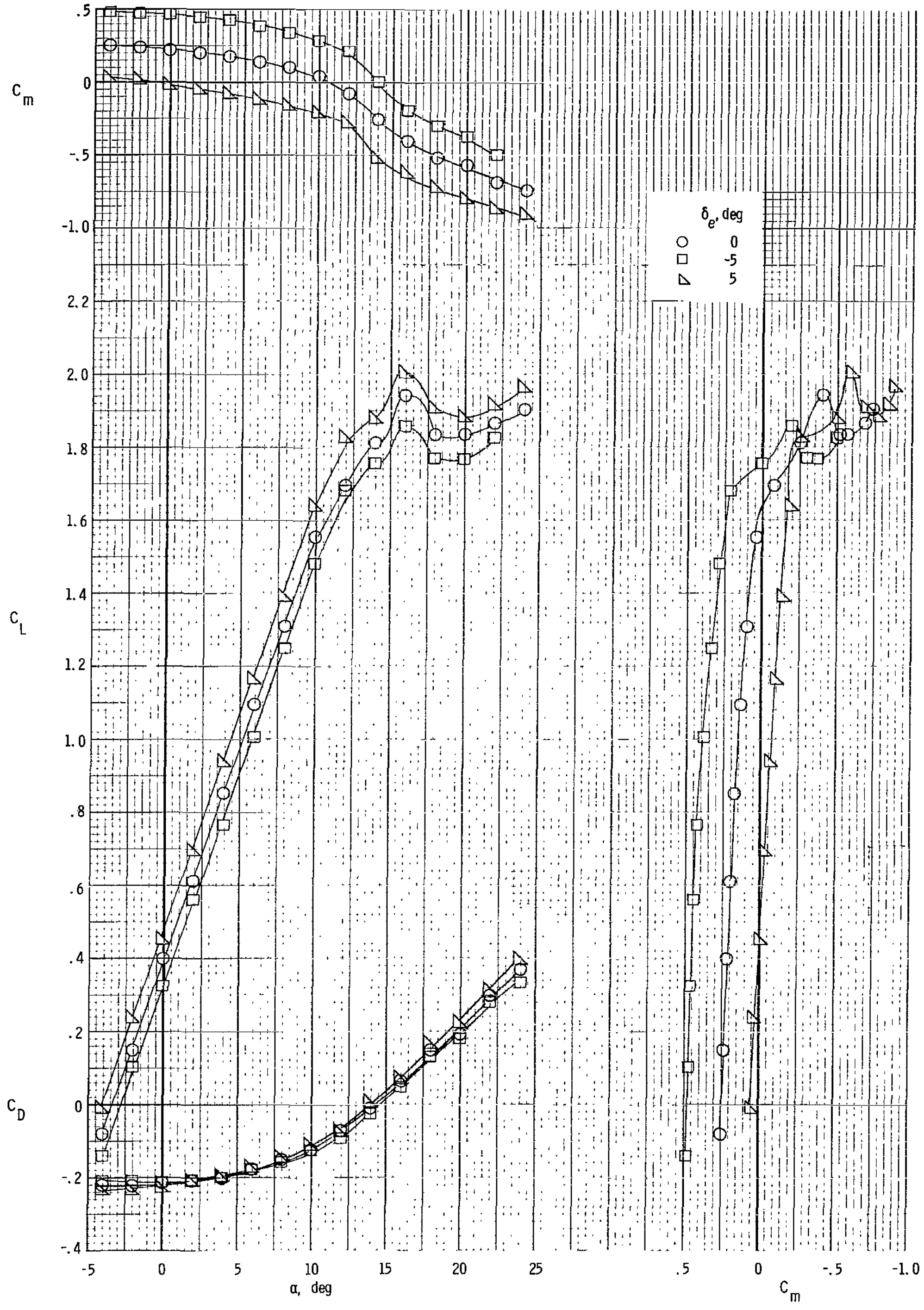

(c) $T_C' = 0.28$.

Figure 15.- Concluded.

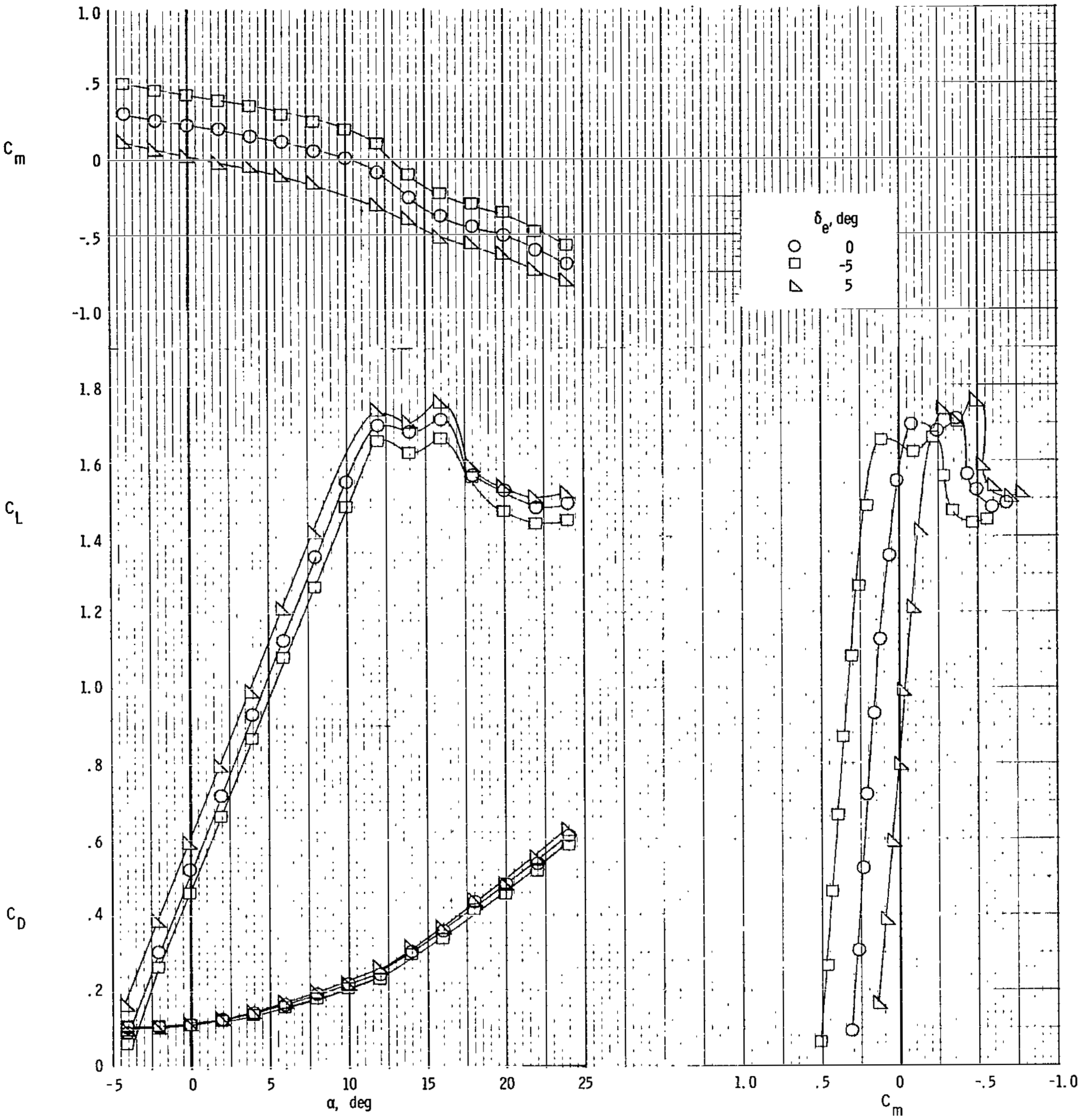

(a) $T_c' = 0$.

Figure 16.- Longitudinal aerodynamic characteristics of model with short nacelle for several thrust coefficients for $\delta_f = 35^0$.

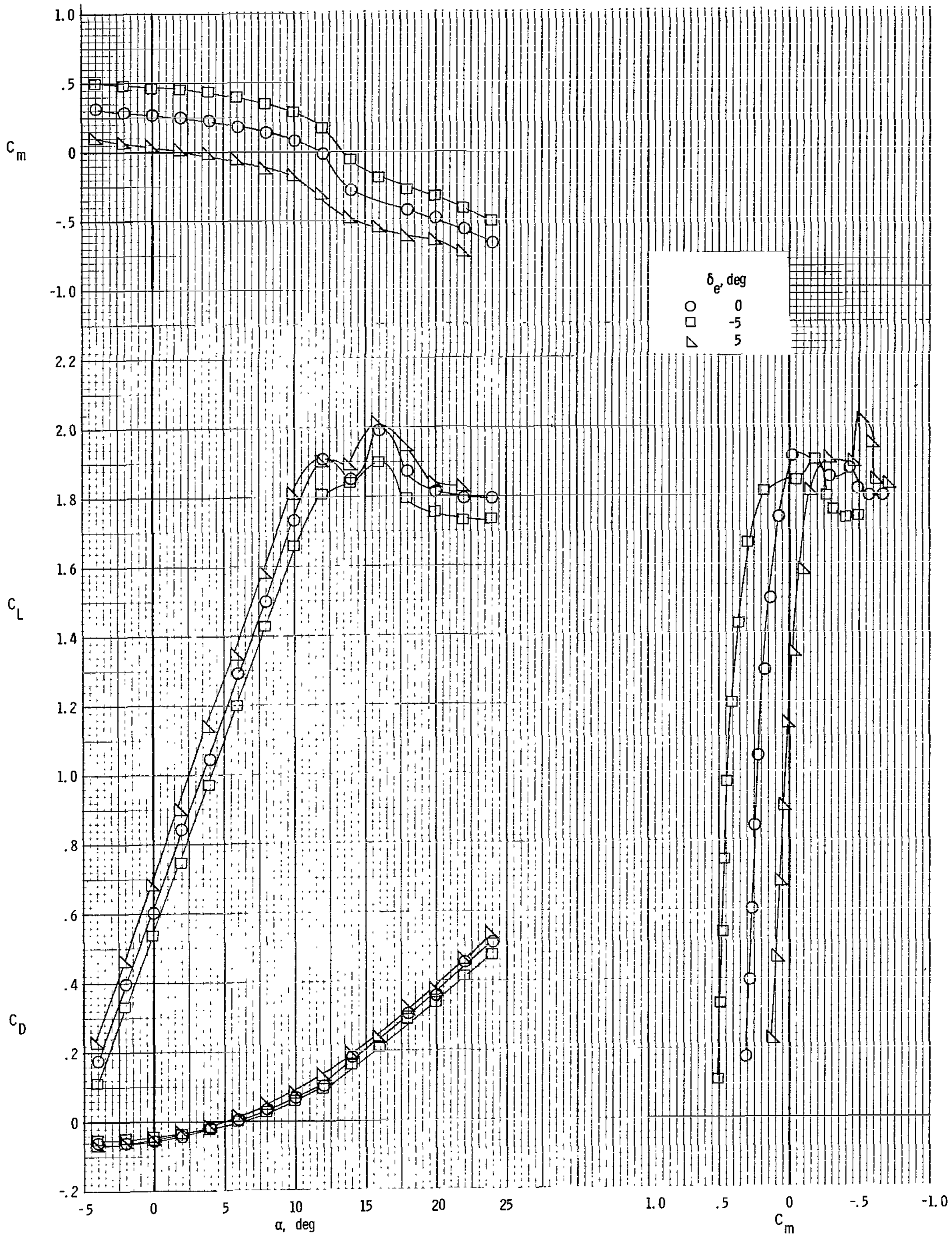

(b) $T_c' = 0.19$.

Figure 16.- Continued.

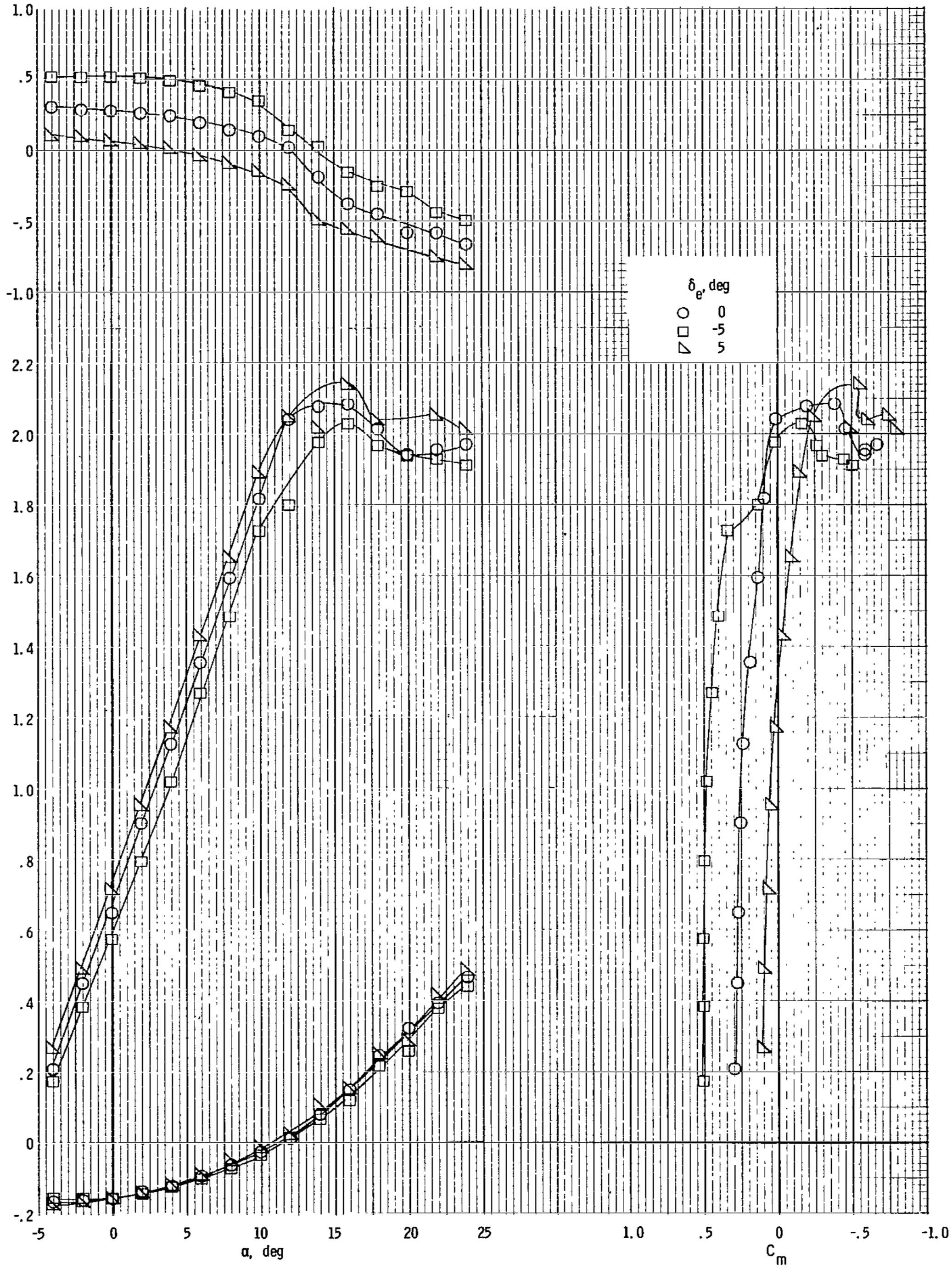

(c) $T_C' = 0.28$.

Figure 16.- Concluded.

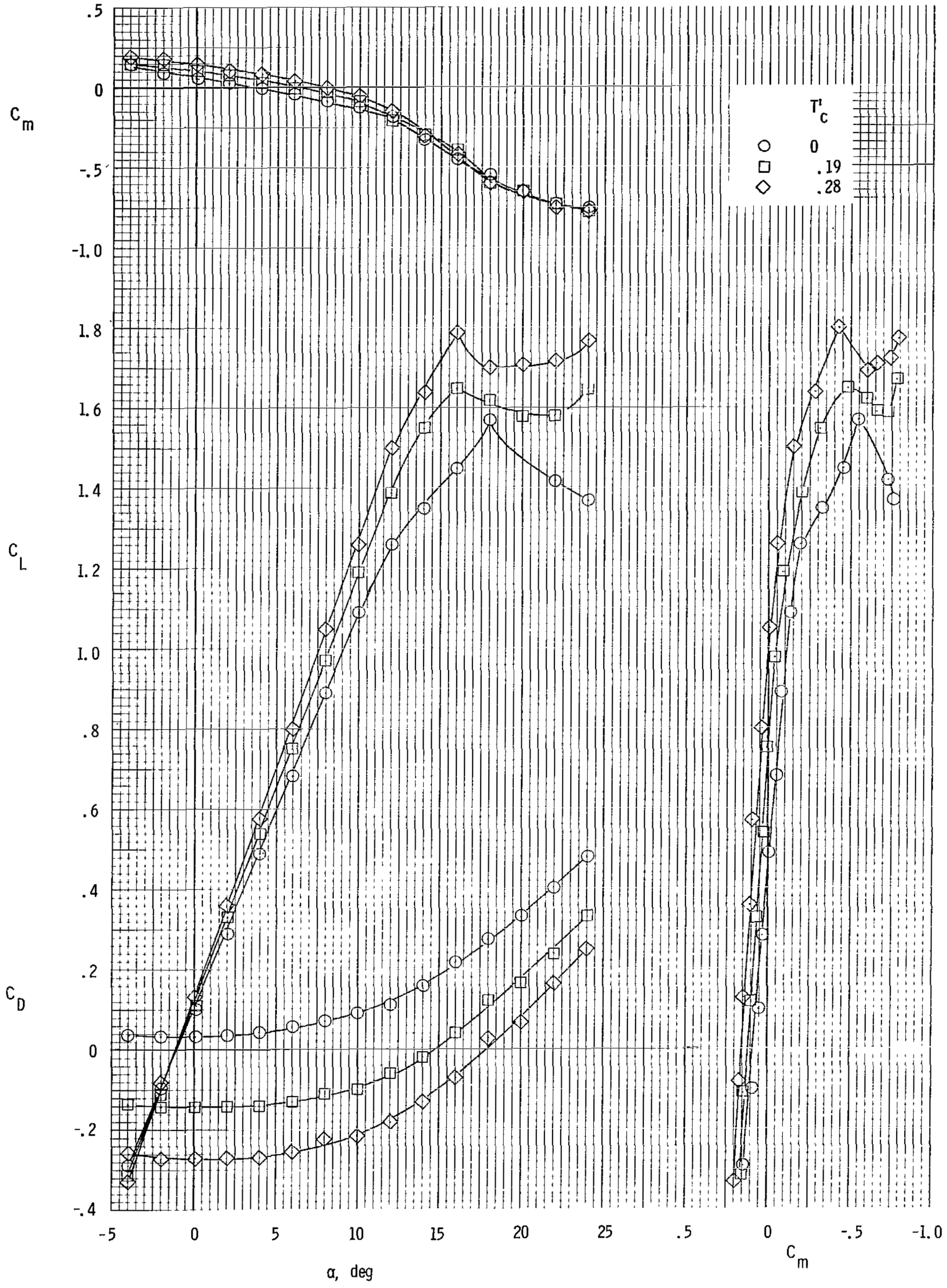

Figure 17.- Longitudinal aerodynamic characteristics of model with cowl modification. $\delta_f = 0^0$; $\beta = 0^0$; $\delta_e = 0^0$.

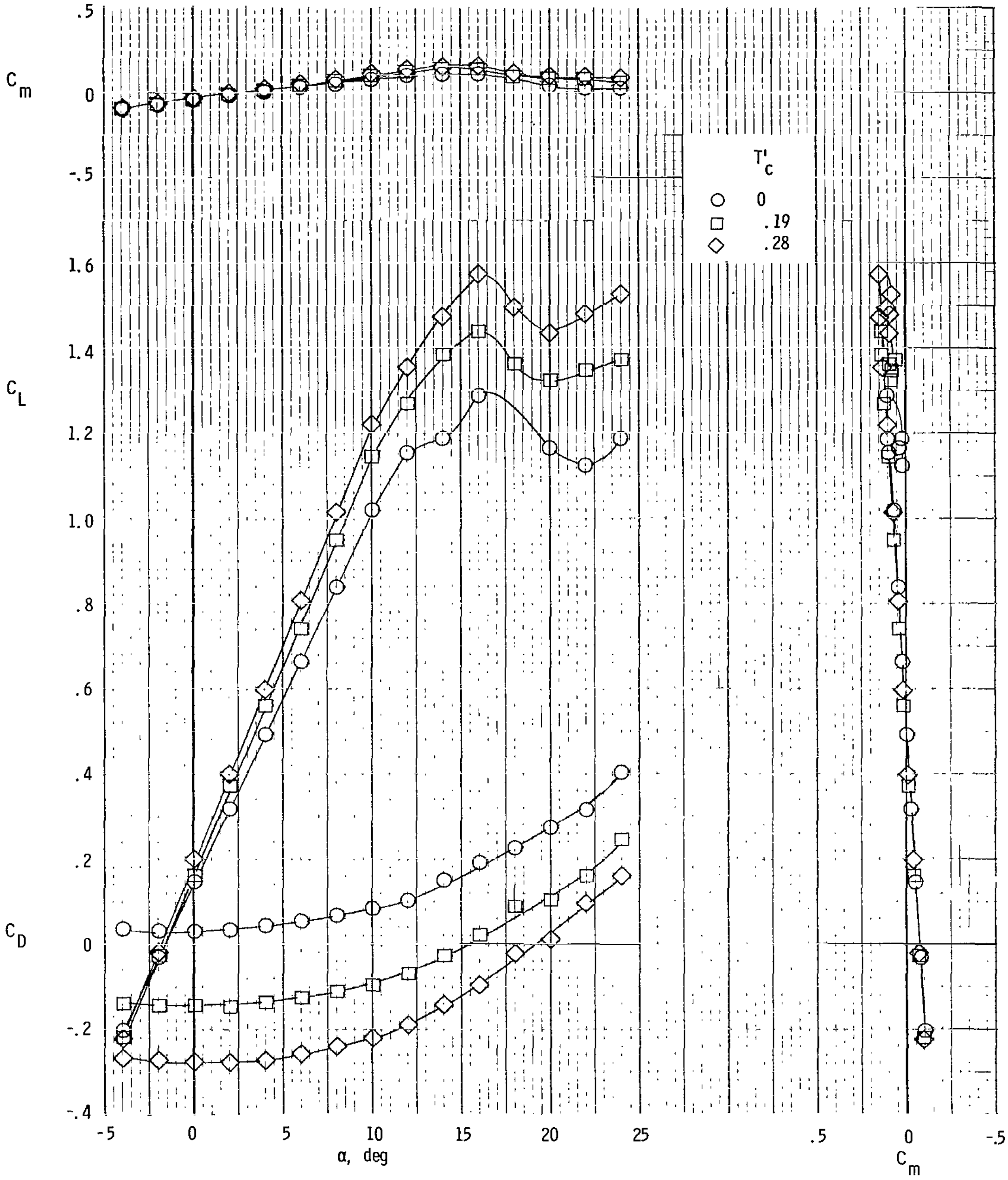

(a) $\delta_f = 0^0$.

Figure 18.- Longitudinal aerodynamic characteristics of model with horizontal tail removed for several flap deflections.

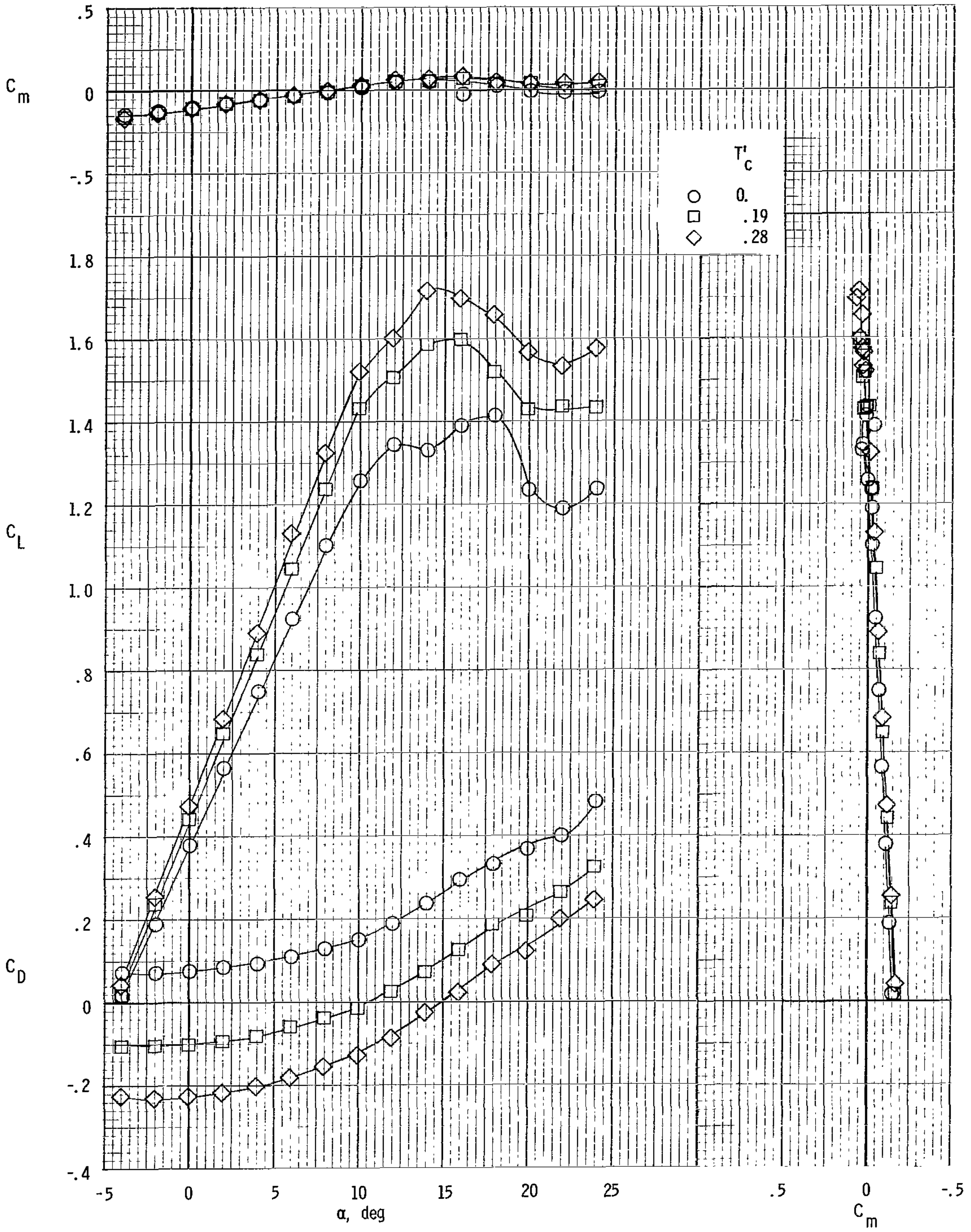

(b) $\delta_f = 15^0$.

Figure 18.- Continued.

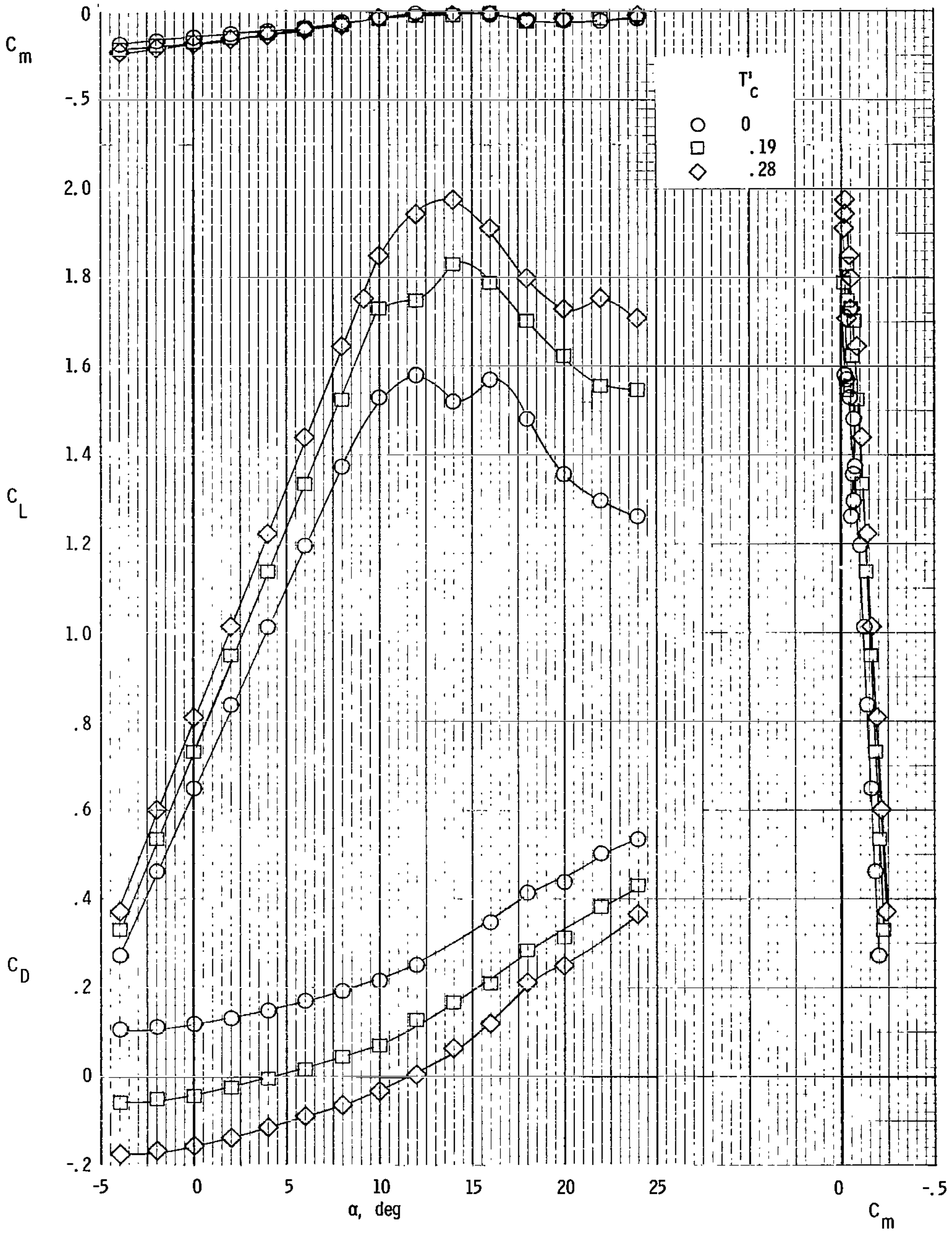

(c) $\delta_f = 35^0$.

Figure 18.- Concluded.

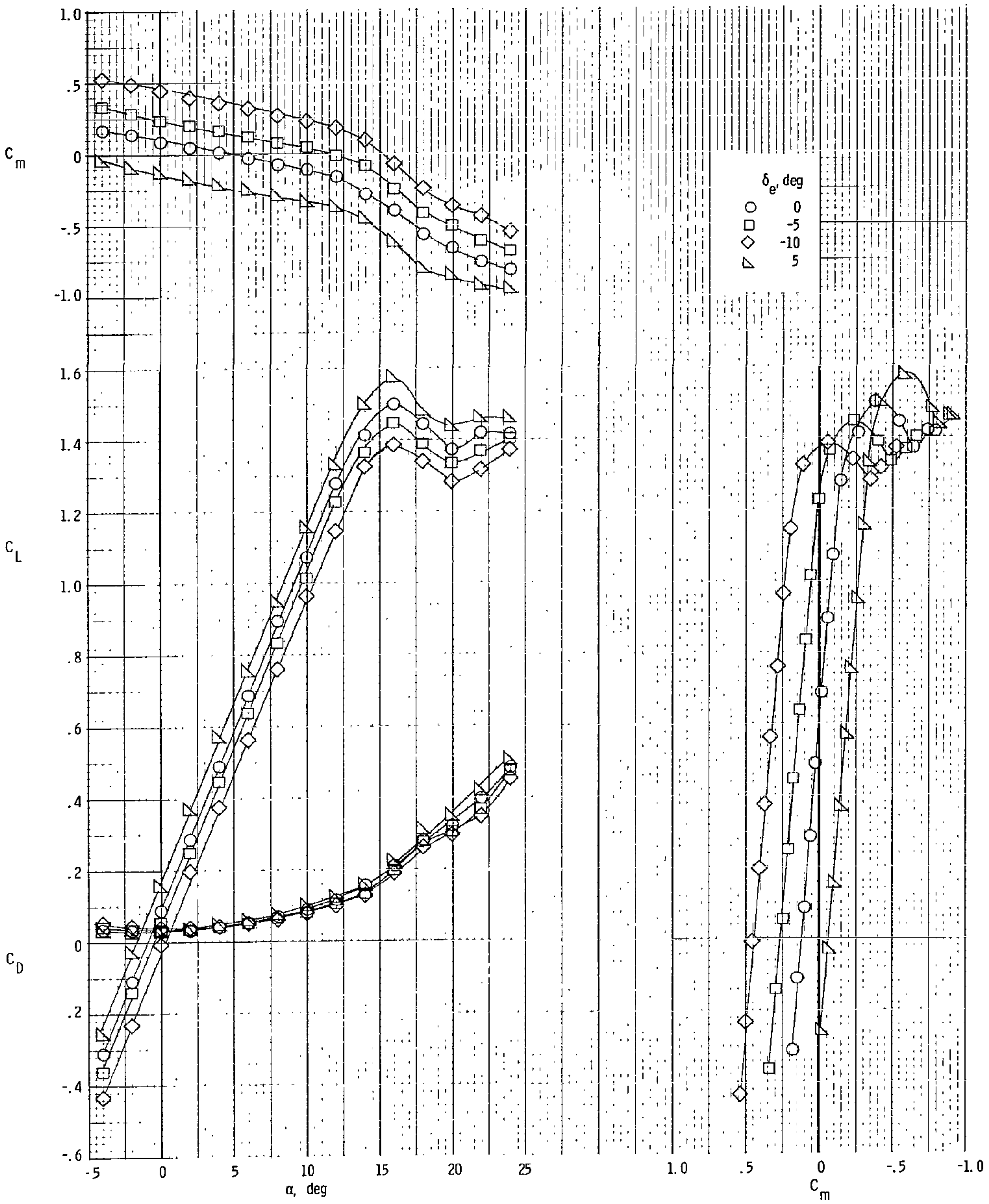

(a) $T_c' = 0$.

Figure 19.- Longitudinal aerodynamic characteristics of model with smooth ice on horizontal tail for $\delta_f = 0^0$.

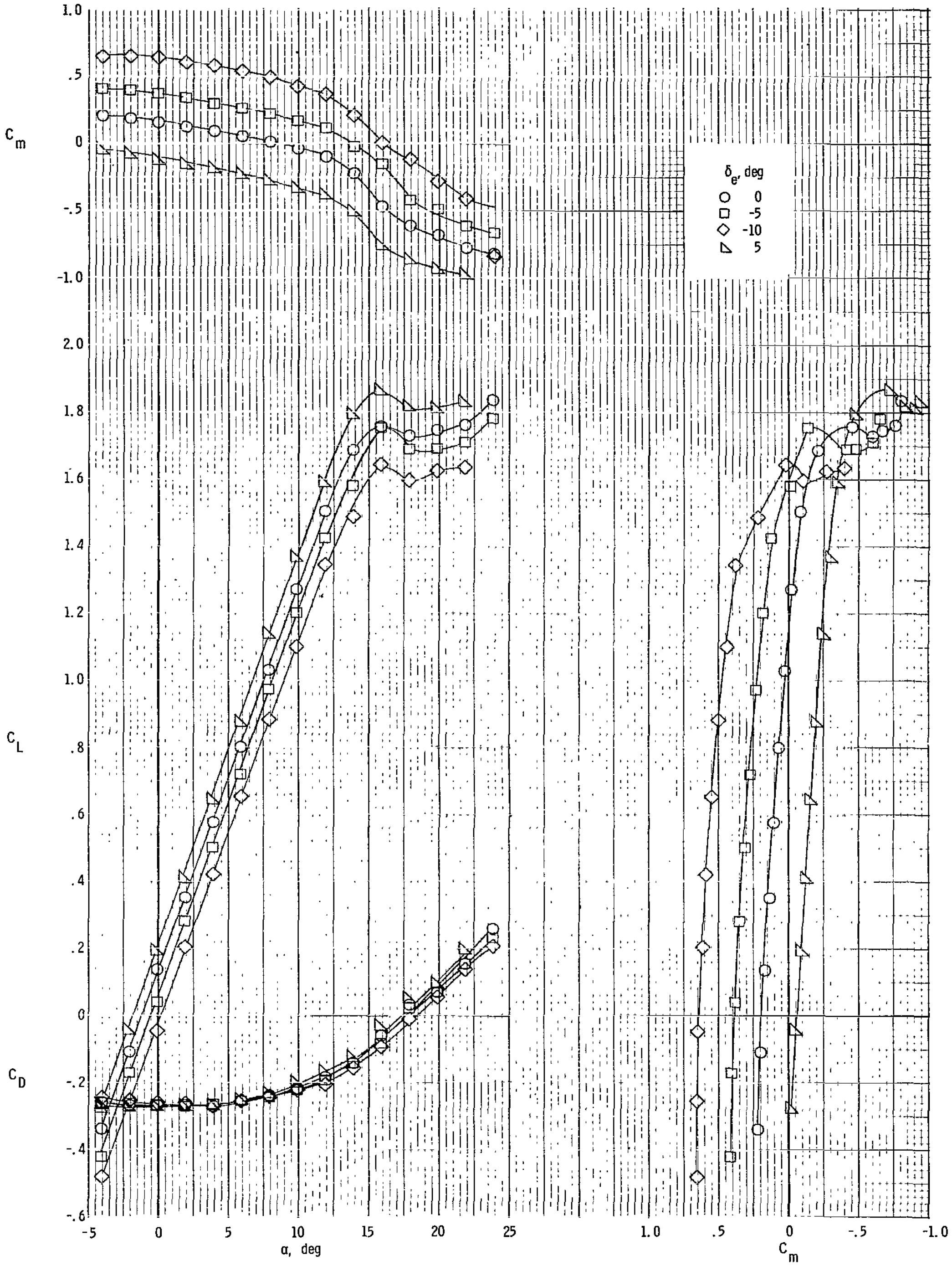

(b) $T_c' = 0.28$.

Figure 19.- Concluded.

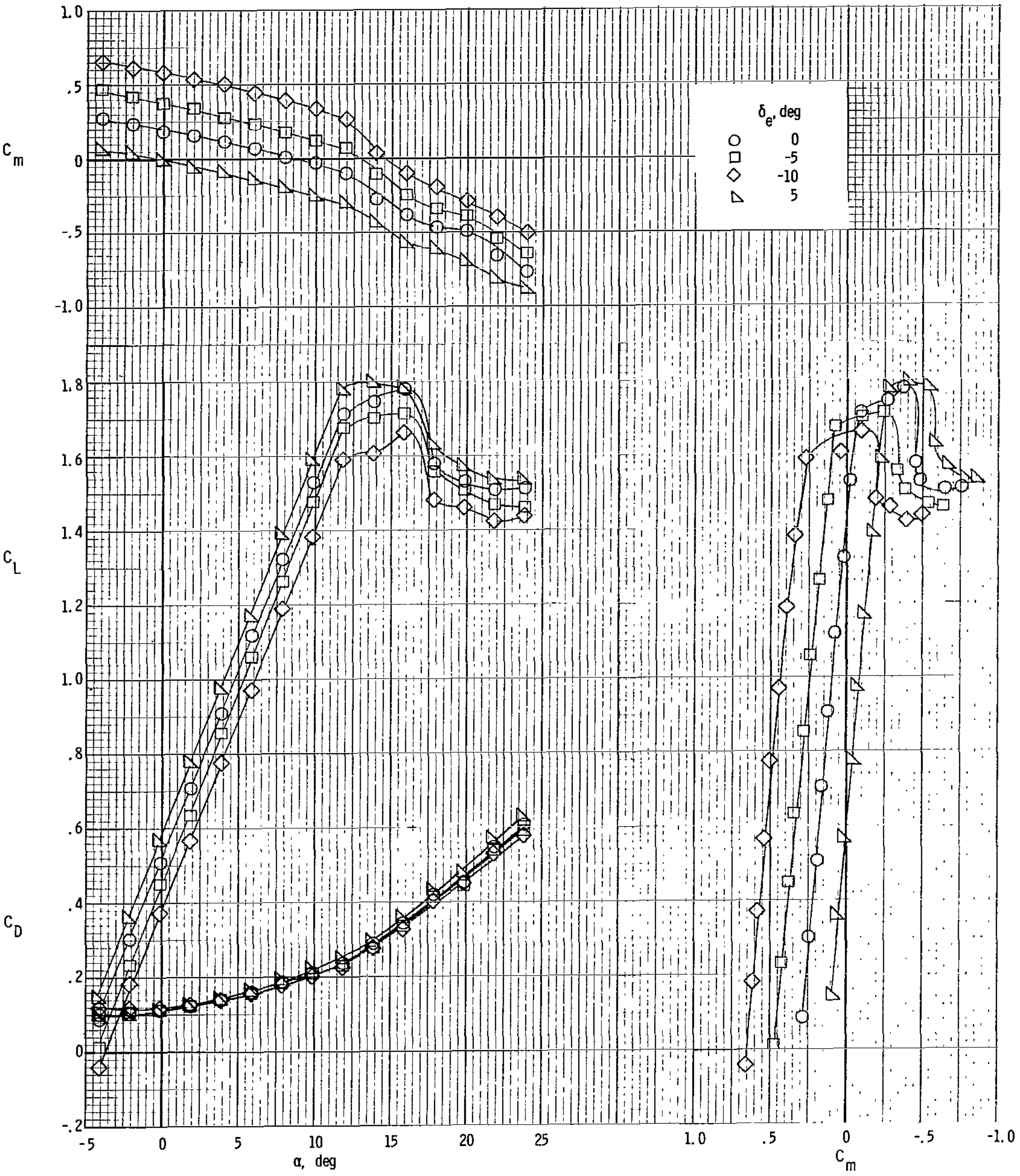

(a) $T_c' = 0$.

Figure 20.- Longitudinal aerodynamic characteristics of model with smooth ice on horizontal tail for $\delta_f = 35^0$.

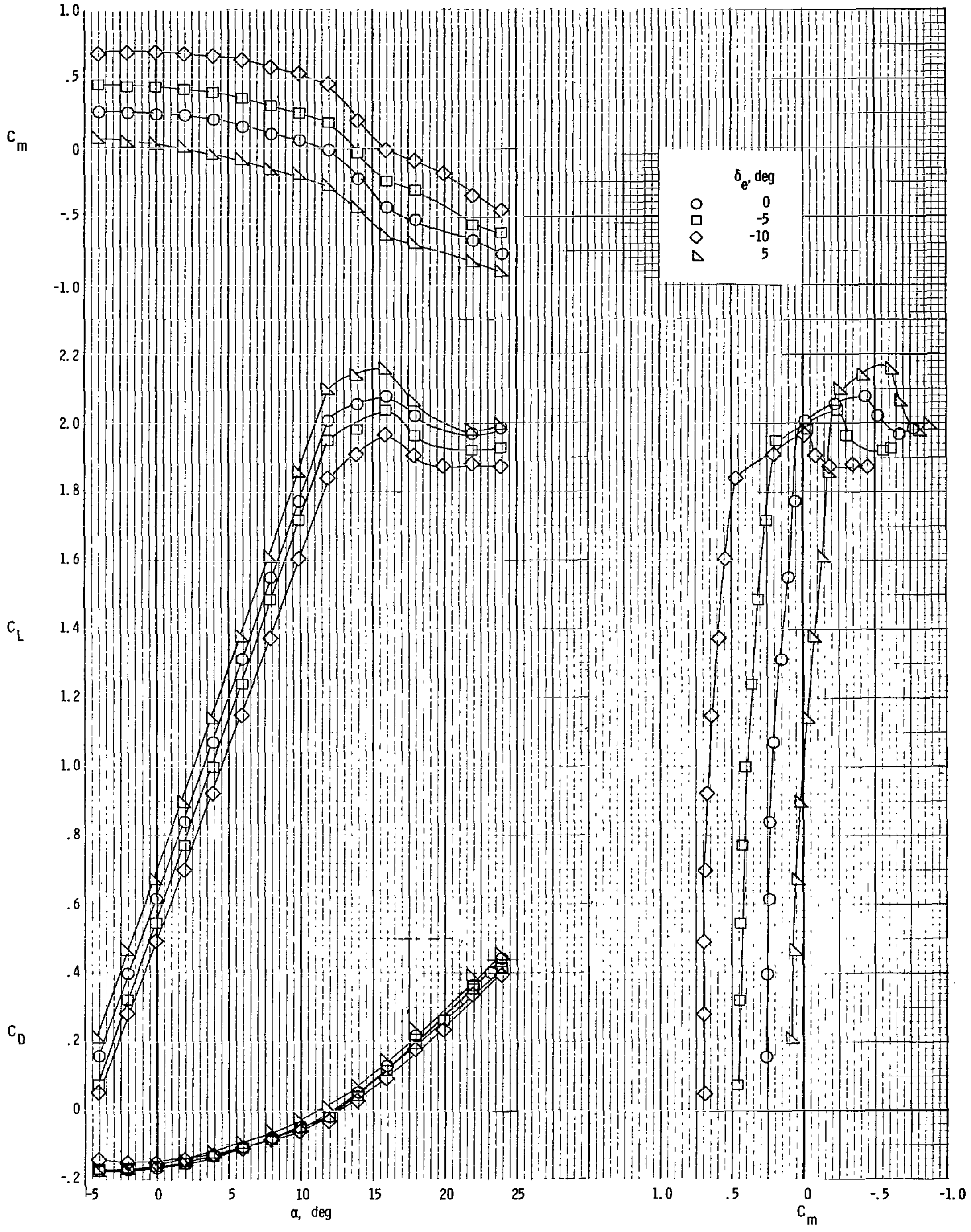

(b) $T_C' = 0.28$.

Figure 20.- Concluded.

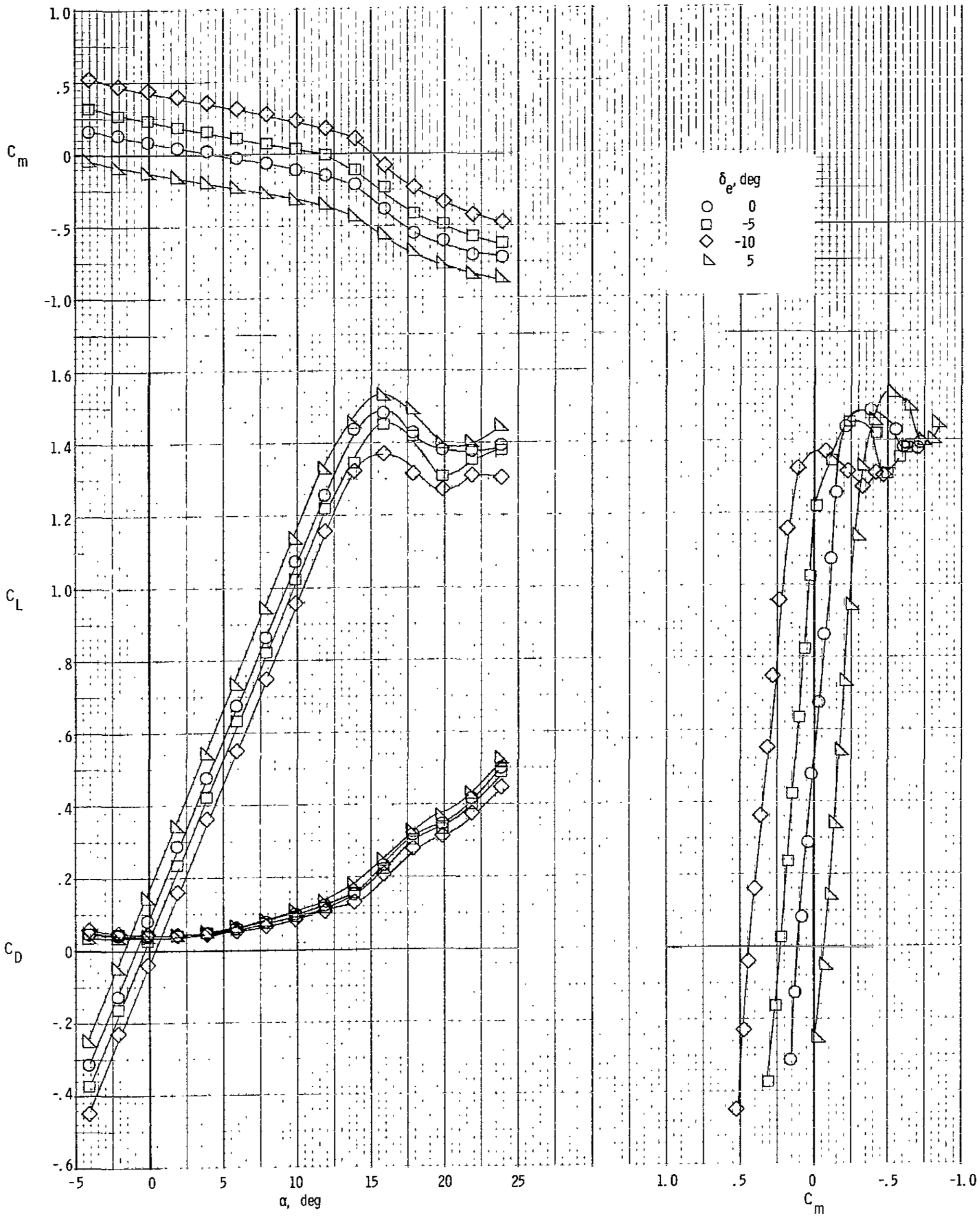

(a) $T'_c = 0$.

Figure 21.- Longitudinal aerodynamic characteristics of model with rime ice on horizontal tail for $\delta_f = 0^0$.

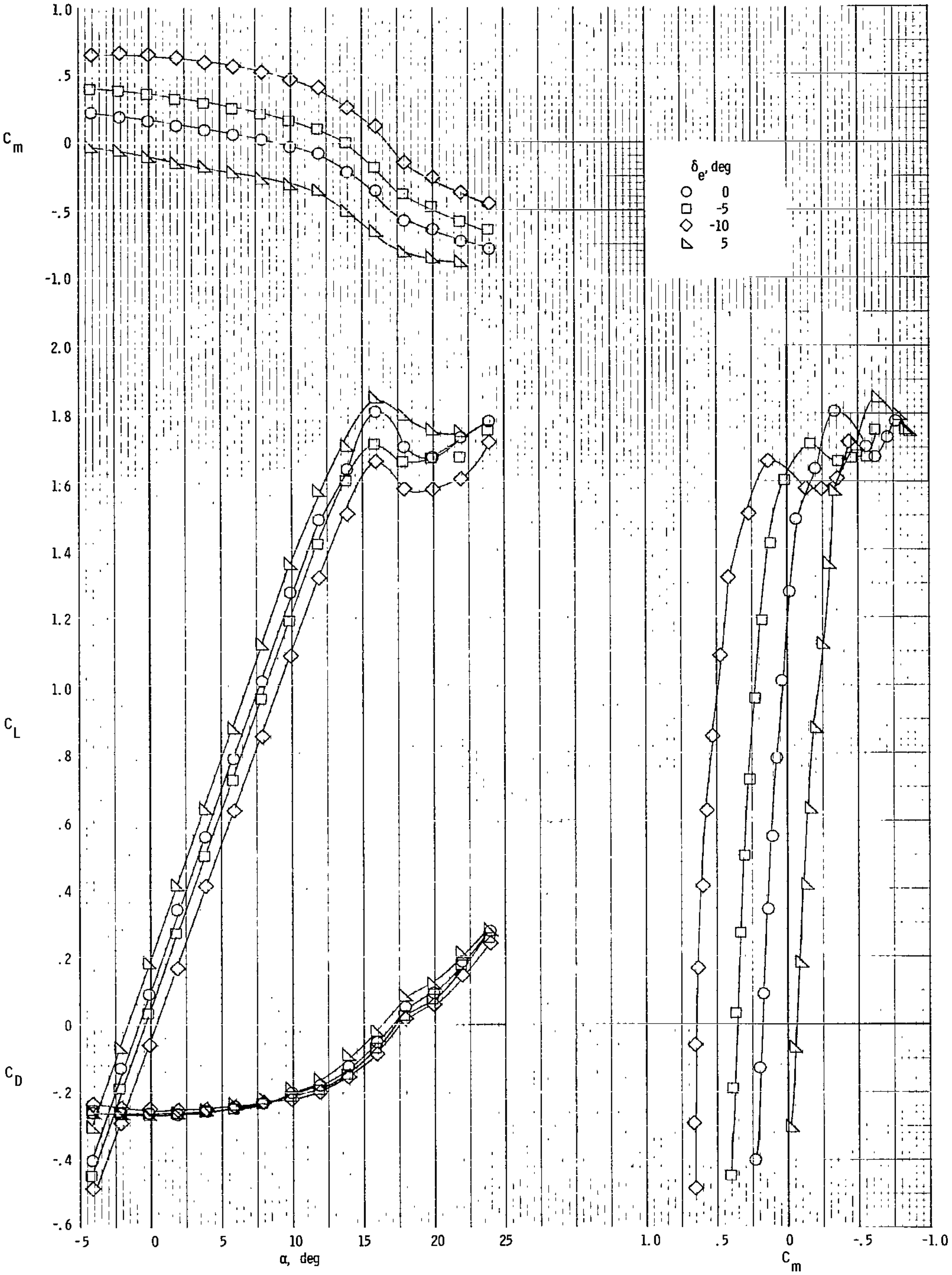

(b) $T_C' = 0.28$.

Figure 21.- Concluded.

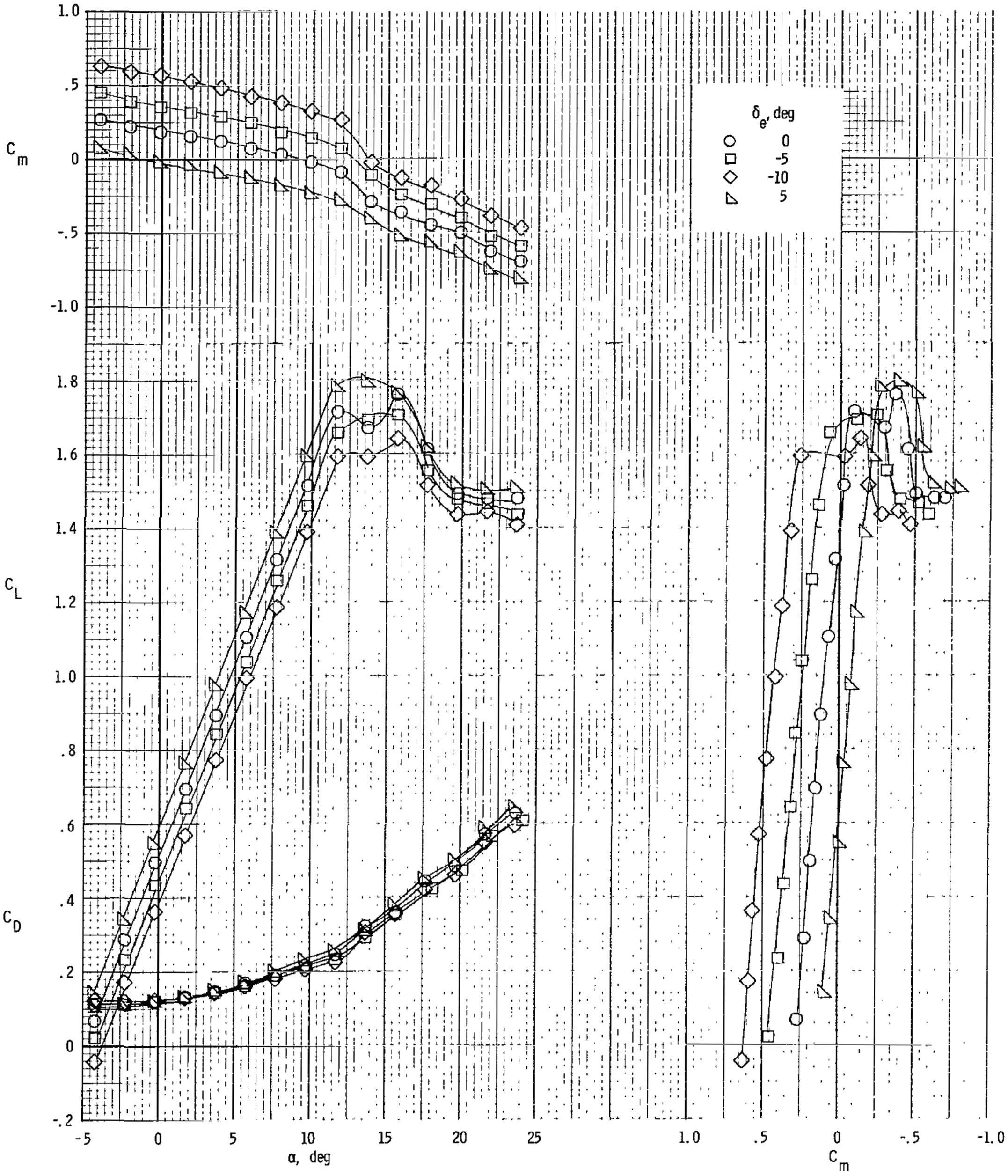

(a) $T_C' = 0$.

Figure 22.- Longitudinal aerodynamic characteristics of model with rime ice on horizontal tail for $\delta_f = 35^0$.

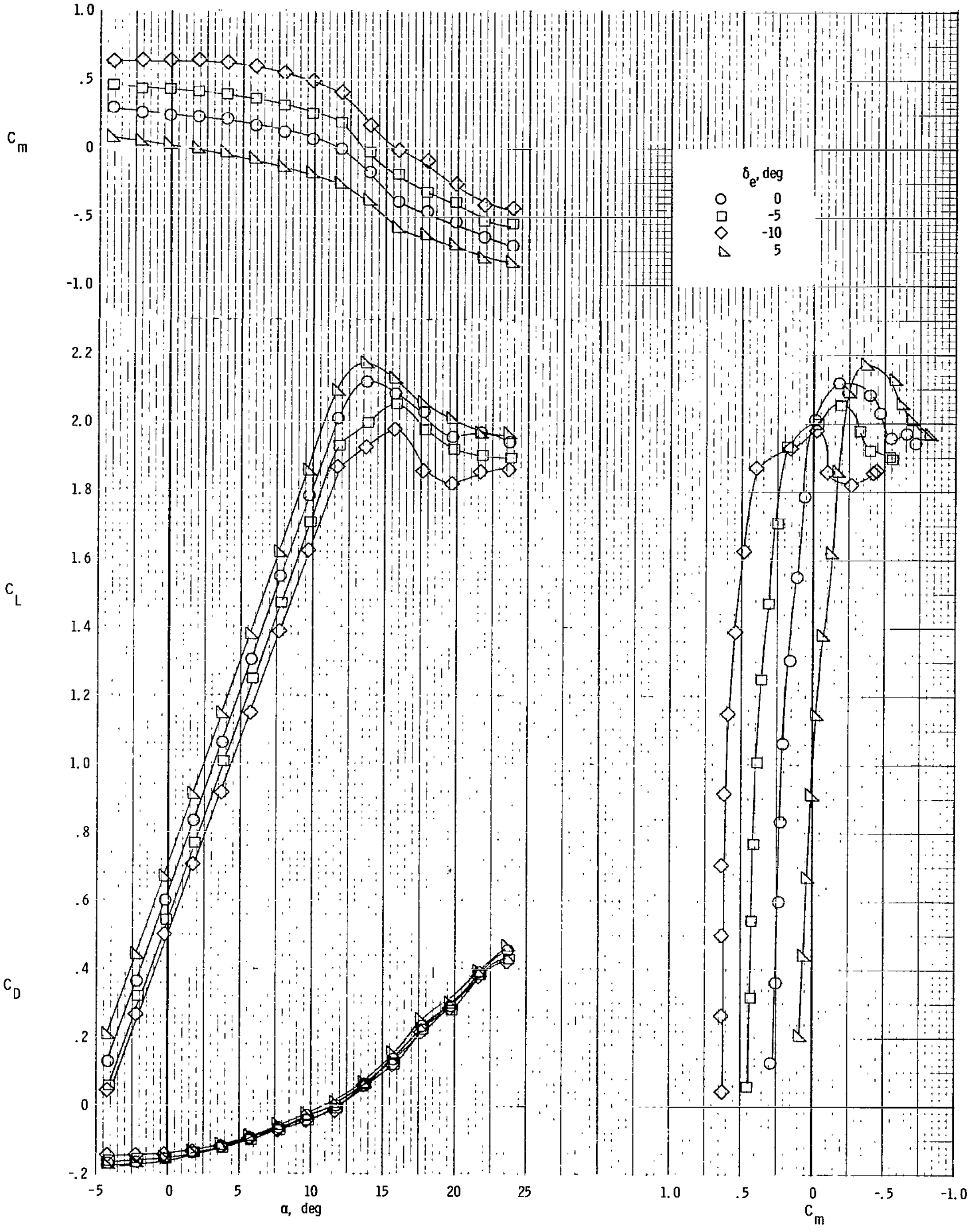

(b) $T'_C = 0.28$.

Figure 22.- Concluded.

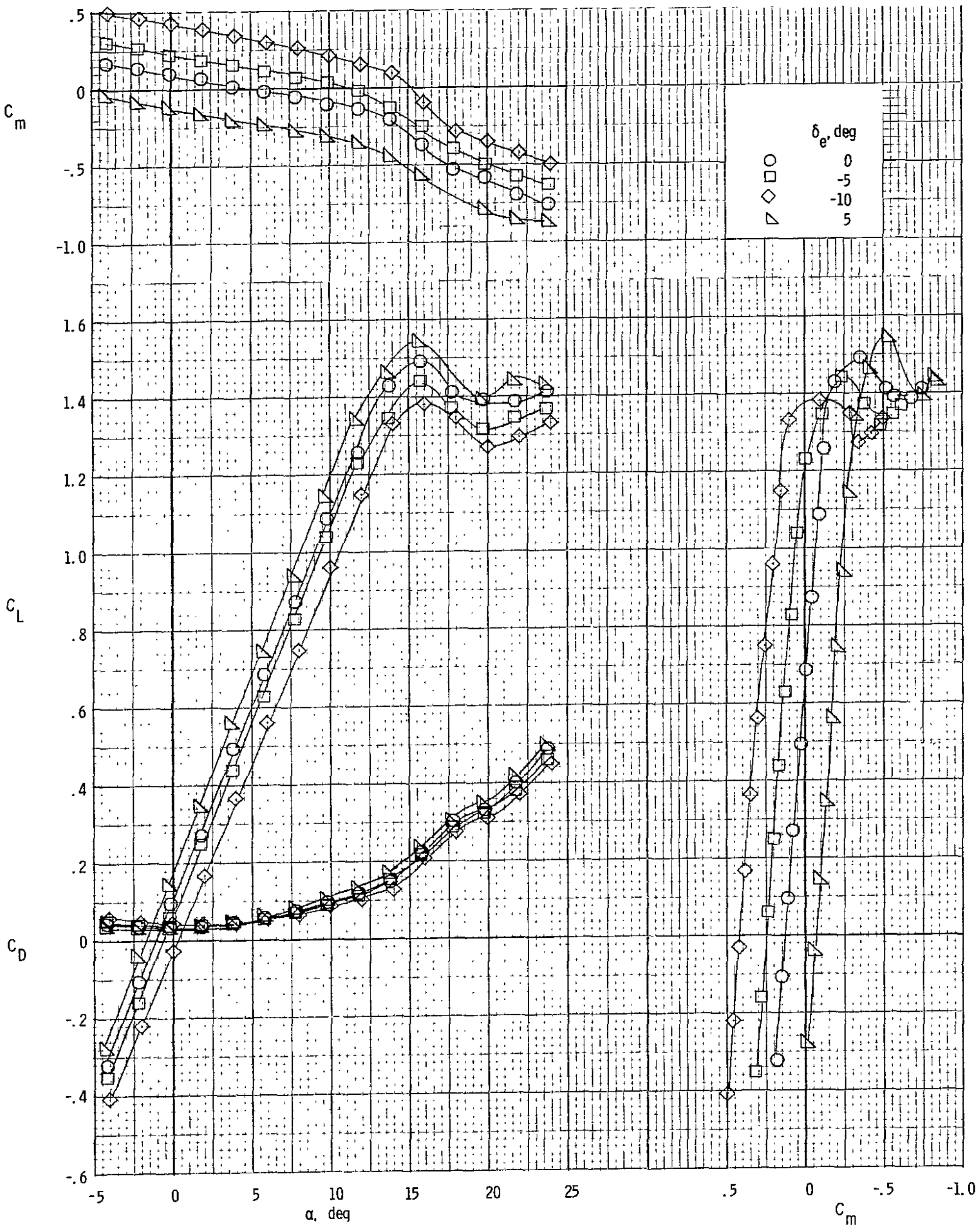

(a) $T'_c = 0$.

Figure 23.- Longitudinal aerodynamic characteristics of model with glaze ice on horizontal tail for $\delta_f = 0^0$.

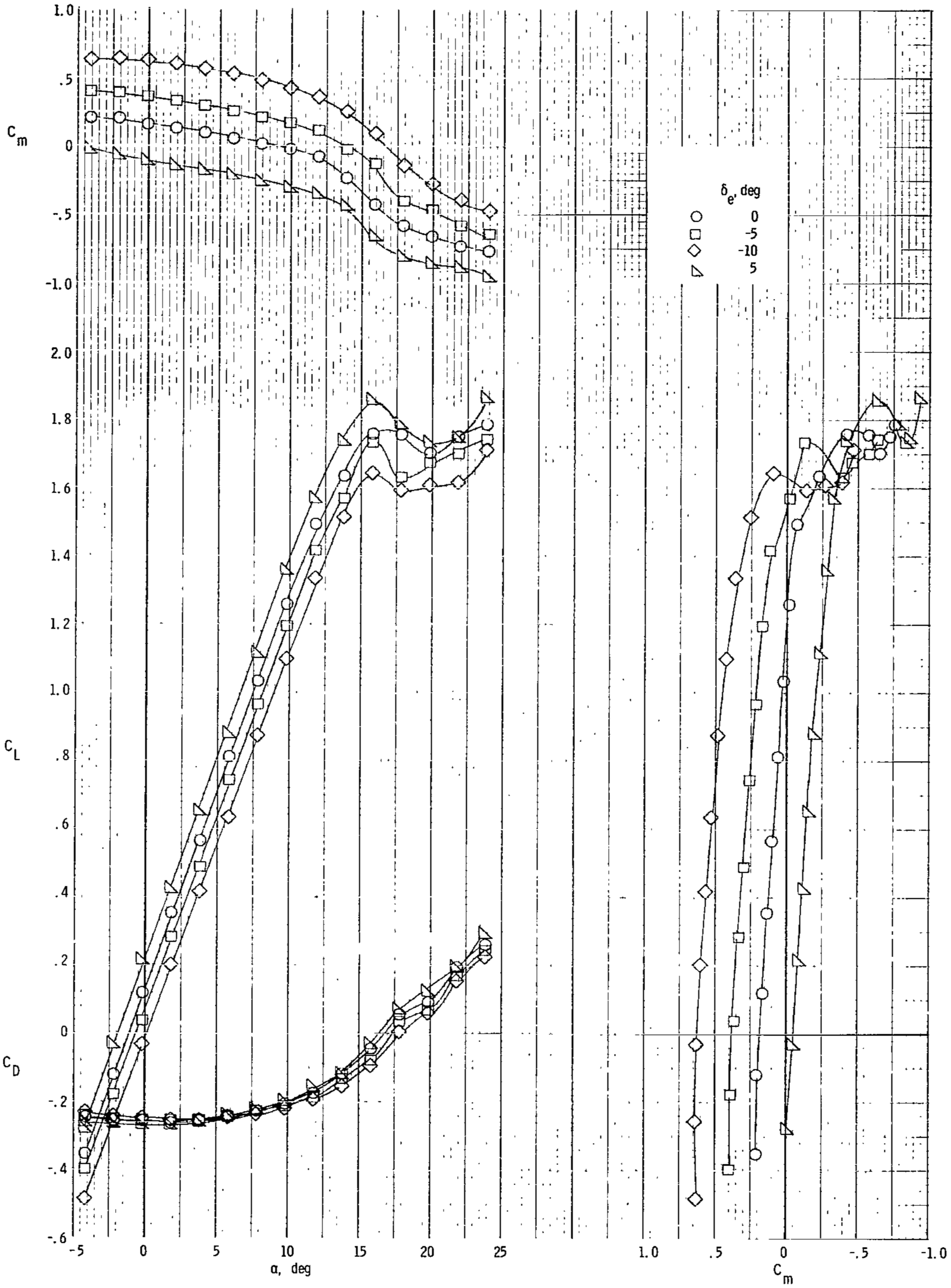

(b) $T'_C = 0.28$.

Figure 23.- Concluded.

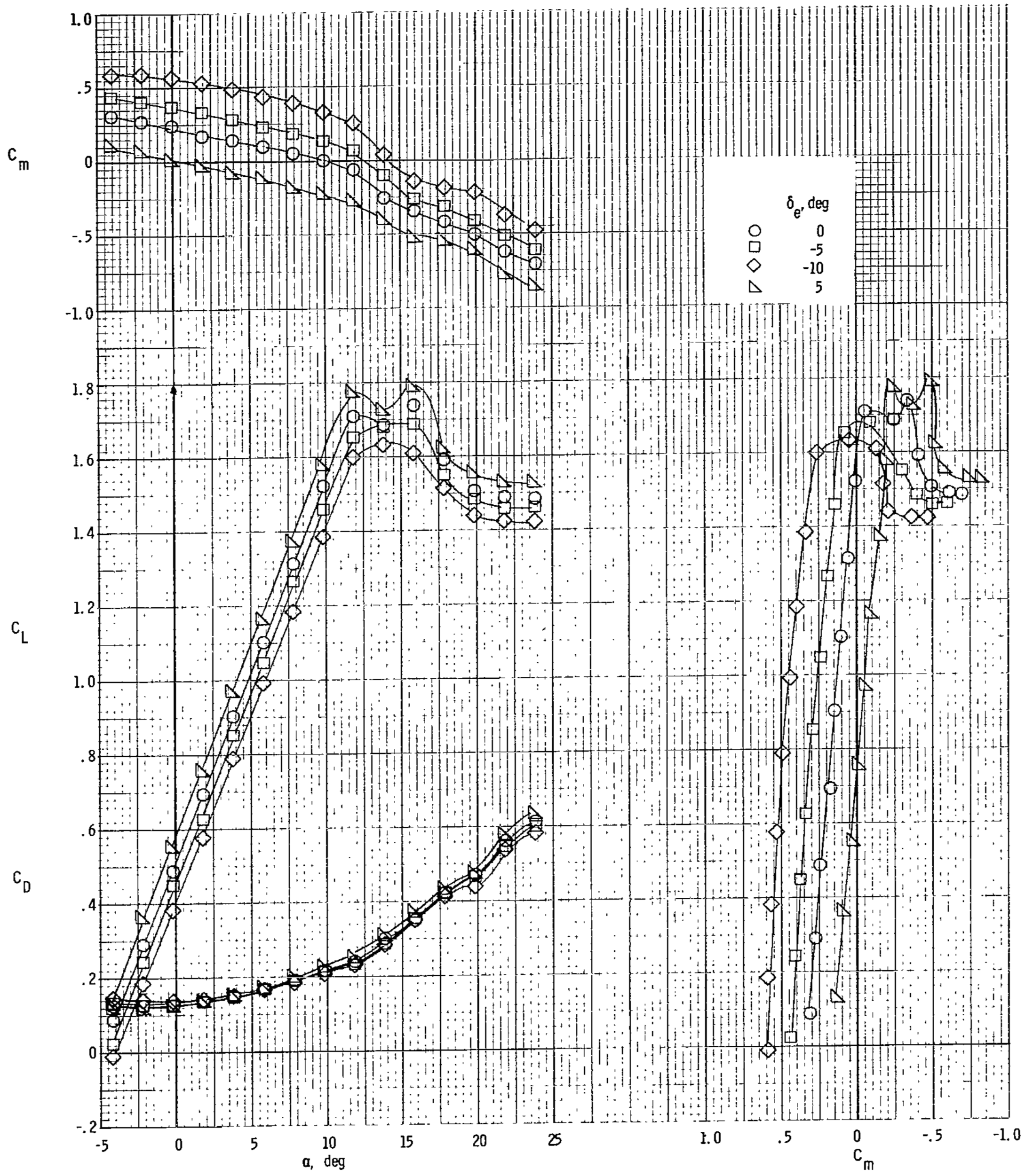

(a) $T_c' = 0$.

Figure 24.- Longitudinal aerodynamic characteristics of model with glaze ice on horizontal tail for $\delta_f = 35^0$.

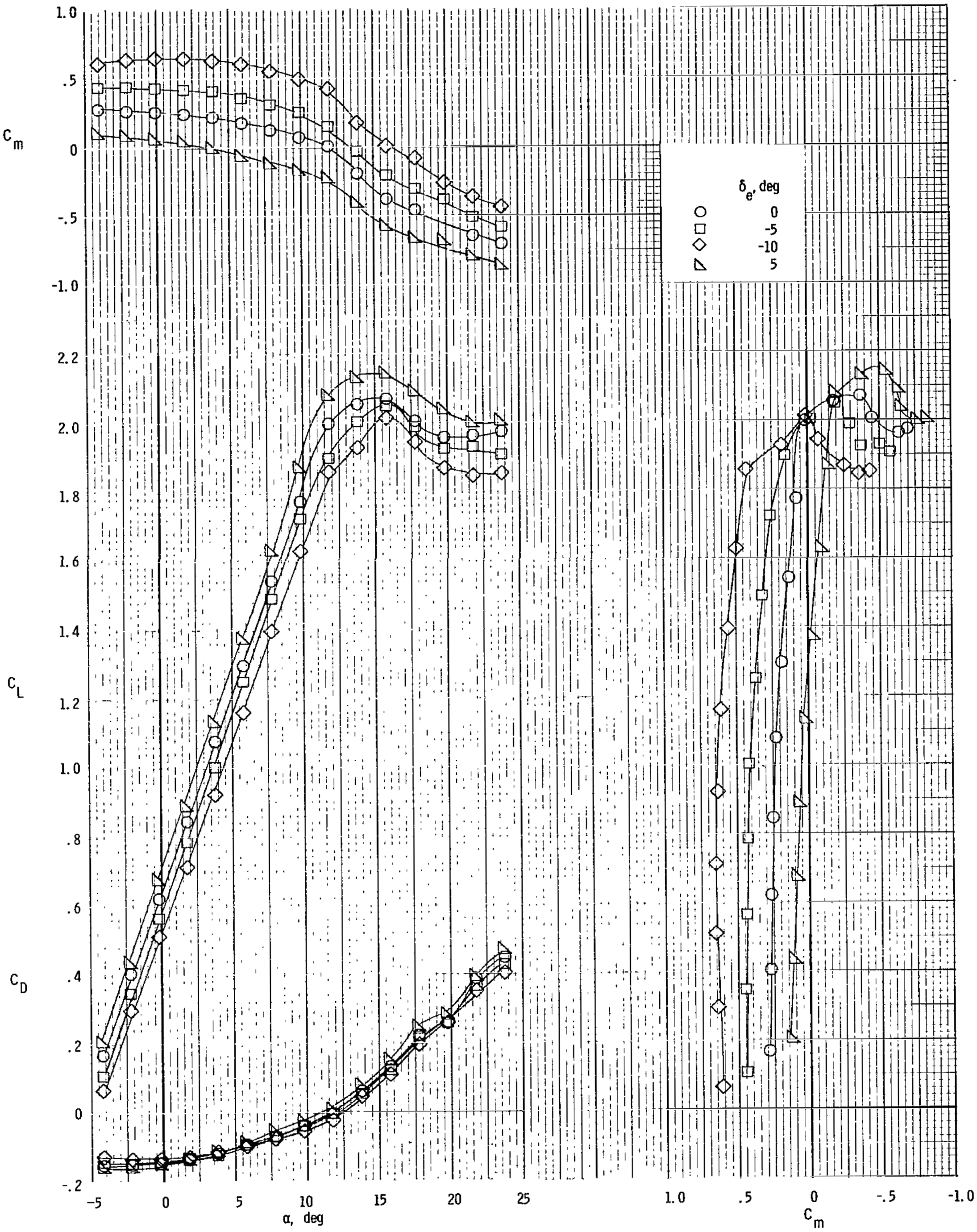

(b) $T'_c = 0.28$.

Figure 24.- Concluded.

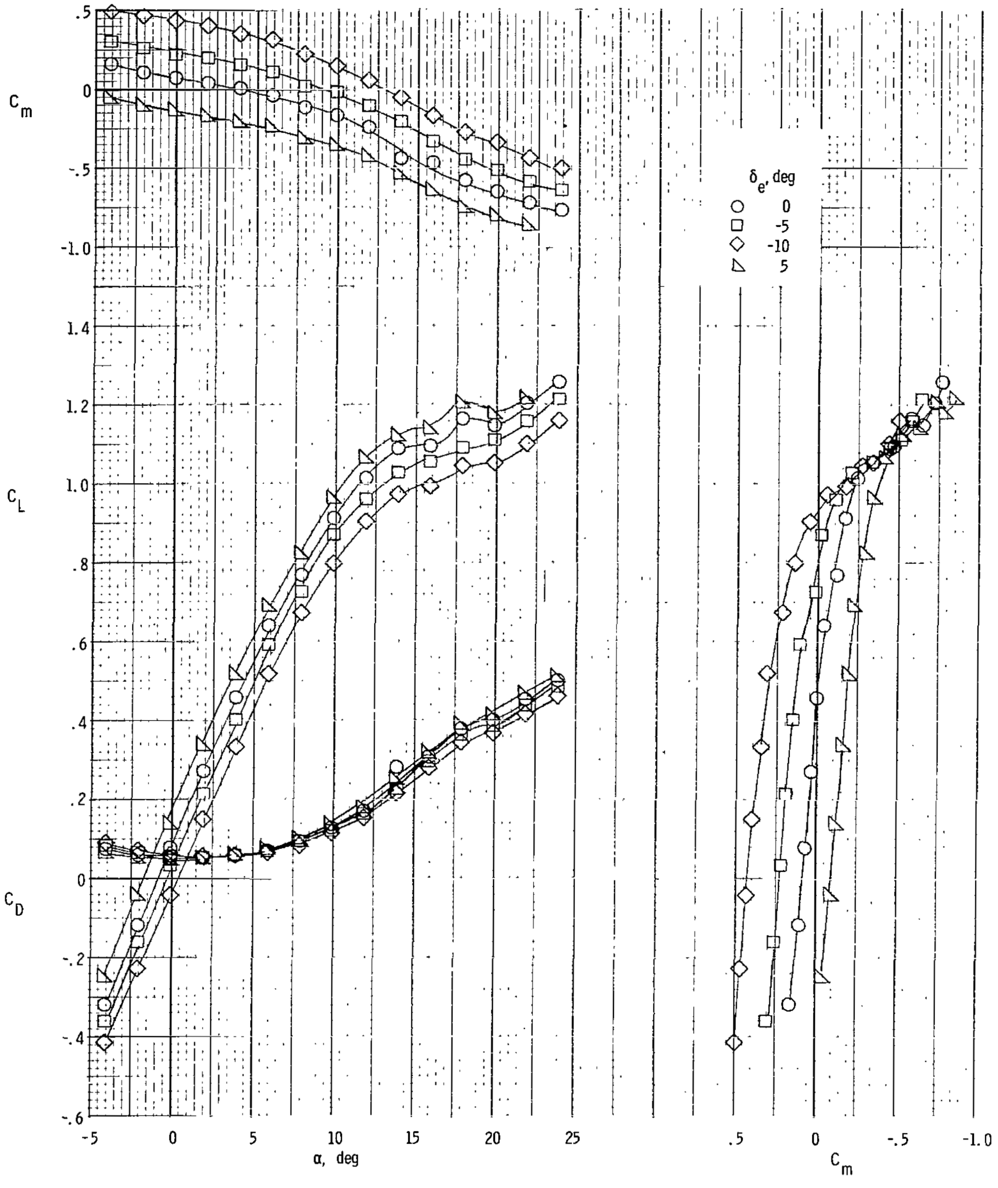

(a) $T_C' = 0$.

Figure 25.- Longitudinal aerodynamic characteristics of model with glaze ice on wing and horizontal tail for $\delta_f = 0^{\circ}$.

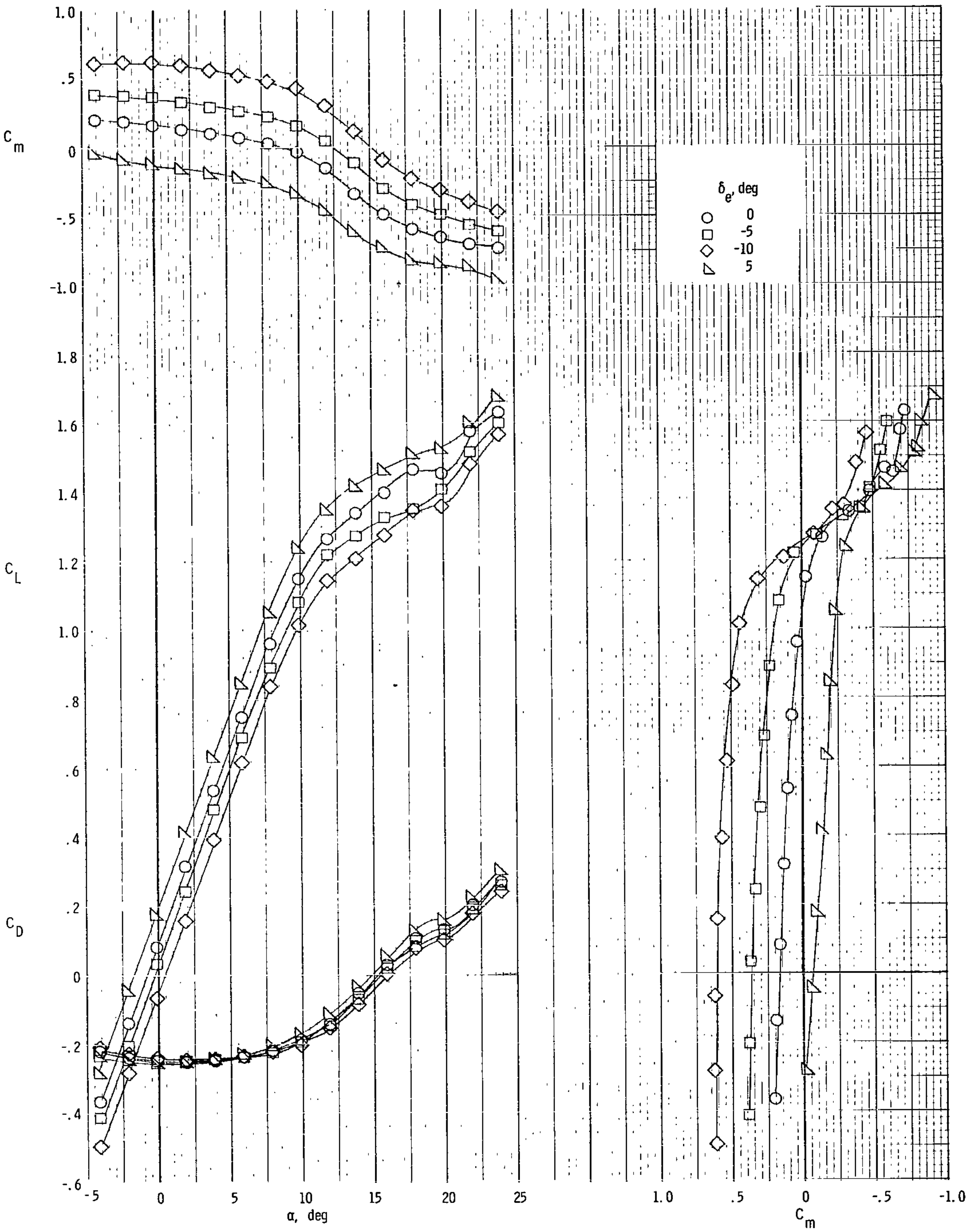

(b) $T_c' = 0.28$.

Figure 25.- Concluded.

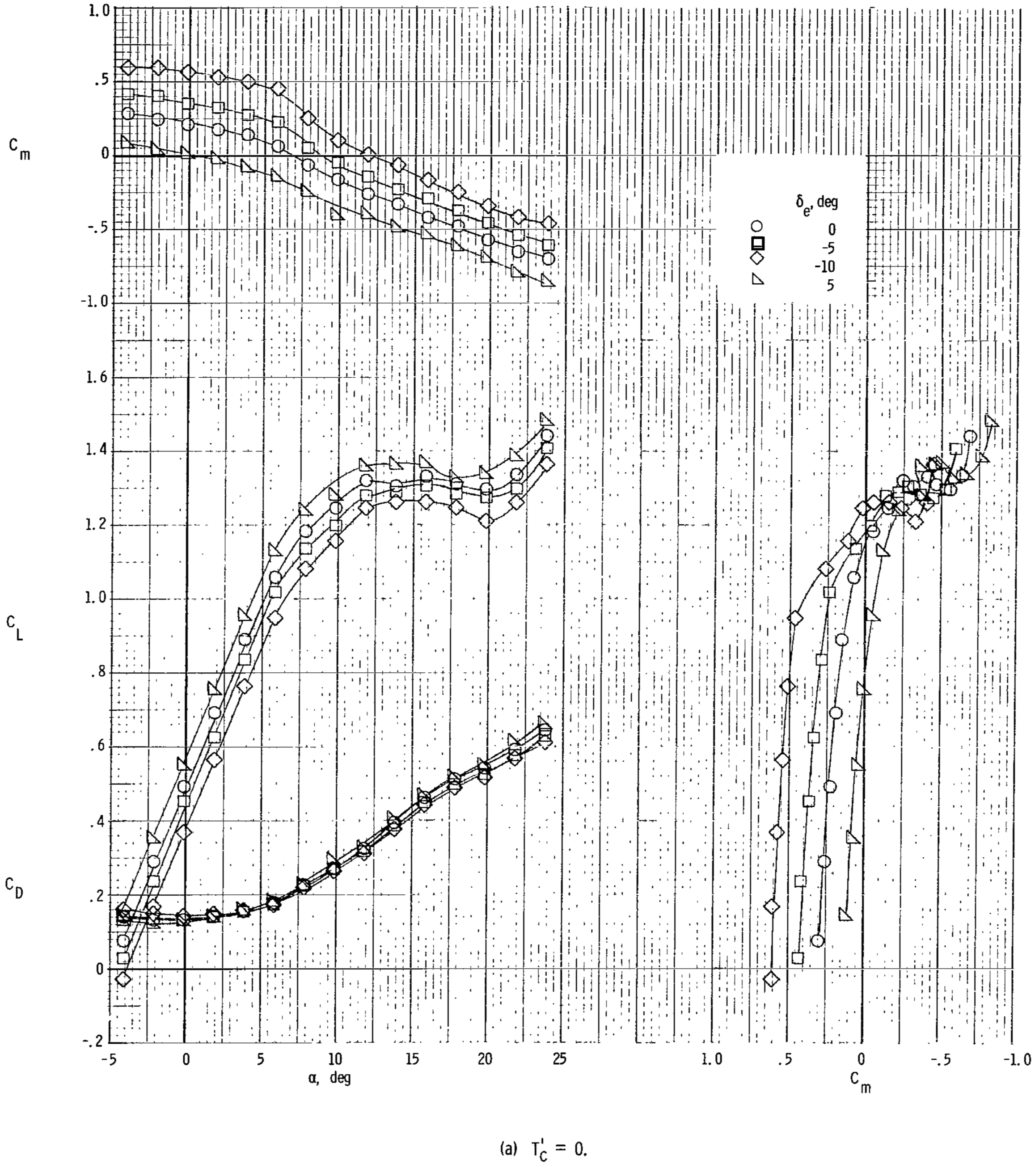

(a) $T'_c = 0$.

Figure 26.- Longitudinal aerodynamic characteristics of model with glaze ice on wing and horizontal tail for $\delta_f = 35^0$.

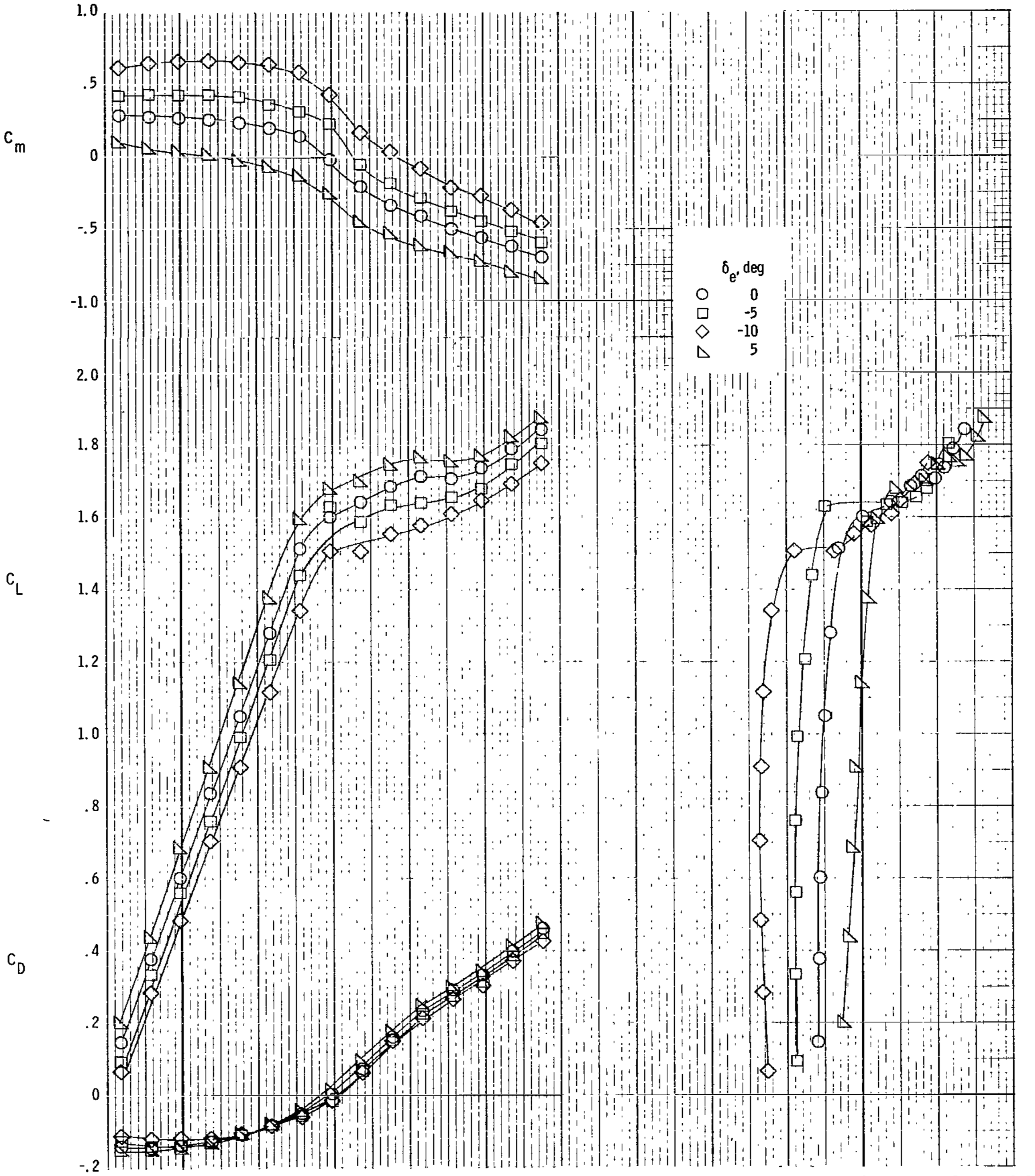

(b) $T'_c = 0.28$.

Figure 26.- Concluded.

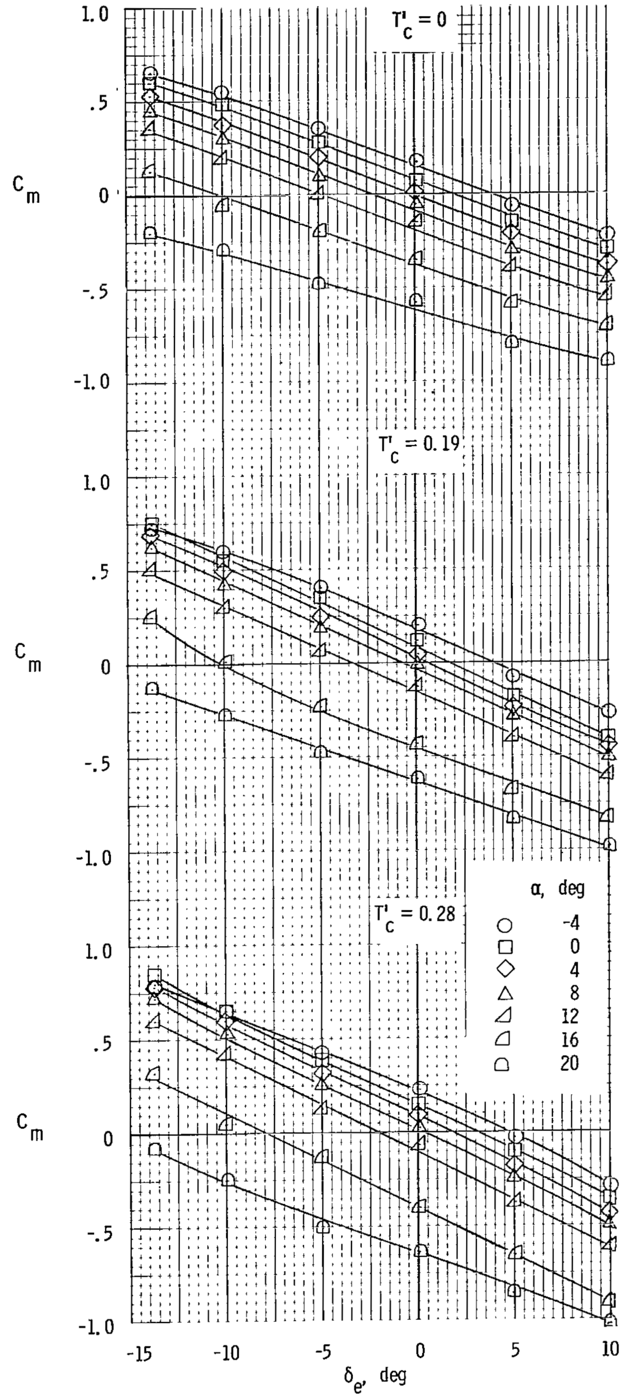

(a) $\delta_f = 0^o$.

Figure 27.- Variation of pitching-moment coefficient with elevator deflection for several power and flap settings.

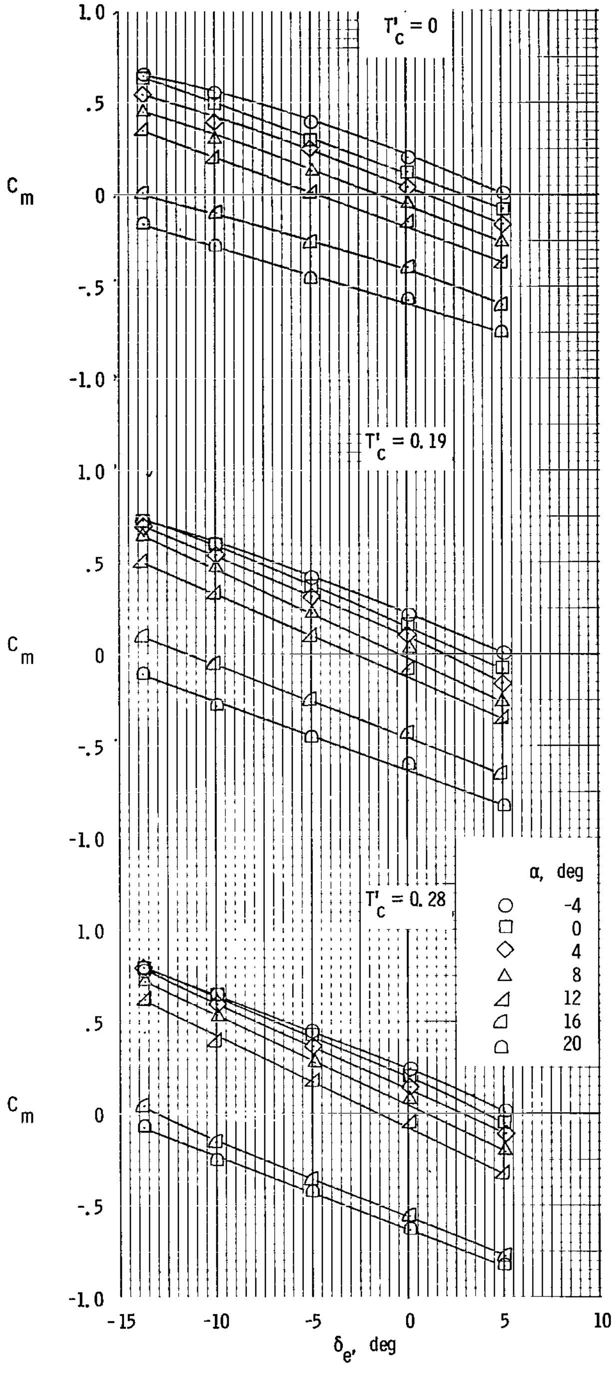

(b) $\delta_f = 15^0$.

Figure 27.- Continued.

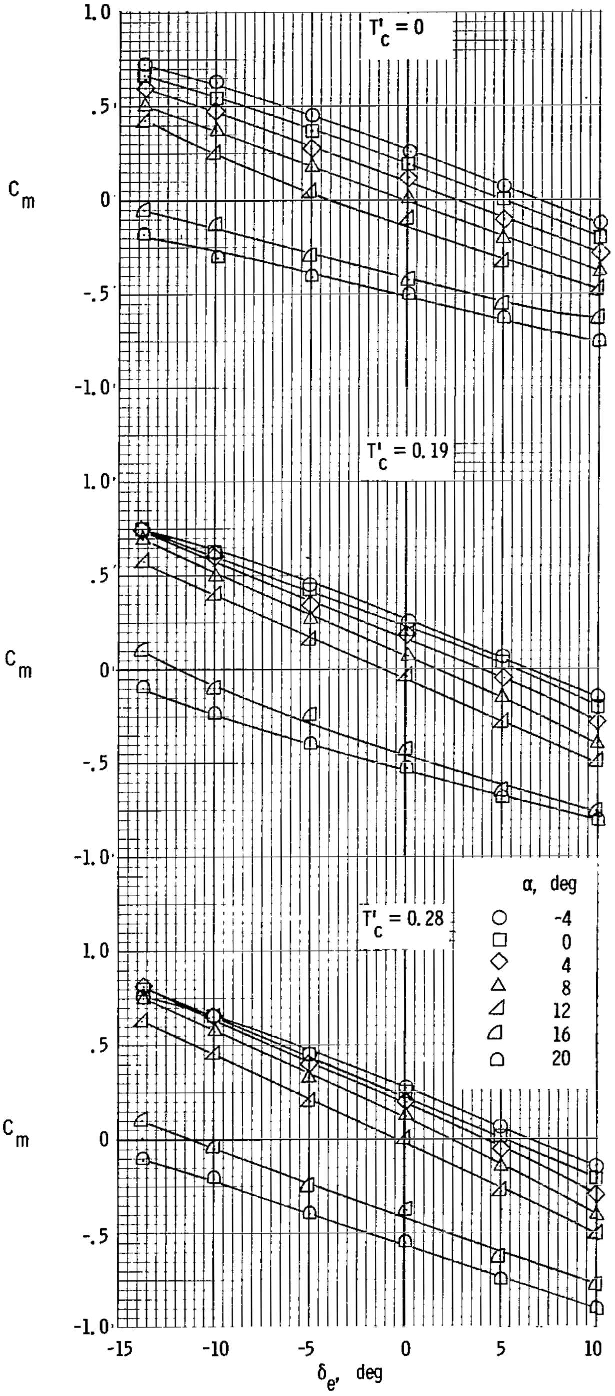

(c) $\delta_f = 35^o$.

Figure 27.- Concluded.

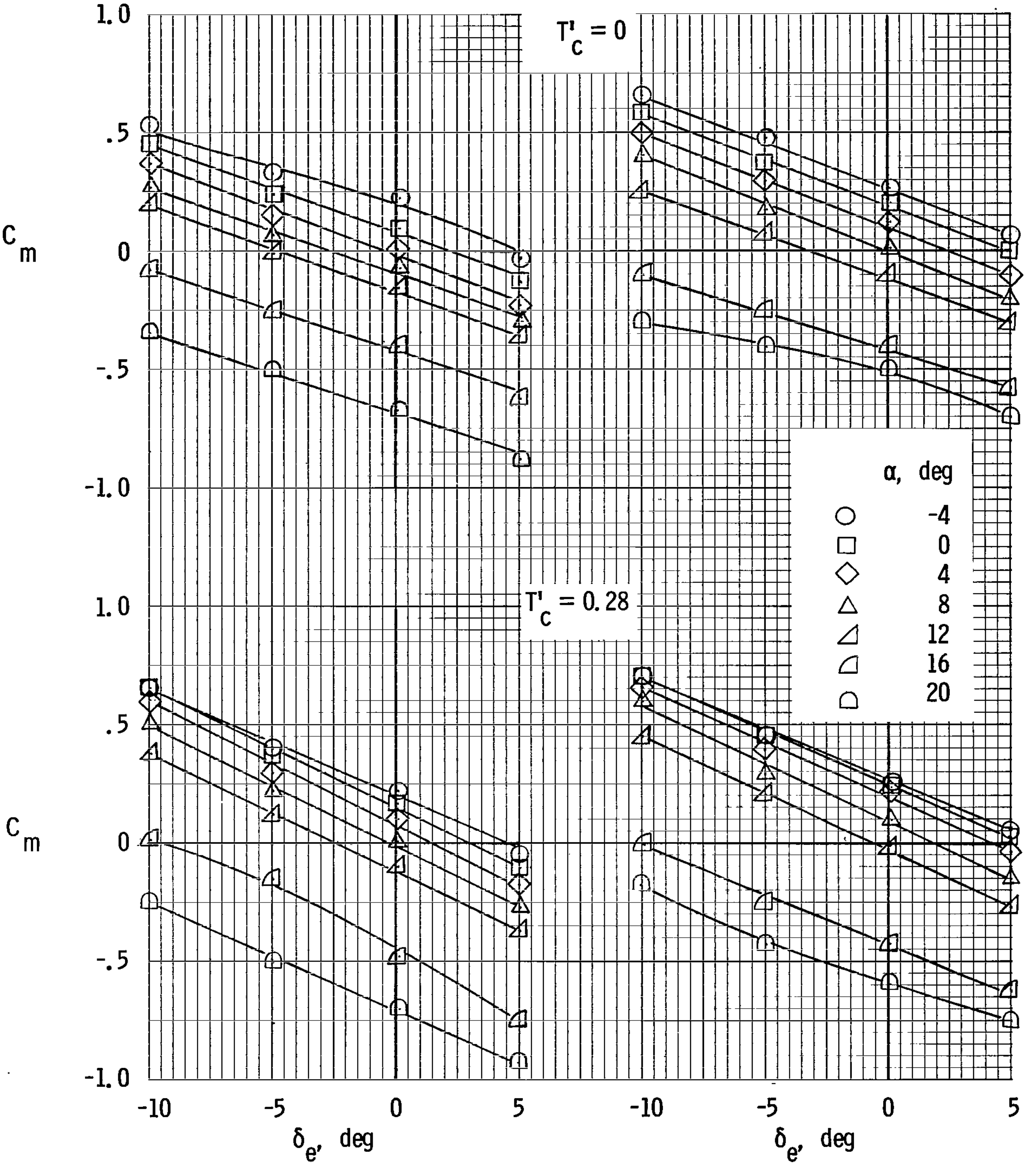

(a) $\delta_f = 0^\circ$.

(b) $\delta_f = 35^\circ$.

Figure 28.- Variation of pitching-moment coefficient with elevator deflection for several power and flap settings with smooth ice on tail only.

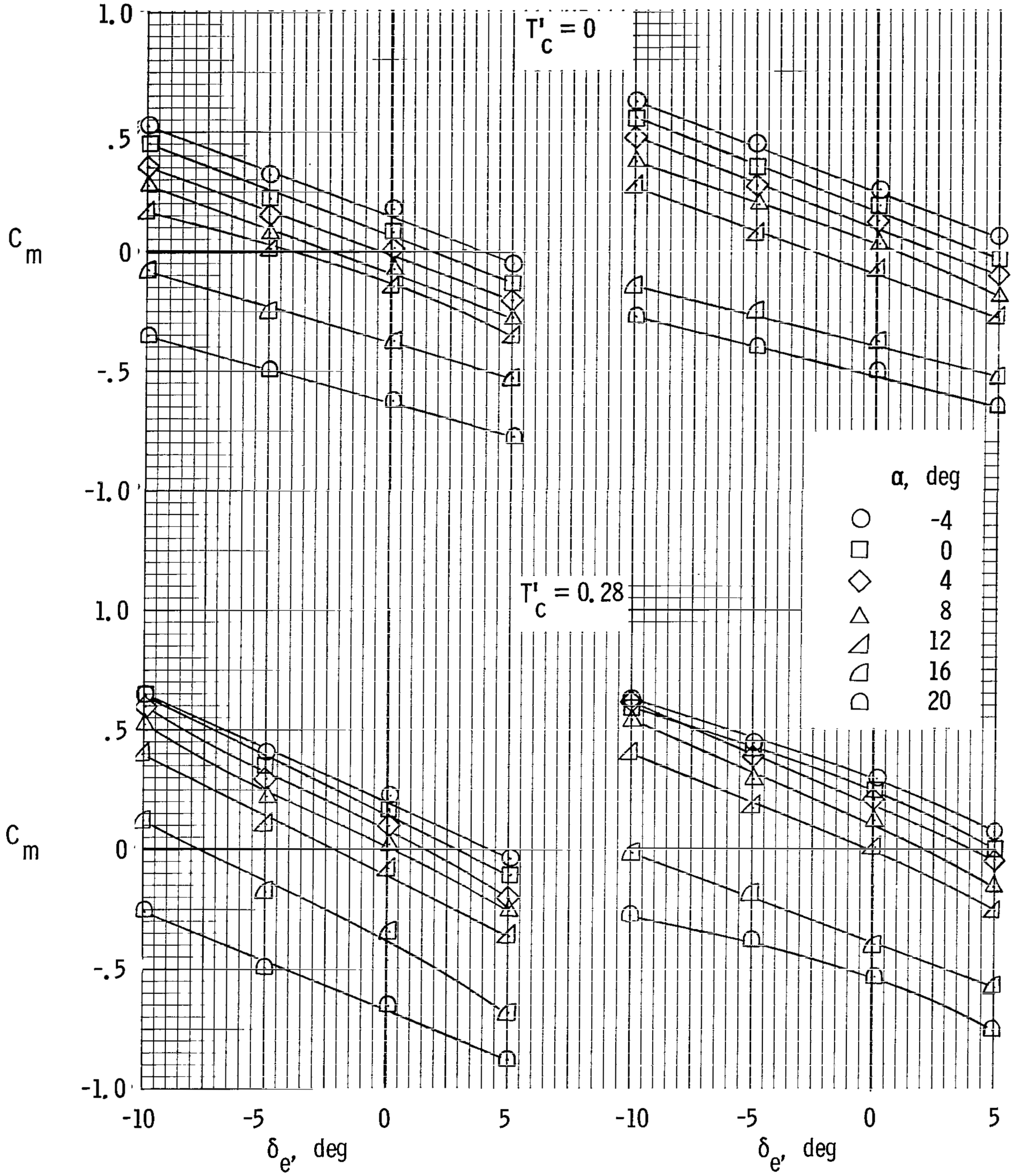

(a) $\delta_f = 0^0$.

(b) $\delta_f = 35^0$.

Figure 29.- Variation of pitching-moment coefficient with elevator deflection for several power and flap settings with rime ice on tail only.

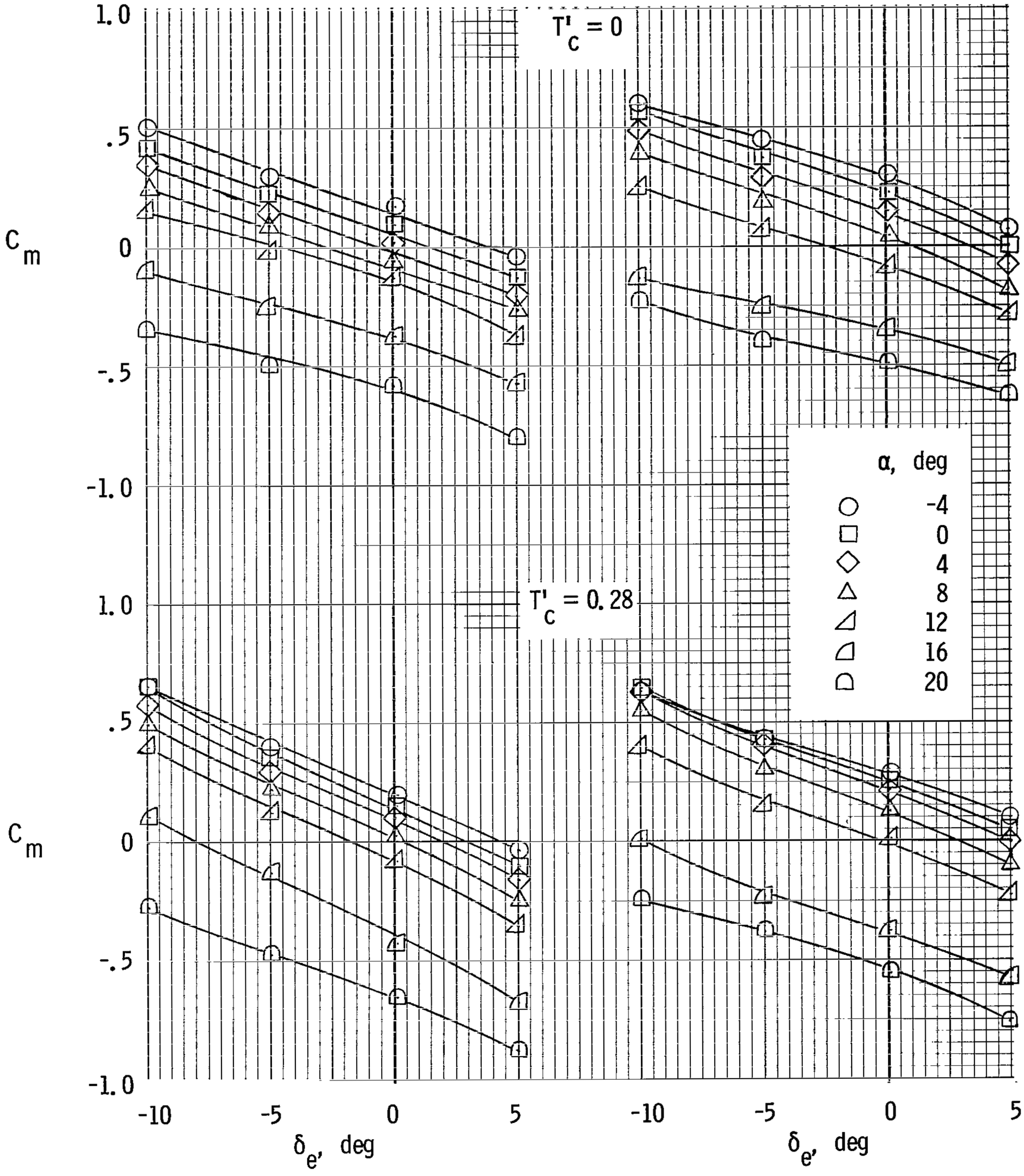

(a) $\delta_f = 0^\circ$.

(b) $\delta_f = 35^\circ$.

Figure 30.- Variation of pitching-moment coefficient with elevator deflection for several power and flap settings with glaze ice on tail only.

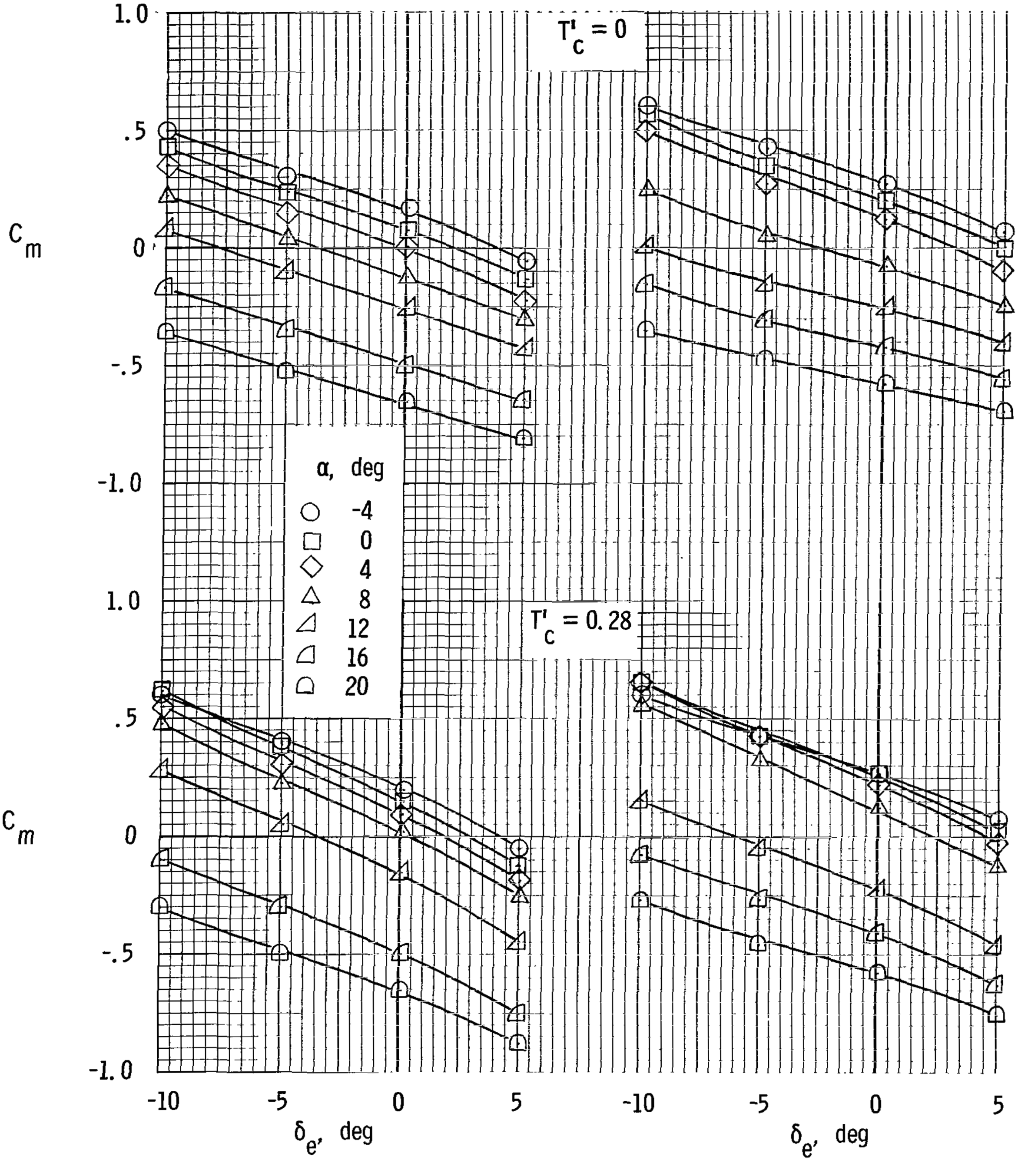

(a) $\delta_f = 0^0$.

(b) $\delta_f = 35^0$.

Figure 31.- Variation of pitching-moment coefficient with elevator deflection for several power and flap settings with glaze ice on wing and tail.

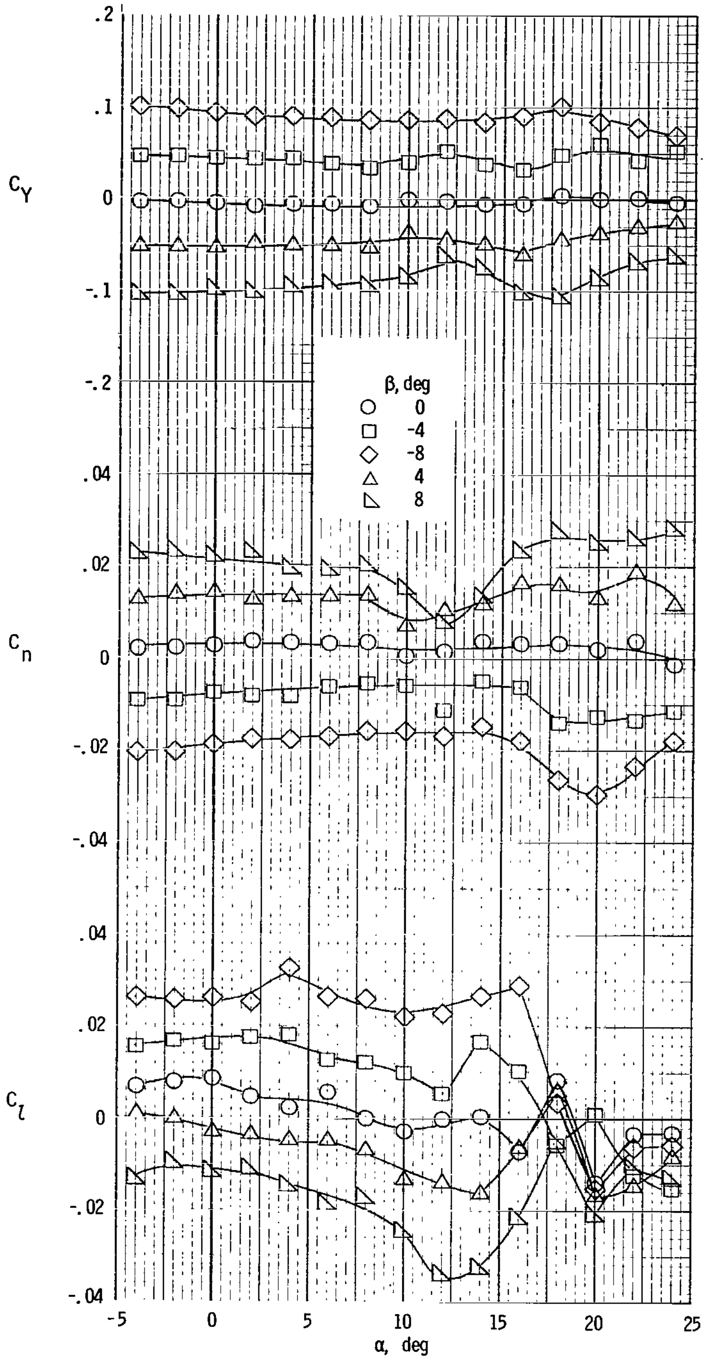

(a) $\delta_f = 0^o$.

Figure 32.- Lateral aerodynamic characteristics of model with propellers removed for several flap deflections.

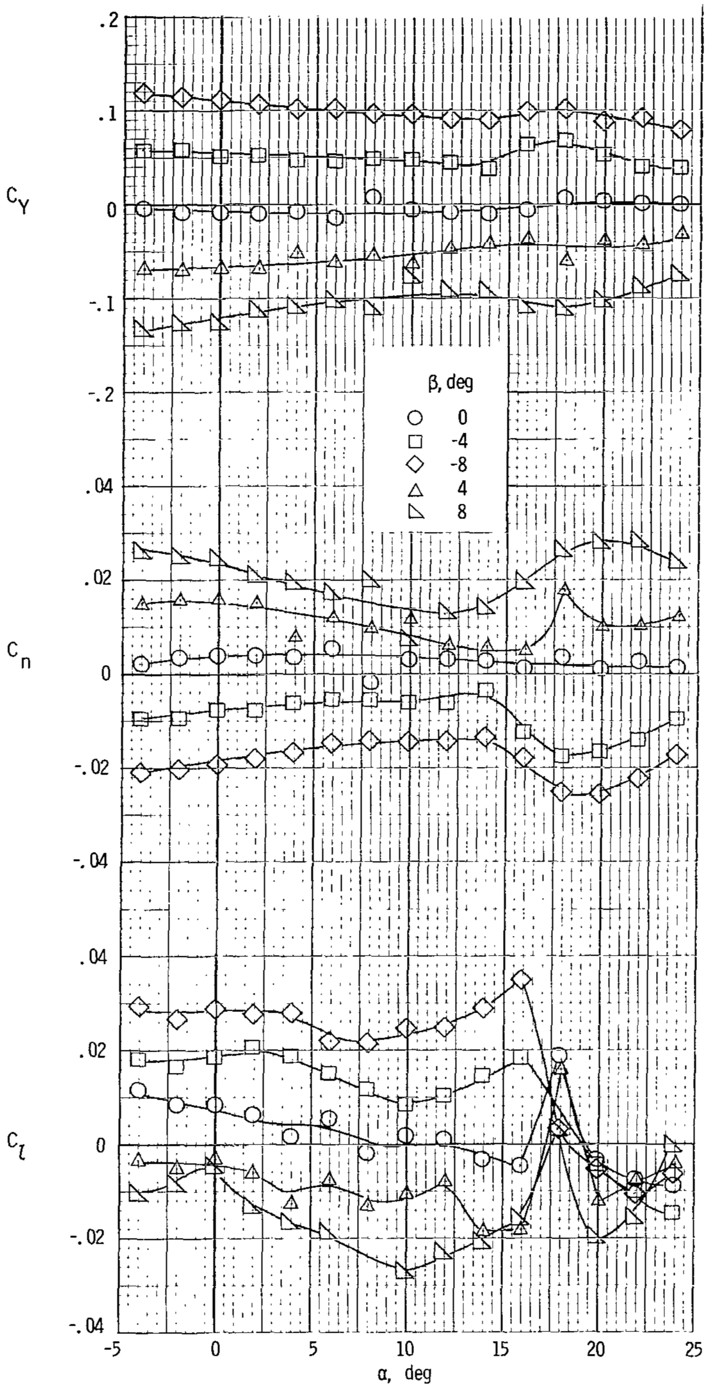

(b) $\delta_f = 15^\circ$.

Figure 32.- Continued.

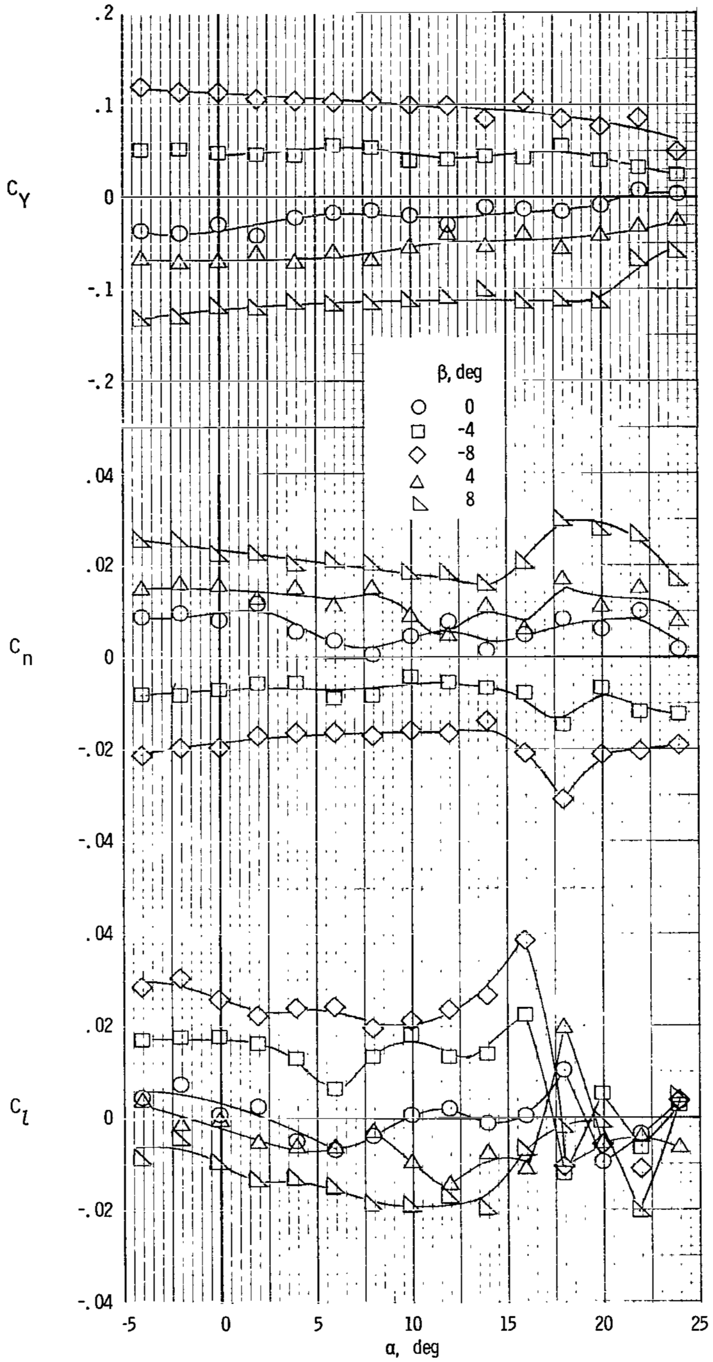

(c) $\delta_f = 35^0$.

Figure 32.- Concluded.

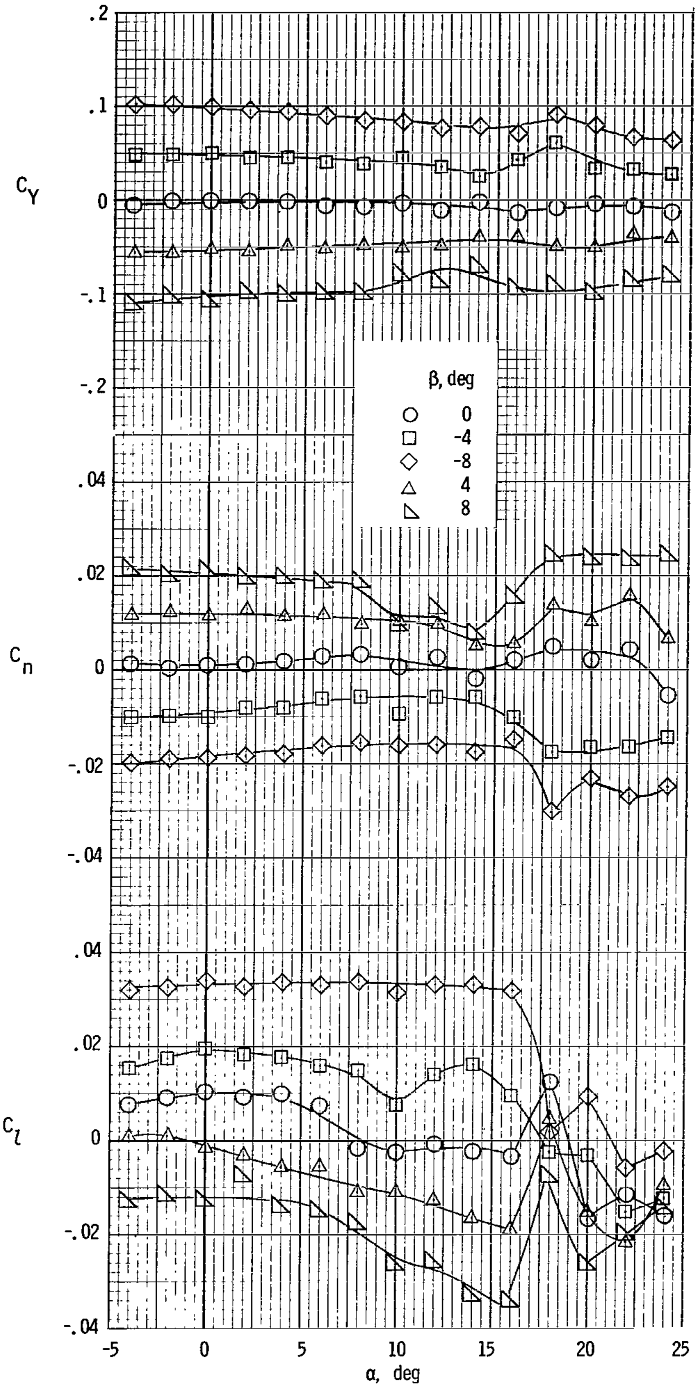

(a) $T_c' = 0$.

Figure 33.- Lateral aerodynamic characteristics of model for several sideslip angles and thrust coefficients for $\delta_f = 0^o$.

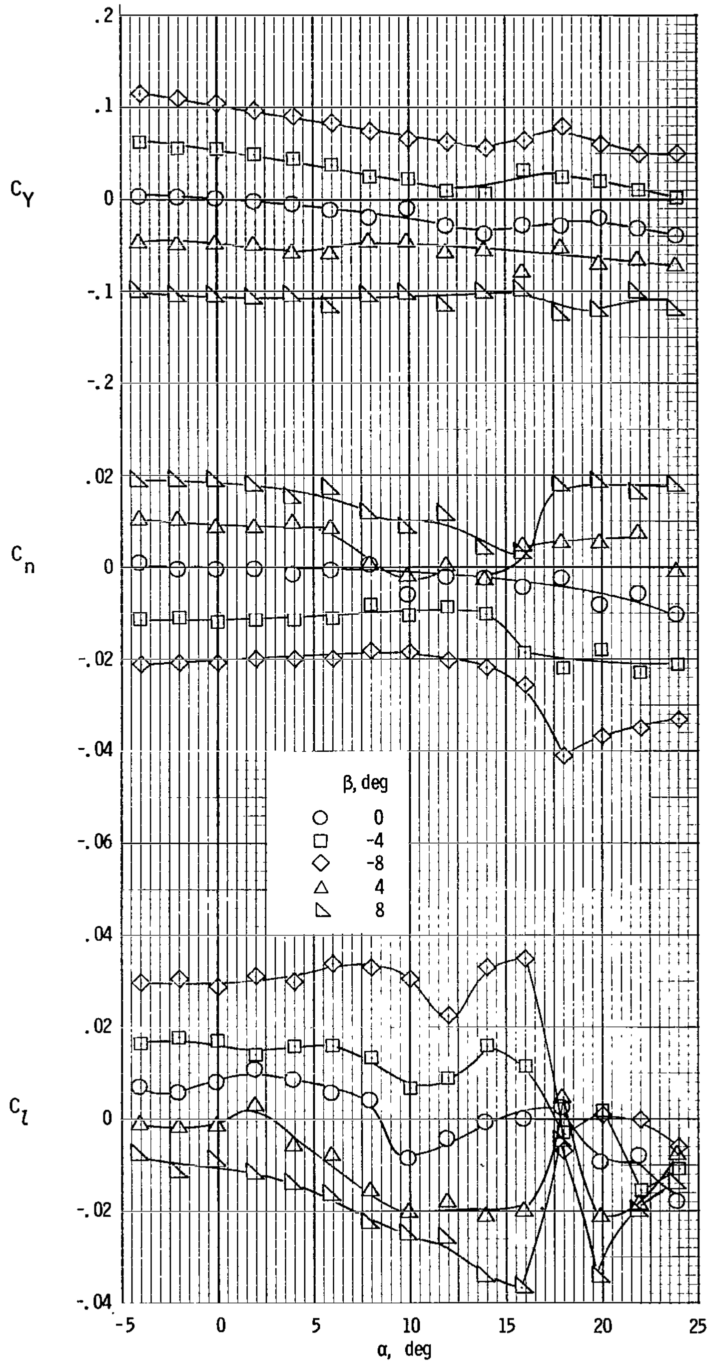

(b) $T_c' = 0.19$.

Figure 33.- Continued.

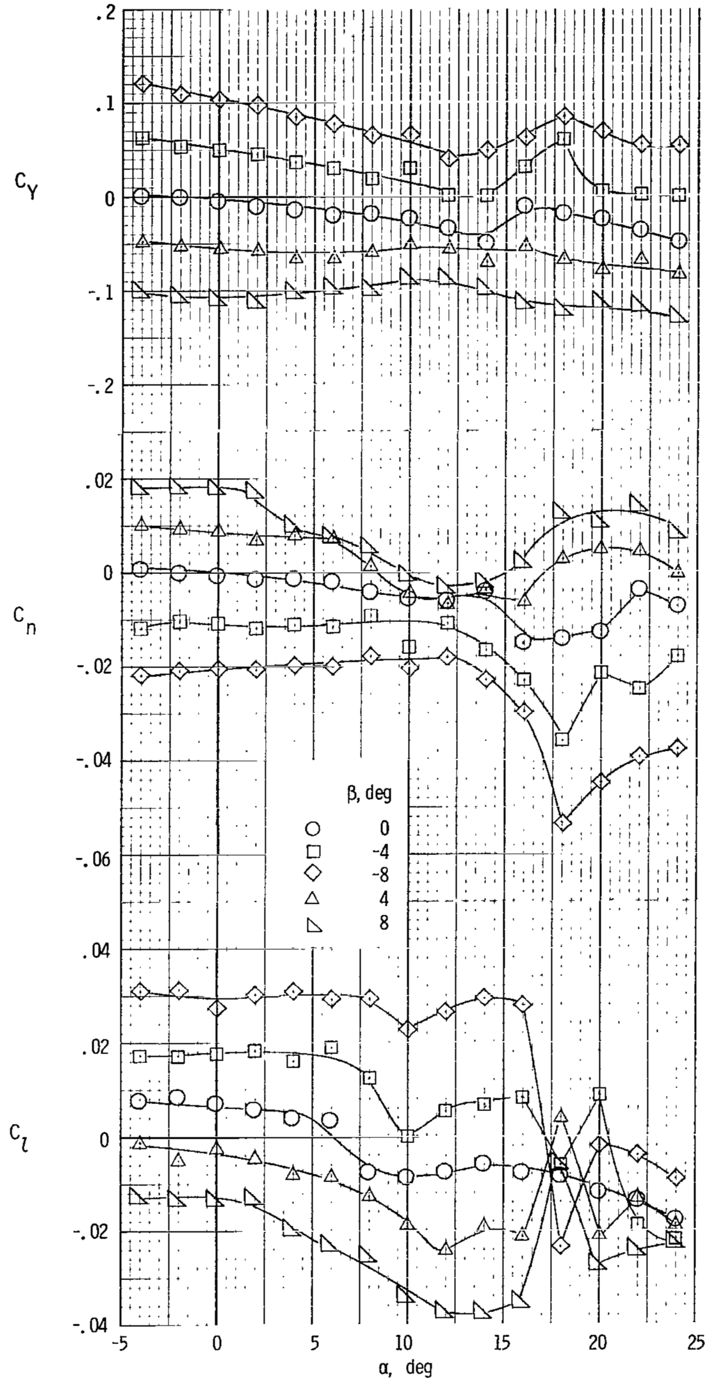

(c) $T_c' = 0.28$.

Figure 33.- Concluded.

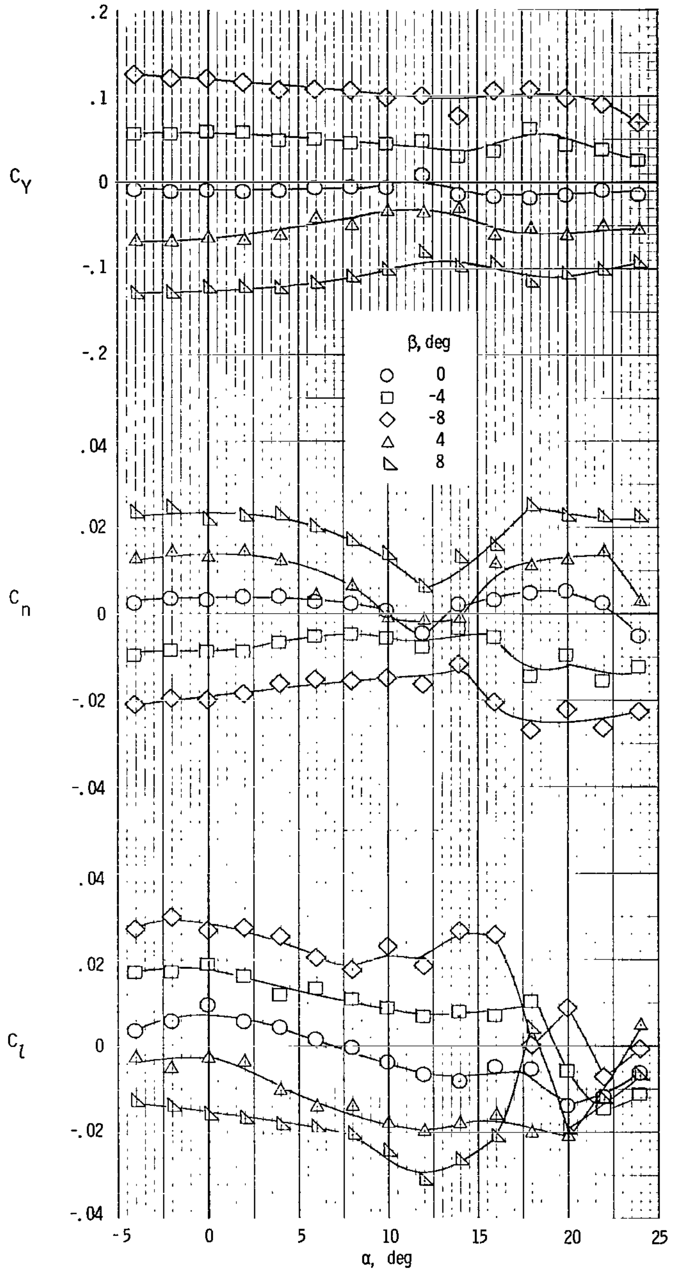

(a) $T'_c = 0$.

Figure 34.- Lateral aerodynamic characteristics of model for several sideslip angles and thrust coefficients for $\delta_f = 15^0$.

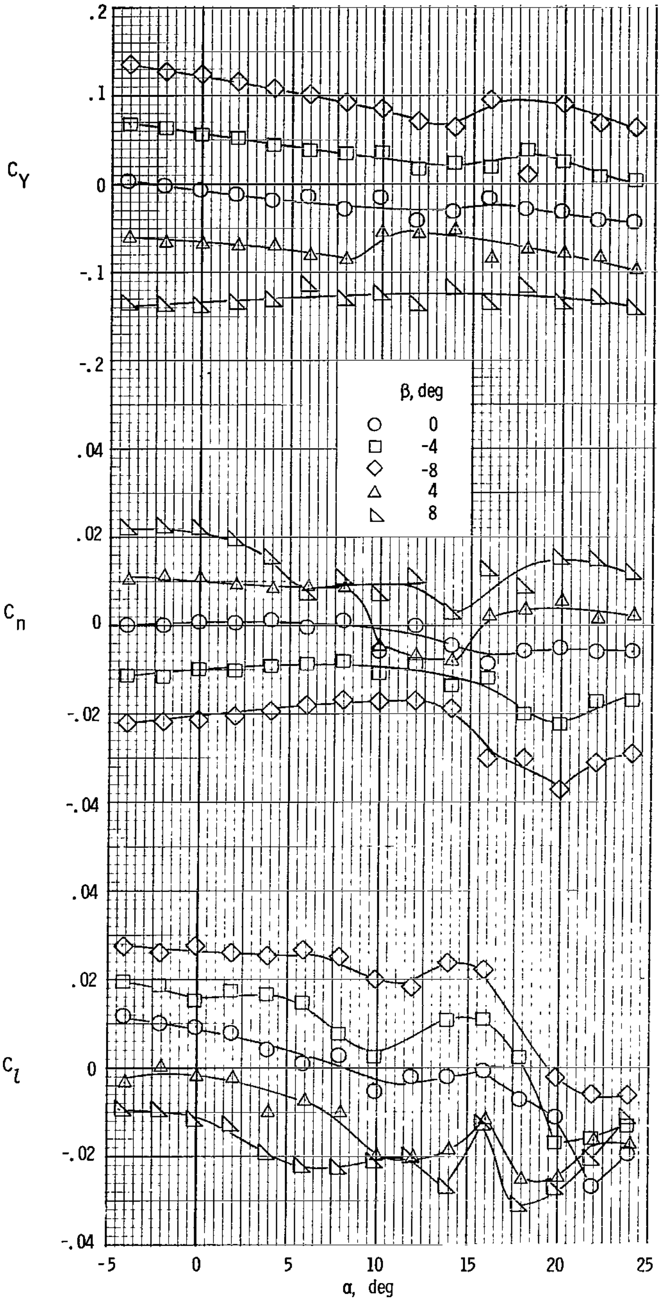

(b) $T'_C = 0.19$.

Figure 34.- Continued.

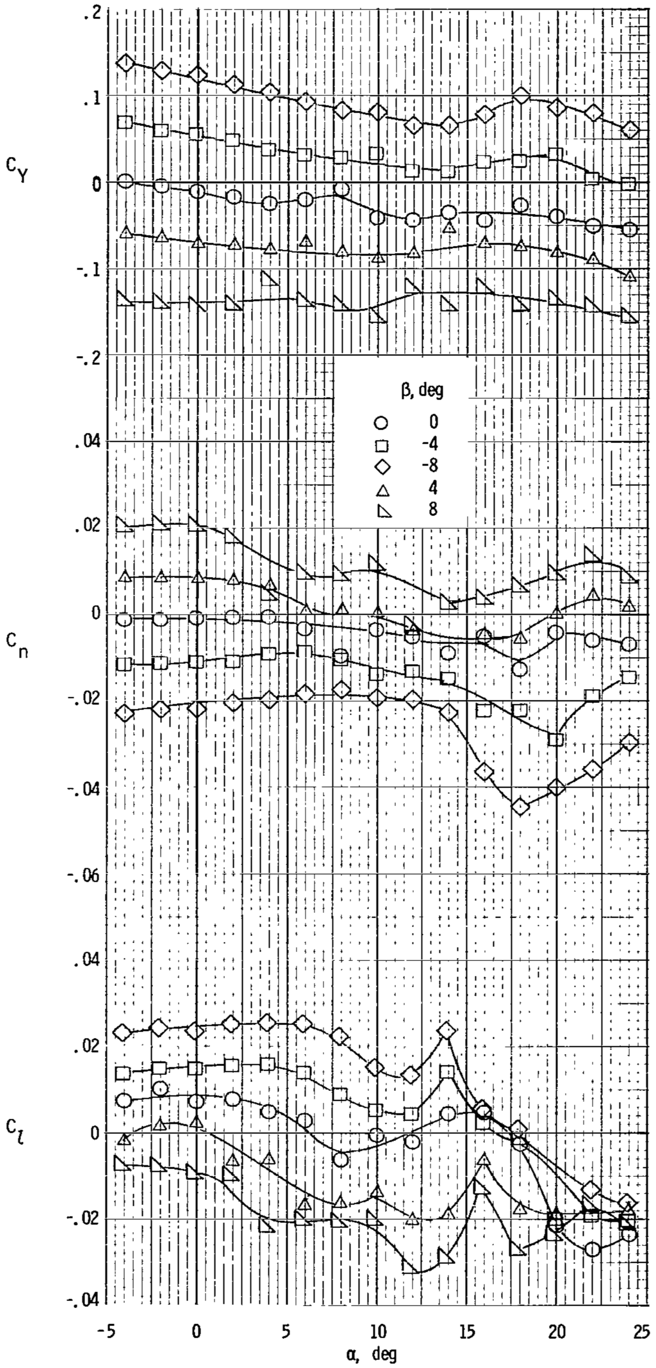

(c) $T_c' = 0.28$.

Figure 34.- Concluded.

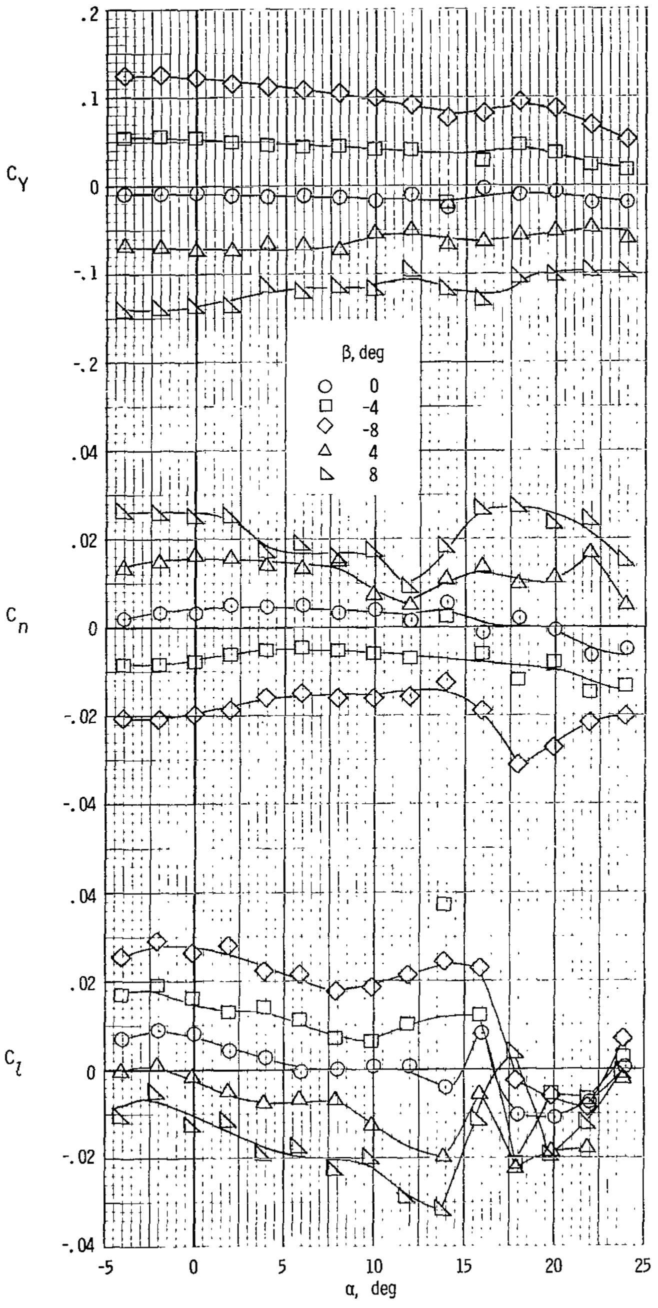

(a) $T_c' = 0$.

Figure 35.- Lateral aerodynamic characteristics of model for several sideslip angles and thrust coefficients for $\delta_f = 35^0$.

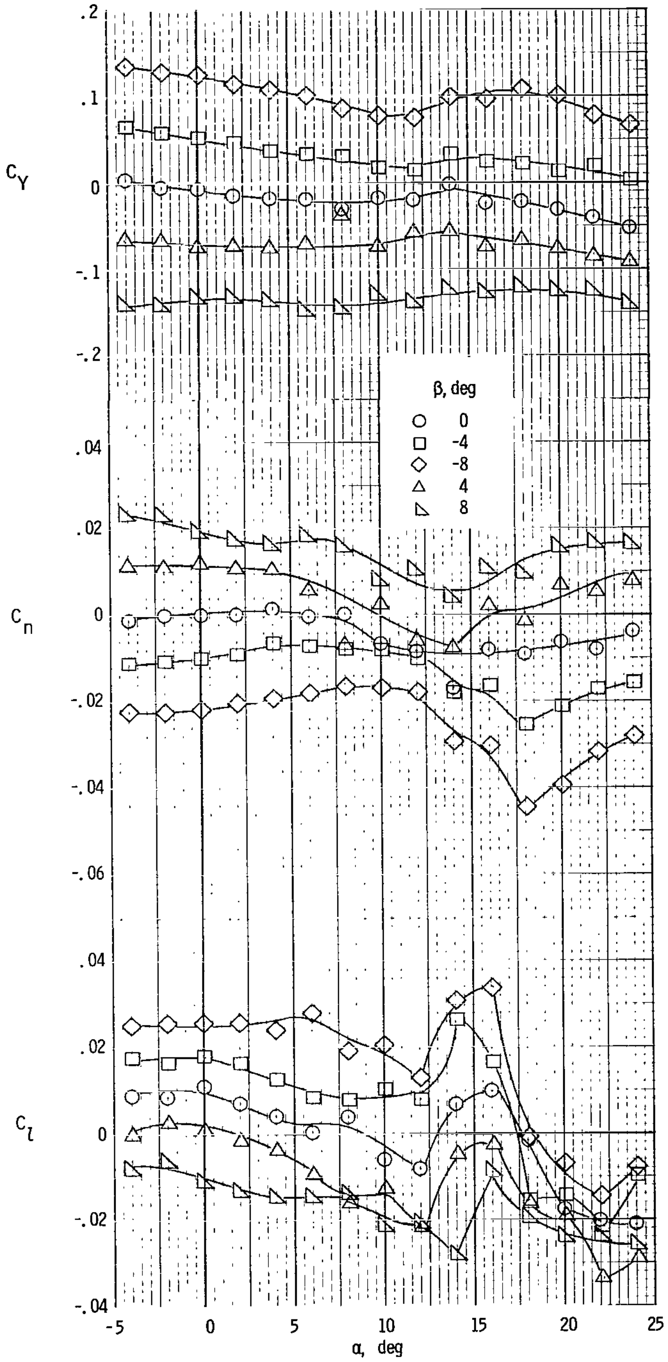

(b) $T_C' = 0.19$.

Figure 35.- Continued.

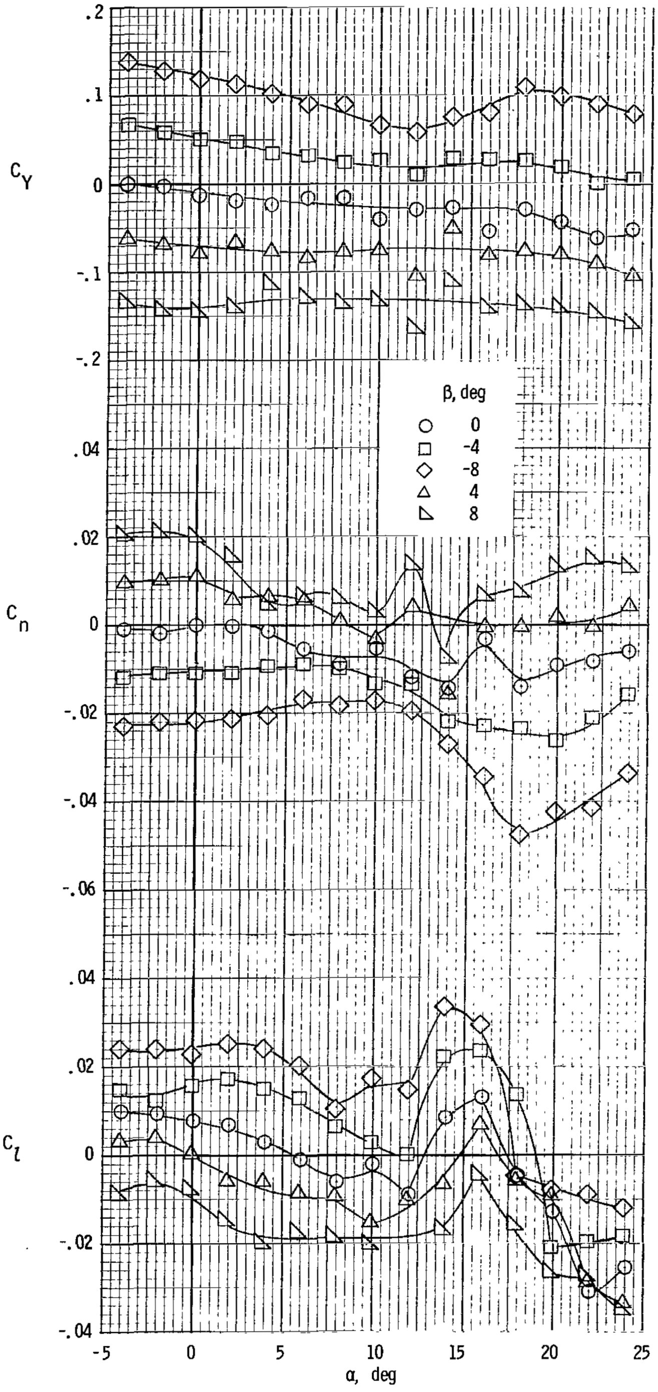

(c) $T_c' = 0.28$.

Figure 35.- Concluded.

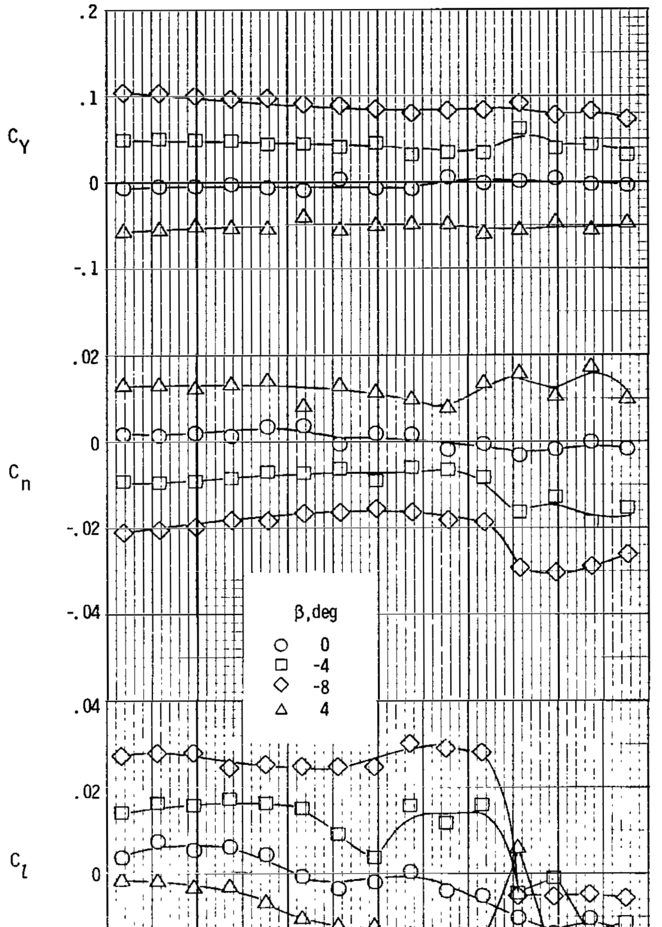

(a) $T_c' = 0$.

Figure 36.- Lateral aerodynamic characteristics of model with short nacelles for several sideslip angles and thrust coefficients for $\delta_f = 0^0$.

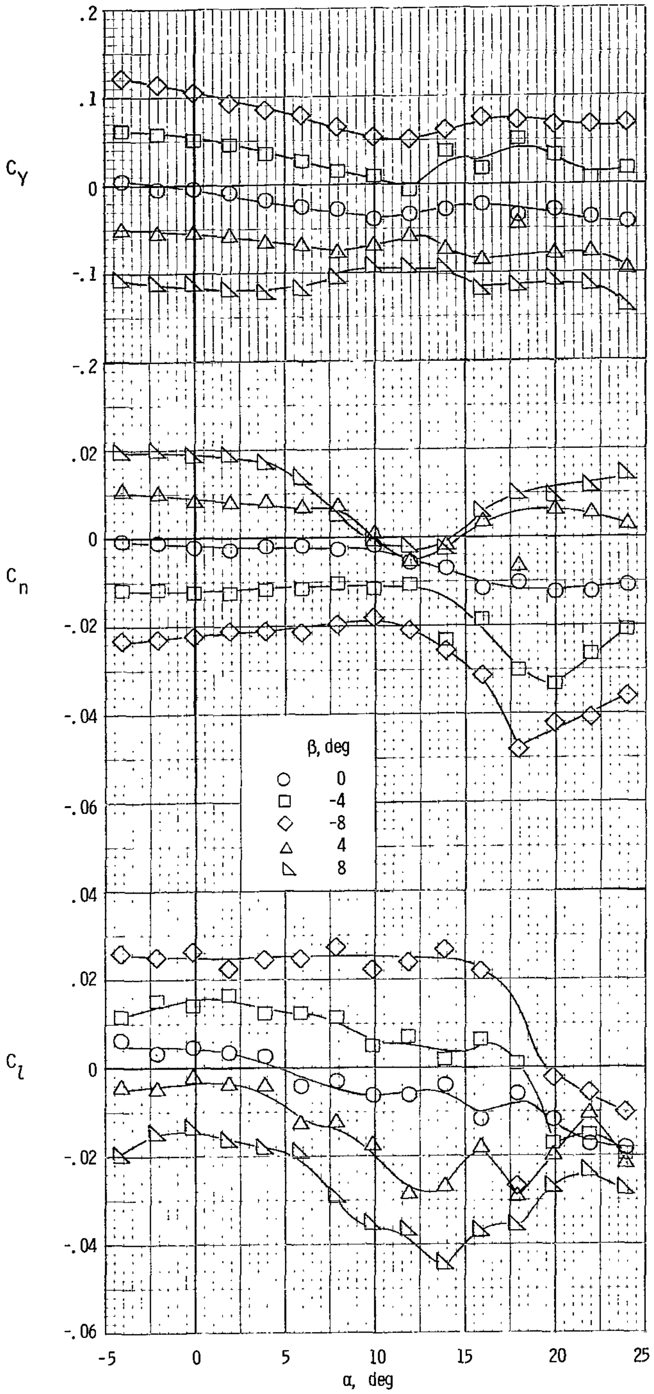

(b) $T_c' = 0.28$.

Figure 36.- Concluded.

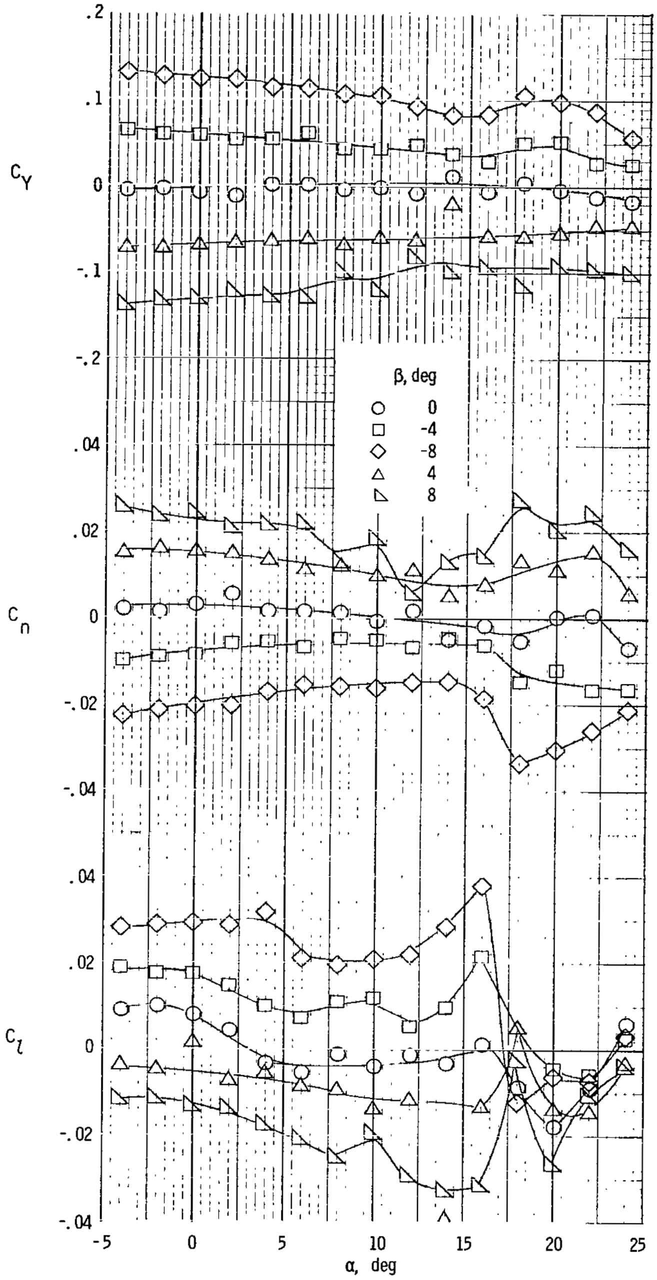

(a) $T'_c = 0.$

Figure 37.- Lateral aerodynamic characteristics of model with short nacelles for several sideslip angles and thrust coefficients for $\delta_f = 35^0$.

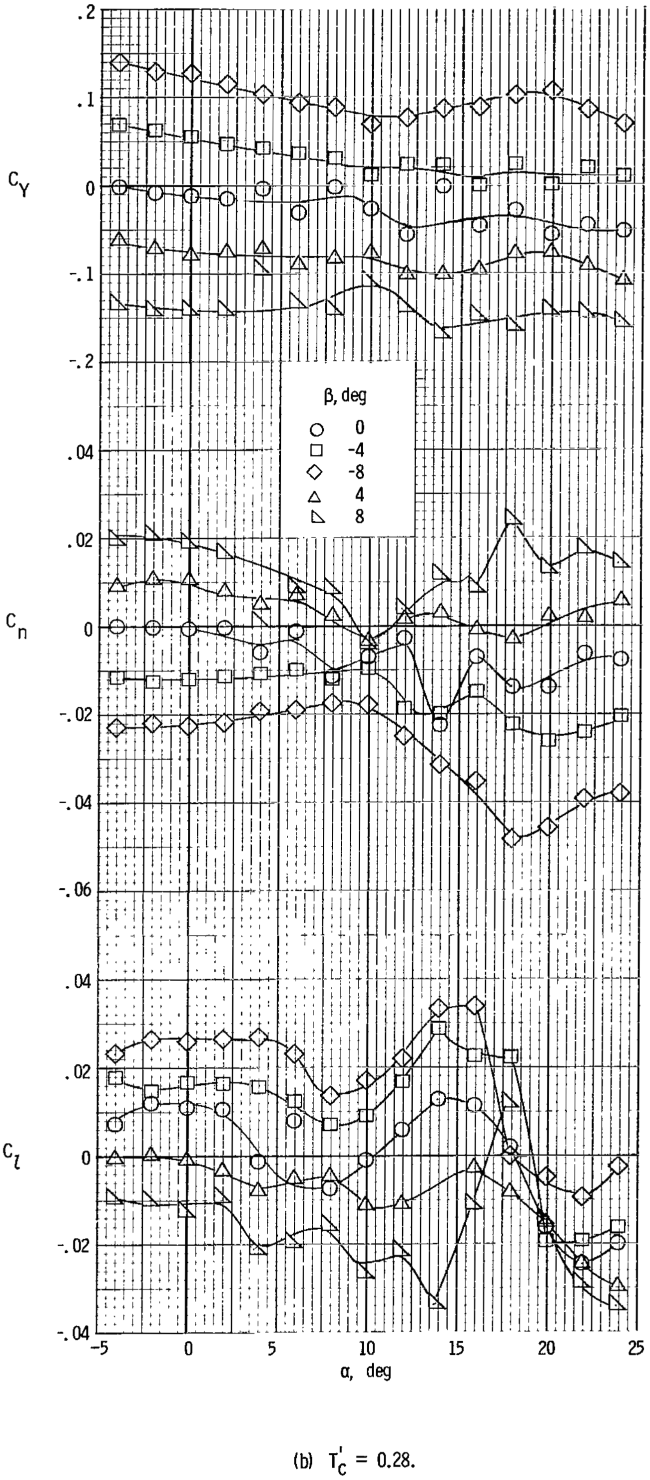

(b) $T_C' = 0.28$.

Figure 37.- Concluded.

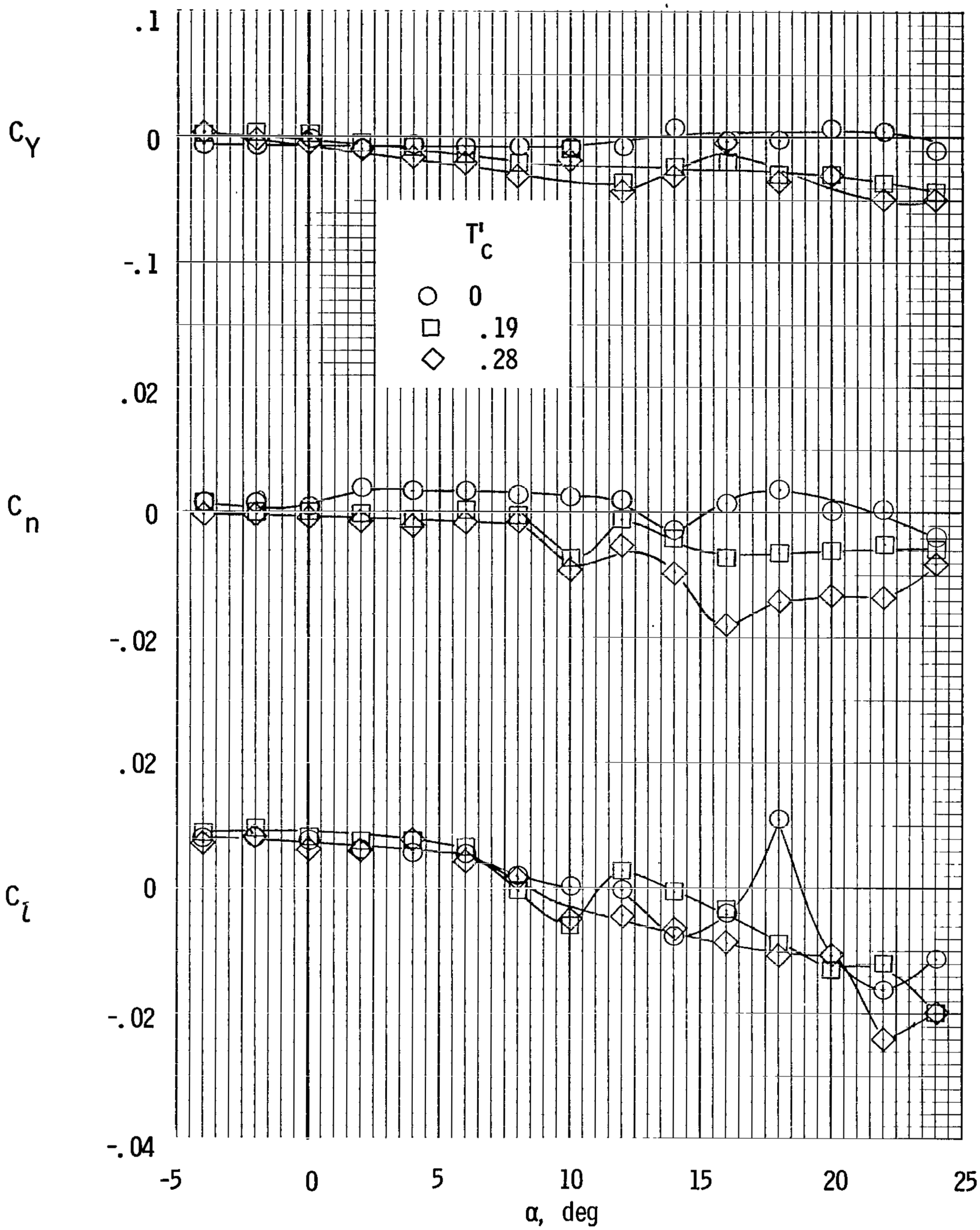

Figure 38.- Lateral aerodynamic characteristics of model with cowl modification. $\delta_f = 0^0$; $\beta = 0^0$.

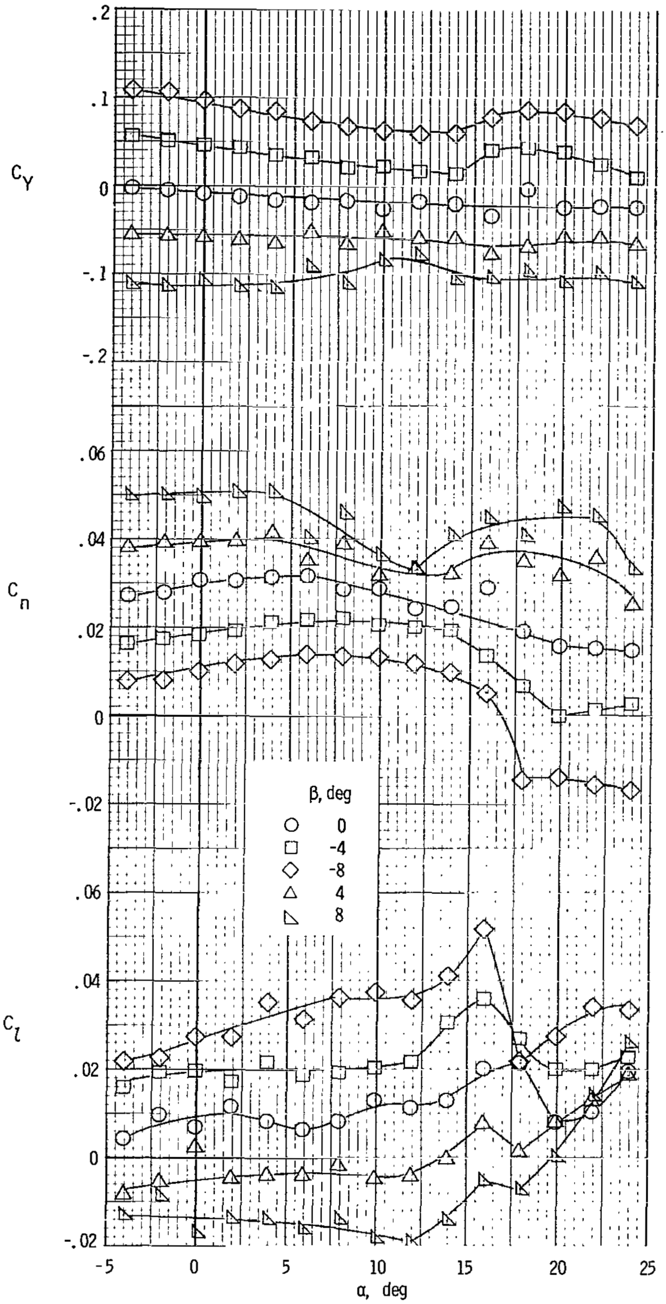

(a) Left engine full; right engine windmilling.

Figure 39.- Lateral aerodynamic characteristics of model with asymmetric power for $\delta_f = 0^0$.

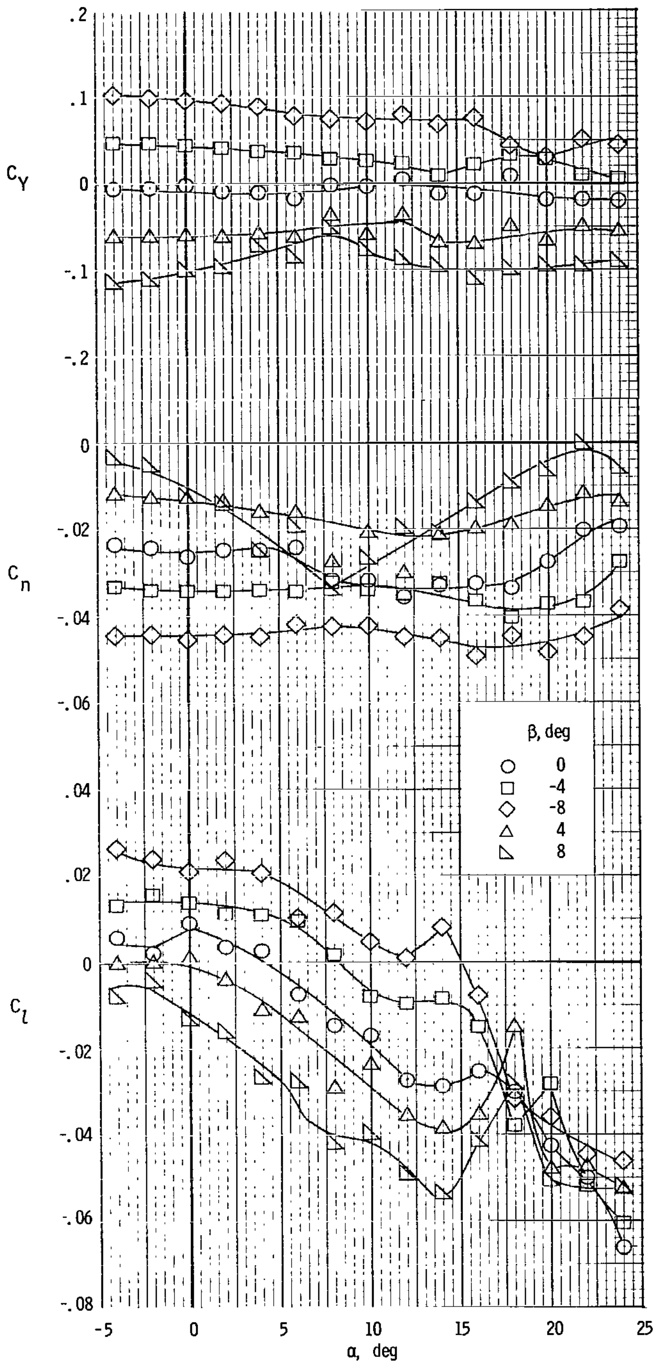

(b) Left engine windmilling; right engine full.

Figure 39.- Concluded.

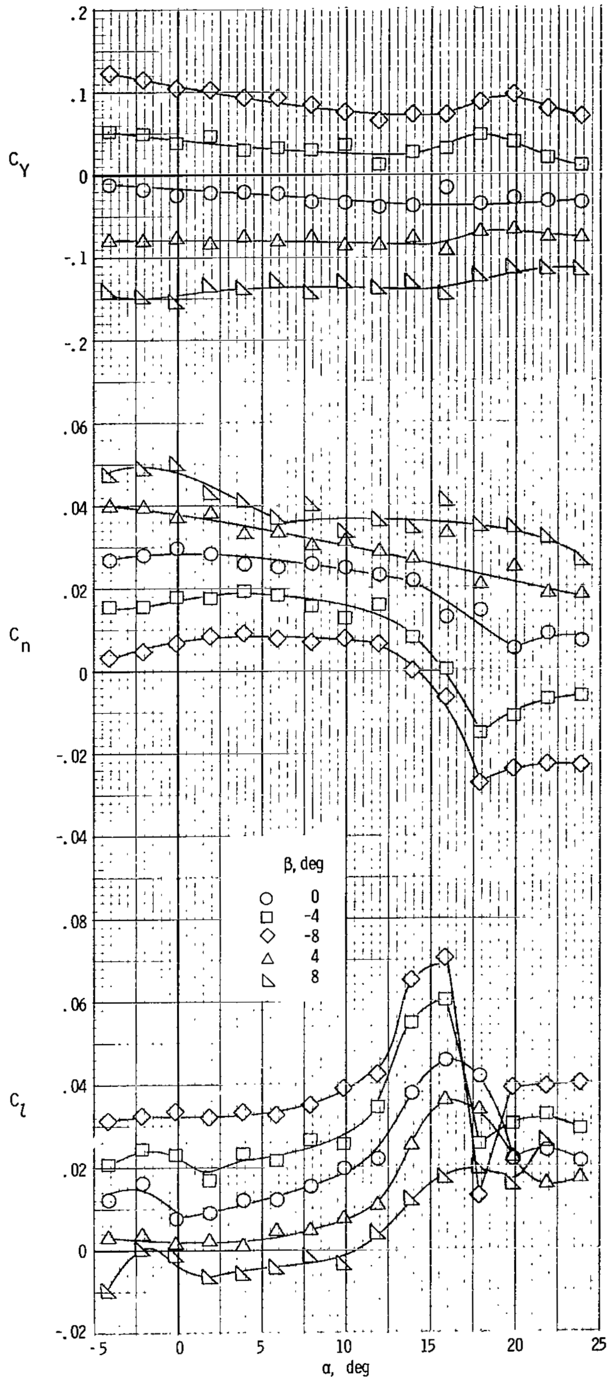

(a) Left engine full; right engine windmilling.

Figure 40.- Lateral aerodynamic characteristics of model with asymmetric power for $\delta_f = 35^0$.

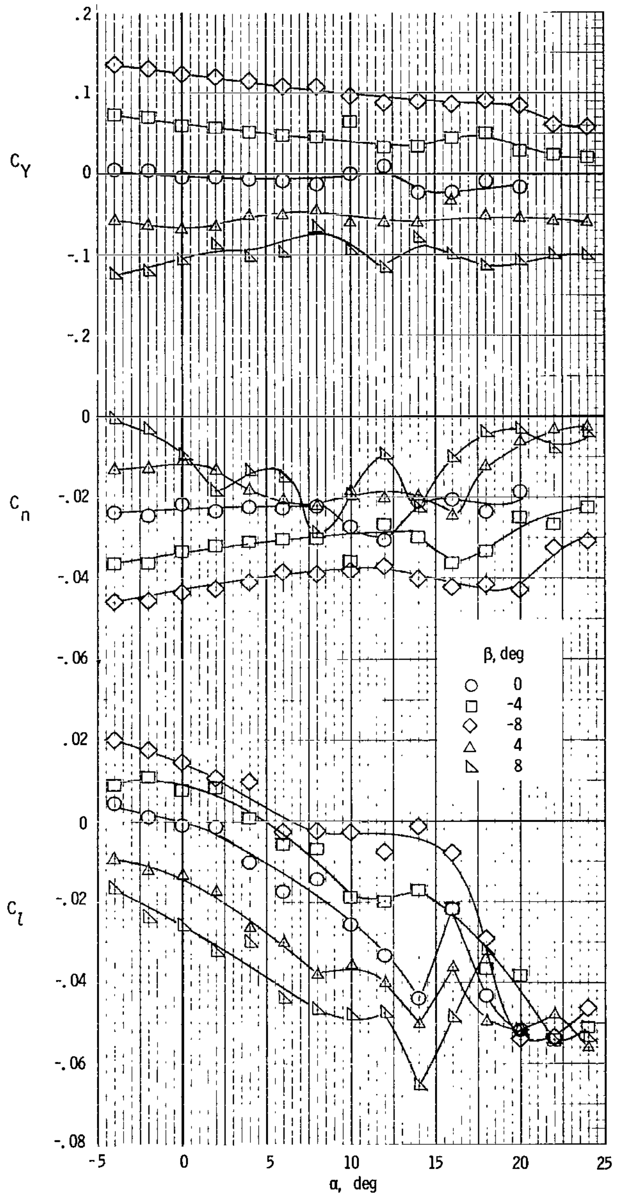

(b) Left engine windmilling; right engine full.

Figure 40.- Concluded.

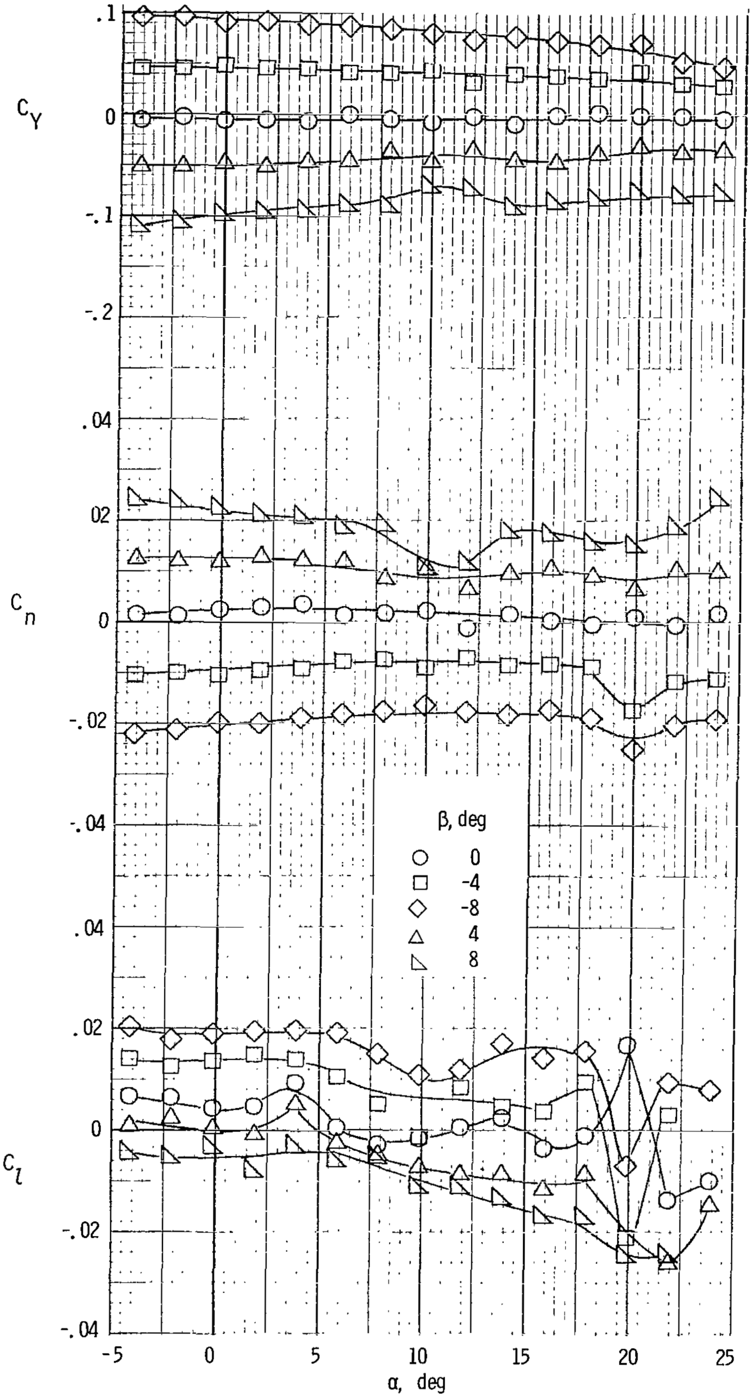

Figure 41.- Lateral aerodynamic characteristics of model with wing-tip tanks removed for $T'_c = 0$ and $\delta_f = 0^0$.

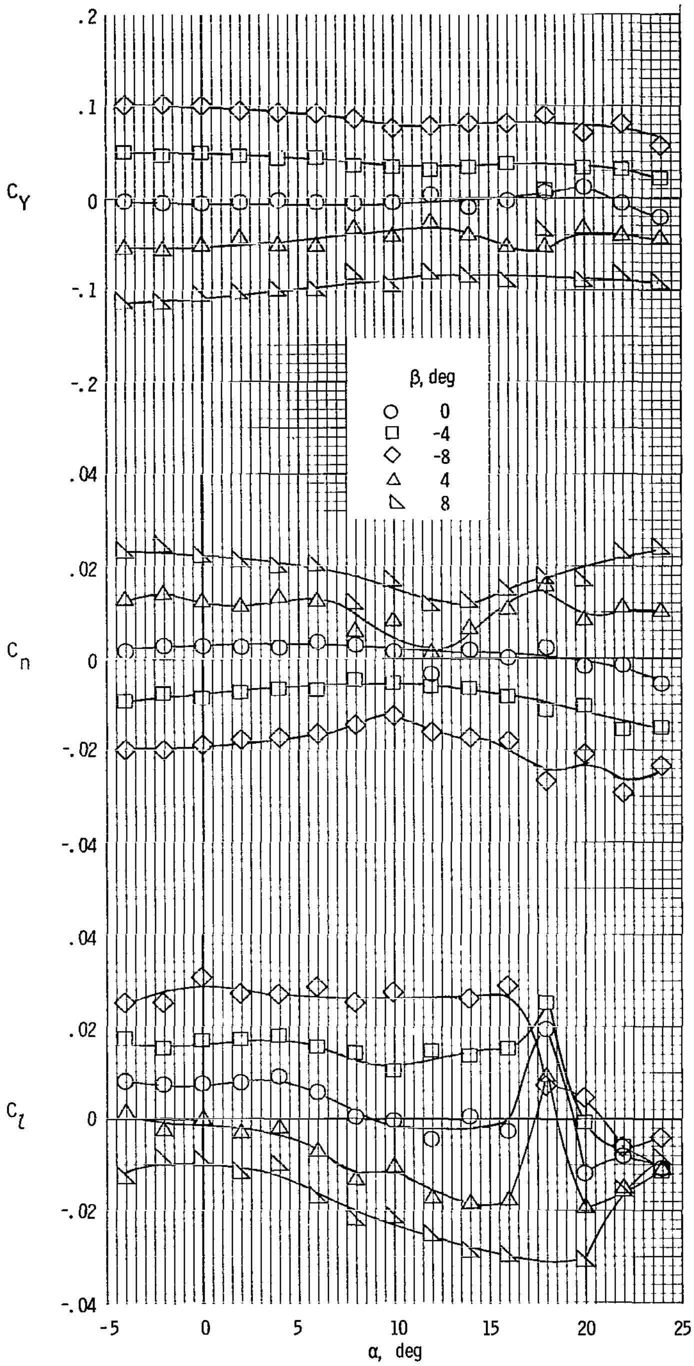

(a) $T_c' = 0$.

Figure 42.- Lateral aerodynamic characteristics of model with ventral fin removed for $\delta_f = 0^o$.

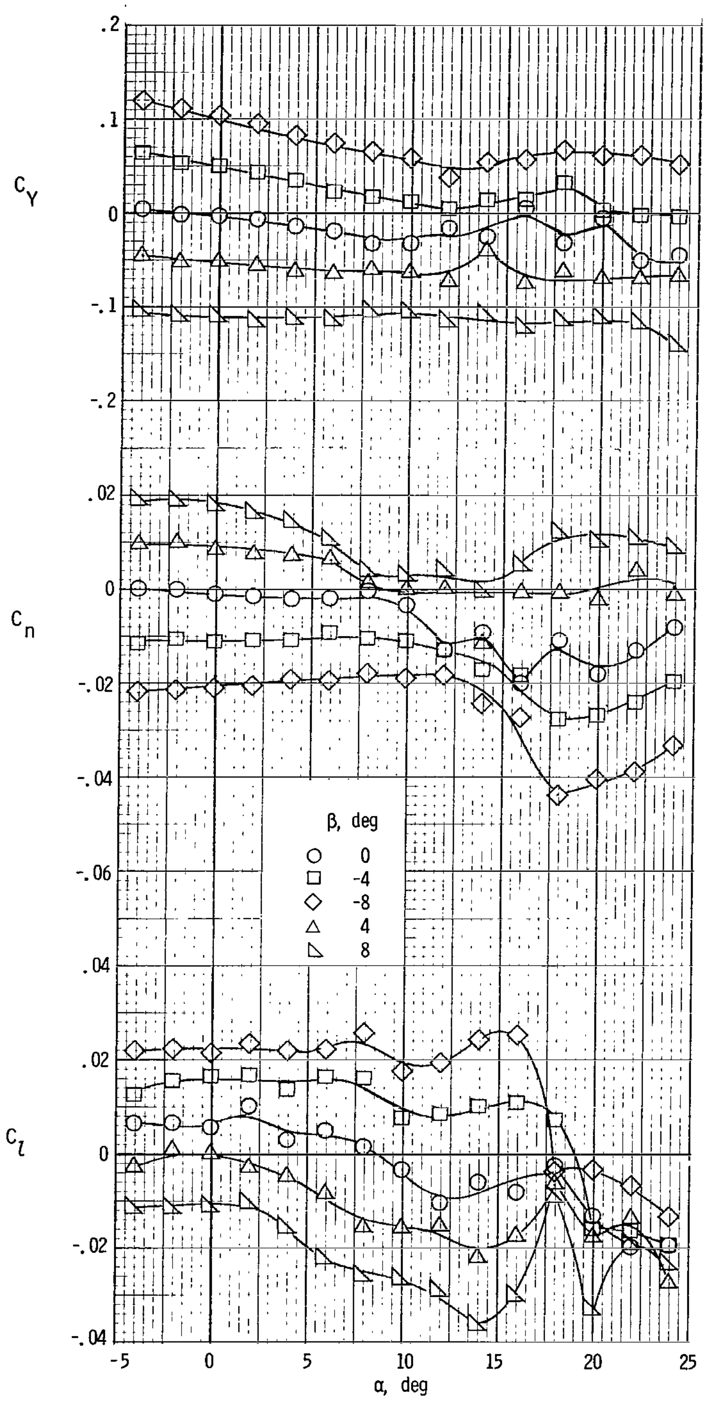

(b) $T_c' = 0.28$.

Figure 42.- Concluded.

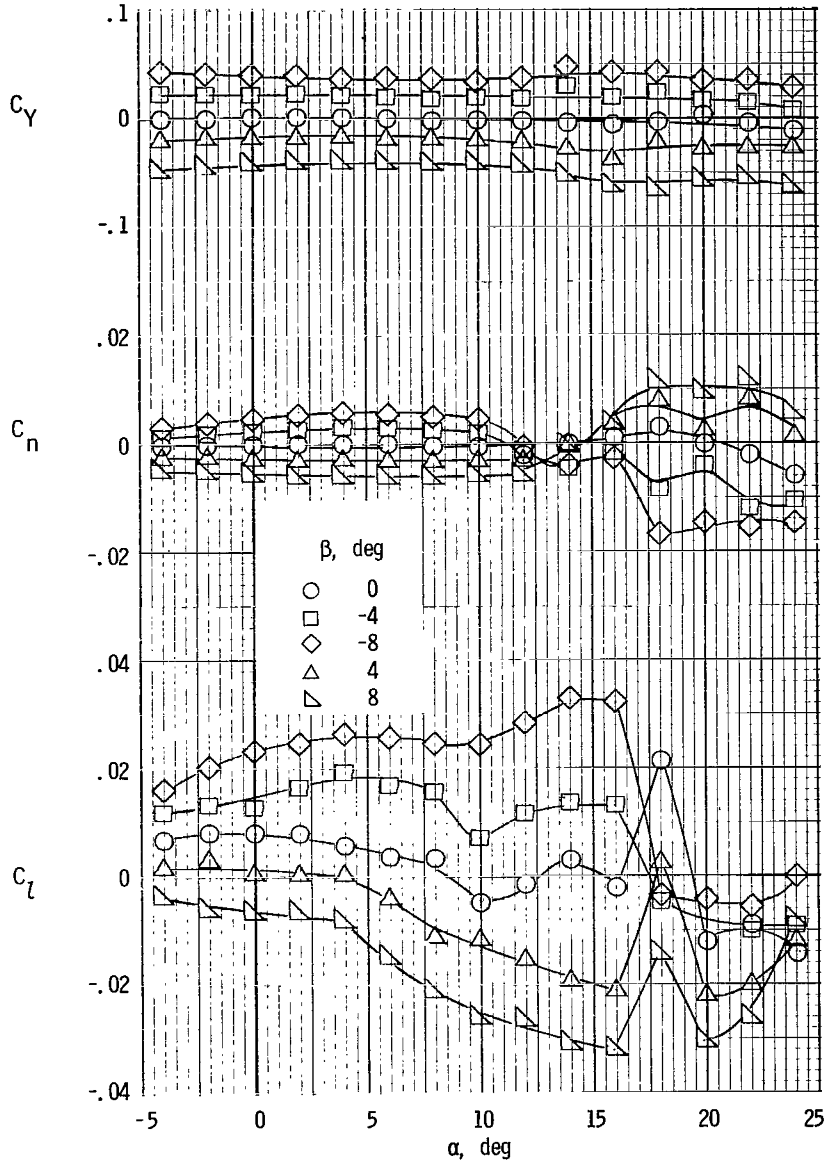

(a) $T'_c = 0$.

Figure 43.- Lateral aerodynamic characteristics of model with vertical tail and ventral fin removed for $\delta_f = 0^o$.

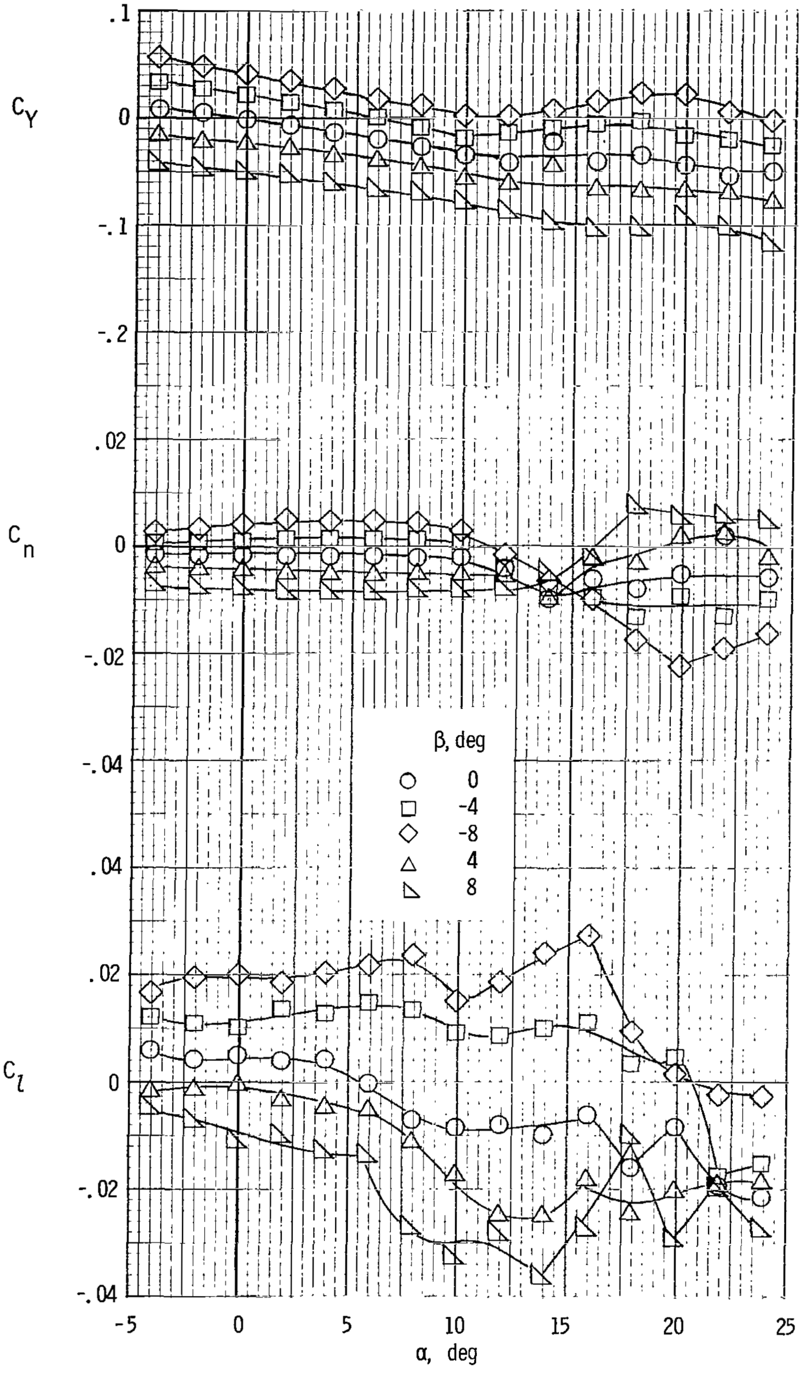

(b) $T_c' = 0.28$.

Figure 43.- Concluded.

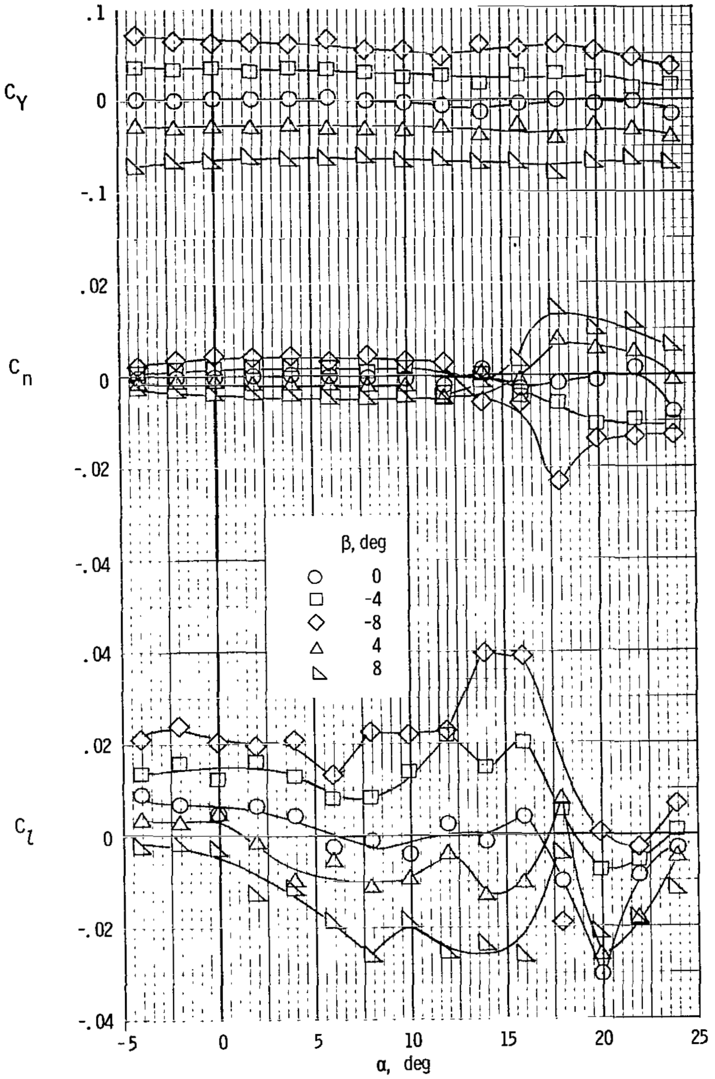

(a) $T_c' = 0$.

Figure 44.- Lateral aerodynamic characteristics of model with vertical tail and ventral fin removed for $\delta_f = 35^0$.

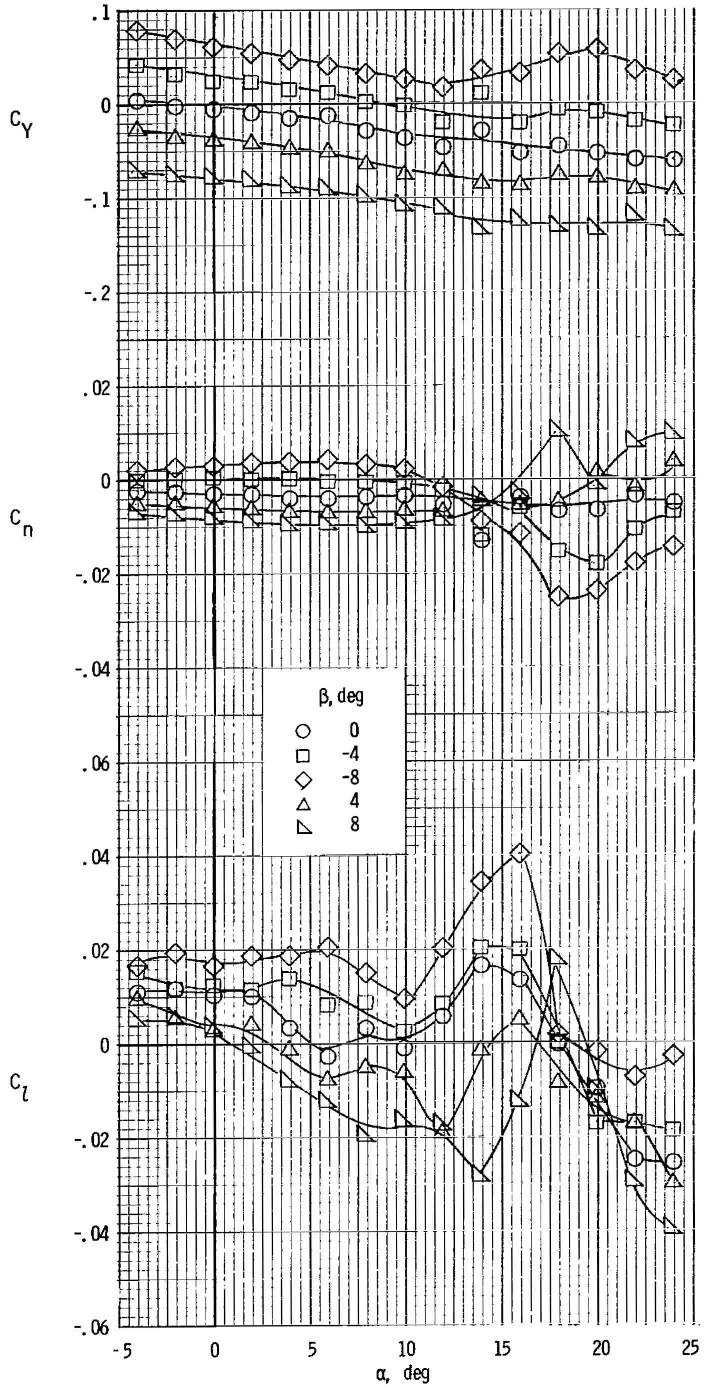

(b) $T'_c = 0.28$.

Figure 44.- Concluded.

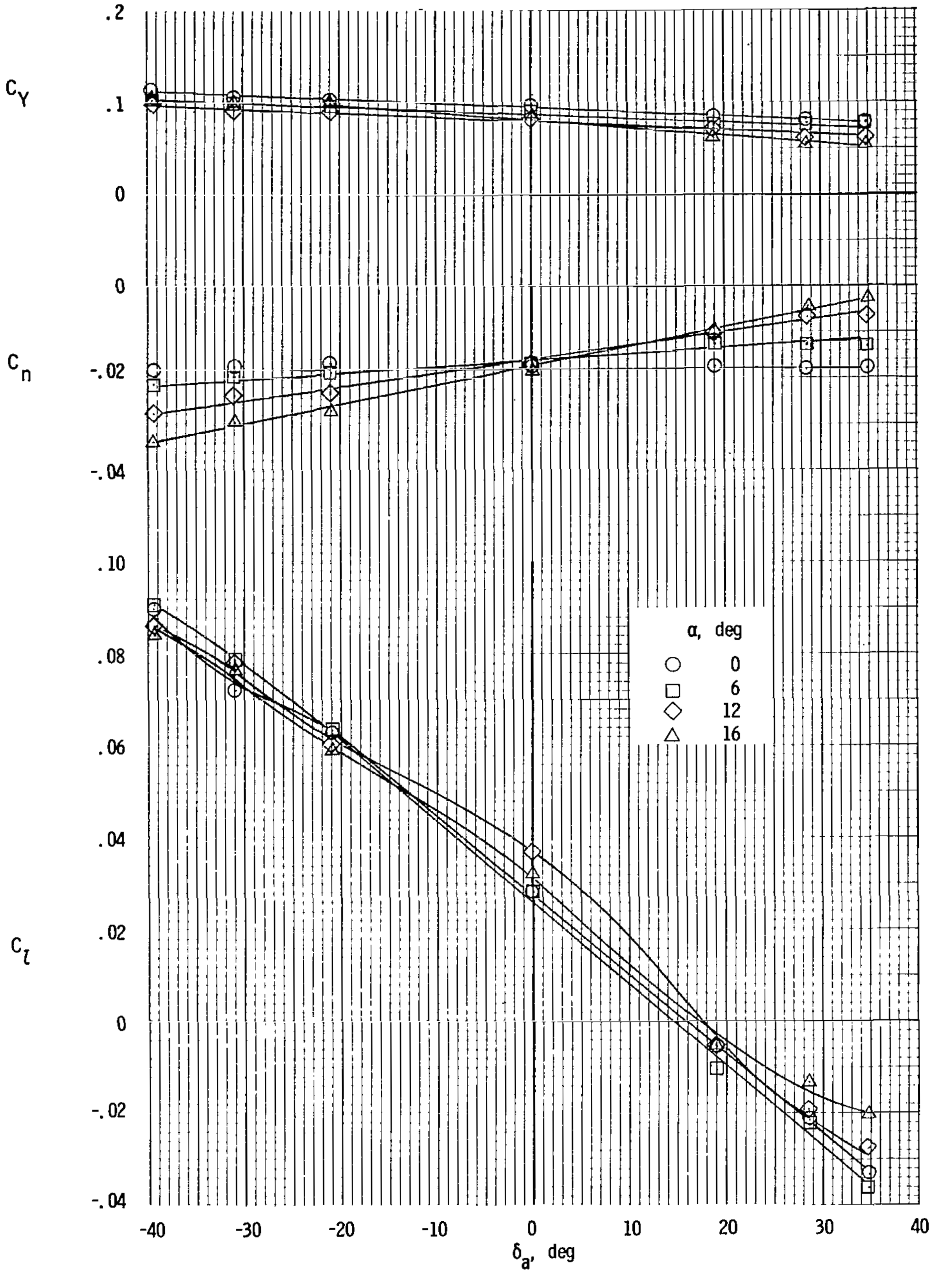

(a) $\beta = -8^0$.

Figure 45.- Variation of lateral aerodynamic characteristics of model with aileron deflection for $\delta_f = 0^0$; $T_C' = 0$.

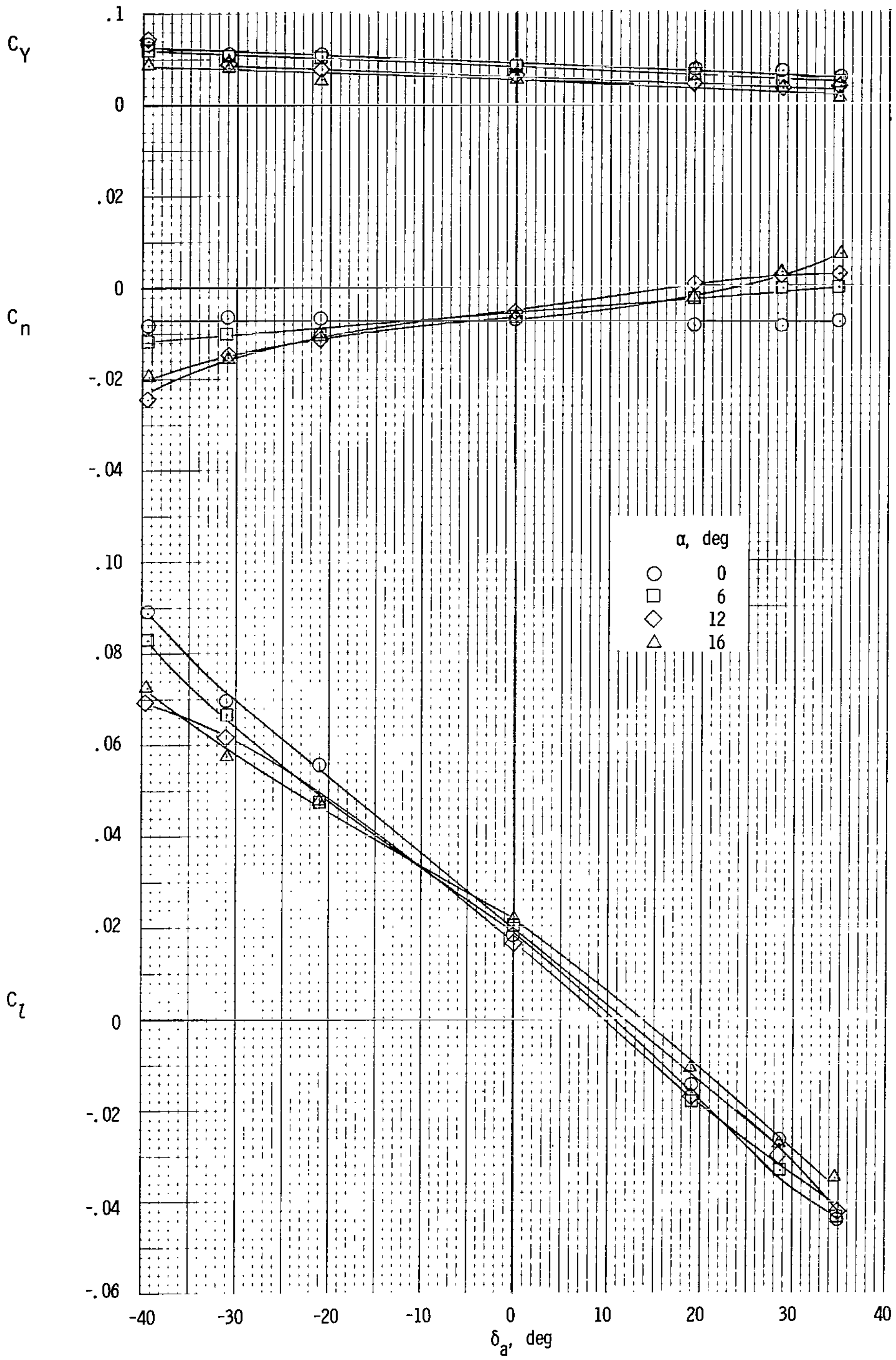

(b) $\beta = -4^0$.

Figure 45.- Continued.

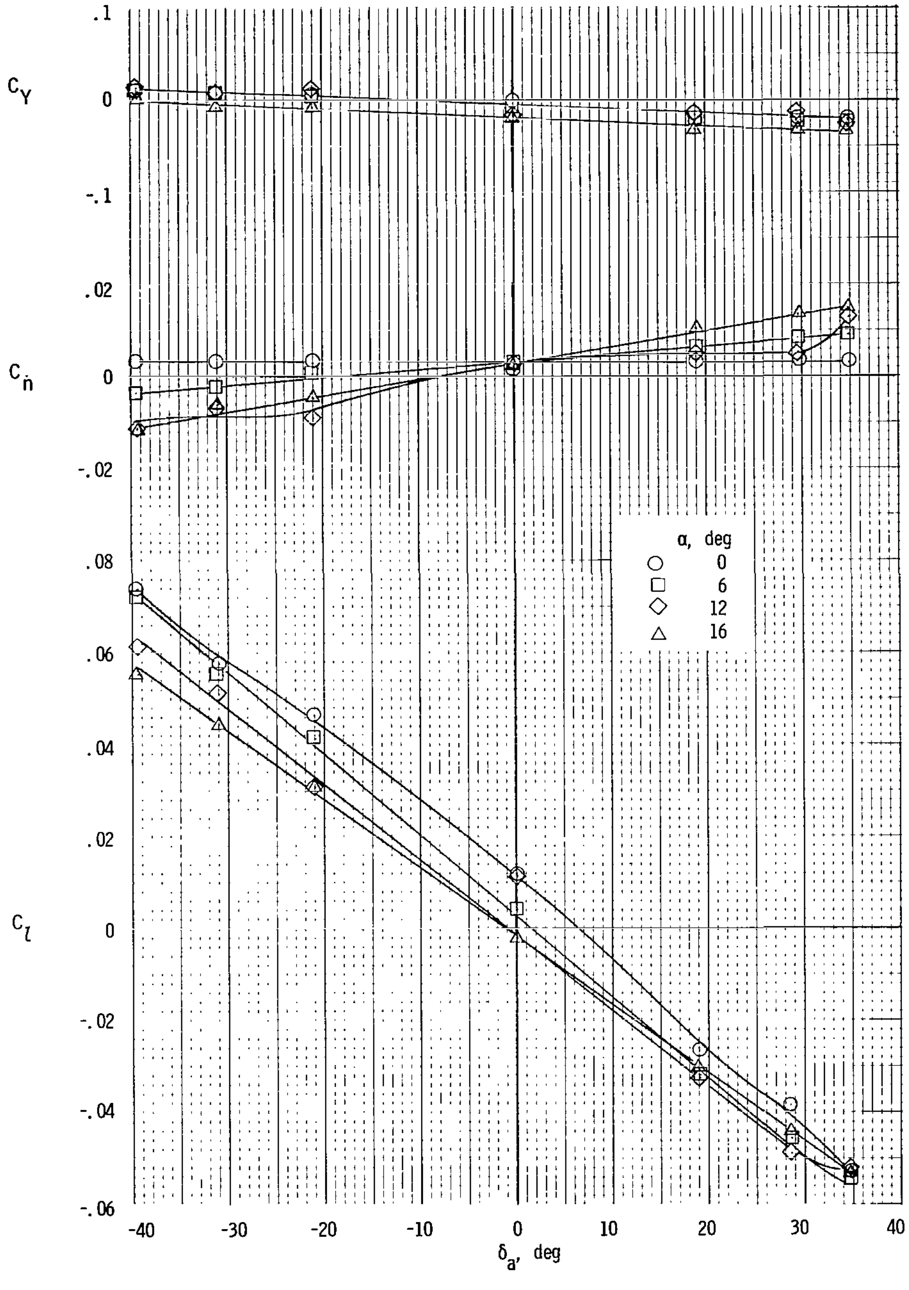

(c) $\beta = 0^{0}$.

Figure 45.- Continued.

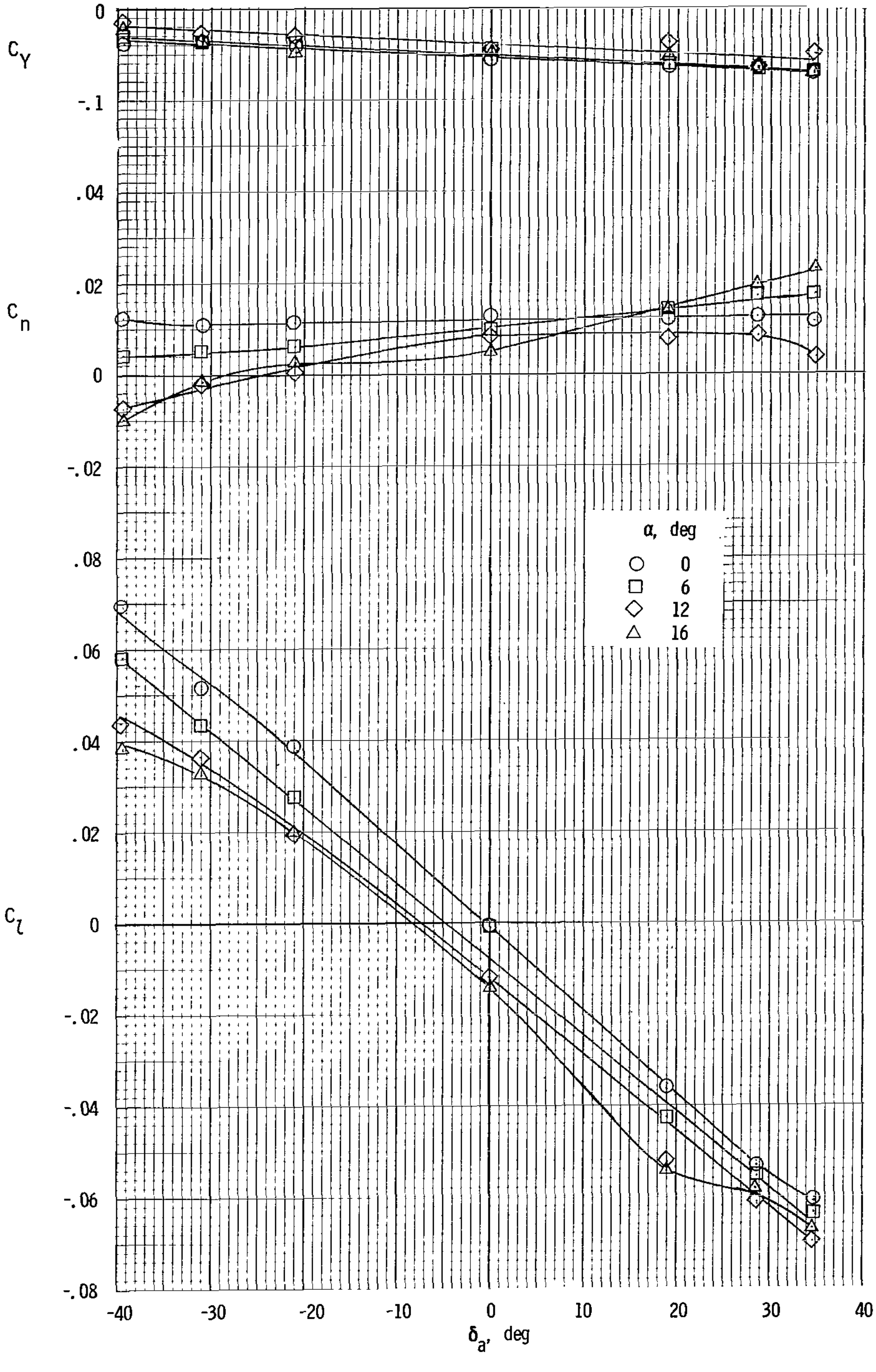

(d) $\beta = 4^{\circ}$.

Figure 45.- Continued.

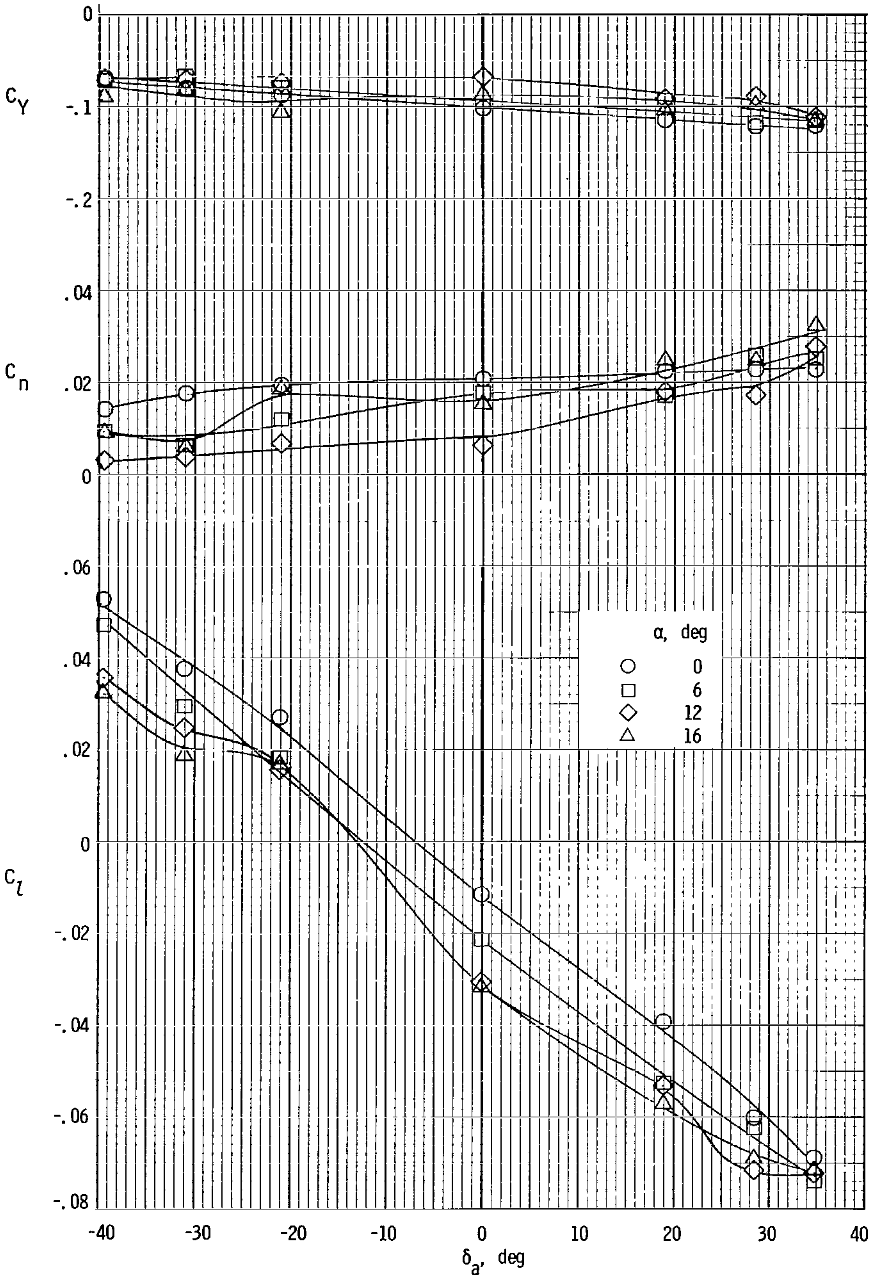

(e) $\beta = 8^{\circ}$.

Figure 45.- Concluded.

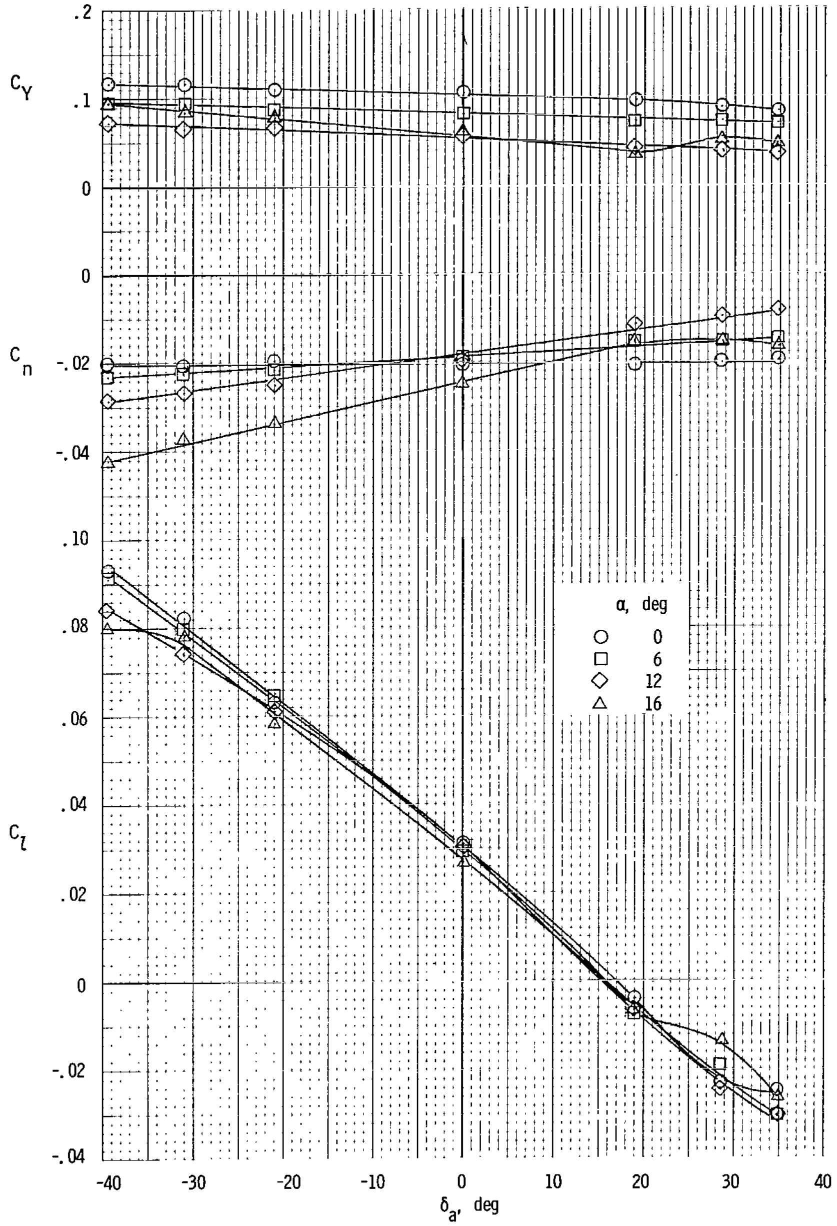

(a) $\beta = -8^0$.

Figure 46.- Variation of lateral aerodynamic characteristics of model with aileron deflection for $\delta_f = 0^0$; $T_c' = 0.19$.

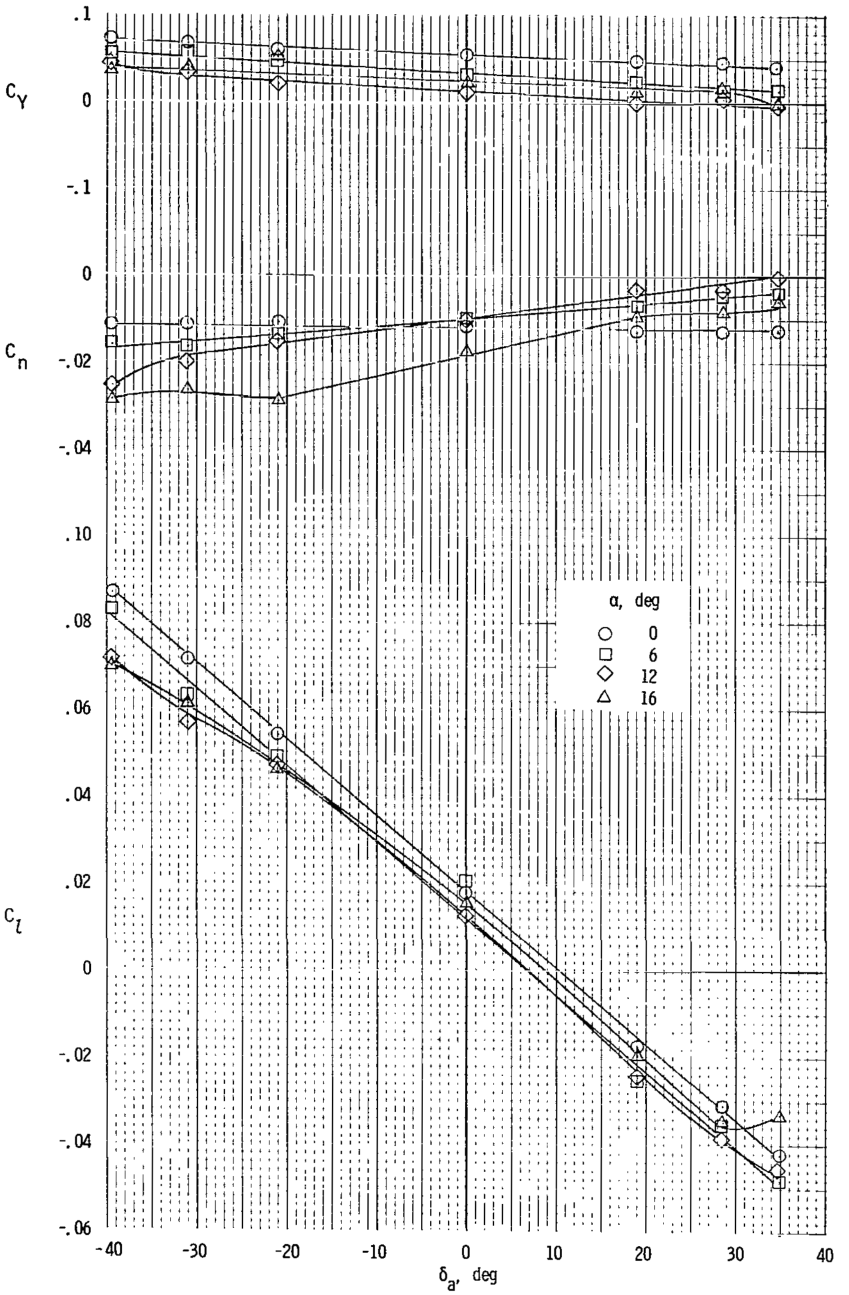

(b) $\beta = -4^0$.

Figure 46.- Continued.

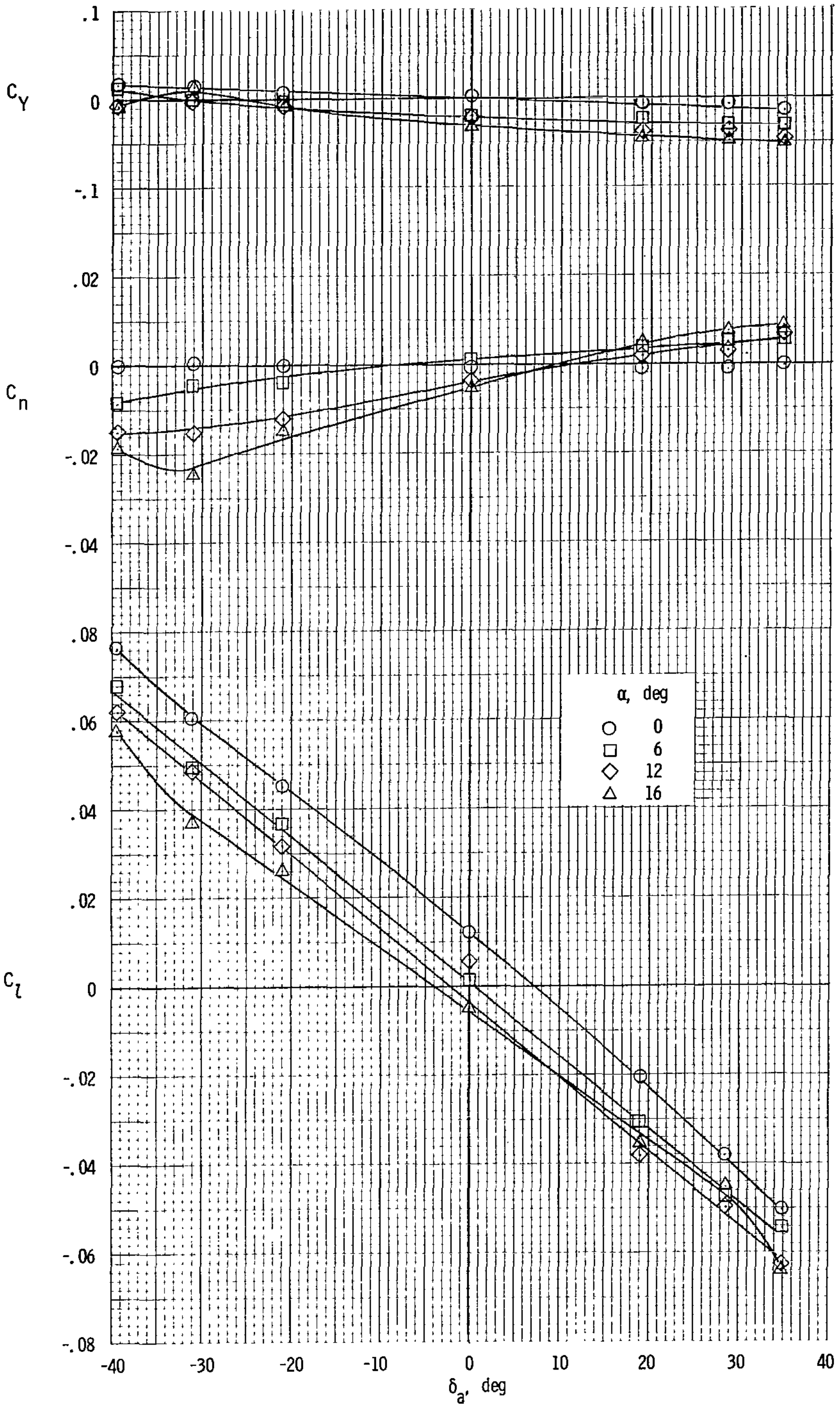

(c) $\beta = 0^0$.

Figure 46.- Continued.

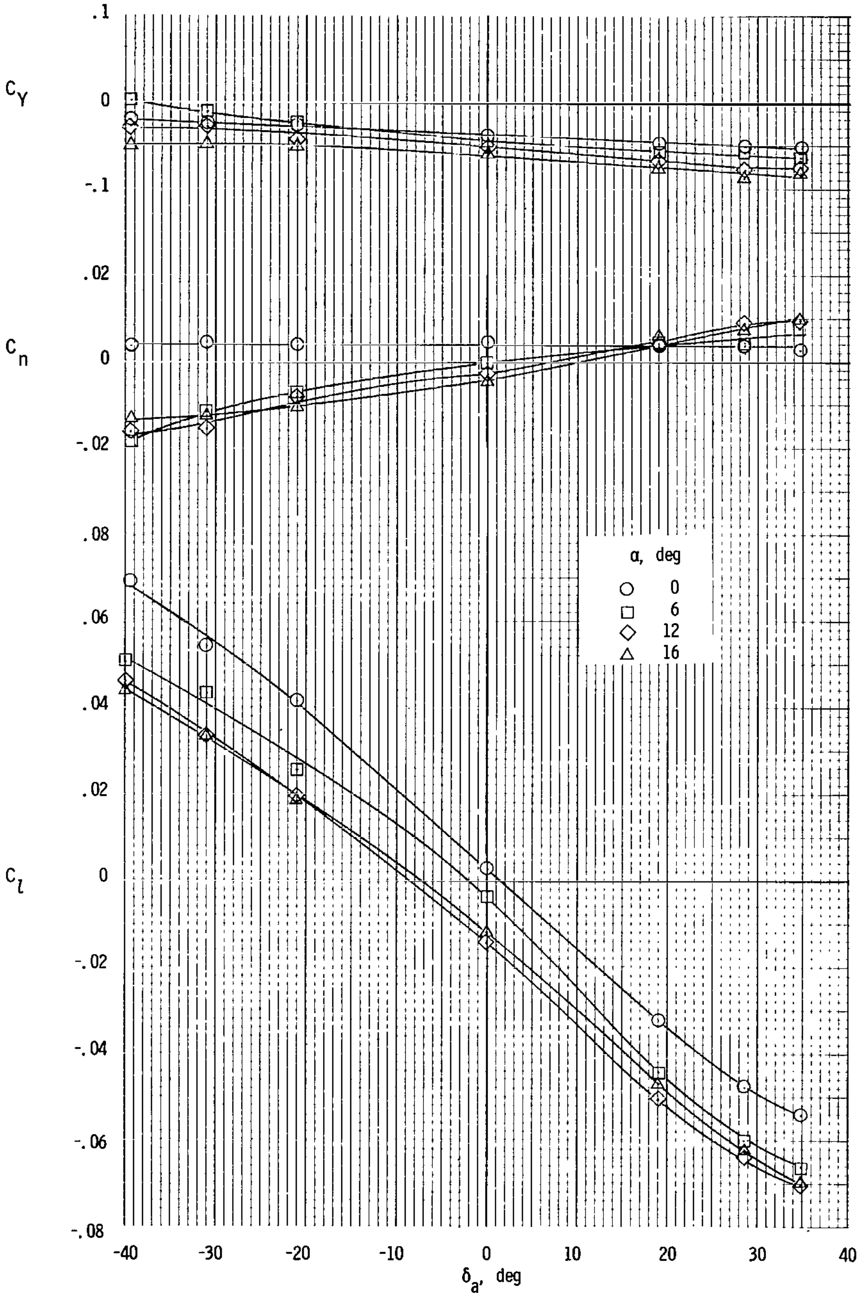

(d) $\beta = 4^o$.

Figure 46.- Continued.

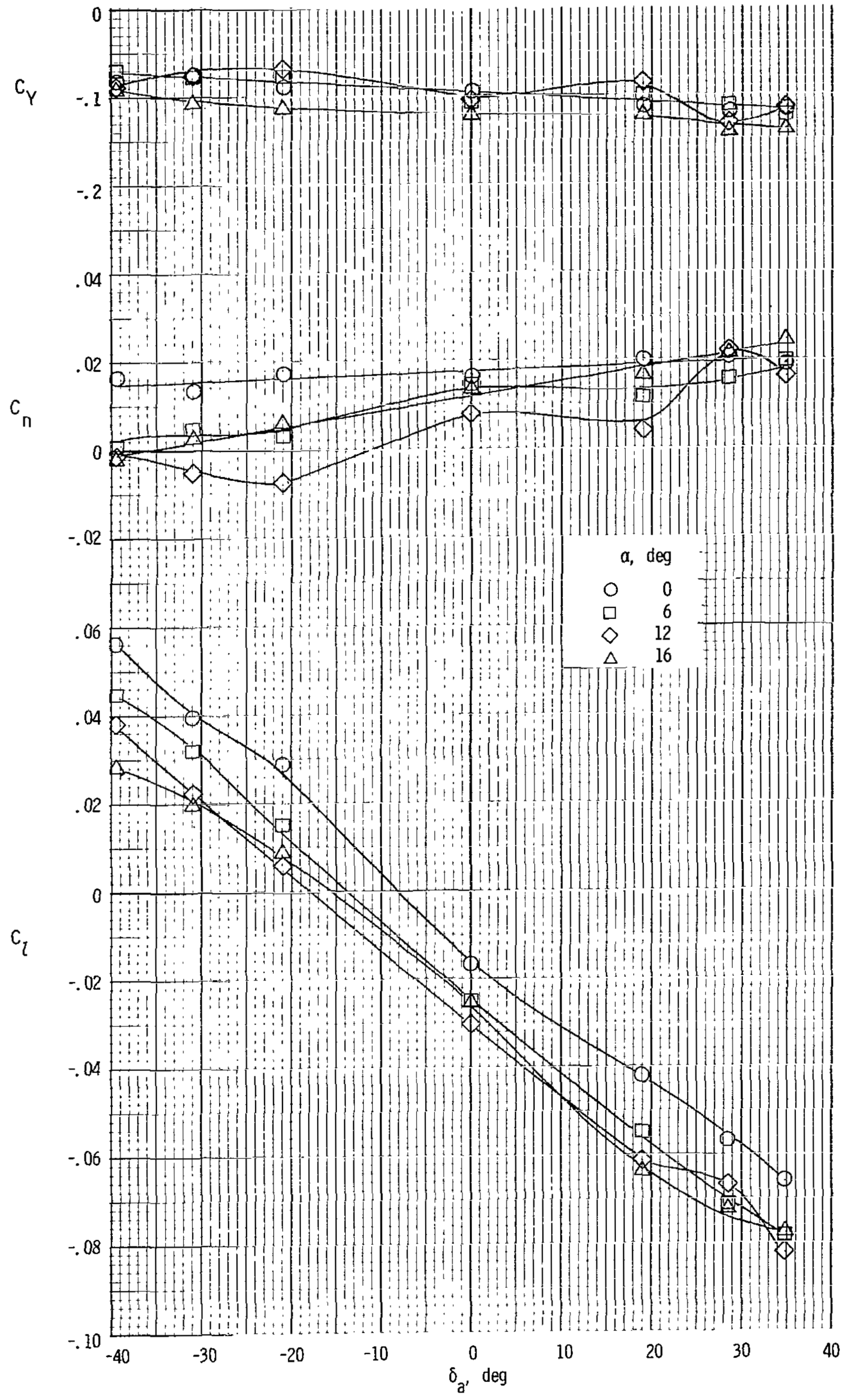

(e) $\beta = 8^{0}$.

Figure 46.- Concluded.

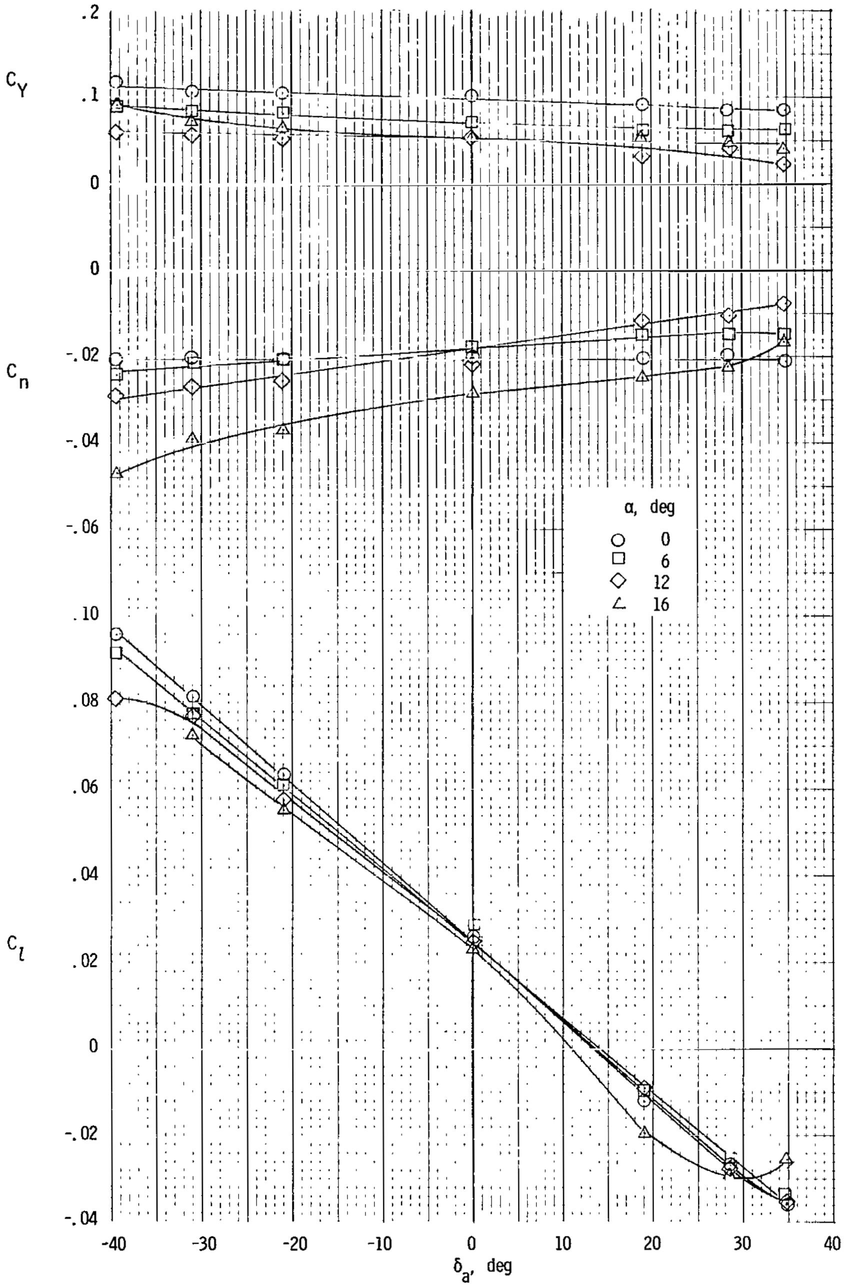

(a) $\beta = -8^{\circ}$.

Figure 47.- Variation of lateral aerodynamic characteristics of model with aileron deflection for $\delta_f = 0^{\circ}$; $T_c' = 0.28$.

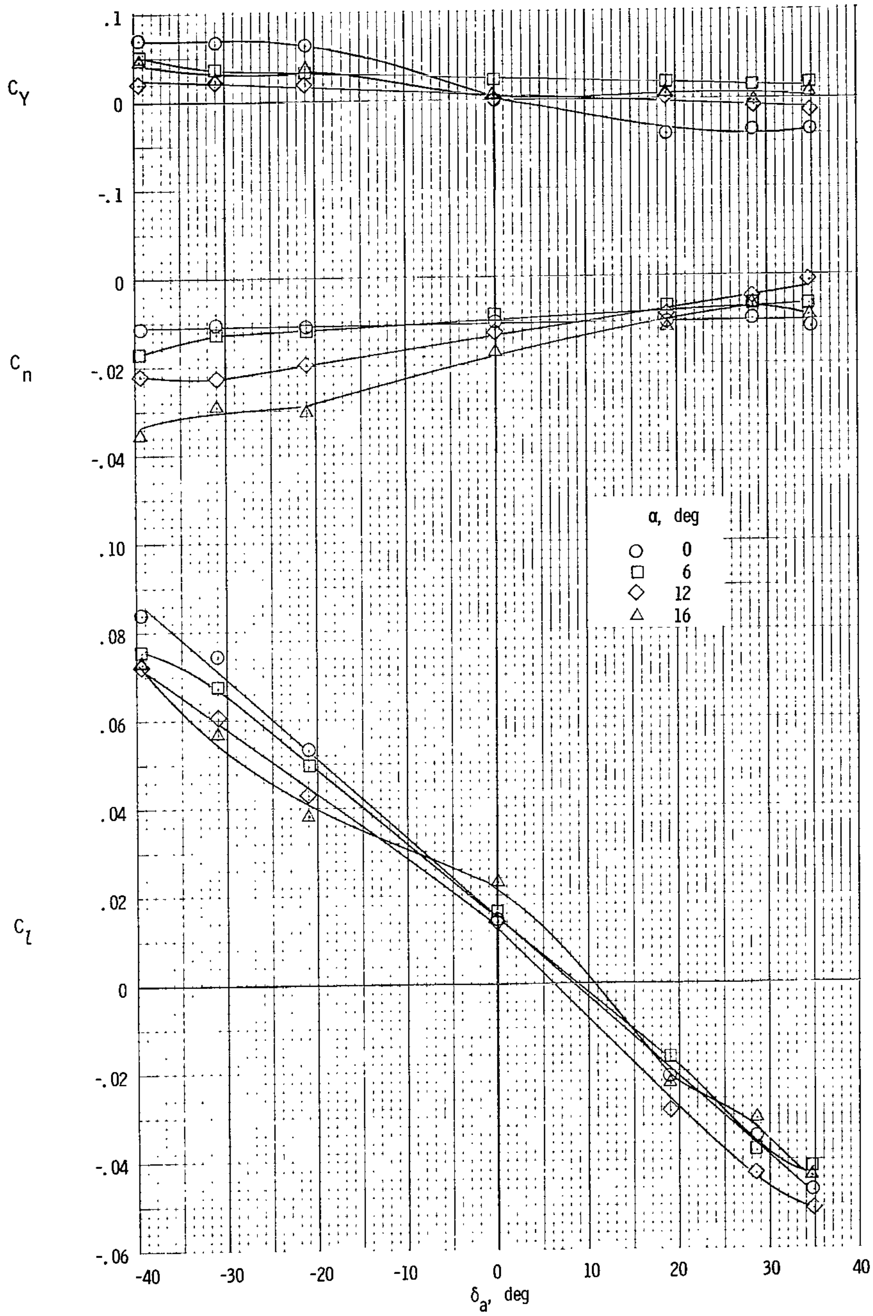

(b) $\beta = -4^{\circ}$.

Figure 47.- Continued.

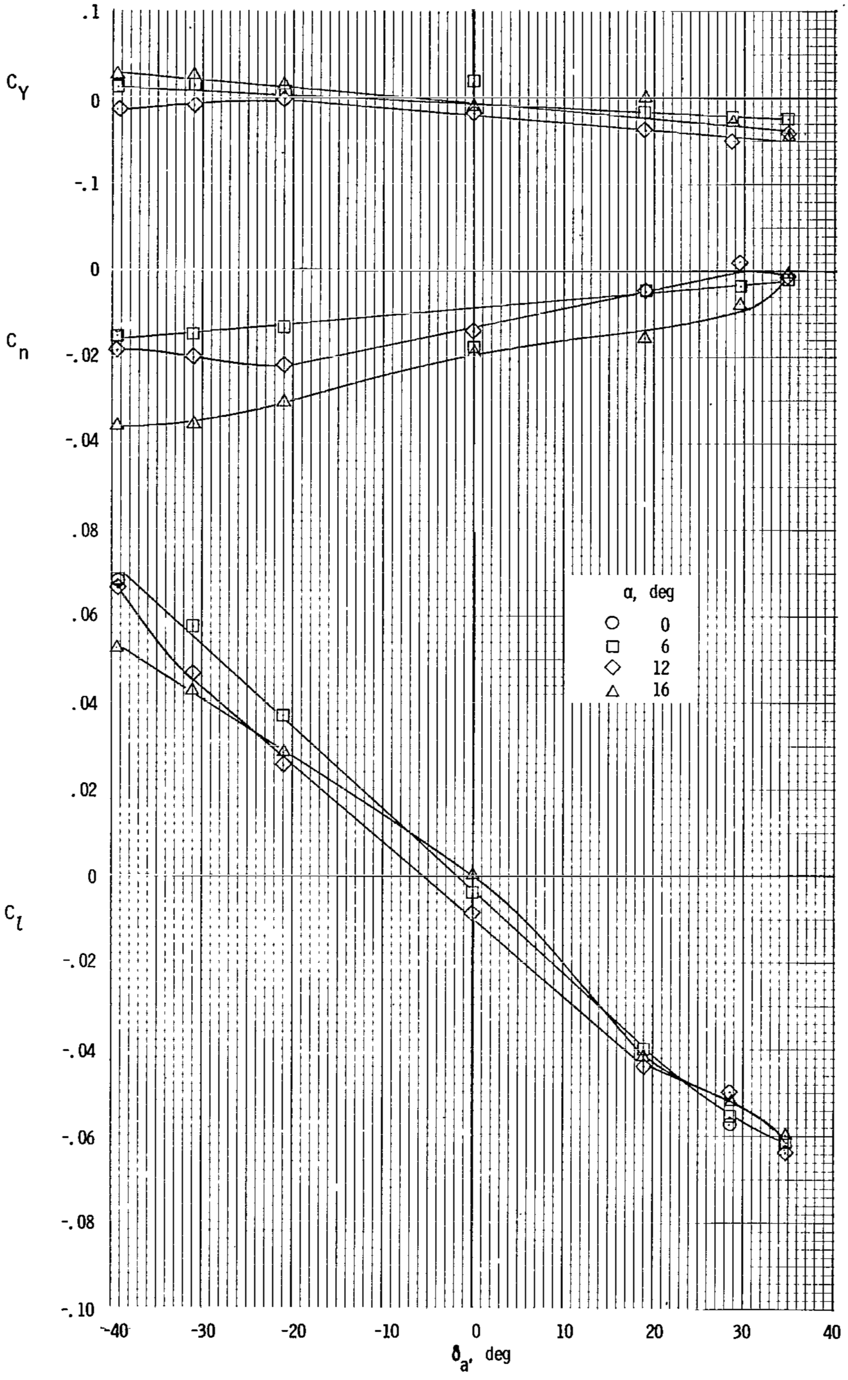

(c) $\beta = 0^{\circ}$.

Figure 47.- Continued.

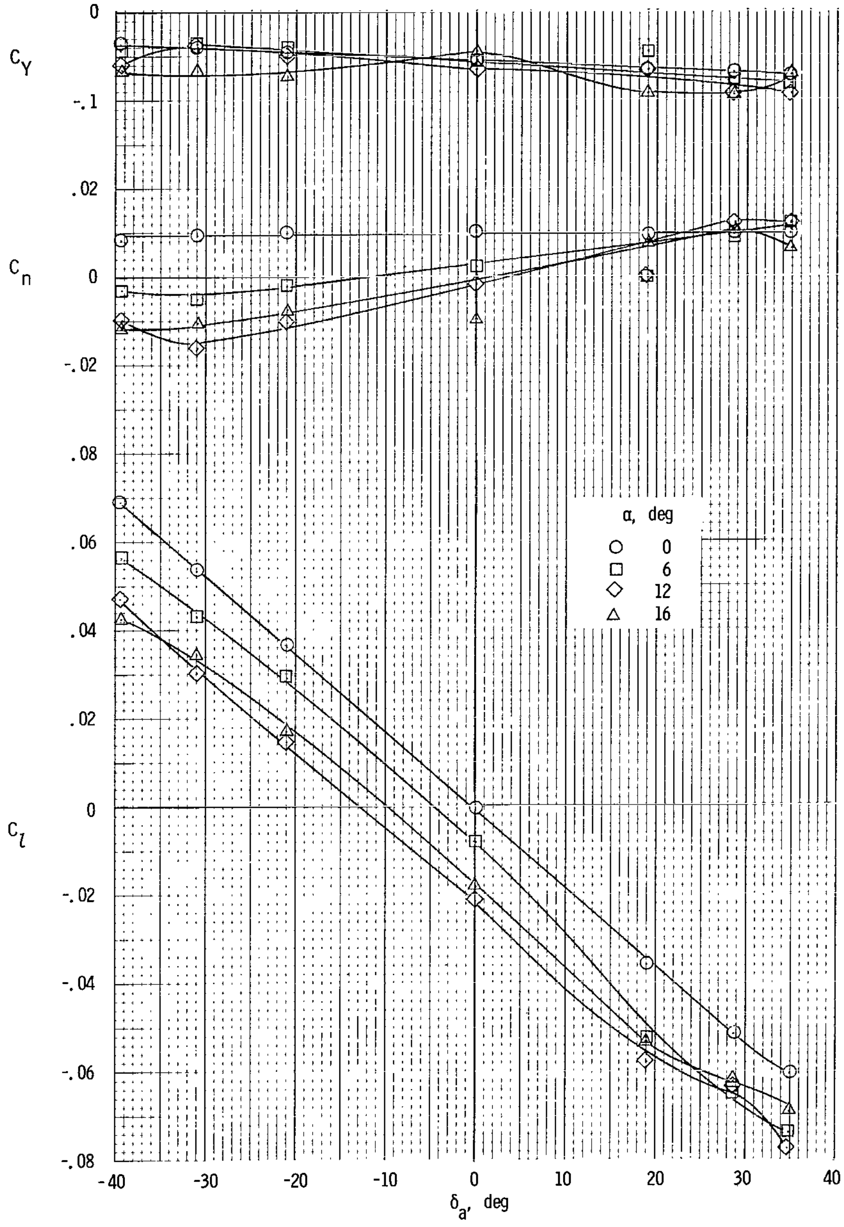

(d) $\beta = 4^{\circ}$.

Figure 47.- Continued.

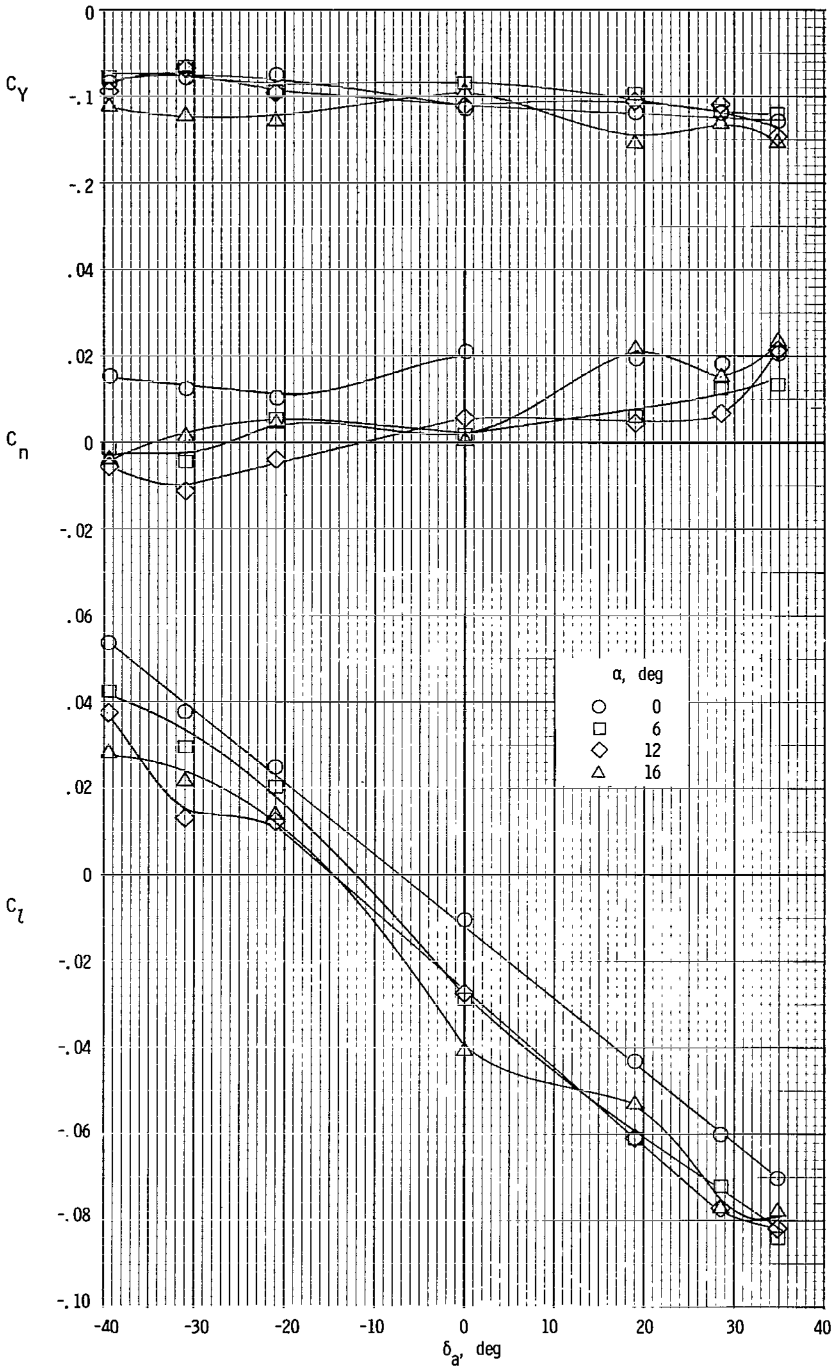

(e) $\beta = 8^0$.

Figure 47.- Concluded.

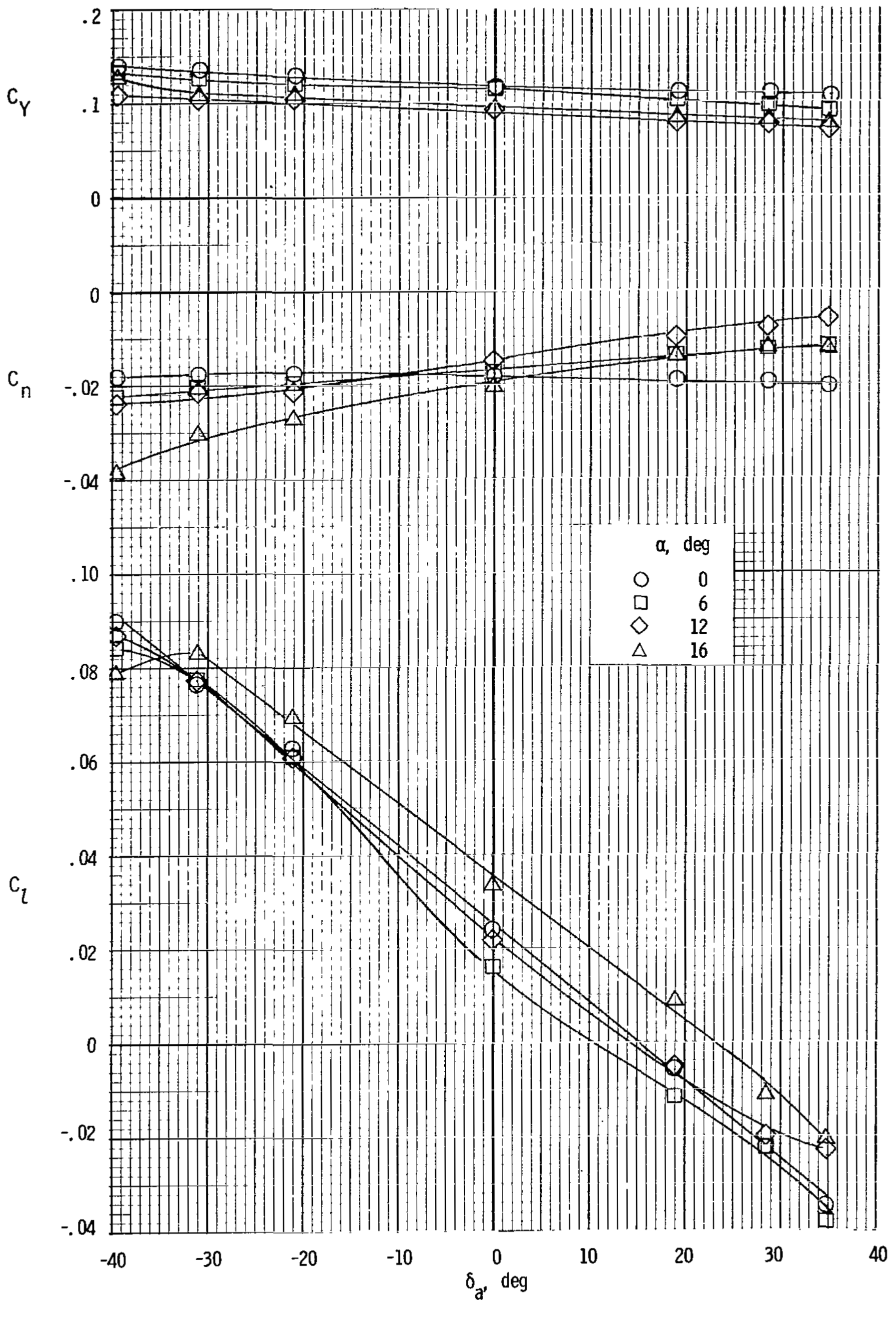

(a) $\beta = -8^{\circ}$.

Figure 48.- Variation of lateral aerodynamic characteristics of model with aileron deflection for $\delta_f = 35^{\circ}$; $T_c' = 0$.

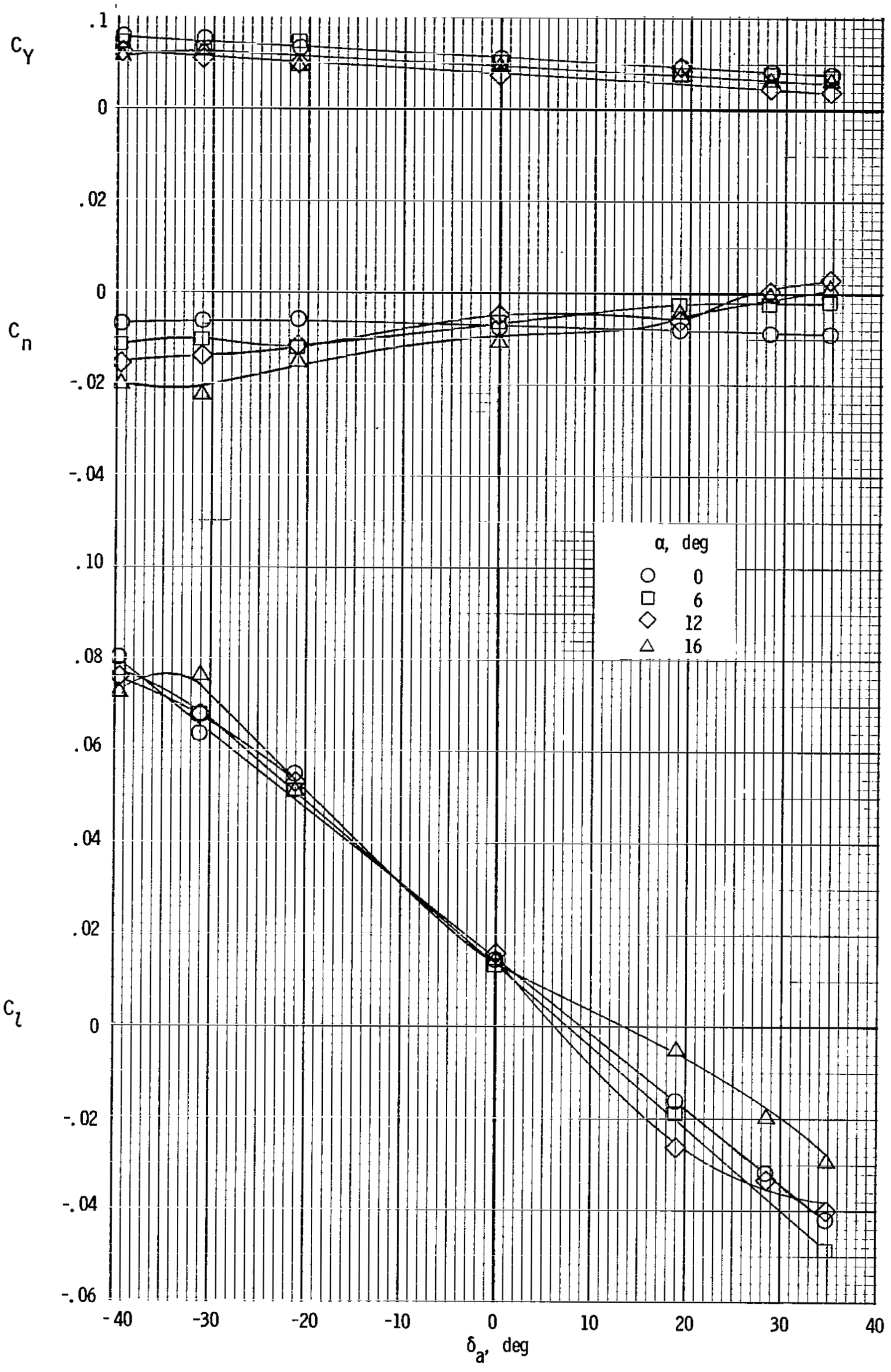

(b) $\beta = -4^\circ$.

Figure 48.- Continued.

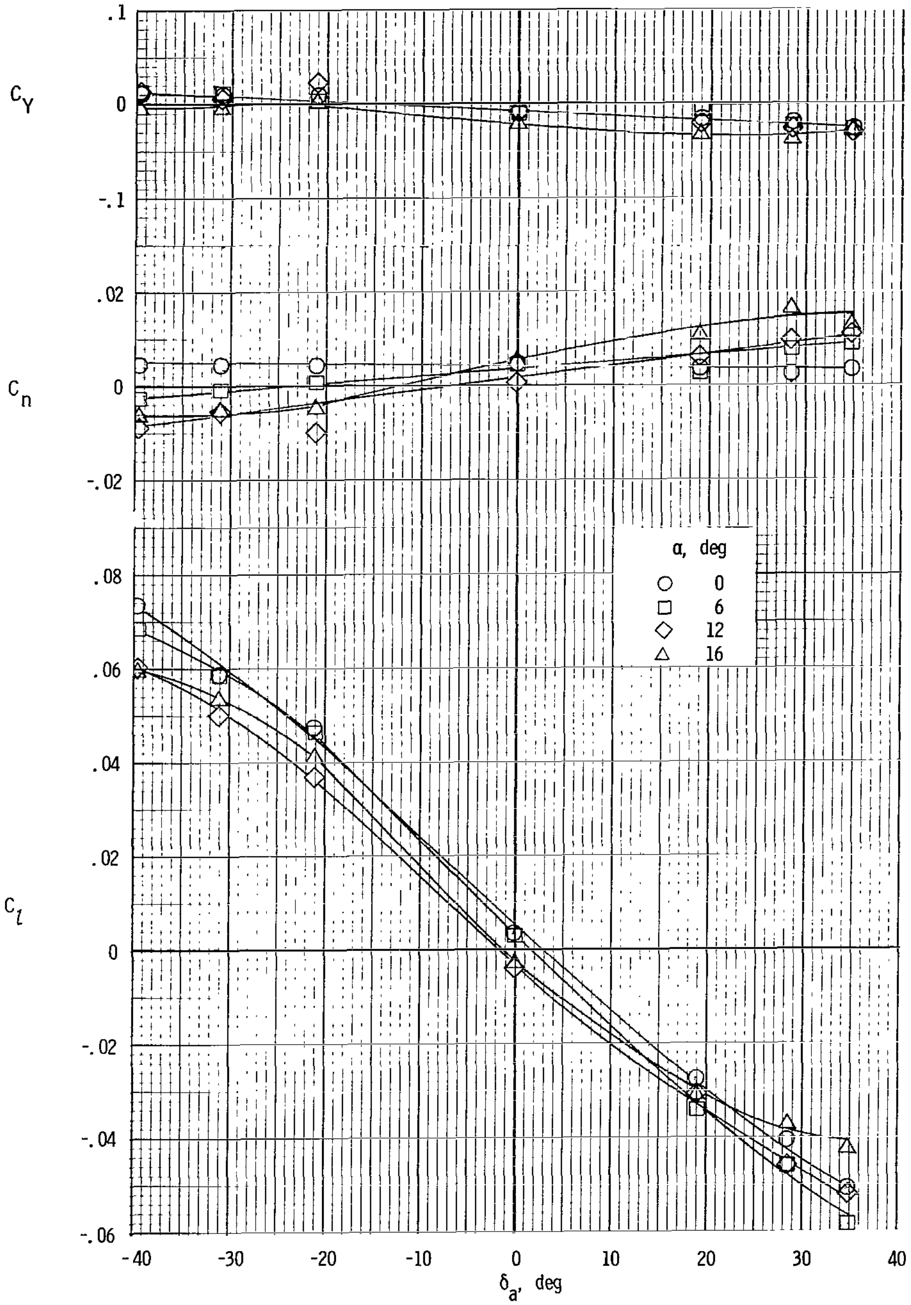

(c) $\beta = 0^{\circ}$.

Figure 48.- Continued.

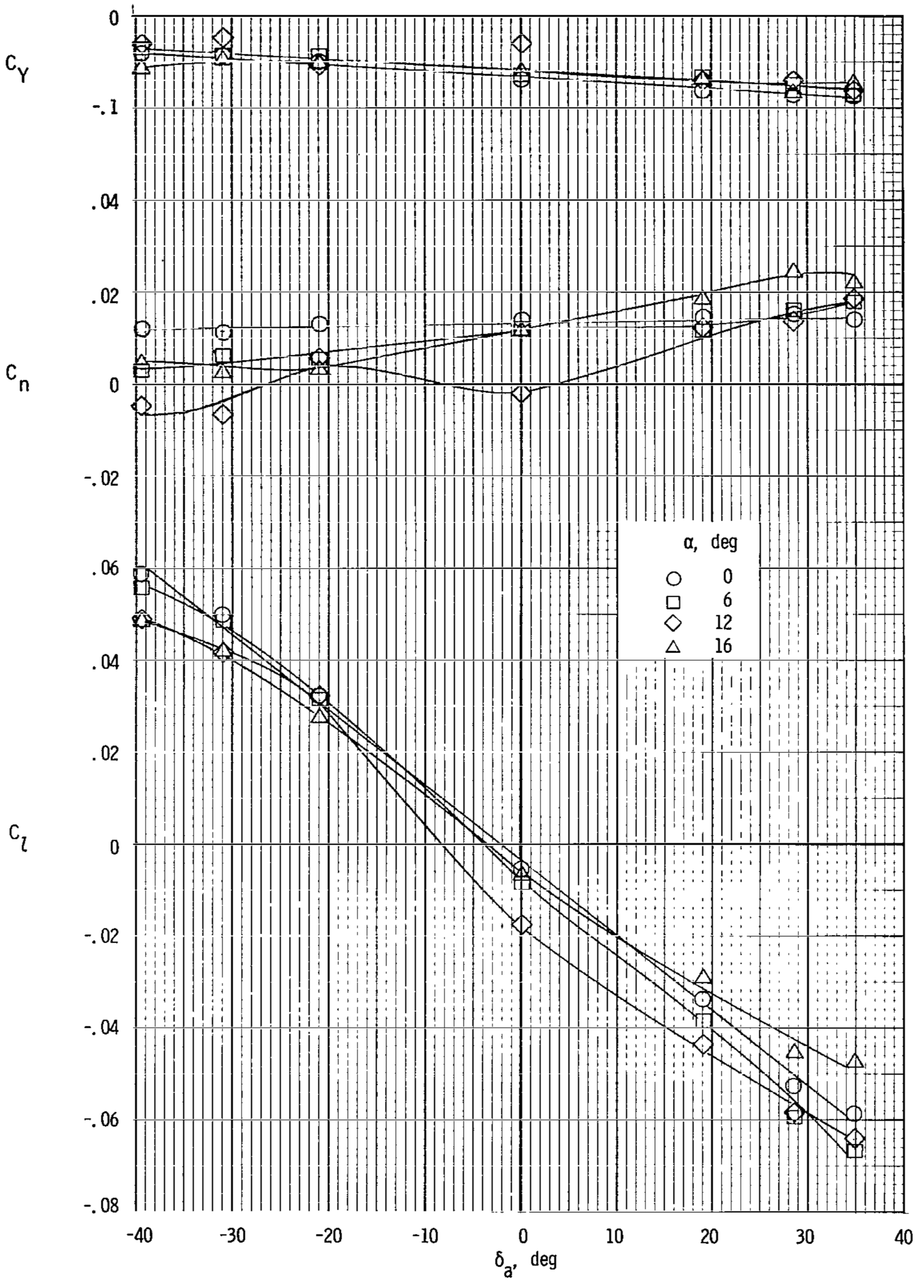

(d) $\beta = 4^{\circ}$.

Figure 48.- Continued.

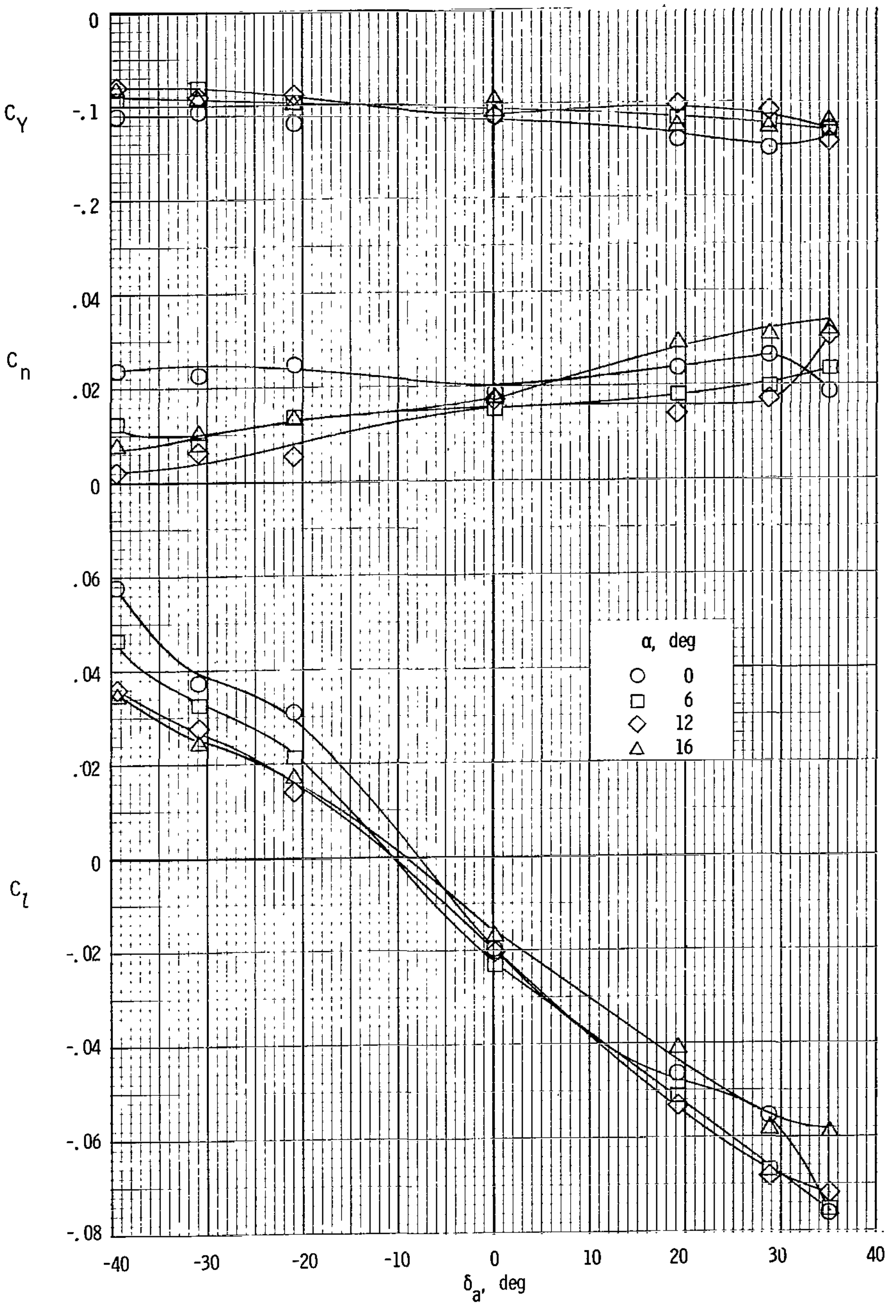

(e) $\beta = 8^0$.

Figure 48.- Concluded.

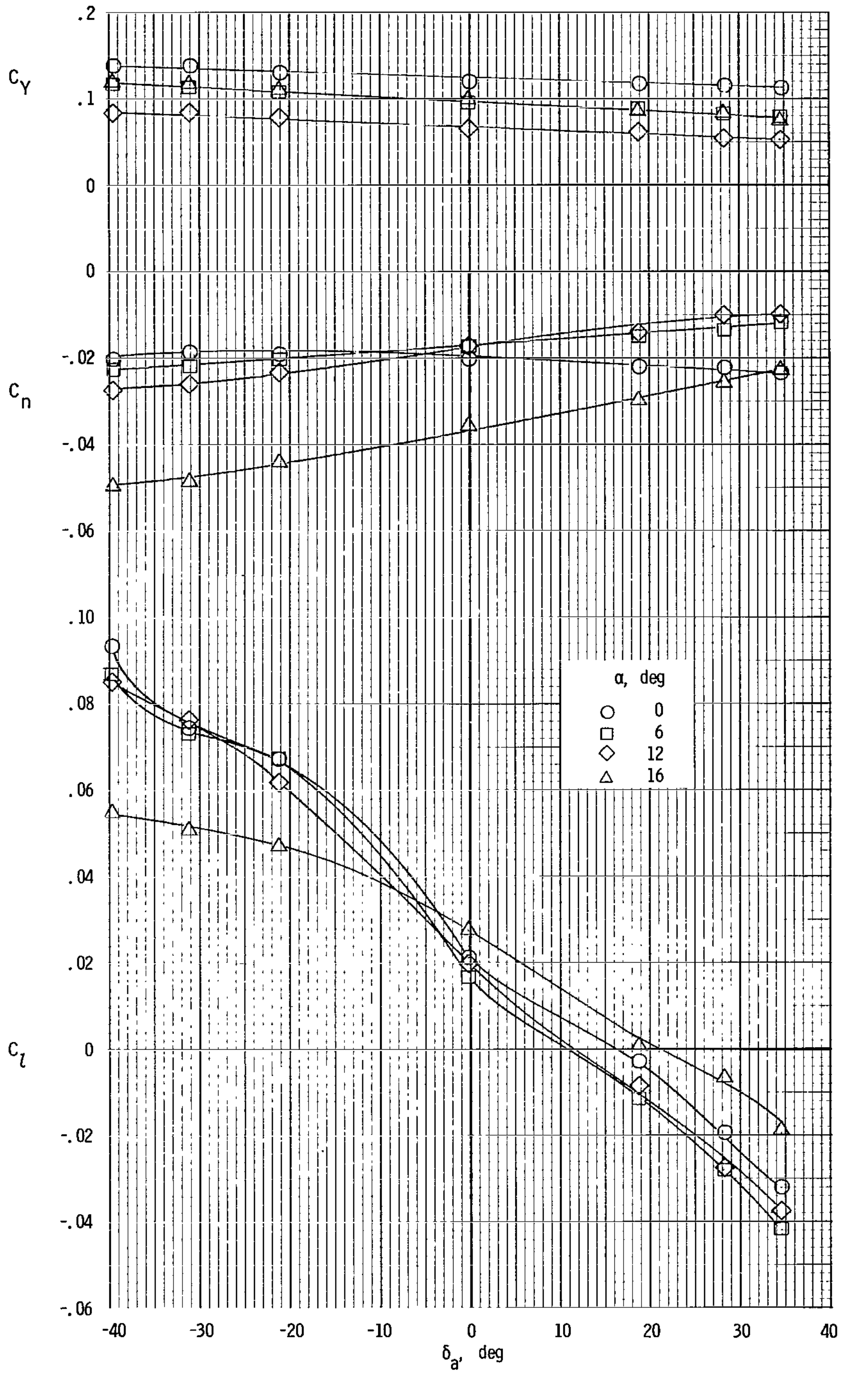

(a) $\beta = -8^\circ$.

Figure 49.- Variation of lateral aerodynamic characteristics of model with aileron deflection for $\delta_f = 35^\circ$; $T_c' = 0.19$.

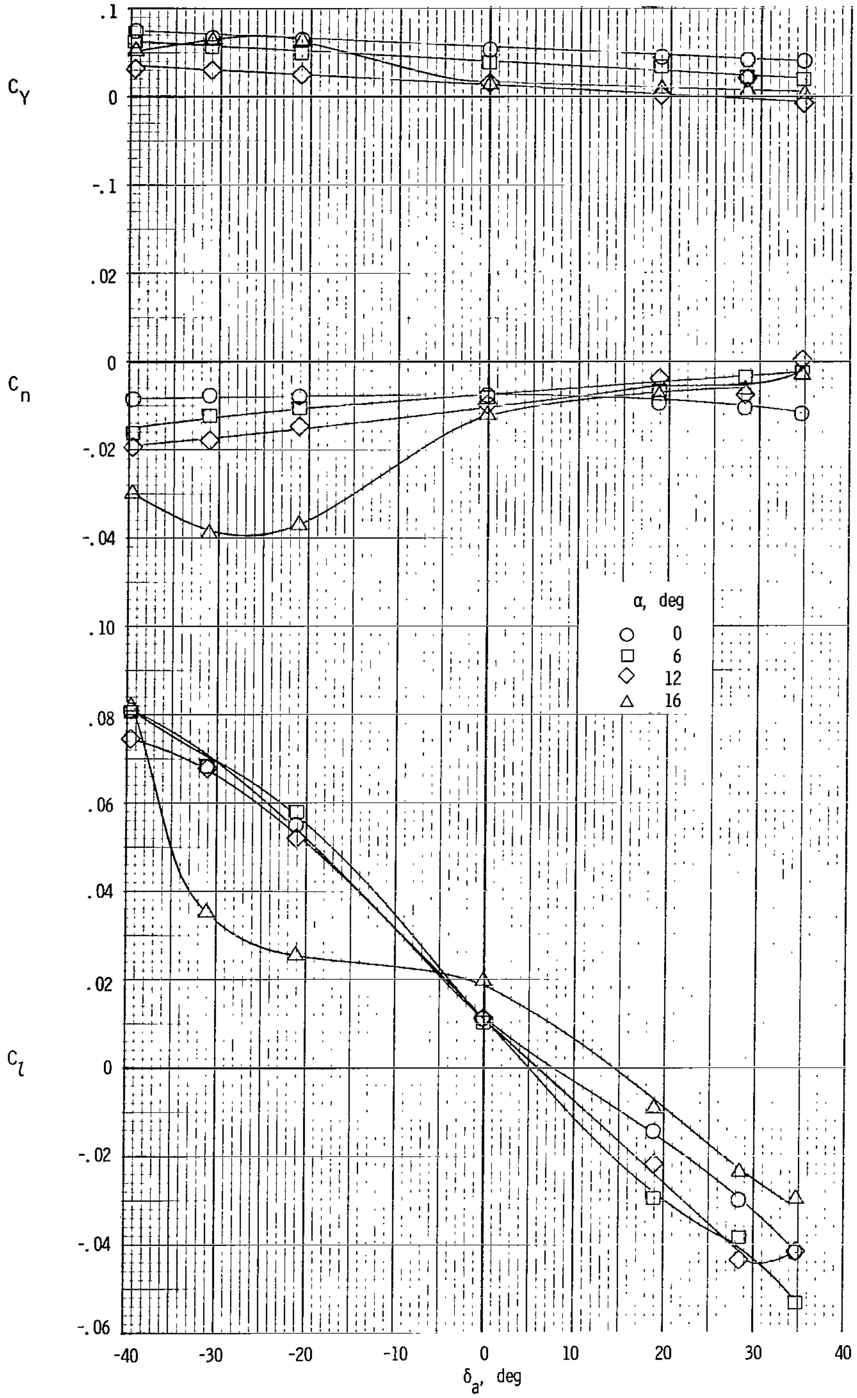

(b) $\beta = -4^{\circ}$.

Figure 49.- Continued.

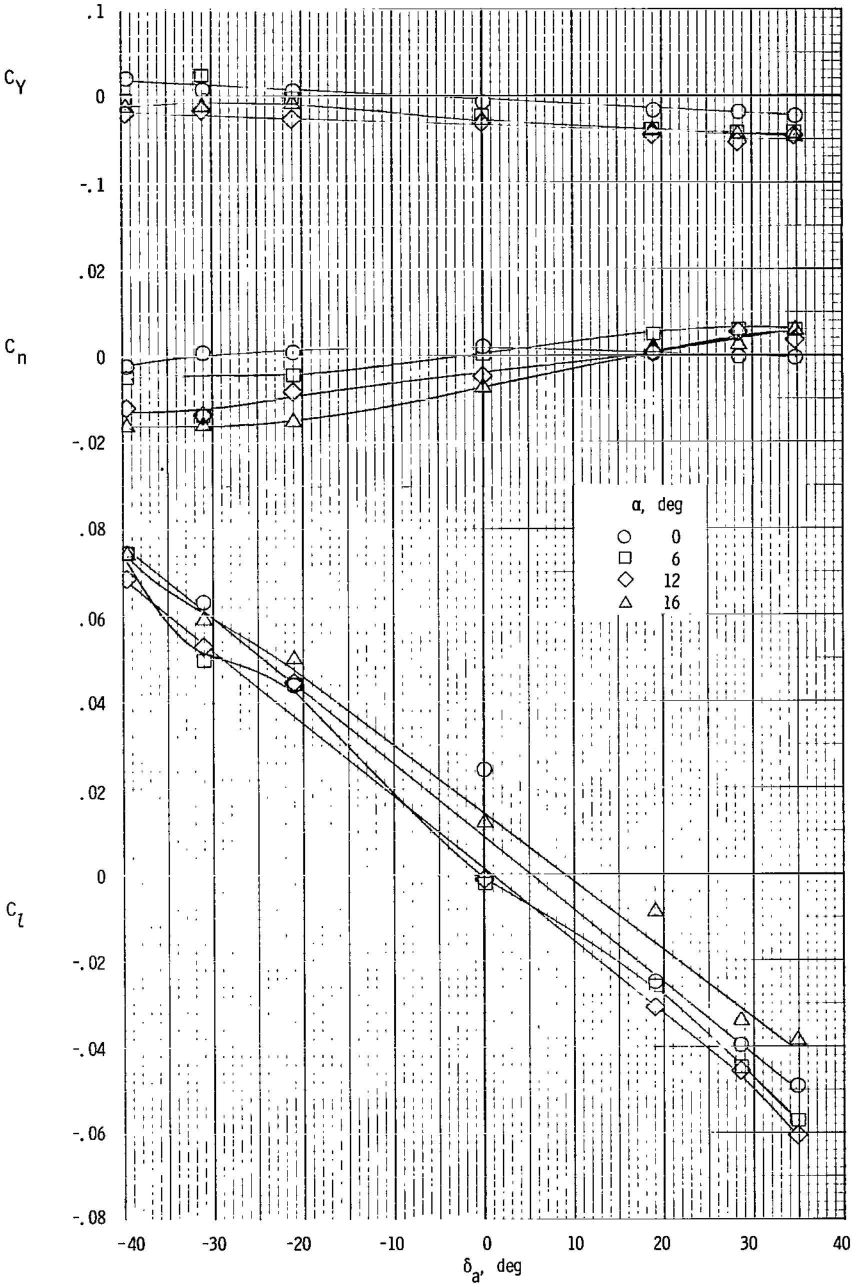

(c) $\beta = 0^o$.

Figure 49.- Continued.

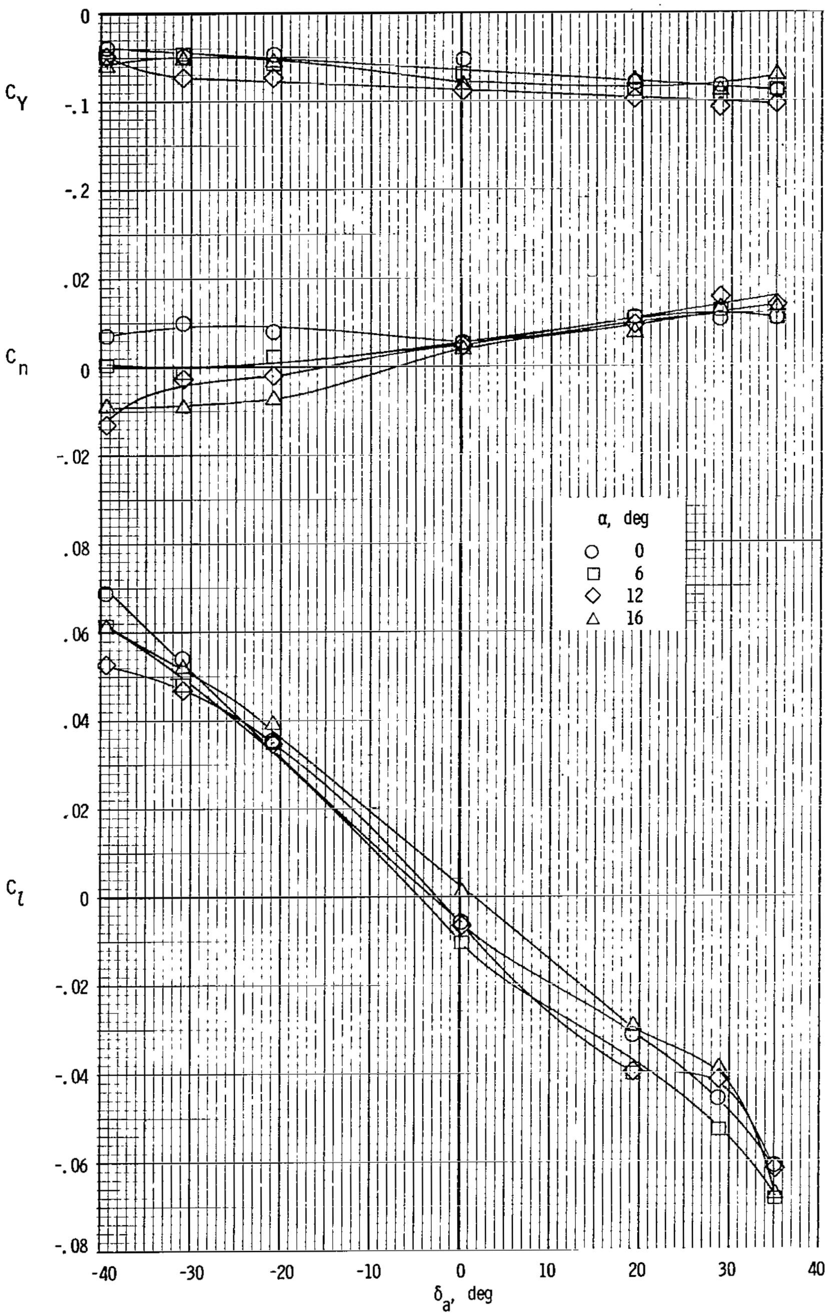

(d) $\beta = 4^o$.

Figure 49.- Continued.

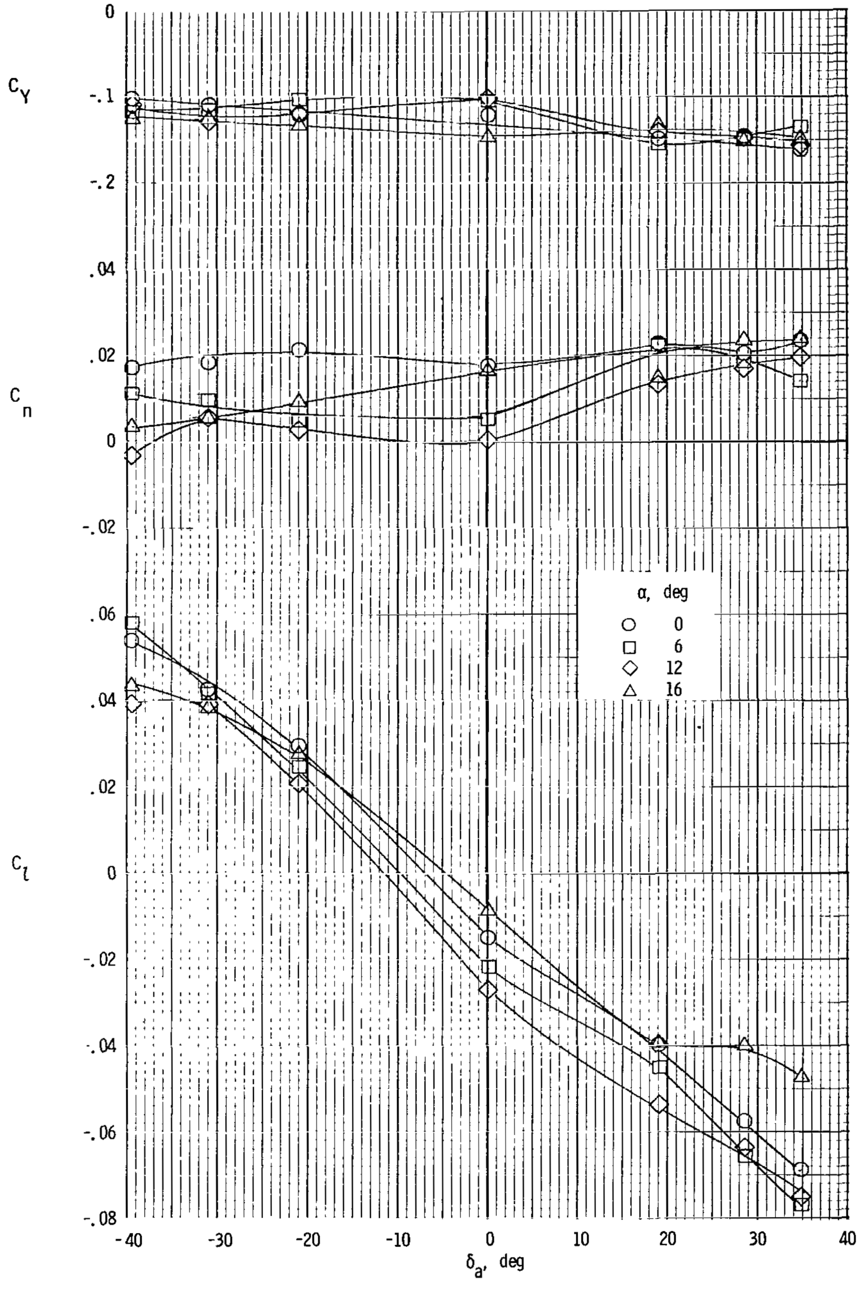

(e) $\beta = 8^0$.

Figure 49.- Concluded.

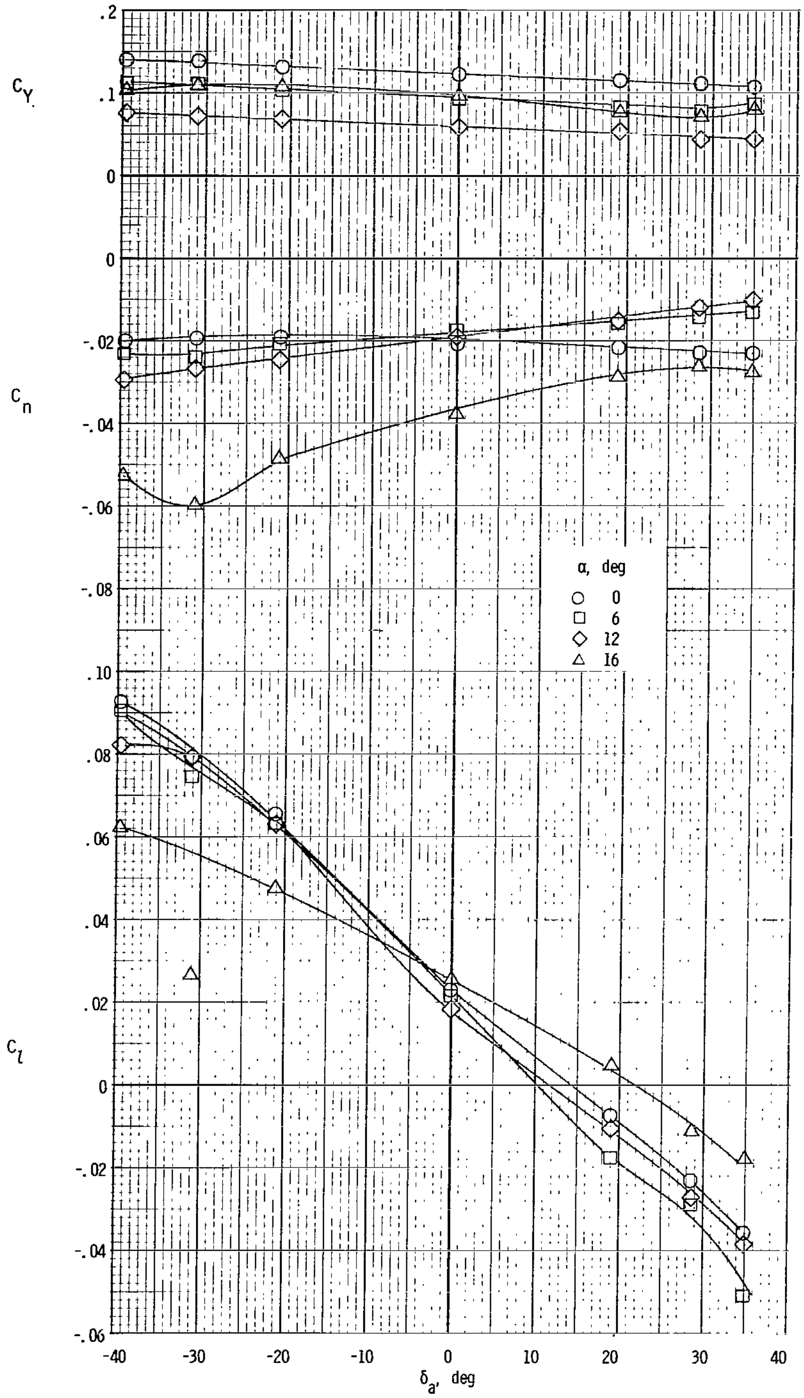

(a) $\beta = -8^0$.

Figure 50.- Variation of lateral aerodynamic characteristics of model with aileron deflection for $\delta_f = 35^0$; $T_c' = 0.28$.

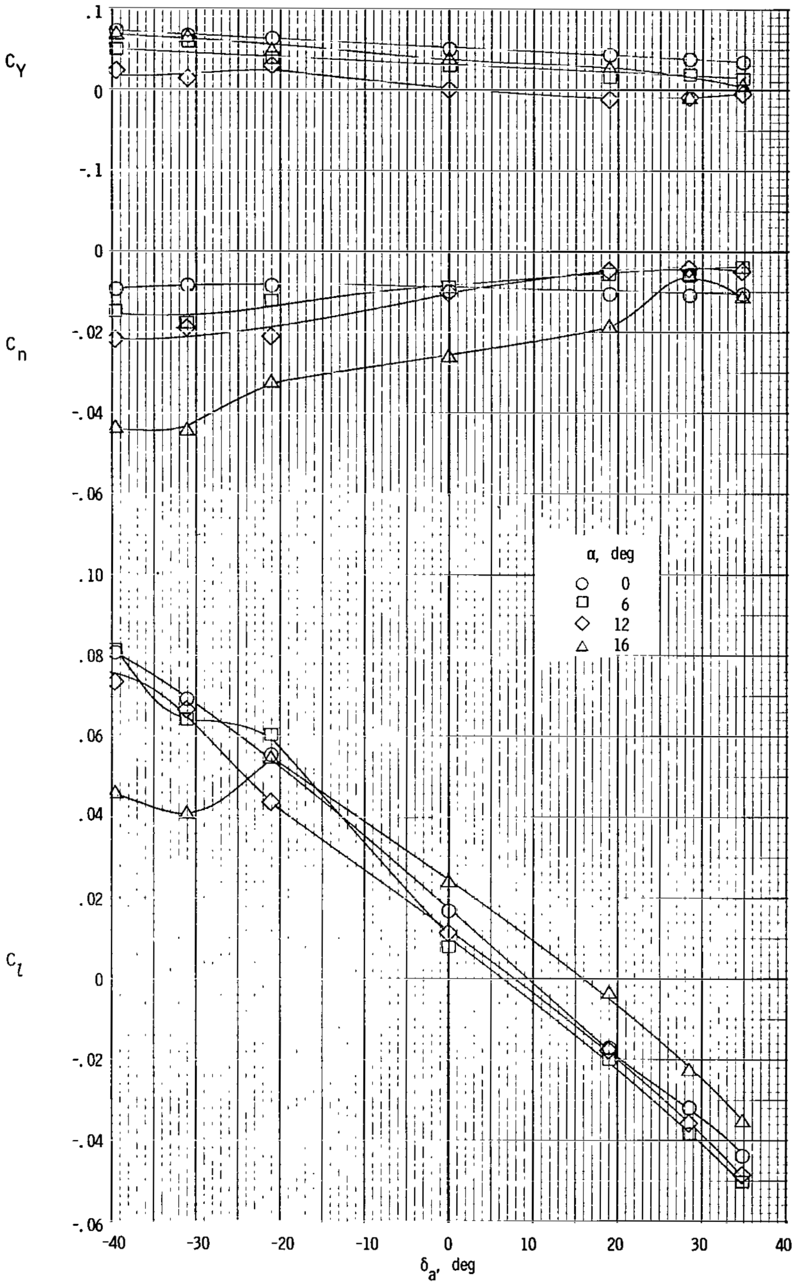

(b) $\beta = -4^{\circ}$.

Figure 50.- Continued.

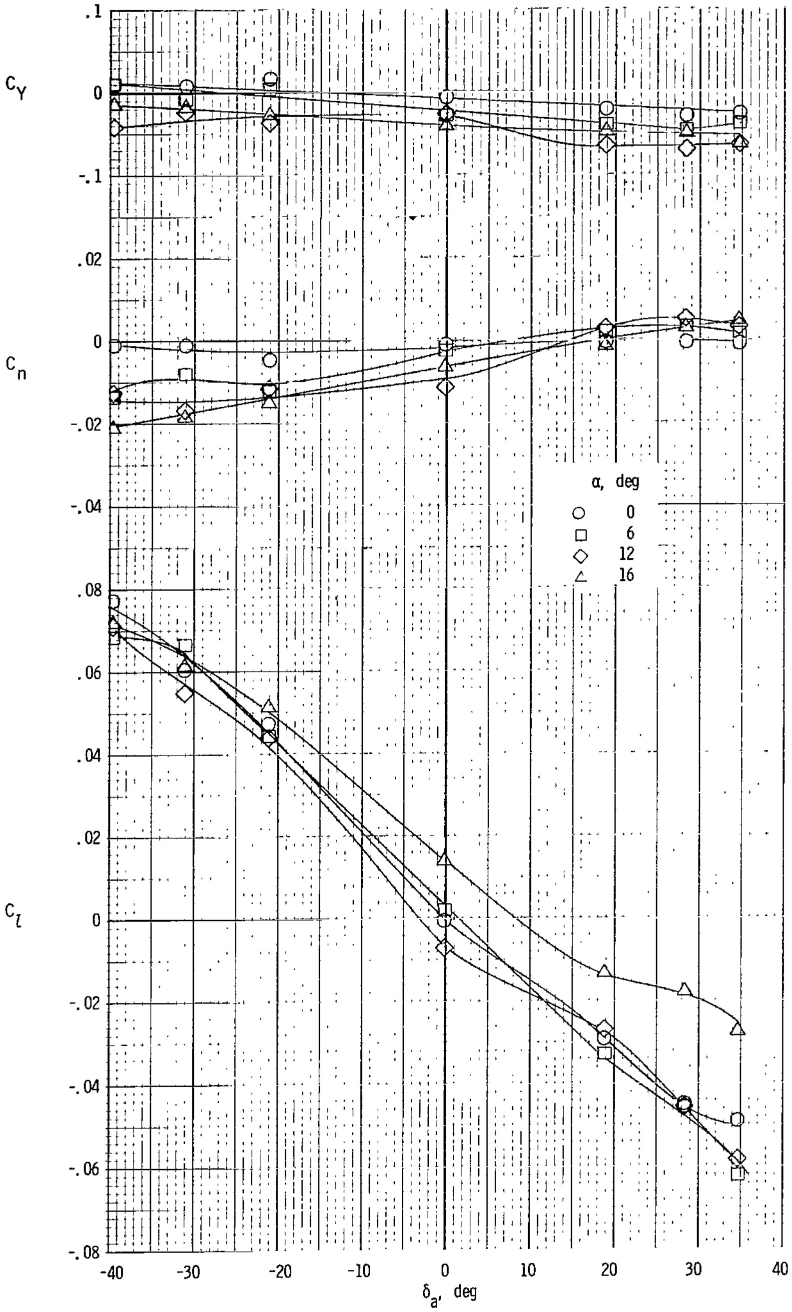

(c) $\beta = 0^{\circ}$.

Figure 50.- Continued.

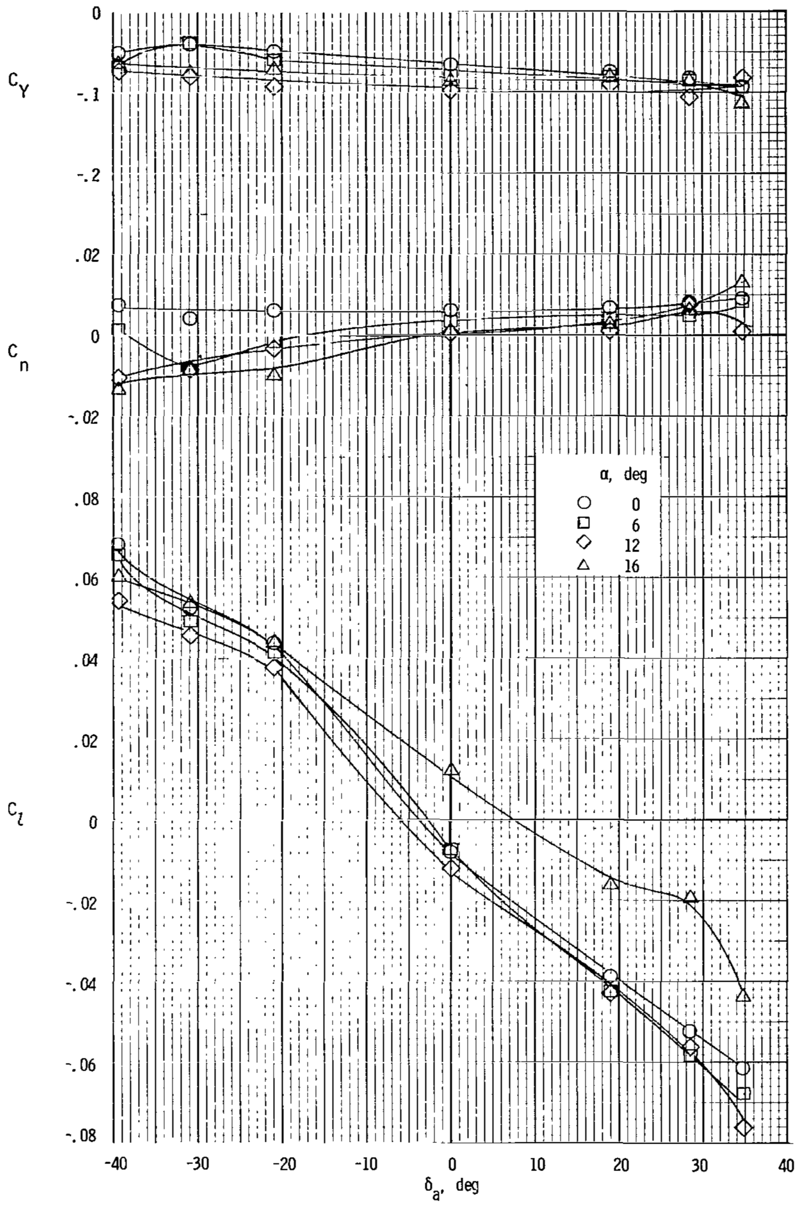

(d) $\beta = 4^0$.

Figure 50.- Continued.

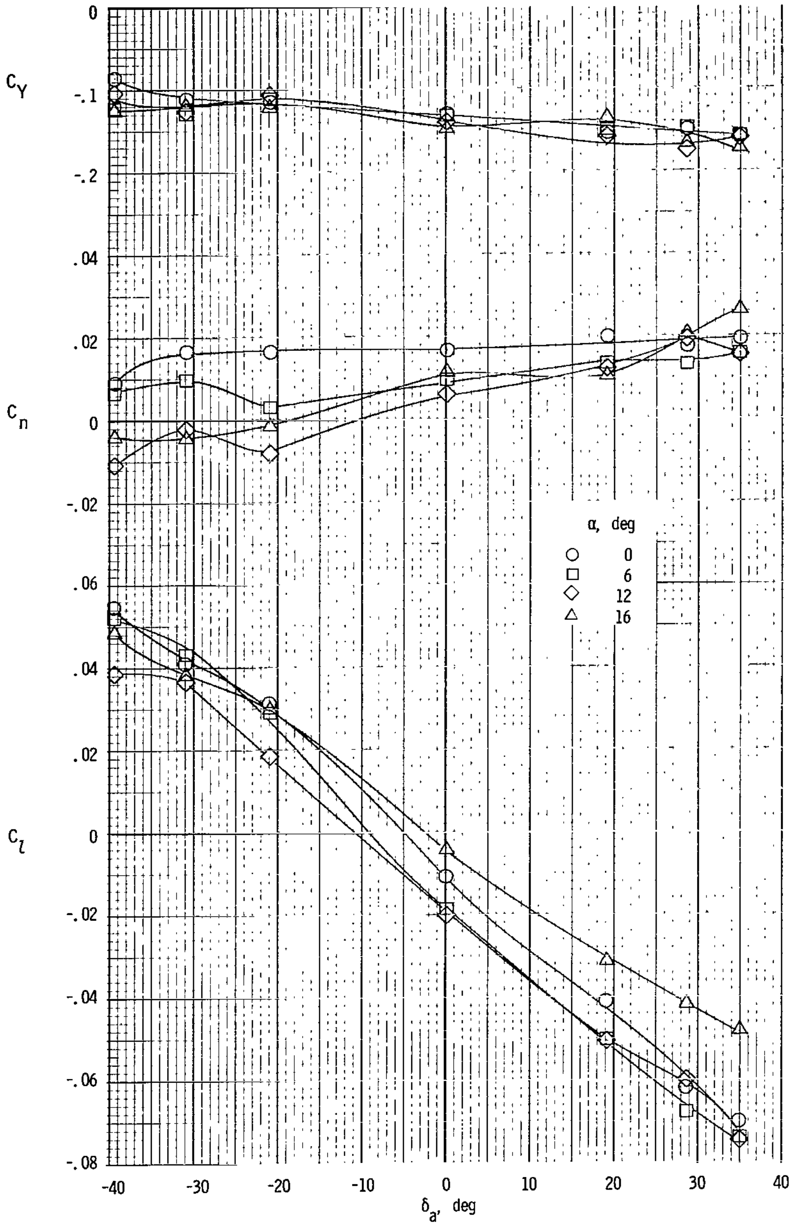

(e) $\beta = 8^0$.

Figure 50.- Concluded.

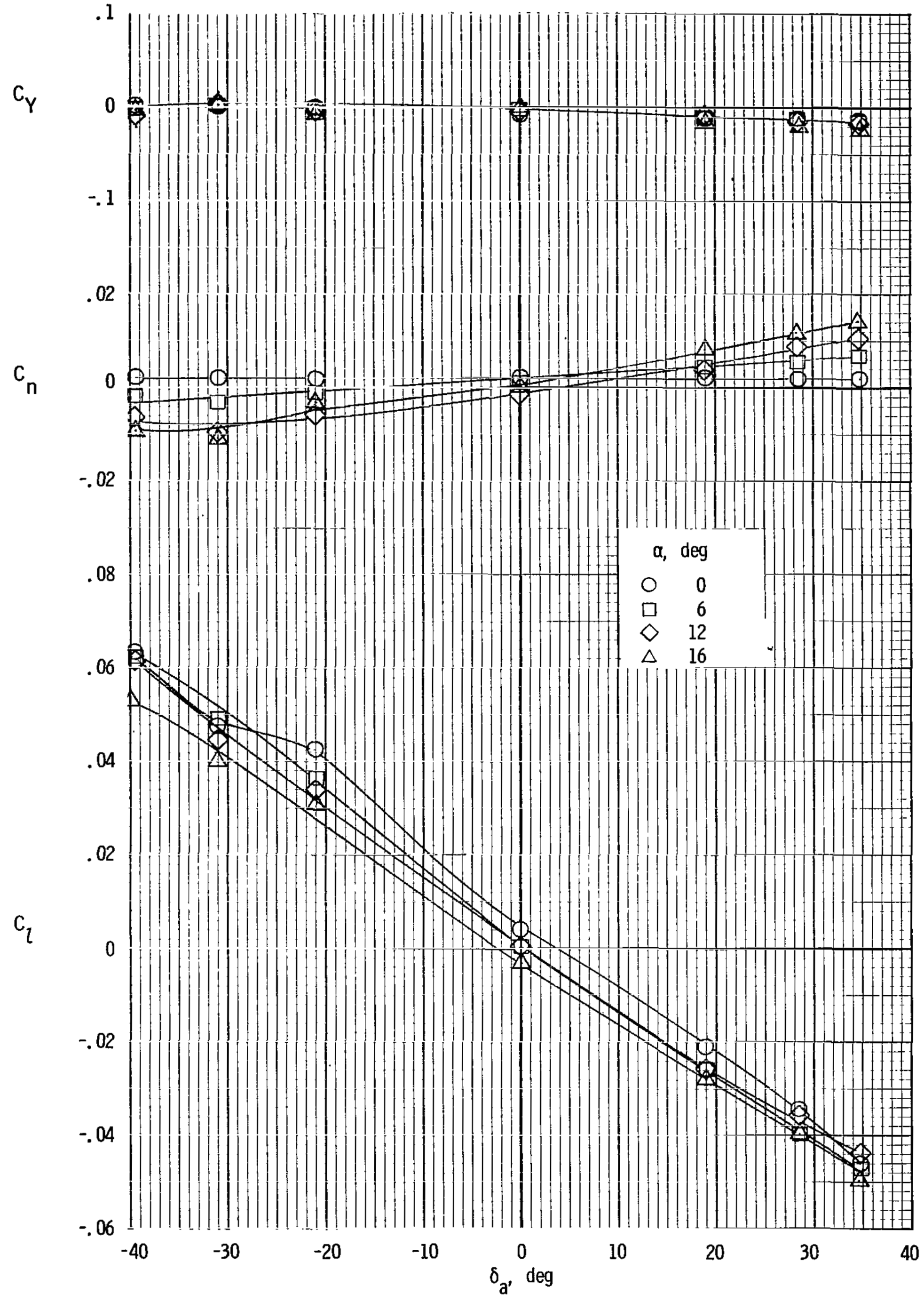

Figure 51.- Variation of lateral aerodynamic characteristics of model with aileron deflection with wing-tip tanks removed for $\delta_f = 0^\circ$; $T_c' = 0$; $\beta = 0^\circ$.

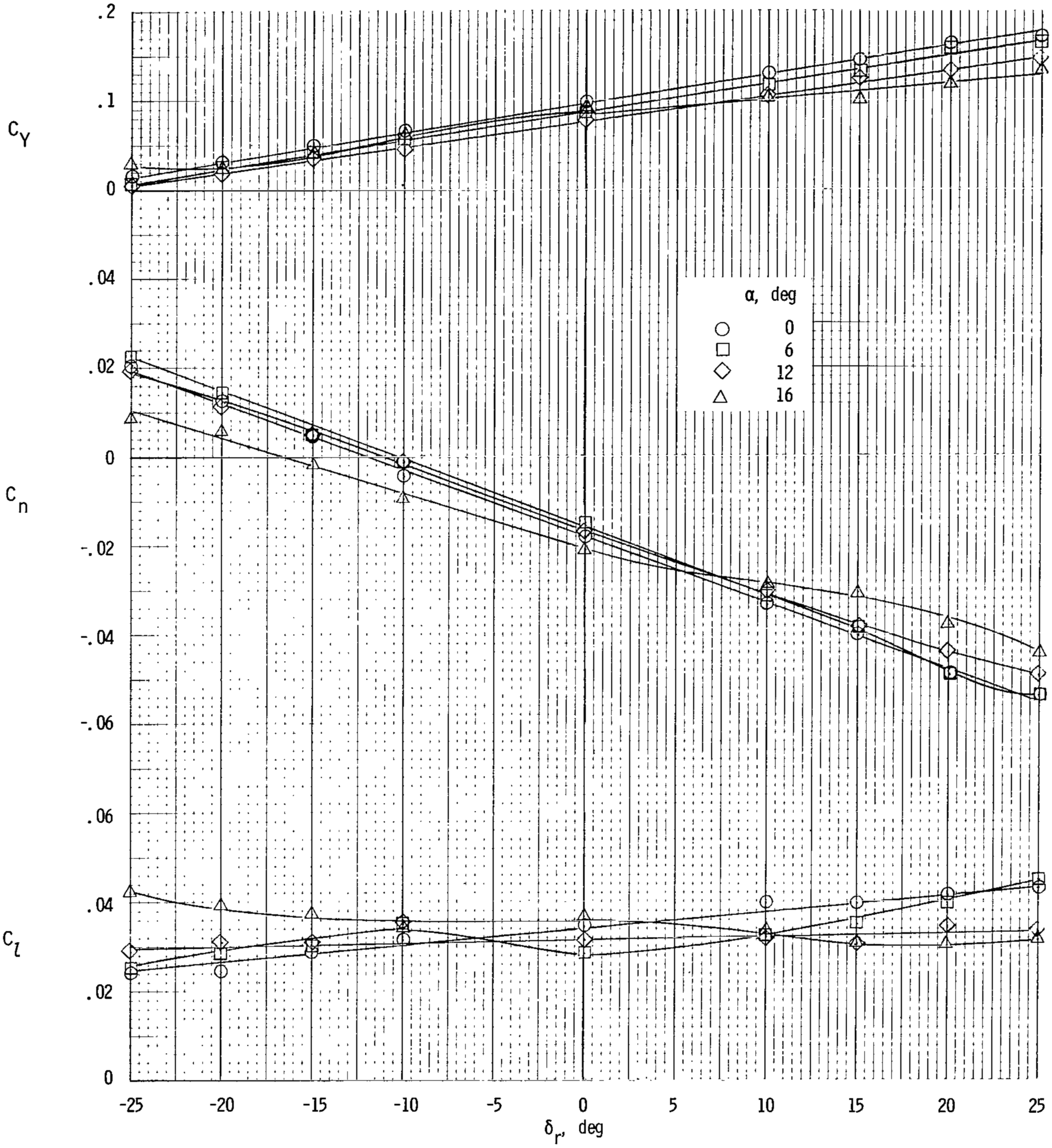

(a) $\beta = -8^0$.

Figure 52.- Variation of lateral aerodynamic characteristics of model with rudder deflection for $\delta_f = 0^0$; $T_c' = 0$.

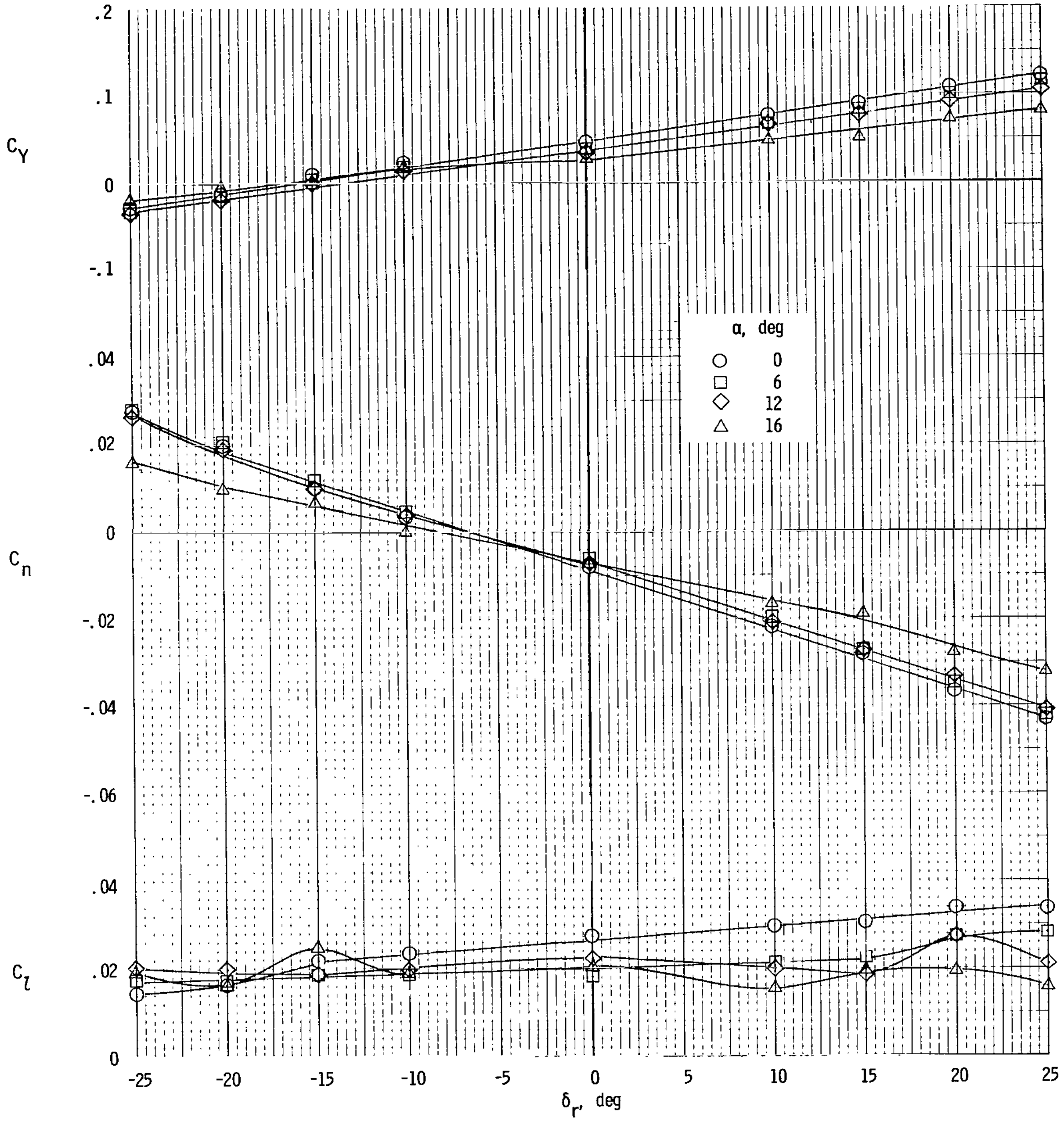

(b) $\beta = -4^{\circ}$.

Figure 52.- Continued.

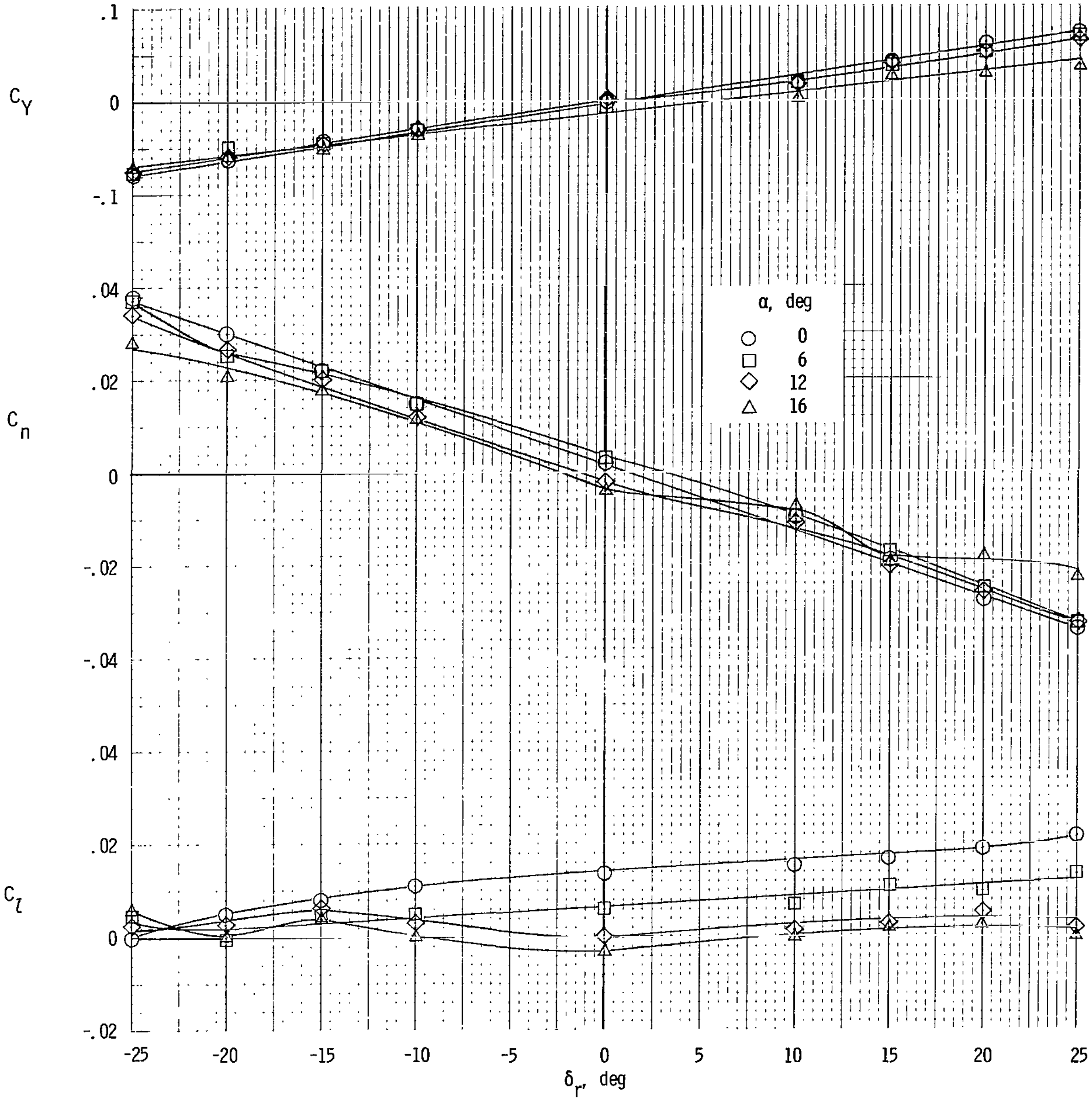

(c) $\beta = 0^o$.

Figure 52.- Continued.

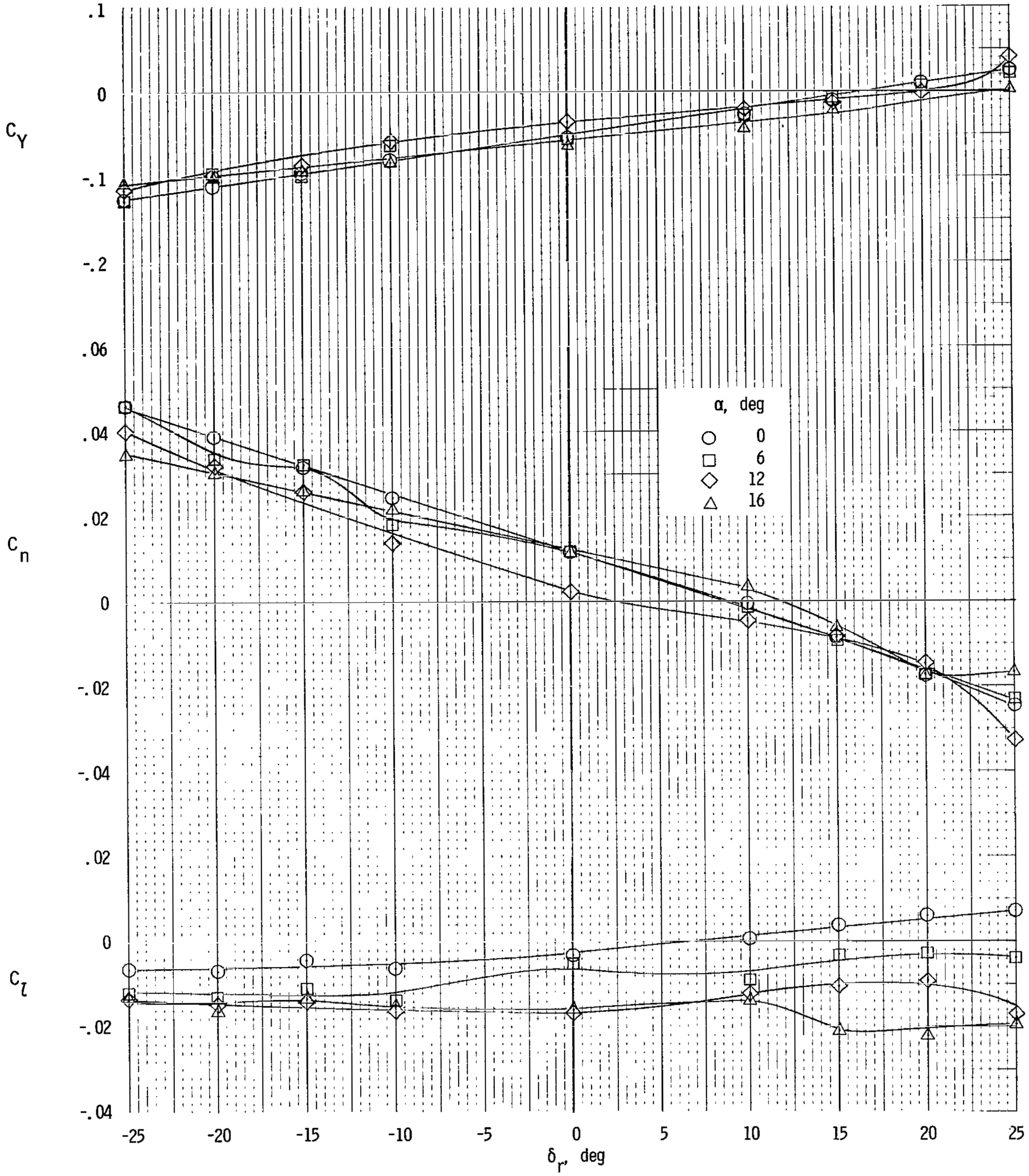

(d) $\beta = 4^0$.

Figure 52.- Continued.

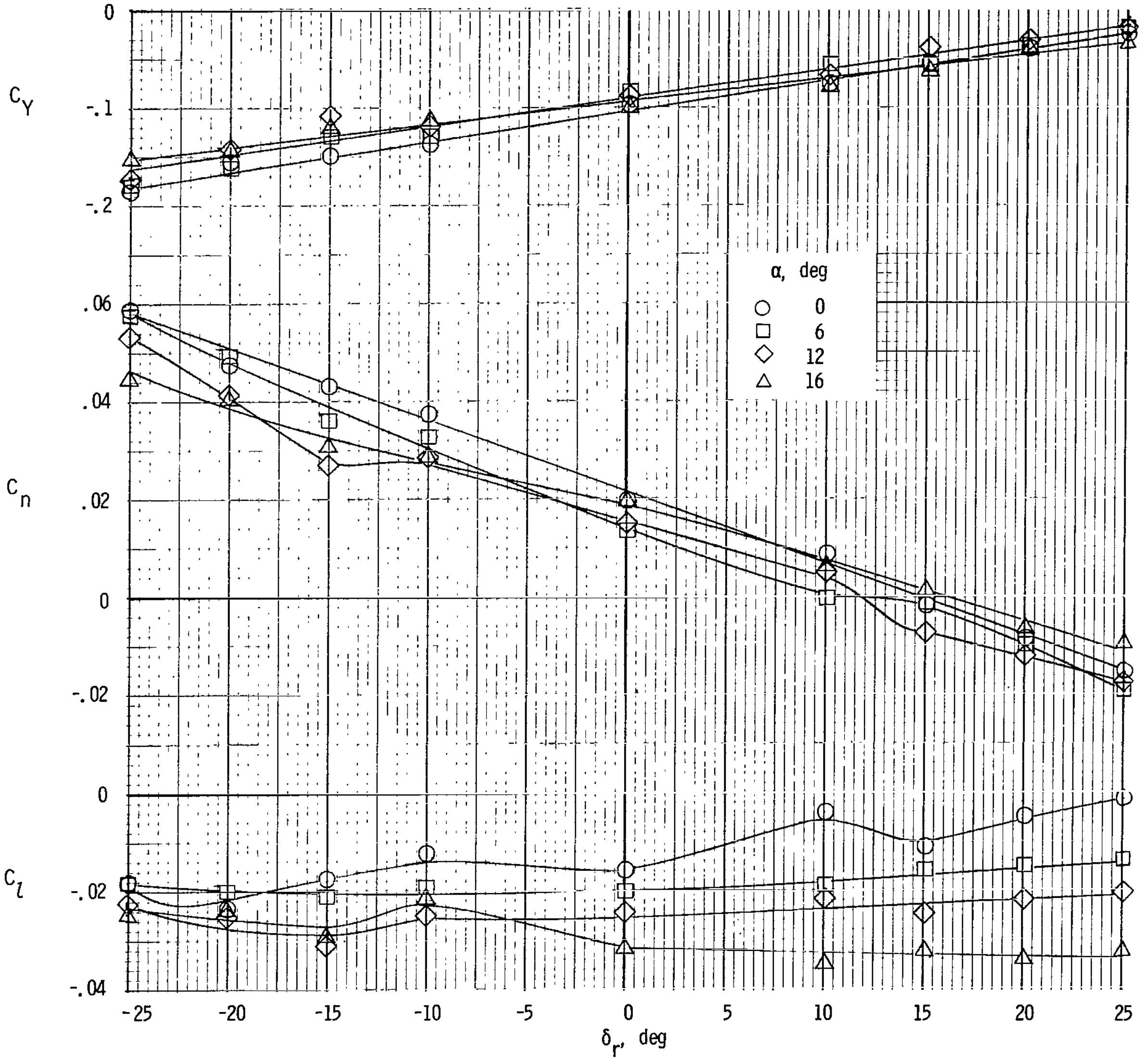

(e) $\beta = 8^0$.

Figure 52.- Concluded.

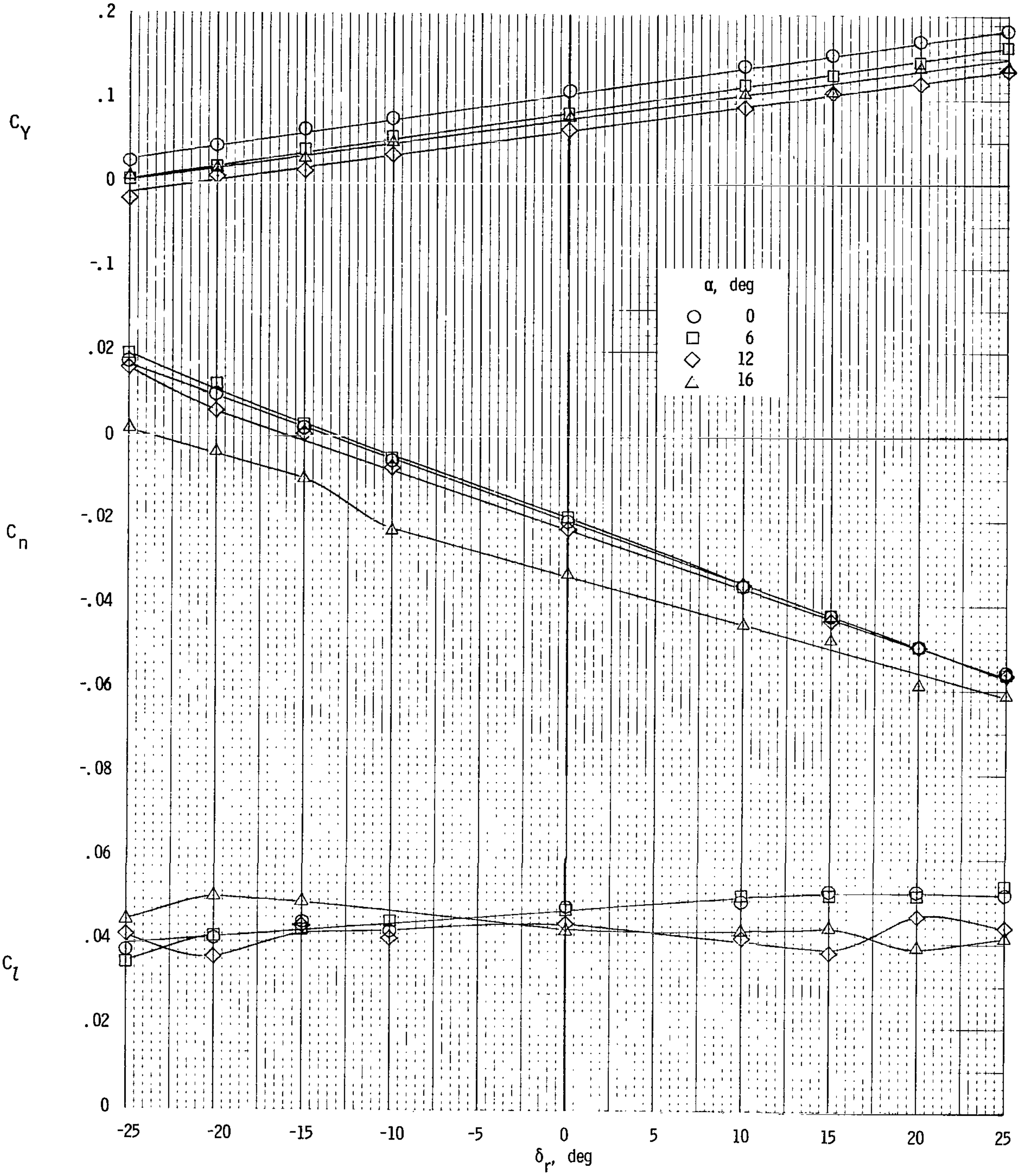

(a) $\beta = -8^0$.

Figure 53.- Variation of lateral aerodynamic characteristics of model with rudder deflection for $\delta_f = 0^0$; $T_c' = 0.19$.

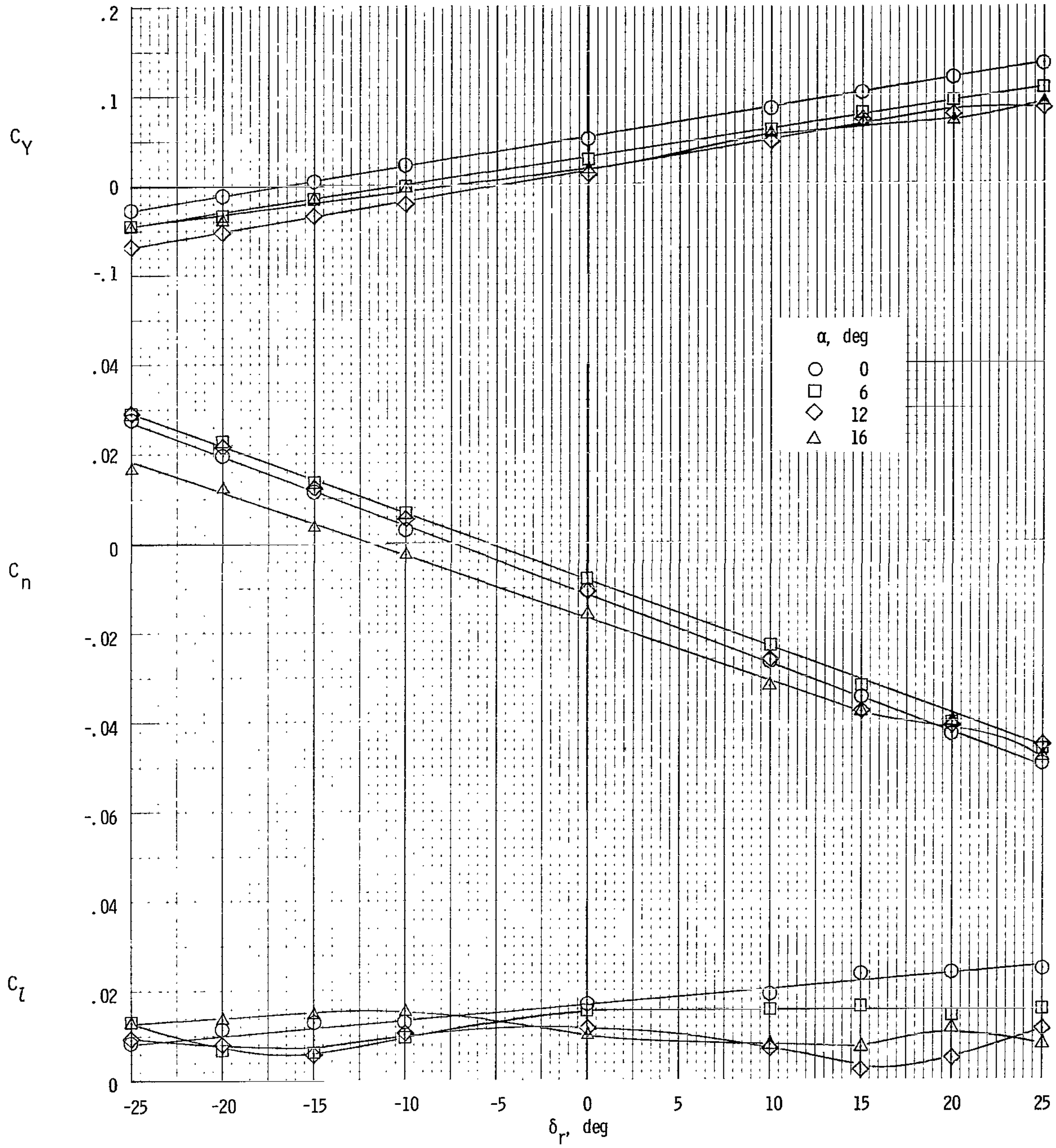

(b) $\beta = -4^0$.

Figure 53.- Continued.

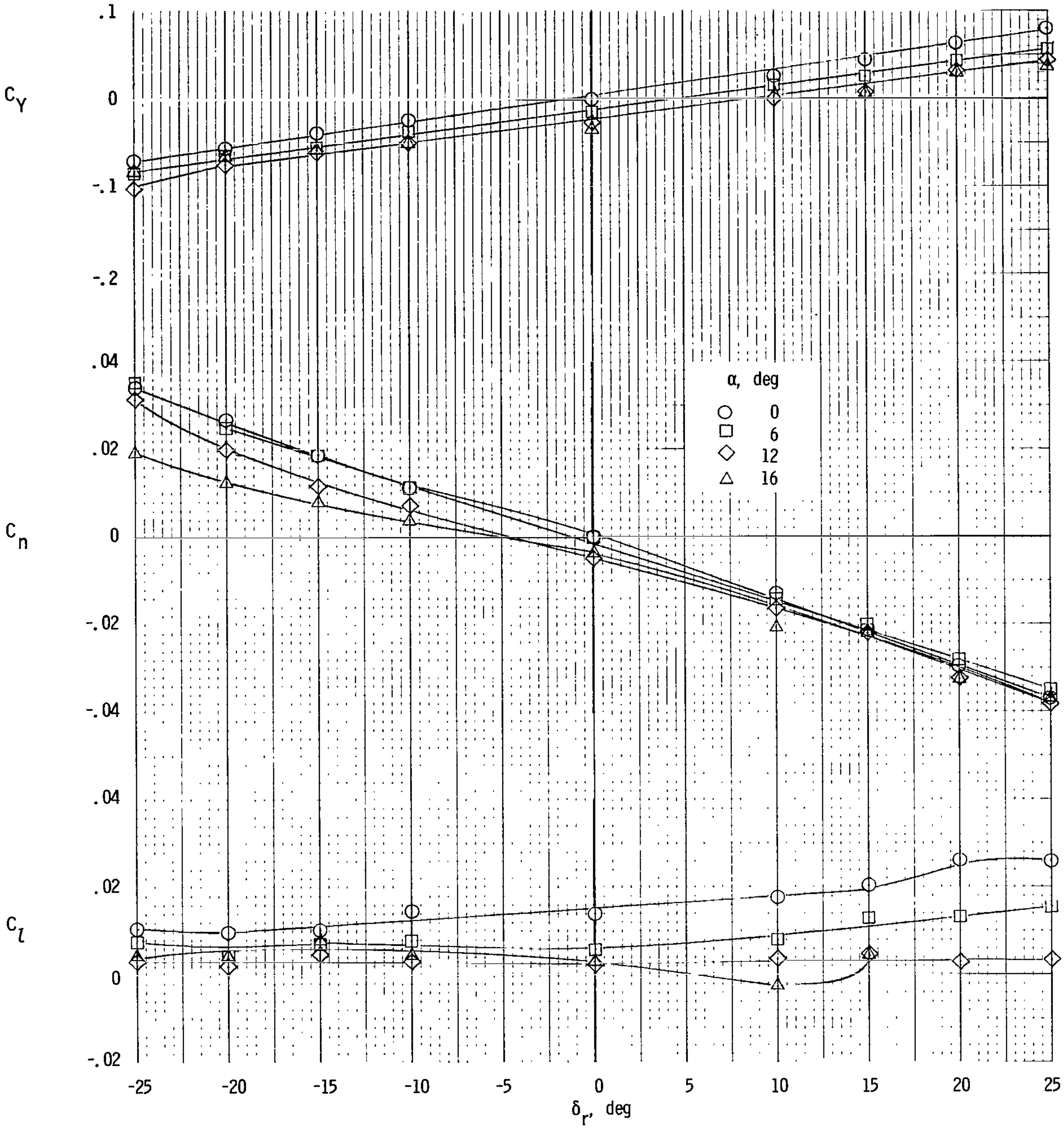

(c) $\beta = 0^0$.

Figure 53.- Continued.

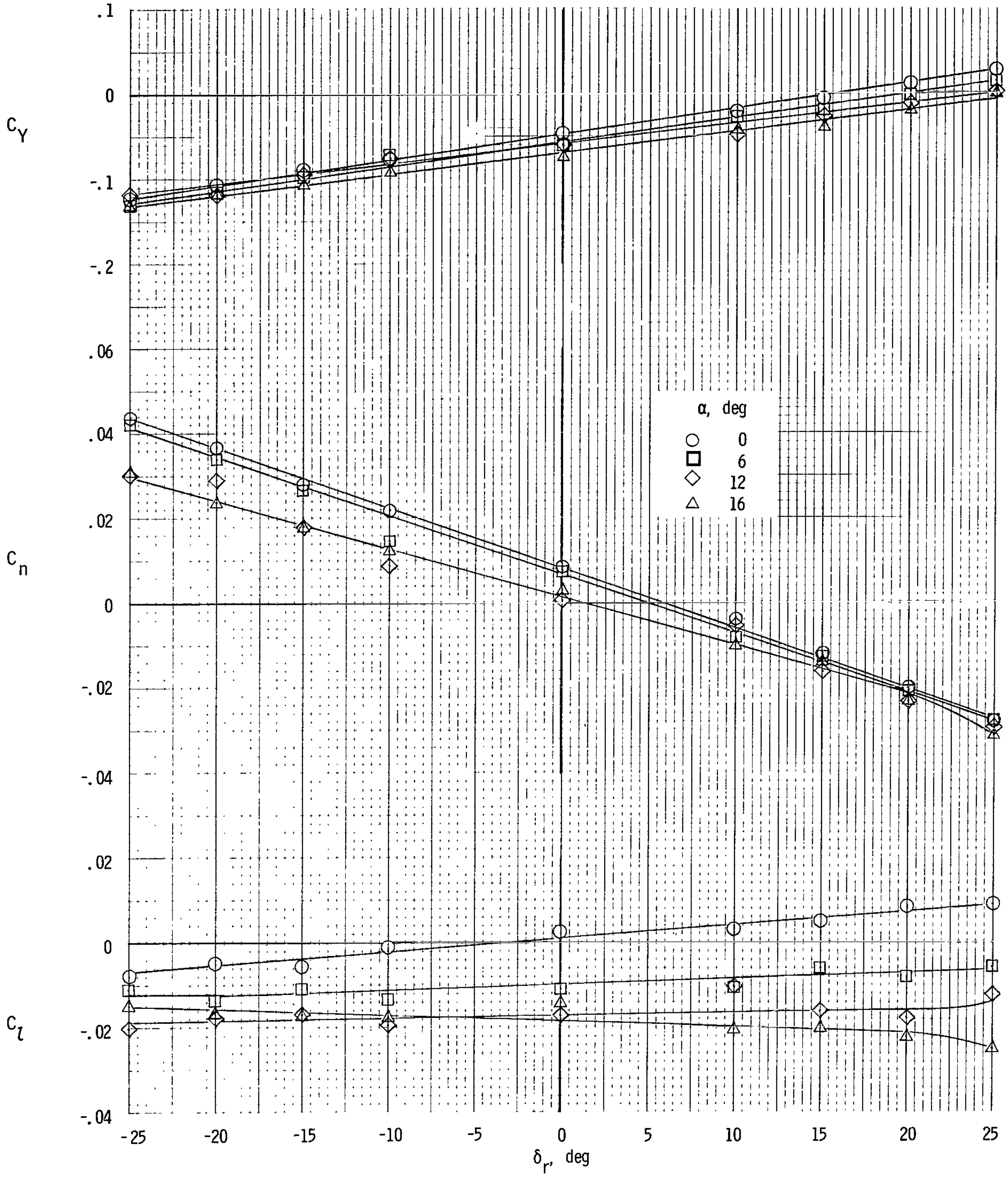

(d) $\beta = 4^0$.

Figure 53.- Continued.

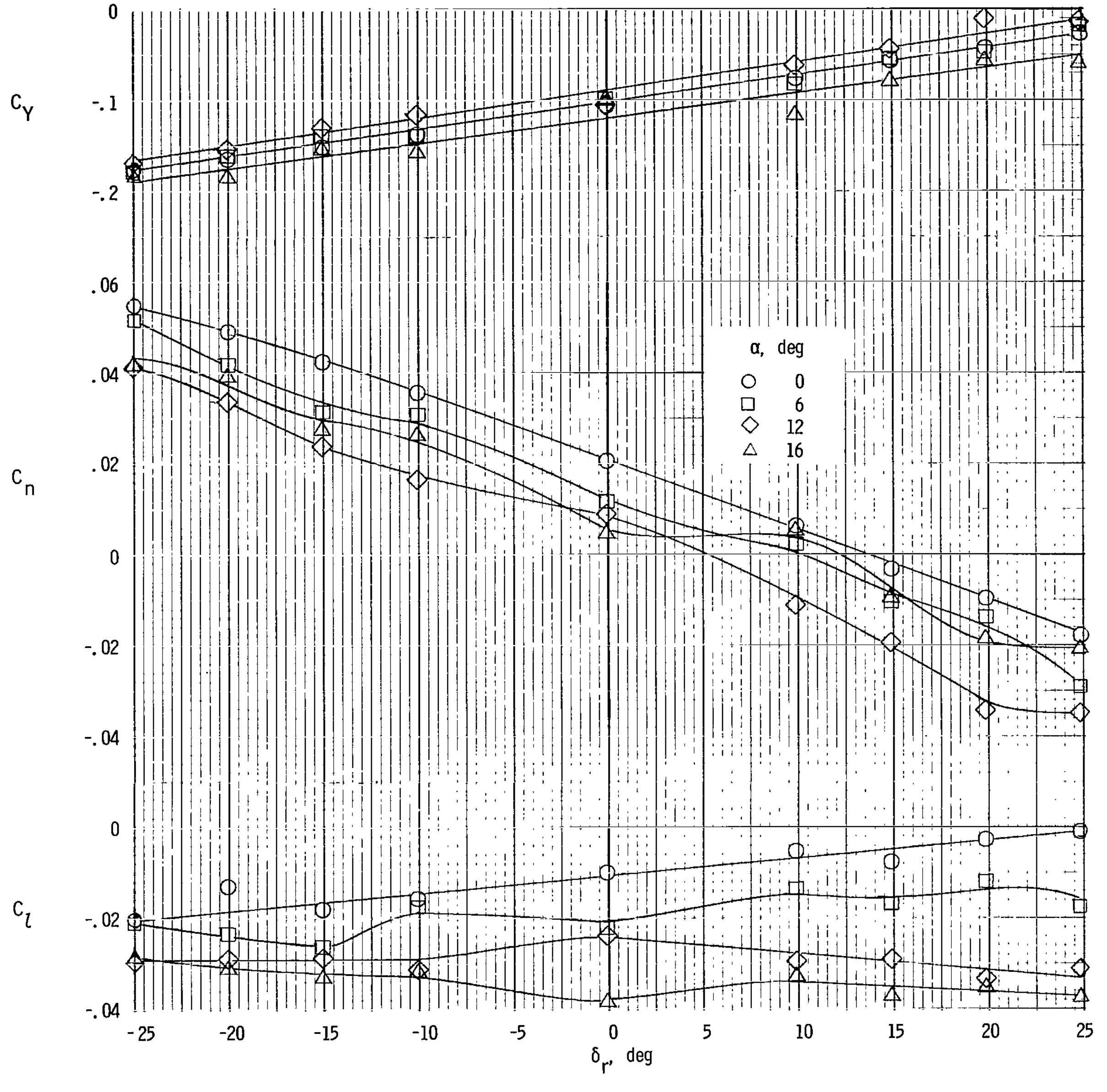

(e) $\beta = 8^o$.

Figure 53.- Concluded.

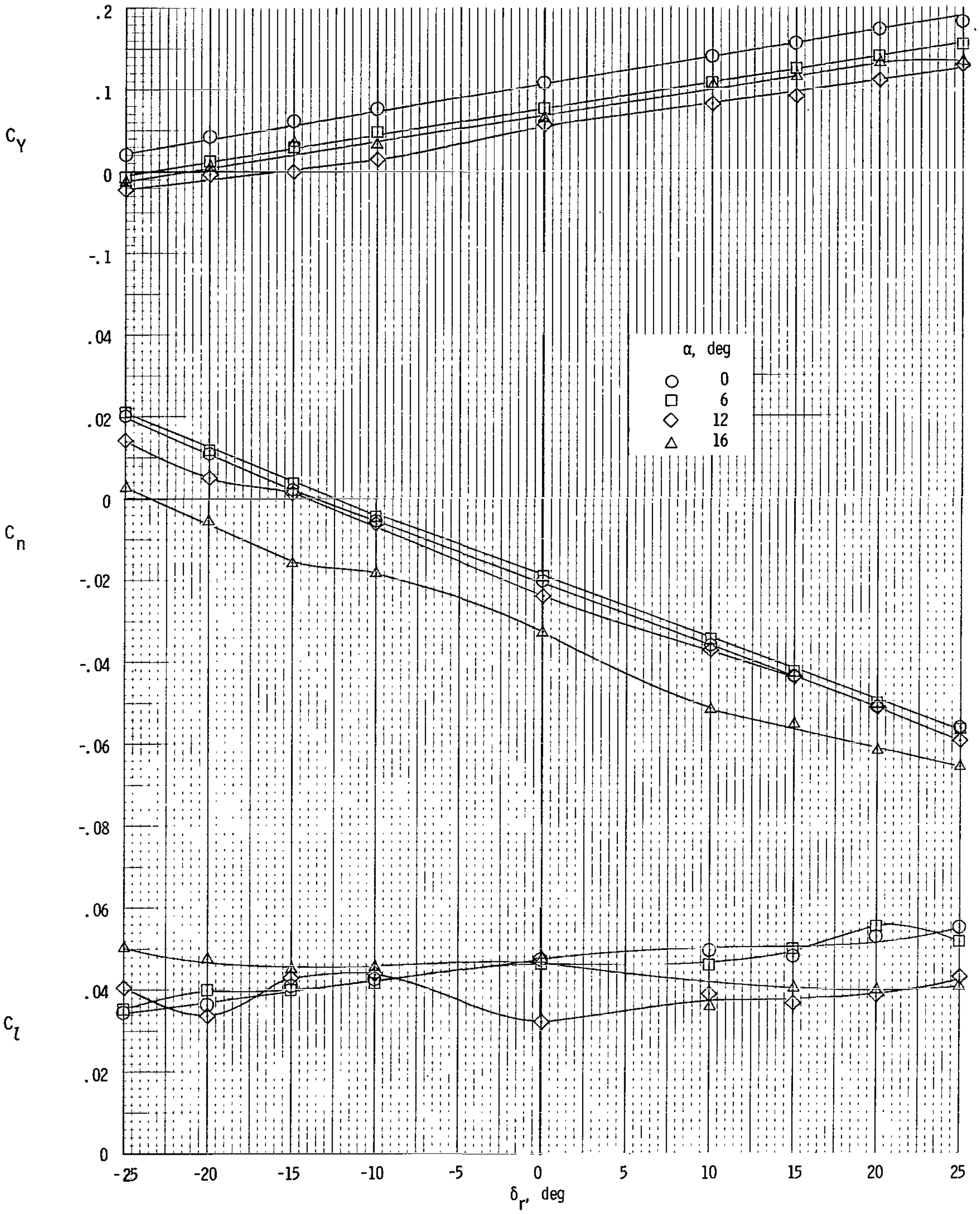

(a) $\beta = -8^0$.

Figure 54.- Variation of lateral aerodynamic characteristics of model with rudder deflection for $\delta_f = 0^0$; $T_c' = 0.28$.

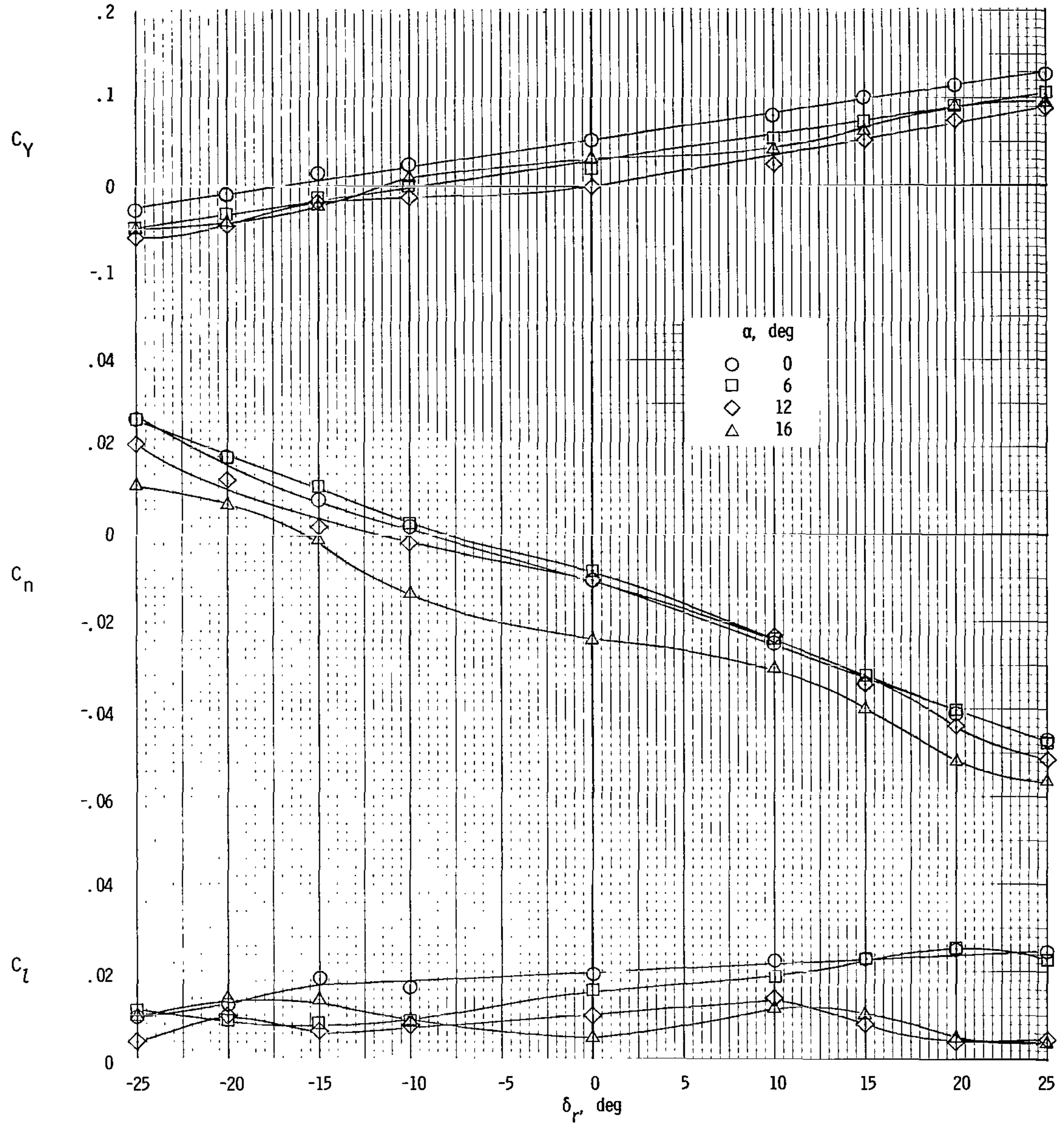

(b) $\beta = -4^{\circ}$.

Figure 54.- Continued.

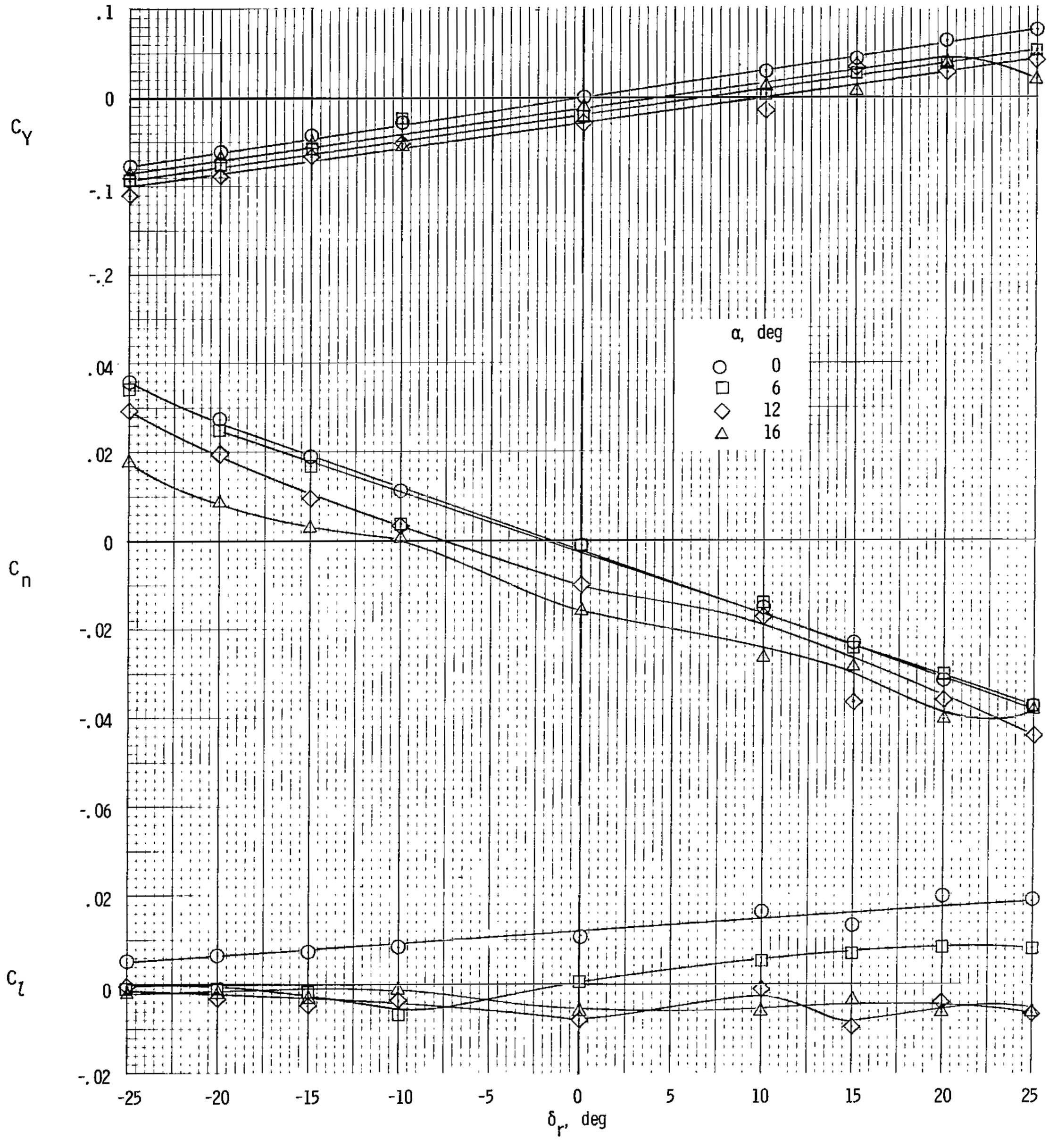

(c) $\beta = 0^{\circ}$.

Figure 54.- Continued.

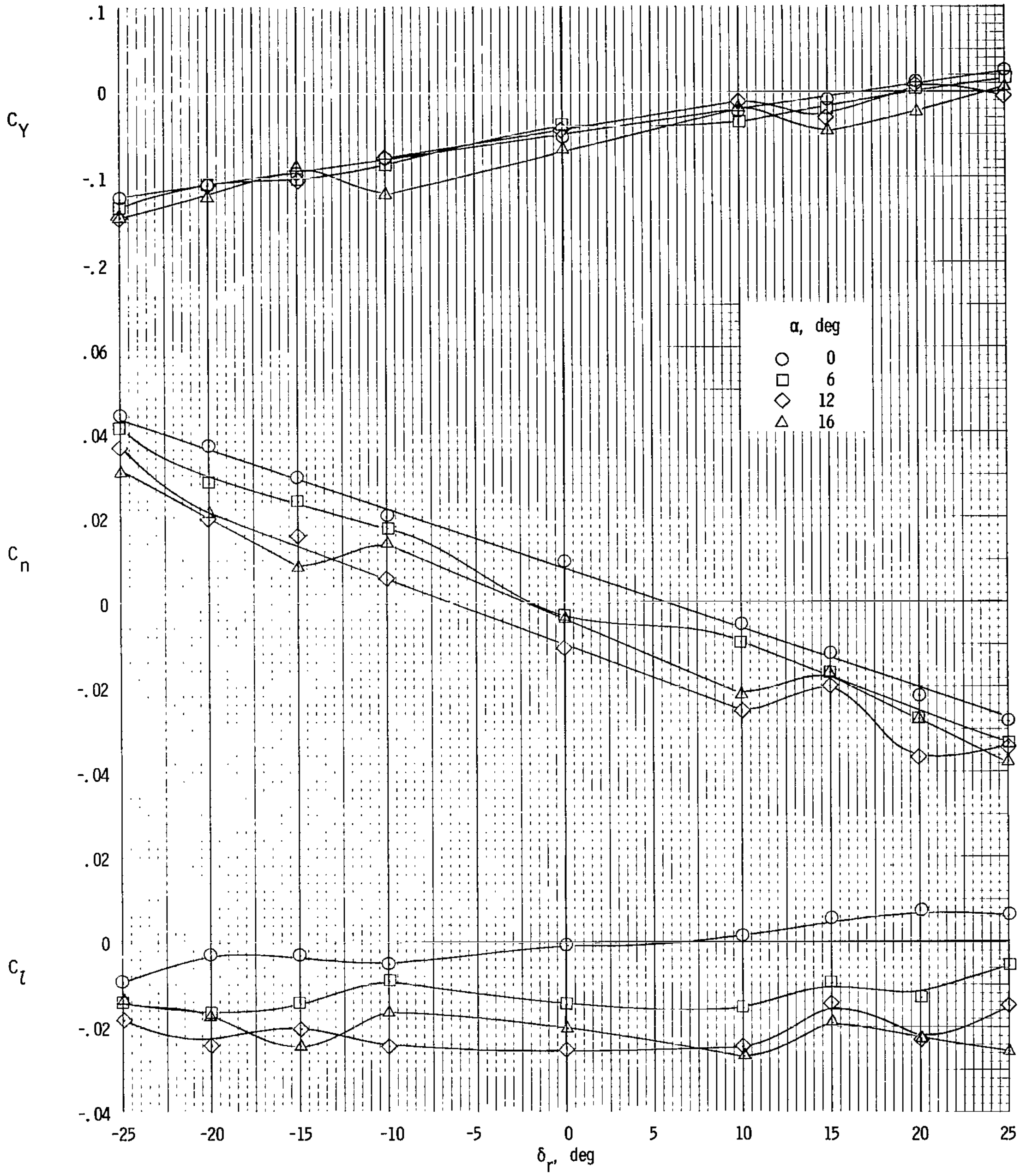

(d) $\beta = 4^o$.

Figure 54.- Continued.

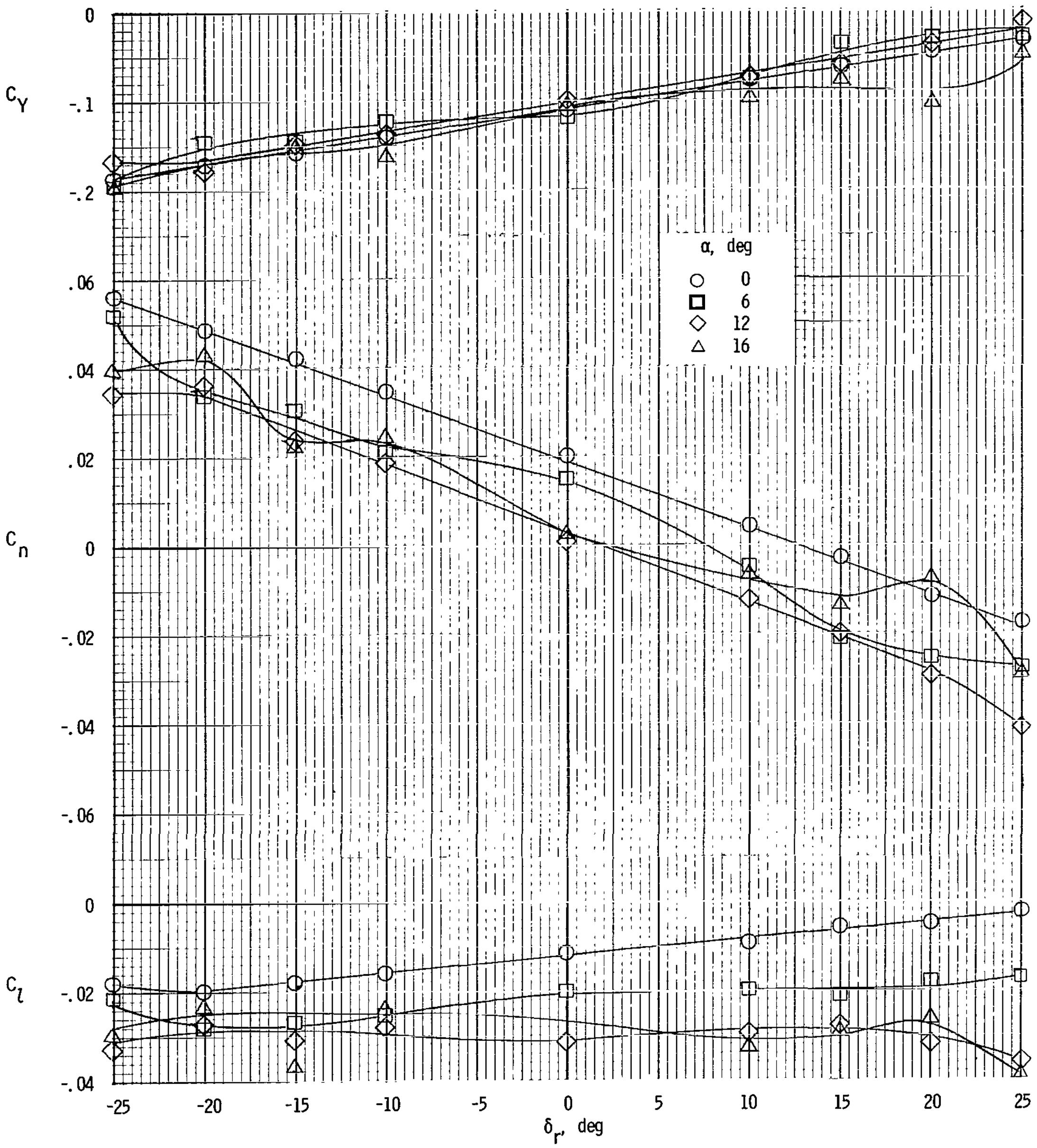

(e) $\beta = 8^o$.

Figure 54.- Concluded.

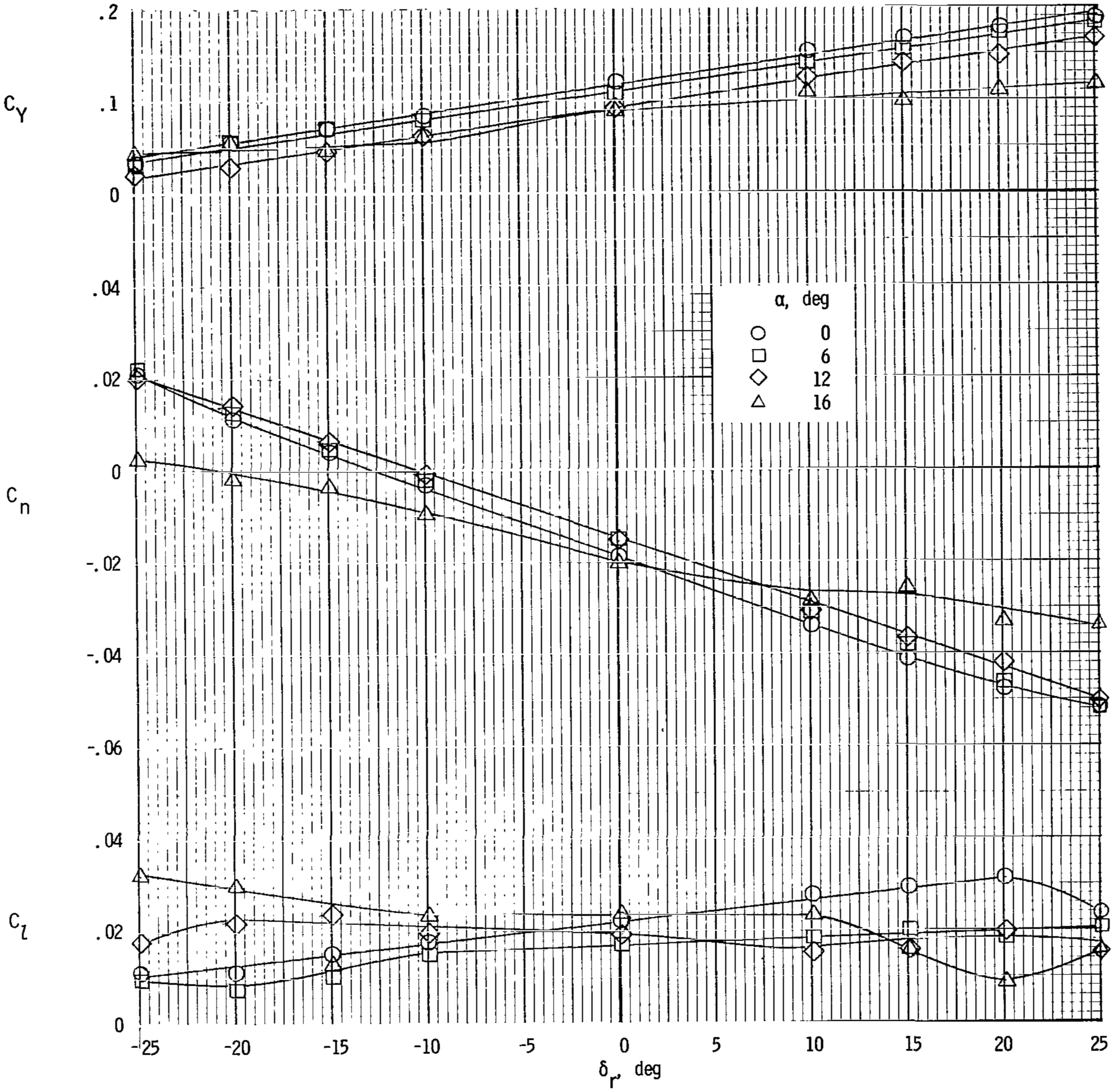

(a) $\beta = -8^0$.

Figure 55.- Variation of lateral aerodynamic characteristics of model with rudder deflection for $\delta_f = 35^0$; $T'_c = 0$.

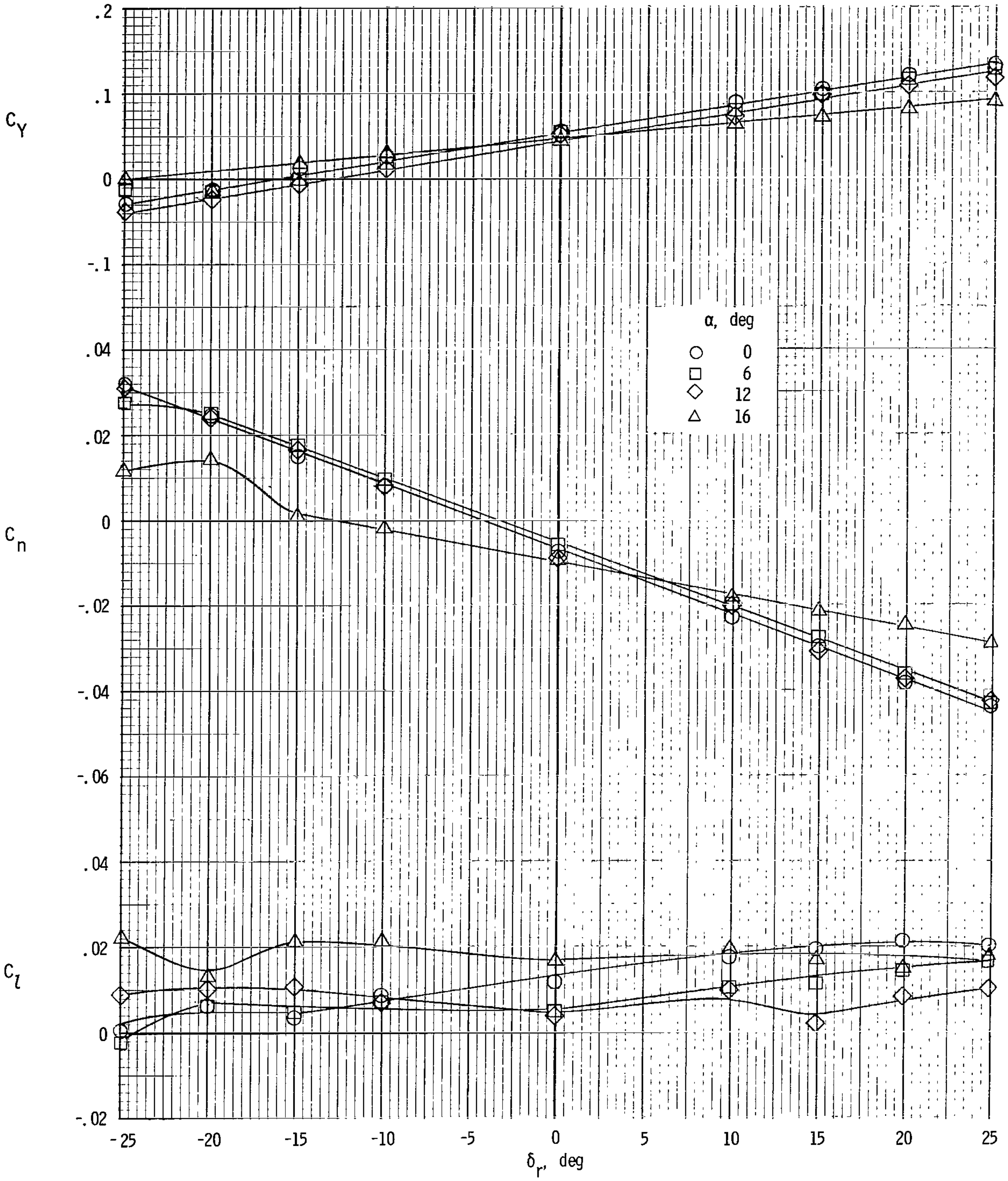

(b) $\beta = -4^0$.

Figure 55.- Continued.

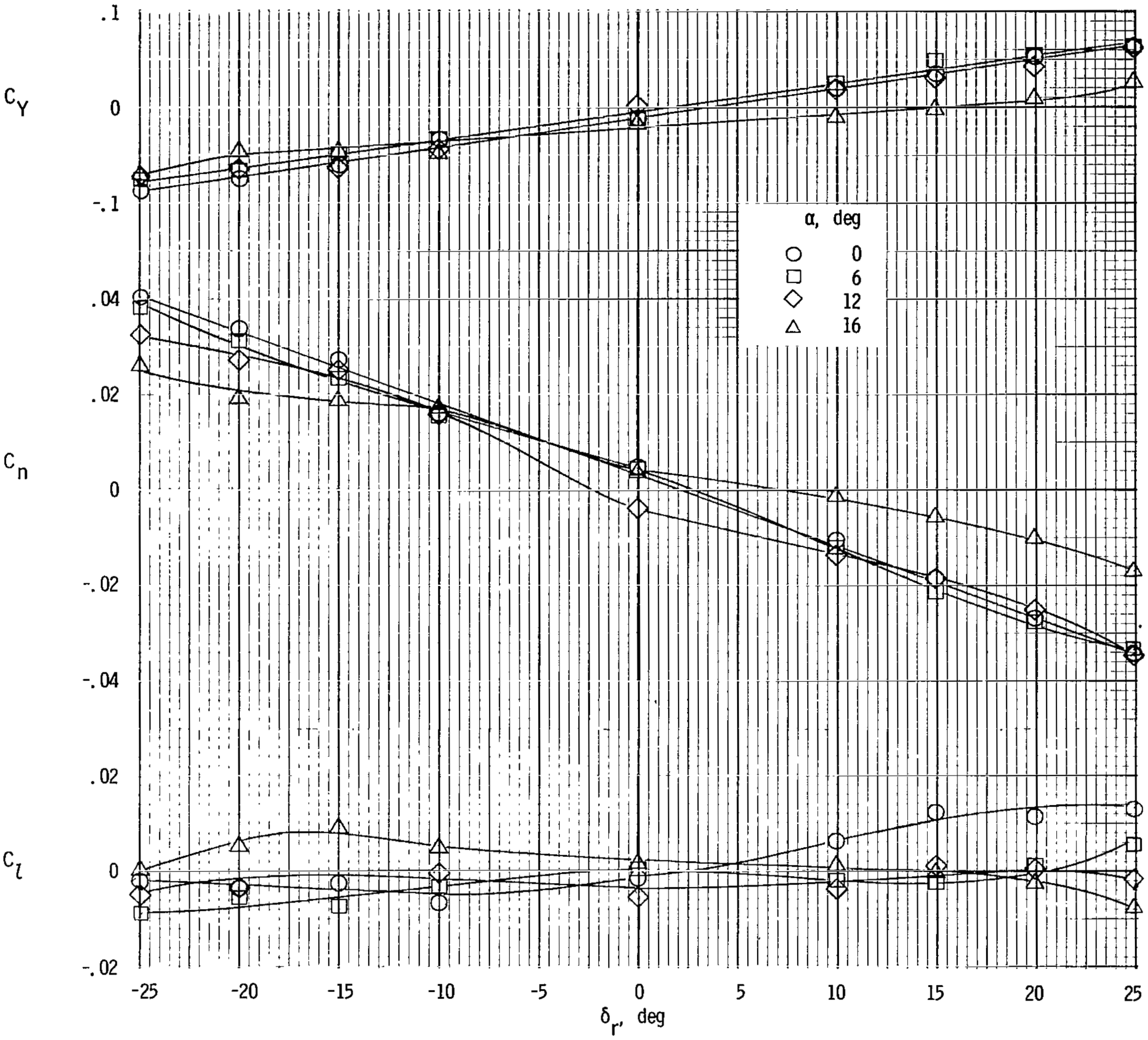

(c) $\beta = 0^{0}$.

Figure 55.- Continued.

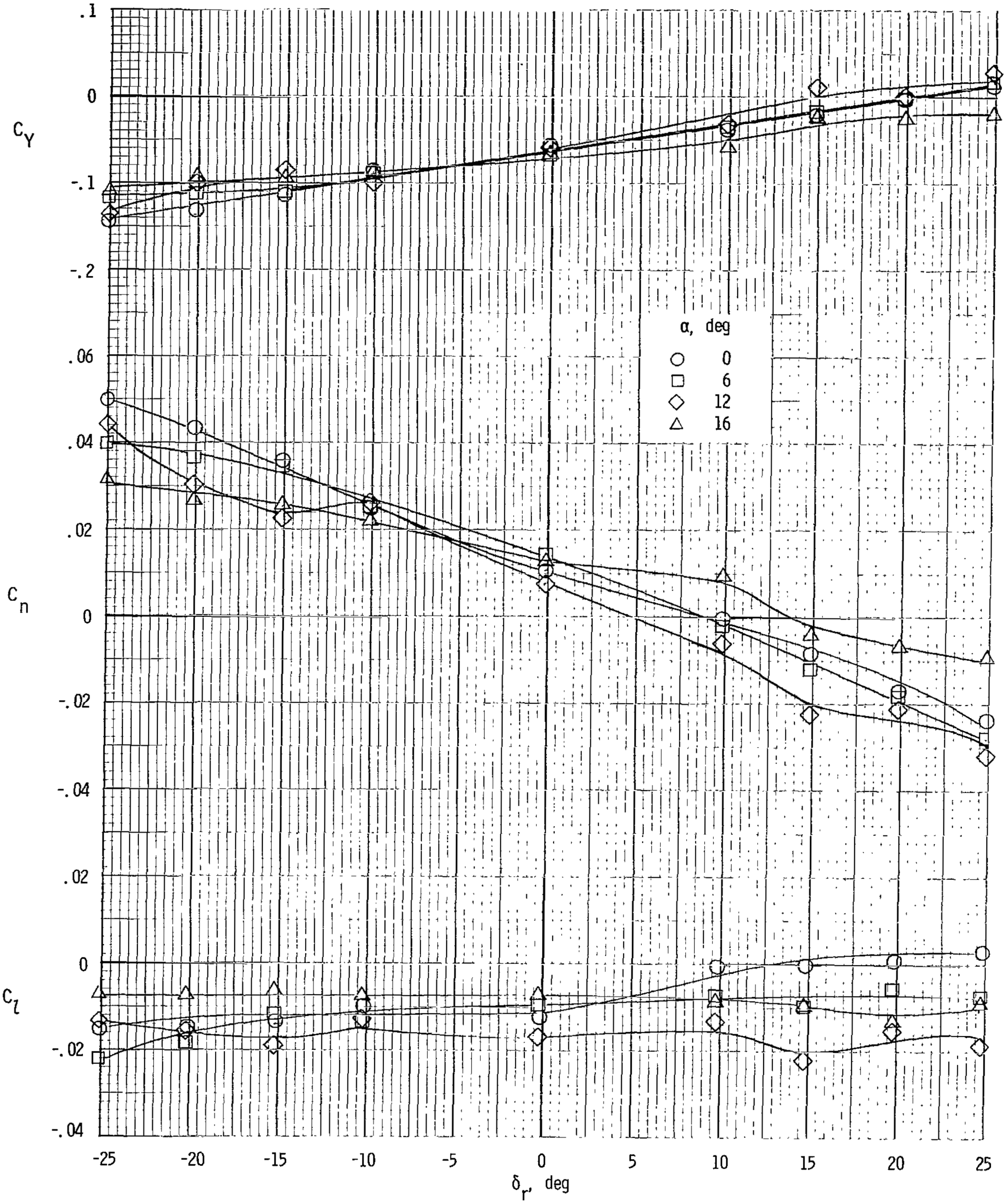

(d) $\beta = 4^{\circ}$.

Figure 55.- Continued.

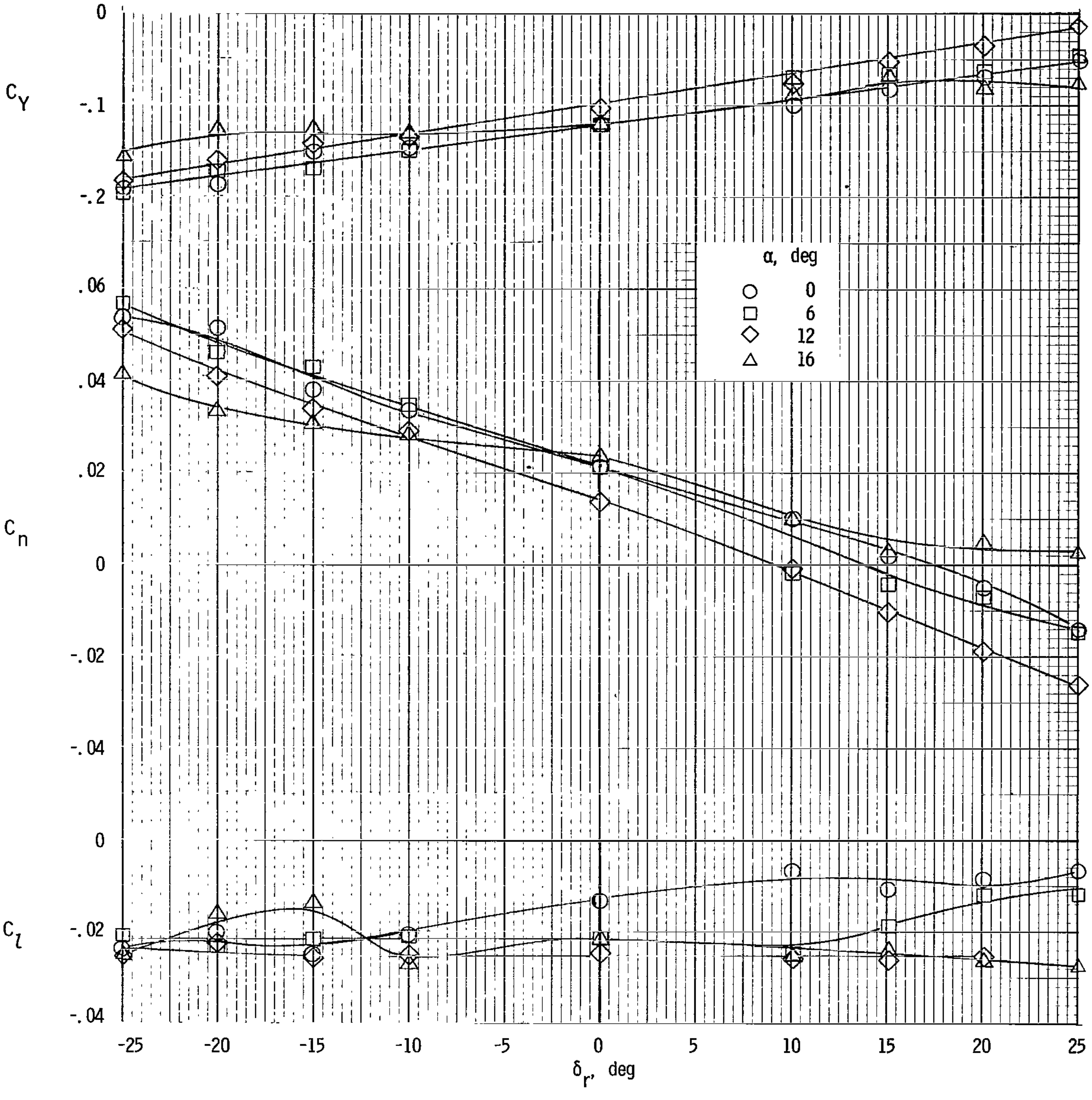

(e) $\beta = 8^{0}$.

Figure 55.- Concluded.

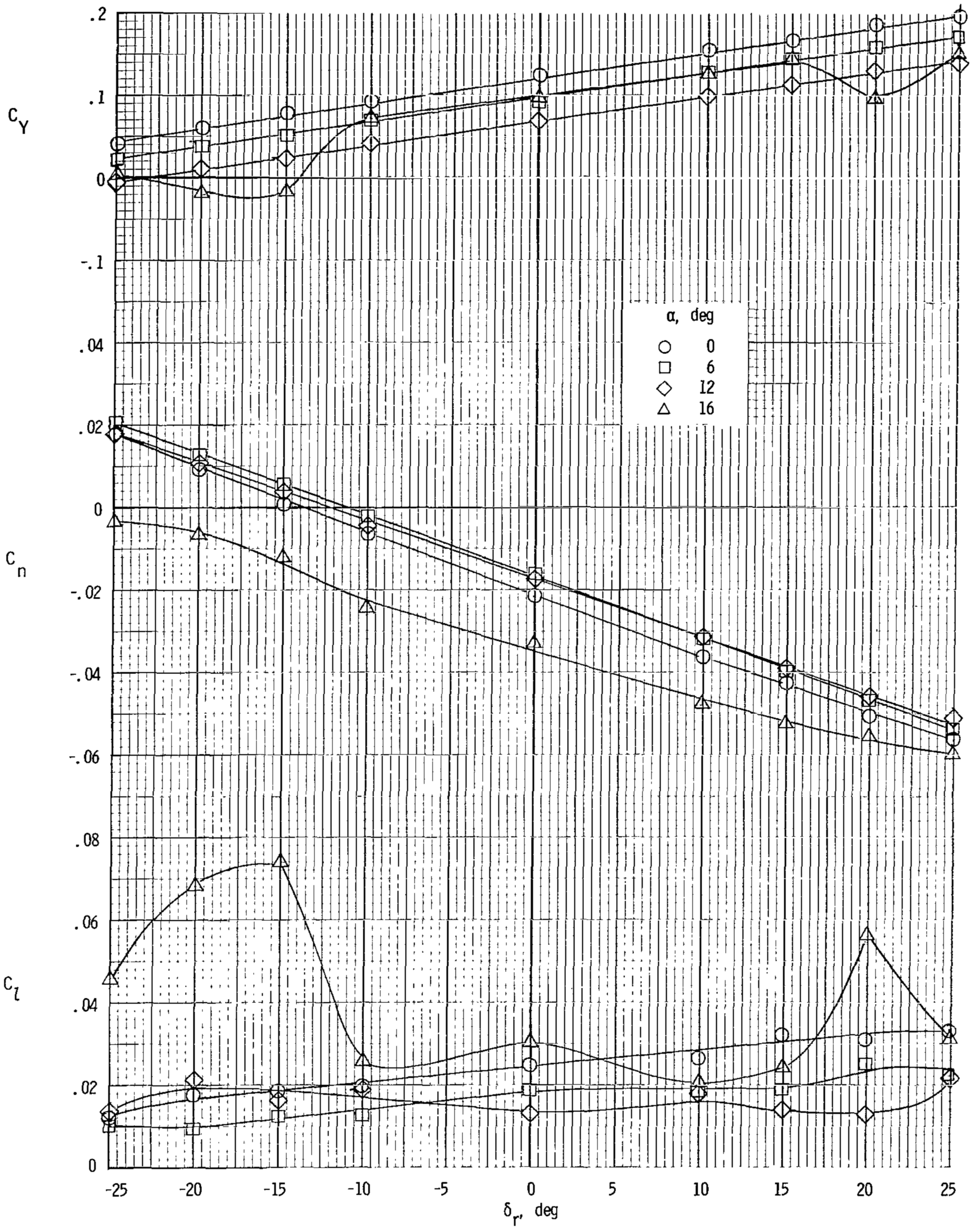

(a) $\beta = -8^{0}$.

Figure 56.- Variation of lateral aerodynamic characteristics of model with rudder deflection for $\delta_f = 35^{0}$; $T_c' = 0.19$.

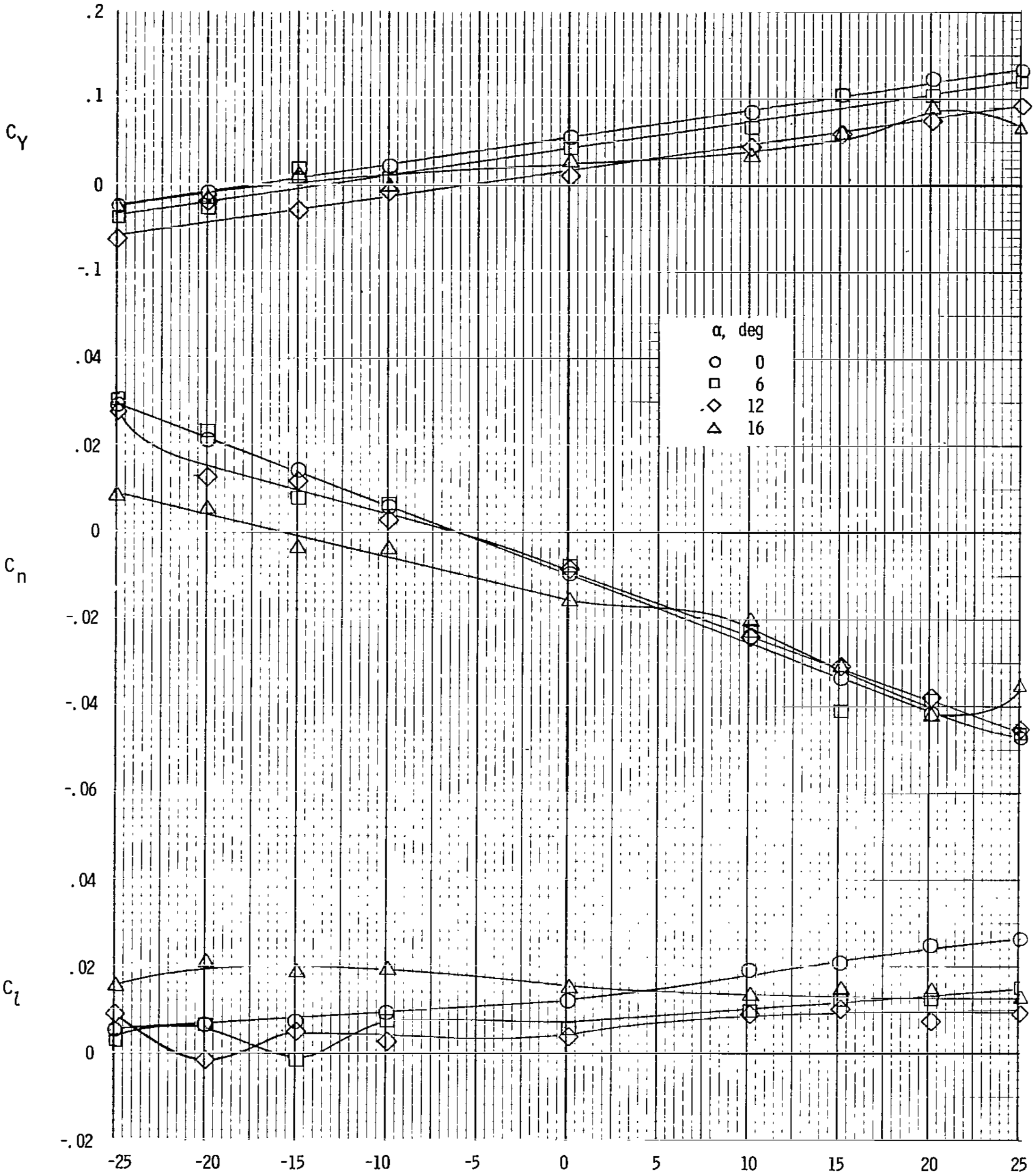

(b) $\beta = -4^{\circ}$.

Figure 56.- Continued.

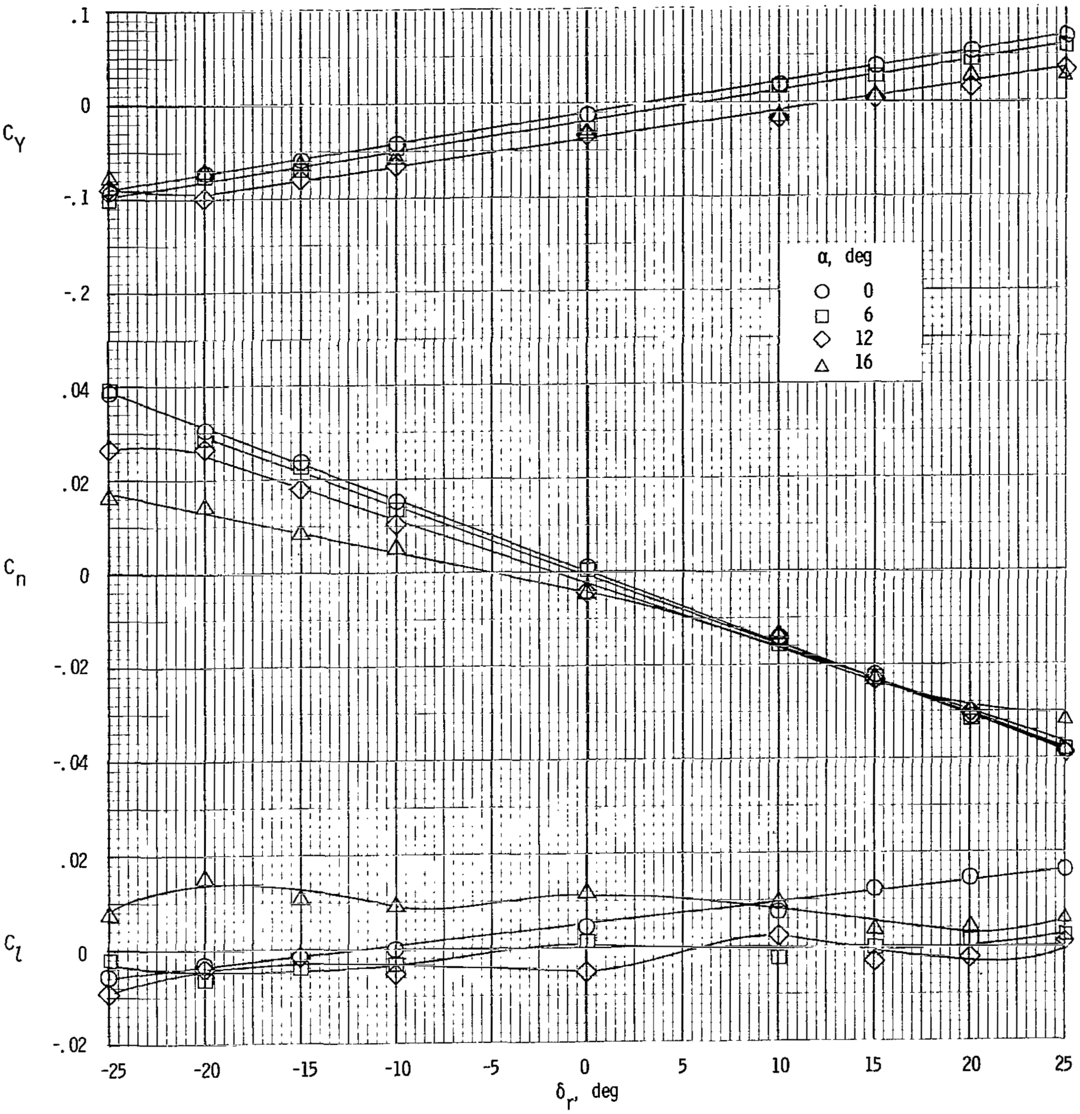

(c) $\beta = 0^0$.

Figure 56.- Continued.

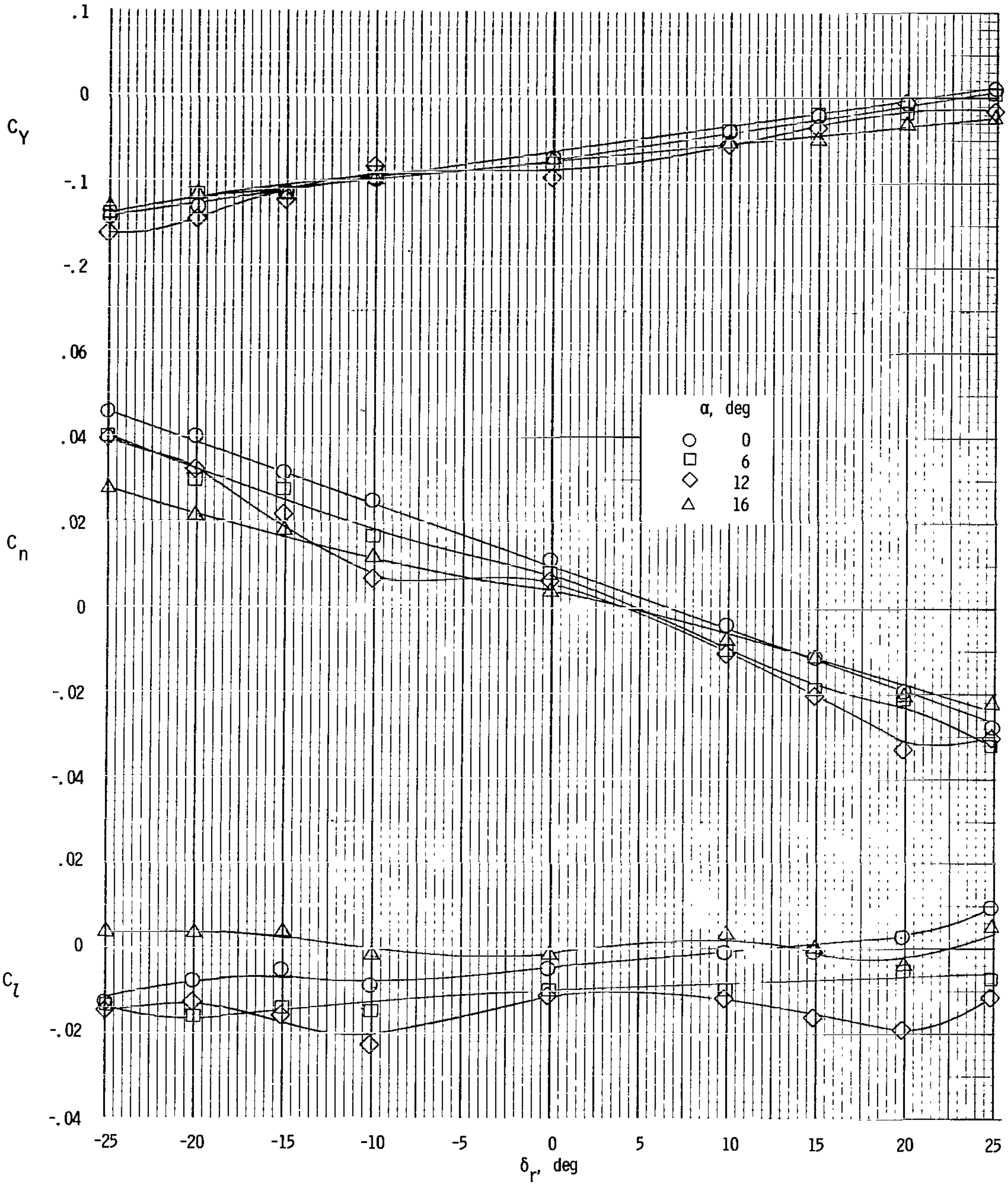

(d) $\beta = 4^o$.

Figure 56.- Continued.

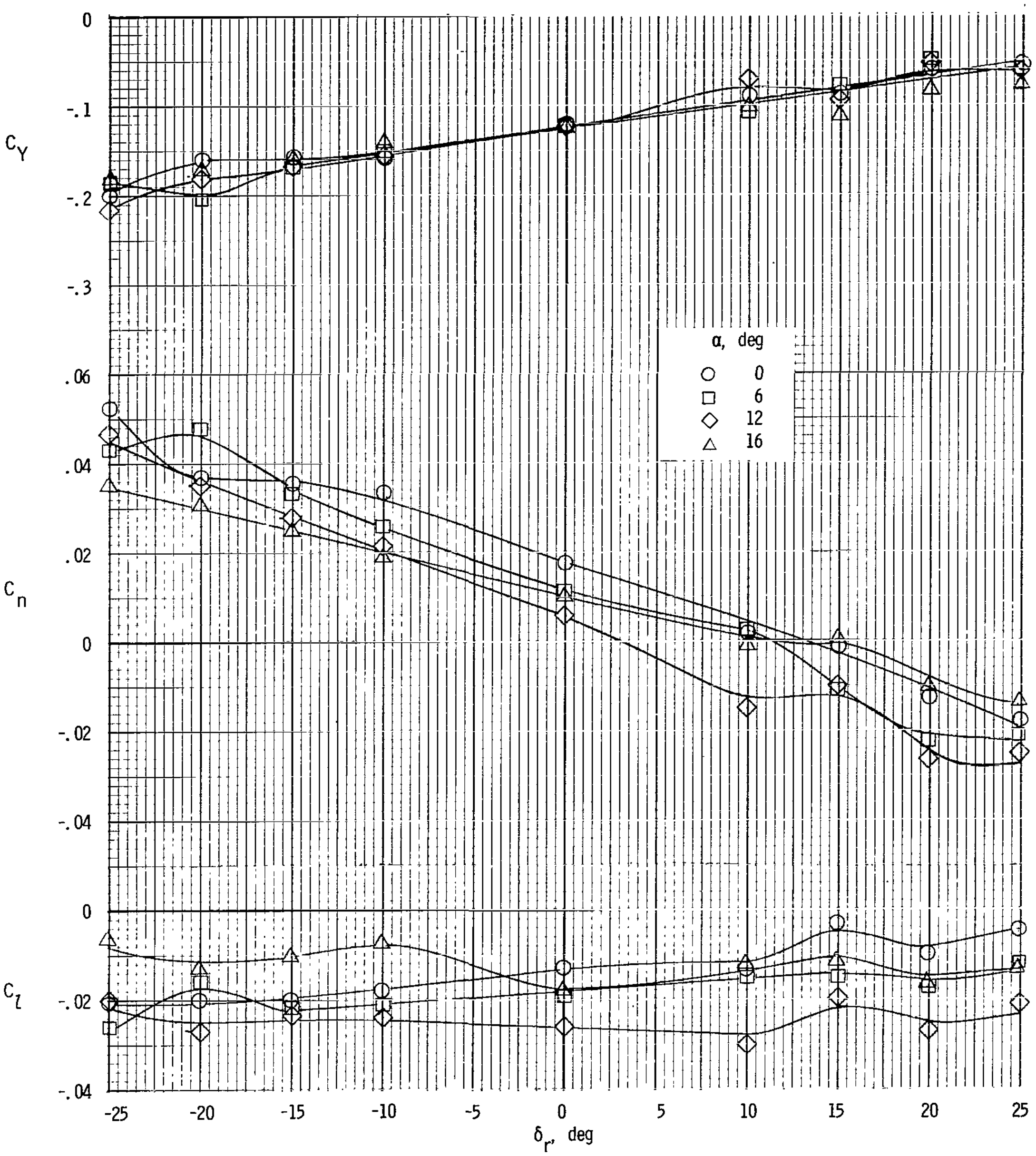

(e) $\beta = 8^o$.

Figure 56.- Concluded.

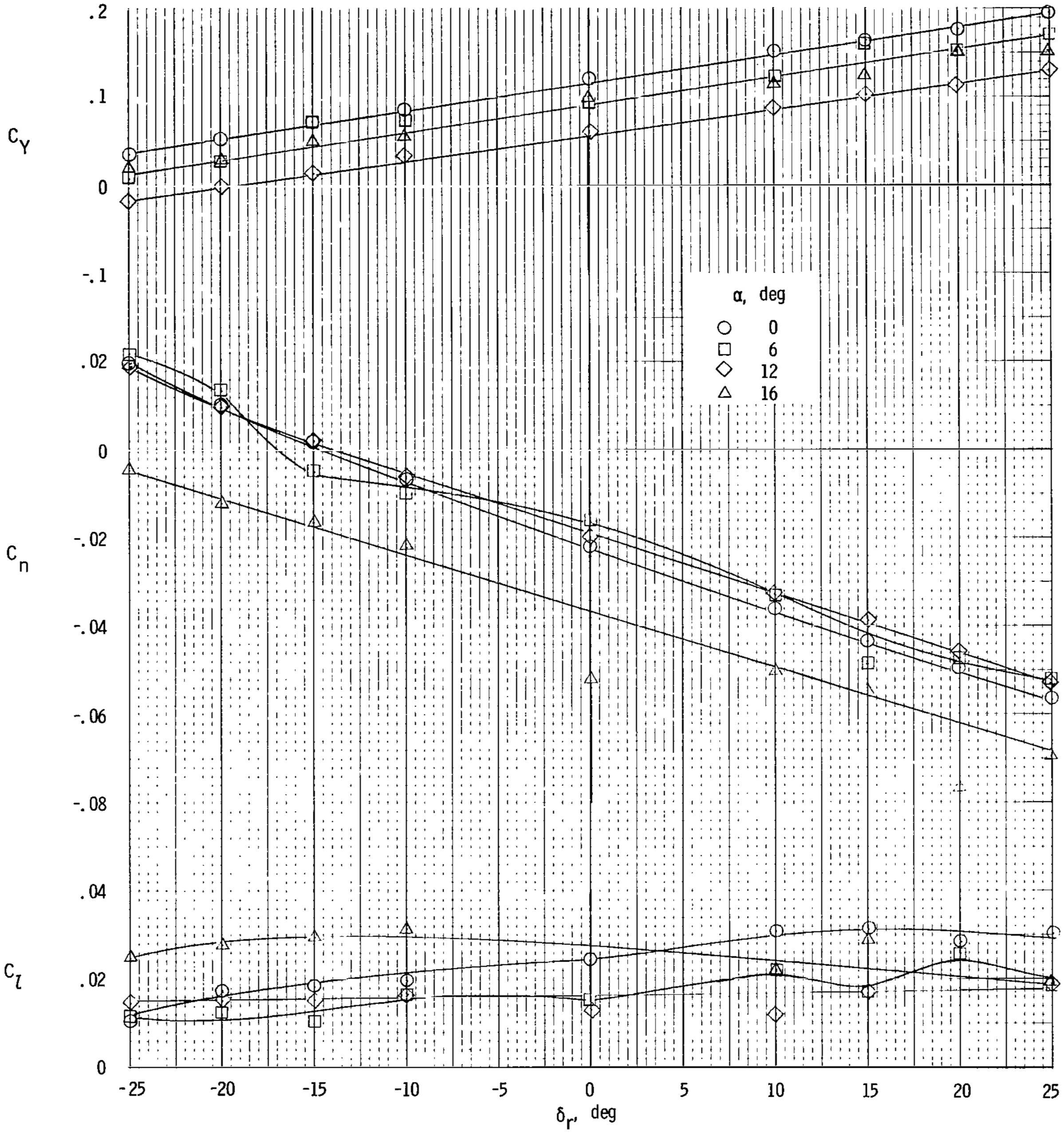

(a) $\beta = -8^0$.

Figure 57.- Variation of lateral aerodynamic characteristics of model with rudder deflection for $\delta_f = 35^0$; $T_c' = 0.28$.

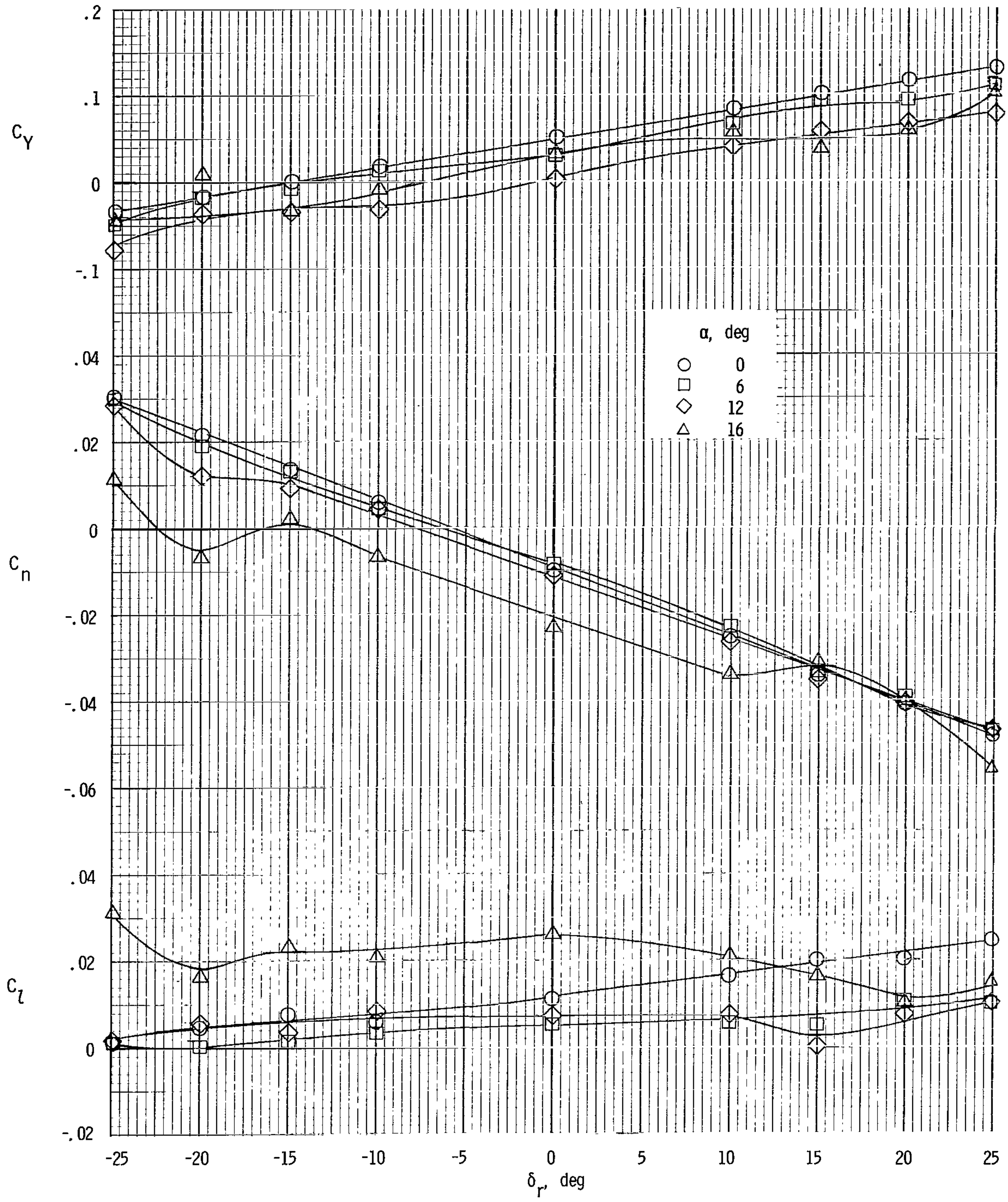

(b) $\beta = -4^0$.

Figure 57.- Continued.

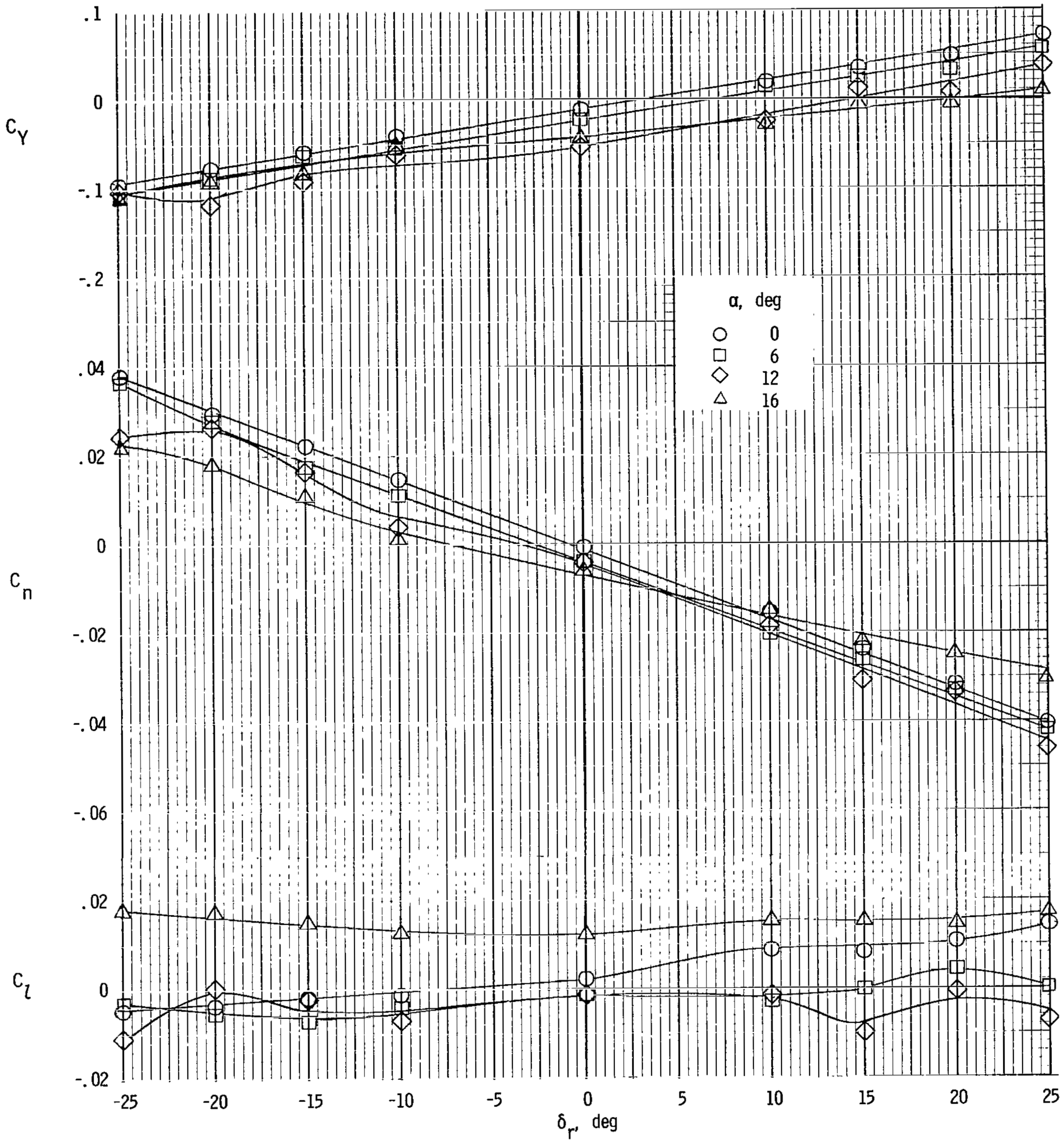

(c) $\beta = 0^0$.

Figure 57.- Continued.

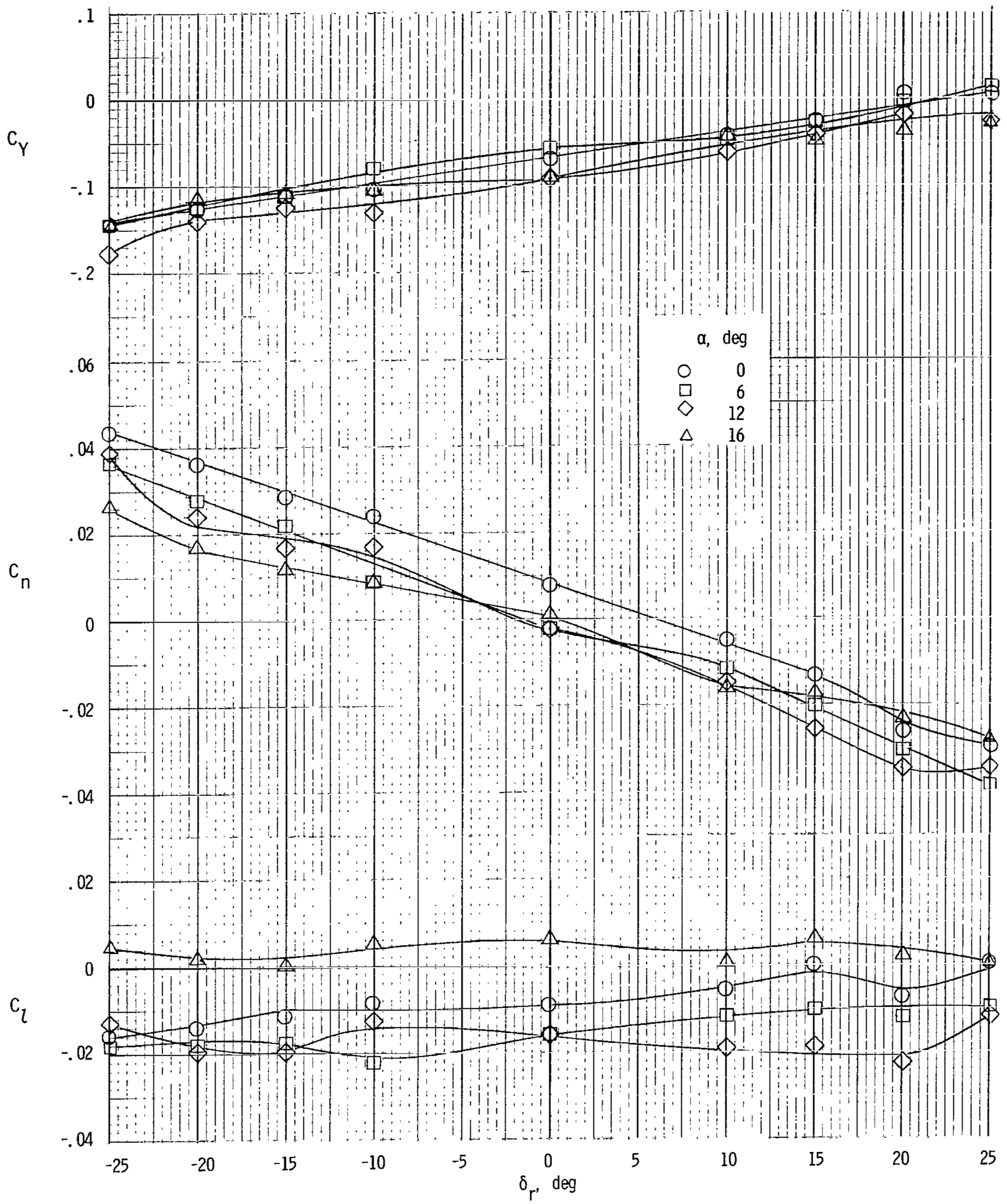

(d) $\beta = 4^{\circ}$.

Figure 57.- Continued.

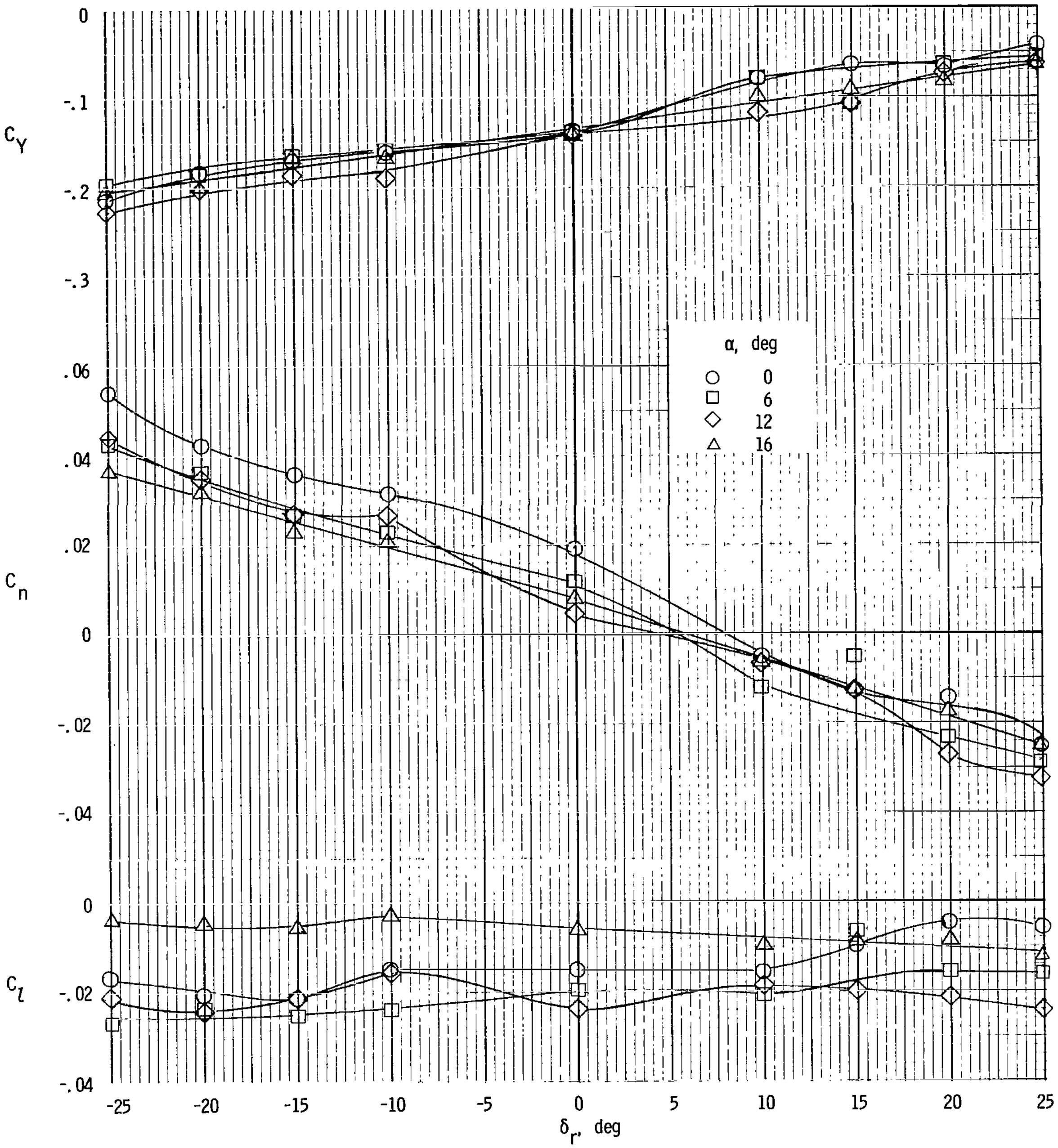

(e) $\beta = 8^{0}$.

Figure 57.- Concluded.

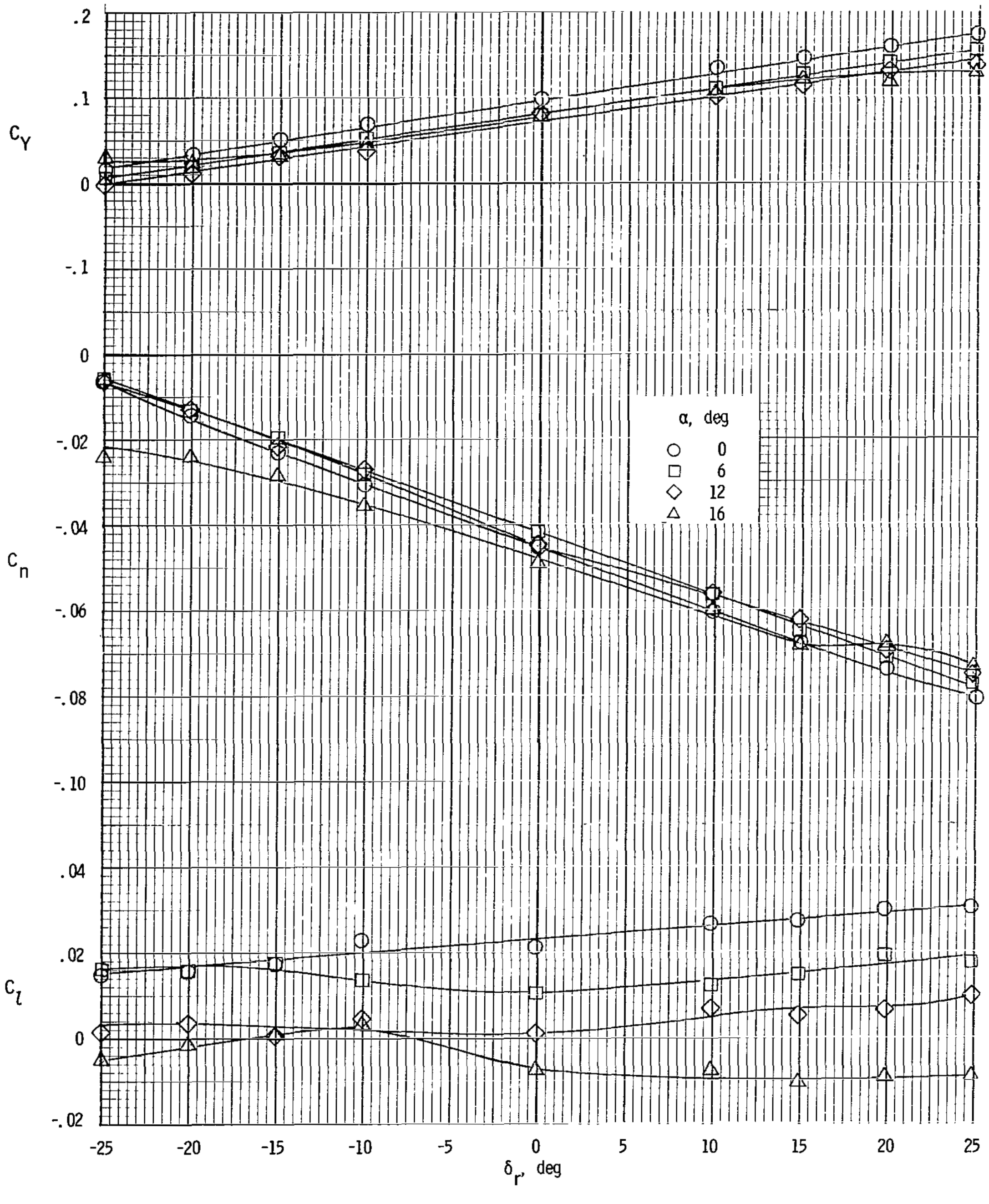

(a) $\beta = -8^0$.

Figure 58.- Variation of lateral aerodynamic characteristics of model with rudder deflection for asymmetric power. $\delta_f = 0^0$. Left engine windmilling; right engine full.

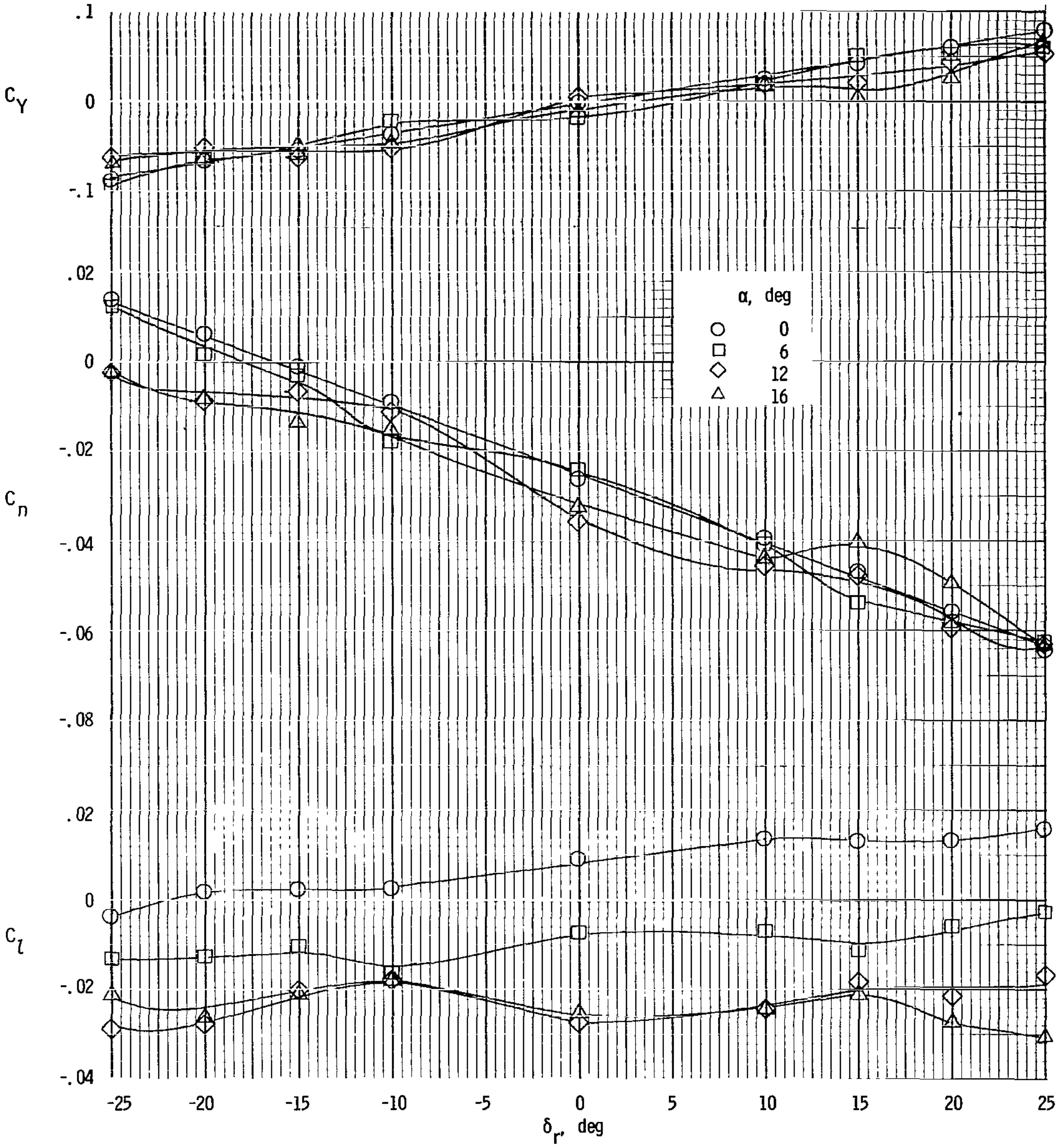

(b) $\beta = 0^0$.

Figure 58.- Continued.

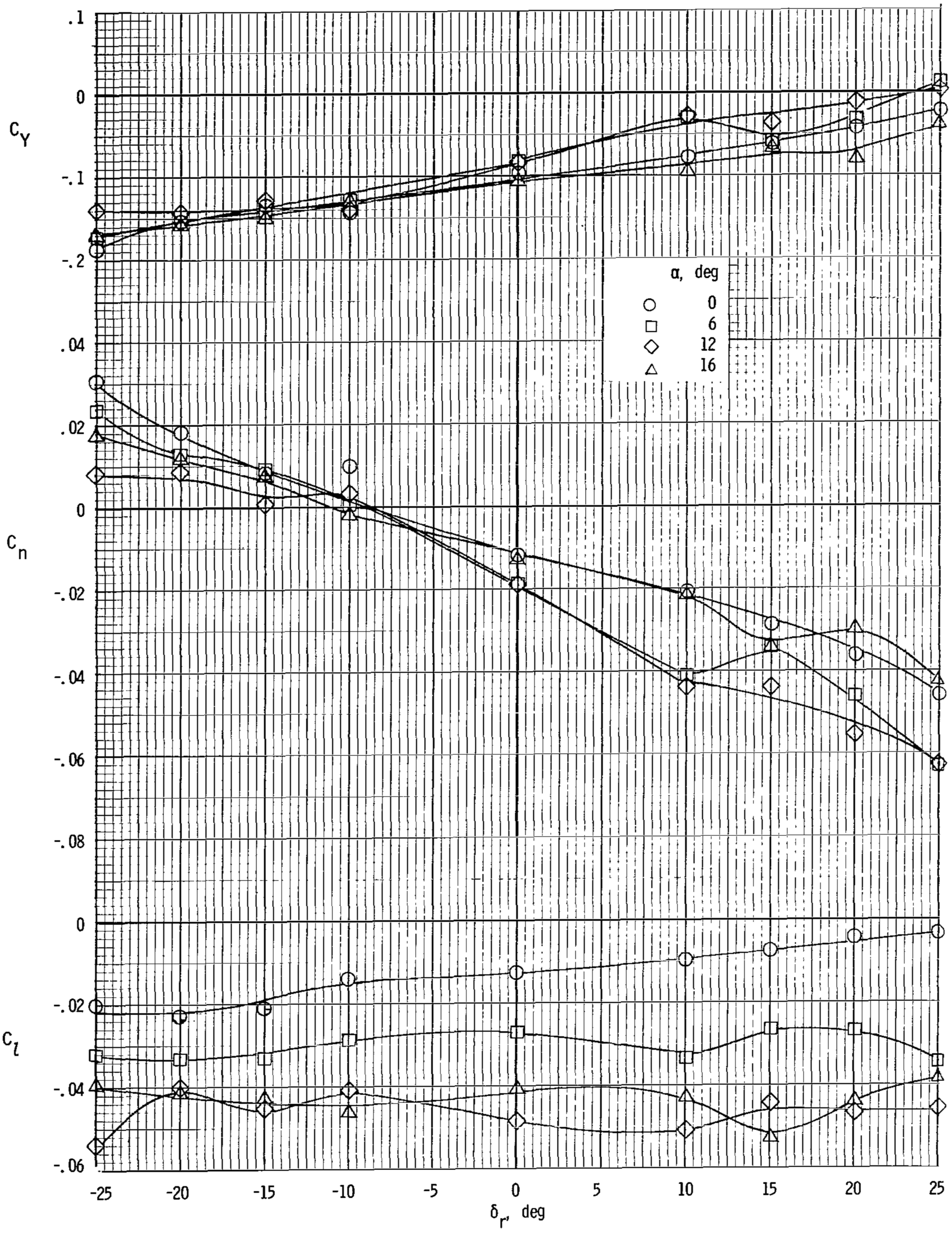

(c) $\beta = 8^0$.

Figure 58.- Concluded.

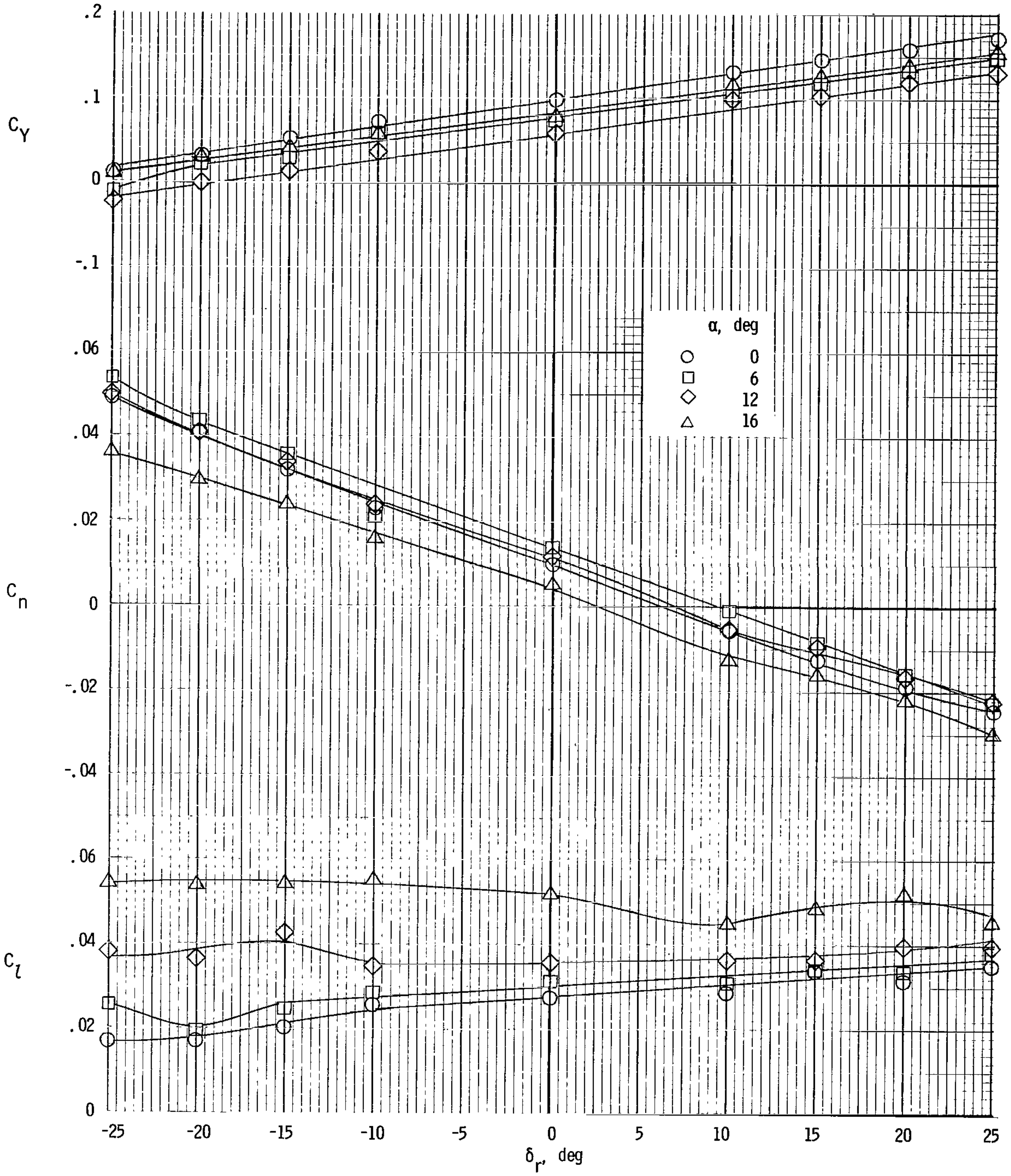

(a) $\beta = -8^0$.

Figure 59.- Variation of lateral aerodynamic characteristics of model with rudder deflection for asymmetric power. $\delta_f = 0^0$. Left engine full; right engine windmilling.

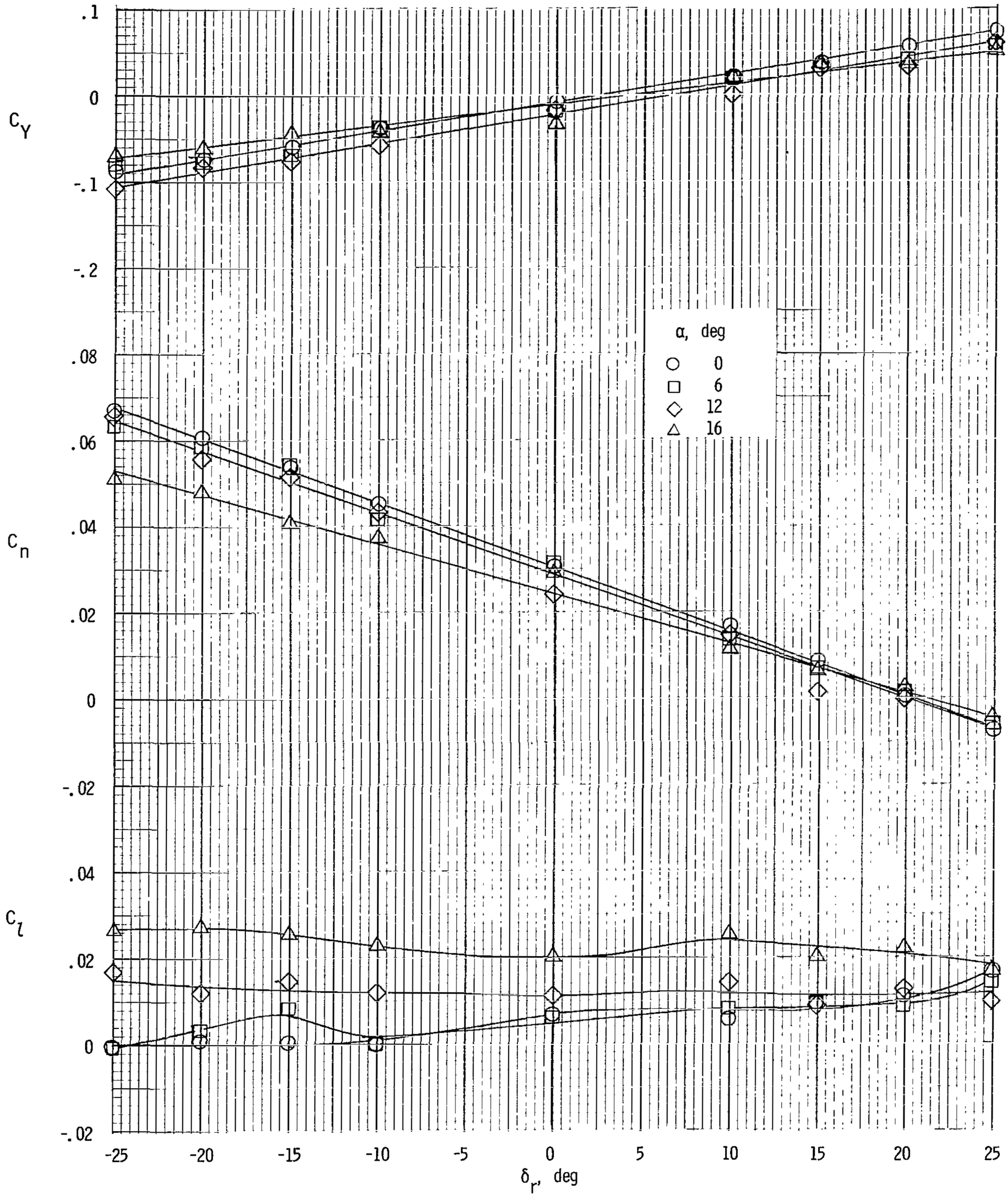

(b) $\beta = 0^0$.

Figure 59.- Continued.

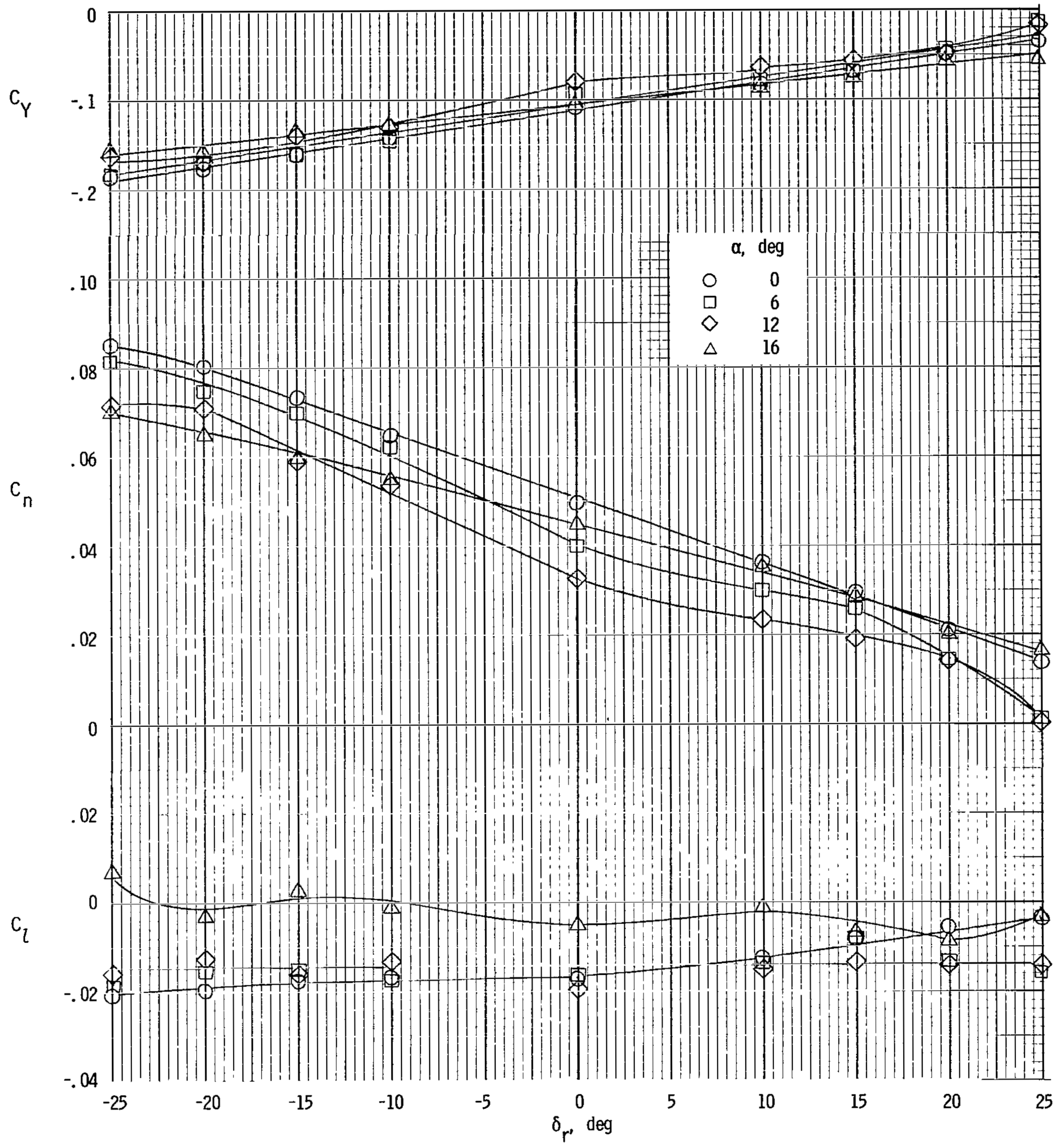

(c) $\beta = 8^0$.

Figure 59.- Concluded.

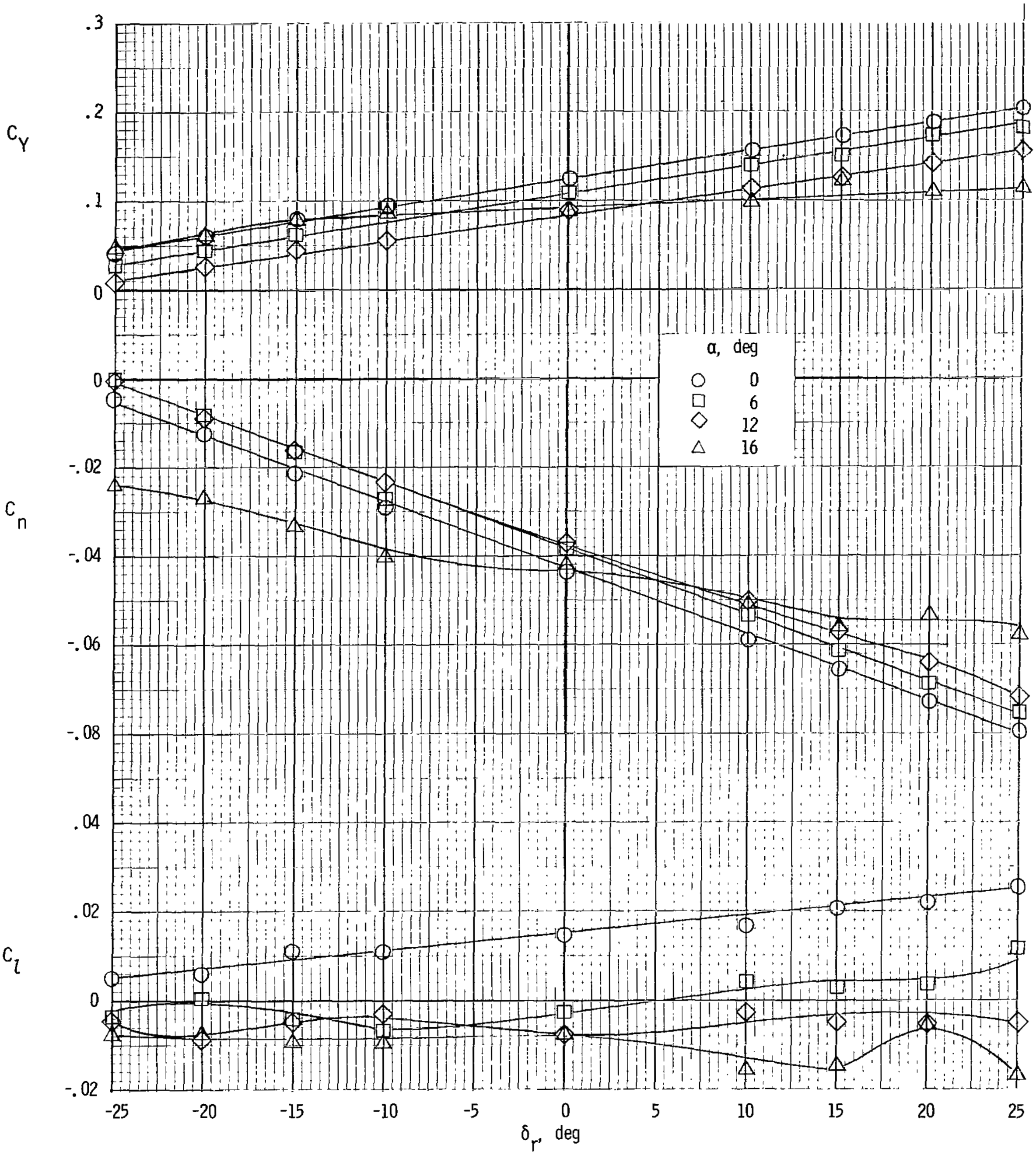

(a) $\beta = -8^0$.

Figure 60.- Variation of lateral aerodynamic characteristics of model with rudder deflection for asymmetric power. $\delta_f = 35^0$. Left engine windmilling; right engine full.

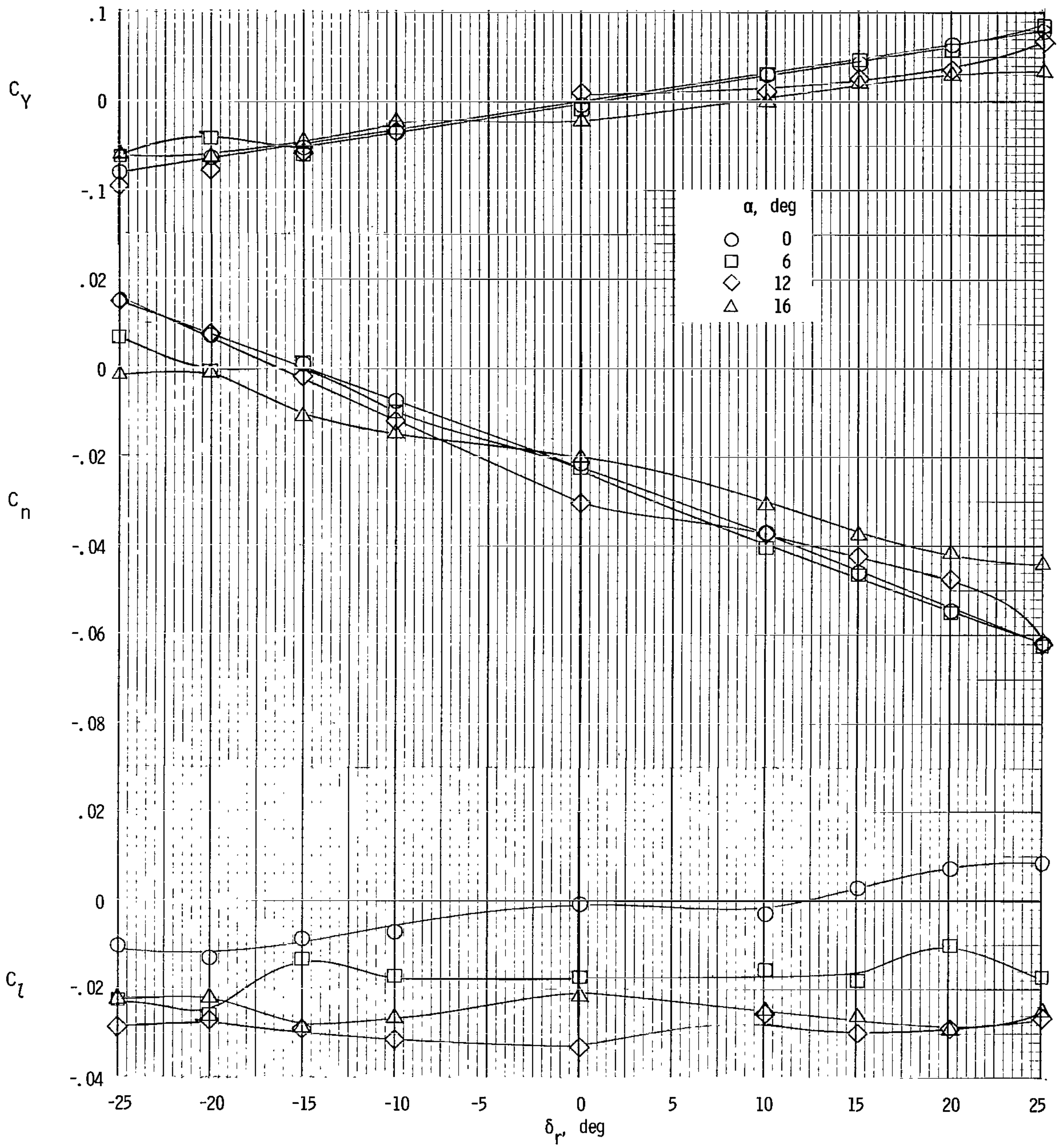

(b) $\beta = 0^0$.

Figure 60.- Continued.

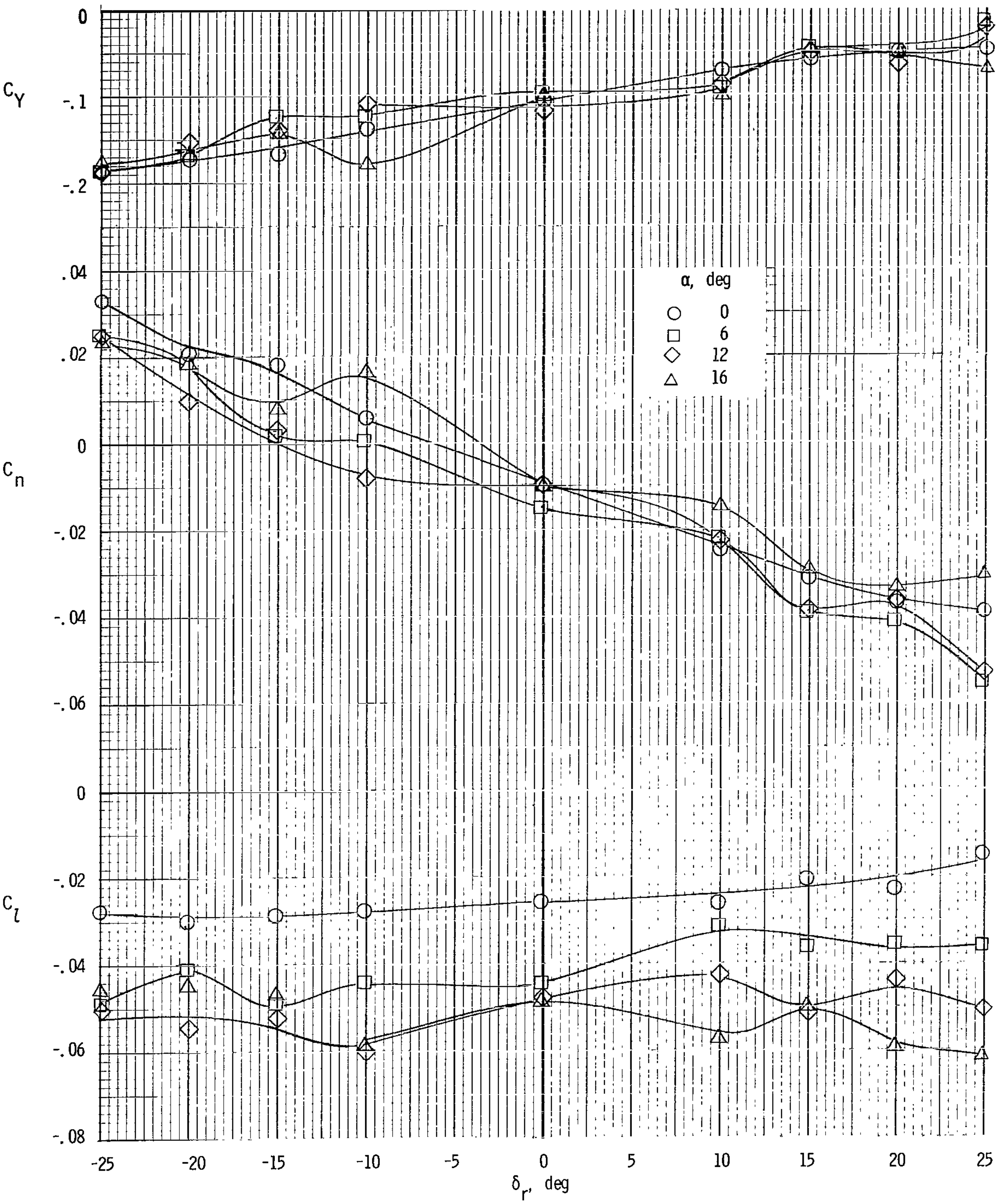

(c) $\beta = 8^0$.

Figure 60.- Concluded.

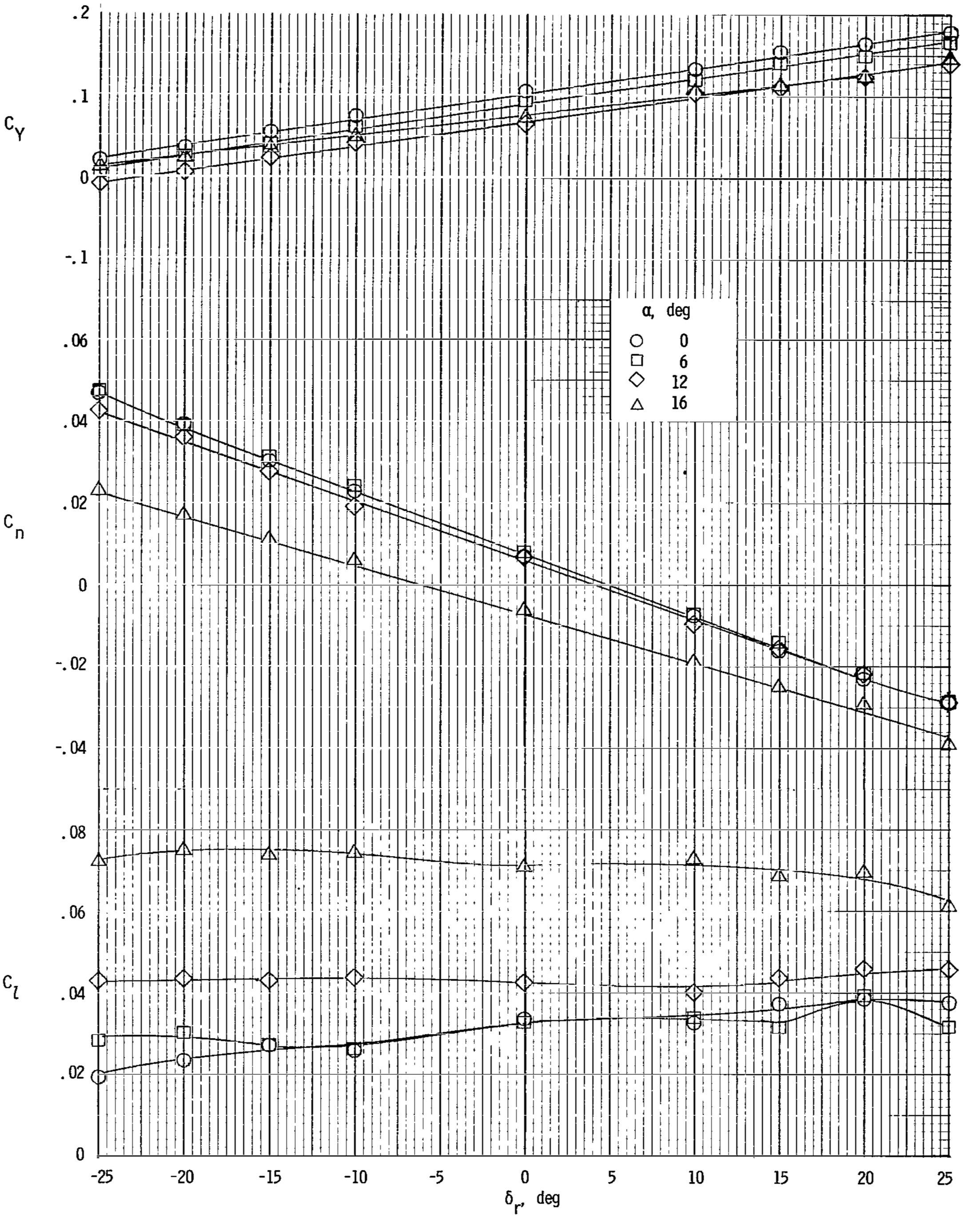

(a) $\beta = -8^{\circ}$.

Figure 61.- Variation of lateral aerodynamic characteristics of model with rudder deflection for asymmetric power. $\delta_f = 35^{\circ}$. Left engine full; right engine windmilling.

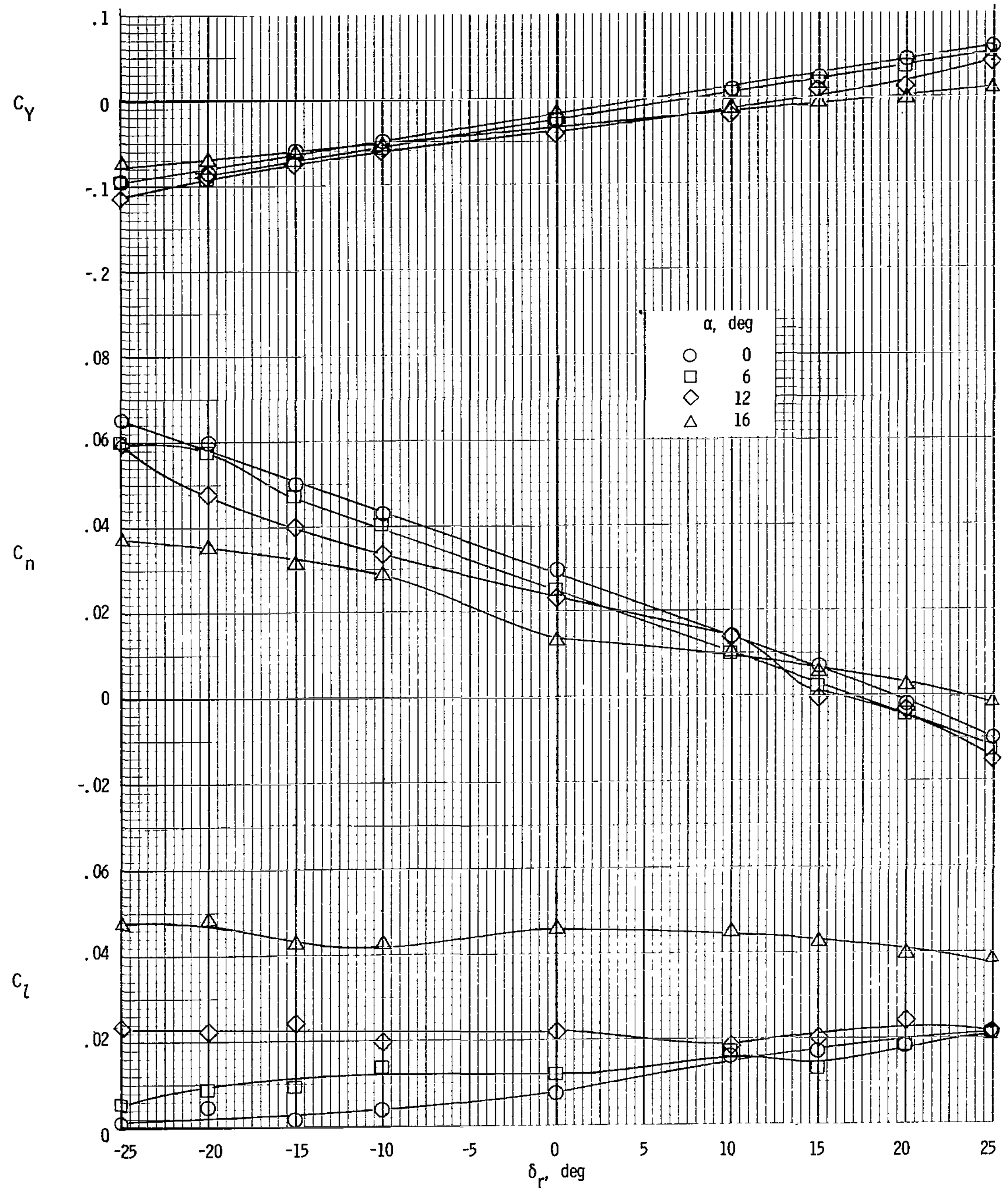

(b) $\beta = 0^{\circ}$.

Figure 61.- Continued.

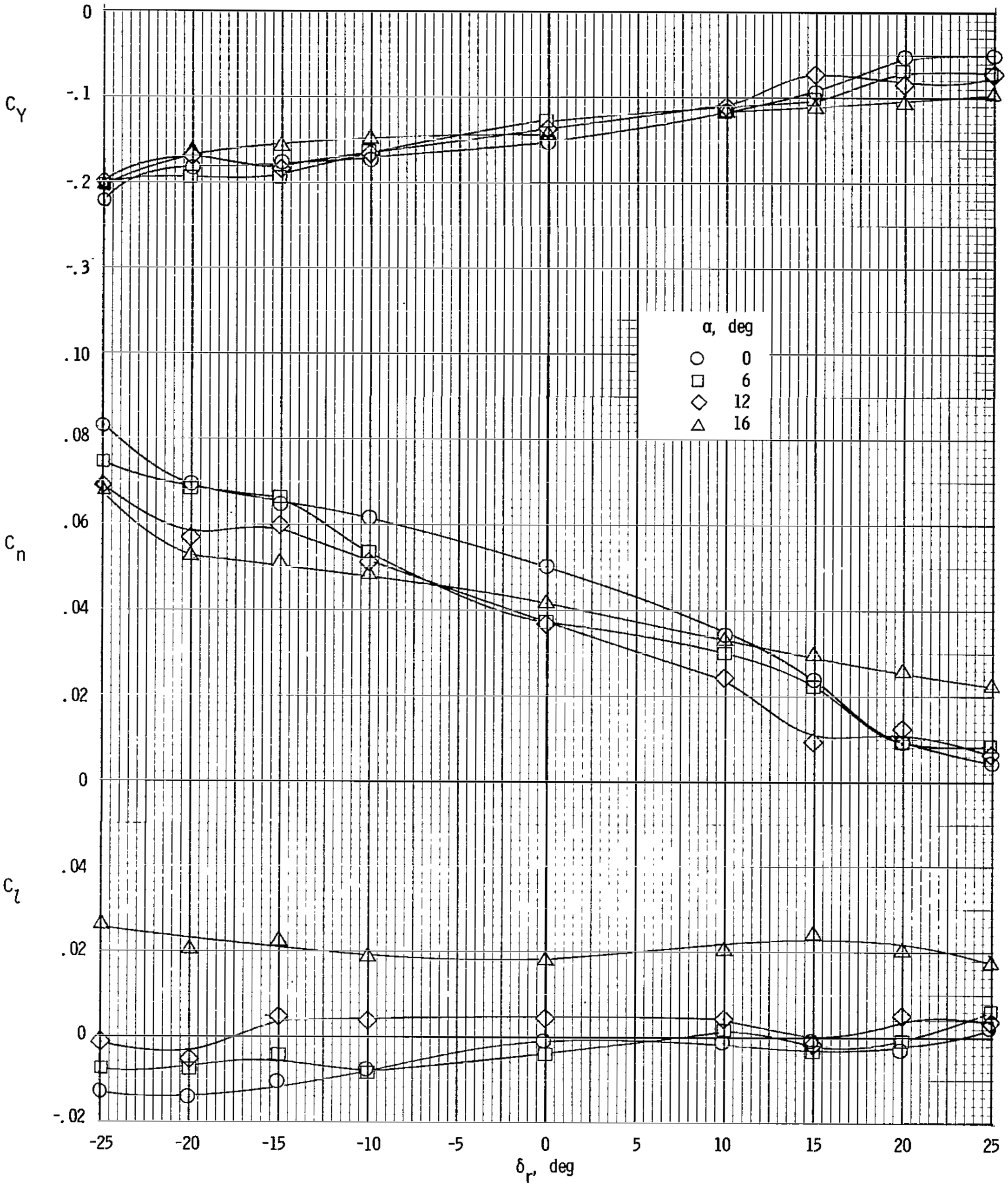

(c) $\beta = 8^0$.

Figure 61.- Concluded.

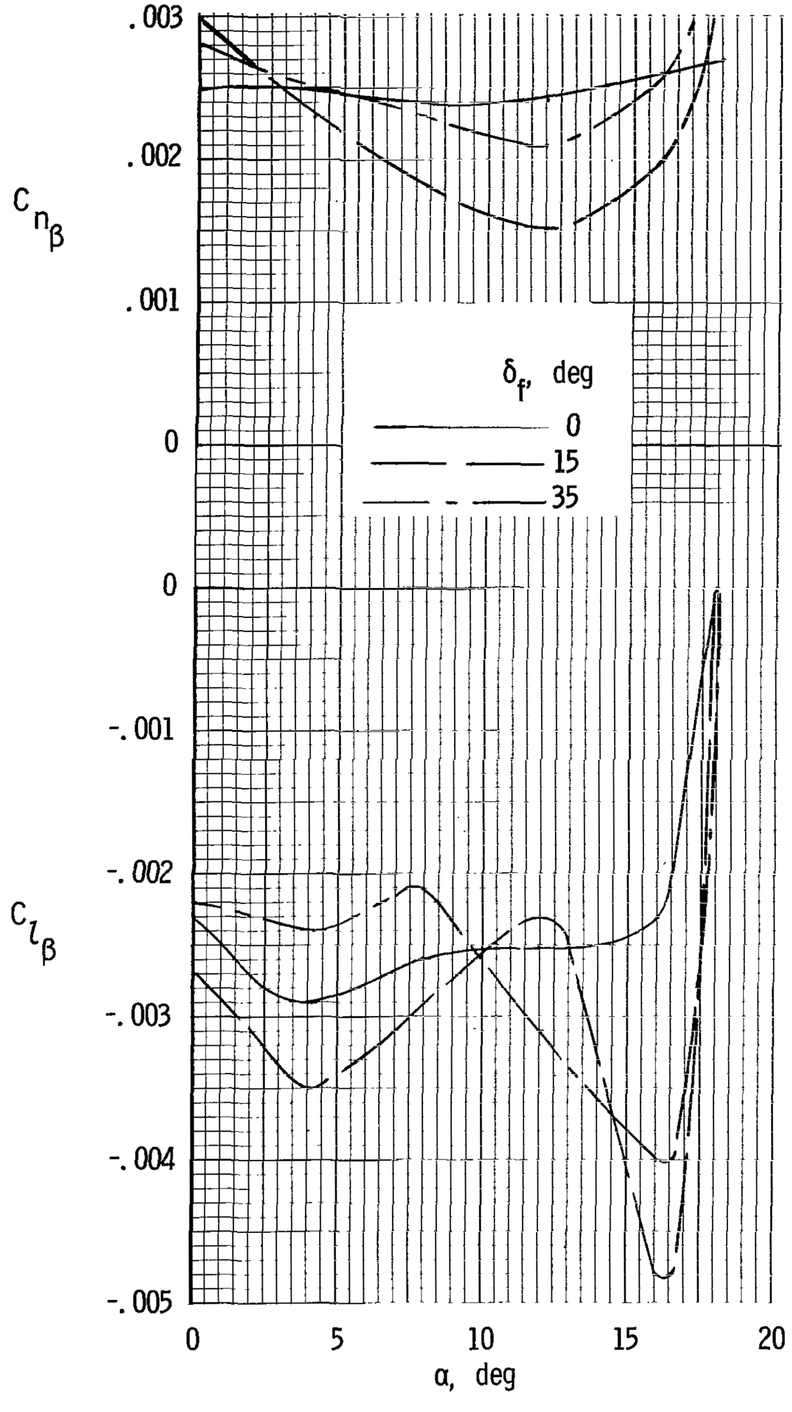

Figure 62.- Variation of effective dihedral and directional stability parameters with angle of attack. Propellers removed.

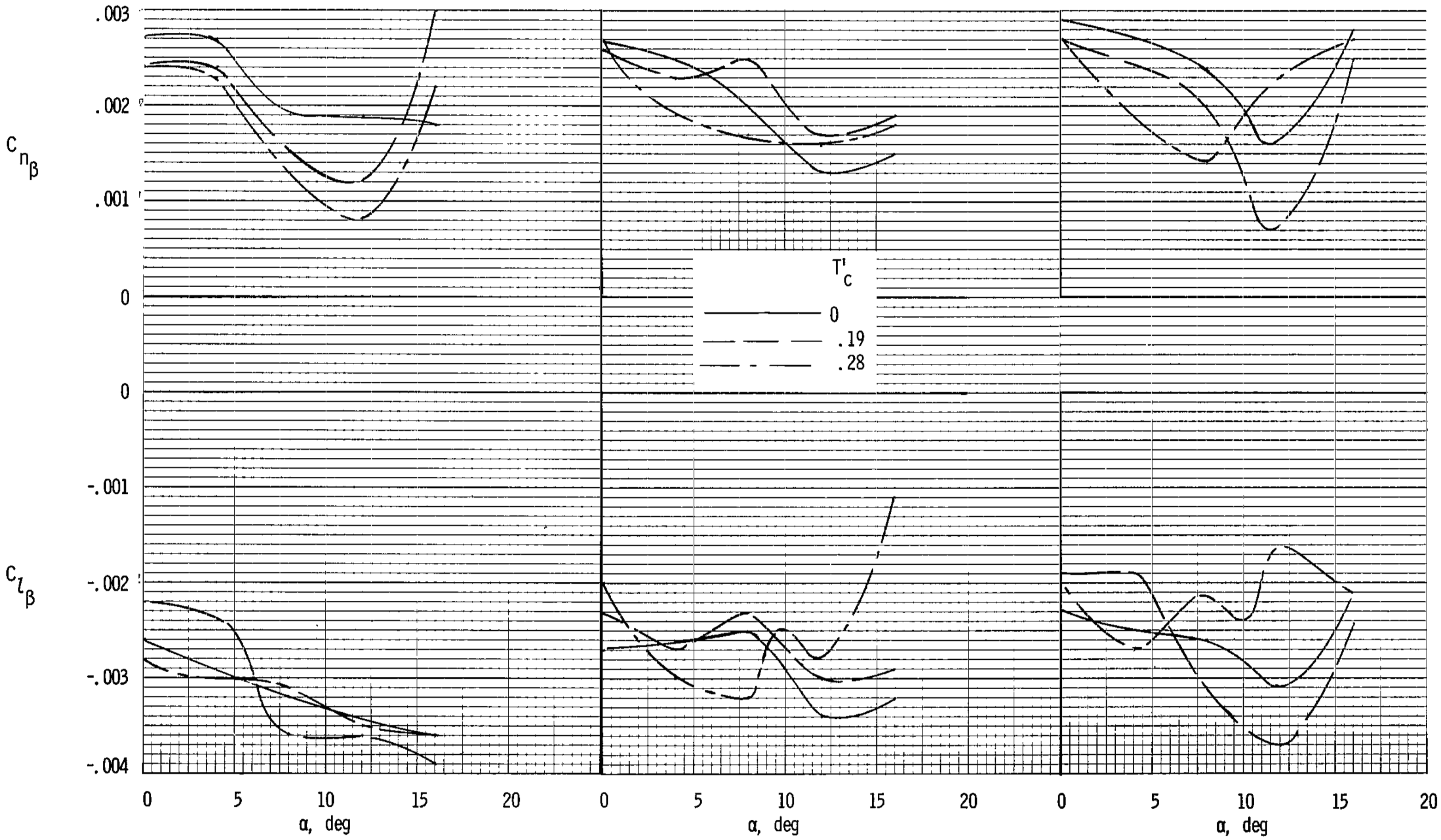

(a) $\delta_f = 0^0$.

(b) $\delta_f = 15^0$.

(c) $\delta_f = 35^0$.

Figure 63.- Variation of effective dihedral and directional stability parameters with angle of attack for several flap deflections and thrust coefficients.

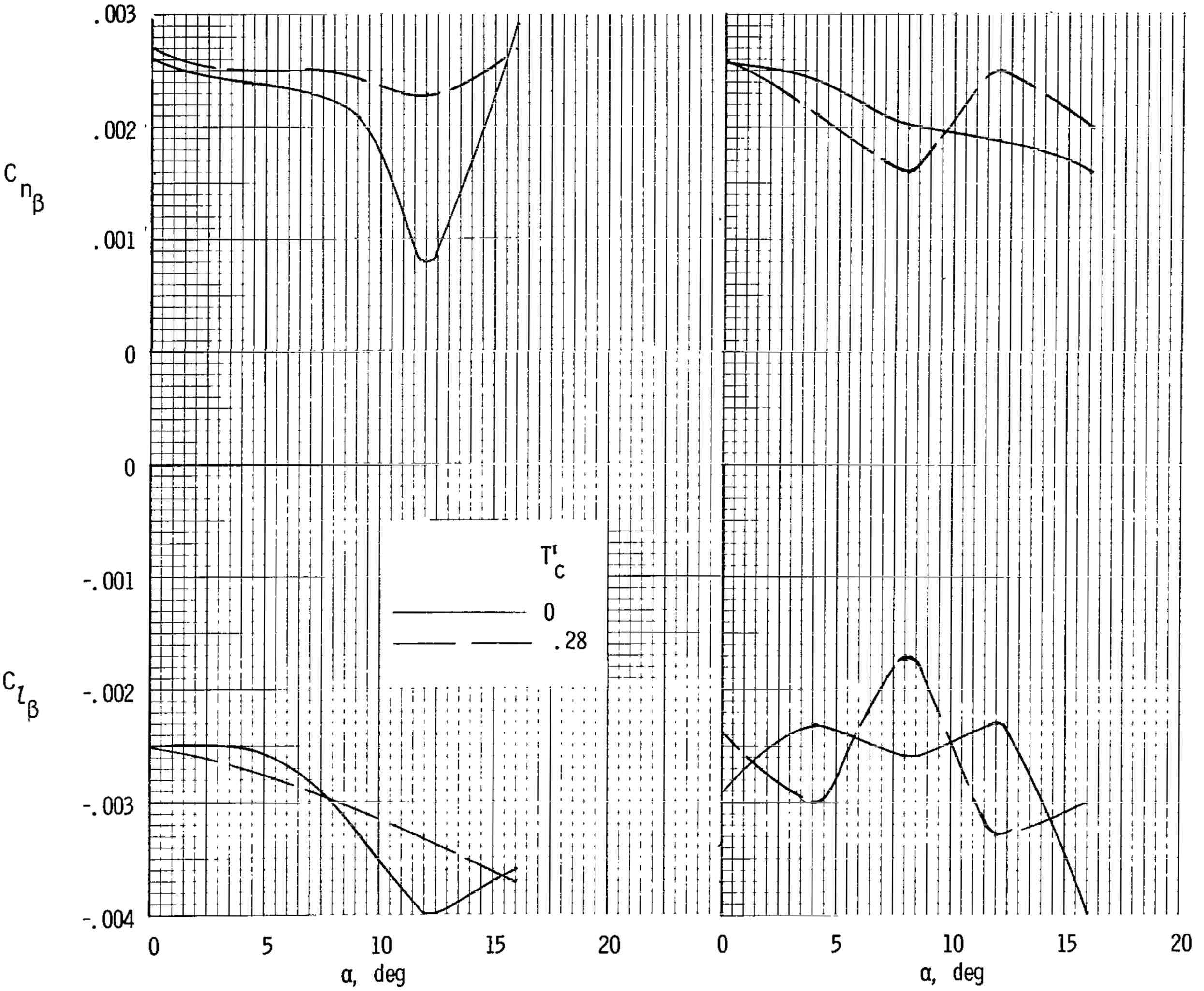

(a) $\delta_f = 0^{\circ}$.

(b) $\delta_f = 35^{\circ}$.

Figure 64.- Variation of effective dihedral and directional stability parameters with angle of attack for the short nacelle configuration.

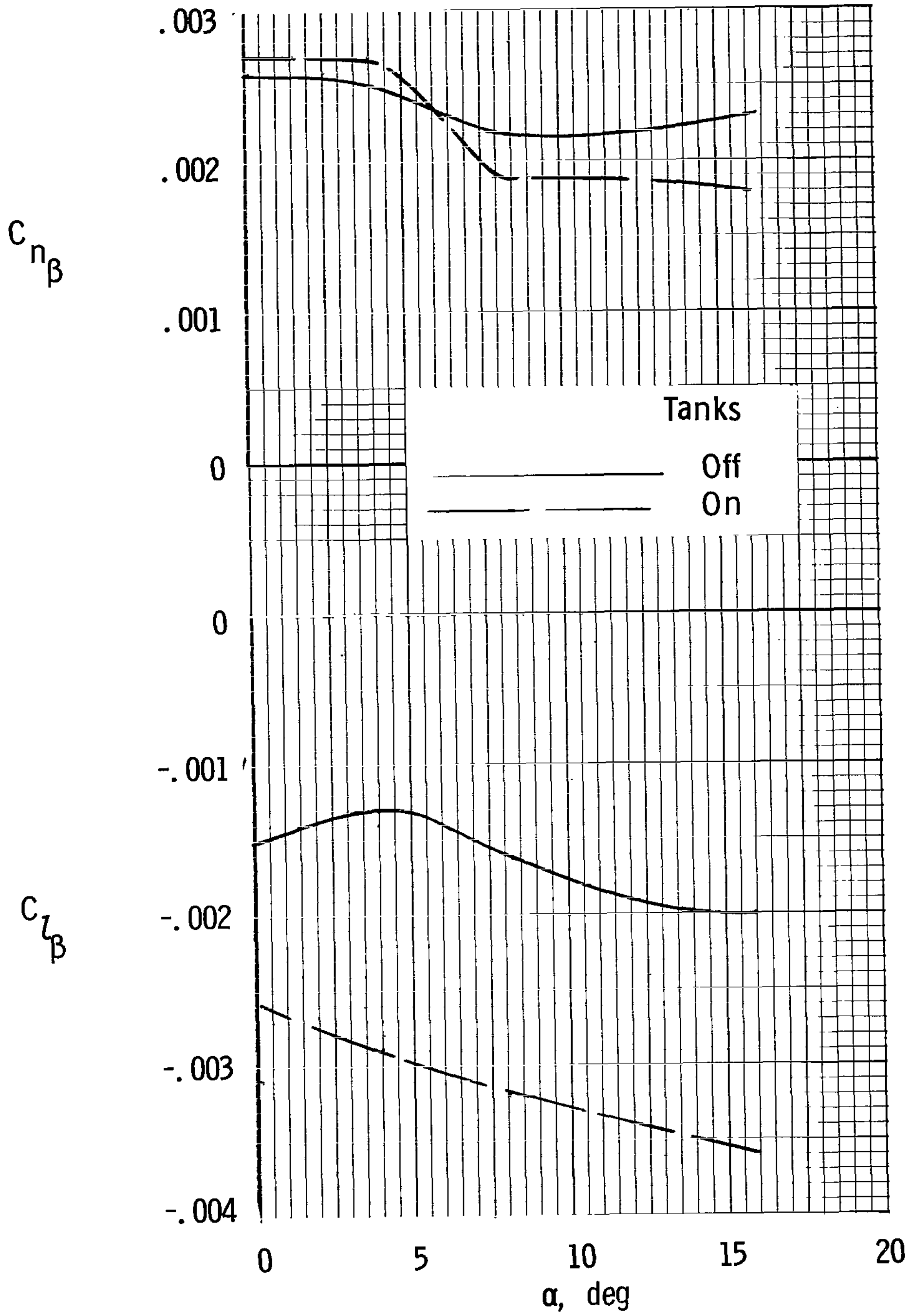

Figure 65.- Comparison of effective dihedral and directional stability parameters of model with and without wing-tip tanks. $\delta_f = 0^0$; $T_c' = 0$.

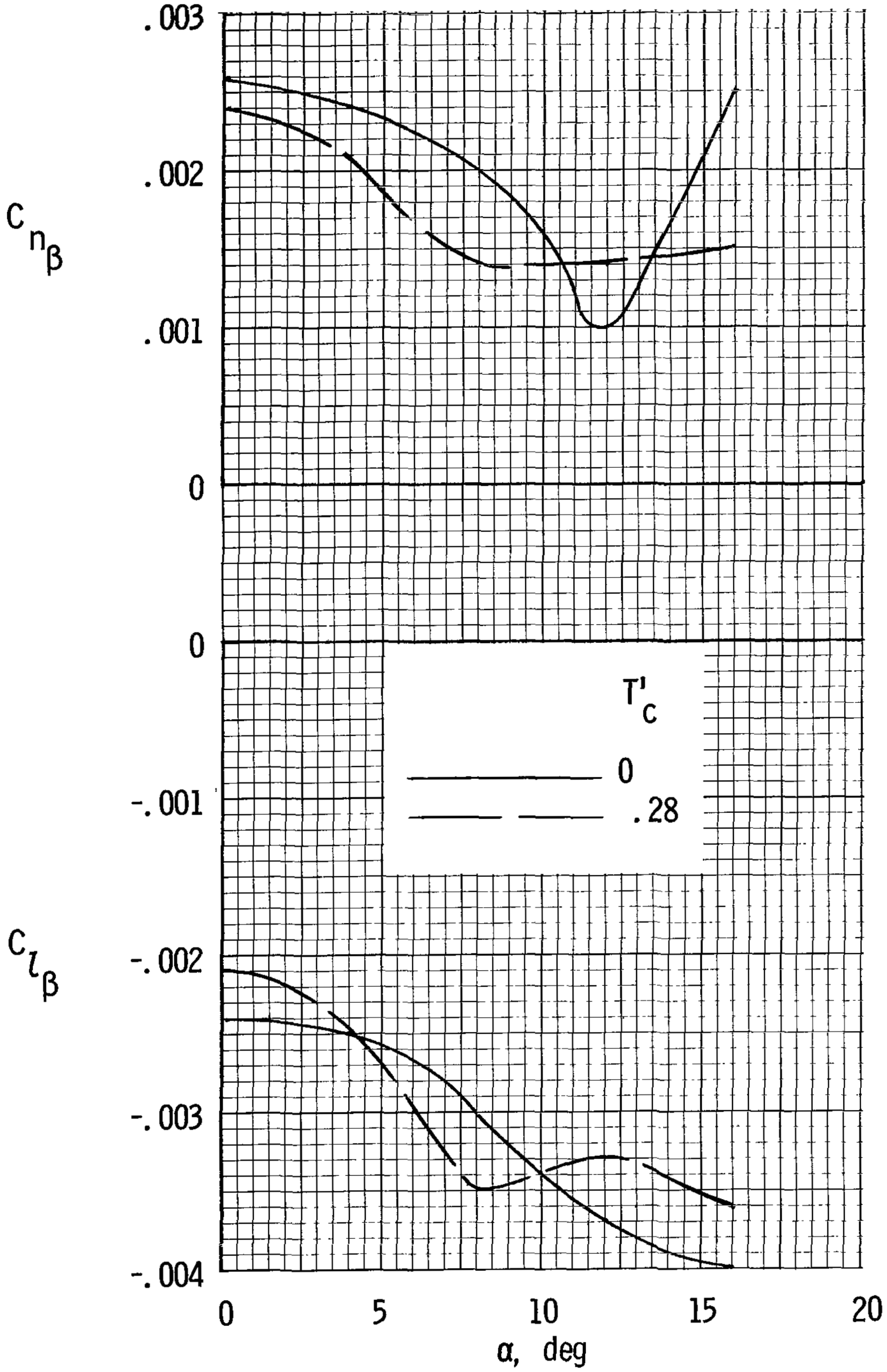

Figure 66.- Variation of effective dihedral and directional stability parameters with angle of attack with ventral fin removed. $\delta_f = 0^0$.

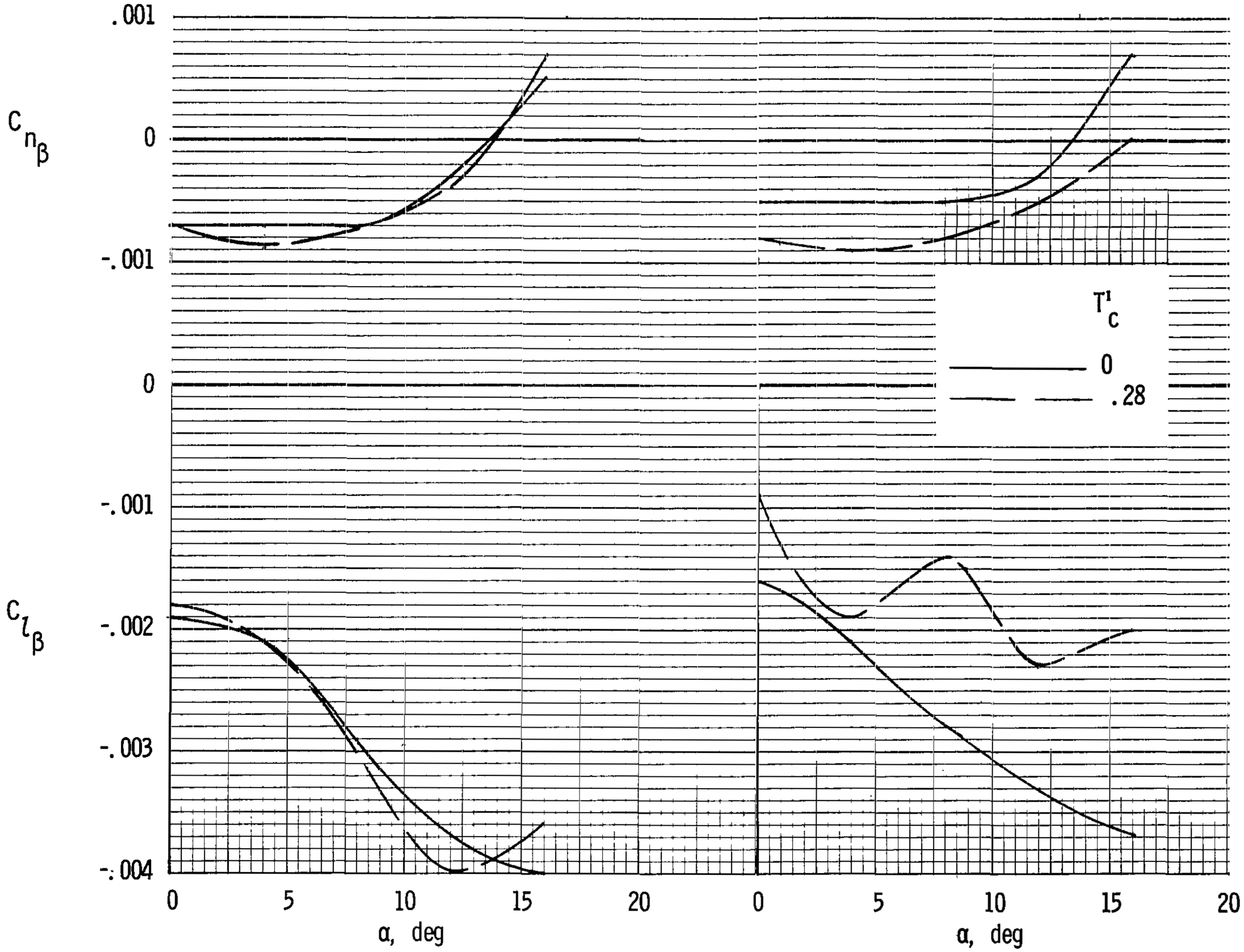

(a) $\delta_f = 0^\circ$.

(b) $\delta_f = 35^\circ$.

Figure 67.- Variation of effective dihedral and directional stability parameters with angle of attack with vertical tail and ventral fin removed.

Error

An error occurred while processing this page. See the system log for more details.

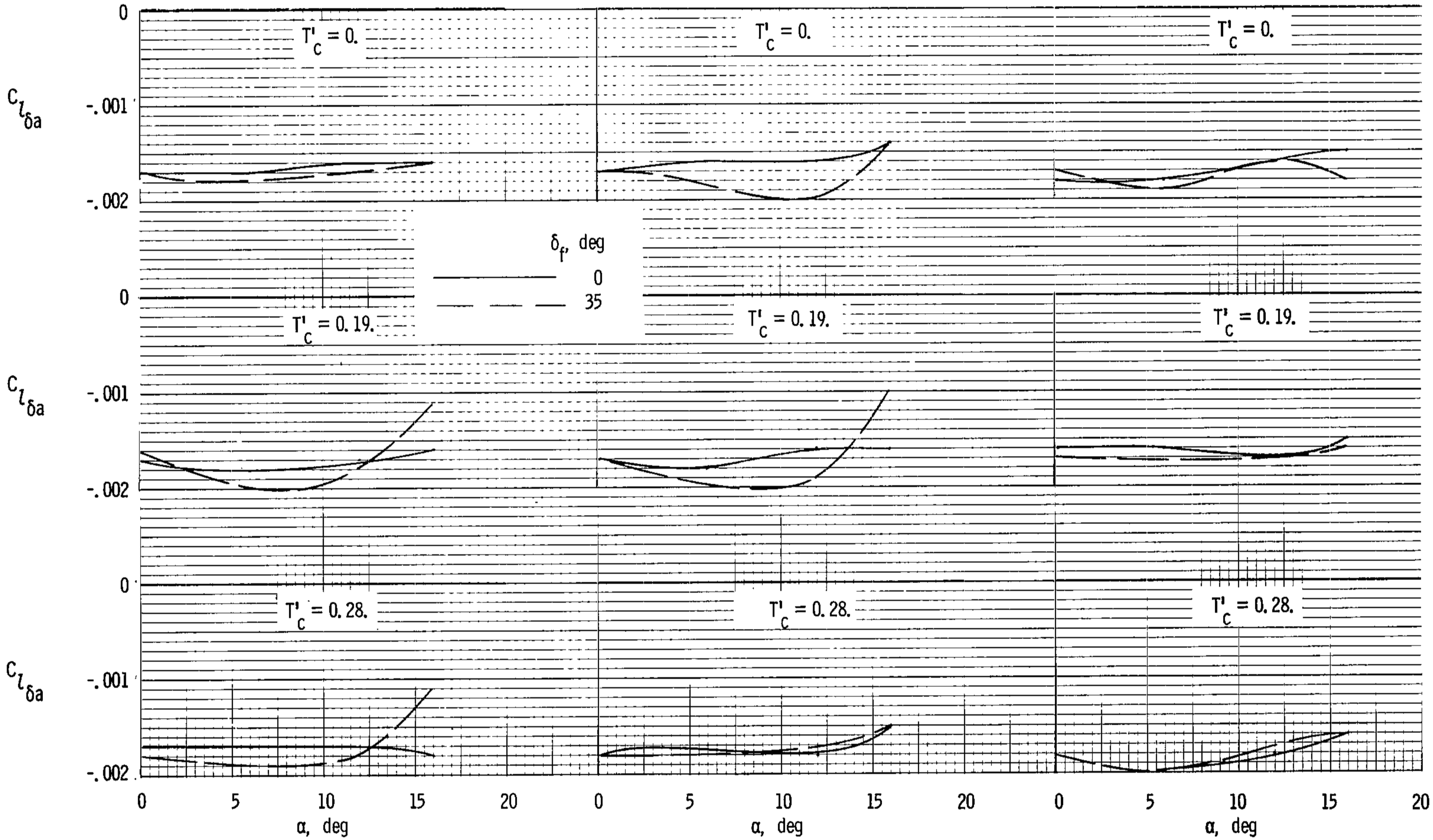

(a) β = -8°.

(b) β = -4°.

(c) β = 0°.

Figure 69.- Variation of aileron effectiveness with angle of attack.

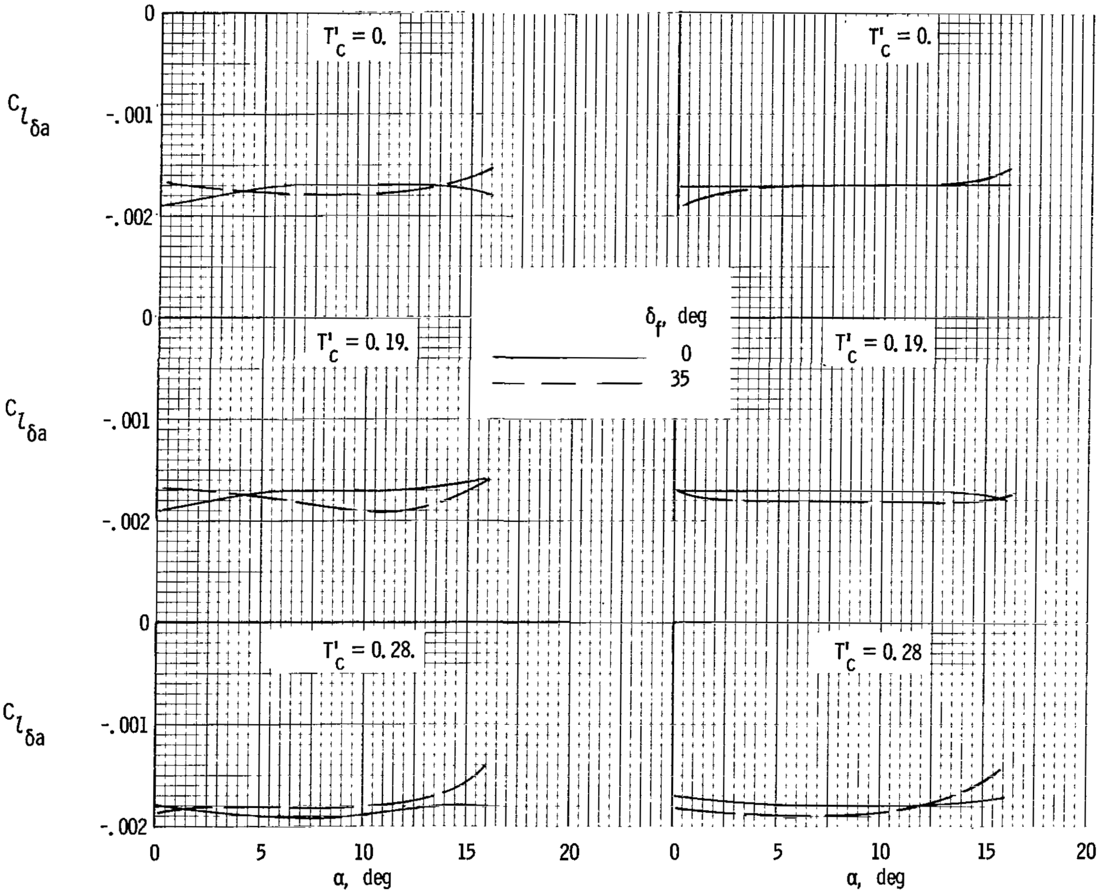

(d) β = 4°.

(e) β = 8°.

Figure 69.- Concluded.

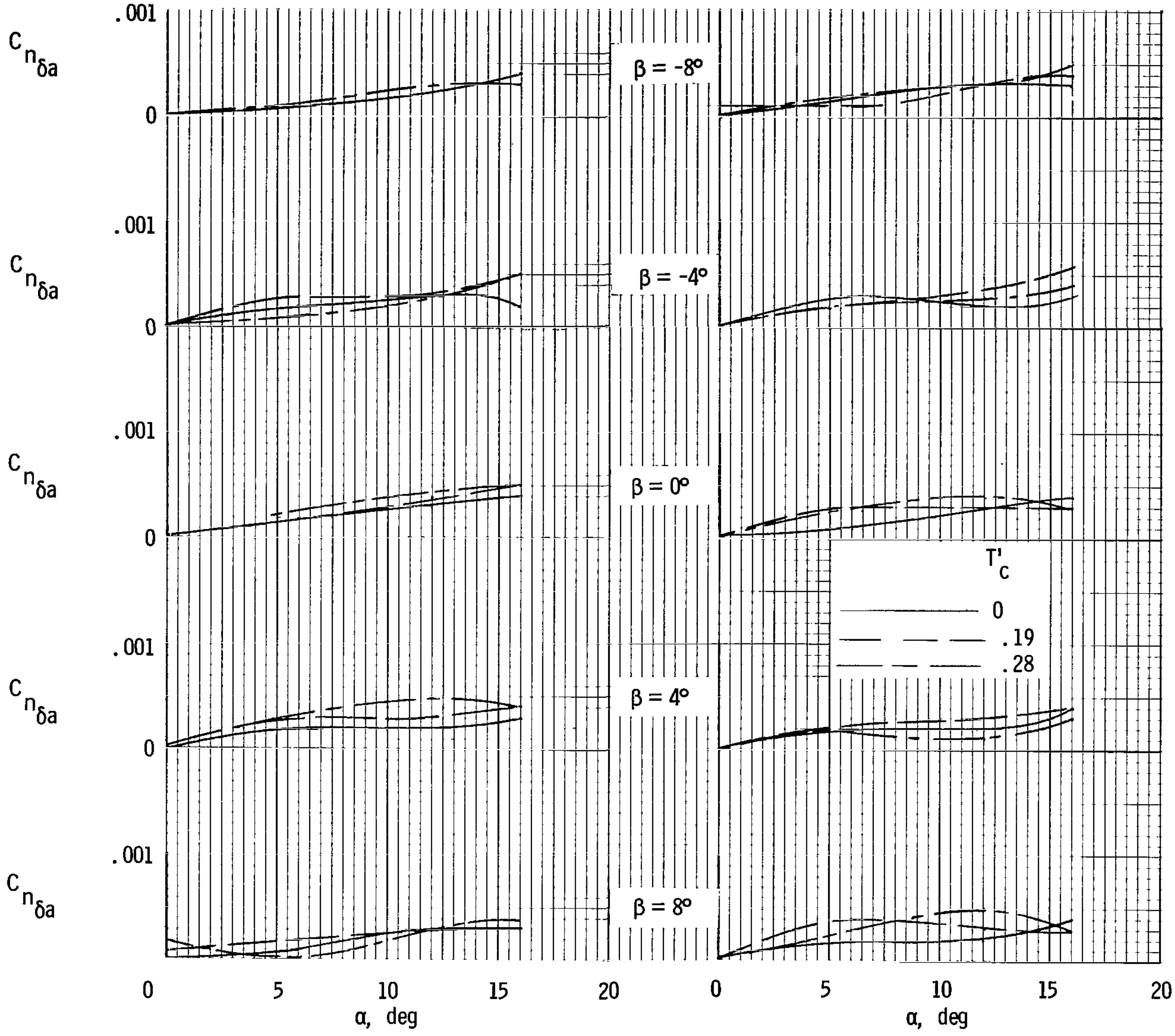

(a) $\delta_f = 0^0$.

(b) $\delta_f = 35^0$.

Figure 70.- Variation of aileron yawing-moment parameter with angle of attack for several flap deflections, sideslip angles, and thrust coefficients.

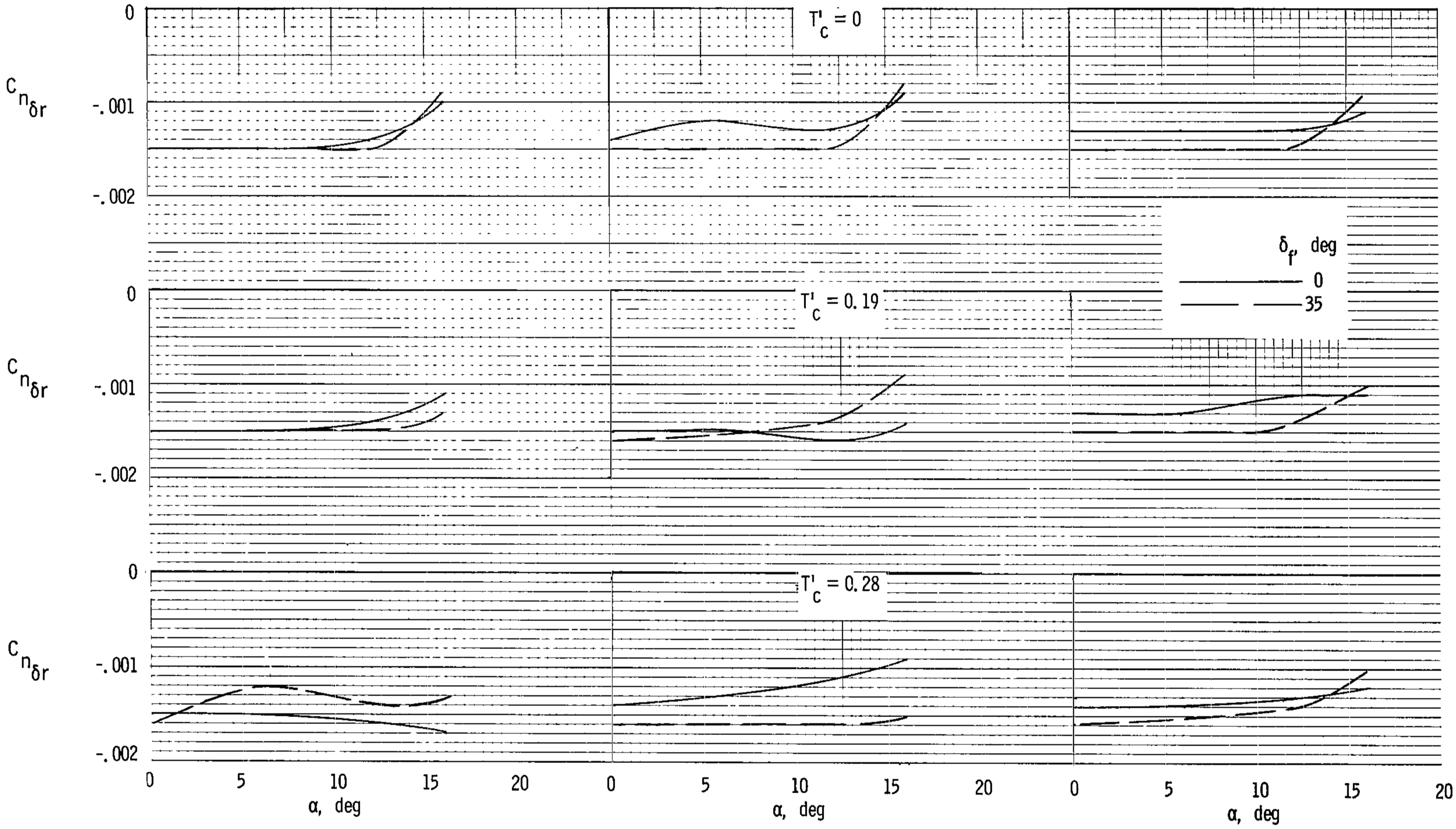

(a) β = -8°.

(b) β = -4°.

(c) β = 0°.

Figure 71.- Variation of rudder effectiveness with angle of attack.

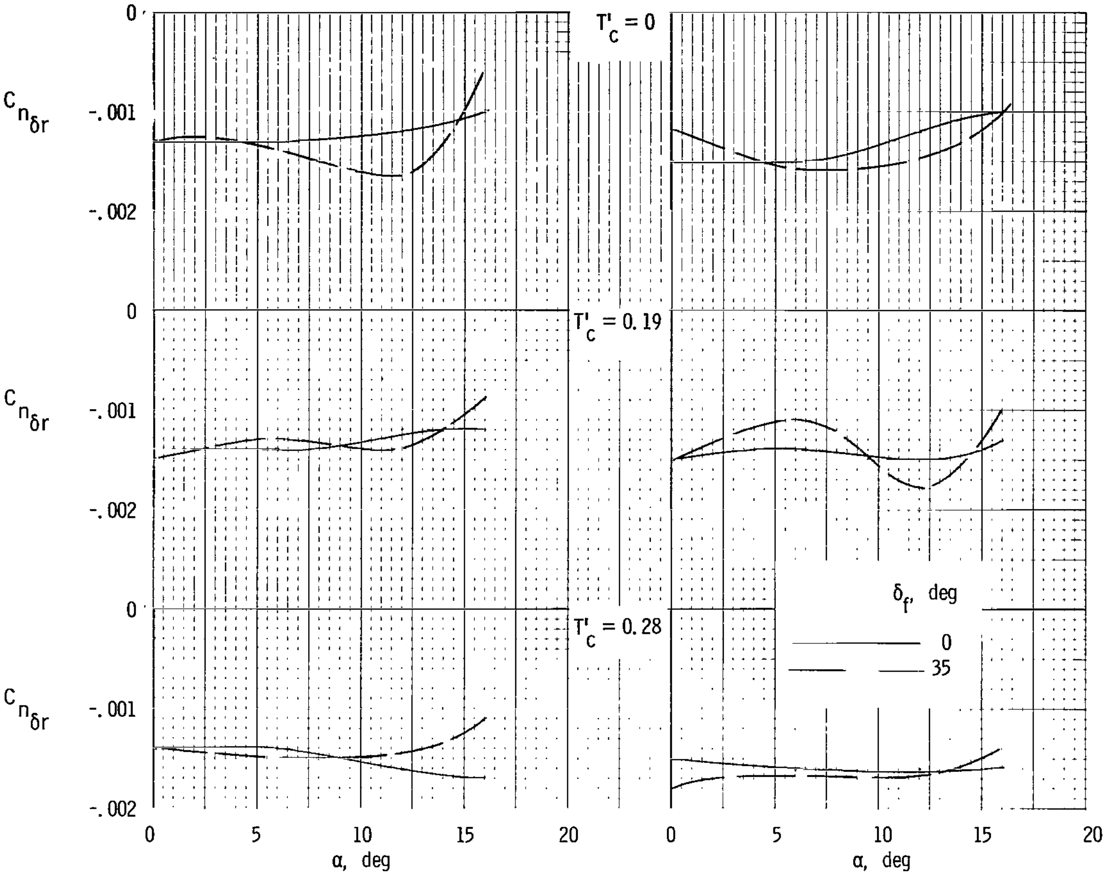

(d) β = 4°.

(e) β = 8°.

Figure 71.- Concluded.

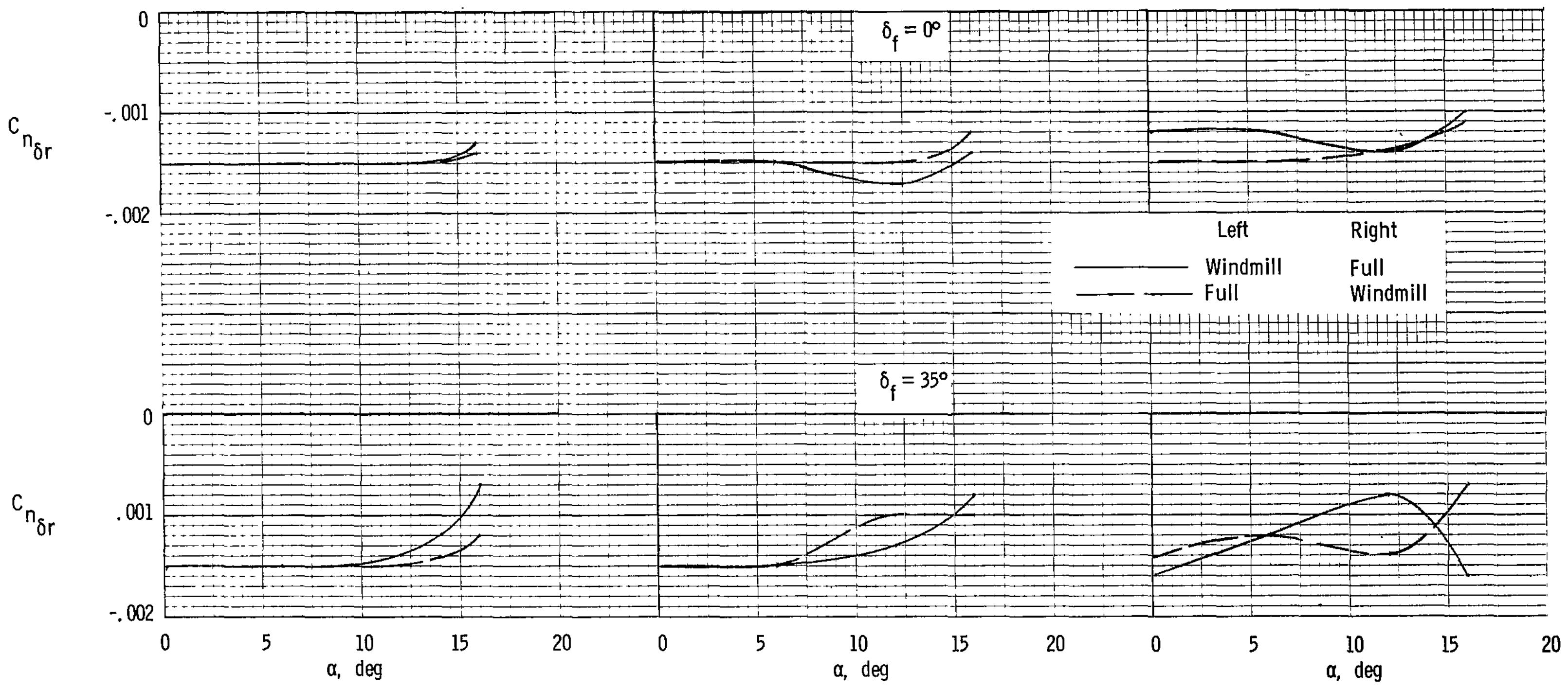

(a) $\beta = -8^0$.

(b) $\beta = 0^0$.

(c) $\beta = 8^0$.

Figure 72.- Variation of rudder effectiveness with angle of attack for asymmetric power.

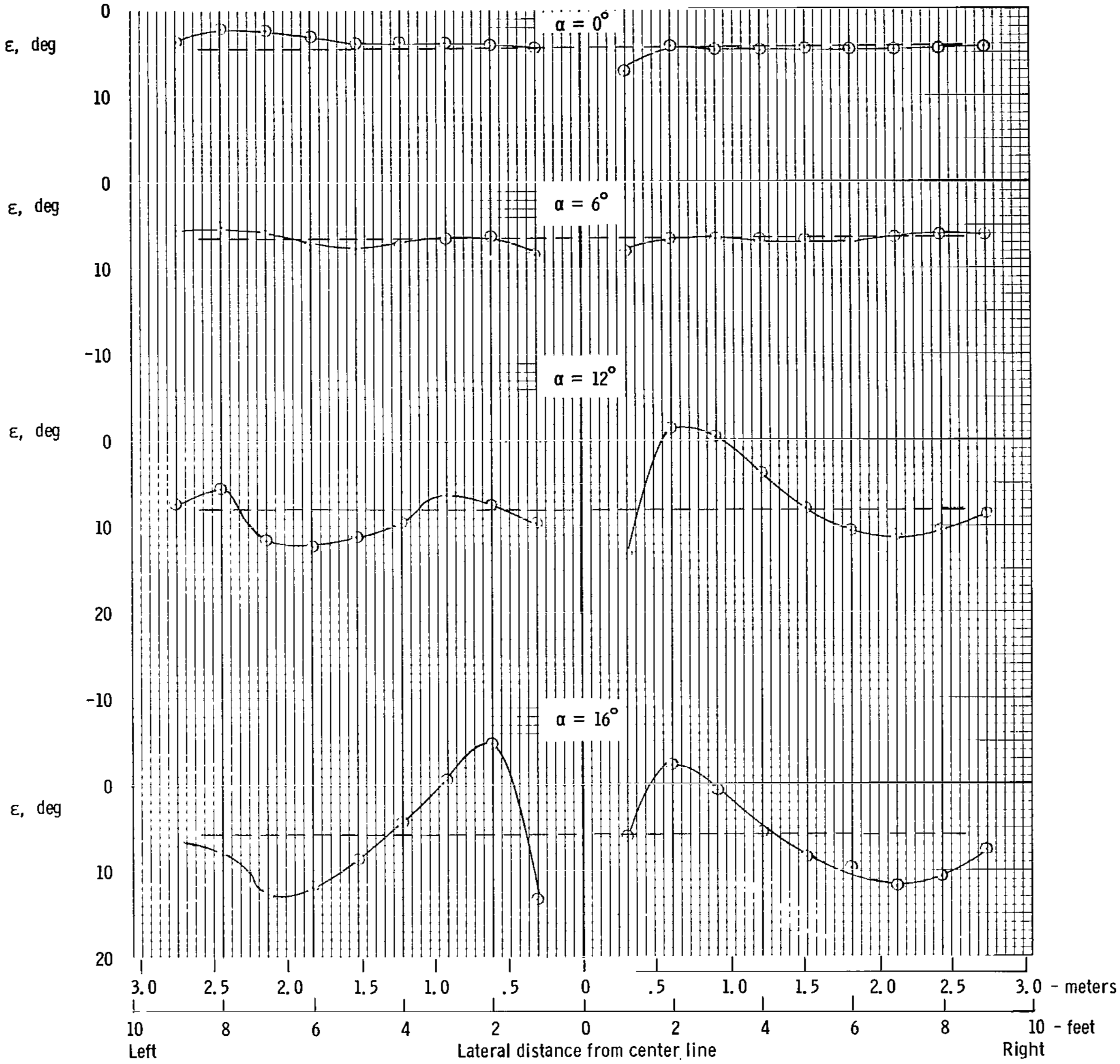

(a) $T'_c = 0$.

Figure 73.- Distribution of downwash across span of horizontal-tail surface. $\delta_f = 0^{\circ}$. Dashed lines are averages integrated over horizontal-tail span.

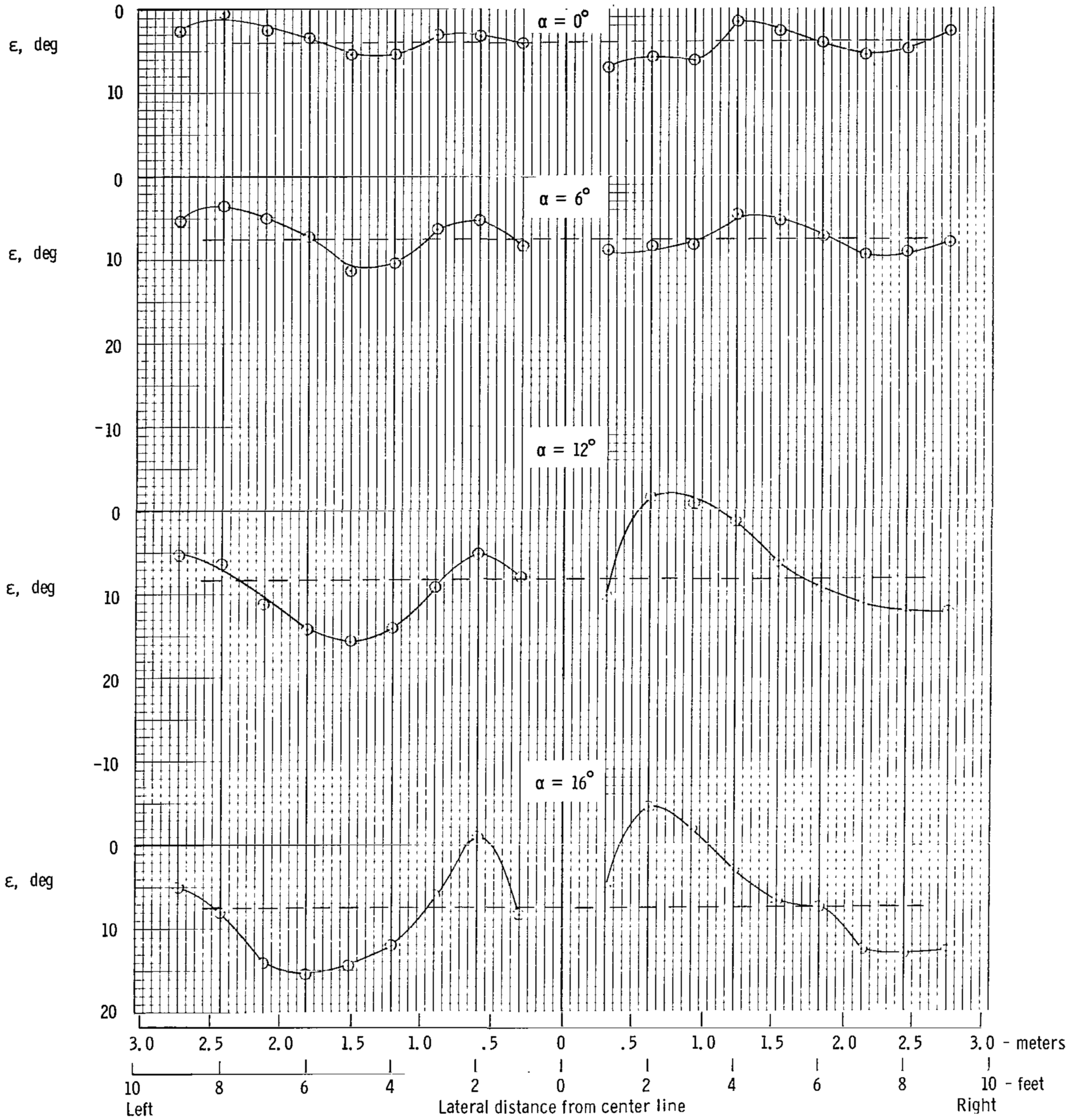

(b) $T_C' = 0.19$.

Figure 73.- Continued.

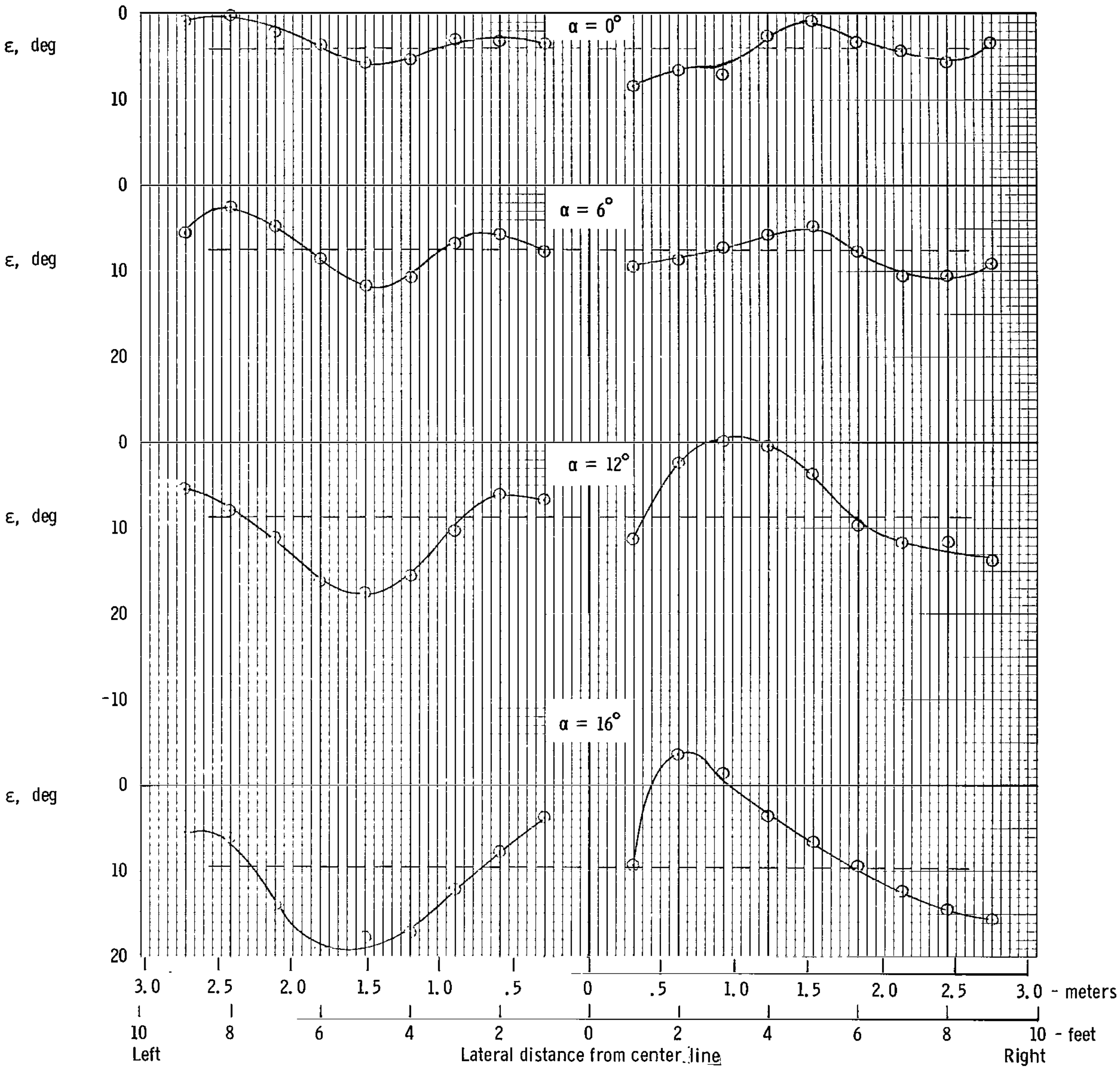

(c) $T_c' = 0.28$.

Figure 73.- Concluded.

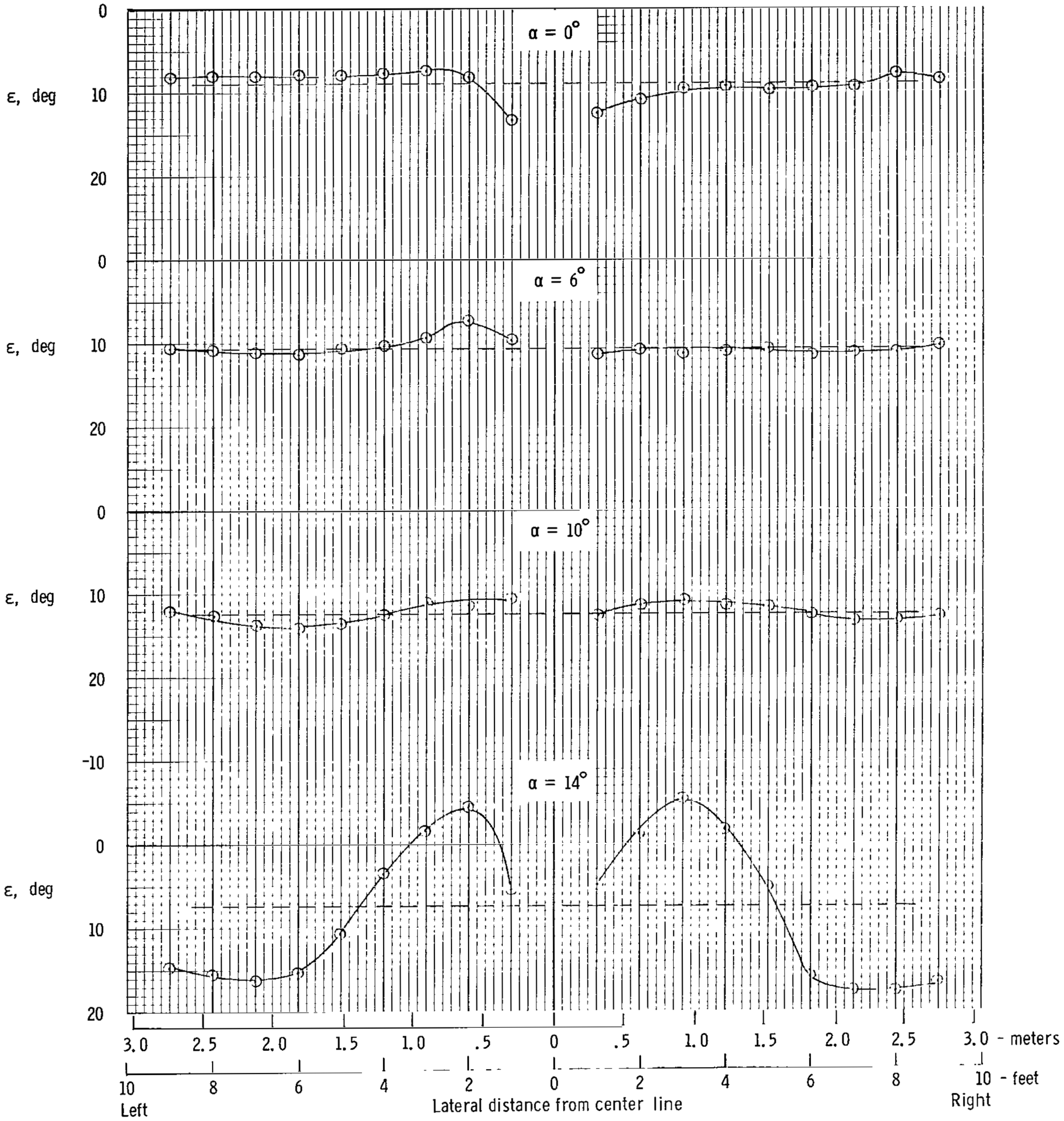

(a) $T_c' = 0$.

Figure 74.- Distribution of downwash across span of horizontal-tail surface. $\delta_f = 35^\circ$. Dashed lines are averages integrated over horizontal-tail span.

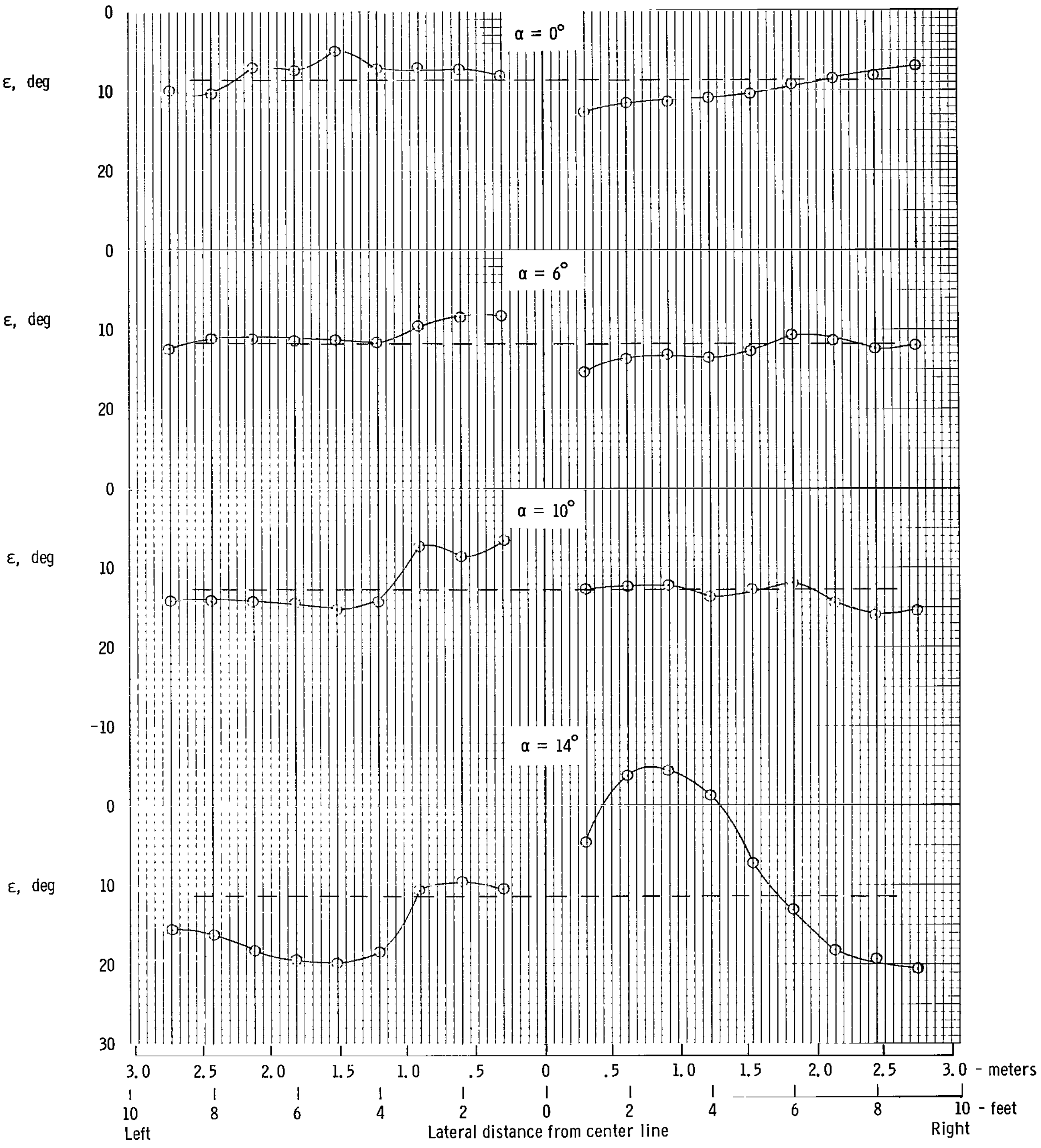

(b) $T_c' = 0.19$.

Figure 74.- Continued.

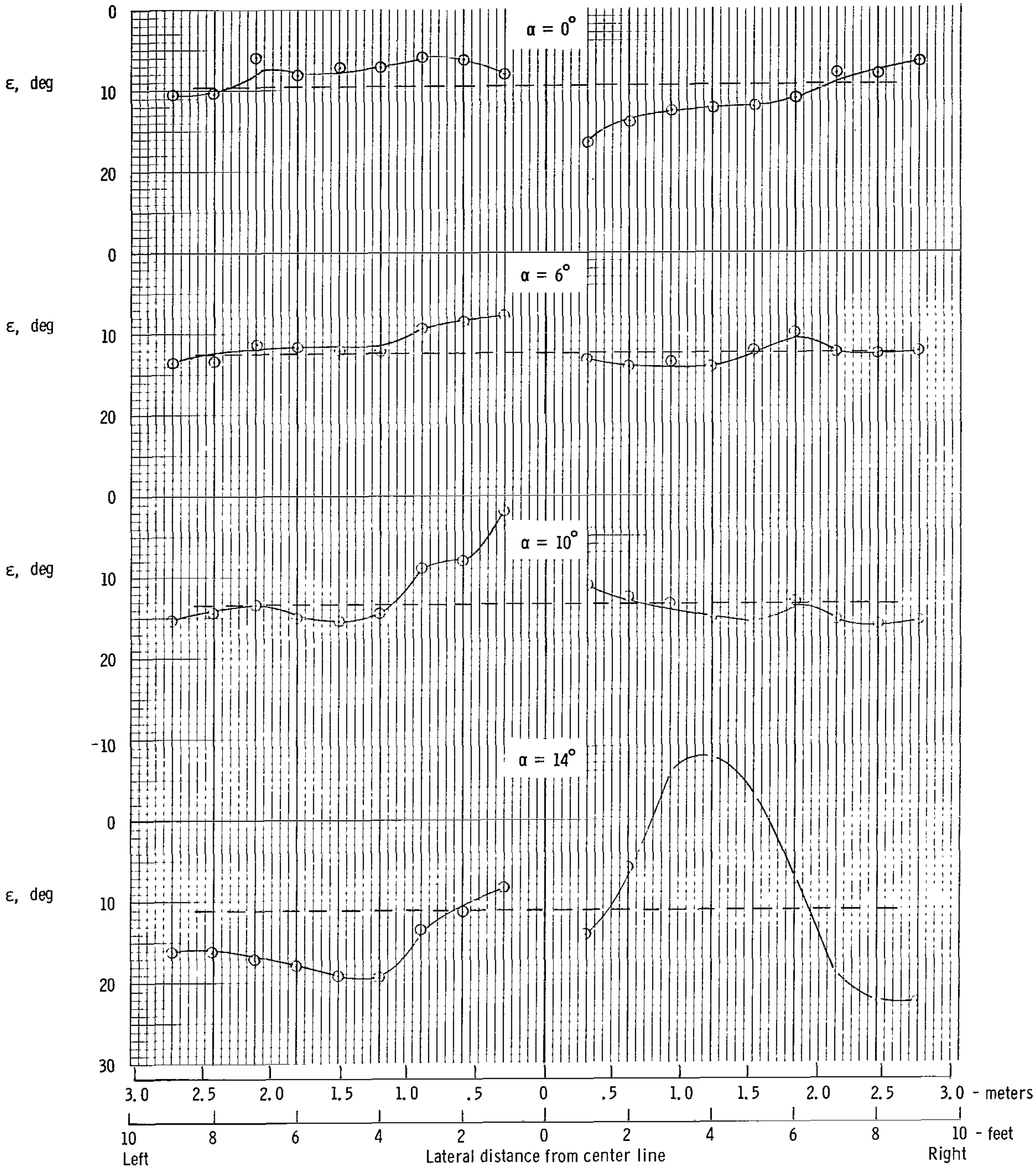

(c) $T_c' = 0.28$.

Figure 74.- Concluded.

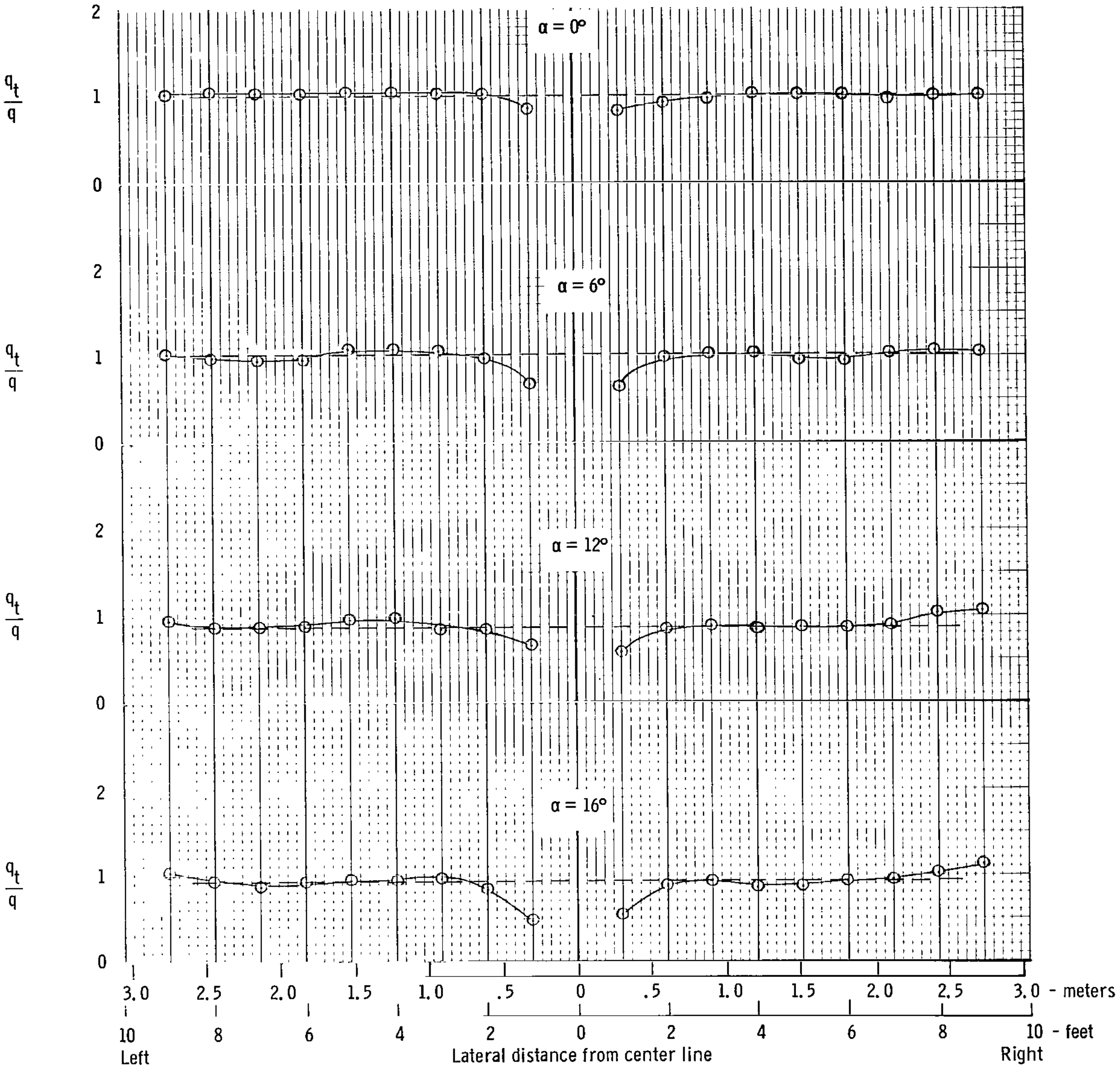

(a) $T'_c = 0$.

Figure 75.- Distribution of dynamic pressure across span of horizontal-tail surface. $\delta_f = 0^0$. Dashed lines are averages integrated over horizontal-tail span.

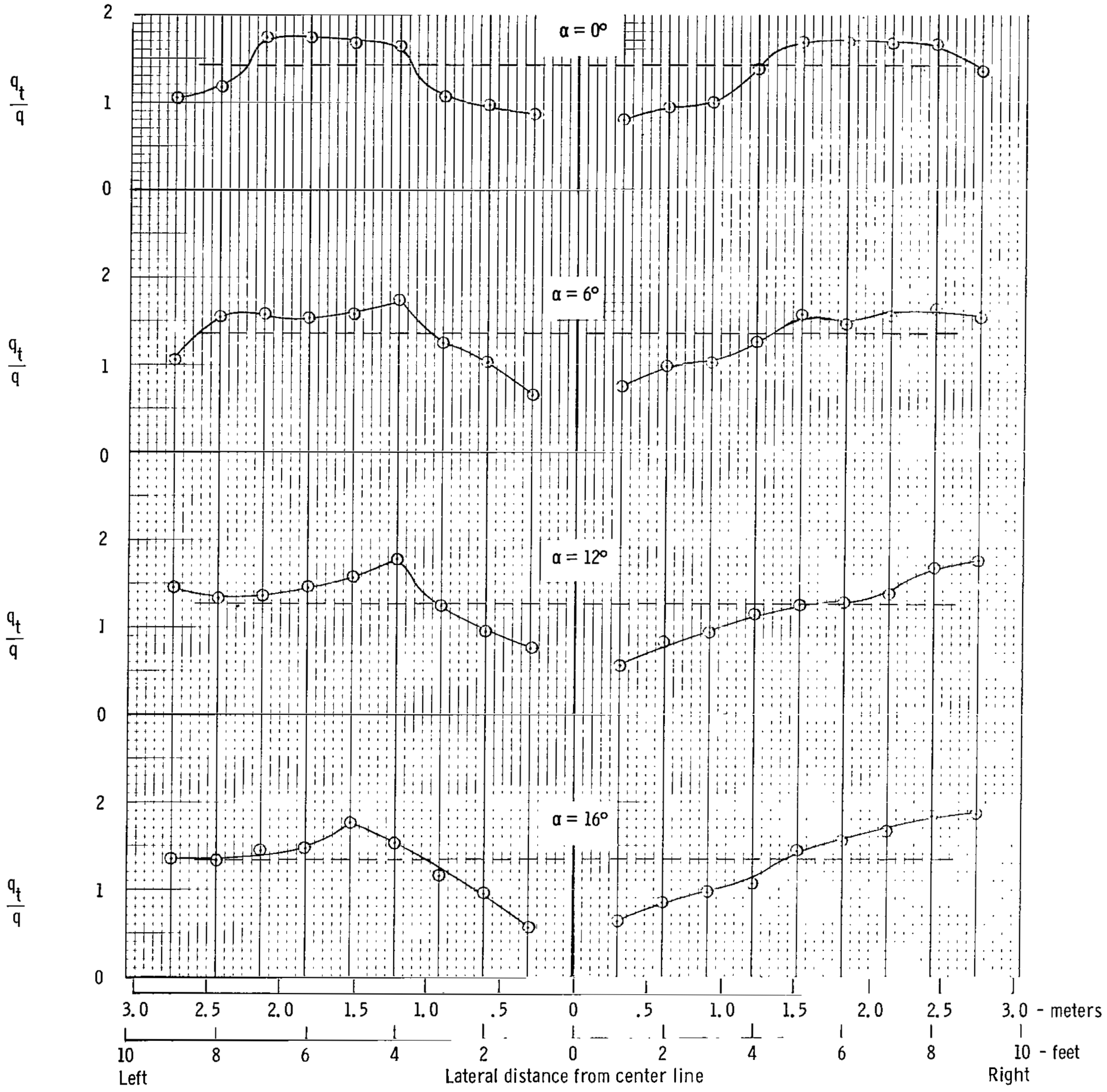

(b) $T_c' = 0.19$.

Figure 75.- Continued.

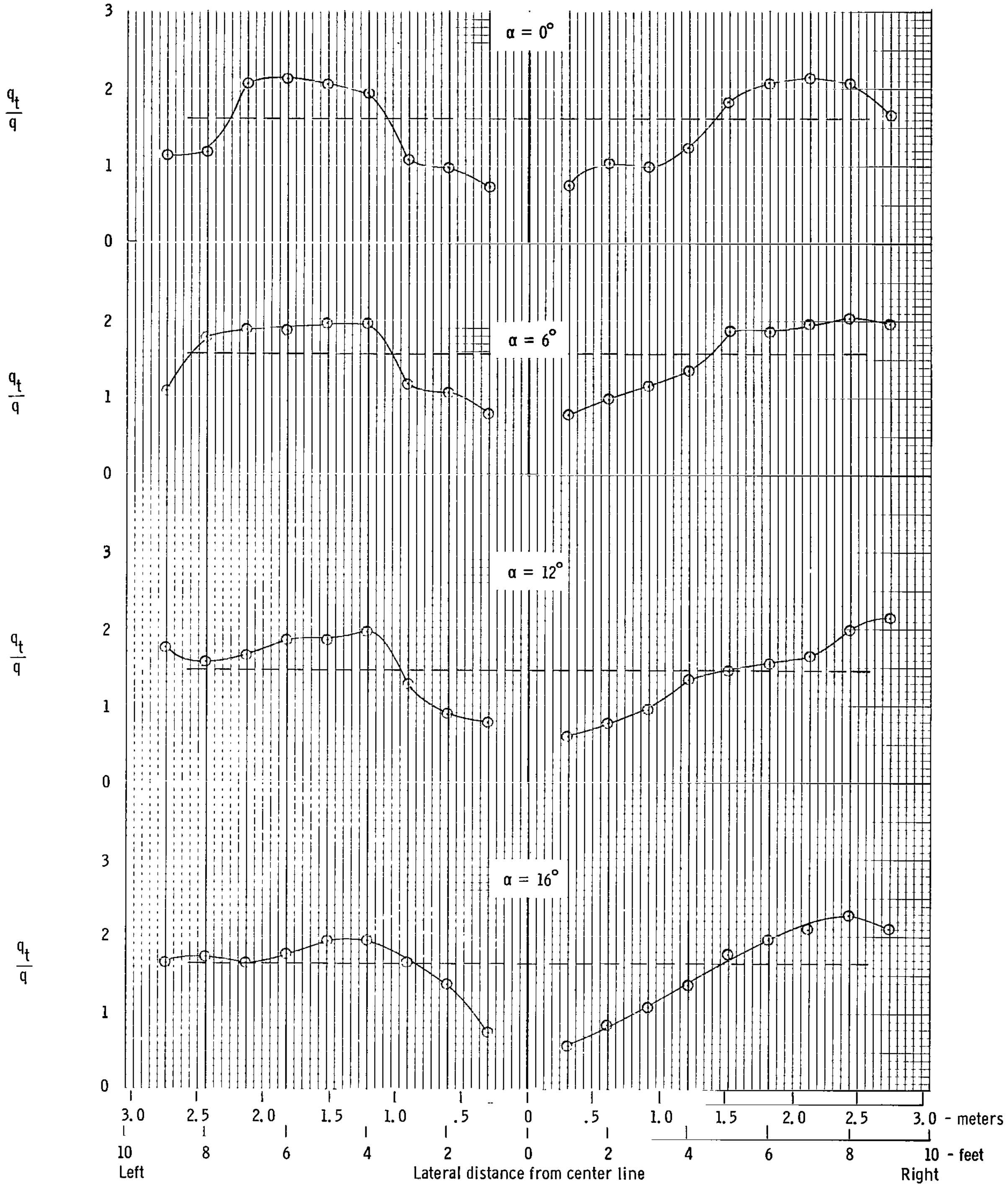

(c) $T_c' = 0.28$.

Figure 75.- Concluded.

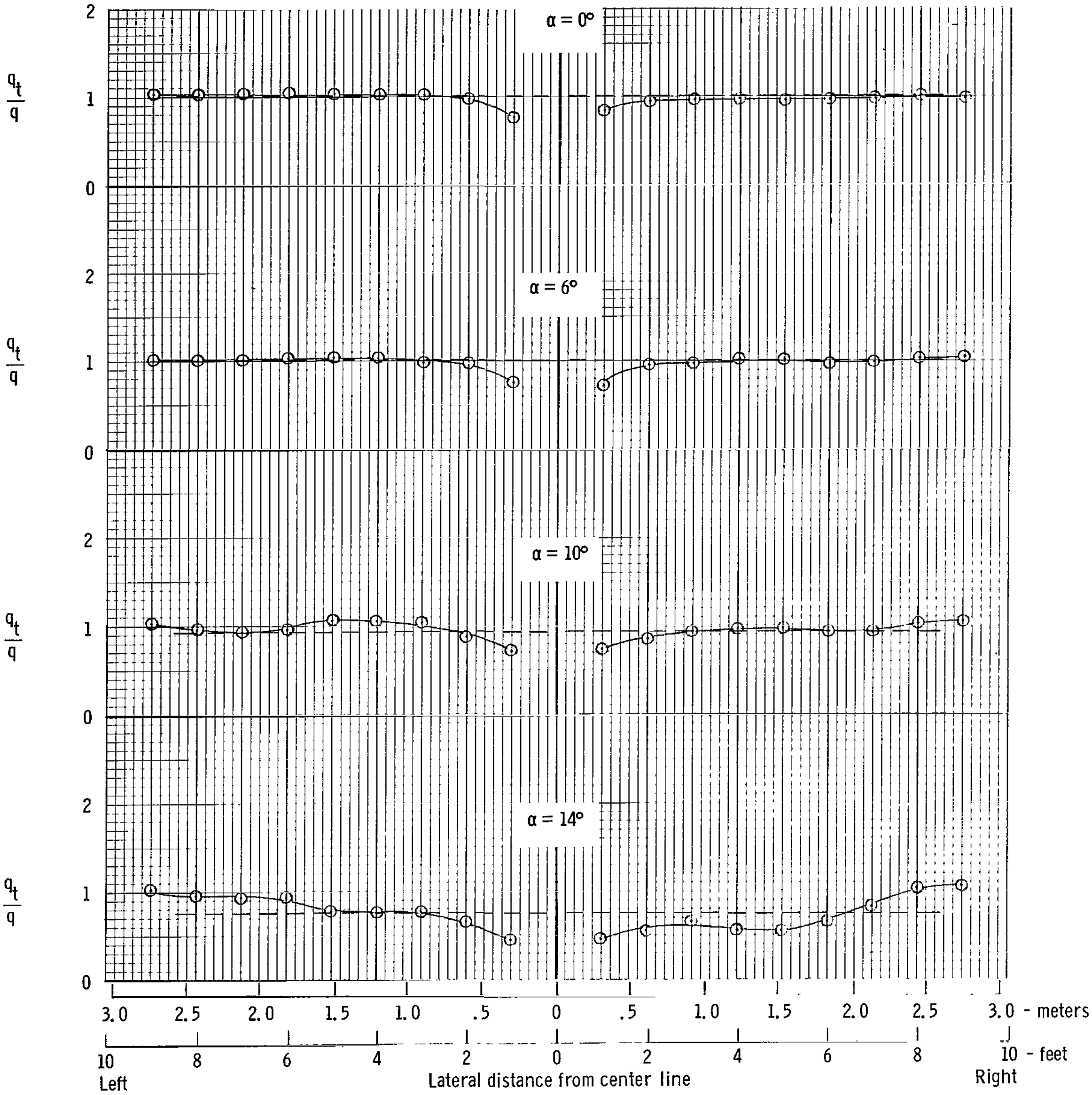

(a) $T_c' = 0$.

Figure 76.- Distribution of dynamic pressure across span of horizontal-tail surface. $\delta_f = 35^0$. Dashed lines are averages integrated over horizontal-tail span.

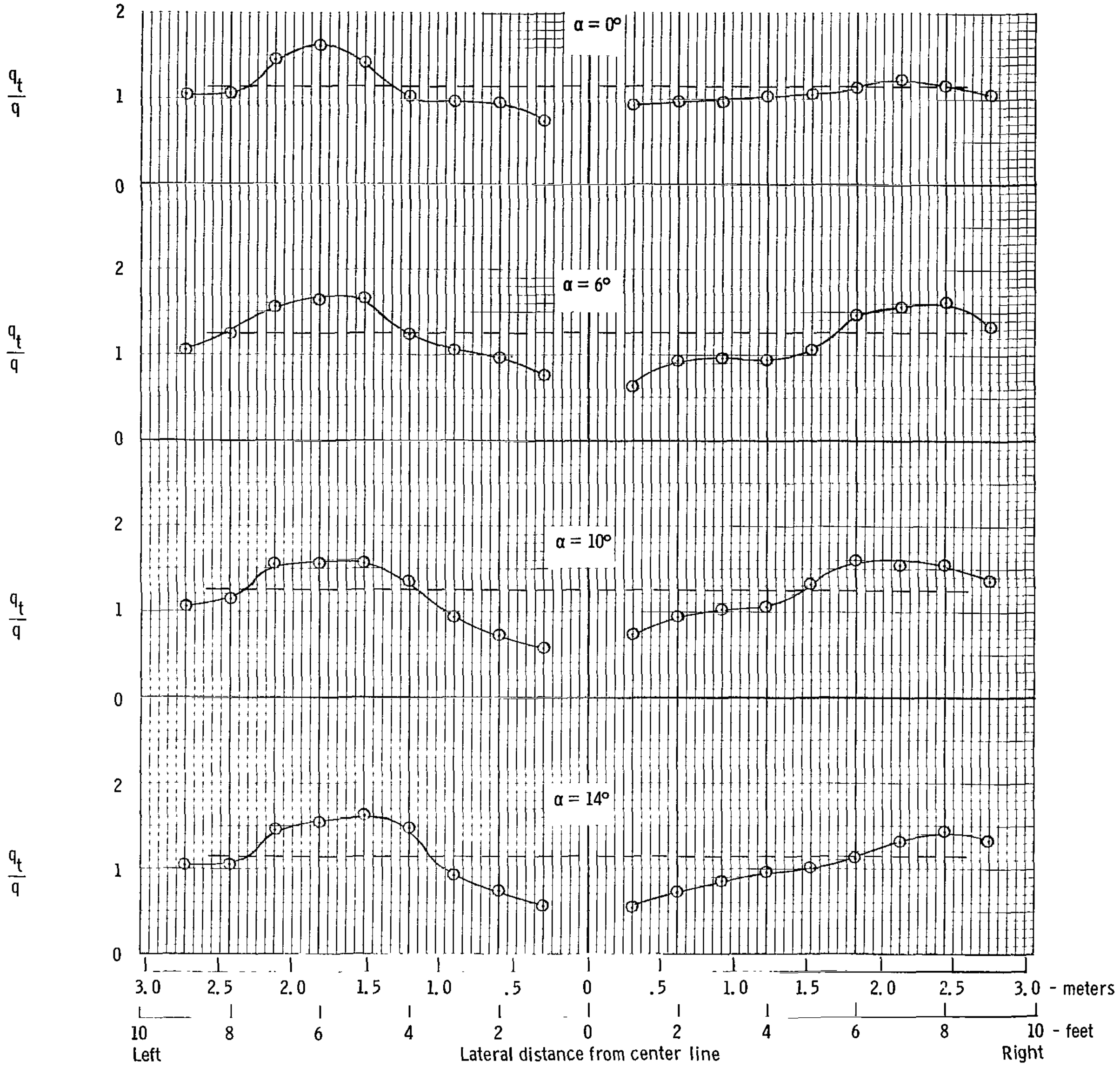

(b) $T_c' = 0.19$.

Figure 76.- Continued.

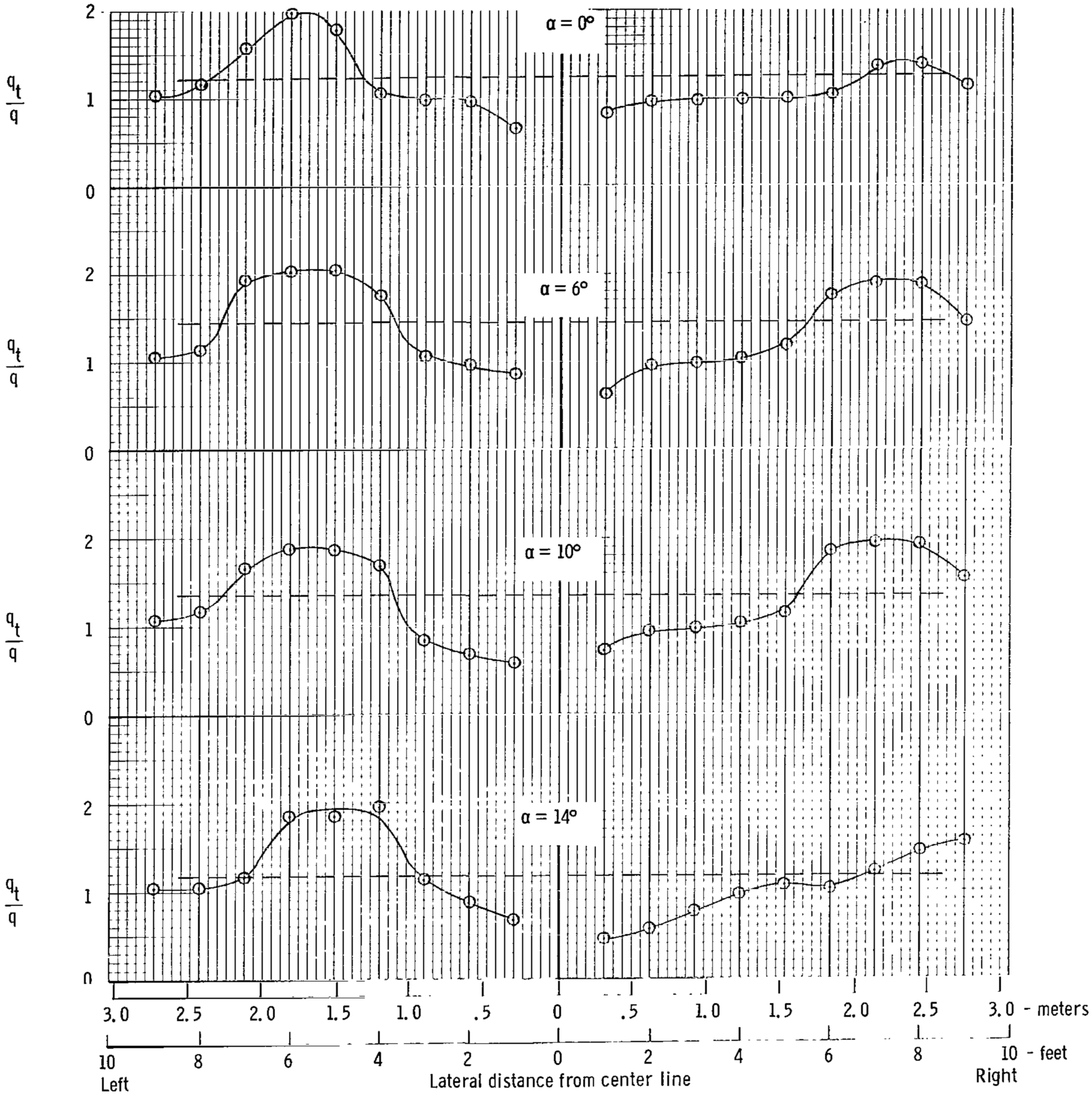

(c) $T_c' = 0.28$.

Figure 76.- Concluded.

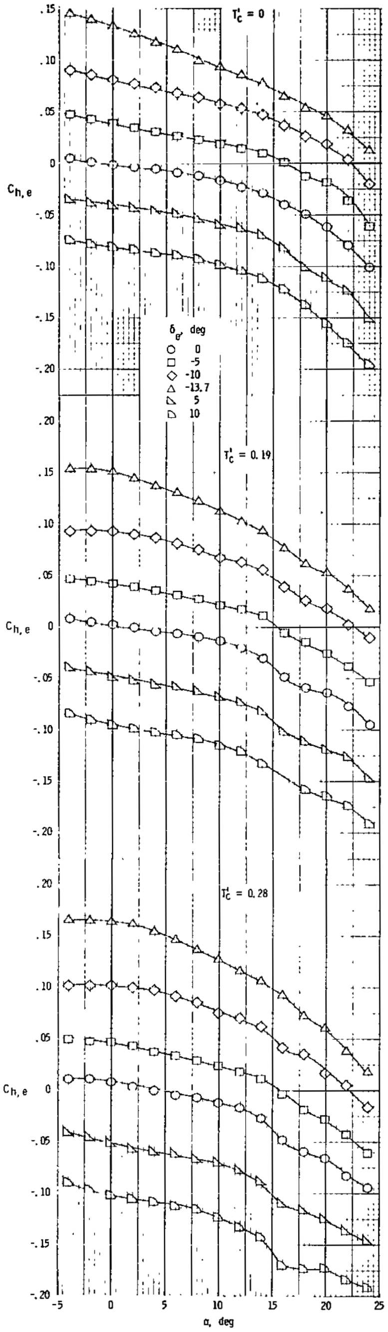

(a) $\delta_f = 0^o$.

Figure 77.- Variation of elevator hinge-moment coefficient with angle of attack for several power and flap settings.

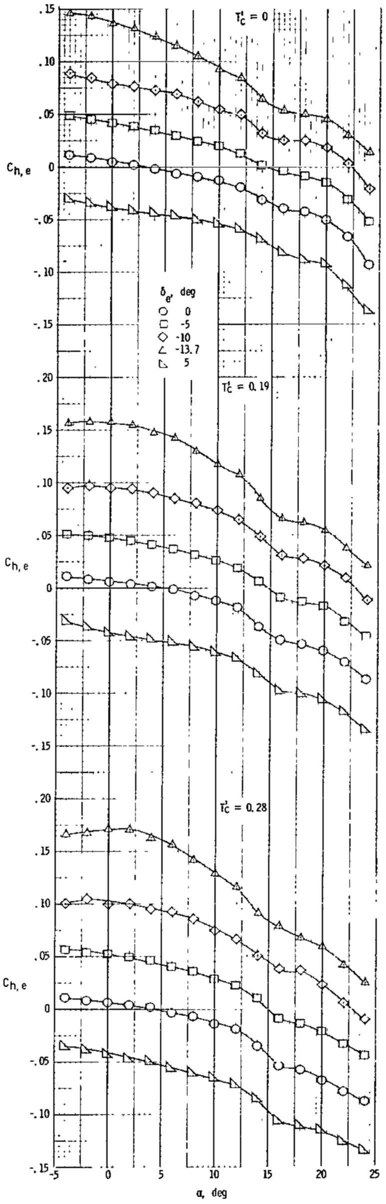

(b) $\delta_f = 15^0$.

Figure 77.- Continued.

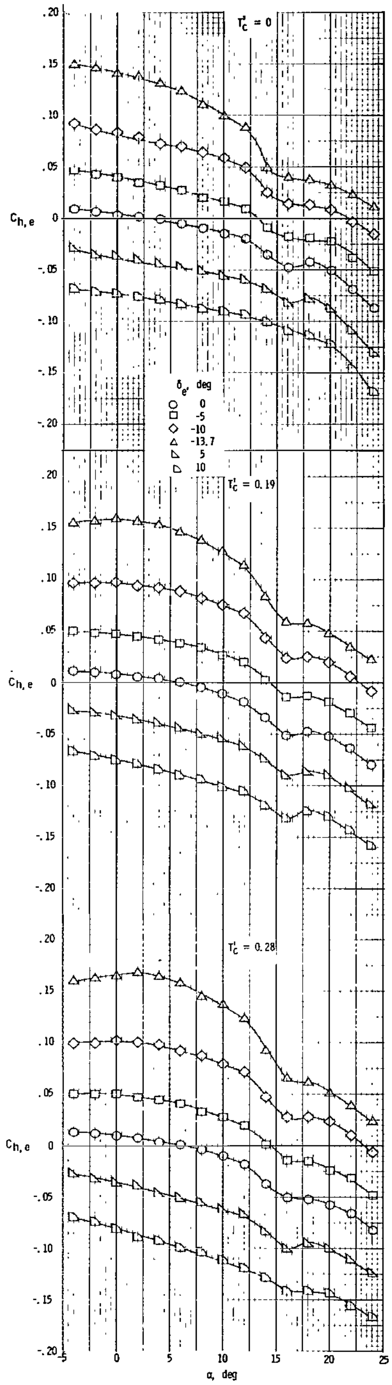

(c) $\delta_f = 35^0$.

Figure 77.- Concluded.

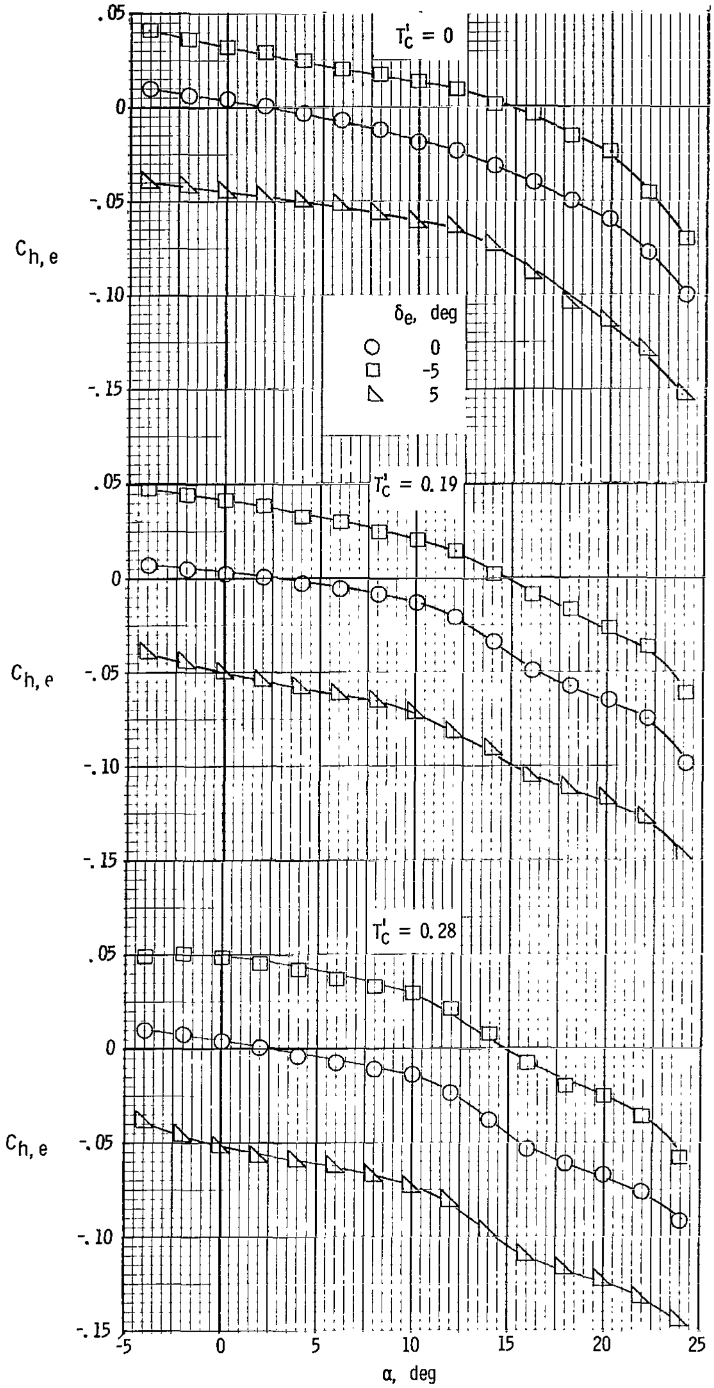

Figure 78.- Variation of elevator hinge-moment coefficient with angle of attack for the short nacelle. $\delta_f = 0^0$; $\beta = 0^0$.

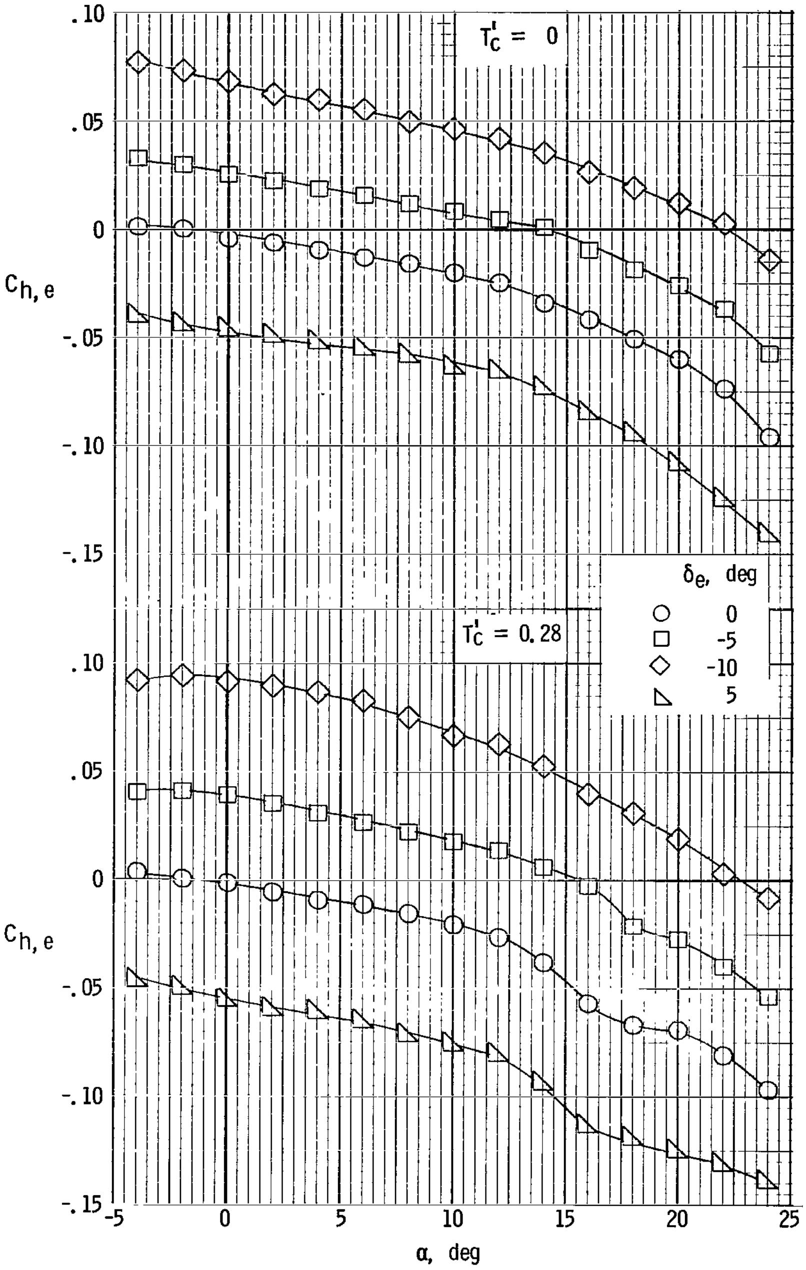

(a) $\delta_f = 0^o$.

Figure 79.- Variation of elevator hinge-moment coefficient with angle of attack with smooth ice on tail only.

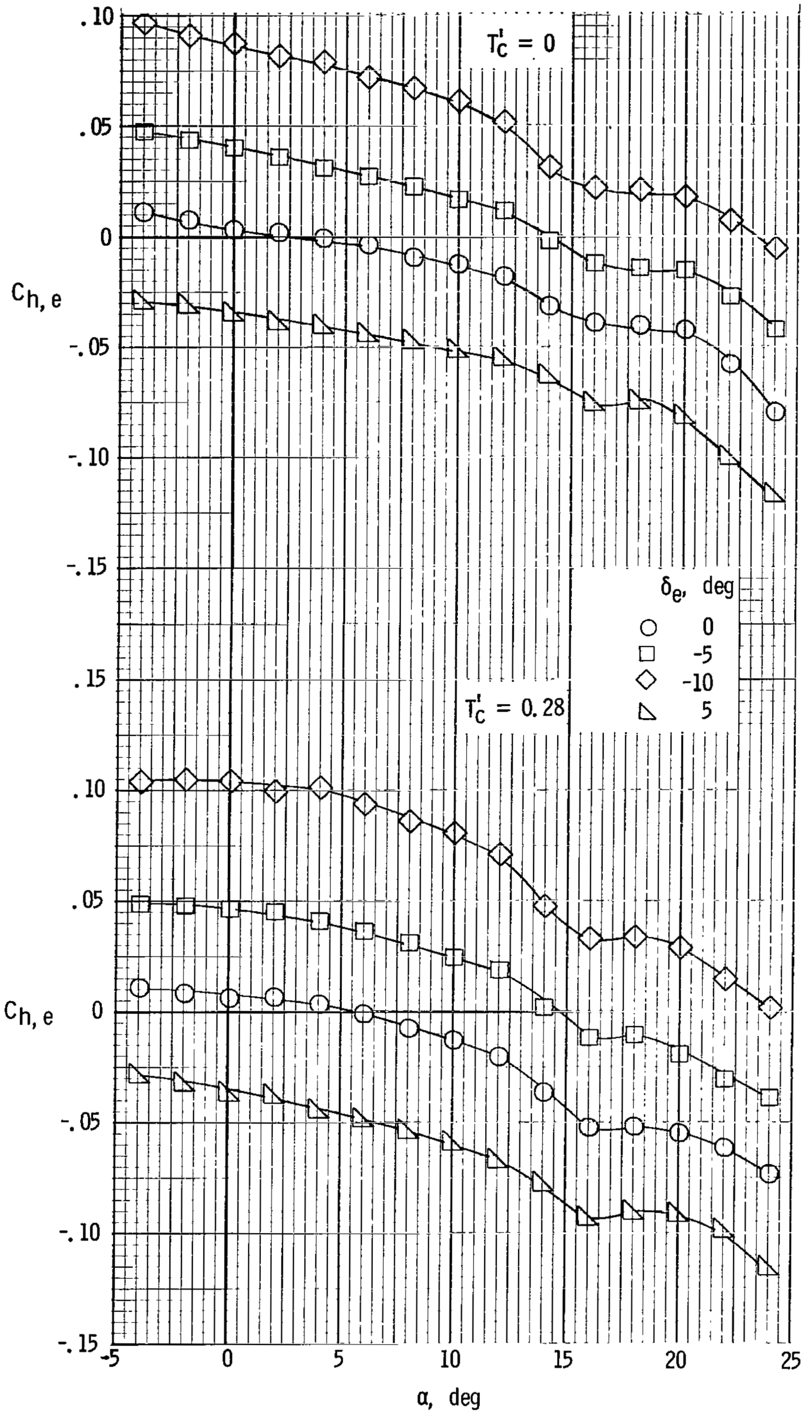

(b) $\delta_f = 35^0$

Figure 79.- Concluded.

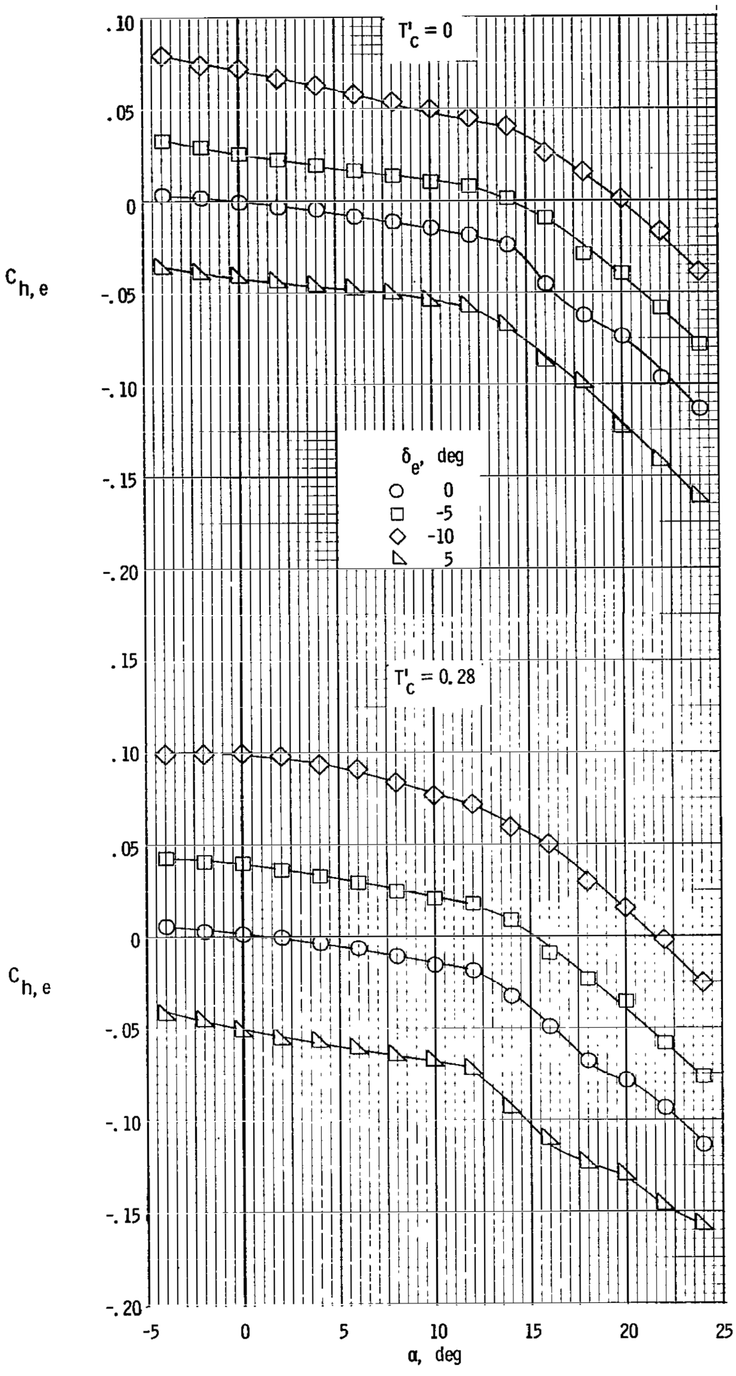

(a) $\delta_f = 0^o$.

Figure 80.- Variation of elevator hinge-moment coefficient with angle of attack with rime ice on tail only.

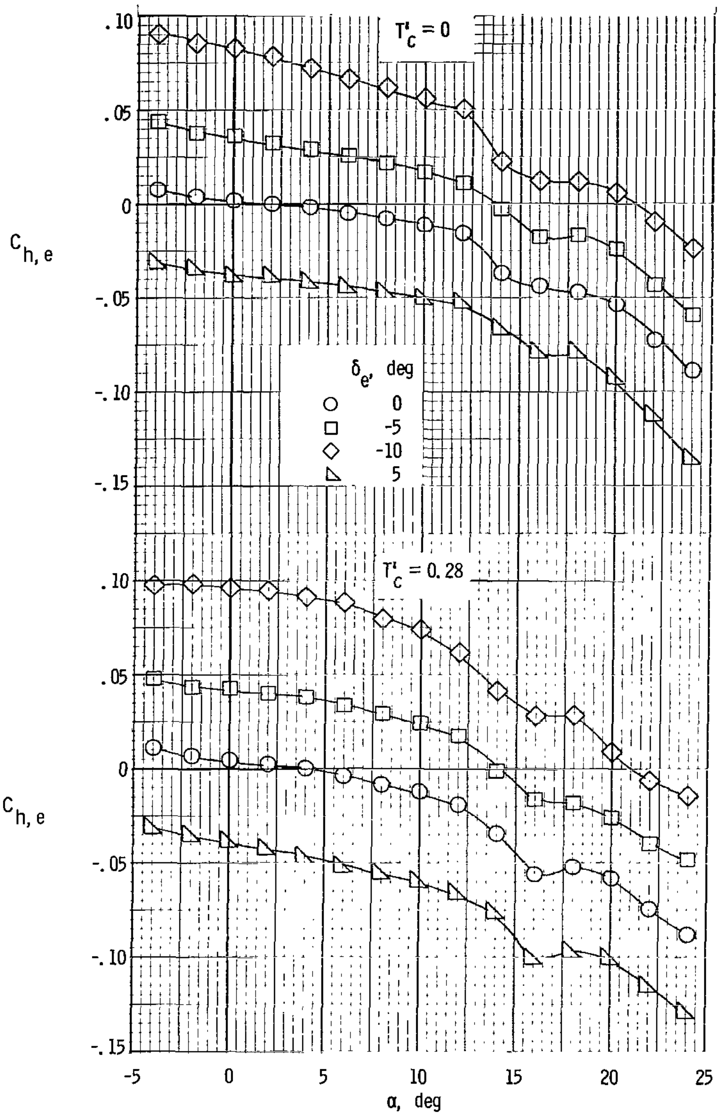

(b) $\delta_f = 35^0$.

Figure 80.- Concluded.

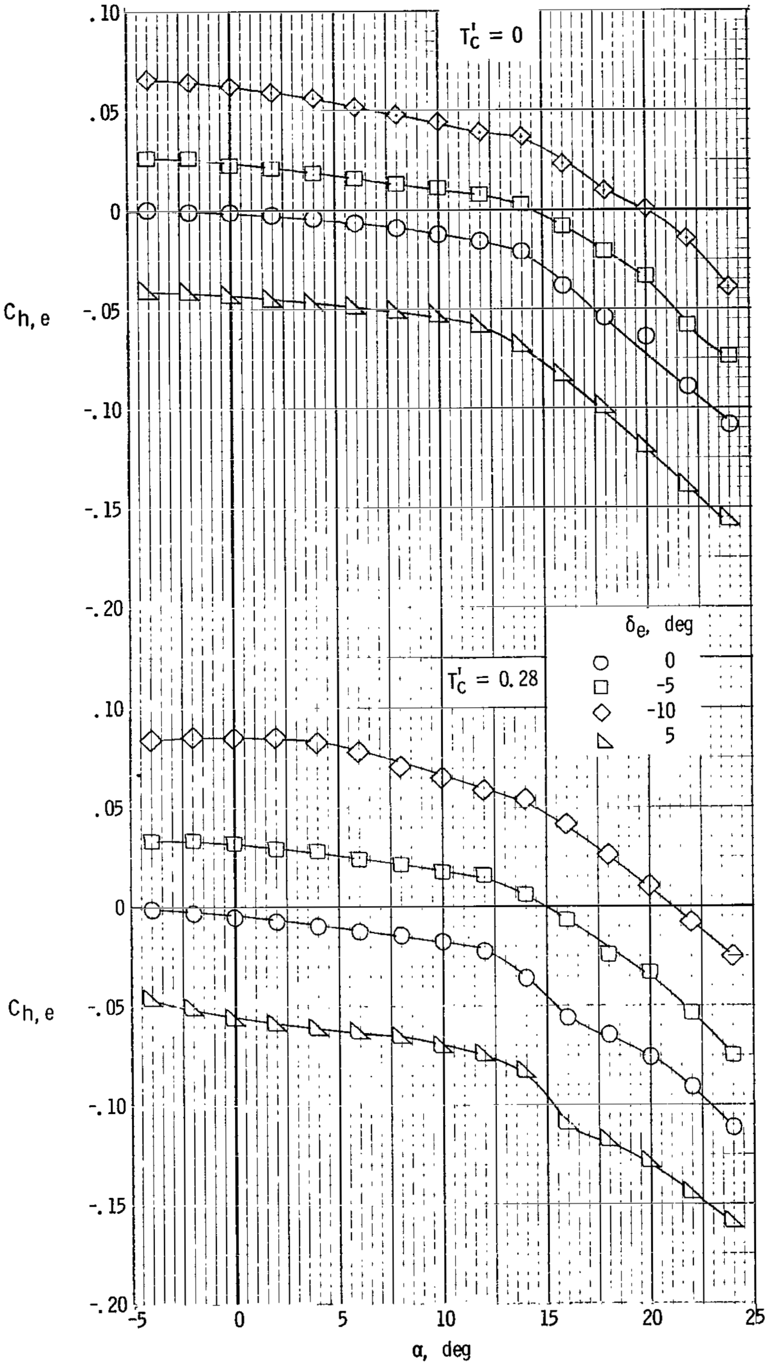

(a) $\delta_f = 0^o$.

Figure 81.- Variation of elevator hinge-moment coefficient with angle of attack with glaze ice on tail only.

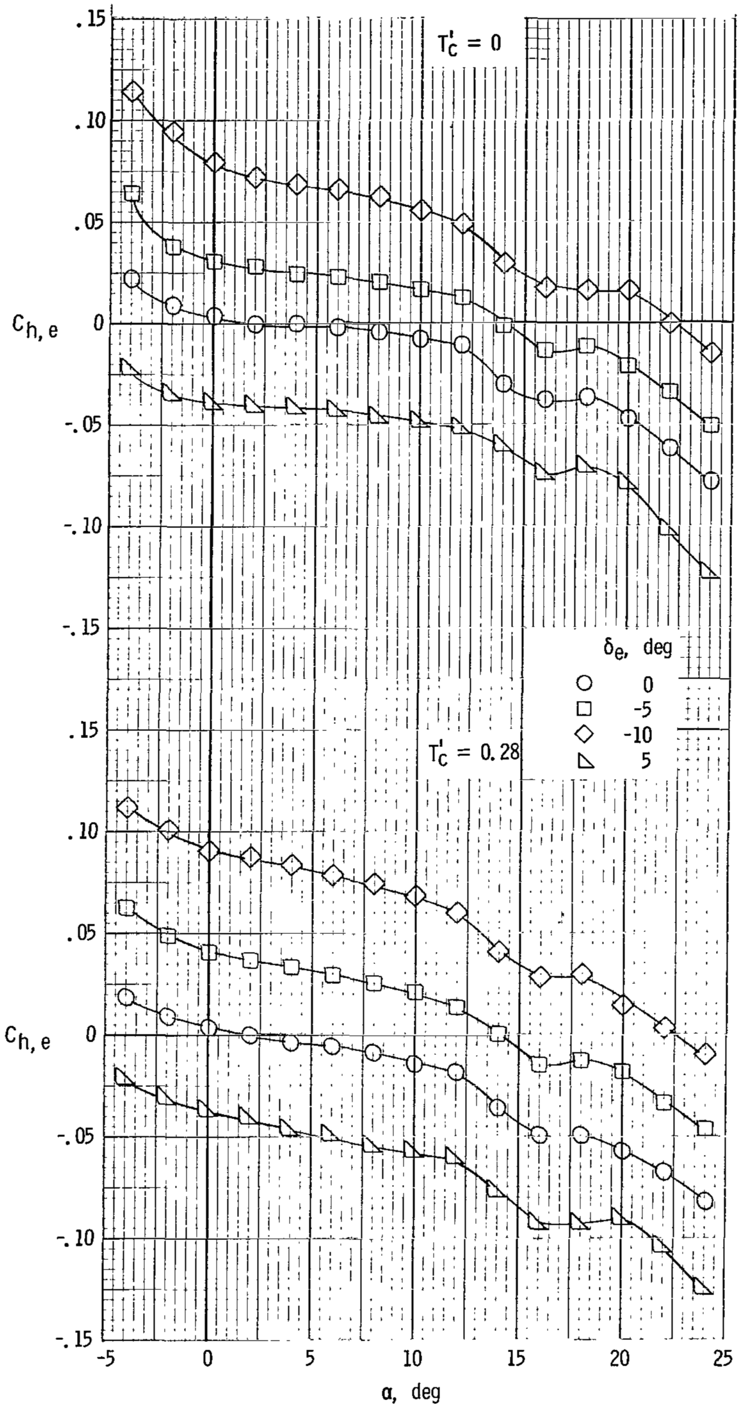

(b) $\delta_f = 35^o$.

Figure 81.- Concluded.

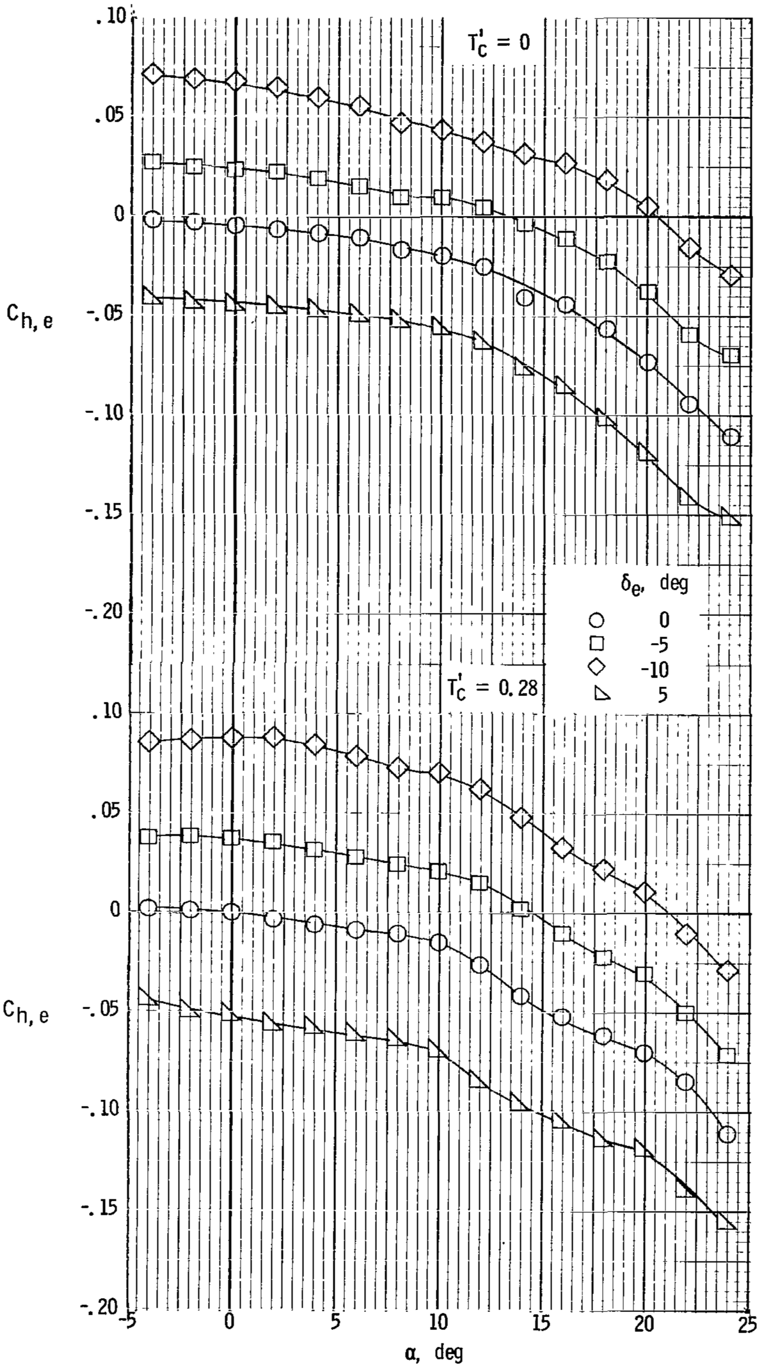

(a) $\delta_f = 0^o$.

Figure 82.- Variation of elevator hinge-moment coefficient with angle of attack with glaze ice on wing and tail.

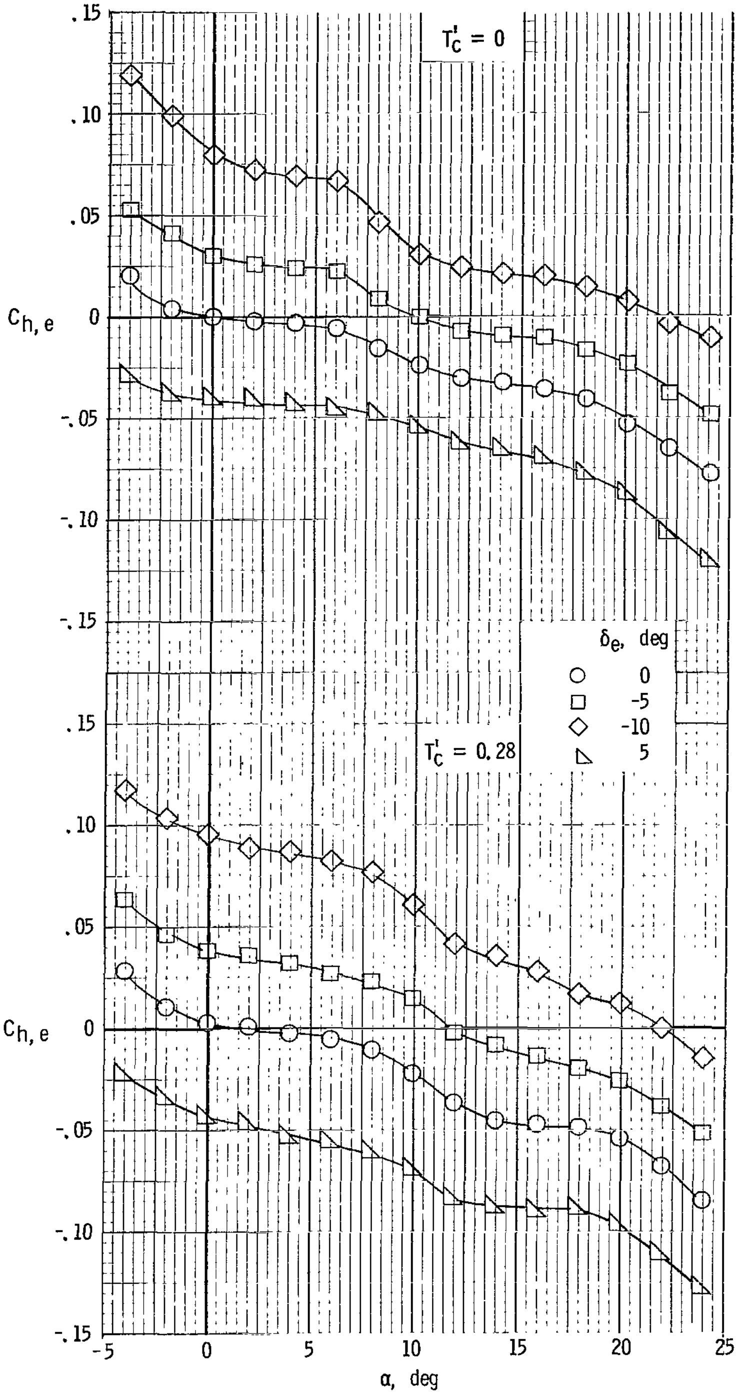

(b) $\delta_f = 35^0$.

Figure 82.- Concluded.

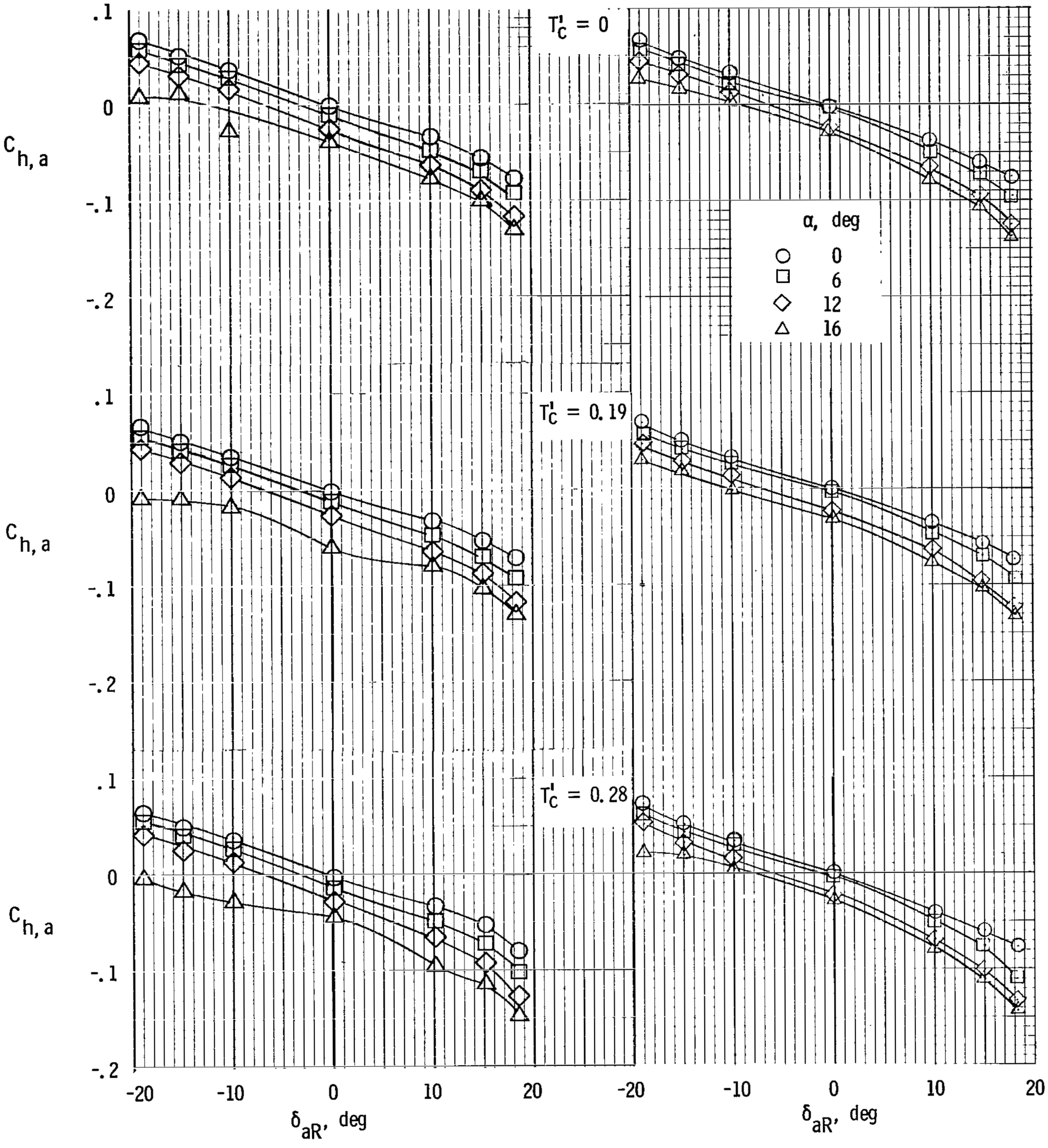

(a) β = 8°.

(b) β = 4°.

Figure 83.- Variation of right aileron hinge-moment coefficient with control deflection. $\delta_f = 0^{\circ}$.

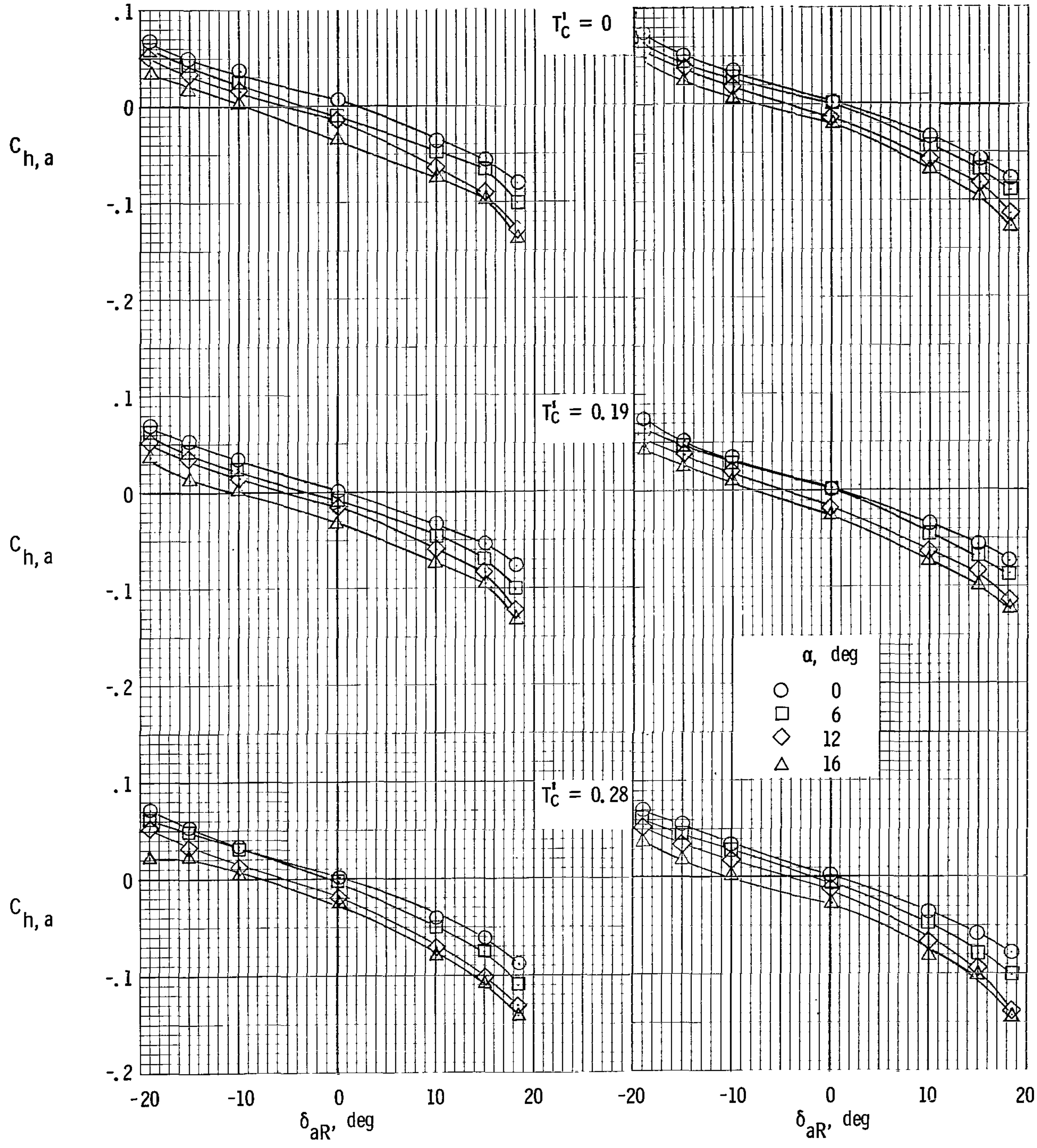

(c) $\beta = 0^0$.

(d) $\beta = -4^0$.

Figure 83.- Continued.

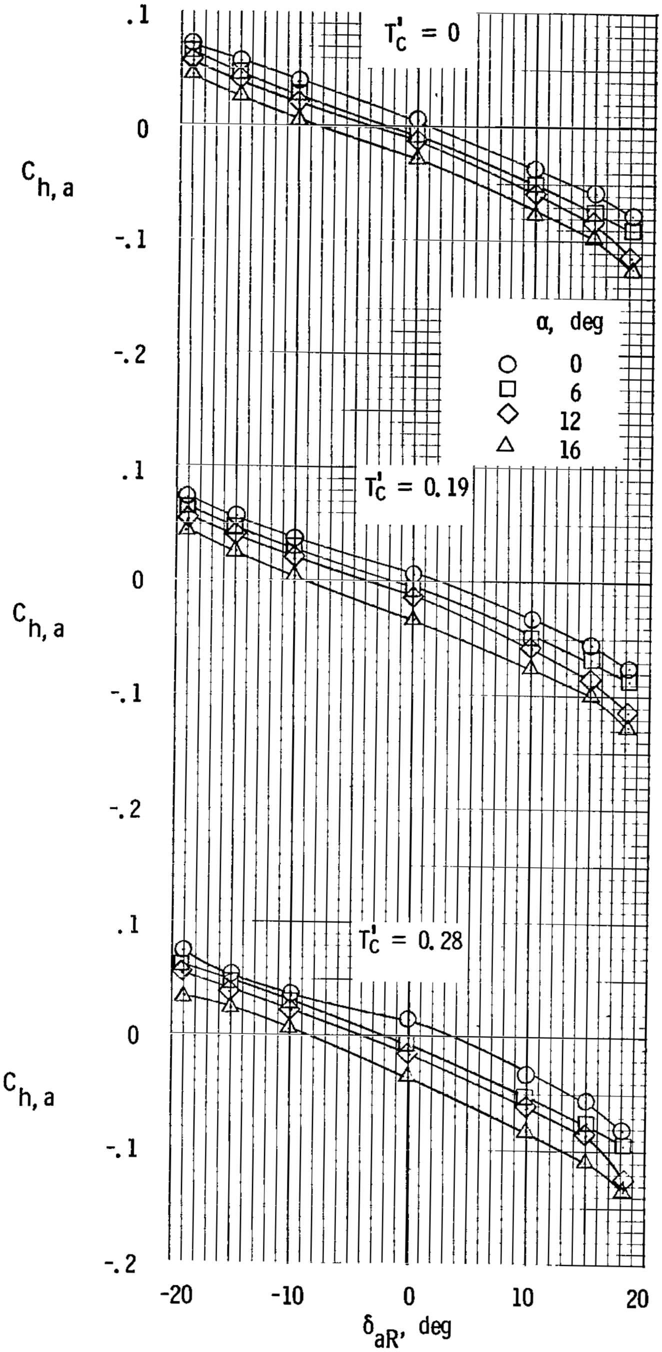

(e) $\beta = -8^{\circ}$.

Figure 83.- Concluded.

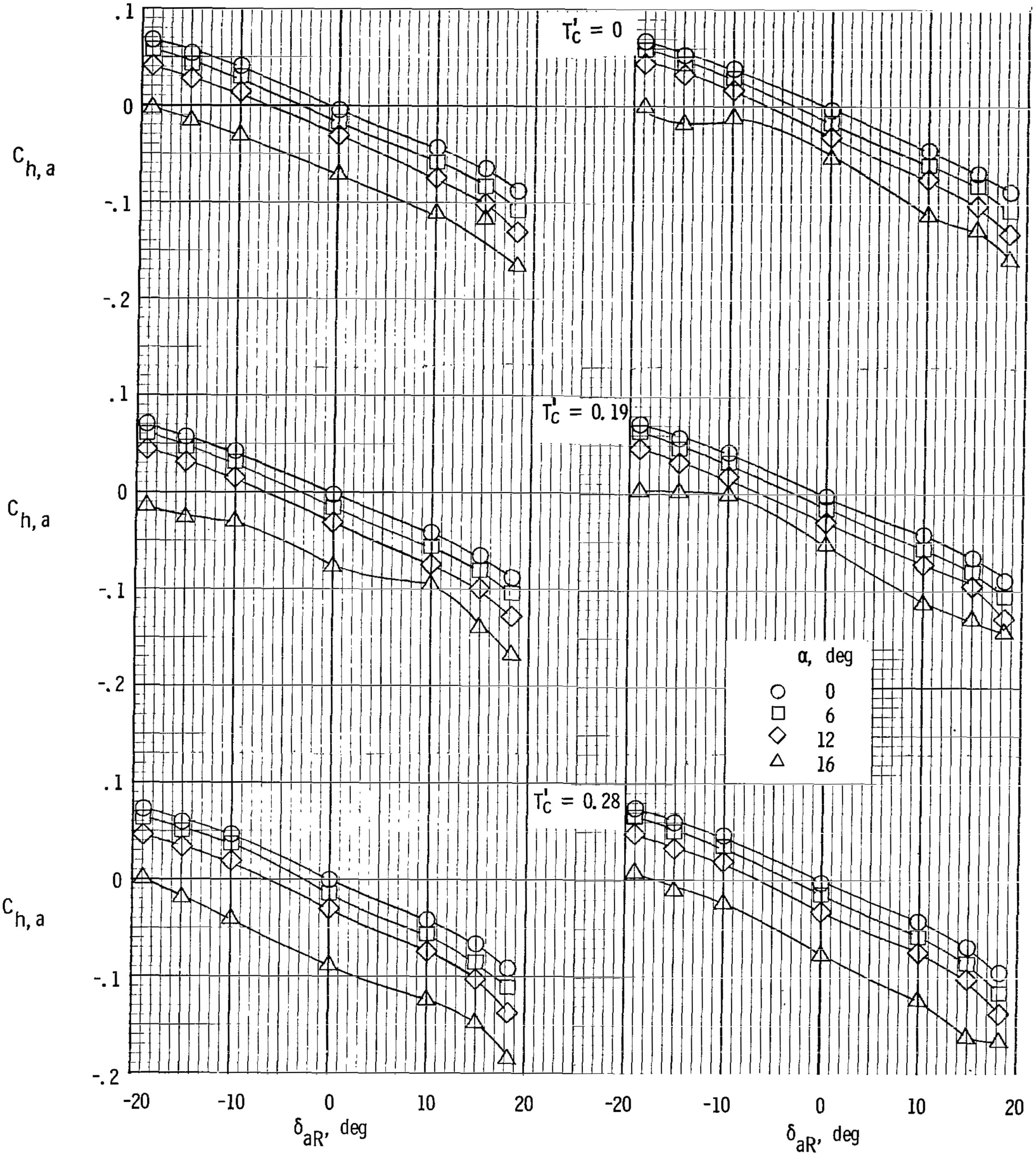

(a) $\beta = 8^0$.

(b) $\beta = 4^0$.

Figure 84.- Variation of right aileron hinge-moment coefficient with control deflection. $\delta_f = 35^0$.

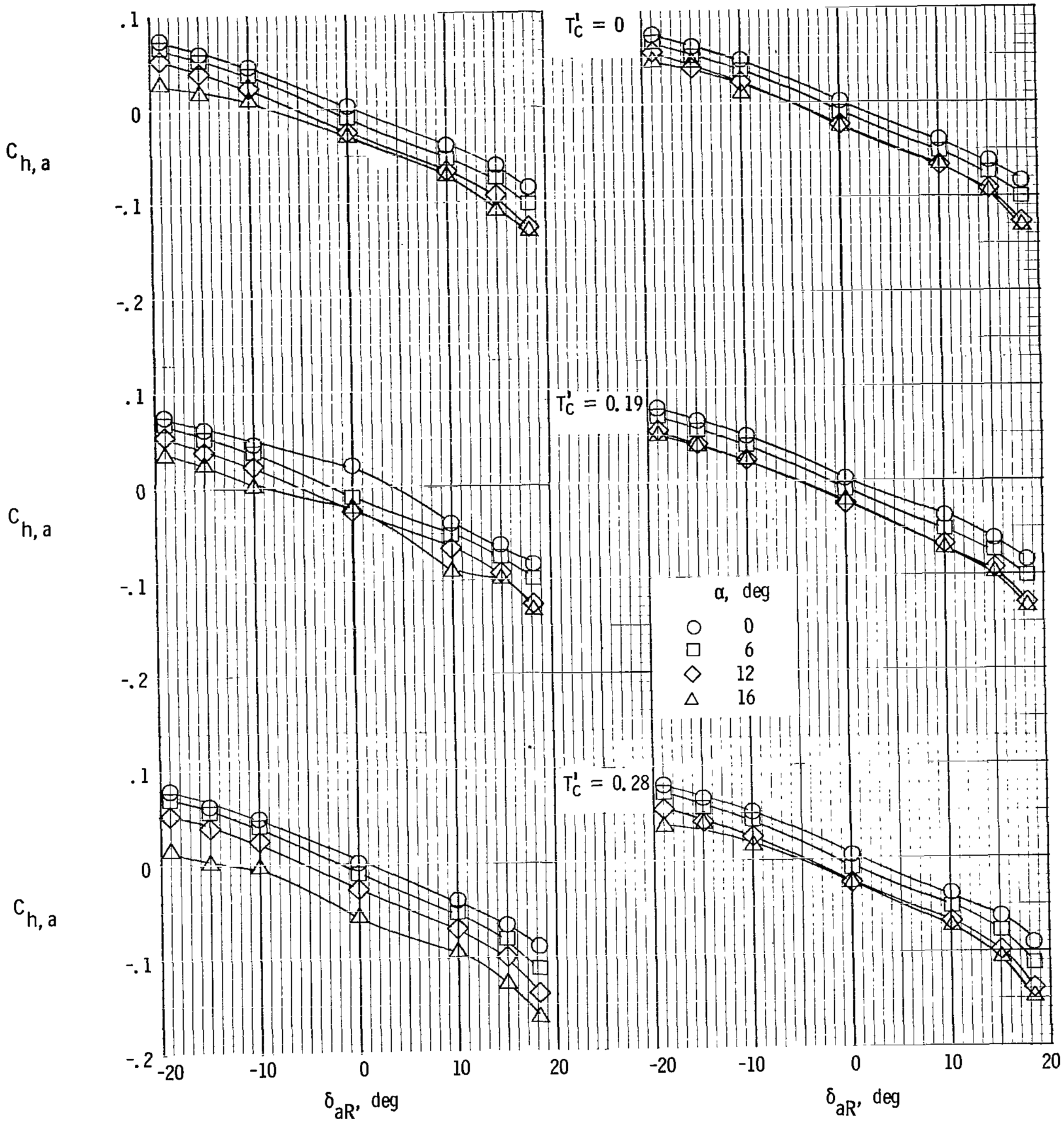

(c) β = 0°.

(d) β = -4°.

Figure 84.- Continued.

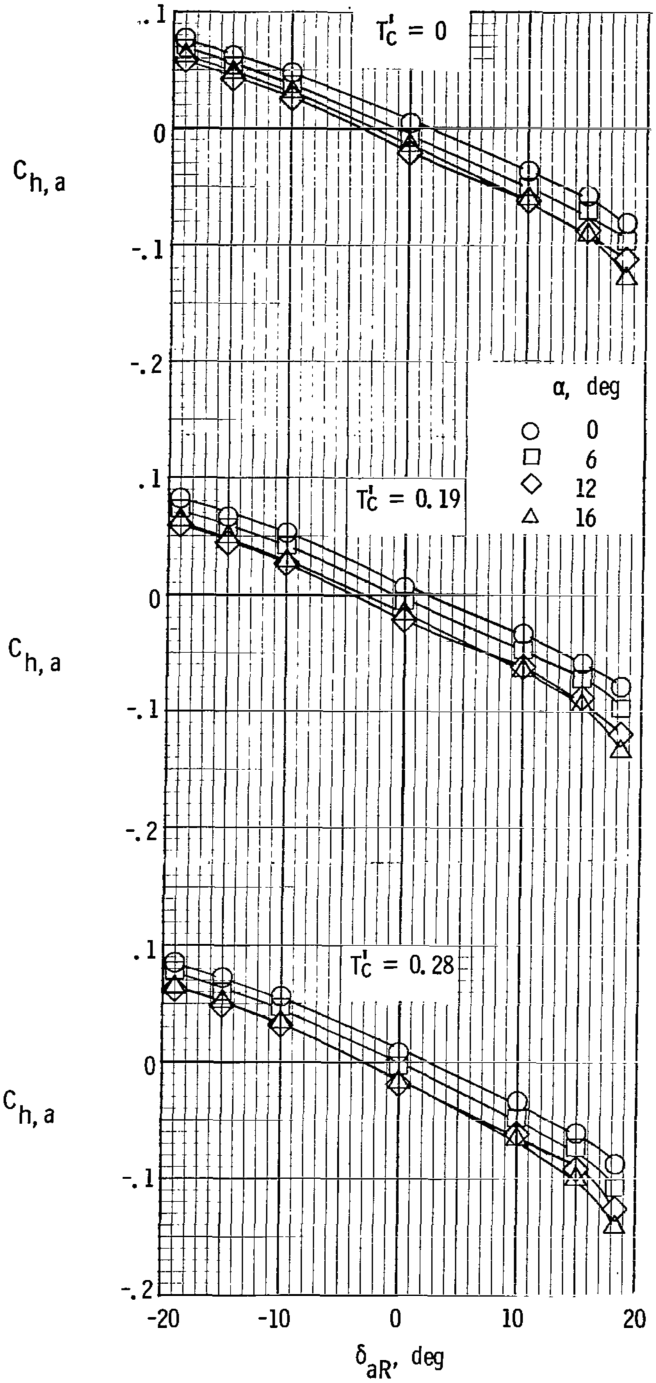

(e) β = -8°.

Figure 84.- Concluded.

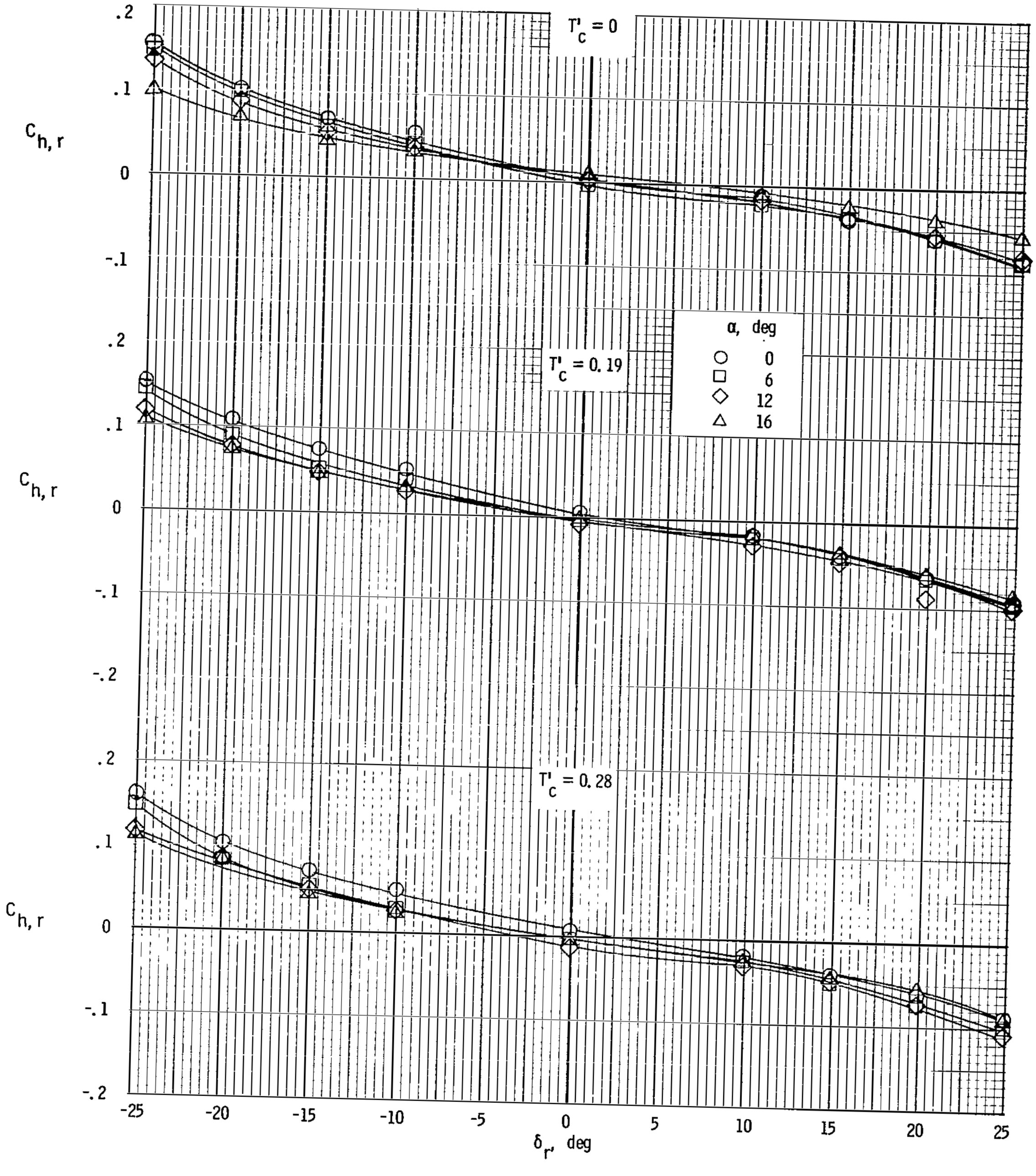

(a) $\beta = 8^0$.

Figure 85.- Variation of rudder hinge-moment coefficient with control deflection. $\delta_f = 0^0$.

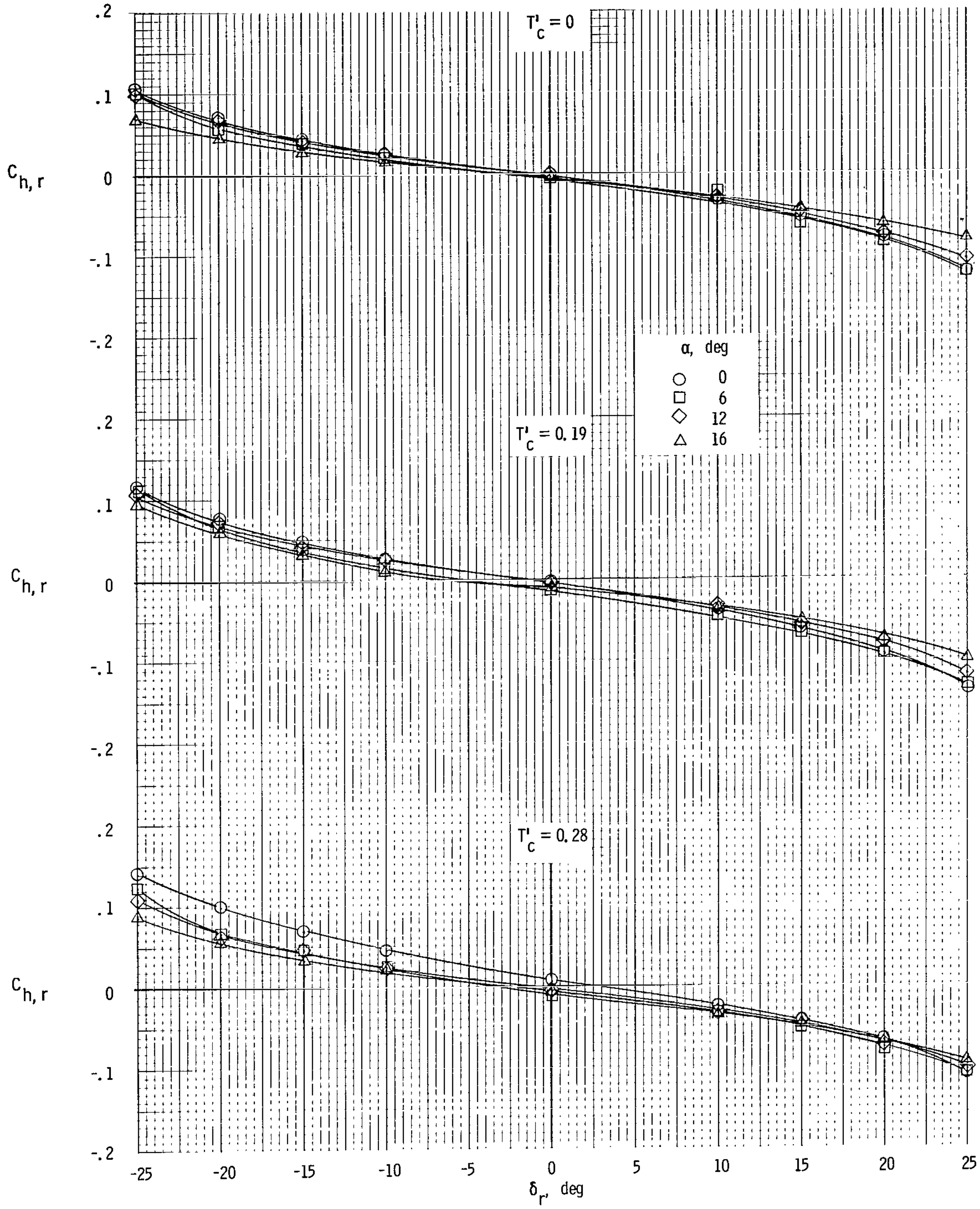

(b) $\beta = 4^{\circ}$.

Figure 85.- Continued.

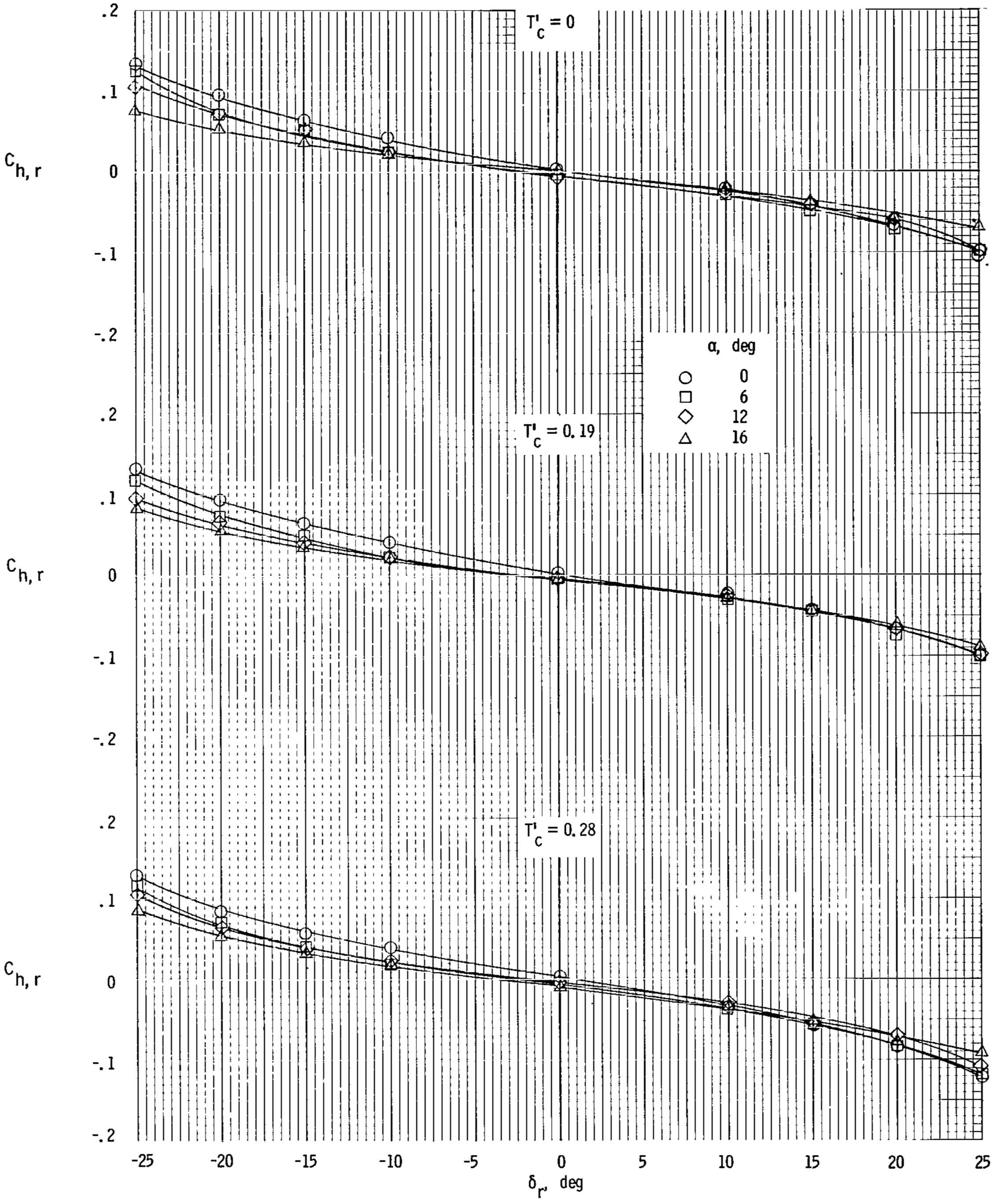

(c) $\beta = 0^0$.

Figure 85.- Continued.

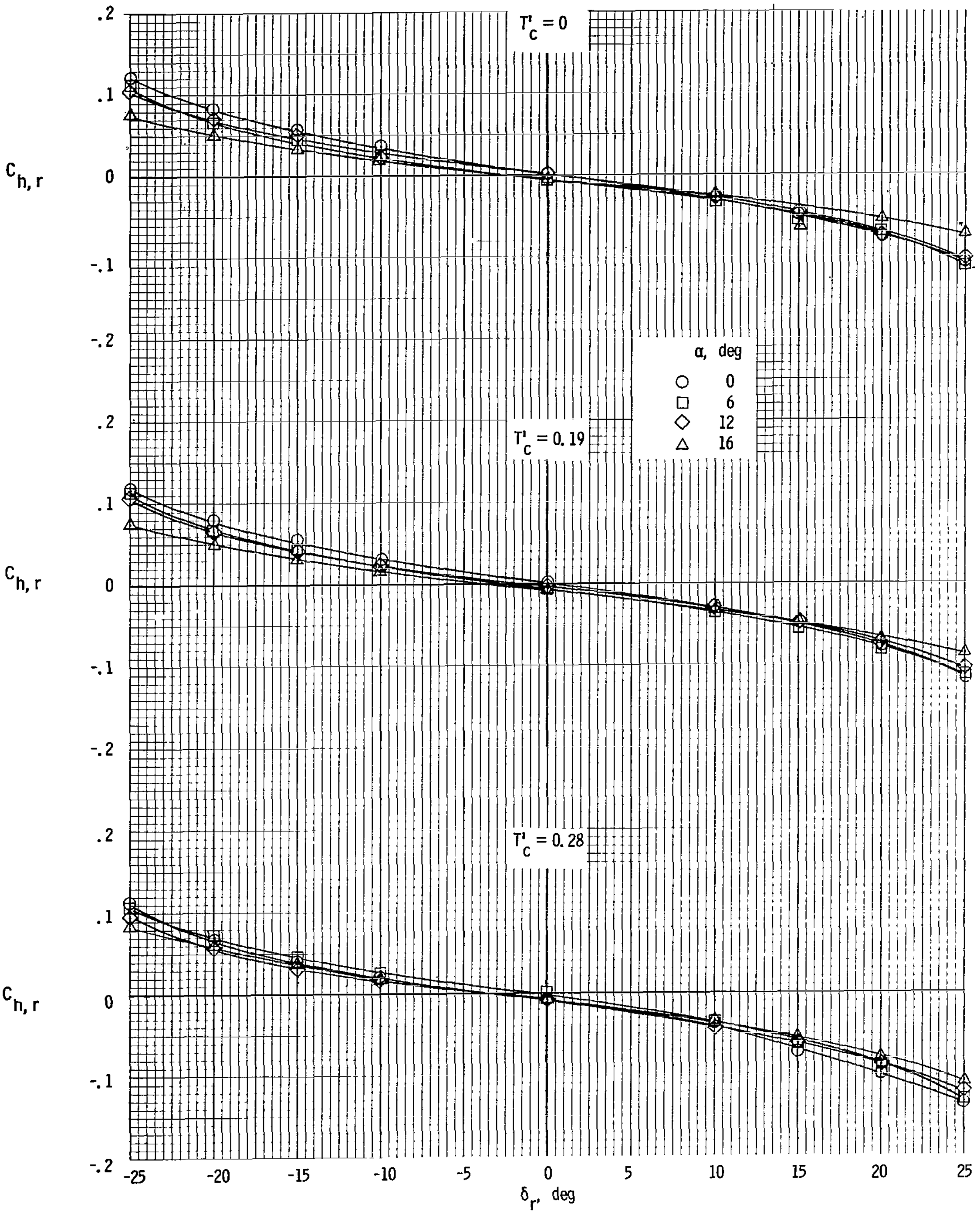

(d) $\beta = -4^\circ$.

Figure 85.- Continued.

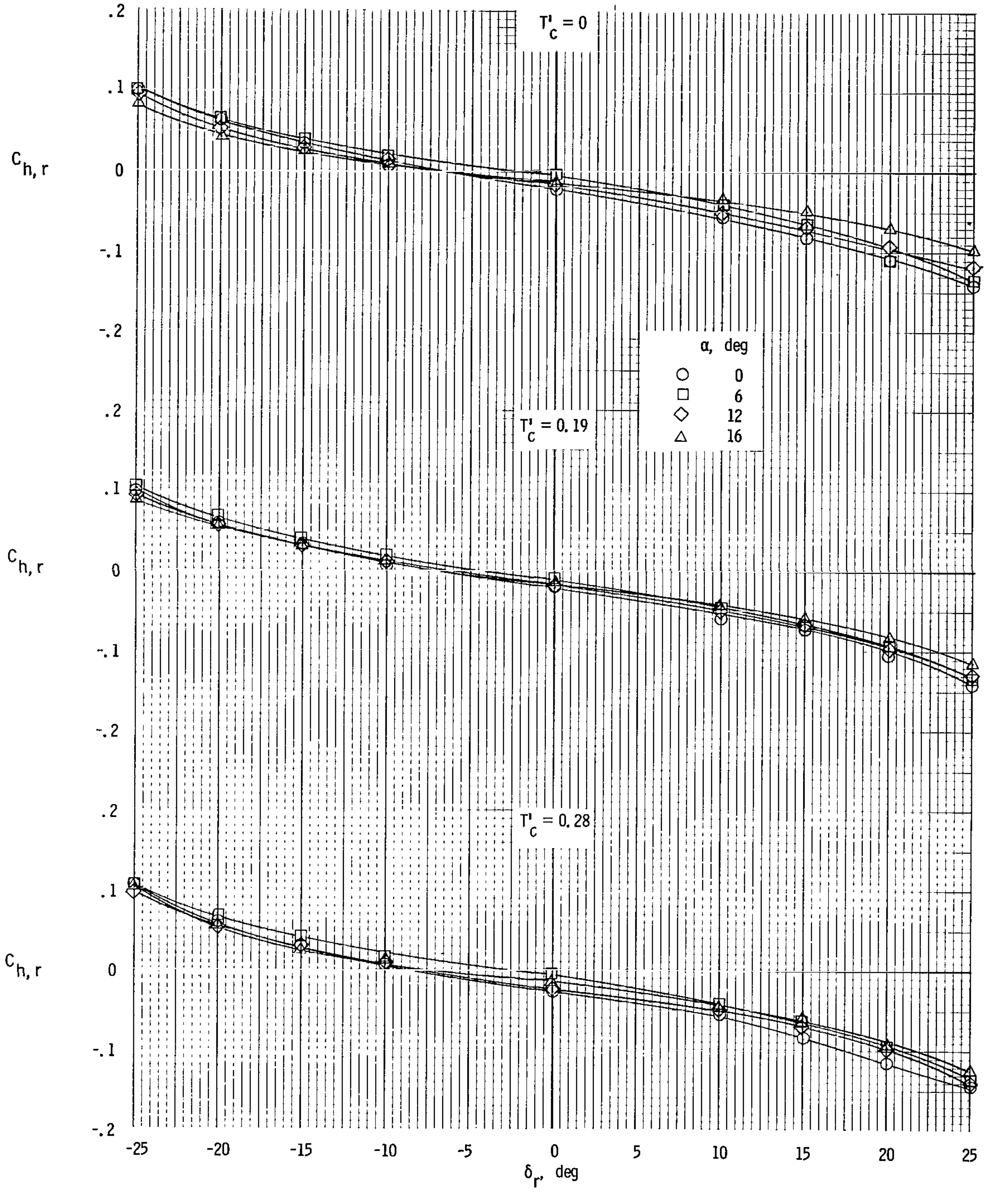

(e) $\beta = -8^0$.

Figure 85.- Concluded.

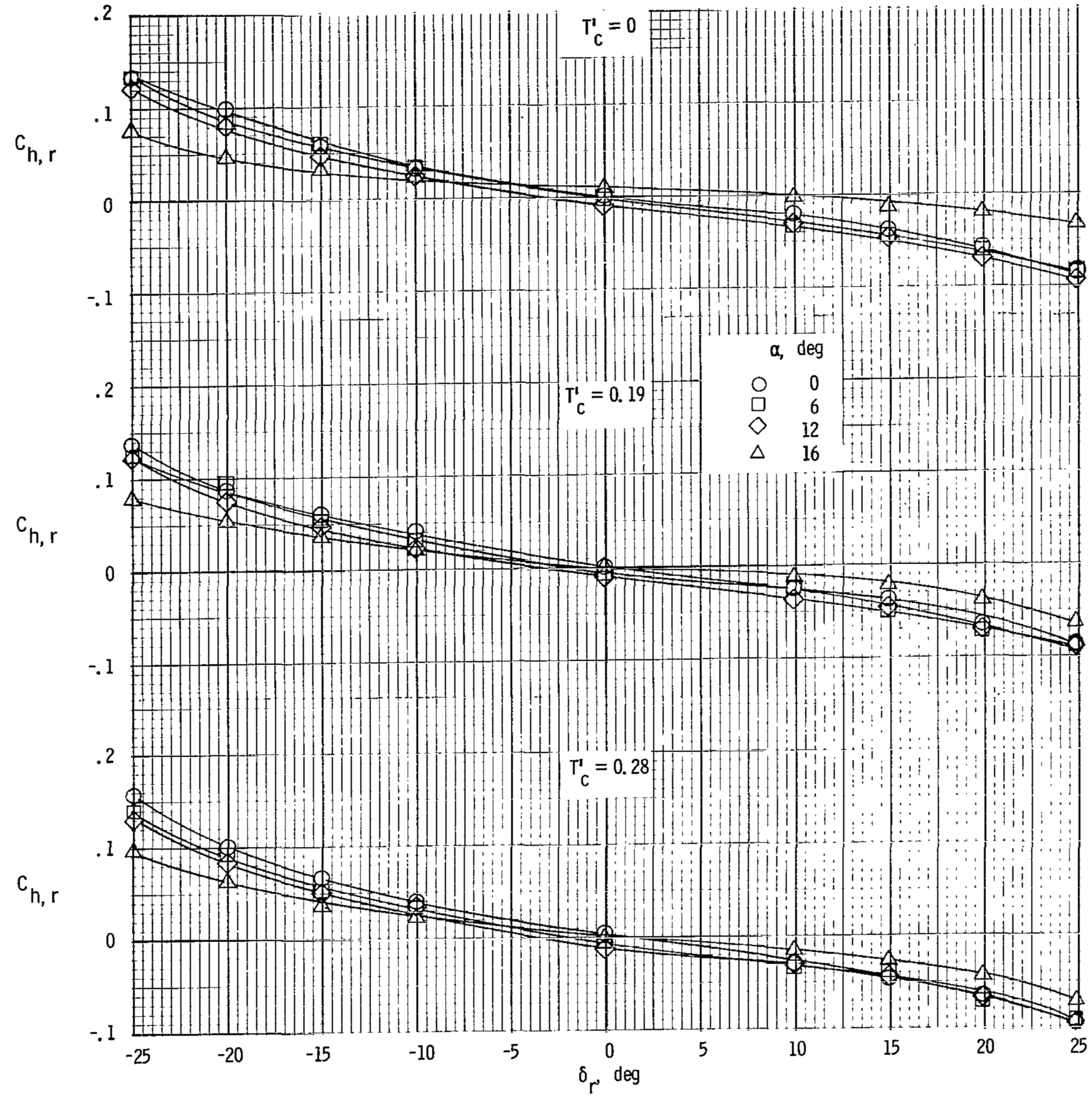

(a) $\beta = 8^0$.

Figure 86.- Variation of rudder hinge-moment coefficient with control deflection. $\delta_f = 35^0$.

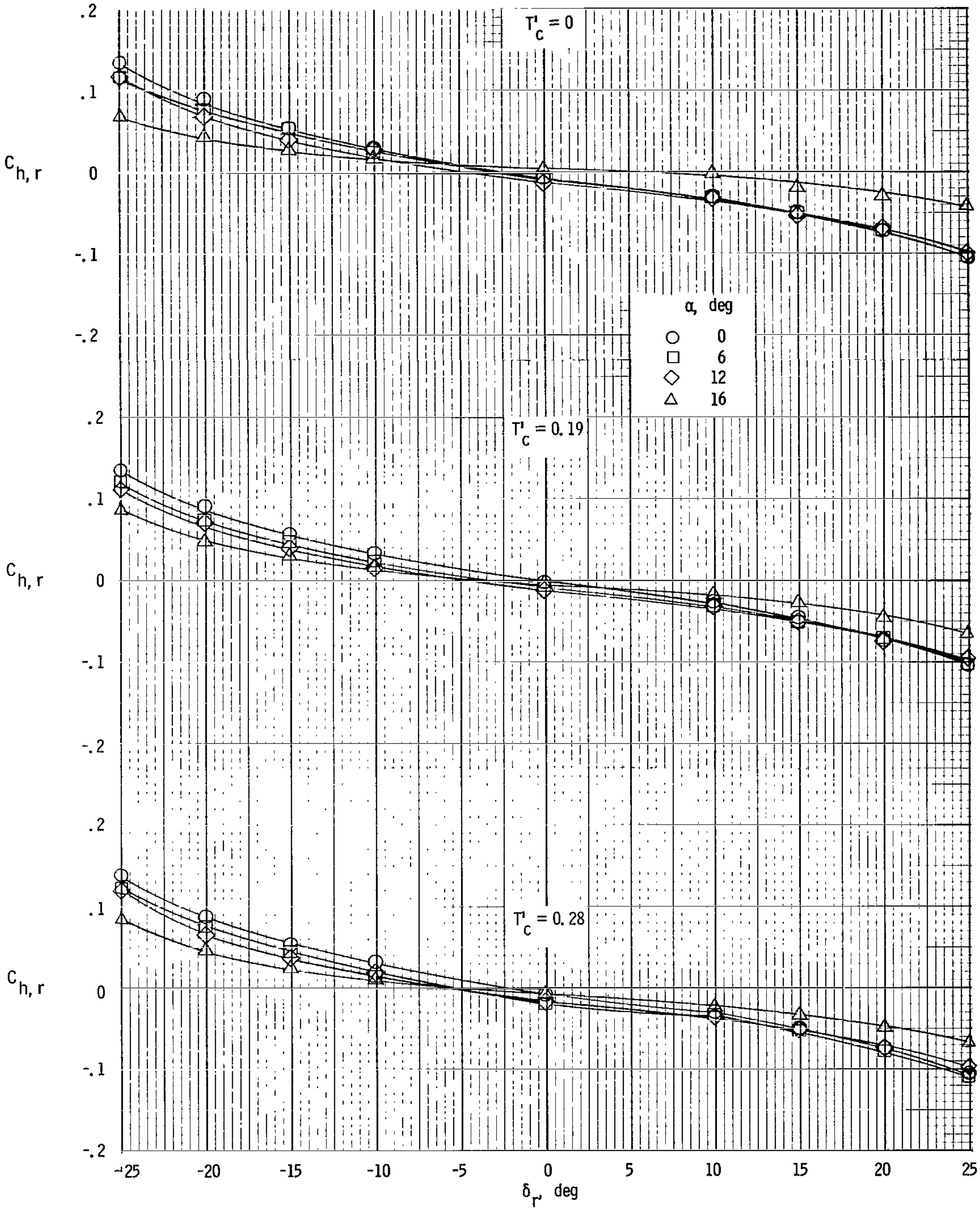

(b) $\beta = 4^{\circ}$.

Figure 86.- Continued.

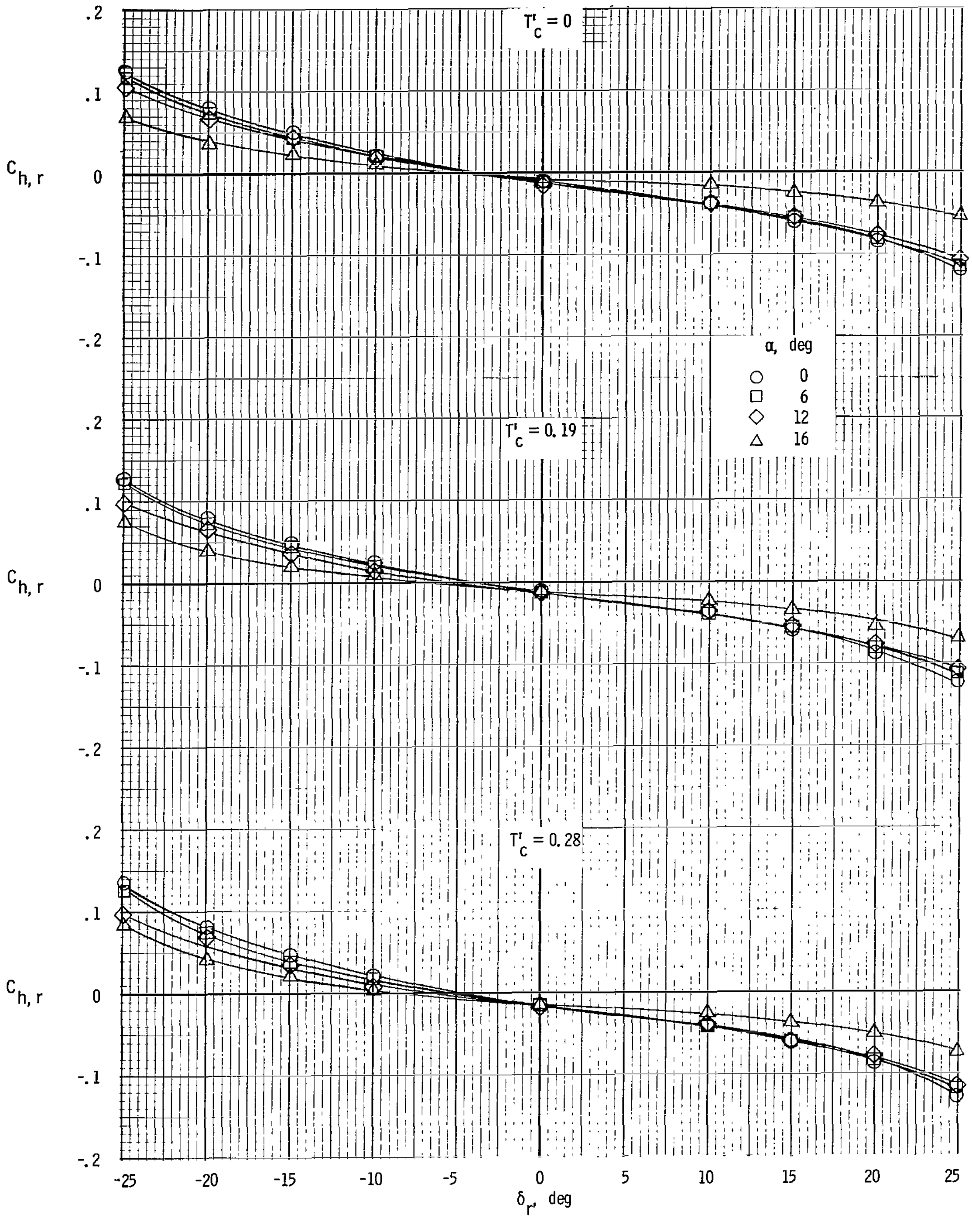

(c) $\beta = 0^0$.

Figure 86.- Continued.

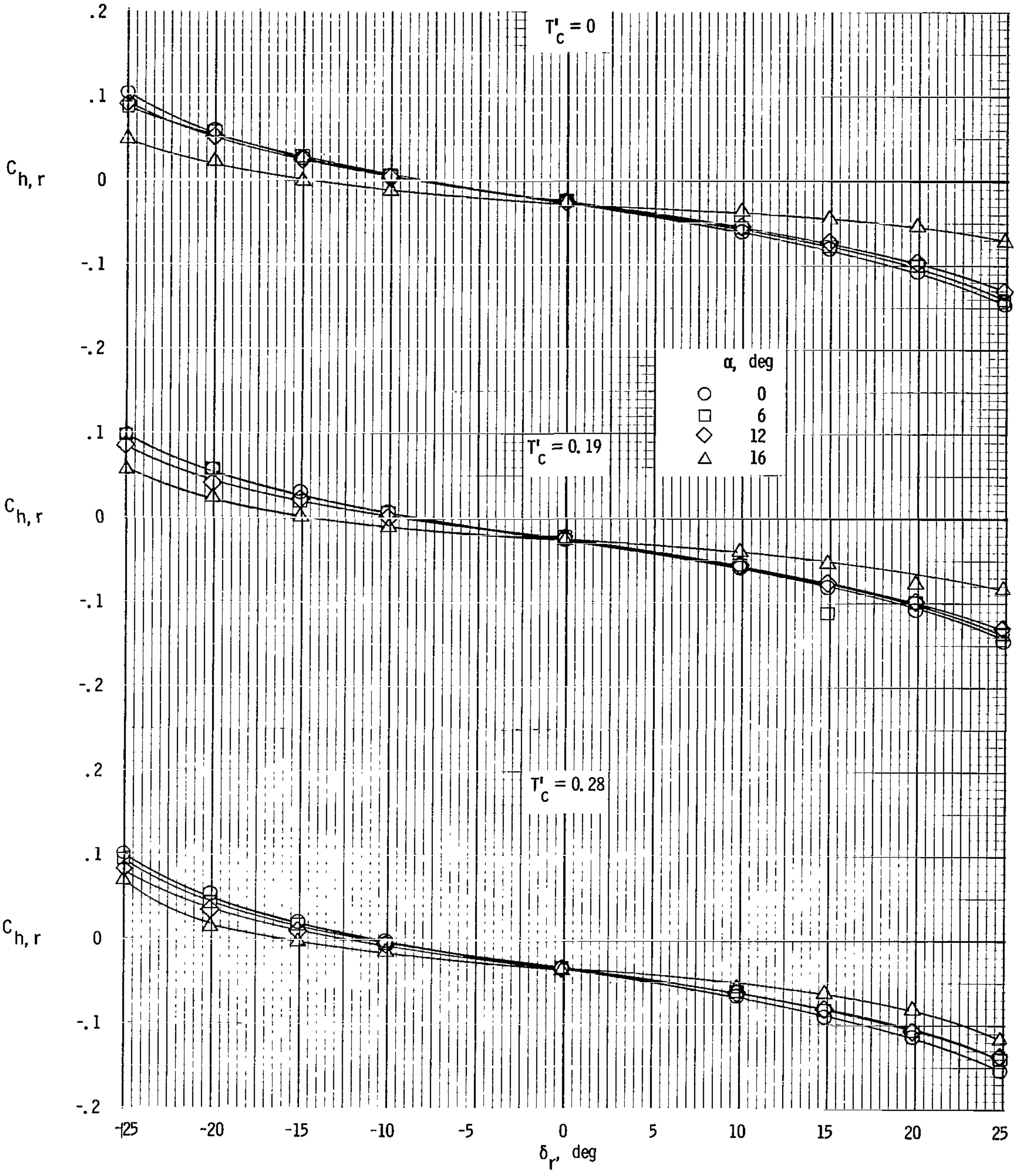

(d) $\beta = -4^{\circ}$.

Figure 86.- Continued.

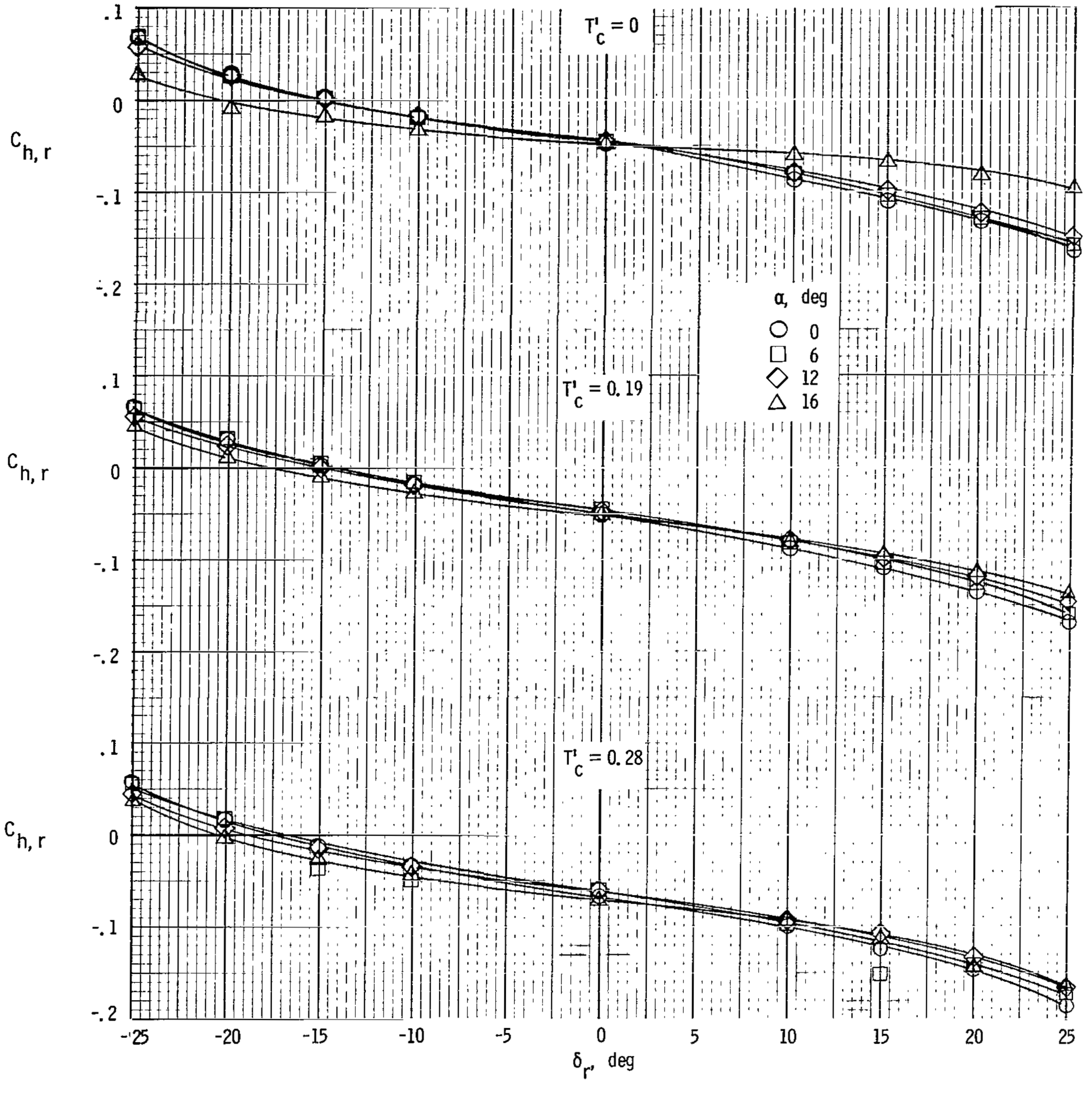

(e) $\beta = -8^0$.

Figure 86.- Concluded.

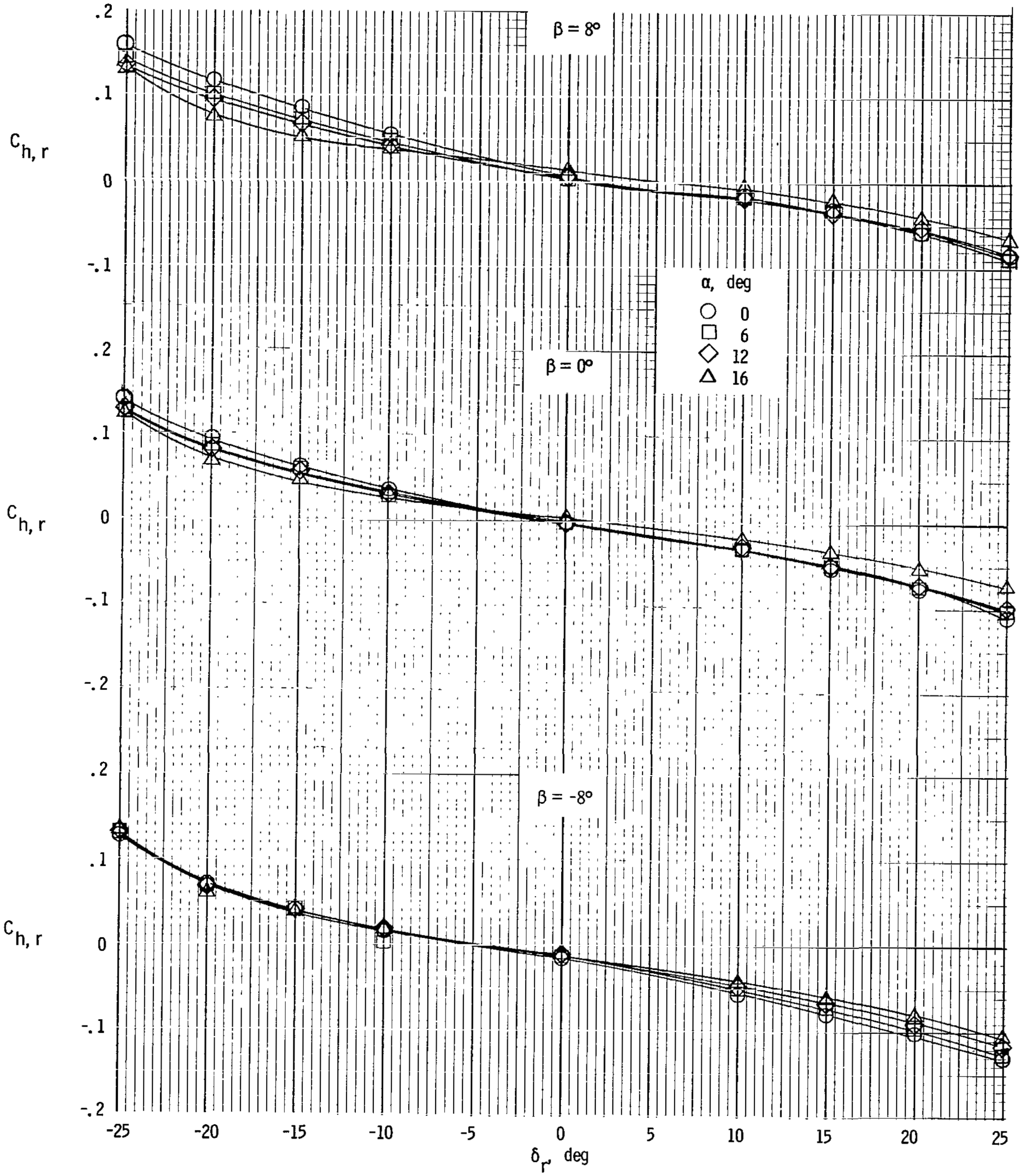

(a) $\delta_f = 0^\circ$.

Figure 87.- Variation of rudder hinge-moment coefficient with control deflection with asymmetric power for left engine full; right engine windmilling.

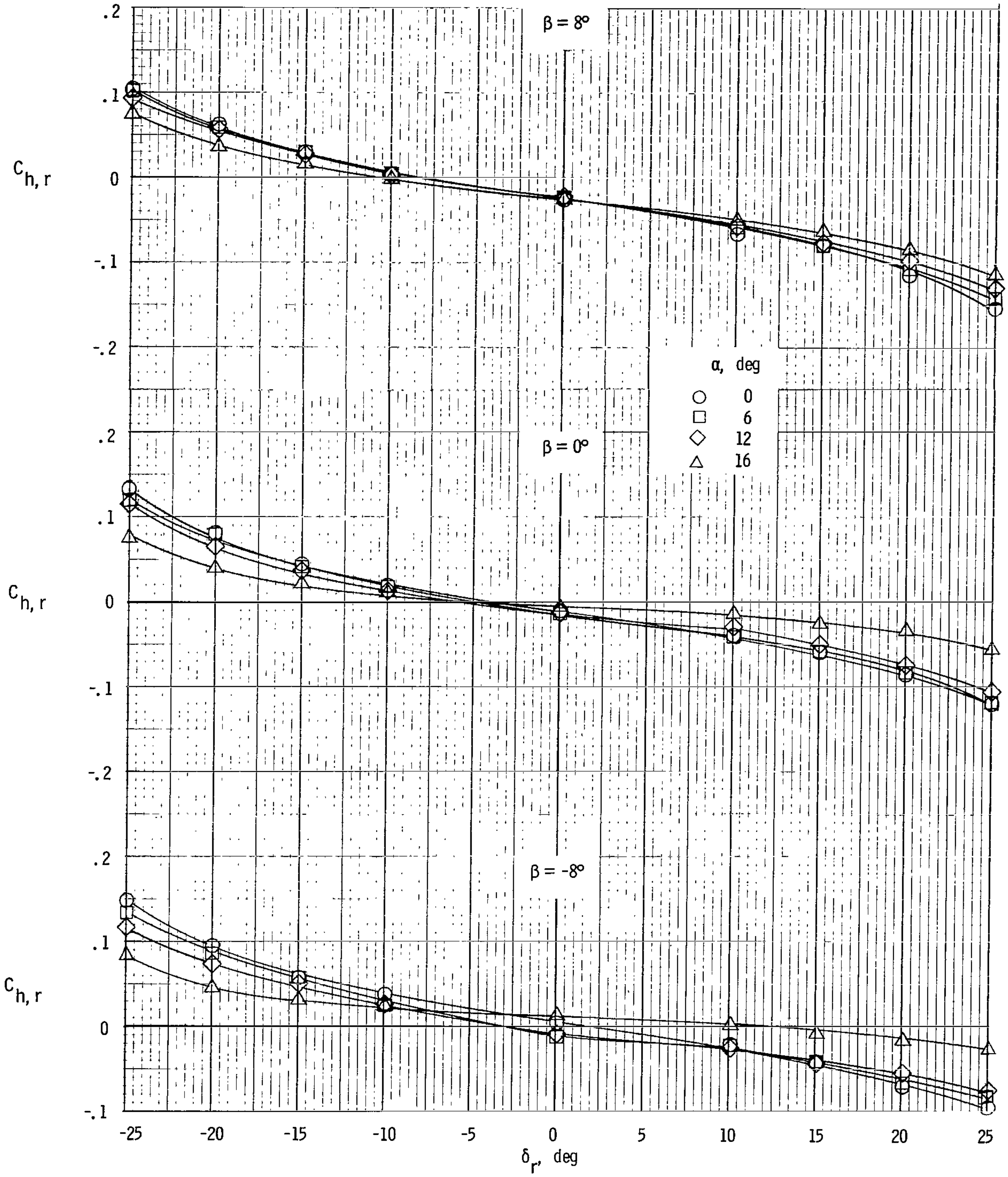

(b) $\delta_f = 35^0$.

Figure 87.- Concluded.

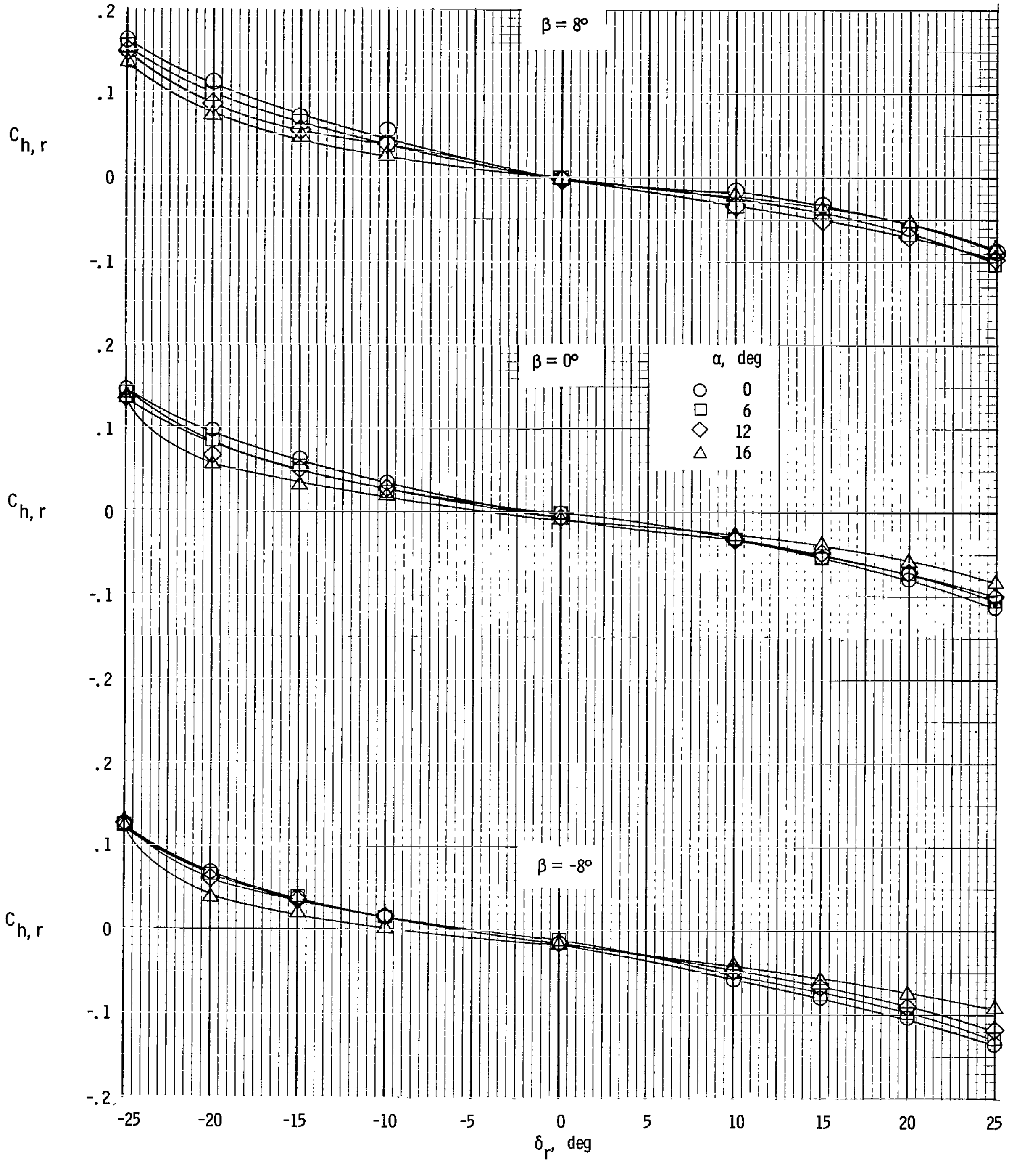

(a) $\delta_f = 0^0$.

Figure 88.- Variation of rudder hinge-moment coefficient with control deflection with asymmetric power for left engine windmilling; right engine full.

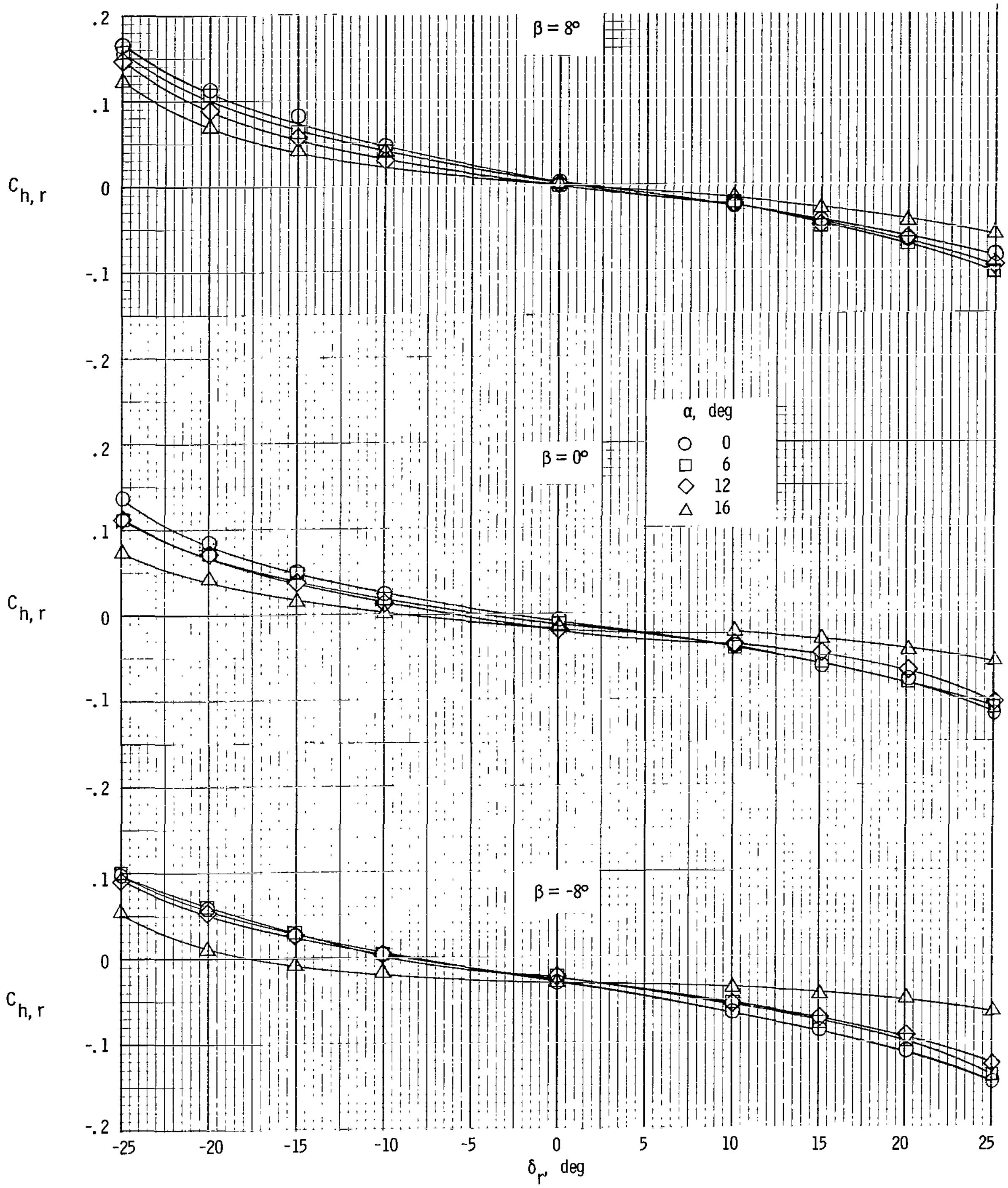

(b) $\delta_f = 35^0$.

Figure 88.- Concluded.

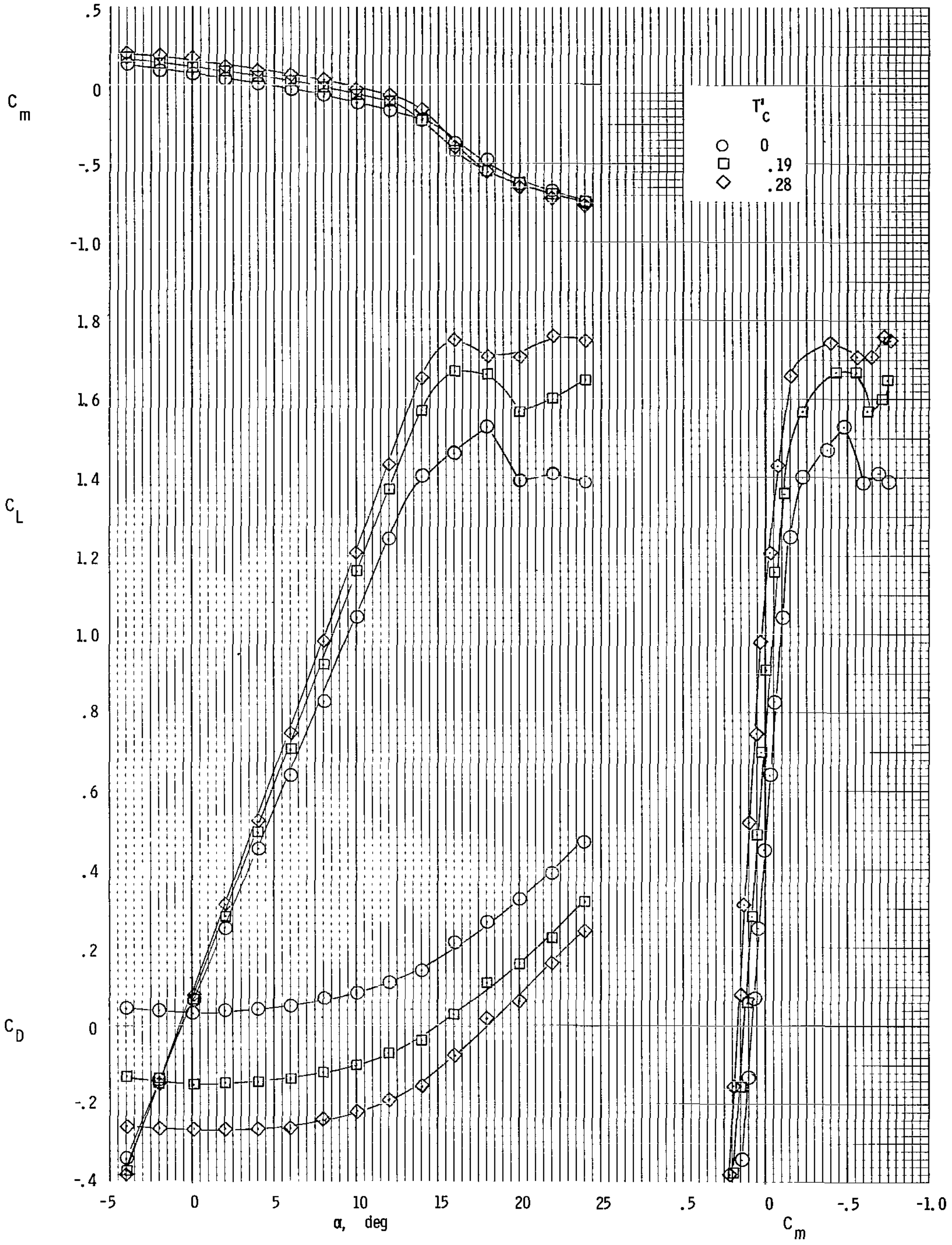

(a) $\delta_f = 0^o$.

Figure 89.- Effect of power on longitudinal aerodynamic characteristics. $\beta = 0^o$; $\delta_e = 0^o$.

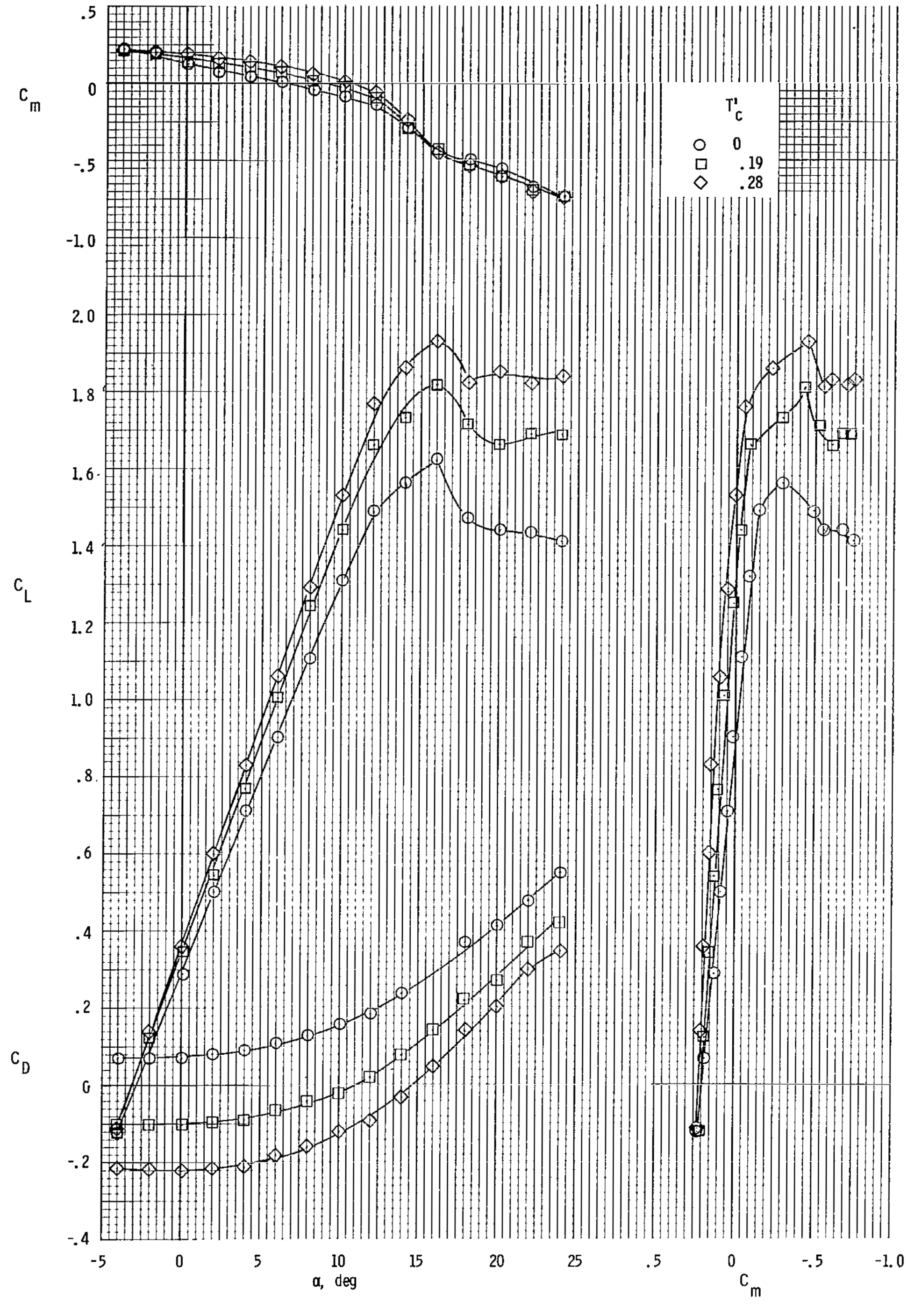

(b) $\delta_f = 15^{\circ}$.

Figure 89.- Continued.

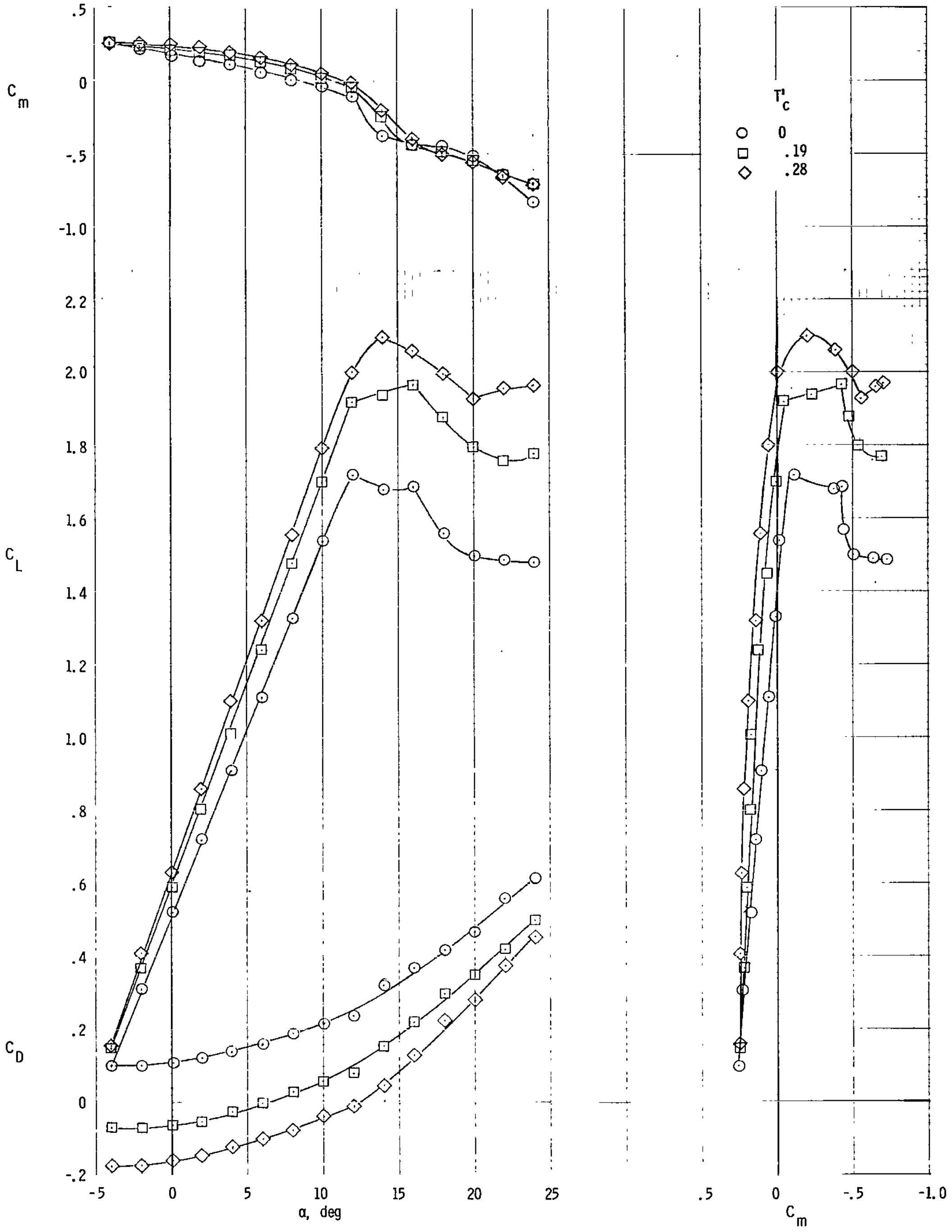

(c) $\delta_f = 35^0$.

Figure 89.- Concluded.

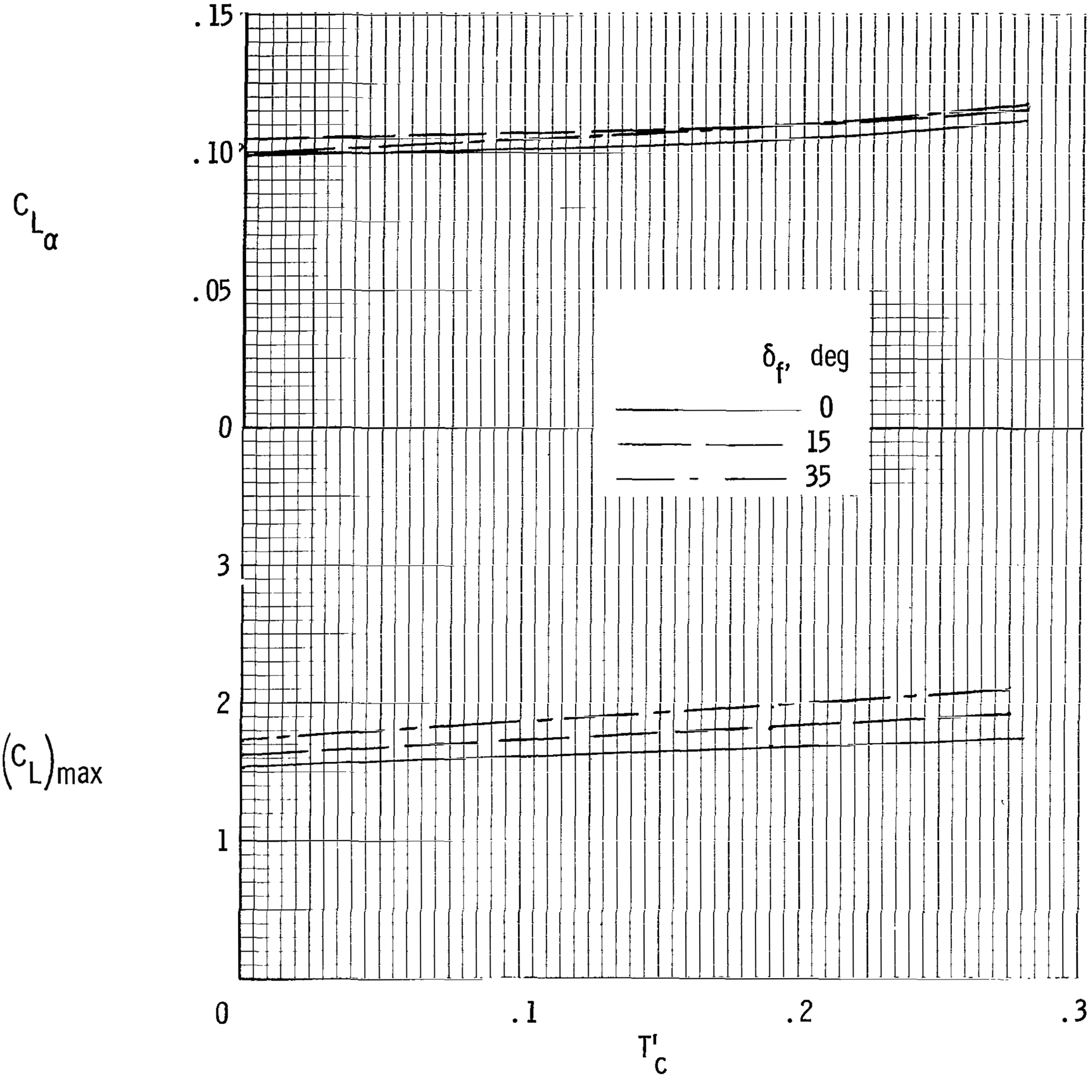

Figure 90.- Effect of power on lift-curve slope and maximum lift coefficient. $\delta_e = 0^0$.

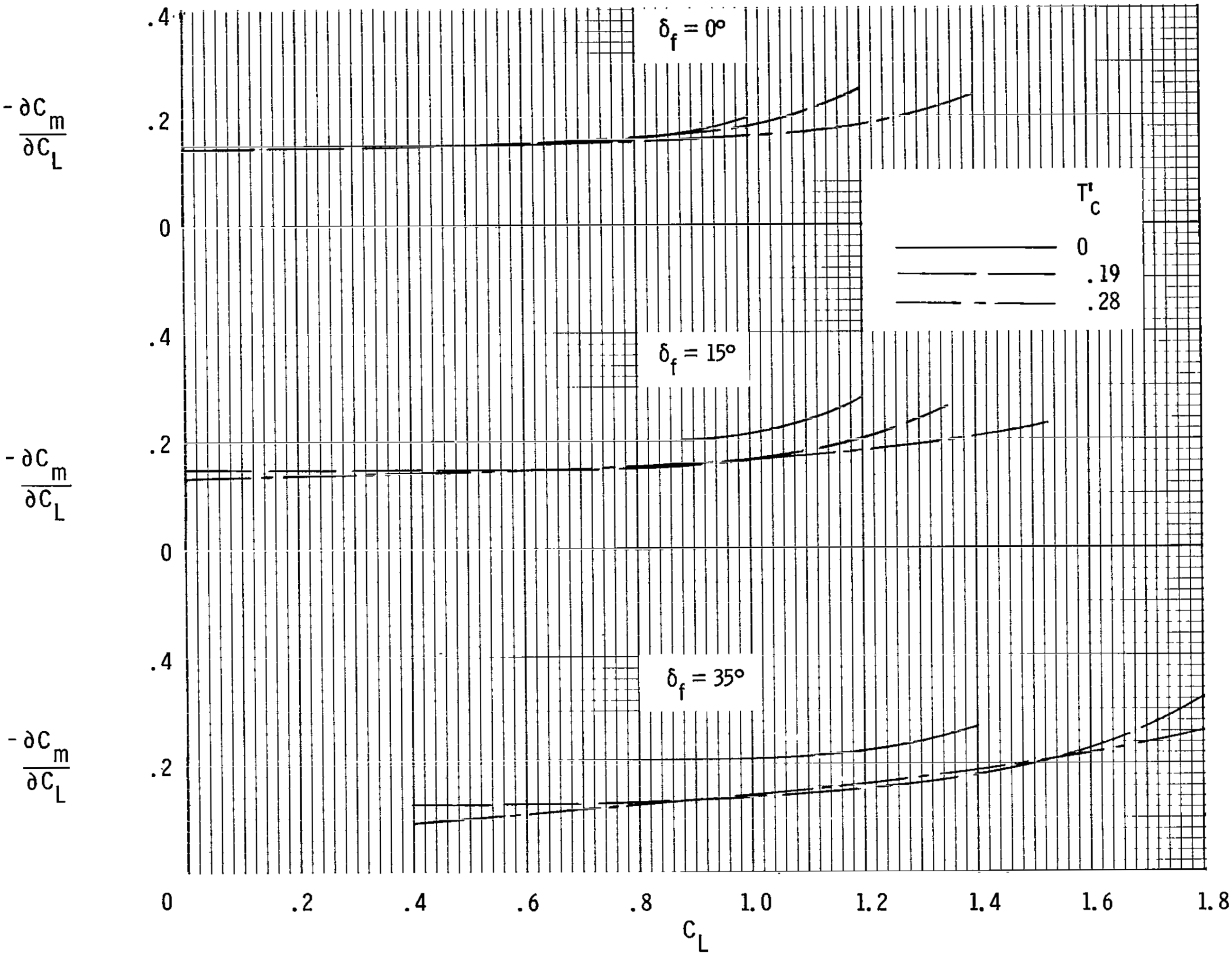

Figure 91.- Variation of stick-fixed longitudinal stability with lift coefficient for several thrust coefficients and flap deflections.

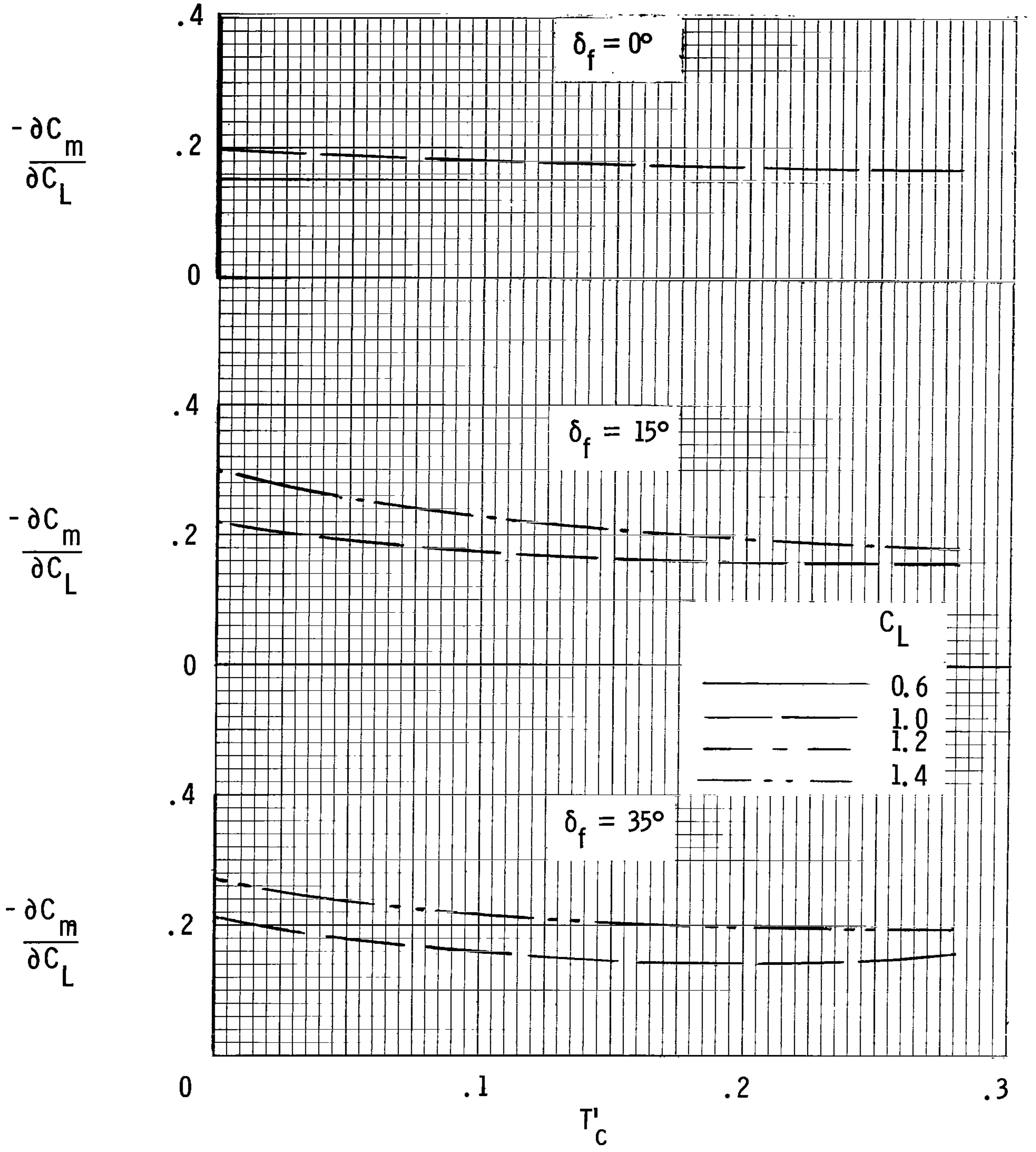

Figure 92.- Effect of power on stick-fixed longitudinal stability characteristics.

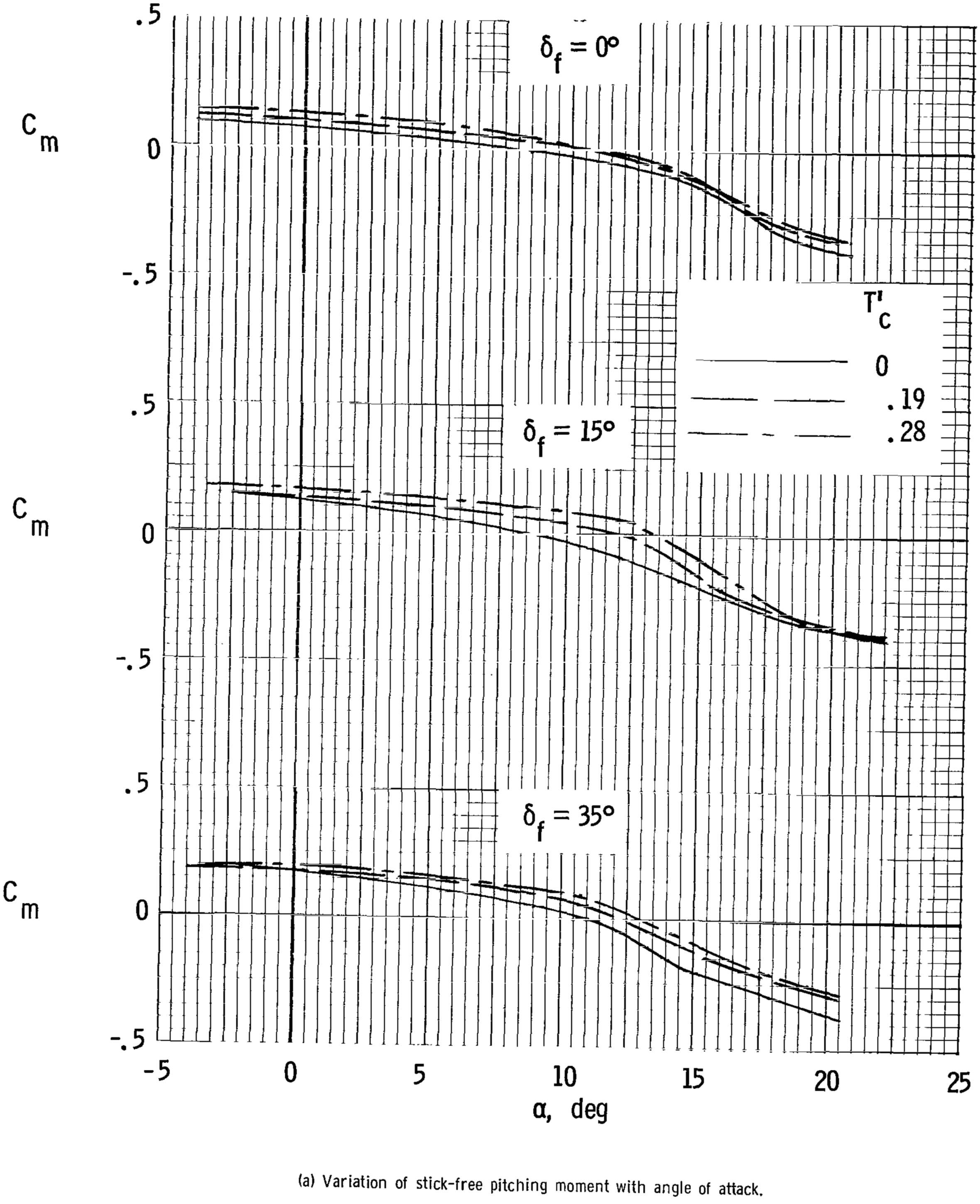

(a) Variation of stick-free pitching moment with angle of attack.

Figure 93.- Stick-free static longitudinal stability characteristics.

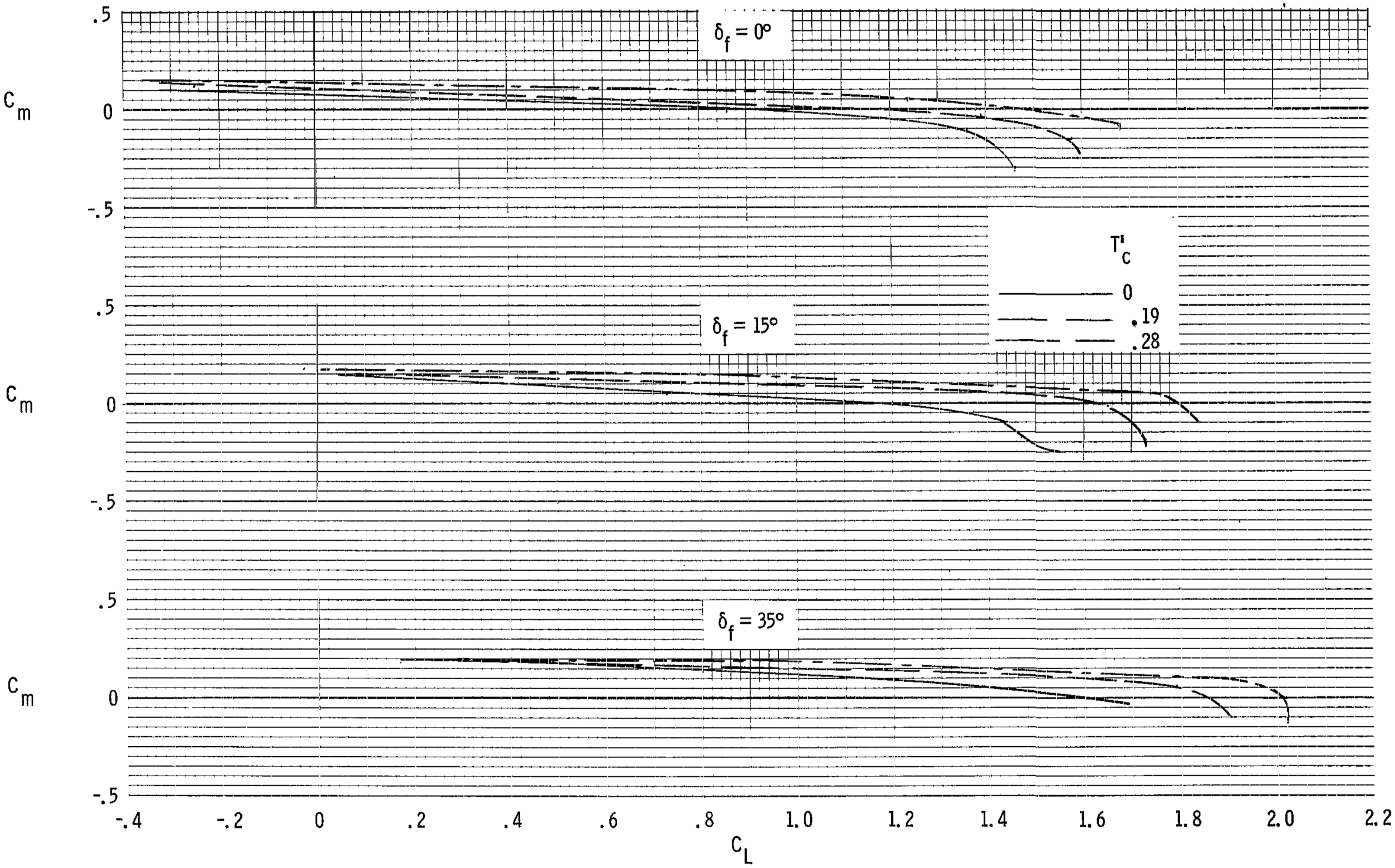

(b) Variation of stick-free pitching moment with lift coefficient.

Figure 93.- Concluded.

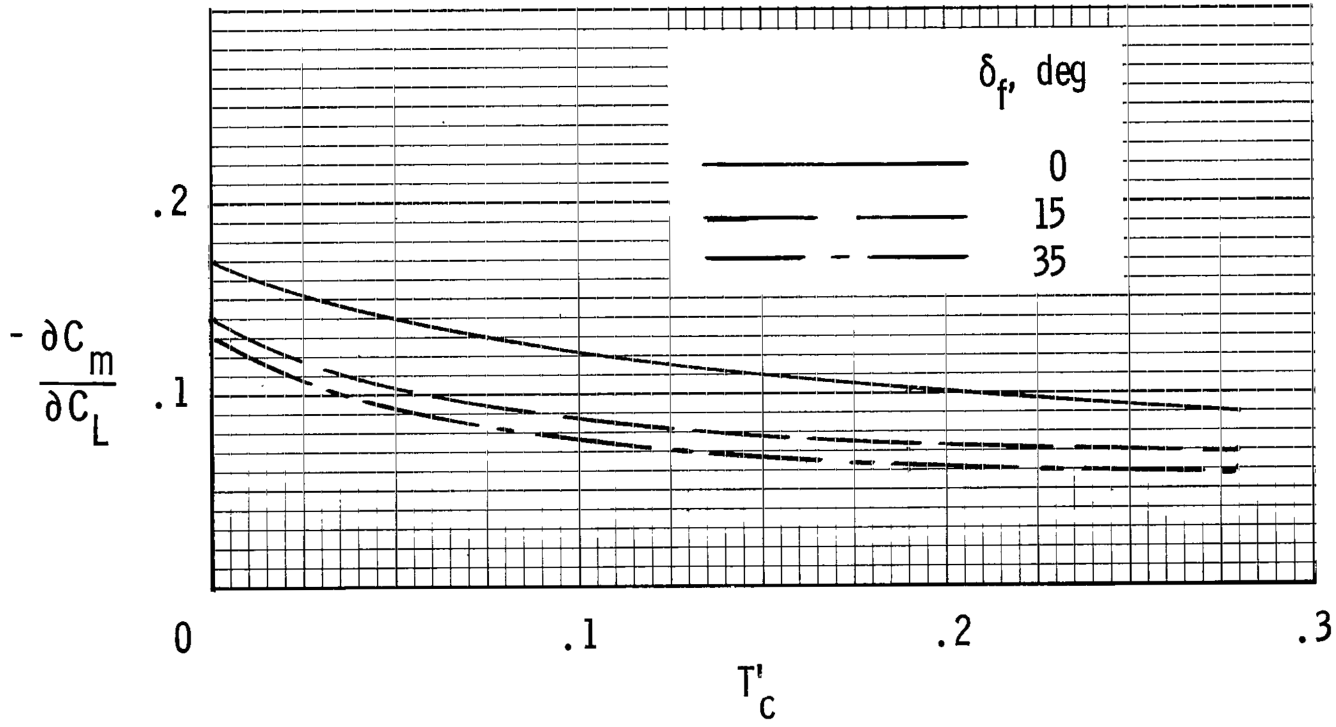

Figure 94.- Effect of power on stick-free longitudinal stability. $C_L = 1.0$.

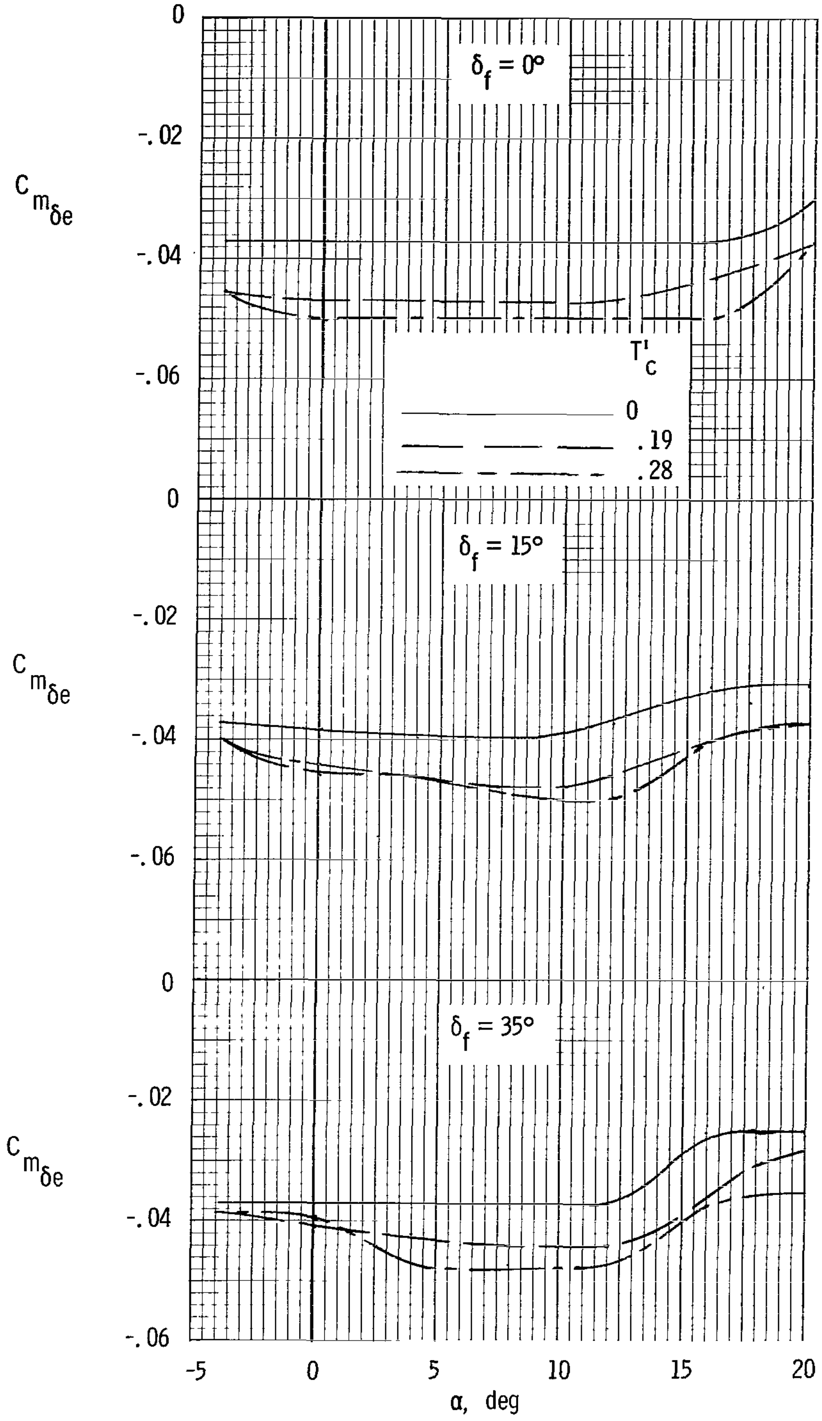

Figure 95.- Variation of elevator effectiveness with angle of attack for several power and flap settings.

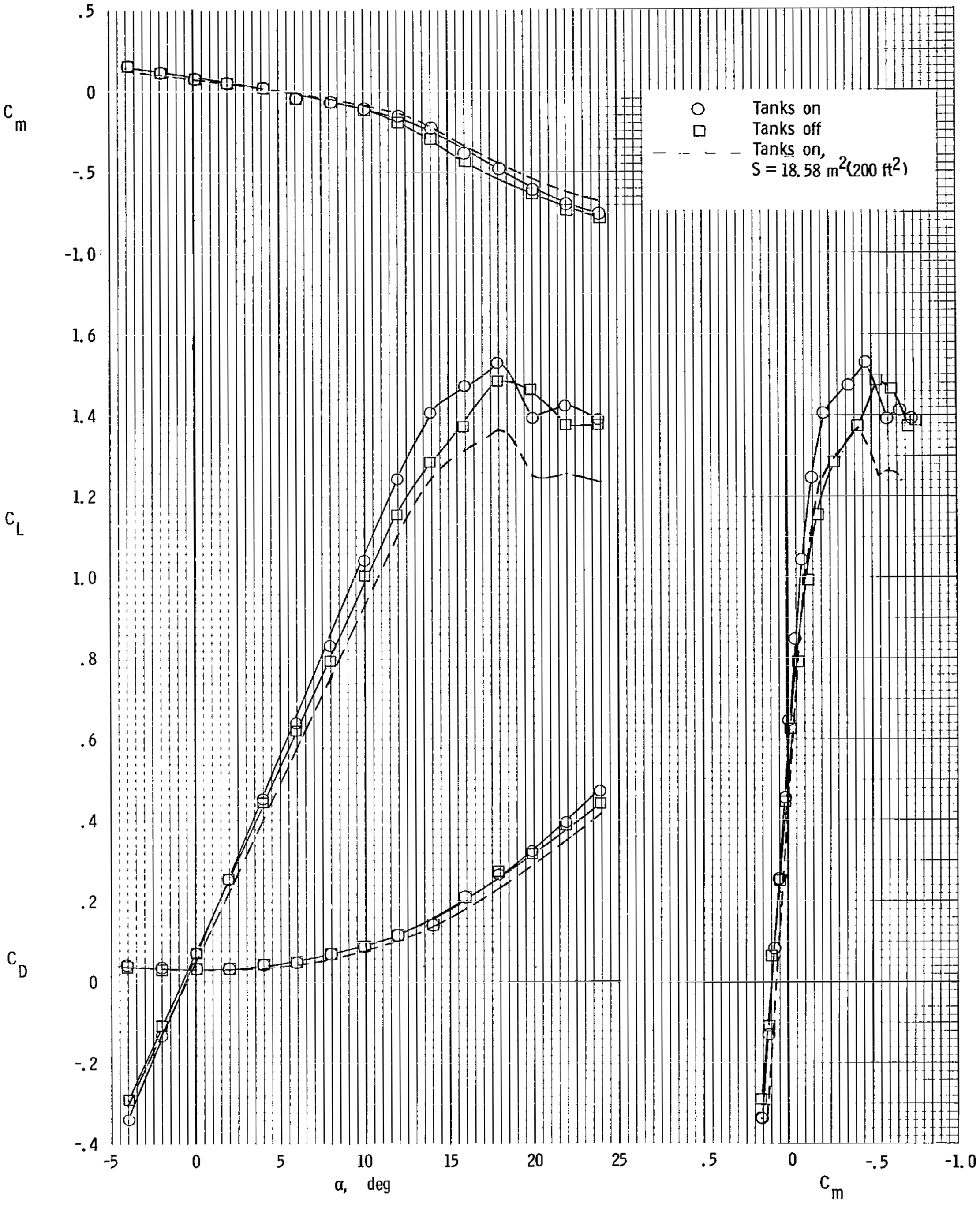

Figure 96.- Comparison of longitudinal aerodynamic characteristics with wing-tip tanks on and off for $\delta_f = 0^o$; $T'_C = 0$.

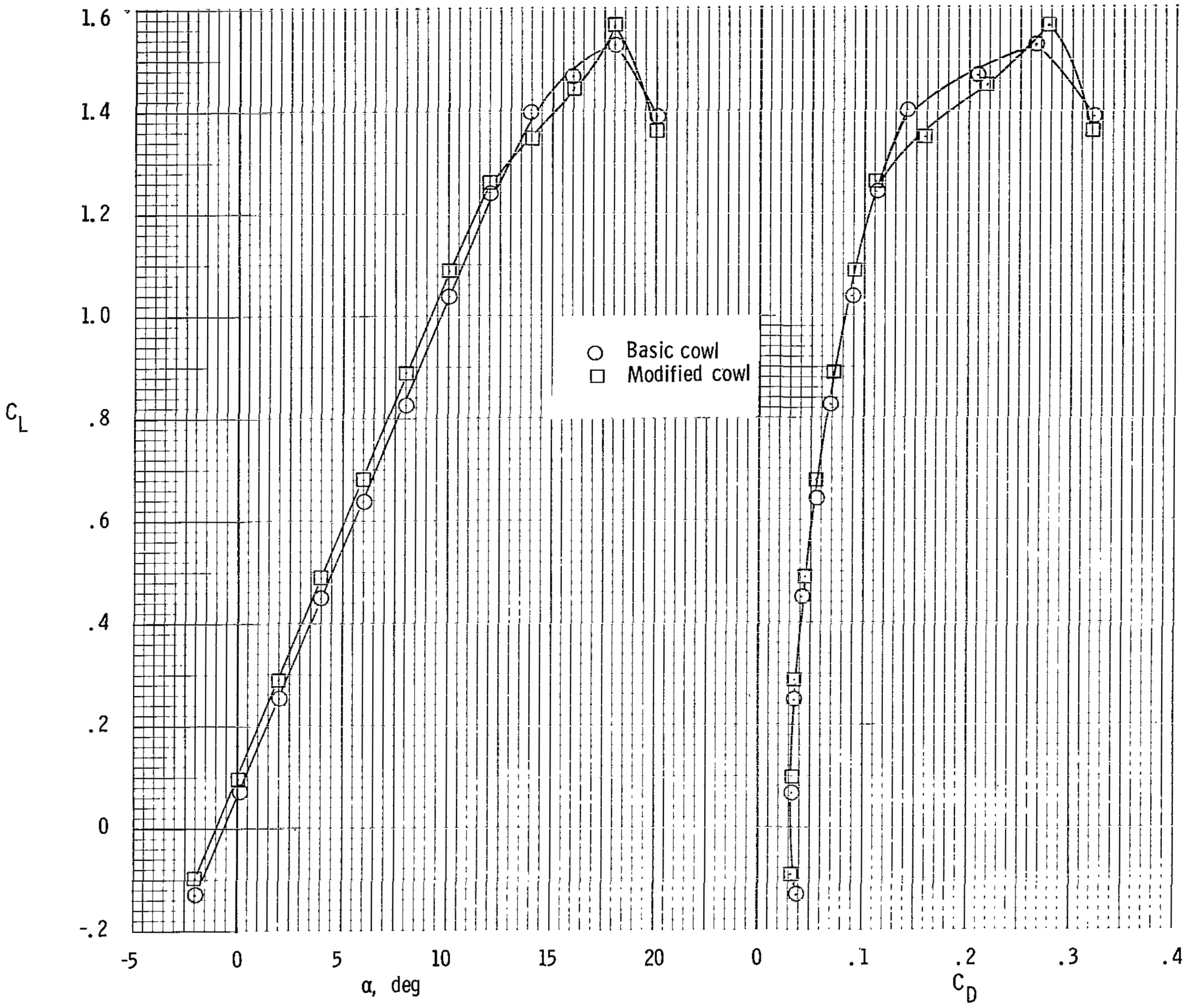

(a) Lift and drag characteristics.

Figure 97.- Comparison of longitudinal characteristics of model with original and modified cowl. $\delta_f = 0^o$; $T'_c = 0$.

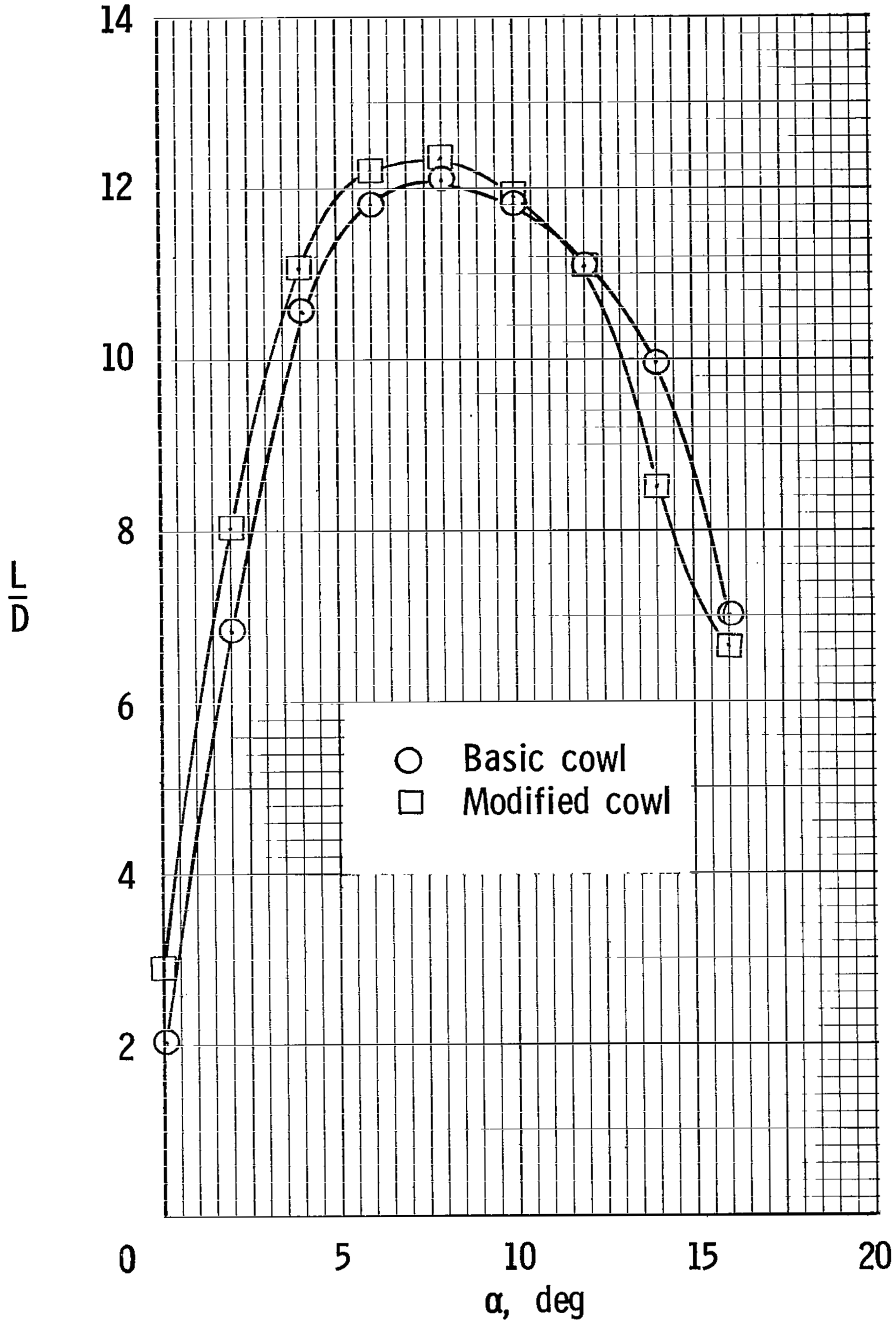

(b) Comparison of lift-drag ratios.

Figure 97.- Concluded.

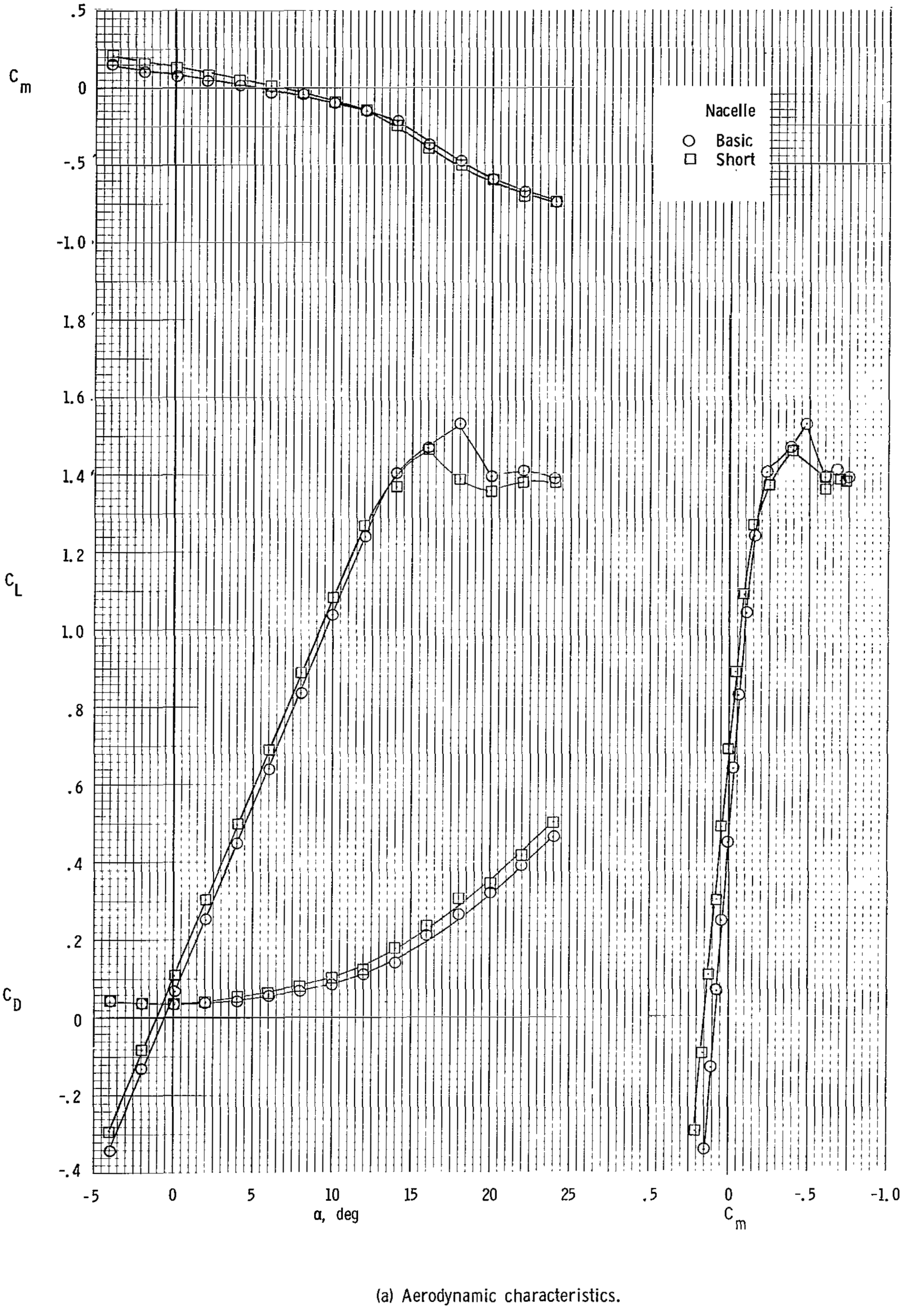

(a) Aerodynamic characteristics.

Figure 98.- Comparison of longitudinal aerodynamic characteristics and L/D for the basic and short nacelle configurations. $\delta_f = 0^o$; $T'_c = 0$.

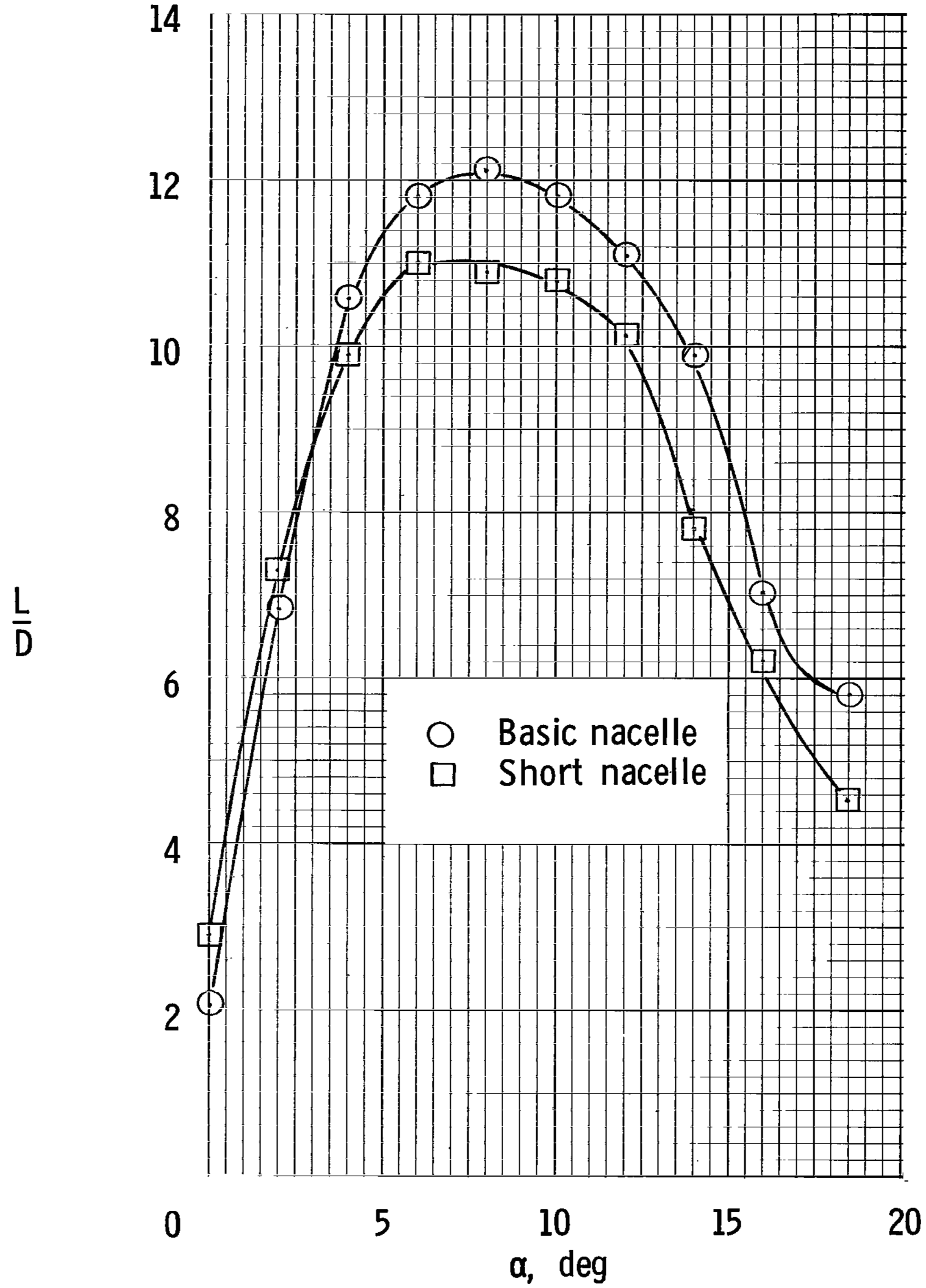

(b) Comparison of lift-drag ratios.

Figure 98.- Concluded.

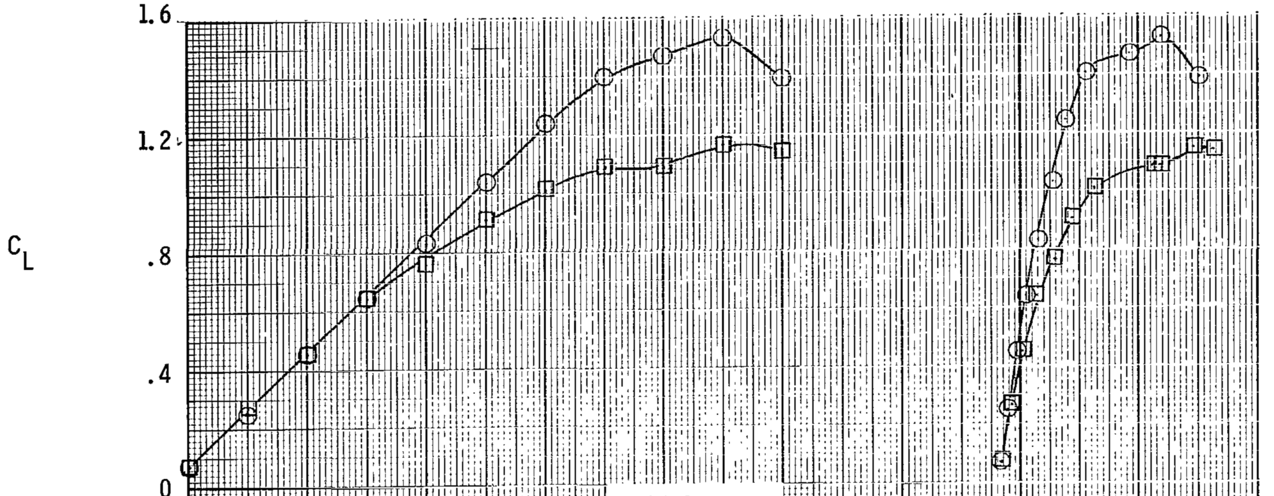

(a) $\delta_f = 0°$.

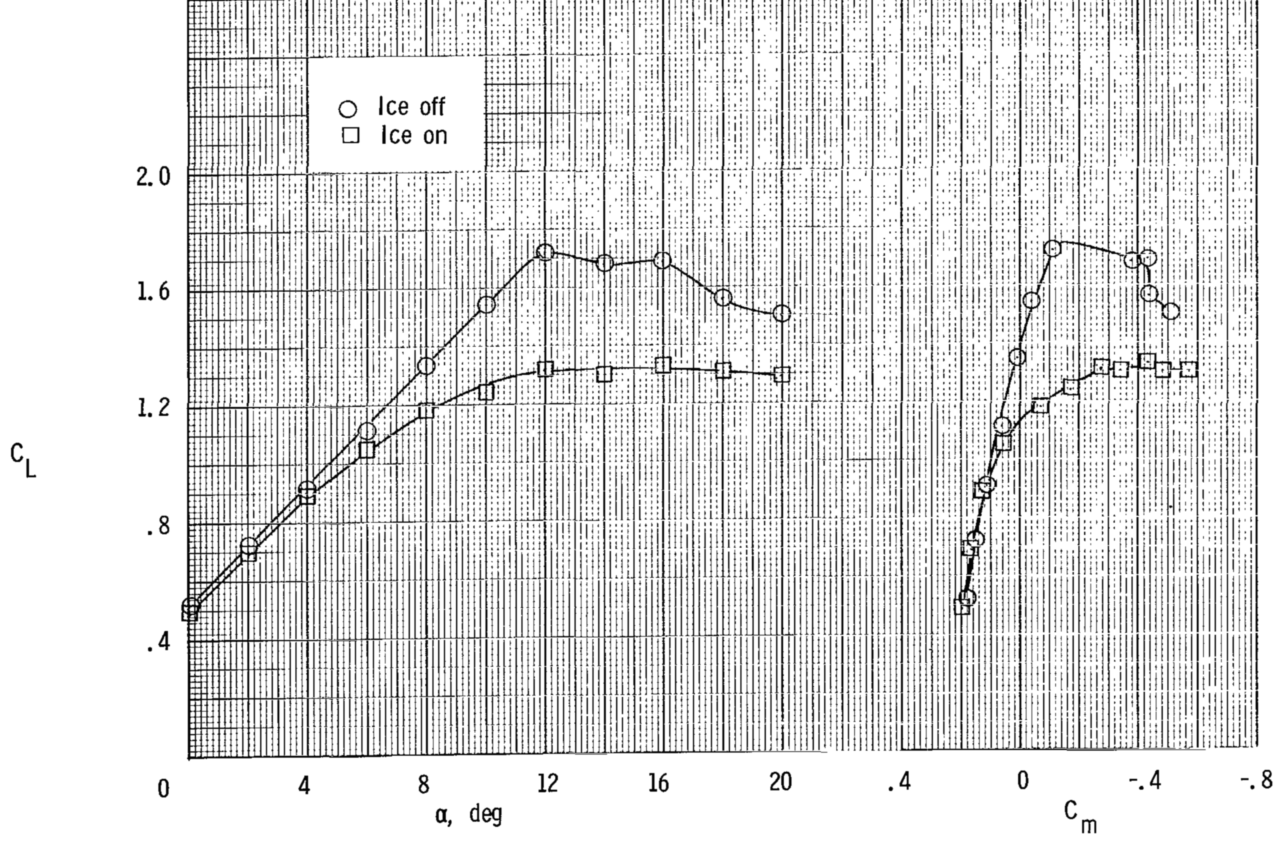

(b) $\delta_f = 35^0$.

Figure 99.- Comparison of longitudinal characteristics with and without glaze ice. $T'_c = 0$; $\beta = 0^0$.

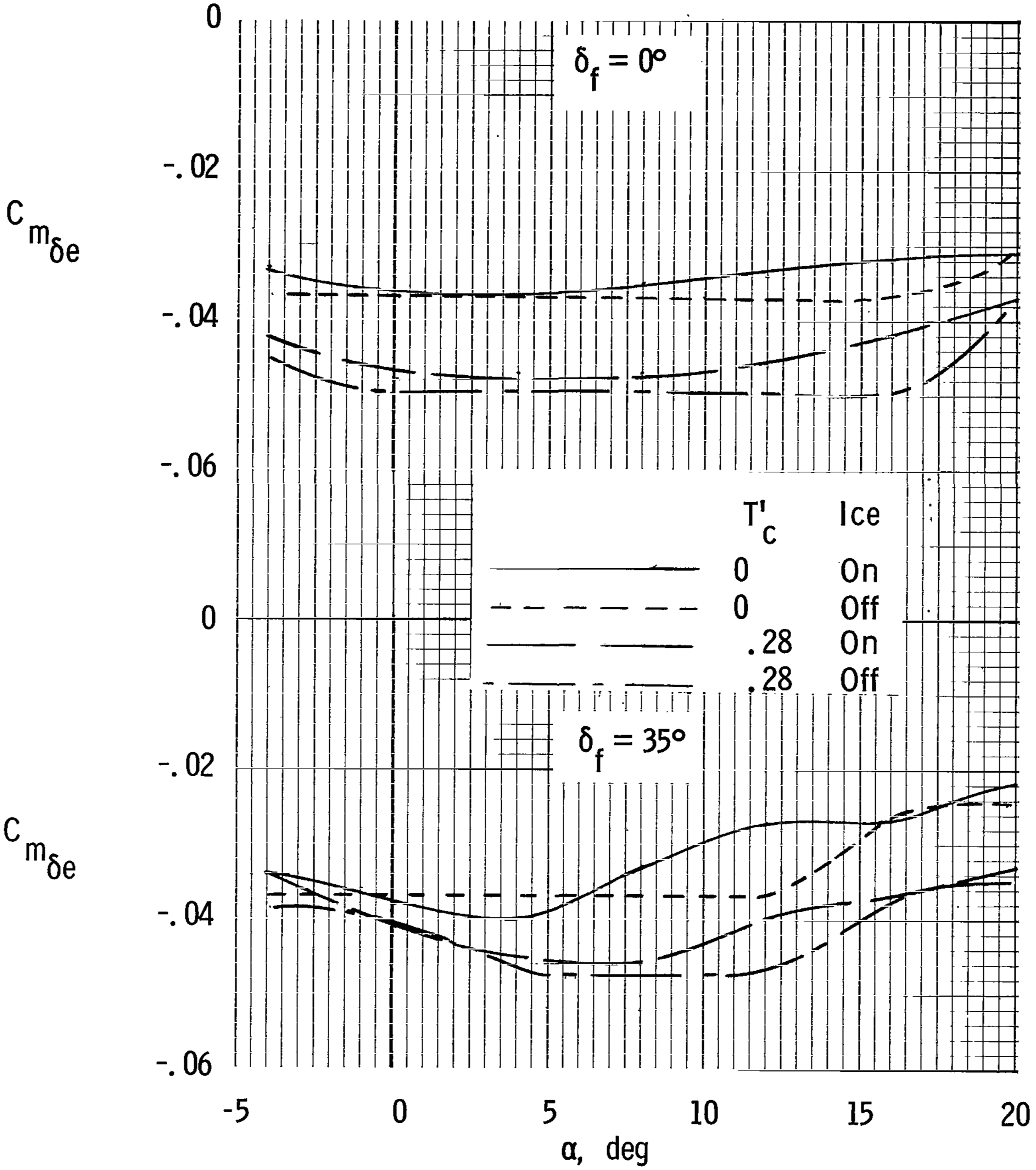

Figure 100.- Variation of elevator effectiveness with angle of attack for several flap and power settings with glaze ice on wing and tail.

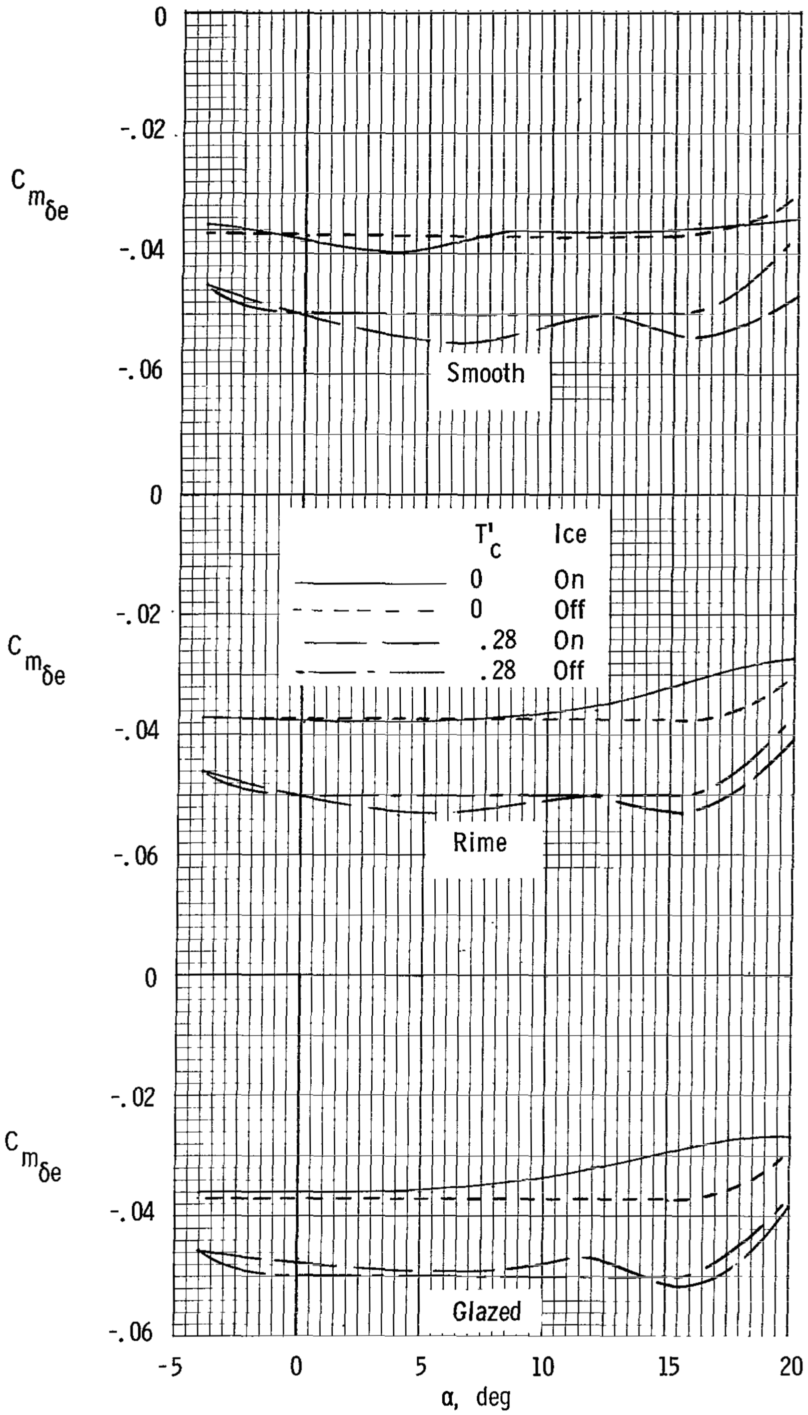

(a) $\delta_f = 0^{o}$.

Figure 101.- Variation of elevator effectiveness with angle of attack for several ice formations on tail only.

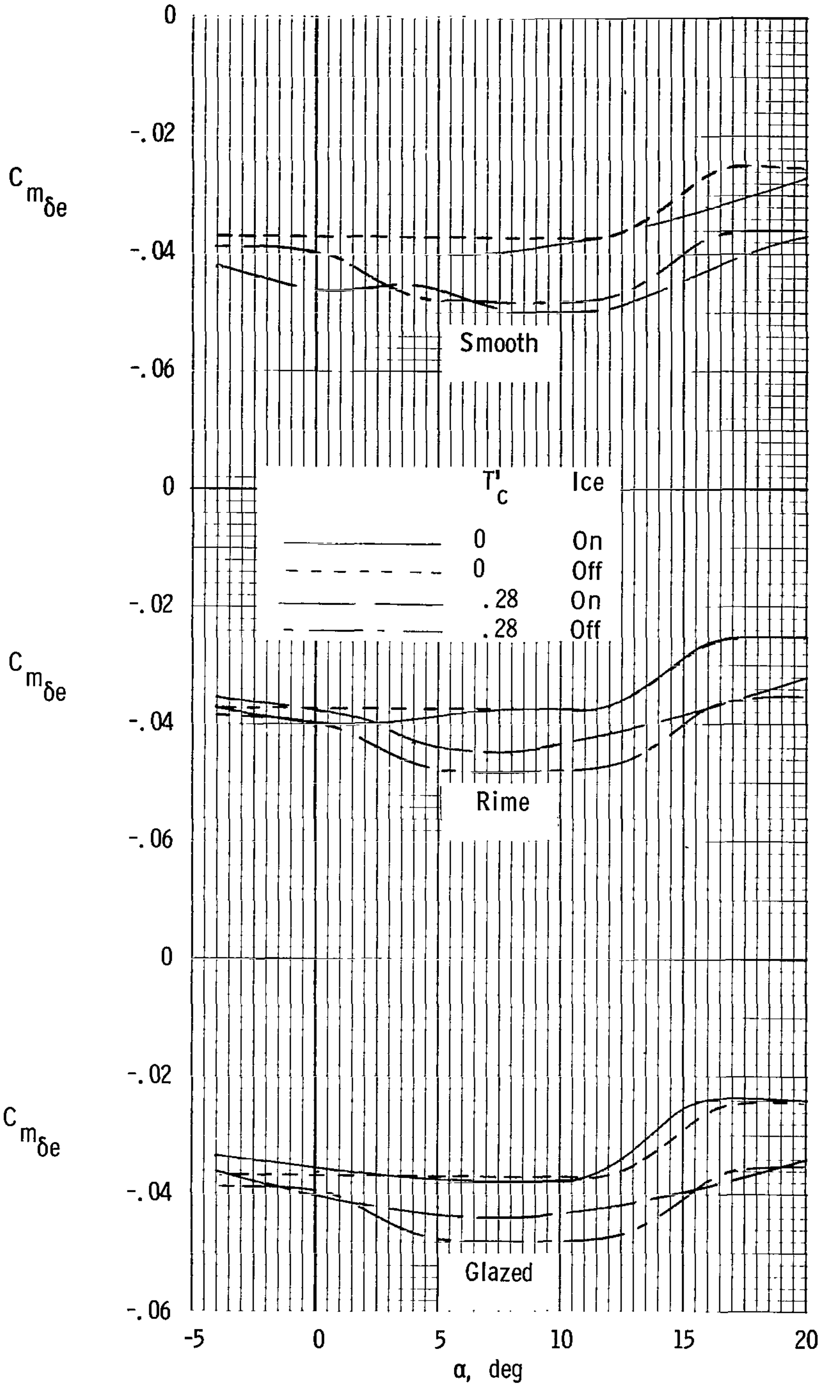

(b) $\delta_f = 35^o$.

Figure 101.- Concluded.

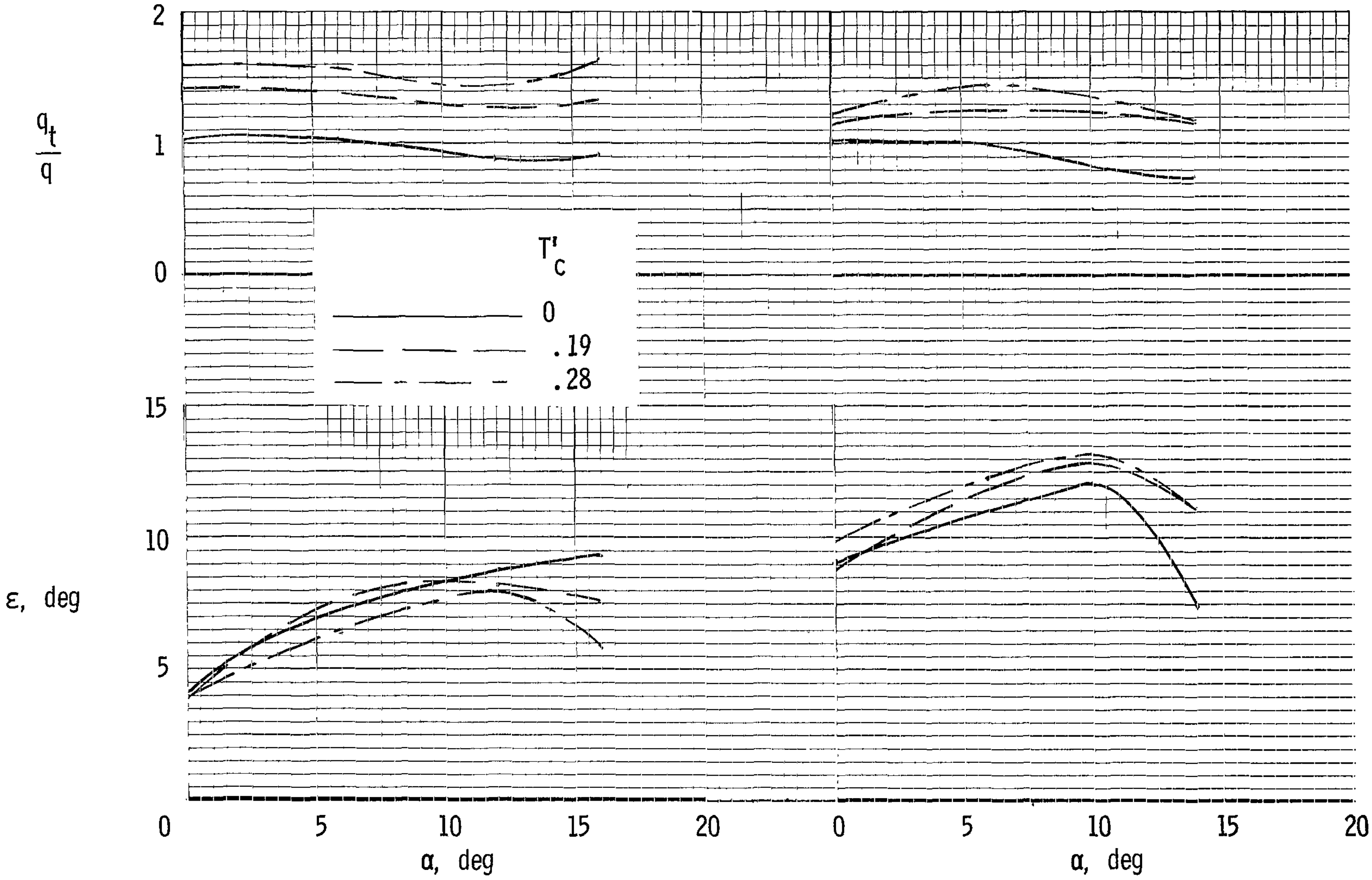

(a) $\delta_f = 0^{\circ}$.

(b) $\delta_f = 35^{\circ}$.

Figure 102.- Variation of average tail downwash angle and dynamic-pressure ratio with angle of attack for various power and flap settings.

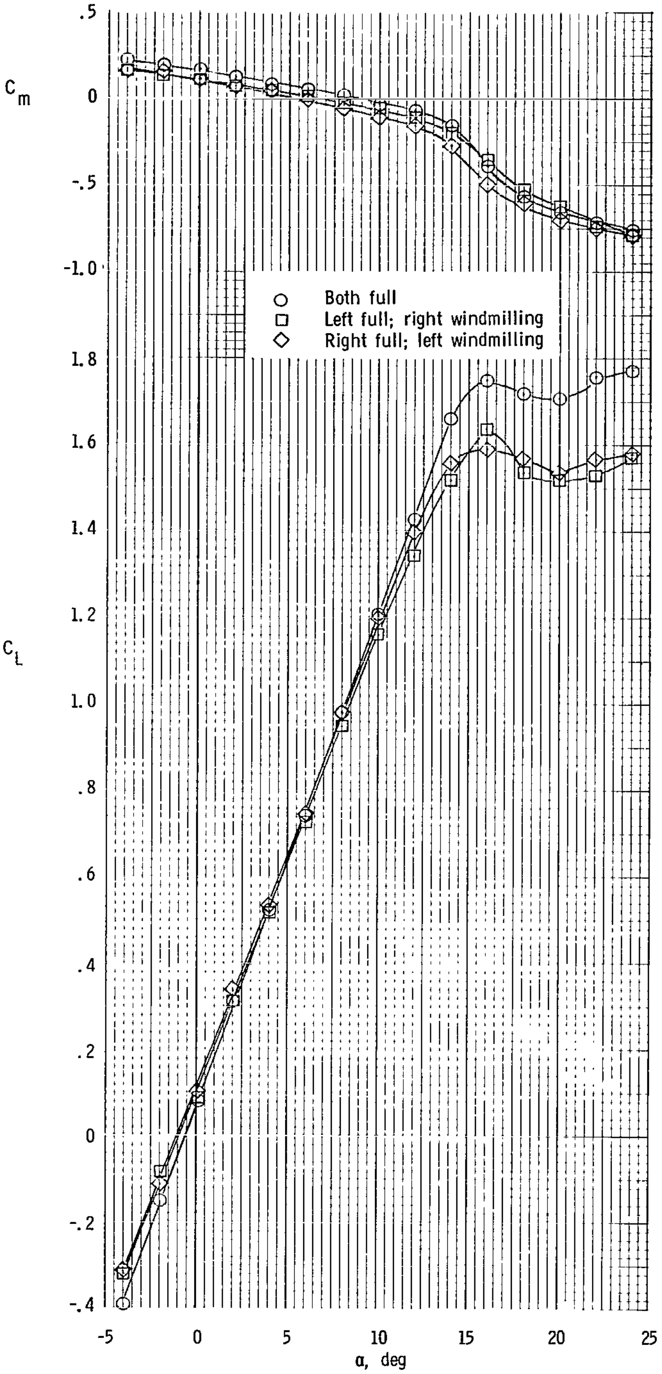

(a) $\delta_f = 0^o$.

Figure 103.- Effect of asymmetric power on longitudinal characteristics. $\beta = 0^o$; $\delta_e = 0^o$.

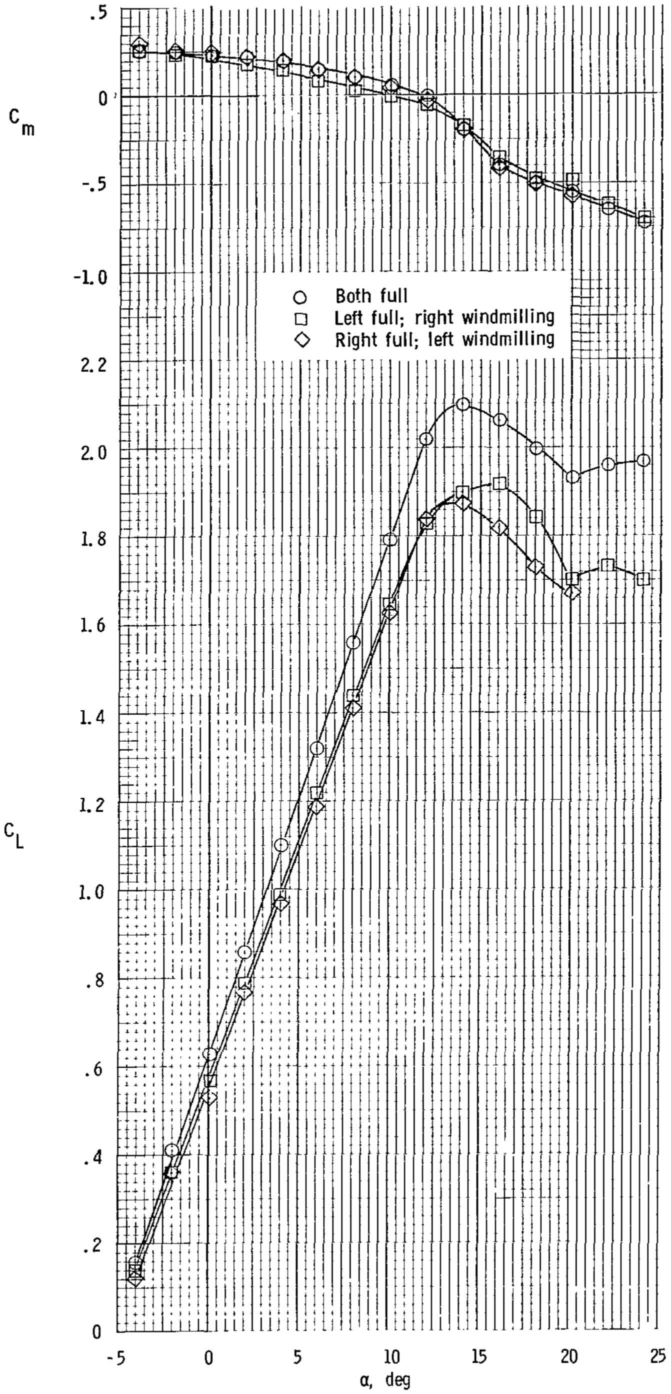

(b) $\delta_f = 35^0$.

Figure 103.- Concluded.

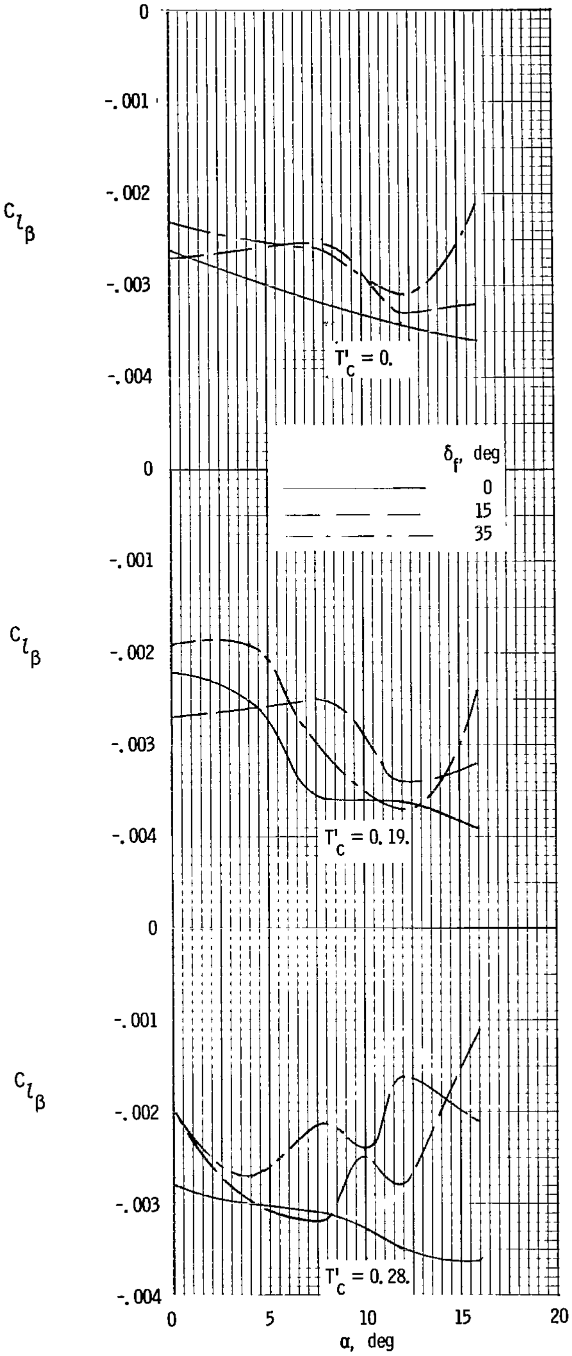

(a) Basic nacelle.

Figure 104.- Effective dihedral characteristics.

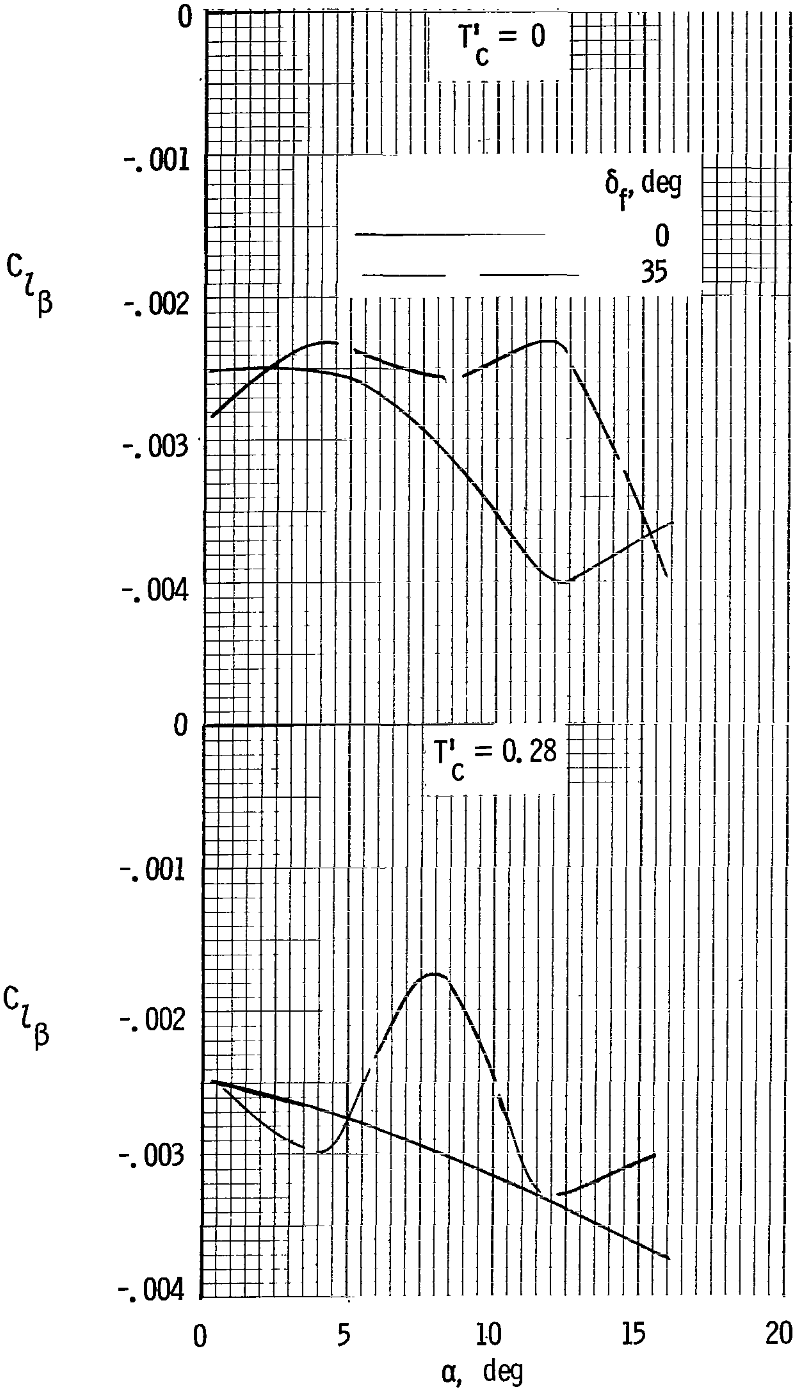

(b) Short nacelle.

Figure 104.- Concluded.

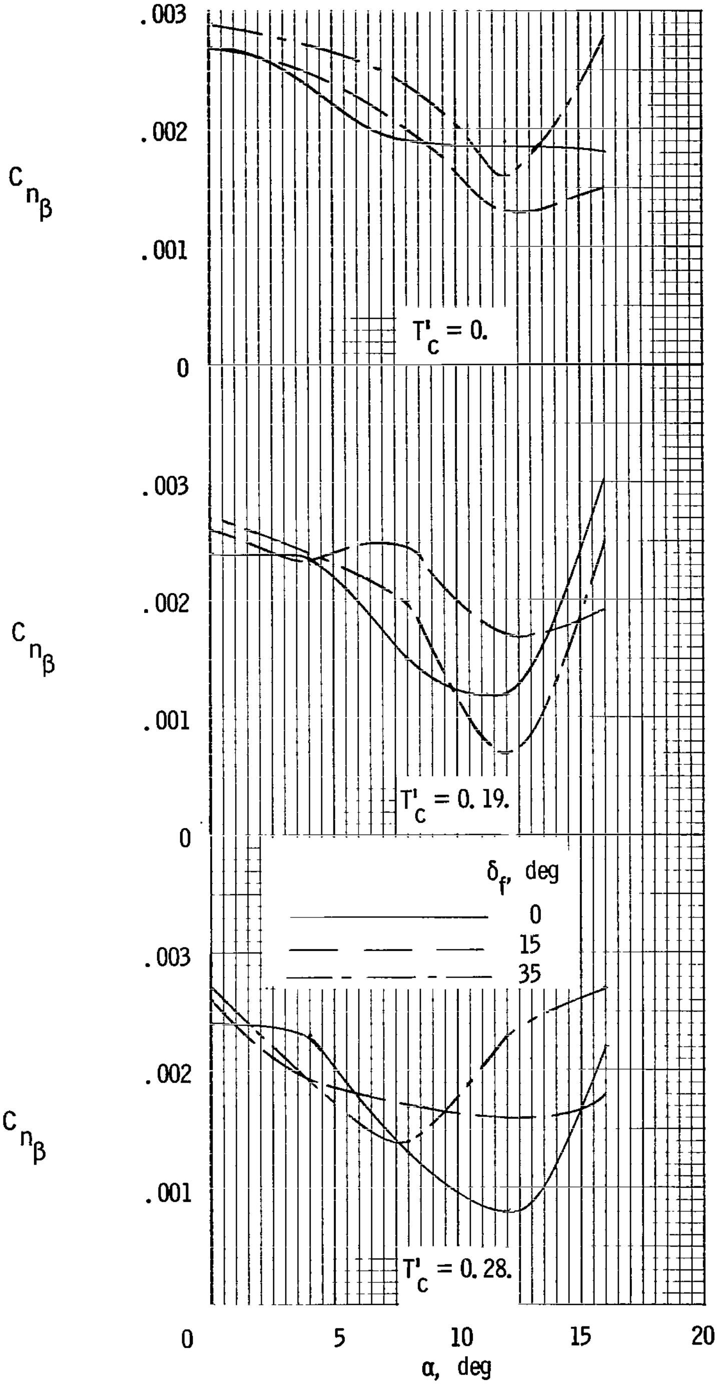

(a) Basic nacelle.

Figure 105.- Directional stability characteristics.

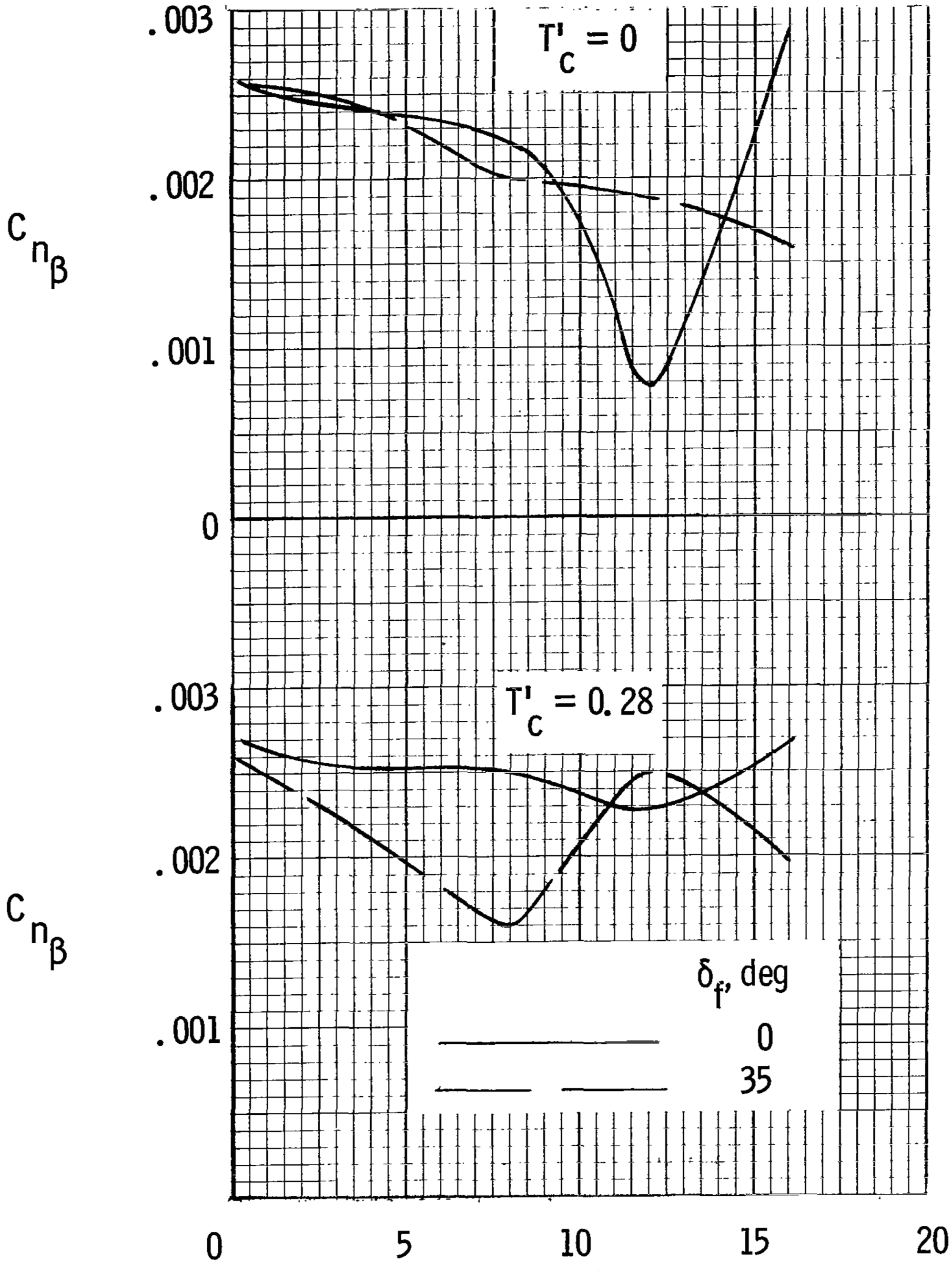

(b) Short nacelle.

Figure 105.- Concluded.

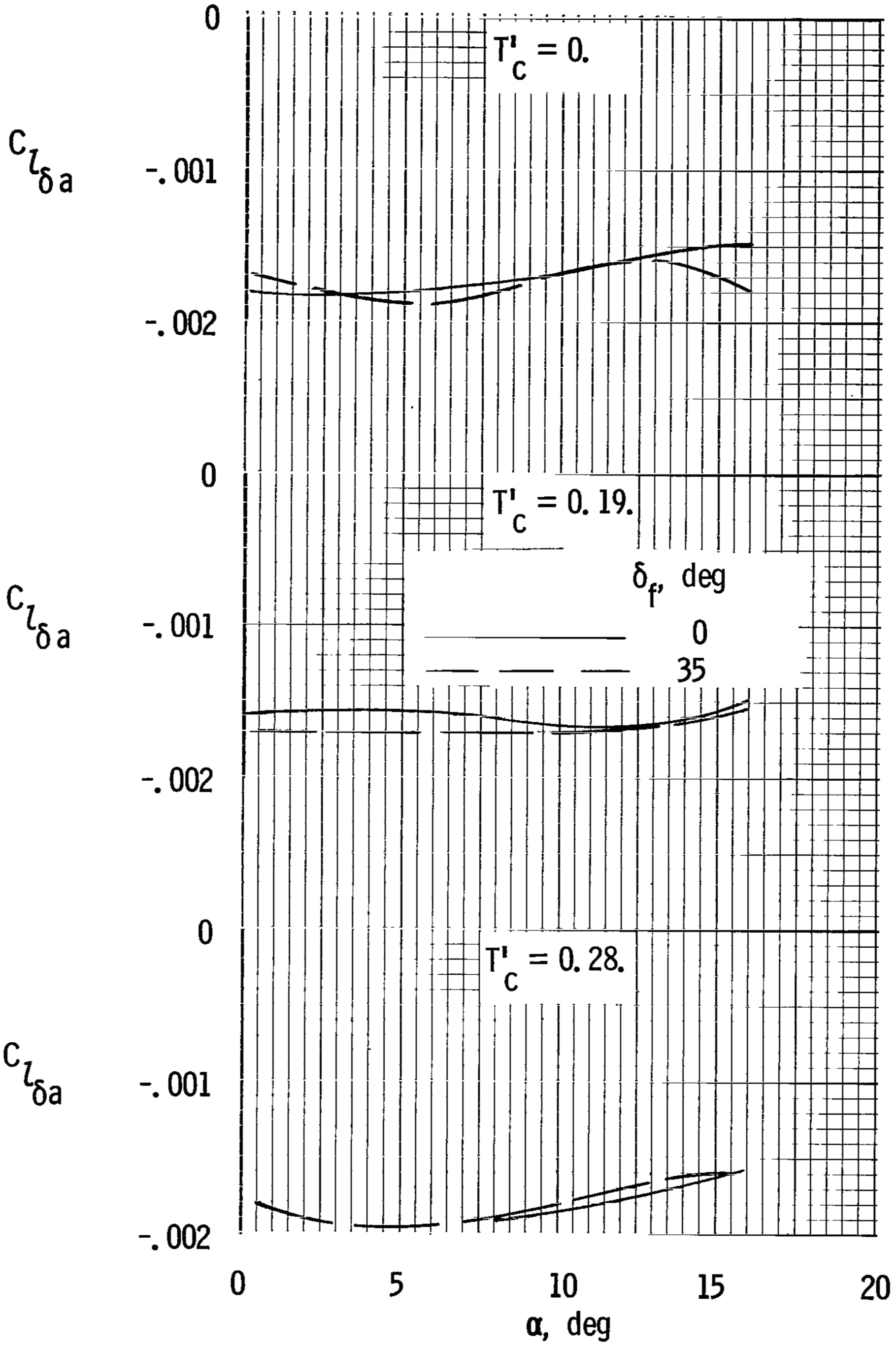

(a) Aileron effectiveness.

Figure 106.- Variation of aileron and rudder effectiveness with angle of attack.

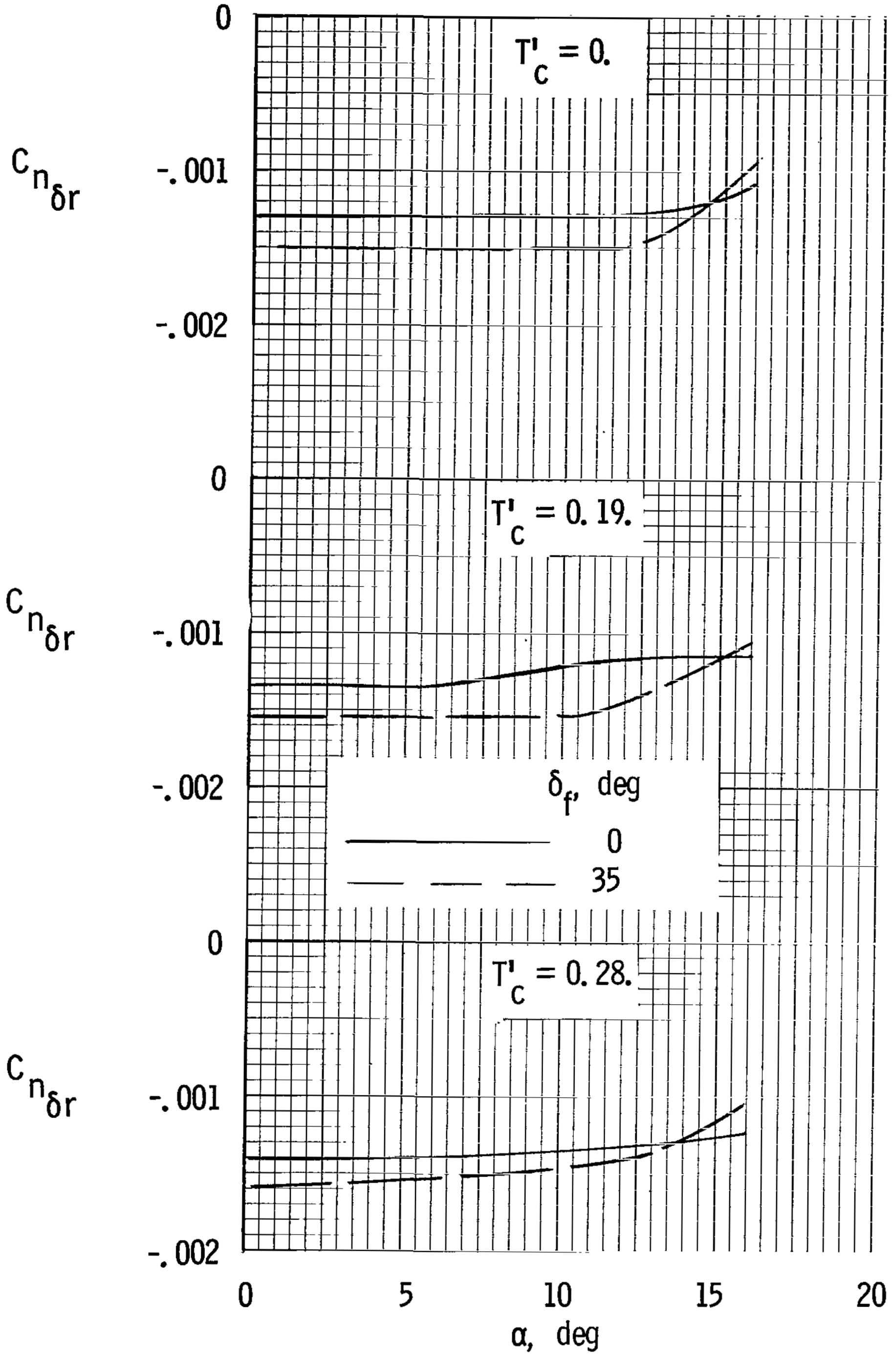

(b) Rudder effectiveness.

Figure 106.- Concluded.

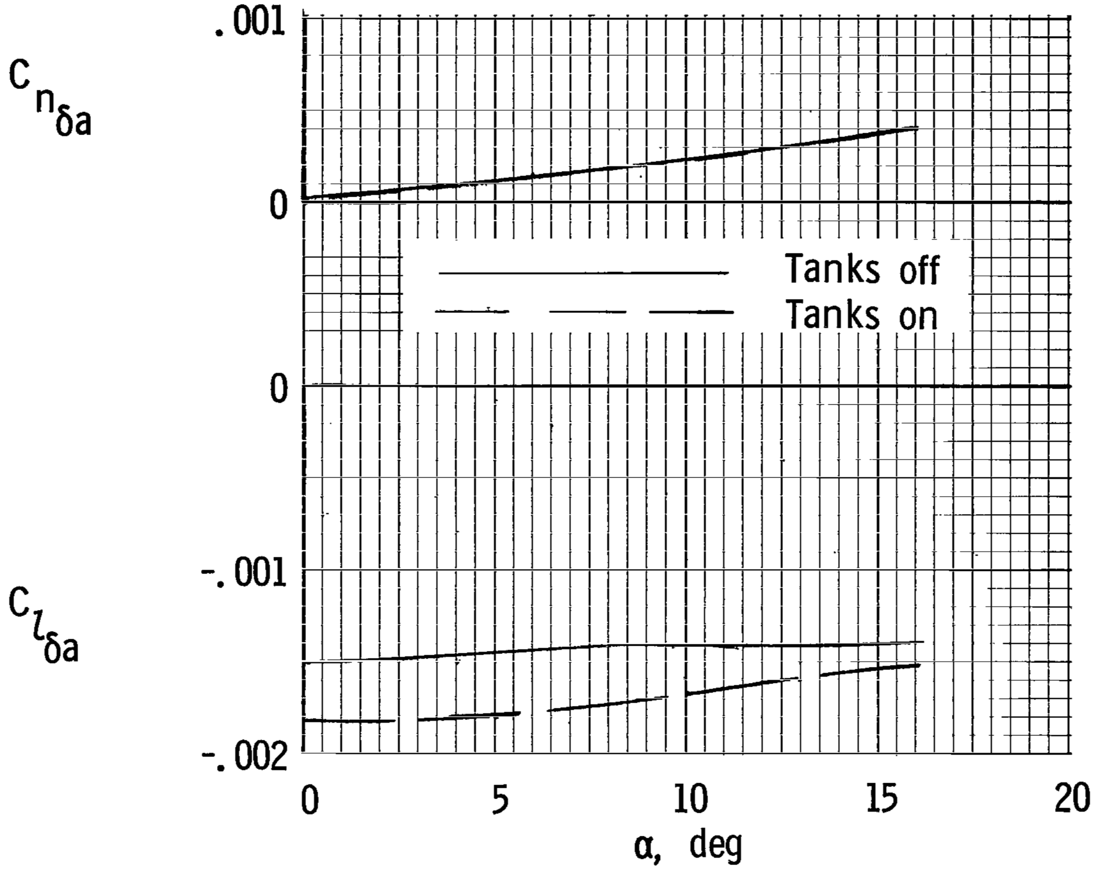

Figure 107.- Effect of wing-tip tanks on aileron characteristics.

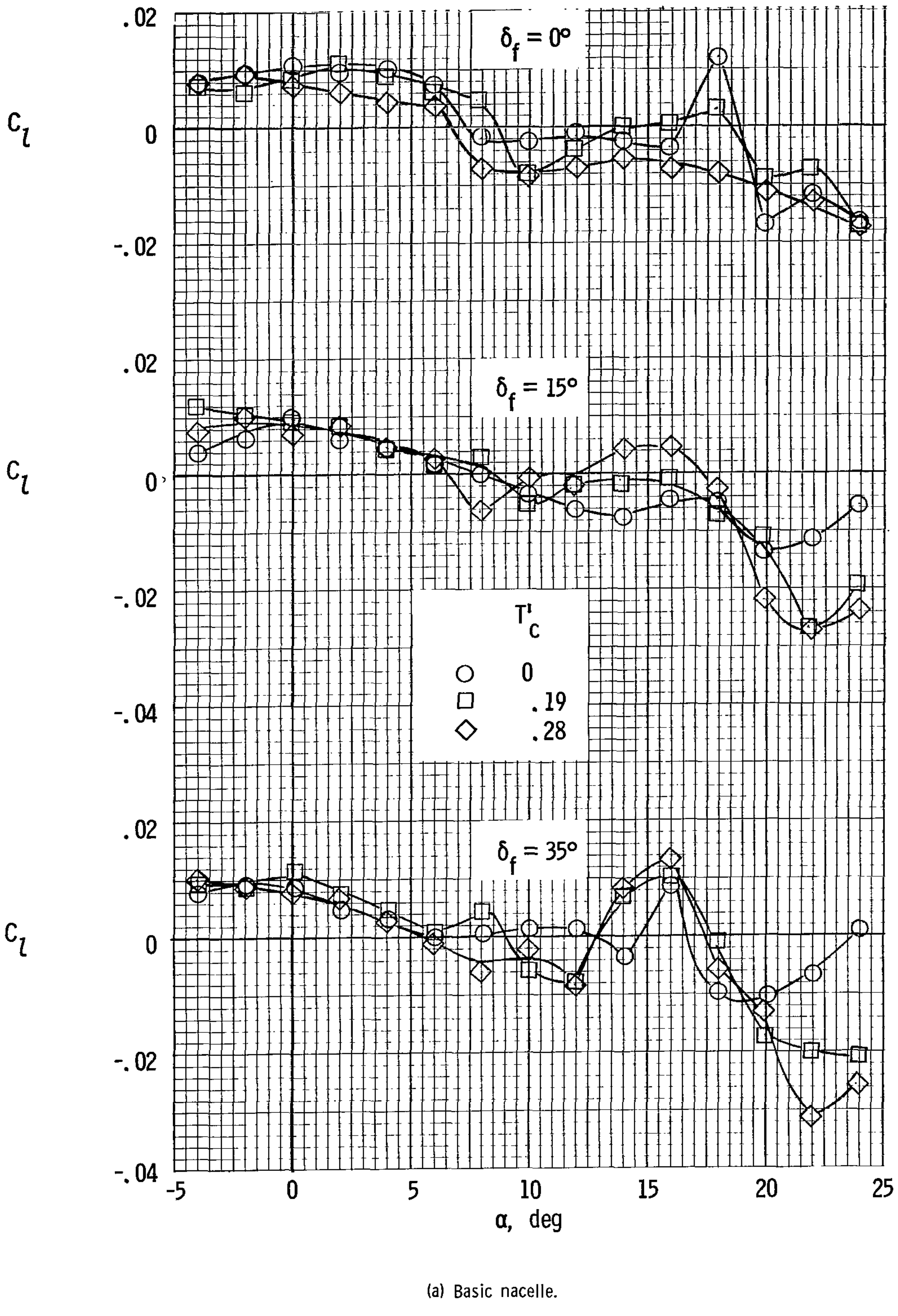

(a) Basic nacelle.

Figure 108.- Variation of rolling-moment coefficient with angle of attack for basic and short nacelle configurations. $\beta = 0^{0}$.

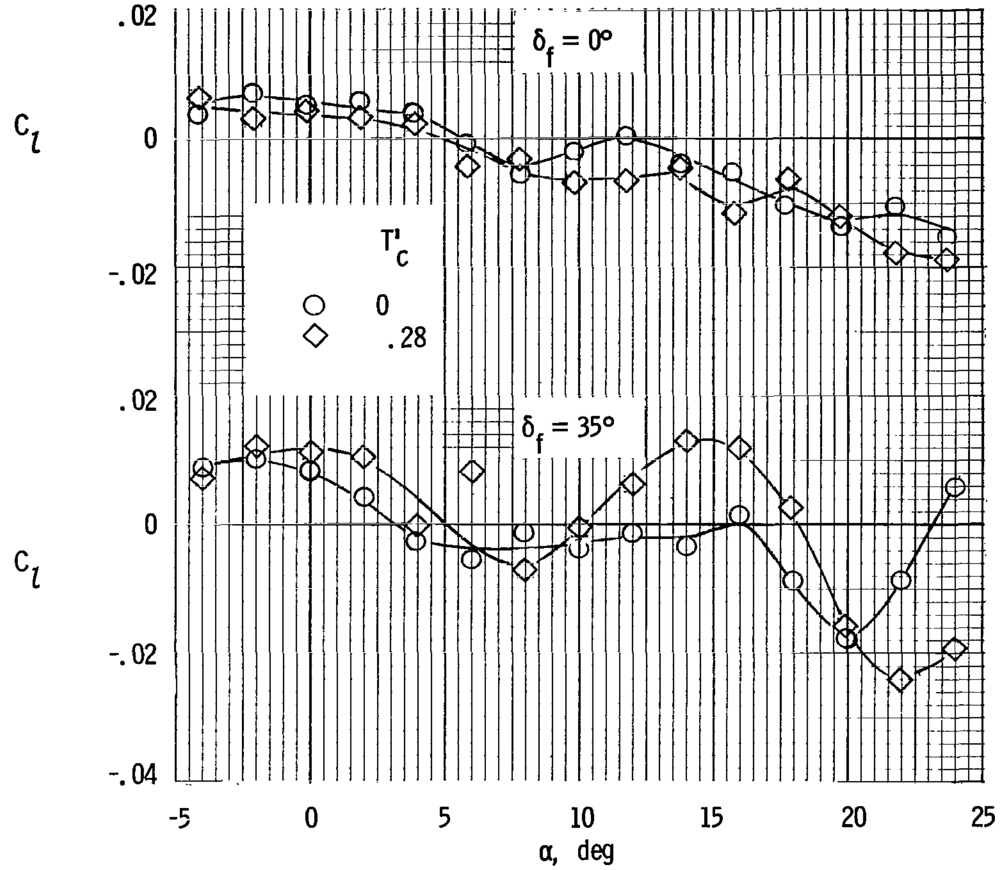

(b) Short nacelle.

Figure 108.- Concluded.

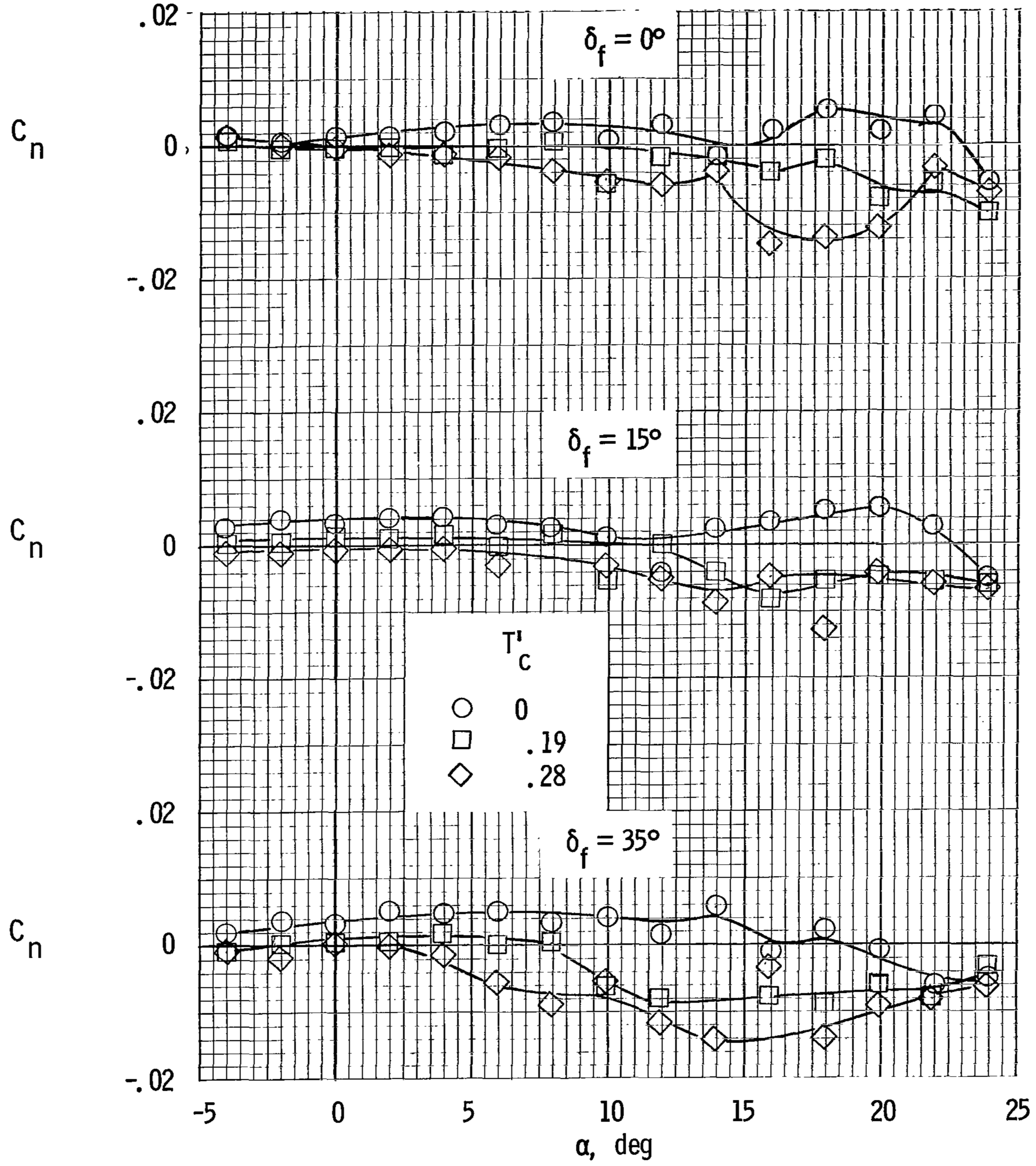

(a) Basic nacelle.

Figure 109.- Variation of yawing-moment coefficient with angle of attack for basic and short nacelle configurations. $\beta = 0^0$

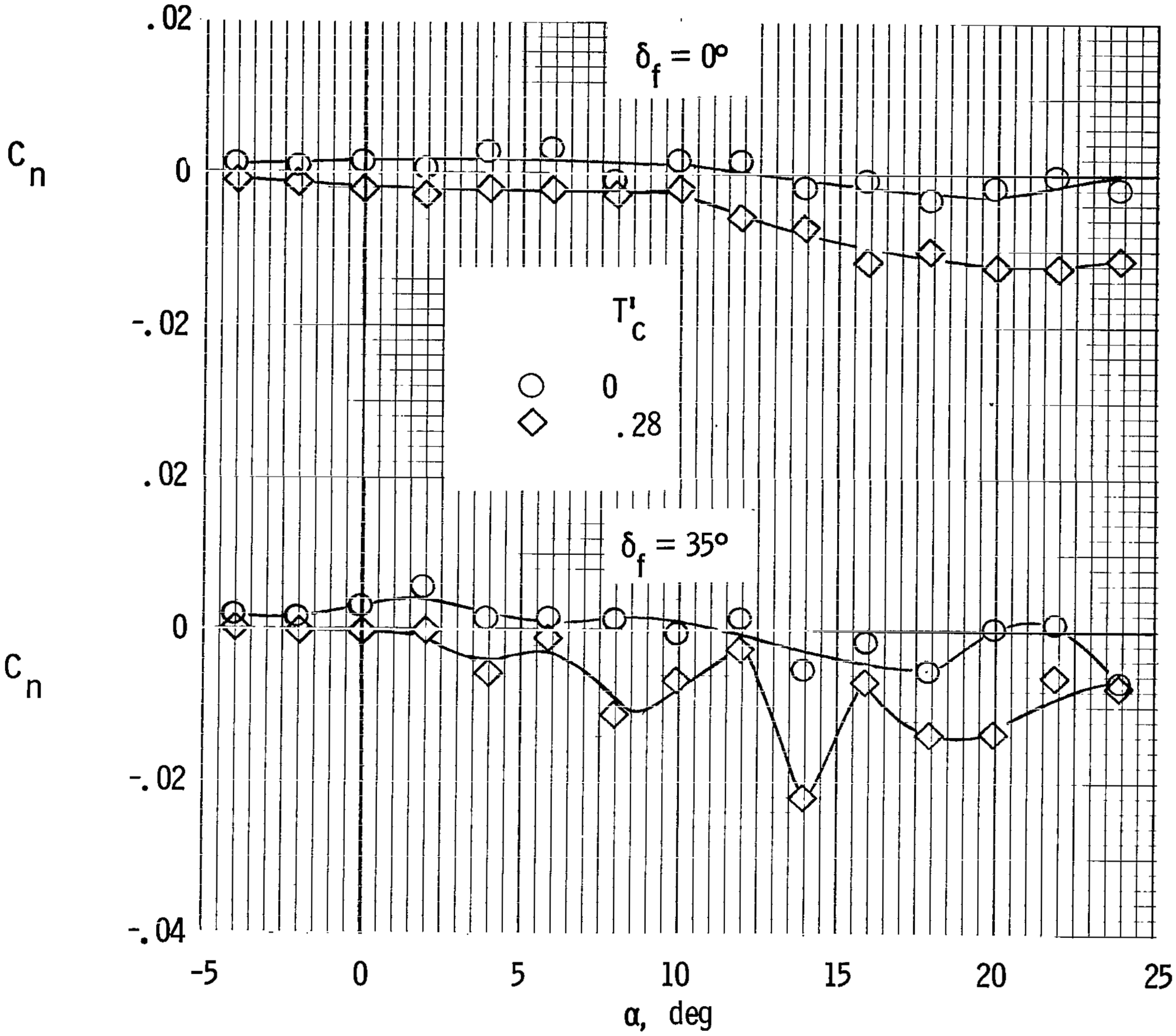

(b) Short nacelle.

Figure 109.- Concluded.

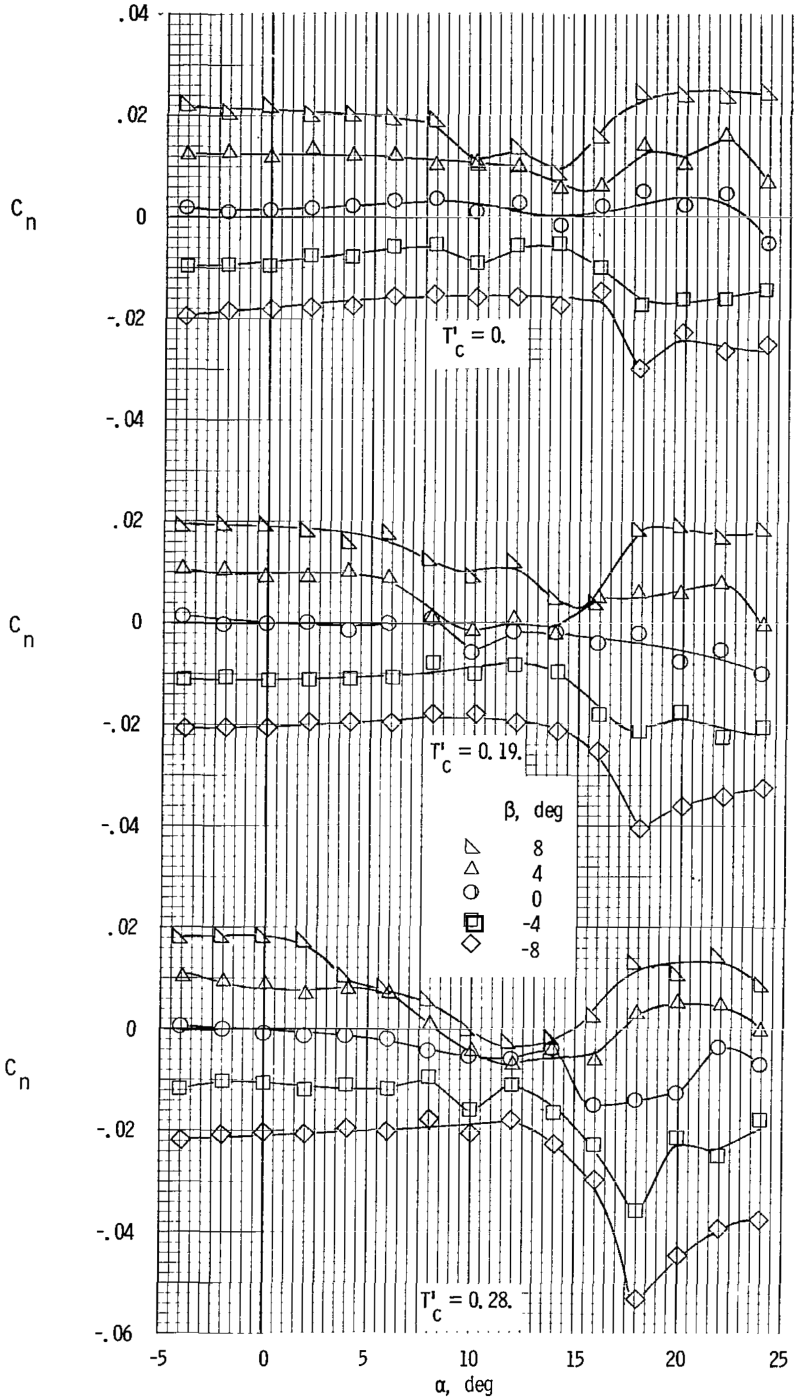

(a) Symmetric power.

Figure 110.- Variation of yawing-moment coefficient with angle of attack for various power conditions. $\delta_f = 0^{\circ}$.

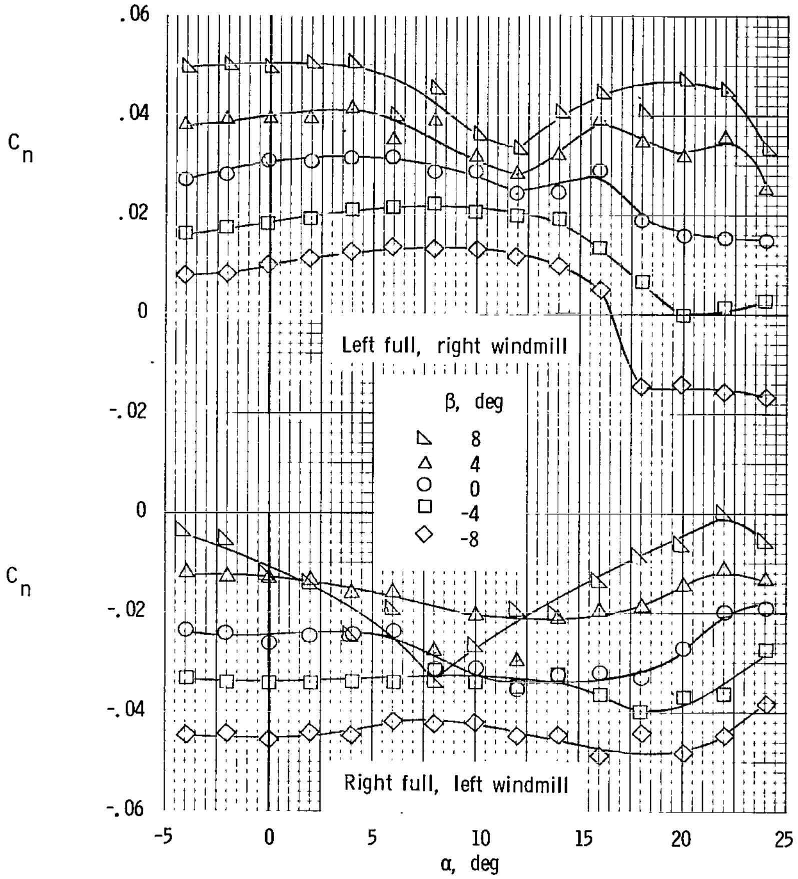

(b) Asymmetric power.

Figure 110.- Concluded.

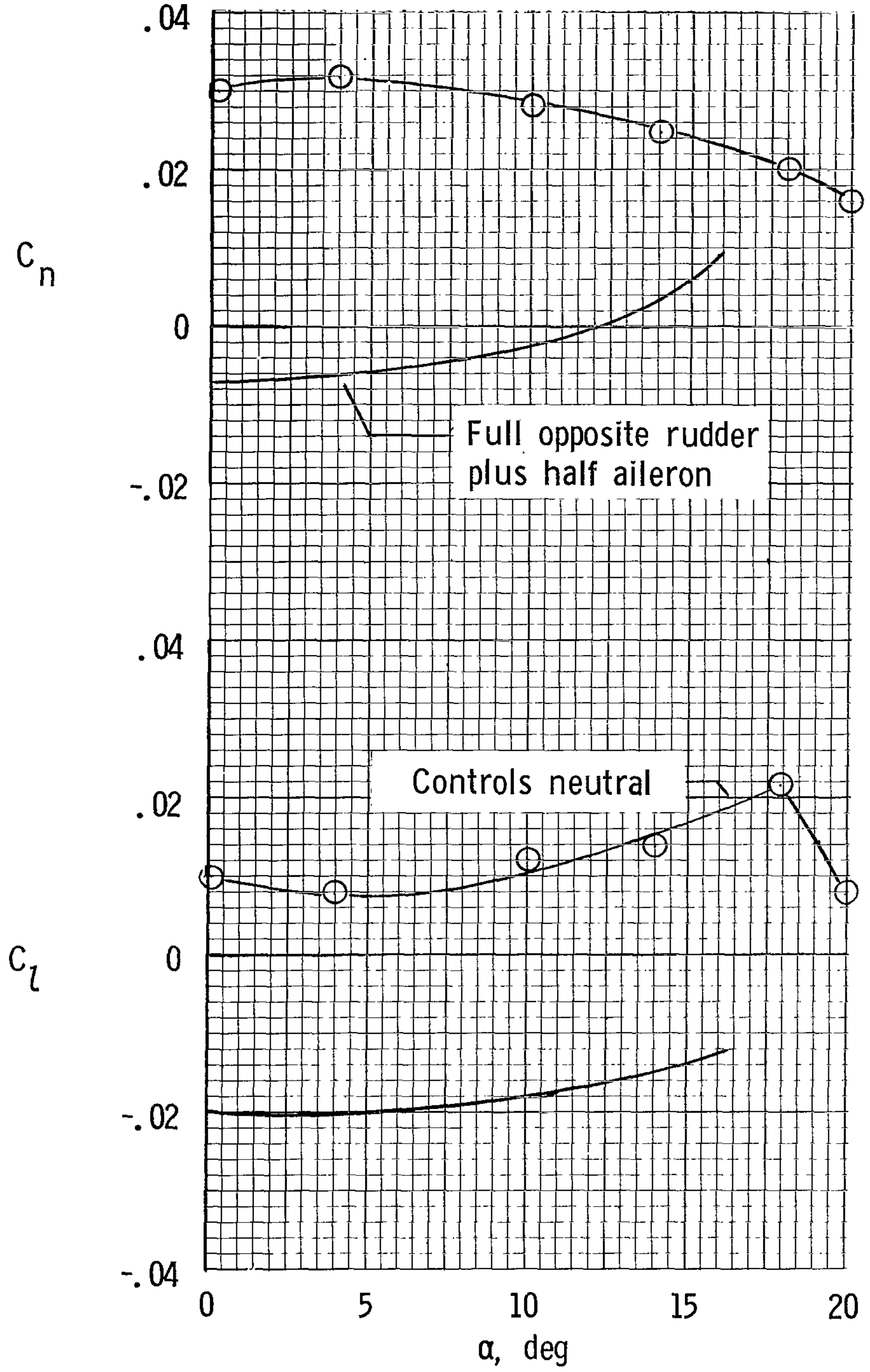

Figure 111.- Control capability for overcoming lateral moments with left engine full; right engine windmilling. $\beta = 0^{\circ}$; $\delta_f = 0^{\circ}$.

NASA-Langley, 1971 —— 2 L-7607

NATIONAL AERONAUTICS AND SPACE ADMINISTRATION
WASHINGTON, D. C. 20546

OFFICIAL BUSINESS
PENALTY FOR PRIVATE USE $300

FIRST CLASS MAIL

POSTAGE AND FEES PAID
NATIONAL AERONAUTICS AN
SPACE ADMINISTRATION

10U 001 27 51 3DS 71.10 00903
AIR FORCE WEAPONS LABORATORY /WLOL/
KIRTLAND AFB, NEW MEXICO 87117

ATT E. LOU BOWMAN, CHIEF,TECH. LIBRARY

POSTMASTER: If Undeliverable (Section 158
Postal Manual) Do Not Retur

> *"The aeronautical and space activities of the United States shall be conducted so as to contribute . . . to the expansion of human knowledge of phenomena in the atmosphere and space. The Administration shall provide for the widest practicable and appropriate dissemination of information concerning its activities and the results thereof."*
>
> —NATIONAL AERONAUTICS AND SPACE ACT OF 1958

NASA SCIENTIFIC AND TECHNICAL PUBLICATIONS

TECHNICAL REPORTS: Scientific and technical information considered important, complete, and a lasting contribution to existing knowledge.

TECHNICAL NOTES: Information less broad in scope but nevertheless of importance as a contribution to existing knowledge.

TECHNICAL MEMORANDUMS: Information receiving limited distribution because of preliminary data, security classification, or other reasons.

CONTRACTOR REPORTS: Scientific and technical information generated under a NASA contract or grant and considered an important contribution to existing knowledge.

TECHNICAL TRANSLATIONS: Information published in a foreign language considered to merit NASA distribution in English.

SPECIAL PUBLICATIONS: Information derived from or of value to NASA activities. Publications include conference proceedings, monographs, data compilations, handbooks, sourcebooks, and special bibliographies.

TECHNOLOGY UTILIZATION PUBLICATIONS: Information on technology used by NASA that may be of particular interest in commercial and other non-aerospace applications. Publications include Tech Briefs, Technology Utilization Reports and Technology Surveys.

Details on the availability of these publications may be obtained from:

SCIENTIFIC AND TECHNICAL INFORMATION OFFICE

NATIONAL AERONAUTICS AND SPACE ADMINISTRATION
Washington, D.C. 20546